Technology Collaboration Programme
by iea

International Energy Agency
Photovoltaic Power Systems Programme

Task 16 Solar Resource for High Penetration and Large Scale Applications

PVPS

Best Practices Handbook for the Collection and Use of Solar Resource Data for Solar Energy Applications: Third Edition

2021

Report IEA-PVPS 16-04:2021

What is IEA PVPS TCP?

The International Energy Agency (IEA), founded in 1974, is an autonomous body within the framework of the Organization for Economic Cooperation and Development (OECD). The Technology Collaboration Programme (TCP) was created with a belief that the future of energy security and sustainability starts with global collaboration. The programme is made up of 6.000 experts across government, academia, and industry dedicated to advancing common research and the application of specific energy technologies.

The IEA Photovoltaic Power Systems Programme (IEA PVPS) is one of the TCP's within the IEA and was established in 1993. The mission of the programme is to "enhance the international collaborative efforts which facilitate the role of photovoltaic solar energy as a cornerstone in the transition to sustainable energy systems." In order to achieve this, the Programme's participants have undertaken a variety of joint research projects in PV power systems applications. The overall programme is headed by an Executive Committee, comprised of one delegate from each country or organisation member, which designates distinct 'Tasks,' that may be research projects or activity areas.

The IEA PVPS participating countries are Australia, Austria, Belgium, Canada, Chile, China, Denmark, Finland, France, Germany, Israel, Italy, Japan, Korea, Malaysia, Mexico, Morocco, the Netherlands, Norway, Portugal, South Africa, Spain, Sweden, Switzerland, Thailand, Turkey, and the United States of America. The European Commission, Solar Power Europe, the Smart Electric Power Alliance (SEPA), the Solar Energy Industries Association and the Cop- per Alliance are also members.

Visit us at: www.iea-pvps.org

What is IEA PVPS Task 16?

The objective of Task 16 of the IEA Photovoltaic Power Systems Programme is to lower barriers and costs of grid integration of PV and lowering planning and investment costs for PV by enhancing the quality of the forecasts and the resources assessments.

Editors

- Manajit Sengupta (NREL), Aron Habte (NREL), Stefan Wilbert (DLR), Christian Gueymard (Solar Consulting Services, Jan Remund (Meteotest AG)

Authors

- Alessandro Betti , Philippe Blanc, Mathieu David, Yves-Marie Saint-Drenan, Anton Driesse, Janine Freeman, Rafael Fritz, Christian Gueymard, Aron Habte, Robert Höller, Jing Huang, Andreas Kazantzidis, Jan Kleissl, Carmen Köhler, Tomas Landelius, Vincente Lara-Fanego, Philippe Lauret , Luis Martin, Mark Mehos, Richard Meyer, Daryl Myers, Kristian Pagh Nielsen, Richard Perez, Carlos Fernandez Peruchena, Jesus Polo, Dave Renné, Lourdes Ramírez, Jan Remund, Jose Antonio Ruiz-Arias, Manajit Sengupta, Manuel Silva, David Spieldenner, Thomas Stoffel, Marcel Suri, Stefan Wilbert, Stephen Wilcox, Frank Vignola, Ping Wang, Yu Xie, Luis F. Zarzalejo

COVER PICTURE

Sahara dust over Switzerland. Sun during event with high levels of aerosols (Jan Remund)

ISBN 978-3-907281-19-2: Best Practice Handbook for the Collection and Use of Solar Resource Data for Solar Energy Application – 3rd Edition

INTERNATIONAL ENERGY AGENCY

PHOTOVOLTAIC POWER SYSTEMS PROGRAMME

Best Practices Handbook for the Collection and Use of Solar Resource Data for Solar Energy Applications: Third Edition

IEA PVPS
Task 16
Solar resource for high penetration and large scale applications

Report IEA-PVPS T16-04:2021
April - 2021

ISBN 978-3-907281-19-2

This report was produced in collaboration with National Renewable Energy Laboratory (NREL) and is also available at https://www.nrel.gov/docs/fy21osti/77635.pdf

TABLE OF CONTENTS

FOREWORD

Solar energy technologies—such as photovoltaics (PV), solar heating and cooling, or concentrating solar power—provide solutions to the growing need for clean energy to mitigate climate change and to improve air quality. During the past few years, the use of solar energy has strongly progressed, in particular thanks to the impressive development of PV, which has become one of the most cost-competitive energy technologies overall. As the markets for the various solar energy systems increase, reliable and precise historical estimates and future projections of the solar resource are relevant not only to predict the energy output of solar installations and power systems but also increasingly to determine their expected competitiveness and economic return.

This third edition of the *Best Practices Handbook for the Collection and Use of Solar Resource Data for Solar Energy Applications* has been prepared under the leadership of the National Renewable Energy Laboratory (NREL) together with a team of worldwide experts comprising 41 authors from 14 countries working within the framework of the International Energy Agency's Photovoltaic Power Systems Programme (IEA PVPS) Technology Collaboration Programme Task 16 on "Solar Resource for High Penetration and Large-Scale Applications." This project is a joint task with the IEA's Solar Power and Chemical Energy Systems (SolarPACES) Technology Collaboration Programme. Building on the previous work under the IEA's Solar Heating and Cooling Technology Collaboration Programme, this handbook is a prominent example of technology collaboration across the different solar energy technologies and the respective IEA technology collaboration programs.

This third edition of the handbook follows only less than four years after the previous edition, published in 2017, and marks the rapid evolution in the field of solar resource assessment and forecasting. It reflects the considerable progress that has occurred since then in the measurement and modeling of solar radiation and related topics. For instance, this edition features a new chapter on other relevant meteorological parameters, such as wind, temperature, humidity, pressure, surface albedo, and spectral distribution. Particular emphasis is on the progress of forecasts using all-sky images as well as on probabilistic and regional forecasts, which increasingly use artificial intelligence. For the practitioner, an important chapter deals with the application of solar resource data to solar energy projects, including performance modeling.

With its comprehensive coverage of the state of the art of solar resource assessment and forecasting, this handbook serves as a reference document for a wide range of target audiences—from science to solar energy professionals. Understanding the nature of solar radiation, its variations across the globe, and forecasting its evolution over time will increasingly contribute to make the use of solar energy more predictable. As the contribution of solar energy to the energy supply increases over time, the improved predictability is crucial for the optimization of future energy systems.

The IEA PVPS Technology Collaboration Programme is pleased to publish the third edition of this handbook together with NREL. Most importantly, I would like to acknowledge the leadership of NREL, in particular Aron Habte and Manajit Sengupta; the IEA PVPS Task 16/IEA SolarPACES Task 5 experts; and the support of the U.S. Department of Energy.

I hope this handbook finds many interested readers and contributes to the further deployment of solar energy worldwide.

Stefan Nowak

Chair, IEA PVPS Technology Collaboration Programme, September 2020

PREFACE

Jan Remund[1] and Dave Renné[2]
[1] *Meteotest AG*
[2] *Dave Renné Renewables, LLC*

As the world looks for carbon-free sources to meet final energy demand associated with heat, electrical power, and transport, energy from the sun stands out as the single most abundant energy resource on Earth. Harnessing this energy is the challenge and opportunity for achieving a carbon-free energy supply by 2050 to fulfil the 1.5°C target set by the Intergovernmental Panel on Climate Change[1] and recommended in the 2015 Paris Agreement. Reducing carbon-dioxide emissions per energy unit and rapidly accessing the huge potential of solar energy will have the largest effects on achieving the 1.5°C target.

Photovoltaics (PV), solar heating and cooling, and concentrating solar power (CSP) are the primary forms of energy applications using sunlight. These solar energy systems use different technologies, collect different fractions of the solar resource, and have different siting requirements and production capabilities. Reliable information about the solar resource is required for every solar energy application. This holds true for small installations on a rooftop as well as for large solar power plants; however, solar resource information is of the most critical interest in the latter case because such projects require a substantial investment, sometimes exceeding $1 billion in construction costs. Before such projects can be undertaken, the best possible information about the quality and reliability of the fuel source (i.e., solar radiation) must be made available. That is, project developers need to have reliable data about the solar resource available at specific locations, including historic trends with seasonal, daily, hourly, and (preferably) subhourly variability to predict the daily and annual performance of a proposed power plant. Without this information or its accuracy requirements, a bankable financial analysis is not possible.

In response to a meeting of prominent CSP developers and stakeholders hosted by the U.S. Department of Energy (DOE) in September 2008, the National Renewable Energy Laboratory (NREL) produced a handbook to provide best practices for the use of solar resource data, which was titled *Concentrating Solar Power: Best Practices Handbook for the Collection and Use of Solar Resource Data*.[2] The content was based on the experiences of scientists and engineers from industry, academia, and DOE for identifying the sources, quality, and methods for applying solar and meteorological data to CSP projects.

During this same time, the International Energy Agency's (IEA's) Solar Heating and Cooling Programme (SHC) was hosting tasks on solar resource knowledge management (Task 36, 2005–2011; Task 46, 2011–2016). This work was then followed by the IEA's Photovoltaic Power Systems Programme (PVPS) Task 16 (2017–2020). These tasks have brought together the world's foremost experts in solar energy meteorology. This group of experts agrees there is a need to maintain a collective document to disseminate the knowledge that was being developed through these tasks. It was decided that combining the efforts of the experts involved in the IEA tasks to build on the information in NREL's original version of the handbook would provide the best use of resources and deliver a handbook of outstanding quality to users. It was also decided that additional solar technologies, such as PV, would be

[1] See https://www.ipcc.ch/report/ar4/syr/.
[2] See https://www.nrel.gov/docs/fy10osti/47465.pdf.

incorporated along with additional aspects of energy meteorology that have become extremely important, such as solar forecasting. As a result, a second edition of the handbook appeared under a revised title, *Best Practices Handbook for the Collection and Use of Solar Resource Data for Solar Energy Applications*, published by NREL in 2017.[3] This served as the final deliverable for IEA SHC Task 46. An update to that document concludes the work of the first phase of IEA PVPS Task 16 and is presented here as the third edition of the handbook. This edition is available in two different formats, as separate NREL and IEA PVPS reports.

The solar PV industry has developed rapidly throughout the last few years based on ongoing technical evolution and shrinking prices. The size of the installations as well as the penetration levels have grown tremendously—both enhancing the needs for accurate solar data for planning and operation. Induced by these needs, there have been significant enhancements in the body of knowledge in the areas of solar resource assessment and forecasting. This third edition of the handbook updates and enhances the initial versions and presents the state of the art in a condensed form for all of its users.

In the coming years, another stage of solar penetration will be reached: solar energy will not be only a small or growing part of power production but will become a major share of the production. This growth will increase the needs for high-quality and reliable resource data. The data needs for this growing industry are summarized in Table P-1.

The structure of the handbook has been slightly updated since the previous editions. Chapter 1 lays out the need for high-quality and reliable solar resource data to support the rapidly growing industry, and Chapter 2, as before, provides a basic tutorial on solar resources. Chapter 3 presents a comprehensive overview of best practices for measuring solar radiation, including information gained under collaborative work completed during Task 16. Chapter 4 summarizes techniques used to develop estimates of solar resources from weather satellite data and numerical model predictions. Chapter 5 is a new chapter describing additional meteorological variables (besides radiation) that are required for accurate performance analysis. Chapter 6 describes an updated list of commonly used data sets available both in the public and private sectors, and Chapter 7 provides important information on both measured and modeled solar data uncertainty. Chapter 8 provides an update on recent developments in the ability to forecast solar resources over time horizons spanning from minutes to hours ahead and days ahead. All this information leads to Chapter 9, which provides data application techniques for the various stages of project development, from prefeasibility to routine operations, as shown in Table P-1. The outlook for future work is summarized in Chapter 10.

[3] See https://www.nrel.gov/docs/fy18osti/68886.pdf.

Table P-1. Data Application Techniques for the Various Stages of Project Development

System Size →

Phase ↓

	Small	Medium	Large
1. Prefeasibility and planning	• Long-term averages • Monthly data • Solar cadastres/ maps • Simple shading analysis	• TMY • Hourly data • Shading analysis	• Long-term satellite data • Hourly data
2. Feasibility			• Satellite data • Time series (>10 year) • Ground meas. (> 1 year) • Shading analysis • Further site- and technology- specific meteo. parameters (e.g., albedo, soiling)
3. Due diligence and finance		• Satellite data • Time series (>10 y) • Minute data • Shading • Further site- and technology- specific meteo. parameters (e.g., albedo, soiling)	• Satellite data • Time series (>10 y) • Ground meas. (> 1 year) • Minute data • Shading analysis • Further site- and technology- specific meteo. parameters (e.g., albedo, soiling)
4. Operation and maintenance	• Simple monitoring	• Local measurements • Forecasts	• Local measurements • Forecasts

Project developers, engineering procurement and construction firms, utility companies, system operators, energy suppliers, financial investors, organizations involved in planning and managing solar research programs, and others involved in solar energy systems planning and development should find this handbook to be a particularly valuable resource for the collection and interpretation of solar resource data. Readers are encouraged to provide feedback to the authors for future revisions and an expansion of the handbook's scope and content.

ACKNOWLEDGEMENTS

The authors acknowledge the U.S. Department of Energy (DOE) Office of Energy Efficiency and Renewable Energy (EERE) Solar Energy Technologies Office (SETO) for supporting this research. Specifically, the authors are grateful to Dr. Anastasios Golnas, the technology manager for the Systems Integration team of SETO, for his support and encouragement. The authors also thank the International Energy Agency Photovoltaic Power Systems Programme Task 16, without which this publication would not have been possible. Finally, the authors thank the National Renewable Energy Laboratory Communications Office for their tireless work during the publication process.

Special thanks to the following experts who spent hours of their valuable time reviewing the chapters and making excellent suggestions that significantly improved the quality of this handbook.

- Hans Georg Beyer, University of the Faroe Islands
- Marion Schroedter-Homscheidt, German Aerospace Center (DLR)
- Lucien Wald, MINES ParisTech
- Jaemo Yang, National Renewable Energy Laboratory
- Peter Gotseff, National Renewable Energy Laboratory
- Nate Blair, National Renewable Energy Laboratory
- Justin Robinson, GroundWork Renewables, Inc.
- Pedro Jimenez Munoz, National Center for Atmospheric Research

This work was authored in part by the National Renewable Energy Laboratory, operated by Alliance for Sustainable Energy, LLC, for the U.S. Department of Energy (DOE) under Contract No. DE-AC36-08GO28308. Funding provided by U.S. Department of Energy Office of Energy Efficiency and Renewable Energy Solar Energy Technologies Office. The views expressed in the article do not necessarily represent the views of the DOE or the U.S. Government. The U.S. Government retains and the publisher, by accepting the article for publication, acknowledges that the U.S. Government retains a nonexclusive, paid-up, irrevocable, worldwide license to publish or reproduce the published form of this work, or allow others to do so, for U.S. Government purposes.

Moreover, this report was supported by the Swiss Federal Office of Energy under contract no. SI/501486-01 and SI/501984-01 and by the German Federal Ministry for Economic Affairs and Energy under contract no. 03EE1010 (SOLREV) based on a resolution of the German Bundestag.

LIST OF ABBREVIATIONS

ABI	Advanced Baseline Imager
ACR	absolute cavity radiometer
AERONET	Aerosol Robotic Network
AI	angle of incidence
AM	air mass
AnEn	analog ensemble
ANN	artificial neural network
AOD	aerosol optical depth
APOLLO	AVHRR Processing scheme Over cLouds, Land, and Ocean
ARM	Atmospheric Radiation Measurement
AS	Ångström scale
ASI	all-sky imager
AU	astronomical unit
AVHRR	Advanced Very High Resolution Radiometer
BIPM	International Bureau of Weights and Measurements
BOM	Australian Bureau of Meteorology
BRDF	bidirectional reflectance distribution function
BRTF	bidirectional transmittance distribution function
BSA	black-sky albedo
BSRN	Baseline Surface Radiation Network
CAL	cloud albedo
CAMS	Copernicus Atmosphere Monitoring Service
CART	classification and regression tree
CCD	charge-coupled device
CDF	cumulative distribution function
CERES	Clouds and the Earth's Radiant Energy System
CIEMAT	Centro de Investigaciones Energéticas, Medioambientales y Tecnológicas
CIMO	Commission for Instruments and Methods of Observation
CLARA	Cloud, Albedo, and surface RAdiation data set
CLARA-A2	CM SAF Cloud, Albedo and Surface Radiation Data Set from AVHRR Data, Edition 2
CLAVR-x	Clouds from AVHRR Extended System
CM SAF	EUMETSTAT's Satellite Application Facility on Climate Monitoring

CMV	cloud motion vector
COD	cloud optical depth
COSMO	Consortium for Small-scale Modeling
COV	coefficient of variation
CPP	cloud physical property
CRPS	continuous ranked probability score
CSIRO	Commonwealth Scientific and Industrial Research
CSP	concentrating solar power
DHI	diffuse horizontal irradiance
DIR	downwelling infrared irradiance
DISORT	DIScrete Ordinates Radiative Transfer
DLR	Deutsches Zentrum für Luft- und Raumfahrt (German Aerospace Center)
DNI	direct normal irradiance
DOE	U.S. Department of Energy
DRY	design reference years
ECMWF	European Center for Medium-Range Weather Forecasts
ENDORSE	ENergy DOwnstReam Services
EPS	Ensemble Prediction System
ESRA	European Solar Radiation Atlas
ESRL	Earth System Research Laboratory
ETR	extraterrestrial radiation
ETS	extraterrestrial spectrum
EUMETSAT	European Organisation for the Exploitation of Meteorological Satellites
FARMS	Fast All-sky Radiation Model for Solar applications
FARMS-NIT	Fast All-sky Radiation Model for Solar applications with Narrowband Irradiances on Tilted surfaces
FLASHFlux	Fast Longwave and Shortwave Radiative Fluxes
FOV	field of view
FPF	firm power forecast
Fraunhofer IEE	Fraunhofer Institute for Energy Economics and Energy System Technology
Fraunhofer ISE	Fraunhofer Institute for Solar Energy Systems
GARCH	Generalized AutoRegressive Conditional Heteroskedasticity
GEM	Global Environmental Multiscale
GEOS	Goddard Earth Observing System
GFS	Global Forecast System

GHI	global horizontal irradiance
GML	Global Monitoring Laboratory
GNI	global normal irradiance
GOES	Geostationary Operational Environmental Satellite
GOME2	Global Ozone Monitoring Experiment–2
GTI	global tilted irradiance
GUM	*Guide to the Expression of Uncertainty in Measurements*
GVF	ground view factor
HARMONIE	HIRLAM ALADIN Regional Mesoscale Operational NWP In Europe
HIRLAM	High Resolution Limited Area Model
HRRR	High-Resolution Rapid Refresh
ICON	ICOsahedral Nonhydrostatic
IDW	inverse distance weighting
IEA	International Energy Agency
IEC	International Electrotechincal Commission
i-EM	Intelligence in Energy Management
IFS	Integrated Forecast System
IPS	International pyrheliometric scale
IRENA	International Renewable Energy Agency
IS	interval score
ISCCP	International Satellite Cloud Climatology Project
ISIS	Integrated Surface Irradiance Study
ISO	International Organization for Standardization
JPSS	Joint Polar Satellite System
KNMI	Royal Netherlands Meteorological Institute
LRS	land constraints, radiation, and slope
MACC	Monitoring Atmospheric Composition and Climate
MADCast	Multisensor Advection Diffusion nowCast
MAE	mean absolute error
McICA	Monte Carlo Independent Column Approximation
MDMS	Meteorological Data Management System
MERRA-2	Modern Era Retrospective analysis for Research and Applications, Version 2
MESOR	Management and Exploitation of Solar Resource Knowledge
METEOSAT	Meteosat Second Generation
MetOp	Meteorological Observation

METSTAT	METeorolgoical-STATistical model
MFG	Meteosat First Generation
MIDC	Measurement and Instrumentation Data Center
MODIS	Moderate Resolution Imaging Spectroradiometer
MOS	model output statistics
MSE	mean square error
MSG	Meteosat Second Generation
MTG	Meteosat Third Generation
MTS	Meteorological Statistical Model
MWCSAF	Nowcasting Satellite Application Facility (NWC-SAF)
NASA	National Aeronautics and Space Administration
NCAR	National Center for Atmospheric Research
NCEP	National Center for Environmental Protection
NIR	near-infrared
NOAA	National Oceanic and Atmospheric Administration
NREL	National Renewable Energy Laboratory
NSRDB	National Solar Radiation Database
NWP	numerical weather prediction
O&M	operation and maintenance
OSI-SAF	Ocean and Sea Ice Satellite Application Facility
PATMOS-x	Pathfinder Atmospheres Extended
PDF	probability density function
PeEn	persistence ensemble
PIMENT	Laboratory of Physics and Mathematical Engineering for Energy and the Environment
PMOD	Physikalisch-Meteorologisches Observatorium Davos
POA	plane of array
POE	probability of exceedance
POWER	Prediction of Worldwide Energy Resources
PR	performance ratio
PSM	Physical Solar Model
PSP	precision spectral pyranometer
PV	photovoltaic
PVGIS	Photovoltaic Geographical Information System
PVPS	Photovoltaic Power Systems Programme

QEERI	Qatar Environment and Energy Research Institute (QEERI), Hamad Bin Khalifa University
RAMS	Regional Atmospheric Modeling System
RBR	red-to-blue ratio
RGB	red-green-blue
RHI	reflected horizontal irradiance
RMSE	root mean square error
RPOA	in-plane rear-side irradiance
RRTM	Rapid Radiation Transfer Model
RRTMG	Rapid Radiation Transfer Model for General Circulation Models
RSI	rotating shadowband irradiometer
RSP	rotating shadowband pyranometer
RSR	rotating shadowband radiometers
SAM	System Advisor Model
SARAH	CM SAF Surface Solar Radiation Data Set - Heliosat
SARAH-E	CM SAF Surface Solar Radiation Data Set - Heliosat – East
SAURAN	Southern African Universities Radiometric Network
SC	solar constant
SCIAMACHY	Scanning Imaging Absorption Spectrometer for Atmospheric Chartography
SD	standard deviation
SDU	sunshine duration
SERI	Solar Energy Research Institute
SEVIRI	Spinning Enhanced Visible and InfraRed Imager
SHC	Solar Heating and Cooling Programme
Si	silicon
SI	Système International
SICCS	Surface Insolation under Clear and Cloudy Skies
SICLONE	Système d'Information pour l'analyse et la prévision des Configurations spatio-temporel Les des Occurrences Nuageus Es
SID	surface incoming direct radiation
SIS	solar surface irradiance
SMARTS	Simple Model of the Atmospheric Radiative Transfer of Sunshine
SO_2	sulfur dioxide
SolarPACES	Solar Power and Chemical Energy Systems
SOLEMI	Solar Energy Mining
Soumi-NPP	Suomi National Polar-Orbiting Partnership

SRB	Surface Radiation Budget
SRRL	Solar Radiation Research Laboratory
SS	Smithsonian scale
SSE	Surface Meteorology and Solar Energy
SUNY	State University of New York
SURFRAD	Surface Radiation Budget Network
SVF	sky view factor
SZA	solar zenith angle
TDY	typical direct normal irradiance year
TGY	typical global horizontal irradiance year
TMM	typical meteorological month
TMY	typical meteorological year
TOA	top of atmosphere
TRY	typical reference year
TSO	transmission system operator
TSI	total solar irradiance
UIR	upwelling infrared irradiance
UPS	uninterruptible power supply
UV	ultraviolet
WEST	Western Energy Supply and Transmission
WHO	World Health Organization
WMO	World Meteorological Organization
WPVS	World Photovoltaic Scale
WRC	World Radiation Center
WRDC	World Radiation Data Center
WRF	Weather Research and Forecasting
WRMC	The World Radiation Monitoring Center
WRR	World Radiometric Reference
WSA	white-sky albedo

1 WHY SOLAR RESOURCE DATA ARE IMPORTANT TO SOLAR POWER

Manajit Sengupta[1] and Richard Meyer[2]
[1] *National Renewable Energy Laboratory*
[2] *Suntrace GmbH*

Sunlight is the fuel for all solar energy technologies. For any solar generation source, knowledge of the quality and future reliability of the fuel is essential for determining the financial viability of any new project. This information is also important during operations for accurate control, analyses, and integration of the generation to the grid. The variability of the supply of sunlight represents the single greatest uncertainty in a solar power plant's predicted performance. Solar resource information is needed for various stages of a plant's development and operation, such as:

- Historical long-term data for site selection during feasibility studies
- Prediction of power plant output for plant design and financing
- Real-time measurement and solar forecasting for plant and grid operations.

Site selection requires information about numerous parameters for prospective project locations, including current land use, grid access, and proximity to load centers. The top priority though is determining if an adequate solar resource exists for a proposed project. For site selection, average annual solar irradiation at the site is the first selection criterion. Other meteorological parameters, such as ambient temperature and wind speed, may also play an important role. Further, lower seasonal variability could also be advantageous because of a more consistent match to the power demand. Because weather patterns can change from one year to another, many years of data are required to determine reliable average irradiation conditions and interannual variability. For this purpose, satellite-derived, high-quality historic solar radiation data sets covering at least 10 years are usually considered necessary for the site selection of large solar energy systems.

As flat-priced electricity feed-in-tariff regulations get phased out, the economic yield of solar power systems increasingly depends on the solar production at specific times of the day as well as during various times of the year. Thus, for solar projects with variable prices, the temporal distribution of solar irradiance to estimate potential yields among competing sites might be critical even during site selection. At this early stage of project development, it is sufficient to study the temporal variability of the energy output throughout the year and typical daily cycles. As an alternative to multiple-year data sets, typical meteorological year (TMY) data for each site might be sufficient at this stage, in particular for smaller installations; however, the TMY cannot characterize interannual variability and might have limited use for certain projects.

If an appropriate site is identified, the development of a power generation project will require more precise and detailed data sets. For site-specific techno-economic optimization of a solar system, the availability of high-resolution data is always beneficial. These data generally exist in the form of satellite-derived time series. To finance large solar power plants, data sets that are validated by ground measurements on or near the site are essential to reduce the yield risk. In addition to accurate solar radiation measurements, specialized meteorological stations usually provide additional environmental parameters that help to optimize the sizing and proper selection of plant components.

Accurate solar and meteorological stations are also valuable during plant commissioning because reliable measurements are the base for acceptance testing to demonstrate proof of fulfillment of technical specifications for heat or electric output. Although temporary measurement equipment can be used for acceptance testing, reliable measurements are essential for estimating real-time plant output to ensure high efficiency of the plant throughout its service life. The evaluation of plant output as a function of solar irradiance is the most important indicator of power plant performance. A reduction in overall efficiency implies a degradation of one or more power plant components or poor maintenance or operation. Although remotely-sensed data can be used for smaller systems, where performance accuracy can be relaxed, larger solar systems usually rely on ground-based measurements, which might be combined with near-real-time satellite-derived solar radiation data. Local ground measurements also assist in site-specific model validation and improvements of solar forecasts.

Proper and accurate solar forecasts are important for the optimized use of solar power plants, both economically and operationally. They help to improve system operations, such as the optimal use of a storage tank in a solar thermal water heating system, a molten salt system for high-temperature applications, or a battery system in a photovoltaic (PV) system. With the fast growth of grid-connected solar electrical systems, solar radiation forecasts have become highly important for safe grid operations and efficient dispatching between power plants. Although short-term solar forecasts in the areas of high solar penetration enable efficient dispatch, day-ahead forecasts enable accurate unit commitment, leading to efficient planning of reserves.

This handbook covers all pertinent aspects of solar radiation that are relevant for the planning and operation of PV plants, solar thermal heating and cooling systems, concentrating solar thermal plants, and the electric grid. Chapter 2 explains the basic concepts and terms that are essential to understanding the subsequent chapters. Chapter 3 describes the state of the art in measuring solar radiation on the Earth's surface and offers methods and protocols to produce a data set that withstands the scrutiny of due diligence. Chapter 4 focuses on modeling solar radiation. It introduces the theory of radiative transfer in the atmosphere, facilitating an understanding of current practices for calculating the incident solar radiation at the Earth's surface. Today, many data sets are calculated using radiative transfer models with observations from operational meteorological satellites as input, and these examples are also presented in Chapter 4.

Chapter 5 introduces additional sources of meteorological and advanced solar parameters that are required for improved accuracy in solar modeling. Several examples of solar resource data sets—both satellite-derived and ground-measured data—are presented in Chapter 6. It is important to understand the uncertainty of any data set, whether measured or modeled; therefore, Chapter 7 provides an understanding of how to estimate and interpret uncertainty in both measured and modeled data sets. Radiative transfer calculations, similar to those described in Chapter 4, are used to forecast solar radiation and are described in Chapter 8. This chapter describes nowcasting (forecasting for a few hours ahead) by extrapolating satellite-derived and ground-mounted observations as well as solar radiation forecasts beyond the first few hours using numerical weather prediction models.

Chapter 9 summarizes various techniques for estimating solar power using data sets described in previous chapters, and it recommends best practices for the application of data to various stages of a solar power project. Significant work remains to improve the accuracy, reliability, and level of detail of solar resource products. Many open questions remain in the field of solar resource assessment, and Chapter 10 provides an overview of how these outstanding issues could be resolved in the future. Research leading to these solutions could be through the development of new or improved techniques, the application of new

measurement techniques, the use of new meteorological satellites, the development of improved weather models, or, ideally, the use of a smart combination of these approaches.

2 OVERVIEW OF SOLAR RADIATION RESOURCE CONCEPTS

Aron Habte,[1] Thomas Stoffel,[2] Christian Gueymard,[3] Daryl Myers,[4] Philippe Blanc,[5] Stefan Wilbert,[6] and Frank Vignola[7]

[1] *National Renewable Energy Laboratory*
[2] *Solar Resource Solutions, LLC*
[3] *Solar Consulting Services*
[4] *National Renewable Energy Laboratory, retired*
[5] *MINES ParisTech*
[6] *German Aerospace Center (DLR)*
[7] *University of Oregon*

2.1 Introduction

Describing the relevant concepts and applying a consistent terminology are important to the usefulness of any handbook. This chapter discusses standard terms that are used to illustrate the key characteristics of solar radiation—the fuel for all solar technologies.

Beginning with the Sun as the source, this chapter presents an overview of the effects of Earth's orbit and atmosphere on the possible types and magnitudes of solar radiation available for energy conversion. An introduction to the concepts of measuring and modeling solar radiation is intended to prepare the reader for the more in-depth treatments in Chapter 3–Chapter 6. This overview concludes with an important discussion of the estimated uncertainties associated with solar resource data as affected by the experimental and modeling methods used to produce the data. The reader is referred to Chapter 7 for a detailed treatment of uncertainty in measurement and modeling.

2.2 Radiometric Terminology

Before discussing solar radiation further, it is important to understand basic radiometric terms. Radiant energy, flux, power, and other concepts used in this handbook are summarized in Table 2-1.

Table 2-1. Radiometric Terminology and Units

Quantity	Symbol	Unit	Unit	Description
Radiant energy	Q	Joule	J	Energy
Radiant flux	Φ	Watt	W	Radiant energy per unit of time (radiant power)
Radiant intensity	I	Watt per steradian	W/sr	Power per unit solid angle
Radiant emittance	M	Watt per square meter	W/m²	Power emitted from a surface
Radiance	L	Watt per steradian per square meter	W/(sr·m²)	Power per unit solid angle per unit of projected source area
Irradiance	E	Watt per square meter	W/m²	Power incident on a unit area surface
Spectral irradiance	E_λ	Watt per square meter per nanometer	W/(m²·nm)	Power incident on a unit area surface per unit wavelength
Irradiation	H	Joule per square meter	J/m²	Energy accumulated on a unit area surface during a period; a more practical energy unit is kilowatt-hours per square meter (1 kWh / m² = 3.6 MJ/m²)

2.3 Extraterrestrial Irradiance

Any object with a temperature above absolute zero Kelvin emits radiation. With an effective surface temperature of ≈5800 K, the Sun behaves like a quasi-static blackbody and emits radiation over a wide range of wavelengths, with a distribution that is close to that predicted by Planck's law (Figure 2-1). This constitutes the solar spectral power distribution, or solar spectrum. For terrestrial applications, the useful solar spectrum, also called the shortwave spectrum (≈290–4000 nm), includes the spectral regions called ultraviolet (UV), visible, and near-infrared (NIR) (Figure 2-1). The latter is the part of the infrared spectrum that is below 4000 nm in the solar spectrum. In contrast, the longwave (or far-infrared) spectrum extends beyond 4 µm, where the planetary thermal emission is dominant. Based on a recent determination (Gueymard 2018a), most spectral irradiance (98.5%) of the extraterrestrial spectrum (ETS), is contained in the wavelength range from 290–4000 nm. In what follows, broadband solar radiation will always refer to this spectral range, unless specified otherwise.

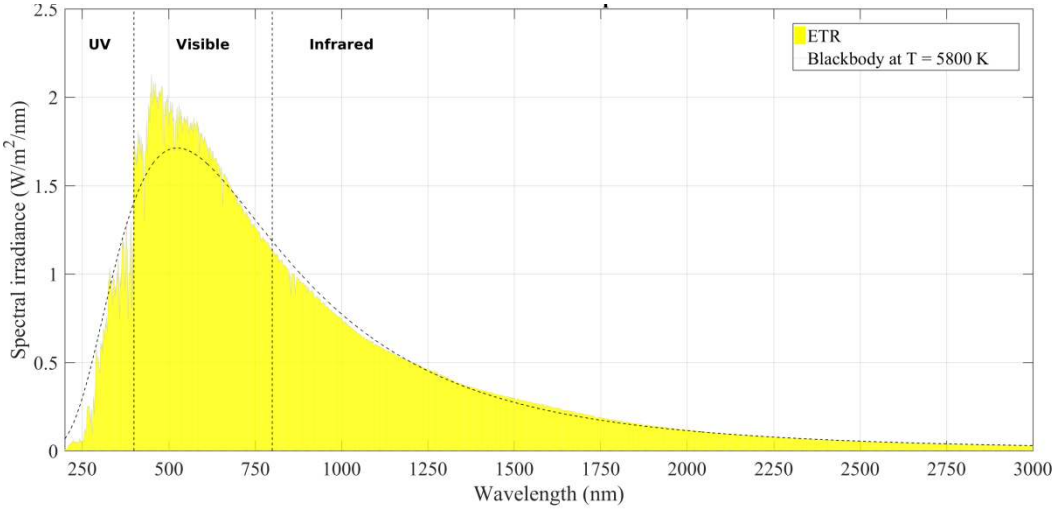

Figure 2-1. Reference ETS (ASTM E490-19) and 5,800 K blackbody distribution using Planck's law. *Image by Philippe Blanc, MINES ParisTech/ARMINES*

Various ETS distributions have been derived based on ground measurements, extraterrestrial measurements, and physical models of the Sun's output. Some historical perspective is offered by Gueymard (2004, 2006, 2018a). All distributions contain some deviations from the current standard extraterrestrial spectra used by ASTM Standard E490 (2019) (Figure 2-1). A new generation of ETS distribution, based on recent spectral measurements from space, was recently published (Gueymard 2018a).

2.4 Solar Constant and Total Solar Irradiance

The total radiant power from the Sun is nearly constant. The solar output (radiant emittance) is called the total solar irradiance (TSI) and can be obtained as the integration of the ETS at 1 AU (astronomical unit, approximate average Sun-Earth distance, discussed in Section 2.5) over all wavelengths. TSI was commonly called the solar constant (SC) until slight temporal variations were discovered (Fröhlich and Lean 1998, 2004; Kopp and Lean 2011). The solar constant is now defined as the long-term mean TSI. Both TSI and solar constant are made independent from the actual Sun-Earth distance by evaluating them at 1 AU. Small but measurable changes in the Sun's output and TSI are related to its magnetic activity. There are cycles of approximately 11 years in solar activity, which are accompanied by a varying number of sunspots (cool, dark areas on the Sun) and faculae (hot, bright spots). TSI increases during high-activity periods because the numerous faculae more than counterbalance the effect of sunspots. From an engineering perspective, these TSI

variations are relatively small, so the solar constant concept is still useful and perfectly appropriate in solar applications.

Figure 2-2 shows the latest version of a composite TSI time series based on multiple spaceborne instruments that have monitored TSI since 1978 using a variety of instruments and absolute scales (Gueymard 2018b). Estimates are also used for the period from 1976–1978 to make this time series start at the onset of solar cycle 21. The solar cycle numbers are indicated for further reference. (Solar cycle 25 is assumed to have started at the end of 2019, but this is still debated as of this writing.) Figure 2-2 shows the solar constant (always evaluated at 1 AU) as a horizontal solid line.

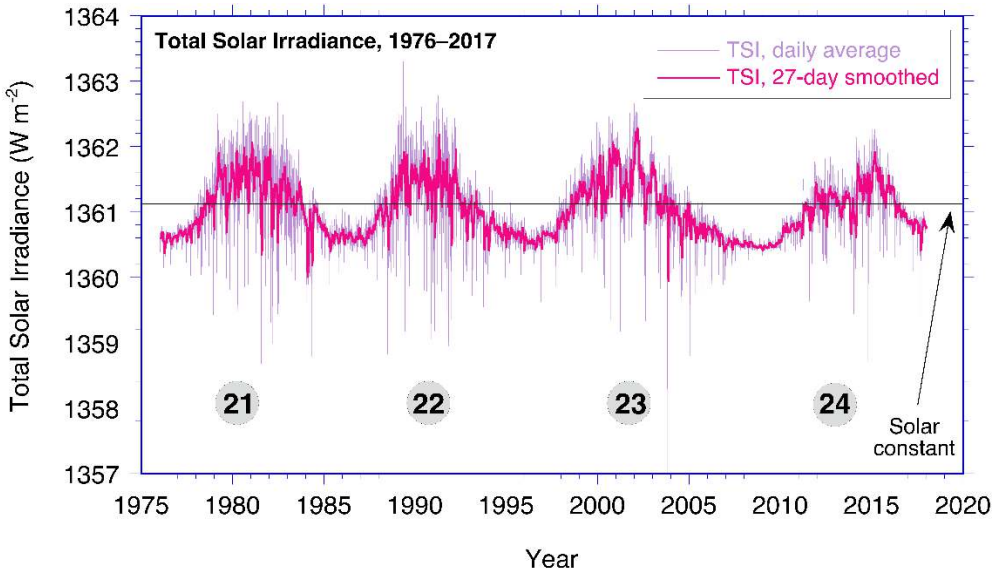

Figure 2-2. Four solar cycles show the temporal variations of daily TSI in a composite reconstruction of the 1976–2017 time series based on observations from spaceborne radiometers after corrections and gap-filling. The thick line indicates the 27-day moving average (corresponding to the 27-day mean solar rotation period), and the circled numbers refer to the solar cycle designation. The horizontal line shows the solar constant (1361.1 W/m^2). *Image based on data published in Gueymard (2018b)*

On a daily basis, the passage of large sunspots results in much lower TSI values than the solar constant. The measured variation in TSI resulting from the sunspot cycle is at most ±0.2%, only twice the precision (i.e., repeatability—not total absolute accuracy, which is approximately ±0.5%) of the most accurate radiometers measuring TSI in space. There is, however, some large variability in a few spectral regions—especially the UV (wavelengths less than 400 nm)—caused by solar activity.

Historic determinations of solar constant have fluctuated throughout time (Gueymard 2006; Kopp 2016). At the onset of the 21st century, it was 1366.1 ± 7 W/m^2 (ASTM 2000; Gueymard 2004). More recent satellite observations using advanced sensors and better calibration methods, however, have shown that the solar constant is somewhat lower: ≈1361 W/m^2. After careful reexamination and corrections of decades of past satellite-based records, Gueymard (2018b) proposed a revised value of 1361.1 W/m^2.

According to astronomical computations such as those made by the National Renewable Energy Laboratory's (NREL's) solar position software (https://midcdmz.nrel.gov/spa/), using SC ≈1361 W/m^2, the seasonal variation of ±1.7% in the Sun-Earth distance causes the irradiance at the top of the Earth's atmosphere to vary from ≈1409 W/m^2 (+3.5%) near January 3 to ≈1315 W/m^2 (–3.3%) near July 4. This seasonal variation is systematic and deterministic; hence, it does not include the daily (somewhat random) or cyclical variability in

TSI induced by solar activity, which was discussed previously. This variability is normally less than ±0.2% and is simply ignored in the practice of solar resource assessments.

2.5 Solar Geometry

The amount of radiation exchanged between two objects is affected by their separation distance. The Earth's elliptical orbit (eccentricity 0.0167) brings it closest to the Sun in January and farthest from the Sun in July, as mentioned. The average Sun-Earth distance is close to the new definition of the AU, which is exactly 149,597,870,700 m, as introduced in 2012 by the International Astronomical Union and recognized as a Système International (SI) unit in 2014 by the International Bureau of Weights and Measures (BIPM). Figure 2-3 shows the Earth's orbit in relation to the northern hemisphere's seasons, caused by the average ≈23.4° tilt of the Earth's rotational axis with respect to the plane of the orbit. The solar irradiance available at the top of atmosphere (TOA) is called the extraterrestrial radiation (ETR). ETR (see Eq. 2-1) is the power per unit area, or flux density, in Watts per square meter (W/m^2), radiated from the Sun and available at the TOA. Just like ETS, ETR varies with the Sun-Earth distance (r) and annual mean distance (r_0):

$$\mathrm{ETR} = \mathrm{TSI}\,(r_0/r)^2 \qquad (2\text{-}1)$$

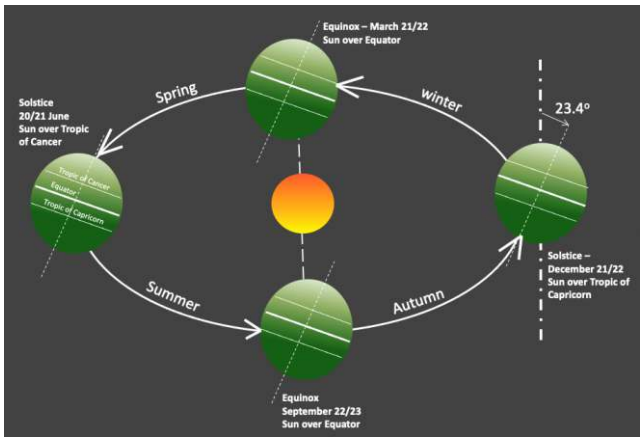

Figure 2-3. Schematic of the Earth's orbit. The Earth's orbit around the Sun is slightly elliptic. *Image by NREL*

As indicated in Section 2.4, it is customary to neglect temporal variations in TSI so that TSI can be replaced by the solar constant in Eq. (2-1) for simplification. The Sun-Earth distance correction factor, $(r_0/r)^2$, in Eq. 2-1 is normally obtained from sun position algorithms, such as those described in Section 2.6.1. Daily values of sufficient accuracy for most applications can also be found in tabulated form—e.g., Iqbal (2012).

From the TOA, the sun appears as a very bright disk with an angular diameter of ≈0.5° (the actual apparent diameter varies by a small amount, ±1.7%, because the Sun-Earth distance varies) surrounded by a completely black sky, apart from the light coming from stars and planets. This angle can be determined from the distance between the Earth and the Sun and the latter's apparent diameter. More precisely, a point at the top of the Earth's atmosphere intercepts a cone of light from the hemisphere of the Sun facing the Earth with a total angle of 0.53°±1.7% at the apex and a divergence angle from the center of the disk of 0.266° (half the apex angle, yearly average). Because the divergence angle is very small, the rays of light emitted by the Sun are nearly parallel; these are called the solar beam. The interaction of the solar beam with the terrestrial atmosphere is discussed next.

2.6 Solar Radiation and the Earth's Atmosphere

The Earth's atmosphere can be seen as a continuously variable filter for the solar ETR as it reaches the surface. Figure 2-4 illustrates the "typical" absorption of solar radiation by atmospheric constituents such as ozone, oxygen, water vapor, or carbon dioxide. The amount of atmosphere the solar photons must traverse, also called the atmospheric path length or air mass (AM), depends on the relative position of the observer with respect to the sun's position in the sky (Figure 2-4). By convention, air mass one (AM1) is defined as the amount of atmospheric path length observed when the sun is directly overhead. As a first approximation, and for low zenith angles, air mass is geometrically related to the solar zenith angle (SZA). Actually, air mass is approximately equal to the secant of SZA, or 1/cos(SZA). Air mass 1.5 (AM1.5) is a key quantity in solar applications and corresponds to SZA = 48.236° (Gueymard, Myers, and Emery, 2002). Air mass two (AM2) occurs when SZA is ≈60° and has twice the path length of AM1. By extrapolation, one refers to the value at the TOA as AM0 (Myers 2013).

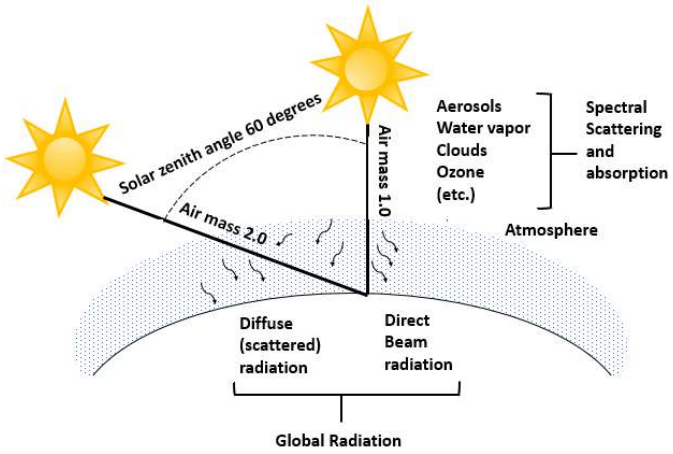

Figure 2-4. Scattering of the direct-beam photons from the sun by the atmosphere produces diffuse radiation that varies with air mass. ***Image by NREL, modified from Marion et al. (1992)***

The cloudless atmosphere contains gaseous molecules and particulates (e.g., dust and other aerosols) that reduce the ETR as it progresses farther down through the atmosphere. This reduction is caused mostly by scattering (a change of a photon's direction of propagation) and also by absorption (a capture of radiation). Finally, clouds are the major elements that modify the ETR (also by scattering and absorption) on its way to the surface or to a solar collector.

Absorption converts part of the incoming solar radiation into heat and raises the temperature of the absorbing medium. Scattering redistributes the radiation in the hemisphere of the sky dome above the observer, including reflecting part of the radiation back into space. The longer the path length through the atmosphere, the more radiation is absorbed and scattered. The probability of scattering—and hence of geometric and spatial redistribution of the solar radiation—increases as the path (air mass) from the TOA to the ground increases.

Part of the radiation that reaches the Earth's surface is eventually reflected back into the atmosphere. A fraction of this returns to the surface through a process known as backscattering. The actual geometry and flux density of the reflected and scattered radiation depend on the reflectivity and physical properties of the surface and constituents in the atmosphere, especially clouds and aerosols.

Based on these interactions between the radiation and the atmosphere, the terrestrial solar radiation is divided into two components: *direct beam radiation*, which refers to solar photons

that reach the surface without being scattered or absorbed, and *diffuse radiation*, which refers to photons that reach the observer after one or more scattering events with atmospheric constituents. These definitions and their usage for solar energy are discussed in detail in Section 2.7.

Ongoing research continues to increase our understanding of the properties of atmospheric constituents, ways to estimate them, and their impact on the magnitude of solar radiation in the atmosphere at various atmospheric levels and at the surface. This is of great importance to those who measure and model solar radiation fluxes (see Chapter 3–Chapter 6).

2.6.1 Relative Motions of the Earth and Sun

The amount of solar radiation available at the TOA is a function of TSI and the Sun-Earth distance at the time of interest, per Eq. (2-1). The slightly elliptical orbit of the Earth around the Sun was briefly described in Section 2.5 and is shown in Figure 2-3. The Earth rotates around an axis through the geographic north and south poles, inclined at an average angle of ≈23.4° to the plane of the Earth's orbit. The axial tilt of the Earth's rotation also results in daily variations in the solar geometry during any year.

In the Northern Hemisphere, at latitudes above the Tropic of Cancer (23.437° N) near midday, the sun is low on the horizon during winter and high in the sky during summer. Summer days are longer than winter days because of progressive changes where the sun rises and sets. Similar transitions take place in the Southern Hemisphere. All these changes result in changing geometry of the solar position in the sky with respect to time of year and specific location. Similarly, the resulting yearly variation in the solar input creates seasonal variations in climate and weather at each location. The solar position in the sky corresponds to topocentric angles, as follows:

- The solar elevation angle is defined as the angle formed by the direction of the sun and the local horizon. It is the complement of SZA, i.e., 90°–SZA.
- The solar azimuth angle is defined as the angle formed by the projection of the direction of the sun on the horizontal plane defined eastward from true north, following the International Organization for Standardization (ISO) 19115 standard. For example, 0° or 360° = due north, 90° = due east, 180° = due south, and 270° = due west.

An example of apparent sun path variations for various periods of the year is depicted in Figure 2-5. Because of their significance in performing any analysis of solar radiation data or any radiation model calculation, the use of solar position calculations of sufficient accuracy is necessary, such as those derived from NREL's Solar Position Algorithm[4] (Reda and Andreas 2003, 2004). This algorithm predicts solar zenith and azimuth angles as well as other related parameters such as the Sun-Earth distance and the solar declination. All this is possible in the period from 2000 B.C. to 6000 A.D. with an SZA standard deviation of only ≈0.0003° (1"). To achieve such accuracy during a long period, this algorithm is very time consuming, with approximately 2300 floating operations and more than 300 direct and inverse trigonometric functions at each time step. Other algorithms exist, differing in the attained accuracy and in their period of validity. Various strategies exist to reduce operations, such as reducing the period of validity while maintaining high accuracy (Blanc and Wald 2012; Grena 2008; Blanco-Muriel et al. 2001) or keeping a long period while reducing the accuracy (Michalsky 1988).

[4] See http://www.nrel.gov/midc/spa/.

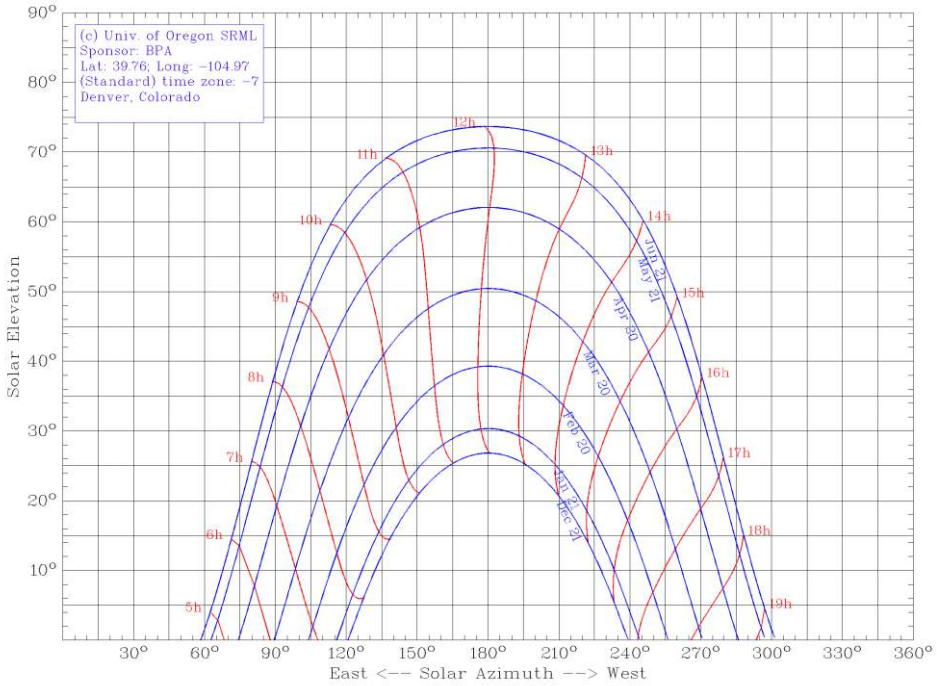

Figure 2-5. Apparent sun path variations during a typical year in Denver, Colorado.
Image from the University of Oregon Solar Radiation Monitoring Laboratory (http://solardata.uoregon.edu/SunChartProgram.php)

2.7 Solar Resource and Components

Radiation can be transmitted, absorbed, or scattered in varying amounts by an attenuating medium, depending on wavelength. Complex interactions of the Earth's atmosphere with solar radiation result in three fundamental broadband components of interest to solar energy conversion technologies:

- Direct normal irradiance (DNI): solar (beam) radiation from the sun's disk itself—of interest to concentrating solar technologies (CST), tracked collectors, and other solar technologies because of incidence angle dependent efficiency
- Diffuse horizontal irradiance (DHI): scattered solar radiation from the sky dome (excluding the sun and thus DNI)[5]
- Global horizontal irradiance (GHI): geometric sum of the direct and diffuse horizontal components (also called the total hemispheric irradiance)
- Global tilted irradiance (GTI): geometric sum of the direct, sky diffuse, and ground-reflected components on a tilted surface. GTI is also referred to as the plane-of-array (POA) irradiance in the photovoltaic (PV) literature.
- Global normal irradiance (GNI): geometric sum of the direct, sky diffuse, and ground-reflected components on a tracking surface that remains perpendicular to the sunbeam.

The radiation components are shown in Figure 2.6.

[5] The diffuse horizontal irradiance is also frequently referred to as DIF in the literature to avoid confusion with the *direct horizontal irradiance*, which is also a quantity of interest in various applications.

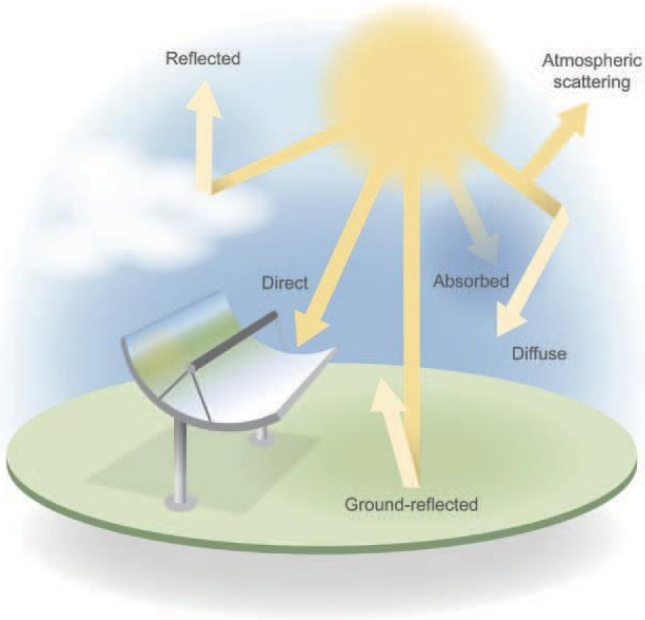

Figure 2-6. Solar radiation components resulting from interactions with the atmosphere. *Image by Al Hicks, NREL*

These basic solar components are related to SZA by the fundamental expression:

$$GHI = DNI \times \cos(SZA) + DHI \tag{2-2a}$$

$$GTI = DNI \times \cos(AI) + DHI \times SVF + RHI \times GVF \tag{2-2b}$$

where AI is the angle of incidence of the solar beam onto the tilted surface, SVF is the sky view factor between the collector and the visible part of the sky, GVF is the ground view factor between the collector and the visible part of the foreground surface, and RHI is the global reflected horizontal irradiance, which is discussed further in Chapter 5, Section 5.11.

2.7.1 Direct Normal Irradiance and Circumsolar Irradiance

By definition, DNI is the irradiance on a surface perpendicular to the vector (i.e., normal incidence) from the observer to the center of the sun caused by radiation that was not scattered by the atmosphere out of the region appearing as the solar disk (WMO 2018). This strict definition is useful for atmospheric physics and radiative transfer models, but it results in a complication for ground observations: it is not possible to measure whether or not a photon was scattered if it reaches the observer from the direction in which the solar disk is seen. Therefore, DNI is usually interpreted in a less stringent way in the world of solar energy. Direct solar radiation is understood as the “radiation received from a small solid angle centered on the sun’s disk” (ISO 2018). The size of this “small solid angle” for DNI measurements is recommended to be $5 \cdot 10^{-3}$ sr (corresponding to ≈2.5° half angle) (WMO 2018). This recommendation is approximately 10 times larger than the angular radius of the solar disk itself based on no-atmosphere geometry, whose yearly average is 0.266°, as mentioned earlier. This relaxed definition is necessary for practical reasons because the instruments used for DNI measurement (pyrheliometers) need to track or follow the sun throughout its path of motion in the sky, and small tracking errors are to be expected. The relatively large field of view (FOV) of pyrheliometers reduces the effect of such tracking errors. Similarly, DHI must be obtained by masking the sun from the pyranometer detector with a small shade. An FOV with a radius of 2.5° is necessary to avoid the impact of tracking errors (e.g., wind-induced tracking errors) and to maintain an FOV complementary to that of the pyrheliometer.

To understand the definition of DNI and how it is measured by pyrheliometers in practice, the role of circumsolar radiation—scattered radiation coming from the annulus surrounding the solar disk—must be discussed. (The reader is referred to the detailed review, based on both experimental and modeling results, found in Blanc et al. (2014).) Because of forward scattering of direct sunlight in the atmosphere, the circumsolar region closely surrounding the solar disk (solar aureole) looks very bright and can alter the observed *sunshape* (Buie et al. 2003). The sunshape—a quantity not to be confused with the "shape of the Sun"—is the azimuthally averaged radiance profile as a function of the angular distance from the center of the sun normalized to 1 at the apparent sun's disc center. The radiation coming from this region is called the circumsolar radiation. For the typical FOV of modern pyrheliometers (2.5°), circumsolar radiation contributes a variable amount, depending on atmospheric conditions, to the DNI measurement. Determining the magnitude of the circumsolar radiation is of interest in CST applications because DNI measurements are typically larger than the beam irradiance that can be used in concentrating systems. This causes an overestimate of CST plant production because the FOV of the concentrators (typically of the order of 1° or even less) is much smaller than the FOV of the pyrheliometers that are used on-site to determine the incident DNI.

The circumsolar contribution to the observed DNI can be quantified if the radiance distribution within the circumsolar region and the so-called penumbra function of the pyrheliometer are known. The latter is a characteristic of the instrument and can be derived from the manufacturer's data. The former, however, is difficult to determine experimentally with current instrumentation. For instance, a method based on two commercial instruments (a sun and aureole measurement system and a sun photometer) has been presented (Gueymard 2010; Wilbert et al. 2013). Other instruments that can measure the circumsolar irradiance are documented in Wilbert et al. (2012, 2018), Kalapatapu et al. (2012), and Wilbert (2014).

To avoid additional measurements, substantial modeling effort is required and might involve estimation of the spectral distribution (Gueymard 2001). Some specific input data are rarely accessible in real time, particularly when a thin ice cloud (cirrus) reduces DNI but considerably increases the circumsolar contribution. Despite these difficulties and because of the special needs of the solar industry, new specialized radiative models have been developed recently to evaluate the difference between the true and apparent DNI using various types of observations (Eissa et al. 2018; Räisänen and Lindfors 2019; Sun et al. 2020; Xie et al. 2020). More research is being conducted to facilitate the determination of the circumsolar fraction at any location and any instant as part of solar resource assessments. Further information on circumsolar radiation can be found in Chapter 5, Section 5.9.

2.7.2 Diffuse Irradiance

A cloudless atmosphere absorbs and scatters some radiation out of the direct beam before it reaches the Earth's surface. Scattering occurs in essentially all directions, away from the specific path of the incident beam radiation. This scattered radiation constitutes the sky diffuse radiation in the hemisphere above the surface. In particular, the Rayleigh scattering theory explains why the sky appears blue (short wavelengths, in the blue and violet parts of the spectrum, are scattered more efficiently by atmospheric molecules) and why the sun's disk appears yellow-red at sunrise and sunset (blue wavelengths are mostly scattered out of the direct beam, whereas the longer red wavelengths undergo less scattering, resulting in a red shift). As mentioned above, the sky radiation in the hemisphere above the local surface is referred to as DHI. A more technical and practical definition of DHI is that it represents all radiation from the sky dome except what is considered DNI; hence, in practice, DHI is the total diffuse irradiance from the whole-sky hemisphere minus the 2.5° annulus around the sun center.

DHI includes radiation scattered by molecules (Rayleigh effect), aerosols (Mie effect), and clouds (if present). It also includes the backscattered radiation that is first reflected by the surface and then re-reflected downward by the atmosphere or clouds. The impact of clouds is difficult to model because they have optical properties that can vary rapidly over time and can also vary considerably over the sky hemisphere. Whereas a single and homogenous cloud layer can be modeled with good accuracy, complex three-dimensional cloud scenes present extreme challenges (Hogan and Shonk 2012).

2.7.3 Global Irradiance

The total hemispherical solar radiation on a horizontal surface, or GHI, is the sum of DHI and the projected DNI to the horizontal surface, as expressed by Eq. 2-2. This fundamental equation is used for data quality assessments, some solar radiation measurement system designs, and atmospheric radiative transfer models addressing the needs for solar resource data. Because GHI is easier—and less expensive—to measure than DNI or DHI, most radiometric stations in the world provide only GHI data. It is then necessary to estimate DNI and DHI by using an appropriate separation model, as discussed in the next section.

2.7.4 Solar Resources for Solar Energy Conversion

Obtaining data time series or temporal averages of the solar radiation components—most importantly, GHI and DNI—that relate to a conversion system is the first step in selecting the site-appropriate technology and evaluating the simulated performance of specific system designs. Systems with highly concentrating optics rely solely on DNI. Low-concentration systems might also be able to use some sky diffuse radiation. Flat-plate collectors, fixed or tracking, can use all downwelling radiation components as well as radiation reflected from the ground if in the collector's FOV.

Solar radiation data are required at all stages of a solar project. Before construction, long time series of historical data are necessary to quantify the solar resource and its variability. During operation, real-time data are typically necessary to verify the performance of the system and to detect problems. In both cases, the required data can be obtained from measurements, modeling, or a combination of both. Typically, measurements are not used exclusively for the early stages of development because (1) long time series of measured irradiance data generally do not exist at the location of interest; (2) measured data, when available, most likely contain gaps that must be filled by modeling; and (3) conducting quality measurements is considerably more costly than operating models (assuming, of course, that the otherwise prohibitively high costs of satellite operations and data management are borne by other agencies). High-quality measurements remain essential, however, because their uncertainty is normally significantly less than that of modeled data (see Chapter 7), and thus they can serve to validate models and even improve the quality of long-term modeled time series through a "site adaptation" process (see Chapter 4). The development and validation of solar radiation models is an intricate procedure that requires irradiance observations obtained with very low measurement uncertainty, typically obtained only at research-class stations.

GHI is measured at a relatively large number of stations in the world (see Chapter 6); however, the quality of such data remains to be verified at most of these stations. Assuming that good-quality GHI data are available at a station of interest, how can the analyst derive the two other components—DNI and DHI—for example, to compute global irradiance on a tilted plane?

There are two possible solutions to this frequent situation. The first is to temporarily ignore the existing GHI data and obtain time series of GHI, DNI, and DHI from a reputable source of satellite-derived data. The modeled and measured GHI data can then be compared for quality assurance and possible bias corrections to the modeled data or, conversely, to determine the quality of the measured data. Both measured and modeled GHI values can incorporate

systematic biases. Understanding the magnitude and nature of these biases and how they can affect the calculation is important when determining the uncertainty in the results (see Chapter 7).

The second method for determining DNI and DHI from GHI data consists of using one of numerous "separation" or "decomposition" models, about which considerable literature exists. Gueymard and Ruiz-Arias (2016) reviewed 140 such models and quantified their performance at 54 high-quality radiometric stations over all continents using data with high temporal resolution (1 minute, in most cases). Previous evaluations had targeted a limited number of models, exclusively using the more conventional hourly resolution—e.g., Ineichen (2008); Jacovides et al. (2010); Perez et al. (1990); and Ruiz-Arias et al. (2010). All current models of this type being empirical in nature are not of "universal" validity and thus might not be optimized for the specific location under scrutiny, particularly under adverse situations (e.g., subhourly data, high surface albedo, or high aerosol loads) that can trigger significant biases and random errors; hence, the most appropriate way to deal with the component separation problem cannot be ascertained at any given location. The solar radiation scientific research community continues to validate the existing conversion algorithms and to develop new ones.

In general, the higher the time resolution, the larger random errors in the estimated DNI or DHI will be. Even large biases could appear at subhourly resolutions if the models used are not appropriate for short-interval data. This issue is discussed by Gueymard and Ruiz-Arias (2014, 2016), who showed that not all hourly models are appropriate for higher temporal resolutions and that large errors might occur under cloud-enhancement situations. A new avenue of research is to optimally combine the estimates from multiple models using advanced artificial intelligence techniques (Aler et al. 2017).

2.7.5 Terrestrial Solar Spectra

Many solar energy applications rely on collectors or systems that have a pronounced spectral response. The performance of solar cells that constitute the building blocks of PV systems are affected by the spectral distribution of incident radiation. Each solar cell technology has a specific spectral dependence (see Figure 3-22). To allow for the comparison and rating of solar cells or modules, it is thus necessary to rely on reference spectral conditions. To this end, various international standardization bodies—ASTM, the International Electrotechnical Commission (IEC), and ISO—have promulgated standards that describe such reference terrestrial spectra. In turn, these spectra are mandated to test the performance of any solar cell using either indoor or outdoor testing methods. Currently, all terrestrial standard reference spectra are for an air mass of 1.5 (noted AM1.5). The reason for this as well as historical perspectives on the evolution of these standards are discussed by Gueymard et al. (2002). The standard reference spectra of relevance to the solar energy community are the following:

- ASTM G173: for GTI on a 37° tilted surface and DNI
- ASTM G197: for the direct, diffuse, and global components incident on surfaces tilted at 20° and 90°
- IEC 60904-3: similar to ASTM G173, with only slightly different values, lower by 0.29%
- ISO 9845-1: replicating ASTM G159 (now deprecated and replaced by G173); ISO is currently preparing an update.

In addition, CIE 241:2020 proposes a number of recommended reference solar spectra for industrial applications at various air masses, and ASTM G177 defines a "high-UV" spectrum at an air mass of 1.05 for material degradation purposes.

It is emphasized that these reference spectra correspond to clear-sky situations and are difficult to realize experimentally (Gueymard 2019). Spectroradiometers are now available that measure the spectral irradiance at high temporal resolution (e.g., each minute) under all possible sky conditions. Although the availability of spectral data are limited, they can be used to test systems under field conditions (see Chapter 3–Chapter 6).

2.8 References

Aler, R., I. M. Galván, J. A. Ruiz-Arias, and C. A. Gueymard. 2017. "Improving the Separation of Direct and Diffuse Solar Radiation Components Using Machine Learning by Gradient Boosting." *Solar Energy* 150: 558–69.

ASTM. 2019. *E490-00a(2019), Standard Solar Constant and Zero Air Mass Solar Spectral Irradiance Tables*. West Conshohocken, PA: ASTM International. www.astm.org.

ASTM. 2020. *ASTM G173-03(2020), Standard Tables for Reference Solar Spectral Irradiances: Direct Normal and Hemispherical on 37° Tilted Surface*. West Conshohocken, PA: ASTM International. www.astm.org.

Blanc, P., and L. Wald. 2012. "The SG2 Algorithm for a Fast and Accurate Computation of the Position of the Sun for Multi-Decadal Time Period." *Solar Energy* 88 (10): 3,072–83. http://doi.org/10.1016/j.solener.2012.07.018.

Blanc, P., B. Espinar, N. Geuder, C. Gueymard, R. Meyer, R. Pitz-Paal, B. Reinhardt, D. Renné, M. Sengupta, L. Wald, and S. Wilbert. 2014. "Direct Normal Irradiance Related Definitions and Applications: The Circumsolar Issue." *Solar Energy* 110: 561–77. http:// doi.org/10.1016/j.solener.2014.10.001

Blanco-Muriel, M., D. C. Alarcón-Padilla, T. López-Moratalla, and M. Lara-Coira. 2001. "Computing the Solar Vector." *Solar Energy* 70 (5): 431–41.

Buie, D., A. G. Monger, and C. J. Dey. 2003. "Sunshape Distributions for Terrestrial Solar Simulations." *Solar Energy* 74 (2): 113–22. https://doi.org/10.1016/S0038-092X(03)00125-7.

CIE. 2002. *CIE 241: 2020—Recommended Reference Solar Spectra for Industrial Applications*.

Eissa, Y., P. Blanc, H. Ghedira, A. Oumbe, and L. Wald. 2018. "A Fast and Simple Model to Estimate the Contribution of the Circumsolar Irradiance to Measured Broadband Beam Irradiance Under Cloud-Free Conditions in Desert Environment." *Solar Energy* 163: 497–509.

Fröhlich, C., and J. Lean. 2004. "Solar Radiative Output and its Variability: Evidence and Mechanisms." *The Astronomy and Astrophysics Review* 12: 273–320. https://doi.org/10.1007/s00159-004-0024-1.

Fröhlich, C., and J. Lean. 1998. "The Sun's Total Irradiance: Cycles, Trends and Related Climate Change Uncertainties Since 1976." *Geophysical Research Letters* 25 (23): 4,377–80.

Grena, R., 2008. "An Algorithm for the Computation of the Solar Position." *Solar Energy* 82 (5): 462–70. https://doi.org/10.1016/j.solener.2007.10.001.

Gueymard, C. A. 2001. "Parameterized Transmittance Model for Direct Beam and Circumsolar Spectral Irradiance." *Solar Energy* 71: 325–46.

———. 2004. "The Sun's Total and Spectral Irradiance for Solar Energy Applications and Solar Radiation Models." *Solar Energy* 76: 423–52.

———. 2006. “Reference Solar Spectra: Their Evolution, Standardization Issues, and Comparison to Recent Measurements.” *Advances in Space Research* 37: 323–40. https://doi.org/10.1016/j.asr.2005.03.104.

———. 2010. “Spectral Circumsolar Radiation Contribution to CPV.” *Proceedings of the CPV6 Conference*, Freiburg, Germany.

———. 2018a. “Revised Composite Extraterrestrial Spectrum Based on Recent Solar Irradiance Observations.” *Solar Energy* 169: 430–40.

———. 2018b. “A Reevaluation of the Solar Constant Based on a 42-Year Total Solar Irradiance Time Series and a Reconciliation of Spaceborne Observations.” *Solar Energy* 168: 2–9.

———. 2019. “The SMARTS Spectral Irradiance Model After 25 Years: New Developments and Validation of Reference Spectra.” *Solar Energy* 187: 233–53.

Gueymard, C. A., and J. A. Ruiz-Arias. 2014. “Performance of Separation Models to Predict Direct Irradiance at High Frequency: Validation Over Arid Areas.” *Proceedings of EuroSun 2014*, ISES, Aix-les-Bains, France.

———. 2016. “Extensive Worldwide Validation and Climate Sensitivity Analysis of Direct Irradiance Predictions From 1-Min Global Irradiance.” *Solar Energy* 128: 1–30.

Gueymard, C. A., D. Myers, and K. Emery. 2002. “Proposed Reference Irradiance Spectra for Solar Energy Systems Testing.” *Solar Energy* 73 (6): 443–67.

Hogan, R. J., and J. K. P. Shonk. 2012. “Incorporating the Effects of 3D Radiative Transfer in the Presence of Clouds into Two-Stream Multilayer Radiation Schemes.” *Journal of the Atmospheric Sciences* 70 (2): 708–24. http://journals.ametsoc.org/doi/pdf/10.1175/JAS-D-12-041.1.

International Electrotechnical Commission (IEC). 2019. *IEC 60904-3:2019 Photovoltaic Devices—Part 3: Measurement Principles for Terrestrial Photovoltaic (PV) Solar Devices with Reference Spectral Irradiance Data*. Geneva, Switzerland.

International Organization for Standardization (ISO). 1992. *ISO 9845-1:1992 Solar Energy -- Reference Solar Spectral Irradiance At The Ground At Different Receiving Conditions -- Part 1: Direct Normal And Hemispherical Solar Irradiance For Air Mass 1,5*. Geneva, Switzerland. https://www.iso.org/standard/17723.html.

Ineichen, P. 2008. “Comparison and Validation of Three Global-to-Beam Irradiance Models Against Ground Measurements.” *Solar Energy* 82: 501–12.

Iqbal, M. 2012. *An Introduction to Solar Radiation*. Elsevier.

Jacovides, C. P., J. Boland, D. N. Asimakopoulos, and N. A. Kaltsounides. 2010. “Comparing Diffuse Radiation Models with One Predictor for Partitioning Incident PAR Radiation Into its Diffuse Component in the Eastern Mediterranean Basin.” *Renewable Energy* 35: 1820–27.

Kalapatapu, R., M. Chiesa, P. Armstrong, and S. Wilbert. 2012. “Measurement of DNI Angular Distribution with a Sunshape Profiling Irradiometer.” *Proceedings of the SolarPACES Conference*, Marrakech, Morocco.

Kopp, G. 2016. “Magnitudes and Timescales of Total Solar Irradiance Variability.” *Journal of Space Weather and Space Climate* 6 (27): A30. https://doi.org/10.1051/swsc/2016025.

Kopp, G., and J. L. Lean. 2011. “A New, Lower Value of Total Solar Irradiance: Evidence and Climate Significance.” *Geophysical Research Letters* (38): L01706. https://doi.org/10.1029/2010GL045777.

Marion, W., C. Riordan, D. Renne. 1992. *Shining On: A Primer on Solar Radiation Data* (NREL/TP-463-4856). Golden, CO: National Renewable Energy Laboratory. https://www.nrel.gov/docs/legosti/old/4856.pdf.

Michalsky, J. 1988. "The Astronomical Almanac's Algorithm for Approximate Solar Position (1950–2050)." *Solar Energy* 40 (3): 227–35.

Myers, D. R. 2013. *Solar Radiation: Practical Modeling for Renewable Energy Applications. Energy and the Environment*. Boca Raton, FL: CRC Press.

Perez, R., R. Seals, A. Zelenka, P. Ineichen. 1990. "Climatic Evaluation of Models That Predict Hourly Direct Irradiance from Hourly Global Irradiance: Prospects for Performance Improvements." *Solar Energy* 44: 99–108.

Räisänen, P., and A. V. Lindfors. 2019. "On the Computation of Apparent Direct Solar Radiation." *Journal of Atmospheric Sciences* 76: 2,761–80.

Reda, I., and A. Andreas. 2003. "Solar Position Algorithm for Solar Radiation Applications." *Solar Energy* 76: 577–89.

Reda, I., and A. Andreas. 2004. "Solar Position Algorithm for Solar Radiation Applications." *Solar Energy* 76: 577–89. External note: Corrigendum, published in 2007 *Solar Energy* 81 (6): 838.

Ruiz-Arias, J. A., H. Alsamamra, J. Tovar-Pescador, and D. Pozo-Vazquez. 2010. "Proposal of a Regressive Model for the Hourly Diffuse Solar Radiation Under All-Sky Conditions." *Energy Conversion and Management* 51: 881–89.

Sun, Z., J. Li, G. Shi, J. Manners, and J. Li. 2020. "Fast Scheme for Determination of Direct Normal Irradiance. Part II: Parameterization of Circumsolar Radiation." *Solar Energy* 199: 256–67.

Wilbert, S., B. Reinhardt, J. DeVore, M. Röger, R. Pitz-Paal, and C. A. Gueymard. 2013. "Measurement of Solar Radiance Profiles with the Sun and Aureole Measurement System." *Journal of Solar Energy Engineering* 135: 041002.

Wilbert, S., 2014. "Determination of Circumsolar Radiation and its Effect on Concentrating Solar Power." Ph.D. thesis, Rheinisch-Westfälische Technische Hochschule Aachen, DLR.

Wilbert, S., M. Röger, J. Csambor, M. Breitbach, F. Klinger, B. Nouri, N. Hanrieder, F.Wolfertstetter, D. Schüler, S. Shaswattam, N. Goswami, S., Kumar, A. Ghennioui, R. Affolter, N. Geuder, and B. Kraas. 2018. "Sunshape Measurements with Conventional Rotating Shadowband Irradiometers." *AIP Conference Proceedings* 2033: 190016. https://doi.org/10.1063/1.5067201.

Wilbert, S., R. Pitz-Paal, and J. Jaus. 2012. "Circumsolar Radiation and Beam Irradiance Measurements for Focusing Collectors." Presented at the ES1002: Cost Wire Workshop, May 22–23, Risö.

World Meteorological Organization (WMO). 2018. *Guide to Instruments and Methods of Observations, Volume I – Measurement of Meteorological Variables: 2018 Edition*. https://library.wmo.int/index.php?lvl=categ_see&id=10586.

Xie, Y., M. Sengupta, Y. Liu, H. Long, Q. Min, W. Liu, and A. Habte. 2020. "A Physics-Based DNI Model Assessing All-Sky Circumsolar Radiation." *iScience* 23: 100893. https://doi.org/10.1016/j.isci.2020.100893.

3 MEASURING SOLAR RADIATION

Stefan Wilbert,[1] Thomas Stoffel,[2] Daryl Myers,[3] Stephen Wilcox,[2] Aron Habte,[4] Frank Vignola,[5] and Anton Driesse[6]
[1] *German Aerospace Center (DLR)*
[2] *Solar Resource Solutions, LLC*
[3] *National Renewable Energy Laboratory, retired*
[4] *National Renewable Energy Laboratory*
[5] *University of Oregon*
[6] *PV Performance Labs*

Accurate measurements of the incoming irradiance are essential to solar power plant project design, implementation, and operations. Because solar irradiance measurements are relatively complex—and therefore expensive—compared to other meteorological measurements, they are available for only a limited number of locations. This is true especially for direct normal irradiance (DNI). Developers use irradiance data for:

- Site resource analysis
- System design
- Plant operation.

Irradiance measurements are also essential for:

- Developing and testing models that use remote satellite sensing techniques or available surface meteorological observations to estimate solar radiation resources
- Site adaptation of long-term resource data sets
- Developing solar resource forecasting techniques and enhancing their quality by applying recent measurements for the creation of the forecast
- Other disciplines not directly related to renewable energy, such as climate studies and accelerated weathering tests.

This chapter focuses on the instrument selection, characterization, installation, design, and operation and maintenance (O&M)—including calibration of measurement systems suitable for collecting irradiance resource measurements—for renewable energy technology applications.

3.1 Instrumentation

Before considering instrumentation options and the associated costs, the user should first evaluate the data accuracy or uncertainty levels that will satisfy the ultimate analyses based on the radiometric measurements. This ensures that the best value can be achieved after considering the various available measurement and instrumentation options.

By first establishing the project needs for solar resource data accuracy, the user can then base the instrument selection and the associated levels of effort necessary to operate and maintain the measurement system on an overall cost-performance determination. Specifically, the most accurate instrumentation should not be purchased if the project resources cannot support the maintenance required to ensure measurement quality that is consistent with the radiometer design specifications and the manufacturer's recommendations. In such cases, alternative instrumentation designed for reduced maintenance requirements and reduced measurement performance—such as radiometers

with photodiode-based detectors and diffuser disks or integrated measurement systems such as rotating shadowband irradiometers (RSIs)—could produce more consistent results (see Section 3.2.5). As stated, however, in this context the *first* consideration is the accuracy required to support the final analysis. If budget limitations cannot sustain the necessary accuracy, a reevaluation of the project goals and resources must be undertaken.

Redundant instrumentation is another important approach to ensure confidence in data quality. Multiple radiometers at the project site and/or providing for the measurement of the solar irradiance components—e.g., global horizontal irradiance (GHI), diffuse horizontal irradiance (DHI), DNI, and global tilted irradiance (GTI, also referred to as plane-of-array (POA) irradiance)—regardless of the primary measurement need, can greatly enhance opportunities for post-measurement data quality assessment, which is required to provide confidence in the resource data.

Measuring other meteorological parameters relevant to the amounts and types of solar irradiance available at a specific time and location can also provide opportunities for post-measurement data quality assessment (see Section 3.3).

3.2 Radiometer Types

Instruments designed to measure any form of radiation are called radiometers. The earliest developments of instrumentation for measuring solar radiation were designed to meet the needs of agriculture for bright sunshine duration to understand evaporation and by physicists to determine the sun's output or "solar constant." During the 19th and 20th centuries, the most widely deployed instrument for measuring solar radiation was the Campbell-Stokes sunshine recorder (Iqbal 1983; Vignola, Michalsky, and Stoffel 2020). This analog device focuses the direct beam by a simple spherical lens (glass ball) to create burn marks during clear periods (when DNI exceeds ≈120 W/m^2) on a sensitized paper strip placed daily in the sphere's focus curve. By comparing the total burn length to the corresponding day length, records of percentage possible sunshine from stations around the world became the basis for characterizing the global distribution of solar radiation (Löf, Duffie, and Smith 1966). The earliest pyrheliometers (from the Greek words for *fire*, *sun*, and *measure*) were based on calorimetry and used by scientists to measure brief periods of DNI from various locations, generally at high elevations to minimize the effects of a thick atmosphere on the transmission of radiation from the sun. By the early 20th century, scientists had developed pyranometers (from the Greek words for *fire* and *measure*) to measure GHI to understand the Earth's energy budget (Vignola, Michalsky, and Stoffel 2020).

This section summarizes the types of commercially available radiometers most commonly used to measure solar radiation resources for solar energy technology applications. Solar resource assessments are traditionally based on broadband measurements—i.e., encompassing the whole shortwave spectrum (0.29–4 µm). More specialized instruments (spectroradiometers) are needed to evaluate the spectral distribution of this irradiance, which in turn is useful to investigate the spectral response of photovoltaic (PV) cells, for instance. Such instruments are described in Chapter 5, Section 5.6.

3.2.1 Pyrheliometers and Pyranometers

Pyrheliometers and pyranometers are two types of radiometers used to measure solar irradiance. Their ability to receive solar radiation from two distinct portions of the sky distinguishes their designs. As described in Chapter 2, pyrheliometers are used to measure DNI, and pyranometers are used to measure GHI, DHI, GTI (aka POA), or the in-plane rear-side irradiance (RPOA). Another important measurement involving pyranometers is the albedo, which can be used to estimate RHI (reflected horizontal irradiance) in Eq. (2-2b) as

well as RPOA. Albedo measurements are described in Chapter 5, Section 5.11. Table 3-1 summarizes some key attributes of these two radiometers.

Table 3-1. Overview of Solar Radiometer Types and Their Applications

Radiometer Type	Measurement	Field of View (Full Angle)	Installation
Pyrheliometer	DNI	5°–6°	Mounted on a solar tracker for alignment with the solar disk
Pyranometer	GHI	2π steradians	Mounted on a stable horizontal surface free from local obstructions[a]
Pyranometer	DHI	2π steradians	Mounted on a solar tracker fitted with shading mechanism or on a manually adjusted shadowband platform to block DNI from the detector's surface[a]
Pyranometer	GTI (POA)	2π steradians	Mounted in the plane of the flat-plate solar collector (fixed or tracked in one or two axes)
Pyranometer	RPOA	2π steradians	Mounted in the plane of the rear side of the flat-plate solar collector oriented toward the ground (fixed or tracked in one or two axes)
Pyranometers	Albedo	2π steradians	Two pyranometers mounted horizontally measuring the downward and upward irradiance, see Chapter 5, Section 5.11.

[a] Optionally, thermopile pyranometers are installed with a powered ventilator and heating system to reduce contamination of optical surfaces and thermal errors. The base of thermopile pyranometers must be shielded from direct sunlight.

Pyrheliometers and pyranometers commonly use either a thermoelectric or photoelectric passive sensor to convert solar irradiance (W/m^2) into a proportional electrical signal (microvolts [µV] DC). Thermoelectric sensors have an optically black coating that allows for a broad and uniform spectral response to all solar radiation wavelengths from approximately 300–3000 nm (Figure 3-1, left). The most common thermoelectric sensor used in radiometers is the thermopile. There are all-black thermopile sensors used in pyrheliometers and pyranometers as well as black-and-white thermopile pyranometers. In all-black thermopile sensors, the surface exposed to solar radiation is completely covered by the absorbing black coating. The absorbed radiation creates a temperature difference between the black side of the thermopile (i.e., "hot junction") and the other side (i.e., "reference" or "cold junction"). The temperature difference causes a voltage signal. In black-and-white thermopiles, the surface exposed to radiation is partly black and partly white. In this case, the temperature difference between the black and the white surfaces creates the voltage signal. Despite having a relatively small thermal mass, their 95% response times are not

negligible, and they are typically 1–30 seconds[6]—that is, the output signal lags the changes in solar flux. Some instruments include a signal post-processing that tries to compensate for this time lag. Recently, new smaller thermopile sensors with response times as low as 0.2 second have been made commercially available as well. A detailed analysis of radiometer response times is found in Driesse (2018).

In contrast to thermopiles, common photoelectric sensors generally respond to only the visible and near-infrared spectral regions from approximately 350–1,100 nm (Figure 3-1, right; Figure 3-2). Pyranometers with photoelectric sensors are sometimes called silicon (Si) pyranometers or photodiode pyranometers. These sensors have very fast time-response characteristics—on the order of microseconds.

For both thermopile and photelectric detectors used in commercially available instruments, the electrical signal generated by exposure to solar irradiance levels of approximately 1000 W/m^2 is on the order of 10 mV DC (assuming no amplification of the output signal and an appropriate shunt resistor for photodiode sensors). This rather low-level signal requires proper electrical grounding and shielding considerations during installation (see Section 3.3.4). Most manufacturers now also offer pyrheliometers and pyranometers with built-in amplifiers and/or digital outputs. Such digital instruments can be of advantage for several reasons. Corrections for systematic errors depending on, e.g., the sensor temperature or the incident angle of the sun can be corrected directly in the instrument, which reduces the effort needed for data treatment and avoids user errors. Their implementation in a data acquisition system can be easier, and errors resulting from the transmission of low-voltage signals might be avoided. On the other hand, such digital sensors are sensitive to transients, surges, and ground potential rise, so the isolation and surge protection of power and communications lines is of high importance (Section 3.3.4).

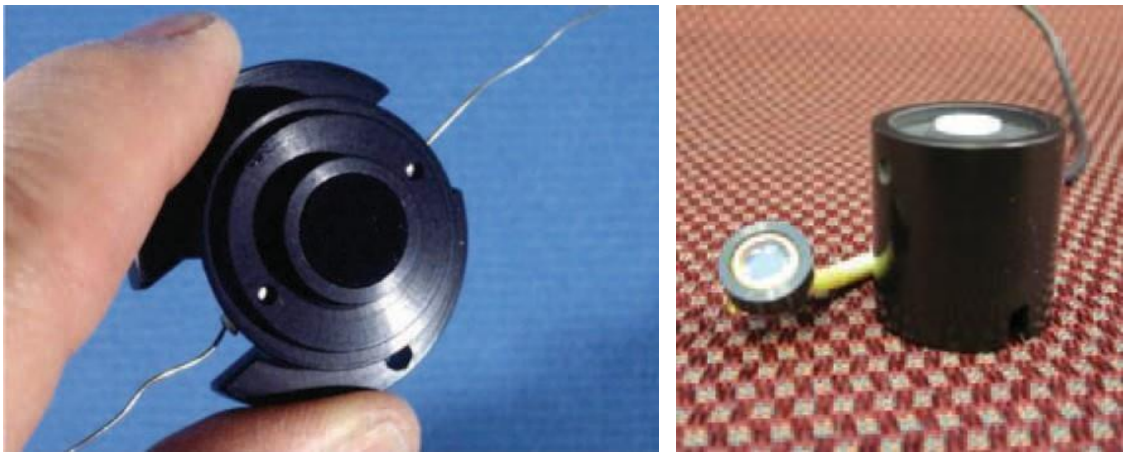

Figure 3-1. (Left) Thermopile assembly used in an Eppley Laboratory, Inc., model PSP and (right) a typical photodiode detector. *Photos used with permission from LI-COR, Inc.*

[6] The given response time represents the time it takes the instrument to reach 95% of the final value. Typically, a steplike change of the incoming irradiance is used to determine the response time.

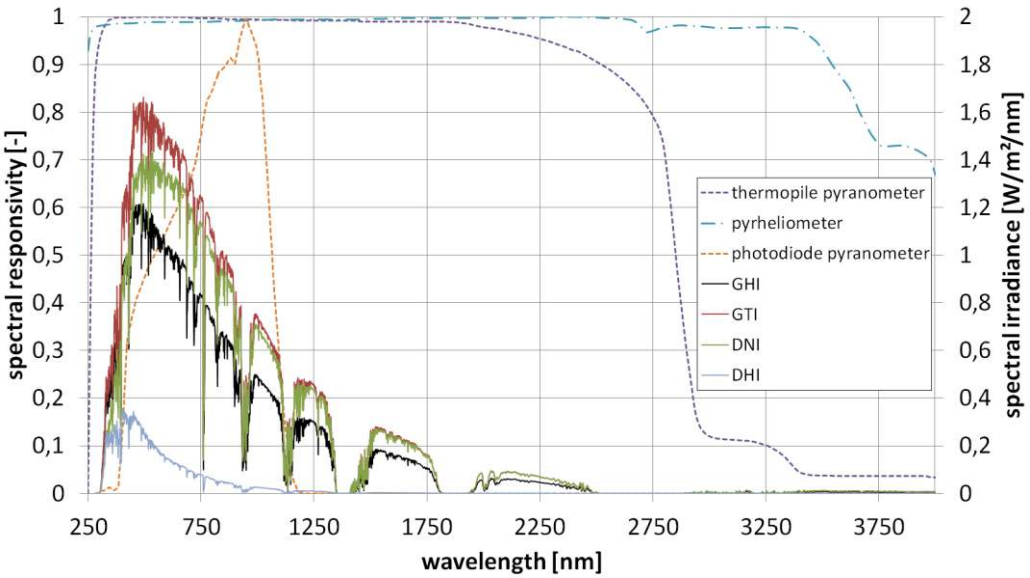

Figure 3-2. Spectral response of LI-COR pyranometer LI200SA, Kipp & Zonen CM21 thermopile pyranometer, and CHP1 pyrheliometer plotted next to the GHI, DNI, DHI, and GTI spectra for ASTM G-173 conditions at AM1.5. *Image by DLR*

3.2.1.1 Pyrheliometers

Pyrheliometers are typically mounted on automatic solar trackers to maintain the instrument's alignment with the solar disk and to fully illuminate the detector from sunrise to sunset (Figure 3-3 and Figure 3-4). Alignment of the pyrheliometer with the solar disk is determined by a simple diopter—a sighting device in which a small spot of light (the solar image) falls on a mark in the center of a target located near the rear of the instrument, serving as a proxy for alignment of the solar beam to the detector. The tracking error is acceptable as long as the solar image is at least tangent to the diopter target. Modern sun trackers use software to compute and precisely track the sun position. These calculations require that the sun tracker is assembled and positioned correctly (horizontally levelled, correct azimuth orientation), and tracking errors occur if the tracker is not installed and positioned correctly. Tracking errors caused by imperfect levelling vary with the sun position. Sun sensors can help to reduce the remaining tracking errors during periods with no direct irradiance; hence, they are used in high-quality stations. The sun sensor is tracked to the sun and uses a four-quadrant sensor placed behind a pinhole or a lens to detect the tracking error. The tracking error is then sent to the tracker software so that it can be corrected. By convention—and to allow for small variations in tracker alignment—view-limiting apertures inside a pyrheliometer allow for the detection of radiation in a narrow annulus of sky around the sun (WMO 2018), called the circumsolar region. This circumsolar radiation component is the result of forward scattering of radiation near the solar disk, itself caused by cloud particles, atmospheric aerosols, and other constituents that can scatter solar radiation. All modern pyrheliometers should have a 5° field of view (FOV), following the World Meteorological Organization (WMO) (2018) recommendations. The FOV of older instruments could be larger, however, such as 5.7°–10° full angle. Depending on the FOV—or, to be more precise, the sensor's penumbra function (see Chapter 2, Section 2.7.1, and references therein)—and tracker alignment, pyrheliometer measurements include varying amounts of circumsolar irradiance contributions to DNI. Although this is usually a very small contribution to the measurement, under atmospheric conditions of high scattering, it can be measurable, or even significant.

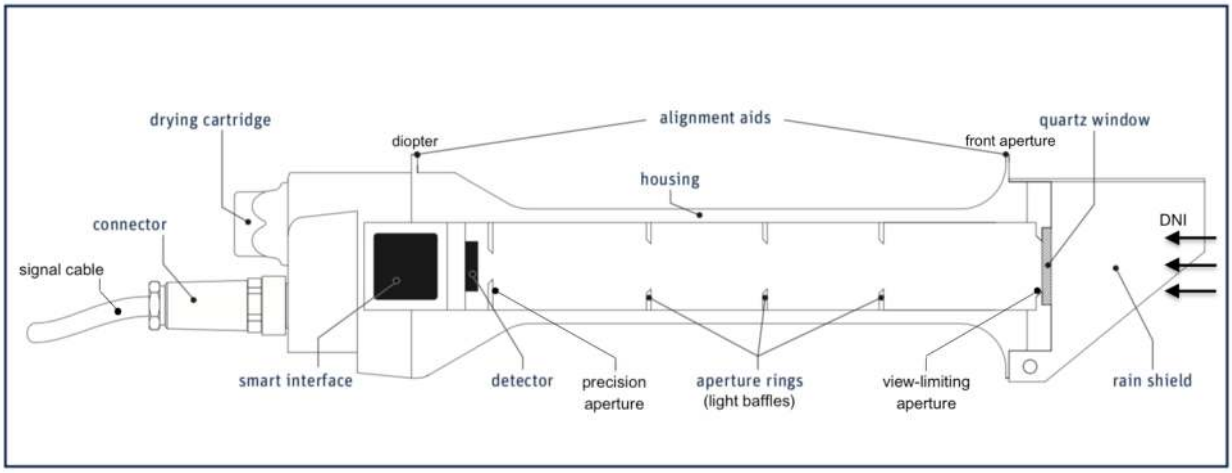

Figure 3-3. Schematic of a Kipp & Zonen B.V., model SHP1—a pyrheliometer with a smart interface. ***Image modified from Kipp & Zonen (2017)***

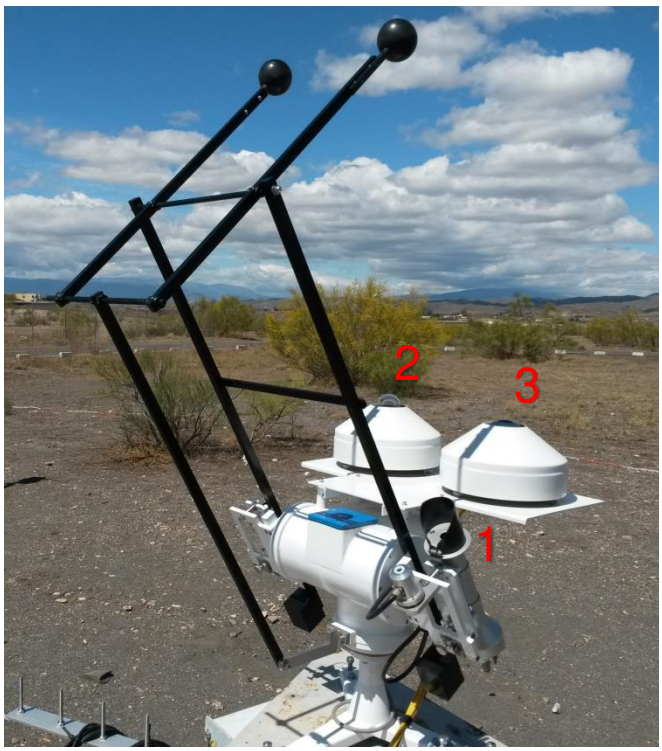

Figure 3-4. A pyrheliometer (1), a shaded pyranometer (2), and a shaded pyrgeometer (3) (See Section 3.2.4) mounted on an automatic solar tracker. ***Photo from DLR***

The most accurate measurements of DNI under stable conditions are accomplished using an electrically self-calibrating absolute cavity radiometer (ACR; see Figure 3-5). This advanced type of radiometer is the basis for the World Radiometric Reference (WRR), the internationally recognized detector-based measurement standard for DNI (Fröhlich 1991). The WMO World Standard Group of ACRs is shown in Figure 3-6. By design, ACRs have no windows and are therefore generally limited to fully attended operation during dry conditions to protect the integrity of the receiver cavity (Figure 3-7). Removable windows and temperature-controlled all-weather designs are available for automated continuous operation of these radiometers; however, the installation of a protective window nullifies the “absolute” nature of the DNI measurement. The window introduces additional measurement

uncertainties associated with the optical transmittance properties of the window (made from either quartz or calcium fluoride) and the changes to the internal heat exchange resulting from the sealed system. Moreover, ACRs need some periods of self-calibration during which no exploitable measurement is possible. This creates discontinuities in the high-accuracy DNI time series that could be measured with windowed ACRs, unless a regular pyrheliometer is also present to provide the necessary redundancy (Gueymard and Ruiz-Arias 2015). Combined with their very high cost of ownership and operation, this explains why ACRs are rarely used to measure DNI in the field.

A unique 10-month comparison of outdoor measurements from 33 pyrheliometers, including ACRs, under a wide range of weather conditions in Golden, Colorado, indicated that the estimated measurement uncertainties at a 95% confidence interval ranged from ±0.5% for windowed ACRs to +1.4%/–1.2% for commercially available instruments (Michalsky et al. 2011). The results also suggested that the measurement performance during the comparison was better than indicated by the manufacturers' specifications.

Figure 3-5. Multiple electrically self-calibrating absolute cavity radiometers mounted on solar trackers with control and data acquisition electronics. *Photo by NREL*

Figure 3-6. The World Standard Group of six absolute cavity radiometers is used to define the WRR or DNI measurement standard. ***Photo by NREL***

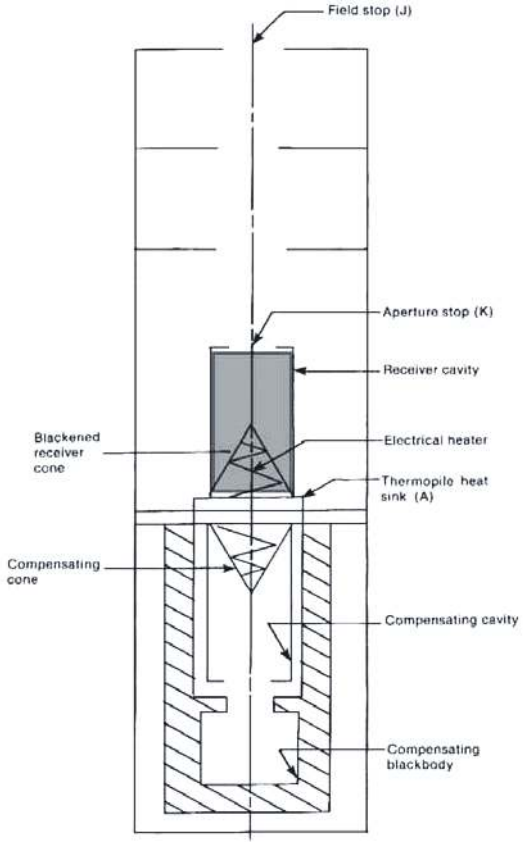

Figure 3-7. Schematic of the Eppley Laboratory, Inc., model automatic Hickey-Frieden absolute cavity radiometer. ***Image modeled from Reda (1996)***

3.2.1.2 Pyranometers

A pyranometer has a thermoelectric or photoelectric detector with a hemispherical FOV (360° or 2π steradians) (see Figure 3-4 and Figure 3-8). This type of radiometer is mounted horizontally to measure GHI. In this horizontal mount, the pyranometer has a complete view of the sky dome. Ideally, the mounting location for this instrument is free of natural or artificial obstructions on the horizon. Alternatively, the pyranometer can be mounted at a tilt

to measure GTI, e.g., in the case of latitude-tilt or 1-axis tracking systems, or vertically for building applications. In an upside-down position, it measures the ground-reflected irradiance. The local albedo is simply obtained by dividing the latter by GHI as further discussed in Chapter 5, Section 5.11.

The pyranometer detector is mounted under a protective dome (made of precision quartz or other high-transmittance optical material) and/or a diffuser. Both designs protect the detector from the weather and provide optical properties consistent with receiving hemispheric solar radiation. Pyranometers can be fitted with ventilators that constantly blow air—sometimes heated—from under the instrument and over the dome (Figure 3-9). The ventilation reduces the potential for contaminating the pyranometer optics caused by dust, dew, frost, snow, ice, insects, or other materials. Ventilation and heating also affect the thermal offset characteristics of pyranometers with single all-black detectors (Vignola, Long, and Reda 2009). The ventilation devices can require a significant amount of electrical power (5–20 W), particularly when heated, adding to the required capacity for on-site power generation in remote areas. Both DC and AC ventilators exist, but current research indicates that DC ventilators are preferable (Michalsky, Kutchenreiter, and Long 2019).

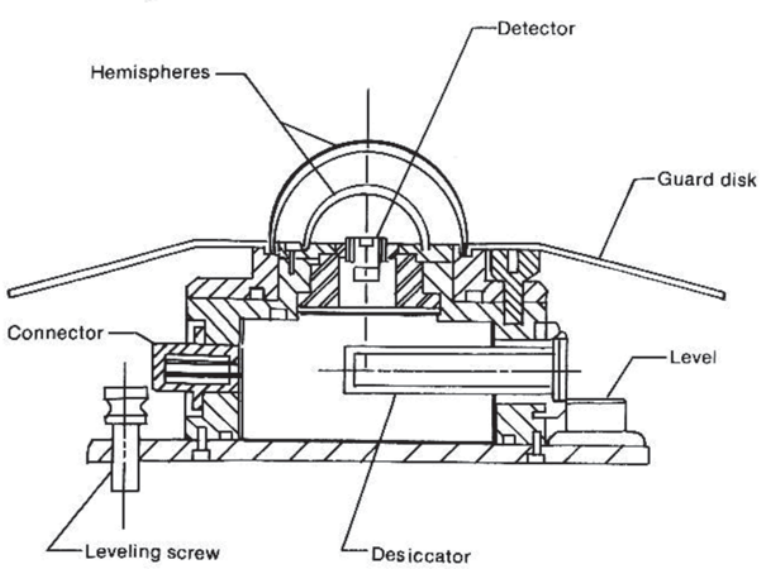

Figure 3-8. Schematic of the Eppley Laboratory, Inc., PSP. ***Image by NREL***

Photodiode pyranometers provide the signal in the form of a photodiode's short-circuit current. The fast response of such photodiode pyranometers makes them interesting for some applications, e.g., the measurement of cloud enhancement or ramping events. Photodiode pyranometers employ a diffuser above the detector (Figure 3-10) to achieve an approximate hemispherical response and to omit the glass dome to reduce cost. The application of a diffuser as an external surface compared to transparent glass domes makes such pyranometers measurably more dust tolerant than pyranometers with optical glass domes (Maxwell et al. 1999). The long-term stability of photodiode pyranometers can vary differently from thermopile-based pyranometers, as shown in Figure 3-11 and as further analyzed in Geuder et al. (2014). These instrument-specific behaviors dictate the need for regular calibrations as recommended by the manufacturers.

Figure 3-9. Kipp & Zonen model CM22 pyranometers installed in ventilated CV2 enclosures. *Photo by NREL*

Figure 3-10. Selected photodiode sensors with different diffusor geometries. *Photos by DLR*

Pyranometers can also be used to measure the diffuse irradiance. The required device for this measurement is known as a diffusometer. It consists of a pyranometer and a shading structure that blocks the direct radiation on its way to the sensor. Shading balls, shading disks, shading rings, or shadowbands are used for that purpose. Shading balls and shading disks must track the sun, and they cover only a small part of the sky corresponding to the angular region defined for measuring DNI (normally 5°). Shading rings and shadowbands cover the complete solar path during a day as seen from the pyranometer. They are built a little bit wider to cover the sun's path on several consecutive days so that readjustments of the shading ring position are not required every day. The shading rings and shadowbands block a significant part of sky diffuse radiation; therefore, correction functions are necessary to determine DHI from the shading device. This explains why the accuracy of such a DHI determination is less than that of a DHI measurement with a shading disk or a shading ball. Shadowbands are further described in Section 3.2.5 in connection with the RSIs.

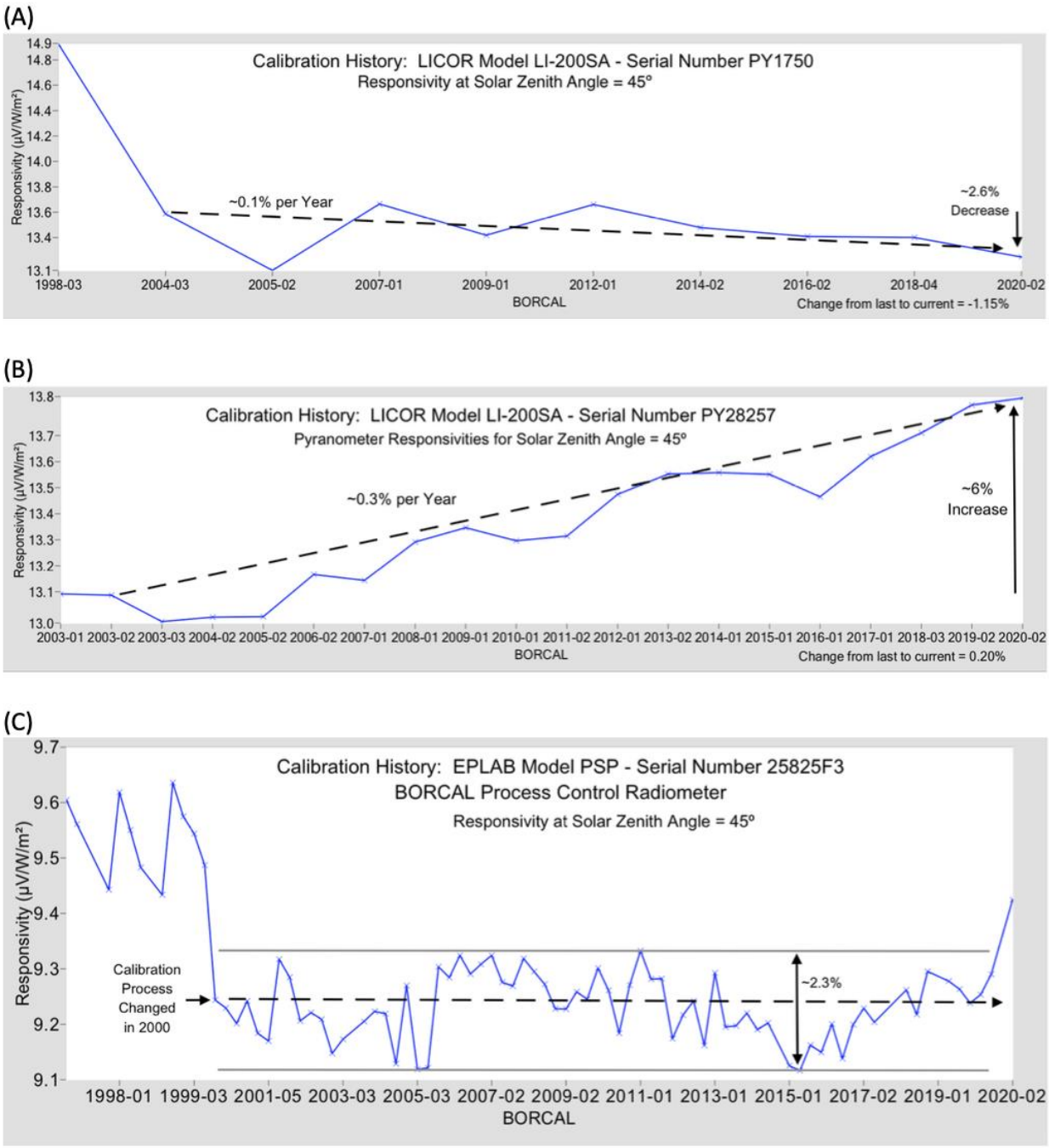

Figure 3-11. Example of long-term calibration responsivity changes for two photodiode-based pyranometers (A and B) with an acrylic diffuser and a thermopile-based pyranometer (C) based on results from periodic NREL Broadband Outdoor Radiometer Calibration events.

3.2.2 Pyrheliometer and Pyranometer Classifications

Both the International Organization for Standardization (ISO) and WMO have established instrument classifications and specifications for the measurement of solar irradiance. Radiometer classification can help to find the correct instrument and to interpret the data. Several instrument properties are used as the basis for these pyrheliometer and pyranometer classifications. The latest ISO specifications for these radiometers are found in ISO 9060 (ISO 2018) and are summarized in Table 3-2 and Table 3-3 based on Apogee

(2019). The standard provides not only acceptance intervals but also corresponding guard bands, which is advantageous because the measurements used to obtain the sensor specifications have nonnegligible uncertainties.

The acceptance intervals provided by ISO 9060 give a general idea of the differences in data quality afforded by instrument classes; therefore, the radiometer classes can be understood as accuracy classes. The current standard also notes, however, that the acceptance intervals shown in the tables cannot be used for uncertainty calculations for measurements obtained at conditions that are different from those defined for the classification. For example, the temperature response limits are defined for the interval from -10°C to 40°C relative to the signal at 20°C. A measurement at 10°C will be connected to a different temperature response error than a measurement at 0°C or even -20°C. For the other parameters, the same principle applies. In particular, the spectral clear-sky irradiance error used for the classification can deviate from the spectral irradiance error for other conditions, e.g., cloudy conditions or other air masses. For pyranometers, it must also be considered that the spectral error for diffuse or tilted radiation is different from the spectral error for global horizontal radiation. A more detailed discussion of the clear-sky spectral error can be found in Wilbert et al. (2020).

The most important changes in the current ISO 9060 compared to the previous version, from 1990 (ISO 1990a), are as follows:

- Simple names are used for the classes (AA, A, B, C), and a new class is introduced mainly for ACRs.
- The clear-sky spectral error is used to classify the spectral properties of the radiometers, allowing photodiode-based radiometers to be also included in the ISO classification. Previously, the spectral selectivity was used, which excluded photodiode radiometers. The spectral selectivity is defined by ISO as the deviation of the spectral responsivity from the average spectral responsivity between 0.35–1.5 µm.
- Additional radiometer classes are defined relatively to their response time and their spectral responsivity. If the 95% response time is less than 0.5 second, the radiometer can be called a “fast response radiometer.” Similarly, “spectrally flat radiometers” are defined using the spectral selectivity. If a radiometer has a spectral selectivity less than 3%, it can be called a spectrally flat radiometer.
- For Class A pyranometers, individual testing of temperature response and directional response is required.
- The final signal of a sensor can be used for classification after the application of specific correction functions (e.g., for temperature response) *if* these corrections are applied within the measurement system (processor within instrument or control unit). Processing errors are also used as a classification criterion.

Including photodiode radiometers was considered helpful because only fast (µs) photodiode sensors can be used for accurate monitoring of extremely rapid fluctuations of solar irradiance. Under such circumstances—typically caused by cloud enhancement events—side-by-side thermopile and photodiode radiometers can disagree by a significant margin (Gueymard 2017a, 2017b). Because the most accurate way to determine GHI involves the combination of DNI and DHI measurements (ISO 2018; Michalsky et al. 1999), the shading balls, shading disks, shading masks, and rotating shadowbands used in RSIs are also defined in the current ISO 9060.

The WMO characteristics of operational pyrheliometers and pyranometers are presented for three radiometer classifications:

1. High quality: near state of the art, suitable for use as a working standard, maintainable only at stations with special facilities and staff
2. Good quality: acceptable for network operations
3. Moderate quality: suitable for low-cost networks where moderate to low performance is acceptable.

Table 3-2. ISO 9060:2018 Specifications Summary for Pyrheliometers Used to Measure DNI

Pyrheliometer Classification List				
Parameter	**Name of Class, Acceptance Interval**			
Name of Class	**AA**	**A**	**B**	**C**
Roughly Corresponding Class from ISO 9060:1990	*Not Defined*	*Secondary Standard*	*First Class*	*Second Class*
Response time for 95% response	No requirement	<10 s	<15 s	<20 s
Zero offset: a) Response to 5 K/h-change in ambient temperature	±0.1 W/m^2	±1 W/m^2	±3 W/m^2	±6 W/m^2
b) Complete zero offset including the effect a) and other sources	±0.2 W/m^2	±2 W/m^2	±4 W/m^2	±7 W/m^2
Non-stability: Percentage change in responsivity per year	±0.01%	±0.5%	±1%	±2%
Nonlinearity: Deviation from the responsivity at 500 W/m^2 because of change in irradiance from 100–1000 W/m^2	±0.01%	±0.2%	±0.5%	±2%
Clear-sky DNI spectral error	±0.01%	±0.2%	±1%	±2%
Temperature response: Percentage deviation because of change in ambient temperature within interval from -10°C–40°C relative to 20°C	±0.01%	±0.5%	±1%	±5%
Tilt response: Percentage deviation from the responsivity from 0°–90° at 1000 W/m^2 irradiance	±0.01%	±0.2%	±0.5%	±2%
Additional signal-processing errors	±0.1 W/m^2	±1 W/m^2	±5 W/m^2	±10 W/m^2

Table 3-3. ISO 9060:2018(E) Specifications Summary for Pyranometers

Pyranometer Classification List			
Specification	**Class of Pyranometer[a]**		
	A	**B**	**C**
Roughly Corresponding Class from ISO 9060:1990	*Secondary Standard*	*First Class*	*Second Class*
Response time: 95% response	<10 s	<20 s	<30 s
Zero offset: a) Response to –200 W/m^2 net thermal radiation	±7 W/m^2	±15 W/m^2	±30 W/m^2
b) Response to 5 K h^{-1} change in ambient temperature	±2 W/m^2	±4 W/m^2	±8 W/m^2
c) Total zero offset including the effects a), b), and other sources	±10 W/m^2	±21 W/m^2	±41 W/m^2
Non-stability: Change in responsivity per year	±0.8%	±1.5%	±3%
Nonlinearity: Percentage deviation from the responsivity at 500 W/m^2 because of change in irradiance from 100–1000 W/m^2	±0.5%	±1%	±3%
Directional response for beam radiation (range of errors caused by assuming that the normal incidence responsivity is valid for all directions when measuring, from any direction, a beam radiation that has a normal incidence irradiance of 1000 W/m^2)	±10 W/m^2	±20 W/m^2	±30 W/m^2
Clear-sky GHI spectral error	±0.5%	±1%	±5%
Temperature response: Deviation because of change in ambient temperature within the interval from -10ºC–40ºC relative to 20ºC	±1%	±2%	±4%
Tilt response: Percentage deviation from the responsivity at 0° tilt because of tilt change from 0–180° at 1000 W/m^2 irradiance	±0.5%	±2%	±5%
Additional signal-processing errors	±2 W/m^2	±5 W/m^2	±10 W/m^2

The WMO characteristics are similar to the classifications presented in the previous version of ISO 9060. The difference between the WMO and the outdated ISO 9060 classification is in the definition of spectral selectivity. The wavelength range used in the WMO definition is from 300–3000 nm; whereas it was from 350–1500 nm in the 1990 version of ISO 9060. The

WMO limits for the selectivity for the different classes were the same or even stricter as in the case of the highest pyranometer class. This led to the unfortunate situation that, apparently, no weather-proof pyrheliometer fulfills the requirements of the WMO classes even though the spectral errors of Class A field pyrheliometers are small. (Clear-sky spectral errors are approximately 0.1% [Wilbert et al. 2020]). Typical pyranometers of the highest class in ISO 9060 are also excluded from the WMO classification (Wilbert et al. 2020). This is true for both the 1990 and the 2018 versions of the standard; therefore, it is currently not recommended to use the WMO classification but instead to work with the most recent version of ISO 9060.

Even within each instrument class, there can be some measurement uncertainty variations. The user should research various instrument models to gain familiarity with the design and measurement performance characteristics in view of a particular application (Myers and Wilcox 2009; Wilcox and Myers 2008; Gueymard and Myers 2009; Habte et al. 2014). Further, the accuracy of an irradiance measurement depends on the instrument itself as well as on its alignment, maintenance, data logger calibration, appropriate wiring, and other conditions and effects that degrade performance. The accuracy of radiometers is further discussed in Chapter 7.

3.2.3 Pyrheliometer and Pyranometer Calibrations

As stated, the signal of field radiometers is a voltage or a current that is ideally proportional to the solar irradiance reaching the detector. A calibration factor is required to convert the current or voltage to a solar irradiance. The calibration factor, $C_{cal,}$ is the inverse of the responsivity, *Rs*. For example, the responsivity of a thermopile pyrheliometer is given in µV per W/m^2. The irradiance, *E*, can be obtained from the voltage signal, $V_{pyr,}$ or from the instrument's responsivity as:

$$E = V_{pyr}/Rs = V_{pyr} \cdot C_{cal} \tag{3-1}$$

These calibration factors can vary over time, which requires periodic recalibrations, as demonstrated by the time-series plot of calibration responsivities of two pyrheliometers shown in Figure 3-12. The instability can be caused by changes in the instrument, the meteorological conditions at the time of calibration, the stability of the calibration reference radiometer(s), the performance of the data acquisition system, and other factors included in the estimated uncertainty of each calibration result.

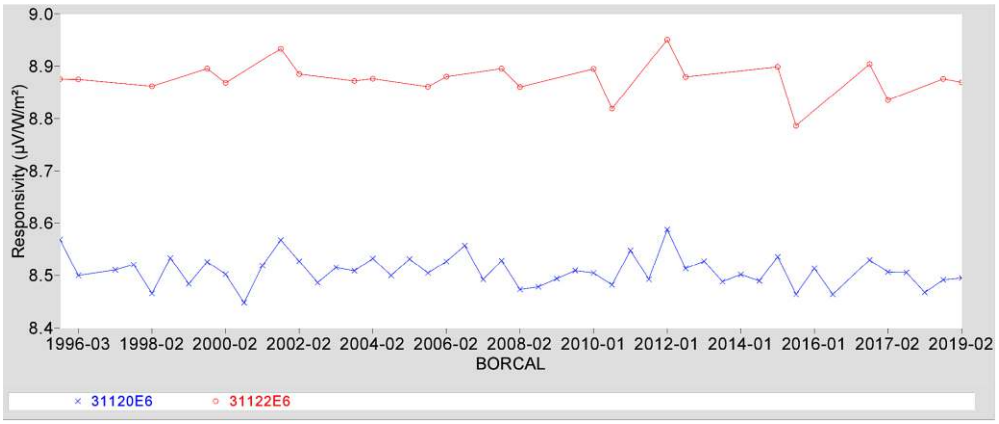

Figure 3-12. Calibration histories for two pyrheliometer control instruments spanning 23 years of Broadband Outdoor Radiometer Calibration events. *Image by NREL*

The calibration of pyrheliometers and pyranometers is described in detail in international standards ASTM G167-05, ASTM E816-05, ASTM E824-05, ASTM G183-05, ISO 9059, ISO

9846, and ISO 9847. The calibration methods described in ISO 9846 (ISO 1993) for pyranometers and in ISO 9059 (ISO 1990b) for pyrheliometers are based on simultaneous solar irradiance measurements with test and reference instruments. ISO 9847 (ISO 1992) describes pyranometer calibrations using a reference pyranometer. These standards will be revised in the next years by the corresponding ISO working groups.

Pyrheliometers are calibrated following ISO 9059 by comparing the voltage signal of the tracked test pyrheliometer to the reference DNI from one or a group of reference pyrheliometers. For each simultaneous measurement pair, a preliminary responsivity can be calculated as the ratio of the test instrument's voltage to the reference DNI (Figure 3-13, right). After rejecting outliers and data collected during unstable conditions, an average responsivity can be determined. Because some pyrheliometers show a noticeable correlation with the solar zenith angle (SZA), specific angular responsivities can also be derived (Figure 3-13, left and bottom). For this calibration method, it is important that clouds do not mask the sun or the circumsolar region. The calibration can be affected if significant levels of circumsolar radiation prevail during the calibration. This risk increases with the instrument's FOV; hence, Linke turbidities should be less than 6 according to the standard method. The Linke turbidity coefficient, T_L, is a measure of atmospheric attenuation under cloudless conditions. It represents the number of clean and dry atmospheres that would result in the same attenuation as the real cloudless atmosphere. One method to derive the Linke turbidity from DNI is presented in Ineichen and Perez (2002).

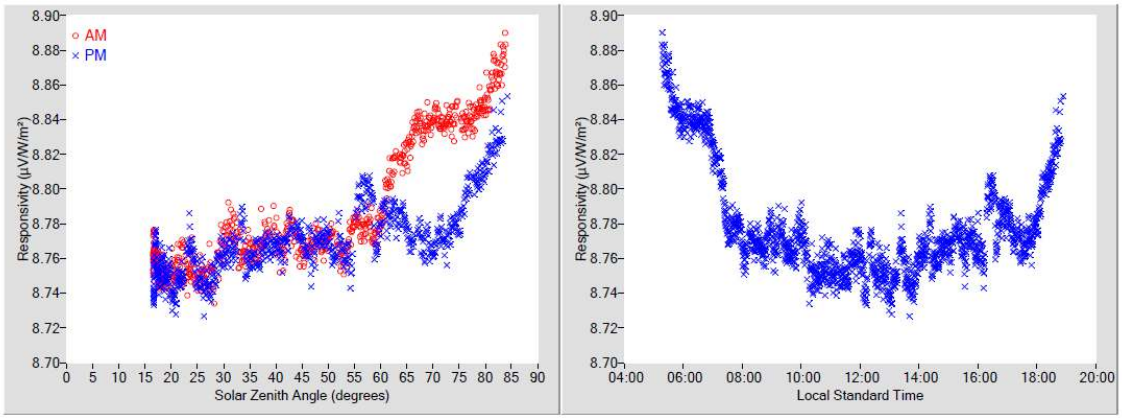

Table 2. Calibration Label Values

RS @ 45° (µV/W/m²) ‡	U95 (%) †	Tilt / Azm
8.7678	+0.80 / -0.62	N/A

† Valid zenith angle range: 30.0° to 60.0°
‡ Estimated thermal offset error during calibration is unspecified.

Figure 3-13. Pyrheliometer calibration results for an Eppley NIP summarizing (left) *Rs* compared to SZA and (right) *Rs* compared to local standard time. *Image by NREL*

As mentioned, the WRR must be used as the traceable reference for the calibration of all terrestrial broadband radiometers, as stipulated by the internationally accepted Système International (SI). This internationally recognized measurement reference is a detector-based standard maintained by a group of electrically self-calibrating absolute cavity pyrheliometers at the World Radiation Center (WRC) by the Physical Meteorological Observatory in Davos, Switzerland. The present accepted inherent uncertainty in the WRR is ±0.3% (Finsterle 2011). All radiometer calibrations must be traceable to the WRR, but that does not mean that all radiometers are calibrated *directly* against the WRR. The calibration chain from the WRR to a field instrument can have several steps. For example, reference ACRs are used as national and institutional standards, and these instruments are calibrated by comparison to the WRR during international pyrheliometer comparisons conducted by the

WRC once every 5 years. Pyranometers calibrated against traceable WRR reference pyrheliometers make these pyranometer calibrations traceable to the WRR.

Pyranometers can be calibrated outdoors with three different methods. One option, as described in ISO 9846, is to compare the DNI output from a reference pyrheliometer to that derived from the test pyranometer using the shade-unshade method. The successive voltages, $V_{unshade}$ and V_{shade}, are proportional to GHI (unshaded) and DHI (shaded), respectively. Using the reference DNI and the relationship between GHI, DHI, and DNI, as described by Eq. (2-2a), the responsivity, *Rs*, of the pyranometer under test for one measurement sequence can be derived:

$$Rs = [(V_{unshade} - V_{shade})/\cos(SZA)]/DNI \quad (3\text{-}2)$$

This method is described in more detail by Reda, Stoffel, and Myers (2003).

For this calibration method, virtually constant atmospheric conditions during the pair of shaded and unshaded measurements are required. Cloud cover must be very low, and the angular distance between clouds and the sun must be high. In addition to cloud cover, aerosol and water vapor variations could affect the calibration. This explains why only data collected for a low T_L (less than 6) should be used for the calibration.

Another option offered by ISO 9846 consists of comparing the voltage signal of the test pyranometer obtained in the GHI measurement position to the GHI calculated from the DNI and DHI measurements of a reference pyrheliometer and a shaded reference pyranometer. The *Rs* of a pyranometer under calibration for one simultaneous set of three measurements can be computed from their unshaded signal ($V_{unshaded}$):

$$Rs = V_{unshaded}/[DNI \cdot \cos(SZA) + DHI] \quad (3\text{-}3)$$

Computing the *Rs* this way is called the "component-summation calibration technique." Again, T_L should be less than 6, and a high angular distance of clouds from the sun should exist during the whole calibration period.

The third option to calibrate pyranometers outdoors is described in ISO 9847. It compares a test pyranometer to a reference pyranometer while both sensors are in the same measurement position (either GHI or GTI). The Rs_i is then obtained as the ratio of the test signal to the reference irradiance. For outdoor pyranometer calibrations using a reference pyranometer (ISO 1992), the sky conditions are less precisely defined than for the other methods described. The calibration interval is adjusted depending on the sky conditions.

The indoor calibration methods from ISO 9847 use irradiance measurements under an artificial light source. For the first option, measurements are taken simultaneously after ensuring that the test and the reference pyranometer receive the same irradiance from an integrating sphere. This is done by switching pyranometer positions during the calibration procedure. The other option is to take consecutive measurements by mounting the test and the reference instrument one after the other in the same position under a direct beam. The indoor calibrations are carried out in a controlled environment that is independent from external meteorological conditions. If measurements with the reference and test pyranometer are made after each other, however, instabilities of the artificial light source increase the calibration uncertainty compared to outdoor calibrations. If simultaneous measurements are used, an additional uncertainty contribution comes from the fact that the test and the reference pyranometer might not receive exactly the same irradiance from the artificial light source, though some of this error can be mitigated by switching the positions of the instruments during the calibration procedure. Further, the incident angle of the radiation is usually not well defined for indoor calibrations. Because of the pyranometer's directional errors (see Table 3-3), this is another source of calibration uncertainty; therefore, in general,

thorough outdoor calibrations with accurate reference instruments have lower uncertainties than indoor calibrations.

The shade/unshade and component summation techniques, when conducted throughout a range of SZA, show that pyranometer responsivities are correlated with it. The variation of *Rs* as a function of SZA is like a fingerprint or signature of each individual pyranometer (Figure 3-14).

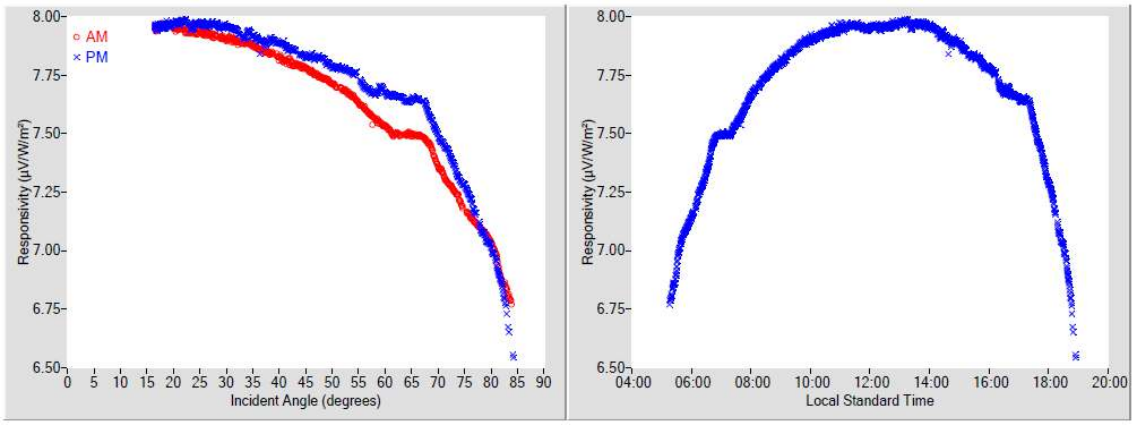

Table 2. Calibration Label Values

RS @ 45° (µV/W/m²) ‡	U95 (%) †	Tilt / Azm
7.8028	+2.61 / -4.08	0.0° / 0.0°

† Valid incident angle range: 30.0° to 60.0°
‡ Estimated thermal offset error during calibration = -20.000 W/m²

Figure 3-14. Pyranometer calibration results for an Eppley PSP summarizing (left) *Rs* compared to SZA and (right) *Rs* compared to local standard time. *Image by Daryl Myers, NREL*

This means that the angular responsivities of different specimens of the same model can differ. Variations of pyranometer *Rs* can be symmetrical with respect to solar noon, or they can be highly skewed, depending on the mechanical alignment of the pyranometer, detector surface structure, and detector absorber material properties. To improve the accuracy in the GHI measurement, using an SZA and azimuth angle-dependent calibration factor for each individual measurement are recommended. This method, however, is applicable only to conditions with high direct radiation contribution to the GHI because the variation of responsivity with SZA is mostly caused by direct radiation and the associated cosine error. For situations when thick clouds mask the sun or for DHI measurements, the angular distribution of the incoming irradiance cannot be approximated well by one incidence angle. For DHI measurements, it is recommended to use the *Rs* for a 45° incidence angle.

For accurate photodiode pyranometer calibration, further considerations beyond these standards are necessary because of the uneven spectral response. A specific calibration method is discussed in Section 3.2.5 for RSI instruments.

3.2.4 Correction Functions for Systematic Errors of Radiometers

Some pyrheliometer and pyranometer measurement errors are systematic and can be reduced by applying correction functions. An example is the correction of the directional errors, as mentioned. Some manufacturers provide one calibration constant for a pyranometer and additional correction factors for different intervals of SZA. This treatment of the incidence angle dependence has the same effect as using an incidence-angle-dependent responsivity.

Moreover, an additional temperature correction can be applied if the internal temperature of pyranometers or pyrheliometers is measured using a temperature-dependent resistor close to the sensor. Correction coefficients are often supplied by the manufacturer.

Measurements from only black (as opposed to black-and-white) thermoelectric pyranometers can be corrected for the expected thermal offset using additional measurements from pyrgeometers (Figure 3-4, right). Pyrgeometers allow for the determination of the downward longwave irradiance between approximately 4.5–40 µm, based on their sensor (thermopile) signal and body temperature. The thermopile is positioned below an opaque window that is transparent only to the specified infrared radiation wavelength range while excluding all visible, near- infrared, and far-infrared radiation. Most pyrgeometers must be positioned below a shading ball or disk to limit window heating by DNI. Ventilation units are also used for pyrgeometers, as in the case of pyranometers. If no pyrgeometer is available, a less accurate correction for the thermal offset can be made based on estimations of the thermal offset from the typically negative measurements collected during the night (Dutton et al. 2000; Gueymard and Myers 2009).

Correction functions for photodiode pyranometers are presented in Section 3.2.5.2.

3.2.5 Systems for Determining Solar Irradiance Components

A measurement system that independently measures the basic solar components—GHI, DNI, and DHI—will produce data with the lowest uncertainty if the instruments are properly installed and maintained. Alternatives exist to reduce the overall cost of such a system while offering potentially acceptable data accuracies, depending on the application. These alternatives are designed to eliminate the expense and complexity of an automatic solar tracker with pyrheliometer and shaded pyranometer.

3.2.5.1 Rotating Shadowband Irradiometers

RSIs use a fast detector that is periodically shaded by a motorized shadowband, which rapidly sweeps back and forth across the detector's FOV (Figure 3-15). The principle of operation of these RSIs is to measure GHI when unshaded and DHI when shaded. The DNI is calculated using the fundamental closure equation relating these three components, Eq. (2-2a):

$$DNI = (GHI - DHI) / \cos(SZA) \quad (3\text{-}4)$$

RSIs are often called rotating shadowband radiometers (RSRs) or rotating shadowband pyranometers (RSPs), depending on the instrument manufacturer. RSI refers to all such instruments measuring irradiance by use of a rotating shadowband. There are two types of RSIs: RSIs with continuous rotation and RSIs with discontinuous rotation.

Figure 3-15. Four commercially available RSIs (clockwise from top left): Irradiance, Inc., model RSR2; Reichert GmbH RSP 4G; Yankee Environmental Systems, Inc., model SDR-1; and CSP-Services GmbH Twin-RSI. ***Photos by (clockwise from top left) Irradiance, Inc.; CSP-Services; NREL; and CSP-Services***

The operational principle of RSIs with continuous rotation is shown in Figure 3-16. At the beginning of each rotation cycle, the shadowband is below the pyranometer in its rest position. The rotation is performed with constant angular velocity and takes approximately 1 second. During the rotation, the irradiance is measured with a high and constant sampling rate (approximately 1 kHz). This measurement is called a burst or sweep. At the beginning of the rotation, the pyranometer measures GHI. The moment the center of the shadow falls on the center of the sensor, it approximately detects DHI; however, the shadowband covers some portion of the sky, so the minimum of the burst is less than DHI. Thus, so-called shoulder values are determined by curve analysis algorithms. Such algorithms are usually implemented in the data logger program and use the maximum of the absolute value of the burst's slope to find the position of the "shoulder values." The difference between GHI and the average of the two shoulder values is added to the minimum of the curve to obtain the actual DHI. Subsequently, DNI is calculated by the data logger using GHI, DHI, and the SZA calculated by the known time and coordinates of the location, as stated. All the RSIs shown in Figure 3-15 (except for the SDR-1 model) work with a continuous rotation.

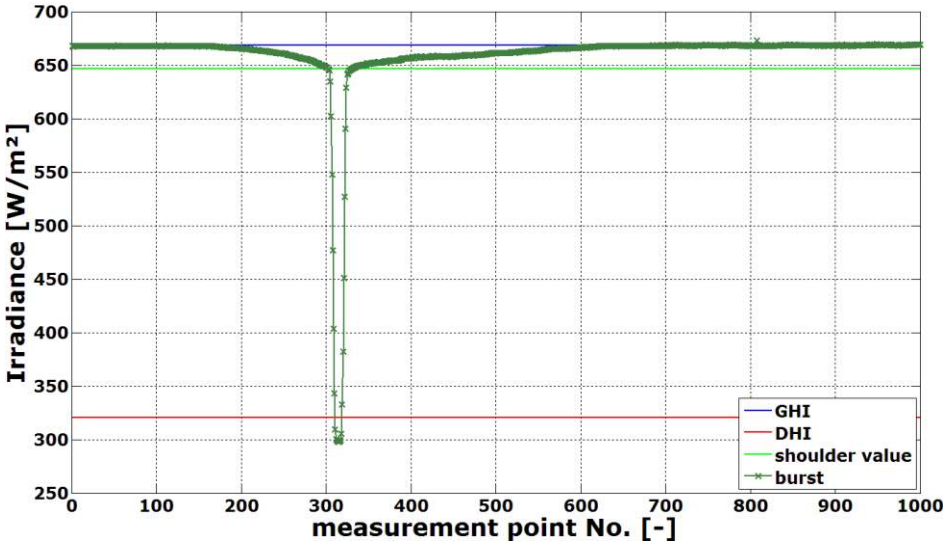

Figure 3-16. Burst (sweep) with sensor signal and the derived GHI, shoulder values, and DHI. *Image from Wilbert (2014)*

RSIs with discontinuous rotation do not measure the complete burst but only four points of it. First, the GHI is measured while the shadowband is in the rest position. Then the shadowband rotates from the rest position toward the position just before it begins shading the diffuser, stops, and a measurement is taken (e.g., during 1 second for the SDR-1 shown in Figure 3-15). Then it continues the rotation toward the position at which the shadow lies centered on the diffuser, and another measurement is taken. The last point is measured in a position at which the shadow has just passed the diffuser. The measurement with the completely shaded diffuser is used equivalently to the minimum of the burst, as shown in Figure 3-16. The two measurements for which the shadow is close to the diffuser are used equivalently to the shoulder values to correct for the portion of the sky blocked by the shadowband.

These two types of RSIs have advantages and disadvantages. An RSI with continuous rotation needs a detector with a fast response time (much less than 1 second—e.g., approximately 10 µs). Because thermopile sensors cannot be used, photodiodes are used instead—typically using Si. An example is the Si-based radiometer model LI-200SA shown in Figure 3-11. Because of the nonhomogeneous spectral response of such Si sensors (see Figure 3-2), the measurement accuracy of highest class thermopile pyranometers cannot be reached. Correction functions for this and other systematic errors must be applied to reach the accuracy required in resource assessments, albeit still not on par with the accuracy of thermopile instruments. These correction functions are discussed in Section 3.2.5.2.

RSIs with discontinuous rotation need sufficiently long measurement times for each of the four points to allow the use of a thermopile detector (e.g., the Yankee TSR-1 thermopile shadowband radiometer, now discontinued); thus, the spectral error of a photodiode can be avoided—at least partly. So far, RSIs with discontinuous rotation typically rely on a diffuser, which has its own uneven spectral transmittance over the shortwave spectrum; hence, the spectral error of such RSIs cannot be neglected. Further, the discontinuous rotation is connected to other disadvantages compared to the continuous rotation. Although RSIs with continuous rotation are not affected by small azimuth alignment errors (within approximately ±5°), the azimuth alignment of RSIs with discontinuous rotation is crucial for their accuracy. Moreover, the accuracy of the sensor's coordinates and sweep time is more important for the discontinuous rotation. If the shadowband stops in the wrong position, the DHI measurement is incorrect. Further, the duration of the measurement with a discontinuous

rotation increases the measurement uncertainty. This is especially relevant if the RSI uses a thermopile sensor and if sky conditions are not stable (e.g., cloud passages). If GHI and the sky radiance distribution change during the four-point measurement, the data used to determine DHI will be inconsistent. In contrast, this complication is less relevant for continuously rotating RSIs because their rotation takes approximately only 1 second.

DHI is typically determined one or four times per minute, but GHI measurements can be sampled at a higher frequency whenever the shadowband does not rotate—for example, every second. The temporal variation of GHI also contains some information about any concomitant change in DNI. Different algorithms are used to determine the averages of DHI and DNI between two DHI measurements using the more frequent GHI measurements. Temporal variation detected by the higher frequency GHI measurement can be used to trigger an additional sweep of the shadowband to update the DHI measurement under rapidly changing sky conditions.

The initial lower accuracy of RSIs compared to ISO 9060 first-class pyrheliometers and secondary standard pyranometers is often compensated by some unique advantages of RSIs. Their simplicity/robustness, low soiling susceptibility (Pape et al. 2009; Geuder and Quaschning 2006; Maxwell et al. 1999), low power demand, and comparatively lower cost (instrumentation and O&M) provide significant advantages compared to thermopile sensors and solar trackers, at least when operated under the measurement conditions of remote weather stations, where power and daily maintenance requirements are more difficult and costly to fulfill.

With neither correction of the systematic deviations nor a matched calibration method, under the best field circumstances RSIs yield an uncertainty of only 5%–10%. This accuracy is notably improved, to approximately 2%–3%, with proper calibration and the application of advanced correction functions (Wilbert et al. 2016), which are described in the following sections. Most instrument providers also offer post-processing software or services that include these correction functions. Users should ask the manufacturer whether such post-processing is part of the instrument package and is readily available.

Because of the stated disadvantages of RSIs with discontinuous rotation and the higher relevance of RSIs with continuous rotation for solar energy applications, the focus here is on RSIs with Si photodiodes and continuous rotation. More information about RSIs with discontinuous rotation can be found in Harrison, Michalsky, and Berndt (1994). Further general information on the accuracy of RSIs can be found in Chapter 7.

3.2.5.2 Correction Functions for Rotating Shadowband Irradiometers

The main systematic errors of RSIs with photodiode sensors are caused by the spectral response of the detector, its cosine response, and its temperature dependence.

Several research groups have developed correction functions that reduce systematic errors in RSI readings. In all cases, the photodiode of the RSI is a LICOR LI-200SA. Whereas temperature correction is similar in all versions (King and Myers 1997; Geuder, Pulvermüller, and Vorbrügg 2008), the methods for the spectral and cosine corrections vary.

Alados-Arboledas, Batlles, and Olmo (1995) used tabular factors for different sky clearness and skylight brightness parameters as well as a functional correction depending on SZA. King and Myers (1997) proposed functional corrections in dependence on air mass and SZA, primarily targeting GHI. This approach was further developed by Augustyn et al. (2002) and Vignola (2006), including diffuse and subsequently direct beam irradiance. The combination of the GHI correction of Augustyn et al. (2002) and of the diffuse correction from Vignola (2006) provides a complete set of corrections for LI-200SA-based RSIs. Independently, a method for DNI, GHI, and DHI correction was developed by the German Aerospace Agency,

Deutsches Zentrum für Luft- und Raumfahrt (DLR), using functional corrections that include a particular spectral parameter obtained from GHI, DHI, and DNI (Geuder, Pulvermüller, and Vorbrügg 2008). Additional corrections in dependence on air mass and SZA were used. Another set of correction functions was later presented in Geuder et al. (2011). Additional new correction methods are on their way (Vignola et al. 2017; 2019; Forstinger et al 2020). An overview of RSI correction functions can be found in Jessen et al. (2017).

3.2.5.3 Calibration Methods for Rotating Shadowband Irradiometers

In addition to the corrections mentioned, special calibration techniques are required for RSIs. As of this writing, RSIs with continuous rotation are equipped with LI-200SA or LI-200R pyranometers. They come with precalibration values from the manufacturer (LI-COR) for GHI based on outdoor comparisons with an Eppley precision spectral pyranometer (PSP) with an accuracy stated as better than 5% (LI-COR Biosciences 2005). Considering that the PSP has only limited performance (Gueymard and Myers 2009), an additional calibration (e.g., on-site or with respect to DHI, DNI, or GHI independently) of the RSIs can noticeably improve their accuracy (Wilbert et al. 2016).

Because of the rather narrow and inhomogeneous spectral response of the photodiodes and the combined measurement of DHI and GHI, only some aspects of the existing ISO standards for pyrheliometer and pyranometer calibrations can be transferred to RSI calibration. Calibrating RSI instruments involves independently field-calibrating them for DNI, DHI, and GHI. Each of these three steps is challenging because each irradiance component has a distinct spectral composition that can change during the day or from one location to another. Because of the spectral response of the Si detectors and/or the diffusers, it is problematic to calibrate an RSI based on only a few short series of measurements. This is possible for thermopile sensors because of their homogenous spectral response covering at least 300–3000 nm (which amounts to >99% of the ASTM G173 DNI spectrum). A similar calibration method of RSIs would need the spectra during the calibration and the additional—but incorrect—assumption that all RSIs from a single manufacturer have exactly the same nominal spectral and cosine response. Then the RSI measurements obtained later in a resource assessment station could be described by nominal correction functions and estimated or measured spectra. A similar approach using a calibration period of several weeks was tested in Forstinger et al. (2020), but it is still not applied for solar projects. Because of the possible variations between the spectral response of different pyranometers of the same model, using separate calibration constants for at least two of the three components (GHI, DHI, and DNI) is recommended; however, some RSI calibration methods include only GHI calibration. The current best practice is to consider a long enough calibration period to include the wide variety of meteorological conditions that are expected at the site where the RSI is planned to be used. Such conditions should be assessed and characterized wisely during the calibration process. The calibration accuracy generally improves when the atmospheric conditions during the calibration closely represent those at the site where the RSI is intended to be operated later, though in reality such conditions will be highly variable. In addition to cloud cover, the effects of aerosols, water vapor, and site altitude on the solar spectrum must be considered (Myers 2011; Wilbert et al. 2016). Calibrations with artificial radiation sources that lack the spectral power distributions of natural solar radiation components usually also lack the variety of natural irradiation conditions; therefore, field calibrations under natural irradiation conditions should yield more accurate calibrations and are thus preferable.

Outdoor RSI calibrations are performed at only a few laboratories, such as the National Renewable Energy Laboratory (NREL), in Golden, Colorado; and DLR at CIEMAT's (Centro de Investigaciones Energéticas, Medioambientales y Tecnológicas) Plataforma Solar de Almería in Spain. Additionally, on-site calibrations are performed by a few specialized

companies. At the Plataforma Solar de Almería, for instance, RSIs are operated parallel to ISO-9060 Class-A pyrheliometers and pyranometers under real-sky conditions (Figure 3-17). The duration of RSI calibrations is from several hours to more than 1 year. These longer calibration periods provide a database for the analysis of systematic signal deviations and measurement accuracy. An analysis of the dependence of the calibration constants on the duration of the calibration period, as well as more details on two possible calibration methods, are presented in Jessen et al. (2016) and Geuder, Affolter, and Kraas (2012). Data quality is analyzed and compared to the reference irradiances. RSI calibrations are performed according to the different methods described. All published calibration techniques are based on the comparison of corrected RSI signals (using the existing correction functions described) to reference irradiance measurements obtained with thermopile sensors.

Depending on the calibration method, one, two, or even three calibration constants are defined. The motivation for determining one calibration constant is that only one pyranometer is used and the calibration based on GHI is less time-consuming than performing separate calibrations for GHI, DHI, and DNI. Because of the Si detector's spectral response, the spectral sensitivities for DHI, GHI, and DNI are not the same; hence, the application of two or three calibration constants is physically reasonable, even though only one sensor is used.

Examples of drift in the GHI calibration constants obtained from Geuder et al. (2008) were later investigated for nine sensors in Geuder et al. (2016) and Jessen et al. (2016). For recalibration periods from 2–3.75 years, changes in this GHI calibration constant were less than 1% in most cases. Recalibration is recommended at least every 2 years. An overview of current RSI calibration methods is presented in Jessen et al. (2016), and more details can be found in Geuder et al. (2008, 2016) and Kern (2010). A case study for the accuracy achievable by different combinations of correction functions and calibration methods is summarized in Chapter 7.

The calibration techniques for RSIs can be partially used for other solid-state radiometers. Further details on RSIs and RSI-specific measurement best practices can be found in Wilbert et al. (2015).

Figure 3-17. RSI calibration station at CIEMAT's Plataforma Solar de Almería. Photo by DLR

3.2.5.4 Other Instruments Used to Derive Diffuse Horizontal Irradiance and Direct Normal Irradiance

In addition to the radiometers described above, other instruments can be used to derive DHI or DNI from irradiance measurements. For example, the scanning pyrheliometer/pyranometer (Bergholter and Dehne 1994, 245ff) or the sunshine duration sensor Soni e3 (Lindner 1984) can be used to derive DNI; however, these two sensors reach only lower accuracies than tracked pyrheliometers, thermopile pyranometers with shading balls, or even RSIs, as documented in Geuder et al. (2006). Note that researchers have developed methods for estimating daily integrated values of DNI from the vast archive of measurements from Campbell-Stokes sunshine recorders (Stanhill 1998; Painter 1981).

Another option for DNI measurements without tracking is the EKO MS-90 instrument (Figure 3-18), which is based on an earlier sunshine recorder sensor (MS-093). The revised design uses a rotating mirror within a fixed glass tube tilted to latitude (–58° to +58°). The mirror reflects the direct beam onto a broadband pyroelectric detector that senses DNI four times per minute. Preliminary tests were conducted against a reference pyrheliometer (EKO MS-57) during the North American Pyrheliometer Comparison held at NREL in September 2016. The tests showed rather small deviations for a simple nontracking instrument when DNI exceeds 600 W/m^2.

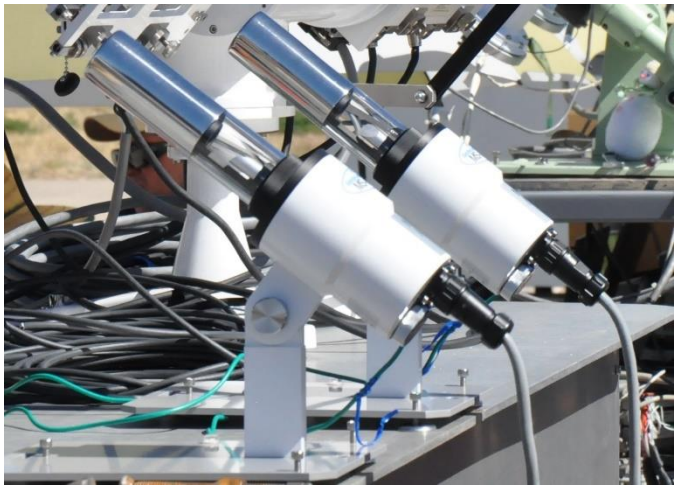

Figure 3-18. EKO MS-90. ***Image by NREL***

Recently, all-sky imagers have also been used to measure solar irradiance (Kurtz and Kleissl 2017). The accuracy of such measurements alone is still too low for their application in resource assessment. All-sky imagers are so far mainly of interest for forecasting applications; hence, these instruments are further discussed in Chapter 8, Section 8.2.11. Another option for estimating DNI from measurements of both DHI and GHI by a single instrument is the SPN1 (Figure 3-19). The SPN1 consists of an array of seven fast-response thermopile radiation detectors that are distributed in a hexagonal pattern under a glass dome. The detectors are positioned under diffuser disks and a special hemispherical shadow mask. The shape of the mask is selected such that for any position of the sun in the sky there is always one or more detectors that are fully shaded from the sun and exposed to approximately half the diffuse radiance (for completely overcast skies). Also, one or more detectors are exposed to the full solar beam for all positions. The minimum and the maximum readings of the seven detectors are used to derive GHI and DHI.

Figure 3-19. Delta-T Devices, Ltd., SPN1. ***Image by NREL***

With this principle of operation, GHI, DHI, and DNI can be derived without any moving parts and without needing alignment other than horizontal leveling. Further, the SPN1's low power demand (the temperature-controlled dome prevents dew and frost) increases its suitability for operation in remote sites compared to DNI or DHI measurements involving solar trackers. Test results indicate that the accuracy of the SPN1's GHI is comparable with RSIs, but its DNI and DHI readings have higher errors than the DNI measured with RSIs (Vuilleumier et al. 2012). Further, SPN1 performance results obtained at six different locations worldwide

can be found in Badosa et al. (2014). An additional comparison with traditional radiometers is presented by Habte et al. (2016).

3.2.6 Photovoltaic Reference Cells for Outdoor Use

The photodiode detectors in the photoelectric pyranometers that are discussed are essentially tiny PV cells, usually only several square millimeters, and their operating principle is identical to the larger cells used in PV modules and PV power plants. The larger cells can also be used as radiometer elements, and when they are mounted in a suitable enclosure for measurement purposes, they are referred to as PV reference cells. Commercial products in this category are quite diverse, as shown in Figure 3-20. Their active cell area ranges from approximately 4–225 cm^2 (from left to right).

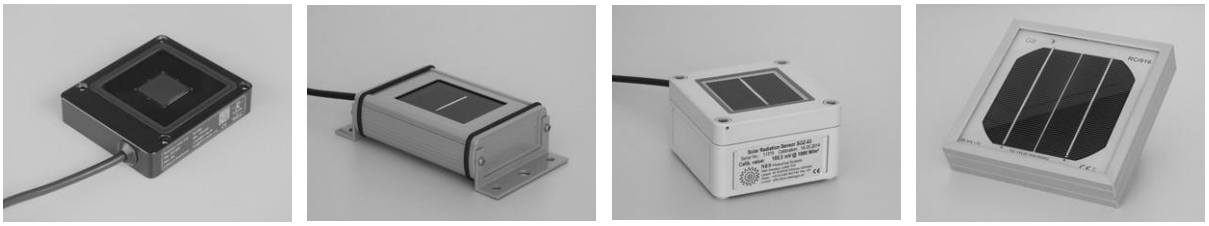

Figure 3-20. A variety of commercial outdoor PV reference cells.
Photos by PV Performance Labs

Although they can be physically diverse, PV reference cells share four main characteristics:

1. The output signal is proportional to the short-circuit current of the detector PV cell, and it is usually the voltage measured across an internal shunt resistor. The cell does not produce electrical power in this configuration, but the measured short-circuit current represents the amount of radiation that could be converted to electric power.
2. The detector PV cells are protected by a flat, transparent window, which leads to reflections at the air-window interface and consequently lower irradiance readings for beam radiation coming at higher angles of incidence. This would be considered a very poor directional response by the definition of the pyranometer classes, but it allows the reference cell readings to more closely track the power output of a PV plant—especially when the window material matches the glass used in the plant's PV modules. Figure 3-21 shows the variations in the angular response from the four commercial reference cells.
3. Like photodiode pyranometers, the spectral response of PV reference cells is narrow and nonuniform (Figure 3-22). This leads to a high spectral error according to the terms of the pyranometer classification, but, again, it allows the reference cells to track the PV plant output more closely. This works best when the technology of the reference cell—and hence its spectral response—matches that of the modules in the PV plant. In some reference cells, a filter glass is used to absorb some of the near-infrared light before it reaches the silicon detector (PV cell), thereby creating an overall spectral response that more closely matches another cell type, such as amorphous silicon or cadmium telluride.

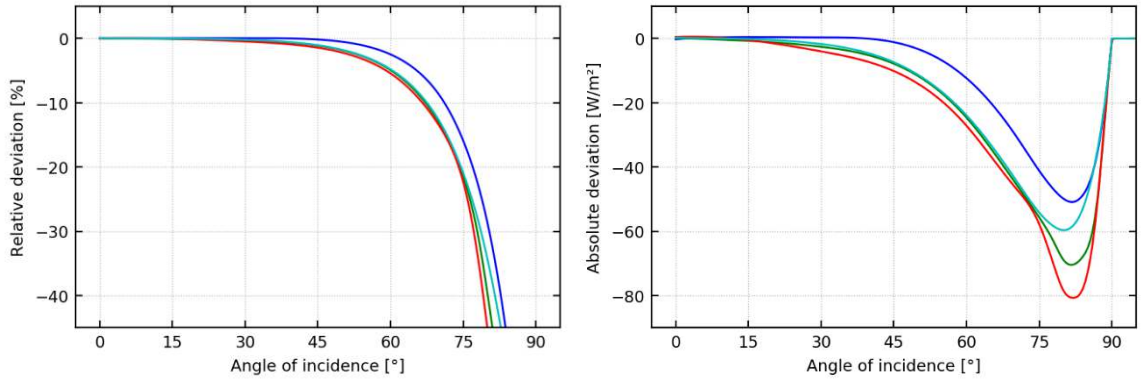

Figure 3-21. Deviations of directional response for four commercial reference cells relative to ideal cosine response. *Measurements and graphics courtesy of Anton Driesse, PV Performance Labs*

4. In practice, the output signal has a pronounced positive temperature dependency. This dependency is primarily a by-product of the spectral response and therefore varies by technology (it is approximately 400–500 ppm/K for crystalline silicon cells); however, it is not the same as the effect of temperature on PV module power output, which decreases with temperature. Reference cell products nearly always include a temperature sensor, and they could offer temperature-corrected or uncorrected irradiance signals as output.

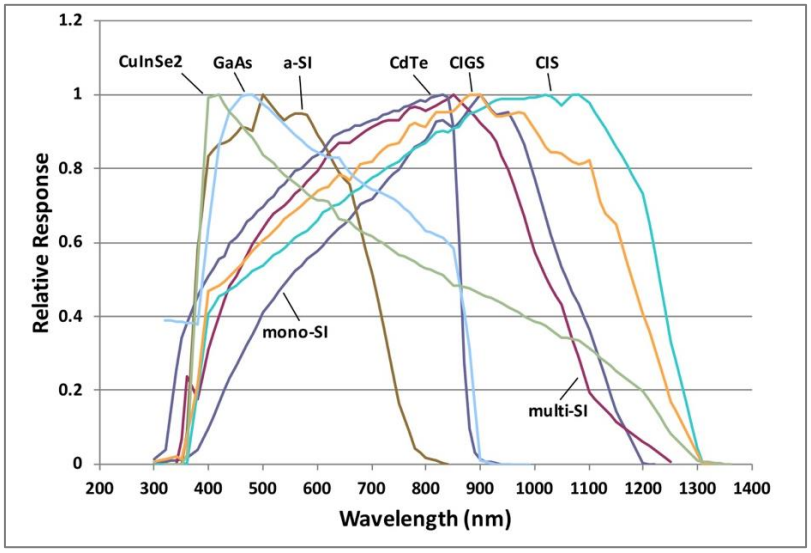

Figure 3-22. Spectral response functions for selected PV materials. *Image courtesy of Chris Gueymard*

Note that this handbook focuses on PV reference cells designed for long-term continuous outdoor measurements. Products outside this category could differ substantially—for example, certain reference cells for indoor use only do not have a protective window. It is also possible to use a regular full-sized PV module as a radiometer by measuring its short-circuit current; however, this is also out of scope.

It is clear from these descriptions that reference cells are fundamentally different from the other types of radiometers discussed in this handbook. These differences are not intrinsically good or bad, but rather they influence which type of radiometer is best suited for a given measurement objective. PV reference cells are not intended to measure broadband hemispherical irradiance; in fact, some product designs would collect water when mounted

horizontally, thus yielding large errors. If a low-cost substitute for a thermopile pyranometer is needed, a photodiode pyranometer is a usually better choice.

3.2.6.1 Standardization of Photovoltaic Reference Cells

Because of their measurement characteristics, reference cells are not consistent with ISO or WMO pyranometer classifications (ISO 2018; WMO 2018). Although many standards apply to PV reference cells directly or indirectly, there is no standard akin to ISO 9060 that would describe precisely and completely how reference cells should behave. In other words, there exists a definition of an ideal pyranometer but not of an ideal reference cell. Nevertheless, IEC 60904-2:2015 – Part 2 (IEC 2015) provides many useful requirements (e.g., linearity better than 0.5% and acceptance angle >160°) and recommendations for reference devices ranging from single cells to whole modules. One of the most important aspects of this standard is the extensive documentation requirement, which states that calibration reports must include spectral responsivity, temperature coefficient, and many other details about the device itself as well as the calibration method and equipment used. Currently, most manufacturers of PV reference cells for outdoor use do not claim to apply this standard.

There is also a de facto World Photovoltaic Scale (WPVS) reference cell standard. This was first established in 1997 by a group of laboratories seeking to establish a reference scale similar to the WRR (Osterwald et al. 1999). WPVS cells conform to IEC 60904-2 and fulfill several very specific additional design criteria (e.g., physical dimensions and connections) that improve long-term stability and repeatability of measurements. Their high cost is more easily justified in a laboratory setting than for fieldwork; nevertheless, outdoor versions of WPVS cells are available.

3.2.6.2 Calibration of Photovoltaic Reference Cells

The responsivity of PV reference cells varies with wavelength, intensity and direction of the incident light, and the temperature of the cell. The calibration value is the response of the device (usually a value in millivolts) under a precisely defined spectral irradiance: the AM1.5 global spectrum (IEC 60904-3, IEC (2019a)) with irradiance 1000 W/m^2; and with a device temperature of 25°C. Combined, these conditions are referred to as the standard test conditions (STC), which apply equally to PV module ratings. Reference cell response is normally linear with irradiance; therefore, the value of the response under STC is equal to the responsivity of the device in mV per 1000 W/m^2 or µV/(W/m^2).

IEC 60904-4:2019 – Part 4 (IEC 2019b) describes four different methods to perform the calibration of primary reference devices with traceability to SI units, so the relationship of reference cells to broadband radiometers is well defined. All these methods consider the narrow spectral response of PV devices by calculating a spectral mismatch factor, which compensates for the fact that the light used during calibration does not normally correspond precisely to the AM1.5 global reference spectrum.

IEC 60904-2:2019 – Part 2 describes how secondary or field reference cells can be subsequently calibrated by comparison to a primary reference device using either natural or simulated sunlight. When the spectral response of the primary reference cell is the same as that of the cell being calibrated, there is no spectral mismatch to be considered.

Primary reference cells are usually calibrated at precisely 25°C so that no temperature correction is required, and when identical devices are used for secondary or field calibrations, the effect of temperature cancels out. When there are differences in devices or device temperatures, however, a correction must be done as part of the calibration. Measurement procedures to determine the temperature coefficient are covered by IEC 60891 (IEC 2009); essentially, they consist of measuring the response over a range of temperatures and determining the slope of a linear fit.

In all calibration situations, the direction of the incident light is predominantly normal to the plane of the cell, implying little or no diffuse irradiance. This minimizes the influence of the directional dependence, but in recent work this aspect has been analyzed more comprehensively, and the use of an angular mismatch factor has been proposed to further improve calibration consistency (Plag et al. 2018).

In the context of calibrations, any adjustments for temperature, spectrum, or direction tend to be small compared to the effects of temperature, spectrum, and direction on field measurements.

3.2.6.3 Deployment Considerations

Because of the four distinct characteristics of PV reference cells, the natural place to deploy them would be in the context of PV projects. The benefit of the application of reference cells in solar resource assessment depends on the technology and the project phase. The benefits of reference cells for a resource assessment before the power plant construction are different from those for PV plant monitoring. The similarity of a PV reference cell to a specific PV technology can be of advantage if this PV technology is used, but other PV technologies will require a different reference cell, and solar thermal systems will require broadband measurements.

For planning large power plants, satellite data sets are adapted to the site using ground measurements to achieve the required high accuracy (see also Chapter 4 and Chapter 9). Traditionally, the available irradiance data were broadband and collected using pyranometers, pyrheliometers, RSIs, or other devices, as described; hence, only broadband irradiance is provided by most satellite data sets, and broadband ground measurements are required for their validation and site adaptation. Only a few satellite-derived data sets include spectral data (Müller et al. 2012; Xie and Sengupta 2018), and such data are not available for the full globe.

Another application of ground measurements collected before the plant construction is PV plant modeling. PV power plant models include effects such as reflectance losses and spectral mismatches to derive the power output from the broadband irradiance. Modeling these effects is related to additional errors, and the reference cells could offer an attractive alternative: If irradiance is measured under a flat glass cover, the reflectance losses do not need to be modeled; and if the irradiance measurement is already weighted by the spectral response of the reference cell, then no spectral correction model is required. In other words, if a PV reference cell is used, then the expected PV system output can be calculated with substantially fewer modeled steps, avoiding the uncertainty those would contribute; therefore, including a tilted reference cell in a ground measurement station is of interest before the plant construction. One drawback for the use of reference cells before actual plant construction is that the exact technology that will be used in the power plant might not be known at the beginning of the measurement campaign. Deviations among the temperature, incidence angle, and spectral effects of different PV products could be bigger than the uncertainty of the PV simulation models for these effects; hence, different reference cells should be used if the PV technology has not been selected before a measurement campaign. Another important limiting factor for the application of reference cells for PV system modeling is the available software used for PV yield simulations. Most do not accommodate selectively bypassing certain model calculation steps, which would be required for adequate use of PV reference cell irradiance measurements. If such a limited software is used, it imposes to some extent the use of a broadband pyranometer.

For PV monitoring, the advantages of PV reference cells are already much clearer, even without significant further research and development. The described accuracy enhancement is of great interest for PV monitoring and capacity testing. The limitation due to the PV

system modeling tools also affects this application if a model using pyranometer-based GTI measurement is contracted for the monitoring; however, PV models used for PV monitoring or capacity testing more frequently allow the application of reference cell measurements as input than models used before the PV plant is built. Moreover, measurements with both pyranometers and reference cells are of interest. In the case of bifacial PV modules, spectrally matched reference cells are also an option to measure the required rear-side irradiance. To measure the rear-side irradiance, the reference cells are mounted on the module racking with an adequate support structure so that they are exposed as similarly as possible as the modules. End row effects are avoided and depending on the size of the PV plant and the variation of the ground and shading properties, several sensors must be used.

To conclude, PV reference cells can be a helpful source of solar resource data, especially for PV monitoring, but currently they cannot replace broadband measurements in the context of general solar resource assessments. It is possible, however, that new, improved resource assessment methods will evolve that are specialized for PV applications and rely primarily on PV reference cells.

General considerations for the instrument selection and the selection of the radiation components that should be measured are presented in Section 3.3.5.

3.2.6.4 Recent and Ongoing Research

The key to the effective use of PV reference cells is to understand their special characteristics and to apply that knowledge when collecting, interpreting, and using the data they produce. One active area of research is to quantify these characteristics for product categories, product models, and individual instruments (see Figure 3-23) (Driesse et al. 2015; Vignola et al. 2018). Directly related to this are studies attempting to apply this knowledge of characteristics to instrument calibration, uncertainty analysis, and modeling (Driesse and Stein 2017).

Although complete knowledge of PV reference cell characteristics is desirable, it is not always practical to acquire and use it, even if it is available. Parallel and complementary efforts are underway to promote increased homogeneity and further standardization (Habte et al. 2018). Future editions of this handbook will expand on these and other topics related to PV reference cells.

Figure 3-23. Test facility to quantify PV reference cell characteristics and compare them with other types of radiometers. *Photo by PV Performance Labs*

3.3 Measurement Station Design Considerations

To collect useful solar resource data, the successful design and implementation of a solar resource measurement station or a network of stations requires careful consideration of the elements summarized in this section. The measurement stations also include additional meteorological instrumentation, such as anemometers, wind vanes, thermometers, and hygrometers. These measurements are described in Chapter 5. The general

recommendations—such as station security and data logging—described in this section also apply to these instruments.

3.3.1 Location

The primary purpose of setting up a solar resource measurement station before the construction of a solar power plant is to collect data that will ultimately allow an analyst to accurately characterize the solar irradiance and relevant meteorological parameters at that specific location. Ideally, the instruments would be within the targeted analysis area. In some cases, however, separation distances might be tolerated depending on the complexities of local climate and terrain variations. Less variability in terrain and climate generally translates to less variability in the solar resource over larger spatial scales. These effects should be well understood before determining the final location of a measurement station. (See Chapter 9 for more discussion of the effect of distance between the station and plant site.) The proximity to the target area must be weighed against operational factors, such as the availability of power, communications, and access for maintenance, as discussed in this chapter. Considerations should also include the possible effects of local sources of pollution or dust—for example, traffic on a nearby dirt road that could impact the measurements.

Solar radiation measurements are also required for medium or large power plants (see Chapter 9). Further, measurements can be helpful for other solar energy purposes, such as testing power plant components or for PV power forecasting for many small PV systems. In power plants and for component or system tests, the position of the station must be such that the measurements reflect the conditions of the power system as well as possible. In large power plants, this means that several distributed stations can be required. For PV systems, IEC 61724-1:2017 defines the number of required radiometers within the PV power plant depending on the system's peak power.

When measurement stations are constructed in metropolitan areas, industrial areas, or near electrical substations or solar power plants, consideration should be given to possible sources of radio frequency signals and electromagnetic interference that could impart unwanted noise in sensors or cables. For example, the same high building that could provide an attractive unobstructed site for solar measurements could also be the ideal location for radio or television broadcast towers or some other apparatus. Such sites should be investigated for interference with the irradiance sensors and monitoring station. See Section 3.3.4 for additional information regarding proper shielding and grounding.

Instrument placement is also an important consideration. If nearby objects—such as trees or buildings—shade the instruments for some period during the day, the resulting measurement will not truly represent the available solar resource in a nearby unshaded part of the site. Distant objects—especially mountains—could be legitimate obstructions because the shadows they cast are likely to produce an influence beyond the area local to the instruments. Conversely, nearby objects can potentially reflect solar radiation onto the instruments, resulting in measurements that do not represent the conditions for the power plant. Such cases could include a nearby wall, window, or other highly reflective object. The best practice is to locate instruments far from any objects that are in view of the instrument detector. The recommendations from WMO (2018) for radiation apply, if not mentioned otherwise.

The easiest way to determine the quality of solar access is to scan the horizon for a full 360° of azimuth and note the elevation of any objects protruding into the sky above the local horizon. Look for buildings, trees, antennae, power poles, and even power lines. Most locations will have some obstructions, but whether they will be significant in the context of the necessary measurements must be determined. Camera-based devices can be used to assess any obstructions including far shading from mountains, trees, etc., and the

assessment can be easily documented and quantified, such as seasonal shade effects. Generally, pyranometers are insensitive to sky blockage within approximately 5° elevation above the horizon. Pyrheliometers, however, are more sensitive because objects can completely block DNI, depending on the daily path of the sun throughout the year. The duration and amount of daily blockage are related to the object's width and height above the horizon. On an annual basis, the number of blockage days depends on where along the horizon the object lies. To be a concern, the object must be in the area of the sun near sunrise or sunset, the time and azimuth of which vary throughout the year. For most of the horizon, objects blocking the sky will not be a factor because the sun rises in a limited angular range in the east and sets likewise in the west during sunset (e.g., at 40° N latitude, sunrise occurs approximately 60° from true north at the summer solstice and 120° from true north at the winter solstice). The farther north in latitude the site is located, however, the greater the angular range of these sunrise and sunset areas of interest. A solar horizon map, or even a sketch of obstructions by elevation and azimuth, will help determine the areas where horizon objects will affect the measurement (see Figure 2-5). Such maps can be created with digital cameras and software. Several commercial products using curved mirrors and also apps for smartphones exist.

Considerations for locating a station should also include environmental factors, such as wildlife habitat, migratory paths, drainage, and antiquities or archeological areas.

3.3.2 Station Security and Accessibility

Measurement stations can cost tens of thousands or even hundreds of thousands of dollars. Although this equipment is typically not the target of thieves seeking property for resale, it is still subject to theft and should be protected. Vandalism might be even more likely than theft. The less visible and accessible the station is to the public, the less likely it will be the target of theft or vandalism. For example, instruments mounted on a rooftop are less likely to attract unwanted attention than those unprotected beside a highway. Lack of visibility is the best defense against vandalism.

Security fences should be used if people or animals are likely to intrude. Within a fenced solar power plant, no additional fences are required. Fencing should be at least 1.8-m tall, preferably with barbed wire and fitted with locking gates in high-profile areas where intrusion attempts are likely. Less elaborate fences might suffice in areas that are generally secure and where only the curious need to be discouraged from meddling with the equipment. In remote venues with few human hazards, cattle fence paneling (approximately 1.2-m tall) might be advisable if large animals roam the area. The fencing should be sturdy enough to withstand the weight of a large animal that might rub against the compound or otherwise be pushed or fall against the fence. It might not be possible to keep smaller animals out of the station compound, and precautions should be taken to ensure that the equipment, cabling, and supports can withstand encounters with these animals. Rodents, birds, and other wildlife could move through the wires or jump over or burrow under fences. Signal cabling between modules or sensors at or near ground level is prone to gnawing by rodents and should be run through a protective conduit or buried. Any buried cable should be either specified for use underground or run through conduit approved for underground use. Underground utilities and other objects should be investigated before postholes are dug or anchors are sunk.

If fences are used, they must be considered a potential obstacle that could shade the instruments or reflect radiation to the instruments. The radiometers should be positioned at least above the line between the horizon and the fence (including barbed wire), if only by a few millimeters, to prevent any shading of the sensor. This assumes that the pyranometer is mounted in a horizontal position and that the pyrheliometer is installed on a solar tracker.

Tilted pyranometers should have an unobstructed view of the ground and sky in front of them. For albedo measurements, fences cause measurement errors if the area under the downward-facing pyranometer is shaded (see also Chapter 5, Section 5.11). This must be considered for the station design. The recommendations from WMO (2018) concerning obstacles should be followed. Deviations between WMO (2018) and the actual station design are acceptable if these deviations affect not only the measurement station but also the solar energy system that is analyzed using the measurements. If nearby towers are unavoidable, the station should be positioned between the tower and the equator (e.g., to the south of the tower in the northern hemisphere) to minimize shading. The radiometers should be positioned as far as possible from the tower—at least several meters—so the tower blocks as little of the sky as possible. Nevertheless, radiometer signal cables should be shorter than 50 m to avoid losses caused by line resistance. The tower should also be painted a neutral gray to minimize strong reflections that could contaminate the solar measurement. These guidelines assume that the tower is part of the measurement station proper and that the site operator has control of the placement or modification of the tower. Without that control, the radiometers should be placed as far as possible from the tower.

Access to the equipment must also be part of a station's construction plan. Because routine maintenance is a primary factor affecting data quality, provisions must be made for reasonable and easy access to the instruments. Factors here could include ease of access to cross-locked property, well-maintained all-weather roads, and roof access that could be controlled by other departments. Safety must also be a consideration. Locations that present hazardous conditions—such as rooftops without railings or that require access using unanchored ladders—must be avoided.

3.3.3 Power Requirements

Ongoing measurements require a reliable source of electrical power to minimize system downtime from power outages. In some areas, power from the utility grid is reliable, and downtime is measured in minutes per year. In other areas, multiple daily power interruptions are routine. Depending on the tolerance of the required analysis to missing data, precautions should be taken to ensure that gaps in the data stream from power outages do not seriously affect the results. The most common and cost-effective bridge for power outages is an uninterruptible power supply (UPS). The UPS can also filter out unwanted or harmful line voltage fluctuations that can occur for a variety of reasons. It has internal storage batteries that are used as a source of power in case of an AC power interruption. When the AC power is interrupted, internal circuitry makes an almost seamless switch from grid-connected AC power to AC provided through an inverter connected to the battery bank. When power is restored, the UPS recharges the internal battery from the AC line power. Power loss is detected quickly, as is switching to the battery, and it is measured in milliseconds or partial line cycles. Some equipment could be particularly susceptible to even millisecond power interruptions during switching and should be identified through trial and error to avert unexpected downtime despite use of the UPS.

The UPS is sized according to:

- Operating power: How much can it continuously supply either on or off grid-connected AC power?
- Operating capacity: How long can the UPS supply power if the grid connection is interrupted?

Users should estimate the longest occurring power outage and size the UPS for the maximum load of attached devices and the maximum period of battery capacity. Batteries should be tested regularly to ensure that the device can still operate per design

specifications. This is most important in hot areas (such as deserts) because batteries could overheat and become inoperative (temporarily or permanently). Internal battery test functions sometimes report errors only when batteries are near complete failure and not when performance has degraded. A timed full-power-off test should be conducted periodically to ensure that the UPS will provide backup power for the time needed to prevent measurement system failure.

In remote locations where utility power is not available, local power generation with battery storage should be devised. Options for on-site electrical power generation include PV or small wind turbine systems (or both) and gasoline- or diesel-fueled generators. The renewable energy systems should be sized to provide enough energy for the maximum continuous load and power through several days of adverse conditions (cloudy weather and/or low wind speeds). This includes sites prone to persistent surface fog. The sizing is a function of the extremes of the solar climate and should consider the longest gap during reduced generation, the shortest recharge period available after discharge, and the generation capacity and storage necessary to provide uninterrupted power for the target location. Some oversizing is necessary to accommodate degradation of PV panels and battery storage, and consideration should be given to ambient temperature, which affects the ability of a battery to deliver energy. Sizing calculators are available to help with this effort.[7]

Equipment should be specified and tested for self-power-on capability in the event of a power outage. This ensures that when power is restored, the equipment will automatically resume measurements and logging without operator intervention. This is an important consideration for remote locations where considerable downtime might occur before personnel can be dispatched to restart a system.

3.3.4 Grounding and Shielding

Station equipment should be protected against lightning strikes and shielded from radio frequency interference that could damage equipment or reduce the validity of the measurements. Several references are available that describe techniques for grounding and shielding low-voltage signal cables (see, e.g., Morrison 1998). Those designing solar resource measurement systems are urged to consult these references and seek expert technical advice. If digital sensors with onboard analog-to-digital converters are used, their sensitivity to transients, surges, and ground potential rise must be considered; therefore, the power and communications lines should be isolated and surge protected with physical isolation, surge protection devices, or other equivalent technology.

In general, the following steps should be taken when designing and constructing a measurement station:

1. Use a single-point ground (e.g., a copper rod driven several feet into the ground) for all signal ground connections to prevent ground loops that can introduce noise or biases in the measurements.
2. Use twisted pair, shielded cables for low-voltage measurements connected as double- ended measurements at the data logger. Double-ended measurements require separate logger channels for + and – signal input conductors. These inputs are compared to each other; therefore, the possibilities for electrical noise introduced in the signal cable are significantly reduced.

[7] See http://pvwatts.nrel.gov/.

3. Physically isolate low-voltage sensor cables from nearby sources of electrical noise, such as power cables. Do not run signal cables in the same bundle or conduit as AC power cables. If a power cable must cross a signal cable, always position the two at right angles to each other. This case is not recommended, but this limited contact will minimize the possibility of induced voltages in the signal cable. Also, the data logger settings should be selected to avoid signal noise (the integration time of the voltage measurement adjusted to AC frequency).
4. Connect metal structures such as masts and tripods to the ground to provide an easy path to the ground in the event of a lightning strike. This will help protect sensitive instruments. Electronic equipment often has a special ground lug and associated internal protection to help protect against stray voltages from lighting strikes. These should be connected with a heavy gauge wire to ground (12 American wire gauge or larger). Metal oxide varistors, avalanche diodes, or gas tubes can be used to protect signal cables from electrical surges such as lightning. These devices must be replaced periodically to maintain effectiveness. The replacement frequency is a function of the accumulated energy dissipated by the unit. The U.S. National Electric Code recommends a ground resistance of less than 5 Ohms for “sensitive” electronic equipment. If that cannot be met with one rod, multiple rods should be used and bonded together. Ground resistance should be measured with a ground resistance tester using the three-pin or four-pin method.

3.3.5 Measurement and Instrument Selection

From among the descriptions, the station designers should choose the instrumentation and the radiation components that will best support the data and uncertainty goals of the project. As discussed, station designers must consider not only the accuracy under optimum maintenance conditions but also the expected accuracy for the likely maintenance conditions. Depending on the project phase, different instruments could be used.

Before constructing large power plants, radiation measurements are used mainly to enhance the accuracy of satellite-derived long-term data sets with different site adaptation methods (see Chapter 4, Section 4.8). For concentrating technologies, only the DNI resource is ultimately of interest, and hence in principle only a pyrheliometer would be needed. This minimalist setup is not recommended, however, because the best data quality control methods rely on the independent measurement of the three radiation components (see Section 3.4.2). For fixed non-concentrating techniques, such as most PV plants, measuring GHI would be the minimal option because long-term GHI data can be site-adapted with the GHI measurement and then converted to POA with decomposition and transposition models. Measuring only GTI on a tilt corresponding to the anticipated POA is not advisable because long-term data sets typically do not provide GTI and because site adaptation methods have only been developed for DNI, GHI, and DHI. Although such minimalistic measurement setups with only one instrument might seem sufficient at first, it is advantageous and hence common to measure further radiation components or to include redundant sensors for the same component. There are several reasons for this. Measuring multiple radiation components in one station increases the accuracy of yield predictions, improves the detection of measurement errors, and gives more flexibility regarding the selection of the power plant technology.

The accuracy of PV yield calculations can be increased by measuring not only GHI but also DNI or DHI. Transposition models used to derive GTI from GHI and DNI are much more accurate than decomposition and transposition models that derive GTI from GHI alone (see Chapter 2, Section 2.7.4). With only the DNI or DHI measurement available at a site, the DNI satellite data can be enhanced with the ground measurements. For more detailed PV system simulations, ground measurements are helpful as direct input. With GHI and DNI data, the

PV simulations are more accurate because one can consider that mainly the direct component is affected by incidence angle and shading.

Additional GTI measurements are advantageous for resource assessment because they can be used to select the best transposition (or decomposition and transposition) model for the site. One must consider that the best transposition (and decomposition) model for open field measurements, however, might not be the best option once the plant is built because the modules affect the incoming radiance distribution. GTI measurements are more accurate than modeled GTI and can be used as direct input for detailed PV modeling. One complication for GTI measurements is selecting the right orientation and tilt of the POA pyranometer before starting the measurement campaign. The optimal orientation depends on the latitude, the meteorological conditions at the site, the shading effects, and the electricity market, among others. Tracked POA measurements might also be of interest, and deploying reference cells should also be considered (Section 3.2.6.3). Reference cells can be valuable for such additional measurements.

A further advantage of radiometers is related to the quality control of the data and to the detection of errors. If global, direct, and diffuse irradiance are known, it is possible—though not advisable—to measure two of the three because the third parameter can be calculated from the other two. The most accurate installations include all three components. This provides not only redundancy in case of instrument failure but also—and more importantly—the basis for the most rigorous data quality protocols, as described in Section 3.4.2. Also, redundant measurements of the same radiation component can be of interest to avoid data gaps and increase accuracy.

Measuring the three radiation components with a solar tracker, a pyrheliometer, a pyranometer, and a shaded pyranometer induces a significant maintenance effort. Without trained personnel providing daily cleaning and prompt corrections in case of tracker or alignment errors, data gaps and increased uncertainties are common. Measurements of DNI or DHI, however, in addition to that of GHI, are recommended for both tracked and fixed utility-scale PV projects and of course also for concentrating collectors; therefore, simple, more robust instruments, such as RSIs (section 3.2.5), at times in combination with a thermopile pyranometer, can be a better option to determine the three radiation components. In this case, only a less effective quality control, as in the case of measurements with two radiometers (e.g., GHI and DNI), is possible because of the principle of operation of these radiometers.

The third main advantage of measuring several radiation components is the increase in flexibility for the selection of the solar technology. The exact technology option or mix might not be selected at the start of the measurement campaign. Depending on the site conditions, tracked PV could be an advantage over fixed PV. If tracked PV is used, DNI measurements are more important than they are for fixed PV systems. A concentrating solar power (CSP) project could be less adequate than PV for a specific site—for example, because of higher than expected aerosol load, which reduces DNI much more than GTI. If PV is selected instead of CSP, GTI must be measured or modeled.

Additional radiometers add to the instrumentation budget, but when considering the overall costs of acquiring the property, building the infrastructure, providing long-term labor for O&M, and underwriting the resources required for processing and archiving, the added cost is nominal, and its inclusion will likely pay off with a valuable dimension of credibility for the project and the associated reduced financing costs.

To operate solar power plants, different measurements are required. For PV, the International Electrotechnical Commission (IEC) standard 61724-1 (IEC 2017) defines the parameters to be measured for PV monitoring. GTI and GHI measurements are required for

the highest accuracy level defined in the standard. Depending on the peak power of the PV system, different numbers of sensors of the same type are required. The IEC standard also defines the instrument types allowed in the classes. PV monitoring Class A systems use the highest ISO 9060 class pyranometers or reference cells with low uncertainty. For PV monitoring Class B systems, less accurate pyranometers and reference cells are allowed. Class B can be of interest for small- or medium-size power plants. For bifacial PV systems, rear-side irradiance and/or albedo (see section 5.11 (Chapter 5)) must also be measured, according to a revision of the standard that is currently under preparation. For CSP, no standard is available that defines the instrumentation that should be used at the power plant; however, virtually all CSP plants use ISO 9060 Class-A pyrheliometers to measure DNI. GHI and DHI are not specifically mentioned, but this is a disadvantage because of the reduced ability to quality-control the radiation measurements. At present, there is no consensus on the required number of DNI measurements per CSP plant. In some instances, only one pyrheliometer is used; whereas in other plants, four or more DNI measurements are taken.

Apart from the radiation measurements, other meteorological parameters are required for resource assessment and during the operation of a solar power plant. These parameters and the corresponding instruments are discussed in Chapter 5.

3.3.6 Data Loggers

Most radiometers output a voltage, current, or resistance that is measured by the data logger, which comprises a voltmeter, ammeter, and/or ohmmeter. The measured output value is subsequently converted to the units of the measurand through a multiplier and/or an offset determined by calibration to a recognized measurement standard.

Data loggers should be chosen to have a very small measurement uncertainty, perhaps 3–10 times smaller than the estimated measurement uncertainty associated with the radiometer. This is the accuracy ratio between the data logger and the radiometer. For example, typical specifications for a good data logger measuring a 10-mV output from the radiometer accurate to 1%, or 0.1 mV (100 µV), are on the order of total uncertainty (accuracy) of better than (less than) 0.1% of reading (or full scale) for the parameter in question, which would be 0.010 mV, or 10 µV.

The logger should also have a measurement range that can cover the signal at near full scale to best capture the resolution of the data. For example, a sensor with a full-scale output of 10 mV should be connected to a logger with a range that is at least 10 mV. A logger with a 1-V range might be able to measure 10 mV but not with the desired accuracy and resolution. Most modern data loggers have several range selections, allowing the user to optimize the match for each instrument. Because of the nature of solar radiation, radiometers (e.g., pyranometers used for GHI measurements) can sometimes produce 200% or more of clear-sky readings under certain passing cloud enhancement conditions, and the logger range should be set to prevent over-ranging during these sky conditions. The absolute GHI limit that can be reached during cloud-enhancement situations is a decreasing function of the measurement time step, but this can be misleading. At a 1-minute resolution, a safe limit seems to be 1800 W/m^2, but it could reach 2000 W/m^2 or more at a 1-second resolution with photodiode radiometers. Because the data logger measures near-instantaneous values regardless of its averaging or recording time step, the range should be set to accommodate the higher values described. See Gueymard (2017a, 2017b) for more details.

Some radiometers use amplifiers to increase the instrument output to a higher range to better satisfy signal range matching requirements; however, such amplifiers will add system complexity and some uncertainty to the data with nonlinearity, noise, temperature dependence, or instability. High-quality amplifiers could minimize these effects and allow a

reasonable trade-off between logger cost and data accuracy. Calibrations should be made of these radiometer systems by coupling the pyranometer or pyrheliometer with its uniquely associated amplifier.

The logging equipment should also have environmental specifications that are compatible with the environment where the equipment will be used. Loggers used inside an environmentally controlled building could have less stringent environmental performance specifications than one mounted outside in a desert or arctic environment. Equipment enclosures can create an internal environment several degrees above ambient air temperature because of solar heating (absorption by the enclosure materials), heat generated by electronic devices mounted inside, and the lack of sufficient ventilation to help purge heat.

The sampling rate and recording rates of the solar resource data should be determined from the desired data analysis requirements. The sampling rate refers to how often the logger measures in a time interval. The recording rate is often also called the reporting rate or the time resolution. It is the length of the time interval that is represented by one data point in the logger's output file. Monthly averages or sums, daily, hourly, minute, or sub-1-minute data records can be of interest. Data loggers can generally be configured to produce output of instantaneous or integrated values at any reasonable time period consistent with the radiometer time-response characteristics. The design should consider the current requirements and, if convenient and practical, future needs for additional analyses. A high-temporal-resolution data-logging scheme can be down-sampled or integrated into longer time periods—but not the other way around. Data logging equipment, data transfer mechanisms, and data storage can generally handle 1-minute data resolution, and this should be considered the recording rate in the data logger. A resolution of 1 minute or better is recommended to allow for accurate data quality control. Because most applications address the solar energy available over time, integrating data of sub-minute samples within the data logger is a common method of data output regardless of the final data resolution required by the analysis. For instance, 1-second signal sampling is recommended for irradiance measurements in the Baseline Surface Radiation Network (BSRN) (McArthur 2005) so that 60 samples are averaged to the reported 1-minute data. The output of the instantaneous samples at longer intervals is much less likely to represent the available energy and should be avoided when configuring a data logger. If the size of a measured data set is a defining issue (e.g., limited data communications throughput), the user can determine the lowest temporal resolution necessary for the application and optimize the data collection accordingly.

3.3.7 Data Communications

Provisions should be made for automatically and frequently transferring data from the data logger to a data processing facility. This is the basis for adequately frequent data checks and timely corrections of outages and errors. Such frequent connections also allow for automatic data logger clock corrections when a local Global Positioning System device, which is preferred, is not available. Noticeable clock corrections of more than 1 second should never be necessary. Historically, data have been captured, transferred, and processed in various ways. Today, electronics and telecommunications allow remote data collection from nearly any location. One option uses a physical connection between logger and a computer that is used for further data analysis or that forwards the data via Internet connection. To avoid a cable connection, a cellphone network can be configured to provide virtual Internet links between a measurement station and the data center. Satellite uplinks and downlinks are also available for data transfers in areas that are not served by either wire- or cell-based phone service. Within the area of an observing station, wireless communications such as radio-frequency connectivity might be useful to minimize the need for long cables between

radiometers and data loggers. Depending on the antennas, data can be transferred over distances of a few kilometers. Such distances can occur between the data logger and the control room in big solar power plants with several megawatts of electrical design power.

To prevent data loss in case of connection problems, the memory of the data logger should be selected appropriately. Memory extensions are available for many data loggers with external cards.

3.4 Station and Network Operations

The protocols and procedures dictating station operations play a fundamental role in the assurance of data quality. These procedures must be established prior to the start of data collection, and then a process must be put into place to carry forth and document adherence to the procedures. Data quality is in great part established the moment the measurement is taken. If errors occur during the measurement, little can be done to improve fundamental quality. For example, a poorly maintained station with dirty optics or misaligned instruments will produce unreliable (large uncertainties or systematic biases) data, and the magnitude of the problem is not likely to be discernable until days or weeks later. Often, one can only guess at which approximate a posteriori adjustments (if any) to make.

In this context, data quality control involves a well-defined supervisory process by which station operators are confident that when a measurement is taken with unattended instruments, the instruments are in a state that produces data of known quality. This process largely encompasses the calibration, inspection, and maintenance procedures discussed in Section 3.4.1, along with log sheets and other items that document the condition of the station. It also includes a critical inspection or assessment of the data to help detect problems not evident from physical inspection of the instruments.

When designing and implementing a data quality plan, keep in mind that eventually the data set will undergo scrutiny for quality. In the best scenario (and a scenario that is certainly attainable), a data analyst will feel comfortable with the quality of the data set and will be willing to move unhindered to the analysis at hand. The plan should eliminate as much as possible any doubts and questions about how the data were collected and whether the values they contain are suitable for the intended purpose. Implementation of the best practices contained in this handbook help eliminate doubts and uncertainties that might jeopardize future projects.

3.4.1 Equipment Maintenance

Proper O&M practices are essential for acquiring accurate solar resource measurements. Several elements in a chain form a quality system. Collectively, these elements produce accurate and reliable solar resource data: station location, measurement system design, equipment installation, data acquisition, and O&M practices. Proper O&M requires long-term consistency, attention to detail, complete and transparent documentation, and a thorough appreciation for the importance of preventive and corrective maintenance of sensitive equipment.

Calibrations are performed with clean instrument optics and a carefully aligned/leveled instrument. To properly apply the calibration factor, the instrument should be kept in the same condition during field measurements as during the calibration. To maintain the calibration relationship between irradiance and radiometer output, proper cleaning and other routine maintenance are necessary. All O&M should be carefully documented with log sheets or preferably with electronic databases that contain enough information to reveal problems and solutions or to assert that the instruments were in good form when inspected. The exact times of the maintenance events should be noted rather than estimated. Time-stamped

pictures taken before and after maintenance with a camera can be extremely useful to evaluate the importance of soiling and misalignment, for example. A button connected to the data logger that is pressed at the beginning and at the end of an inspection is also recommended. The O&M information enables an analyst to identify potentially bad data and provides important documentation to determine and defend the overall quality of the measurements.

The maintenance process includes:

- Checking the alignment/leveling of the detector. Pyrheliometers must be accurately aligned with the solar disk for accurate DNI measurements. Pyranometer detectors must be horizontal for GHI and DHI measurements and accurately tilted (or aligned with a flat-plate collector) for GTI measurements. The radiometer orientation should be checked periodically using the features described earlier in this chapter.
- Cleaning the instrument optics. To properly measure the solar irradiance, no contaminant should block or reduce the radiation falling on the detector. The outdoor environment provides many sources of such contamination, such as dust, precipitation, dew, frost, plant matter, insects, and bird droppings. The sensors should be cleaned regularly to minimize the effect of contaminants on the measurements. In many cases, this can require daily maintenance of radiometers, especially in the case of pyrheliometers. Different standards require or recommend different cleaning frequencies between daily and weekly.
- Documenting the condition of the radiometer. For analysts to understand limitations of the data, conditions that affect the measurements must be documented. This includes substandard measurement conditions, but it is equally important to document proper operations to add credibility to the data set. Observations and notes provide a critical record of conditions that positively and negatively affect data quality.
- Documenting the environment. As a consistency check, note the sky and weather conditions at the time of maintenance. Note any ground surface changes, such as vegetation removal or the presence of snow. This information is valuable when interpreting data from the radiometer, including measurements with unusual values.
- Documenting the infrastructure. The whole measurement station should be examined for general robustness. Any defects should be noted and corrected.

Maintenance frequency depends on prevailing conditions that soil the instruments. This includes dust, rain, dew, snow, birds, and insects. It also depends on instrument type. Radiometer designs based on optical diffusers as the surface separating the inside of the instrument from the environment are less susceptible to the effects of dust contamination than instruments with clear optics, such as domed pyranometers (Myers et al. 2002). This is because fine soiling particles scatter much more than they absorb solar radiation. Absorption affects instruments with clear optics and diffusers the same way. In contrast, the scattering-induced soiling effect has less impact on instruments with diffusers because the latter can transmit most of what the particles have scattered. The scattered radiation (mostly in the forward direction) hence reaches the detector in nearly the same way that radiation would enter a clean diffuser. Conversely, the scattering often causes the incoming radiation to miss the detector in instruments with clear optics because the latter is some distance from the former. This is especially relevant for pyrheliometers (Geuder and Quaschning 2006). Soiling of windowed or domed radiometers can quickly affect their reading and increase their measurement uncertainty. This explains why thermopile radiometers must be cleaned very frequently (e.g., daily). As described earlier, using a ventilator for a pyranometer can reduce this risk of contamination; thus, it is important to consider the frequency and cost of maintenance for proper instrument specification. Although sensors with diffusers, such as

RSIs, are not prone to strong soiling effects, they still require regular cleaning (e.g., twice per month). Note that a diffuser below a clear entrance window/dome does not have an advantage compared to a thermopile below the same clear entrance window/dome.

Daily cleaning for sensors with clear optics or cleaning twice per month for sensors with diffusers as an outer surface is appropriate in most cases; however, different standards require or recommend different cleaning frequencies between daily (ISO TR9901) and weekly (IEC 61724-1). It is recommended to determine the cleaning interval for each site depending on the climate conditions of similar sites or, e.g., by analyzing the immediate effect of cleaning on the measurement signal. Depending on the noted period after which soiling significantly influences the measurement, the cleaning interval can be adjusted so that the degradation in sensitivity is limited to an acceptable level (e.g., <1% for high-quality stations). Each cleaning period and the state of the sensors should be documented, and the measurement values should be checked to evaluate the effect of cleaning on the recorded values.

Radiometers should be carefully cleaned at each inspection, even if soiling appears minimal. Cleaning is generally a very short procedure. A recommendation for the cleaning procedure is as follows. First, remove any loose particles from the entrance window with a soft brush or compressed air. Then clean the entrance window, dome, or diffuser with a dry cloth. If dirt remains after this step, wet a second cloth with distilled water (or methyl hydrate), and wipe the window/diffusor/dome clean. If ice sticks to the surface, try melting the ice with one's hands. Avoid using a hair dryer to melt the ice because the heat can crack the cold optics. More aggressive methods might damage the entrance windows and are therefore not recommended.

Collimators without entrance windows (as used in active cavity radiometers and at least one new commercially available, low-cost pyrheliometer) greatly reduce the accumulation of dust on the sensor's entrance optics, but they could still be affected by insects or spiders because they can enter the collimators, causing strong signal reductions. Even a single fiber of a spiderweb can significantly reduce the signal; therefore, such collimators must be inspected frequently.

At remote sites that could be too difficult to maintain during extended periods, a higher class windowed instrument might not be optimal, despite its potential for better measurements. The cost of maintenance for a remote site could dominate the estimated cost of setting up and operating a station. This aspect should be anticipated when planning a measurement campaign. Often, less maintenance-intensive sensors with initially lower accuracy than windowed instruments can be a better choice, at least until the station becomes permanently serviceable on a sufficiently frequent basis.

Additional spot inspections should be conducted after significant weather events (e.g., dust storms, snowstorms, heavy rainfall, rainfall during periods with high aerosol loads, and storms). Radiometer optics might not necessarily soil within a 24-hour period, but the effects of soiling can be best mitigated with frequent inspection.

Maintenance at remote measurement sites away from institutional or corporate employment centers will require finding a qualified person nearby who can perform the necessary maintenance duties. The qualifications for maintenance are generally nontechnical, but they require someone with the interest and disposition to reliably complete the tasks. As a rule, compensating these people for time and vehicle mileage—rather than seeking volunteers—becomes a worthwhile investment in the long run because it sets up a firm contractual commitment to perform all necessary maintenance duties. Without that formal relationship, it can become difficult to assert the need for reliable and regular attention.

A general conclusion is that a conservative maintenance schedule will support the credibility of the measurement data set and provide the analyst with a base of justification when assigning confidence intervals for the data.

3.4.2 Data Inspection

The collection of quality data cannot occur without careful and ongoing inspection of the data stream for evidence of error or malfunction. Although the maintenance procedures discussed in the previous section rely heavily on the physical appearance of the equipment to detect malfunction, some sources of error are so insidious that they cannot be revealed by simple physical observation; thus, an operations plan must include a careful inspection of the data itself for unrealistic values that might appear only with mathematical analysis. As with the inspections during equipment maintenance, inspection of data should be done with a frequency great enough to avoid prolonged error conditions that would impose a significant bias on the eventual statistical characterization of the data set.

3.4.2.1 Data Quality Control and Assurance

A successful quality-control process requires elements of quality assessment and feedback. Figure 3-24 depicts a quality-assurance cycle that couples data acquisition with quality assessment and feedback.

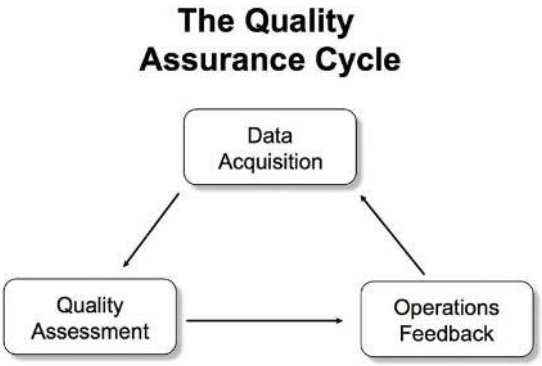

Figure 3-24. Information flow of a quality-assurance cycle. *Image by NREL*

As shown in Figure 3-24, the information flows from data acquisition to quality assessment, where criteria are applied to determine data quality. The results of the quality assessment are analyzed and formed into feedback that goes back to the data acquisition module. The activities in the boxes can take several forms. For example, quality assessment could be the daily site inspection, and the analysis and feedback could be a simple procedure that adjusts the equipment malfunctions. Alternatively, the quality assessment could be a daily summary of data flags, and the analysis would then provide a determination of a specific instrument problem that is transmitted back to maintenance personnel, instructing them to correct deficiencies or to further troubleshoot problems.

The faster the cycle runs, the sooner problems will be detected. This reduces the amount of erroneous data collected during failure modes. Conversely, if the site is inspected infrequently, the chances increase that a large portion of the data set would be contaminated with substandard measurements. More than one quality-assurance cycle can—and likely will—run at any time, each with a different period and emphasis, as noted: daily inspection, weekly quality reports, and monthly summaries.

One practical aspect of this cycle is the importance of positive feedback—a regular report back to site personnel of high-quality operations. This positively reinforces a job well done and keeps site operators cognizant that data are being used and checked and that their

efforts are an integral part of an ongoing process. It is often helpful to have an on-site person handle maintenance and address problems and a central facility that runs quality checks and spots potential problems with the data. Maintenance reports can advantageously include a photographic record of each radiometer, e.g., before and after cleaning or leveling.

The quality-assurance cycle is important, and thus it should be well defined and funded to maintain consistent data quality over time. After the quality of the data is determined, corresponding conclusions must be made for further use of the data. In every case, the quality-assurance data must be included in the data set as metadata. In some cases, the completeness of the data can even be improved based on the quality assurance. For example, data gaps from one sensor can be filled with the redundant data from related sensors. Gap filling is a complex topic that is not described in detail here. To calculate daily, monthly, or yearly sums, gap filling will nearly always be necessary, and it is recommended that the reader consider various publications concerning the topic for this type of correction (Hoyer-Klick et al. 2009; Espinar et al. 2011; Schwandt et al. 2014). Because data gaps can rarely be completely avoided in long time series, and because gap filling might not always work during long periods of missing data, a critical problem is then to obtain correct estimates of the long-term (e.g., monthly or annual) averages, which are of utmost importance in solar resource assessments. Practical methods have been developed to overcome this problem with the minimum possible loss of accuracy, as described by Roesch et al. (2011a, 2011b). But in the context of this section, an investment in planning and funding for maintaining the quality of ongoing data collection can repay manifold in the believability of the final data set.

Another systematic bias that savvy analysts might be able to address concerns the instrument's calibration. If the recalibration of a sensor shows a noticeable change relative to the calibration factor that was used shortly before the recalibration, the data might be reprocessed with a corrected, time-variable calibration factor. For sun photometers, this kind of post processing is applied to the Aerosol Robotic Network (AERONET) Level 1.5 data to elevate them to Level 2 (Holben et al. 1998). A distinct change in calibration factor can be assumed to be linear in time, and the data between two calibration periods are then reprocessed with a time series of this linearly corrected calibration factor.

Finally, the systematic effects of soiling on measured irradiance data can be reduced a posteriori—at least to some extent. This requires any change in irradiance following the sensor cleaning to be documented. Examples of data correction methods can be found in Geuder and Quaschning (2006), Bachour et al. (2016), and Schüler et al. (2016); however, such a correction can result in acceptable accuracy only if the soiling effect is small (e.g., <1%). The availability of such a rough soiling correction method does not eliminate the stated requirement that instrument cleaning must be done frequently. For example, station operators cannot assume that a discontinuity observed at a single cleaning event can be generalized to encompass conditions leading up to all such cleaning events. As stated previously, the effect of soiling (and conversely, cleaning) on pyranometers with diffusing optics is generally less than that seen on pyranometers with clear optics (Maxwell et al. 1999); however, certain meteorological events can produce anomalous effects, even with instruments less prone to soiling. Figure 3-25 shows data from an RSI with diffusing optics, the effect of cleaning the day after a dust storm revealed a 5% attenuation in the measured value prior to maintenance. Documenting the magnitude of such occurrences can be difficult, particularly with a large measurement network. In extreme situations, the data analyst must simply be aware that some increase in measurement uncertainty is necessary.

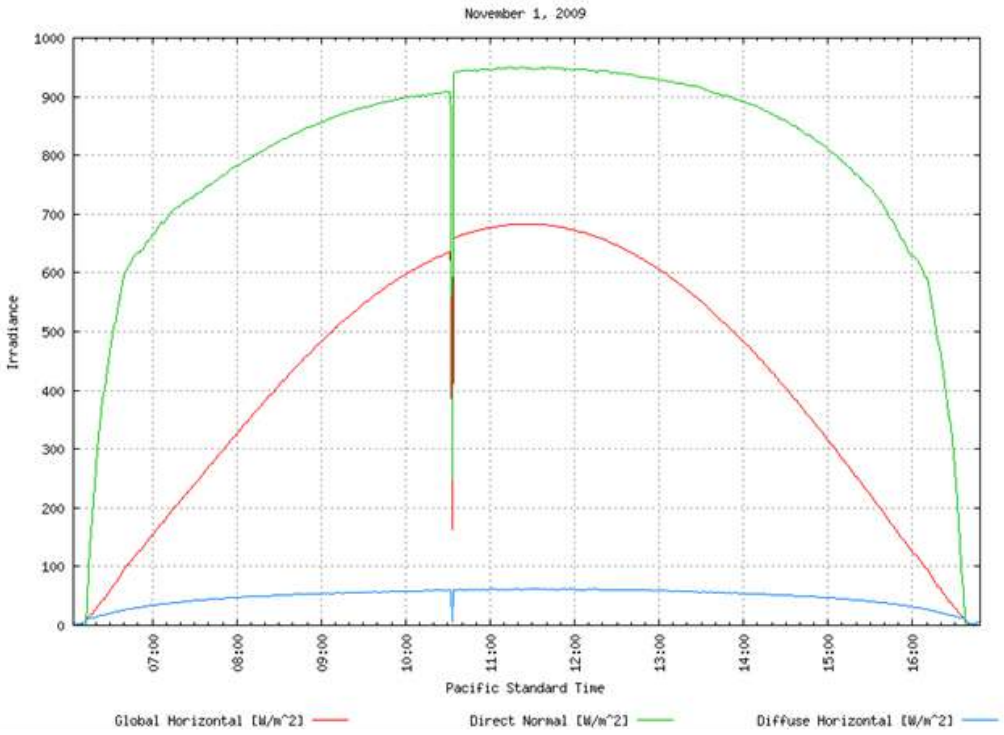

Figure 3-25. Cleaning effect (~5%) on an RSI using a pyranometer with diffusing optics. *Image by NREL*

3.4.2.2 Data Quality Assessment

When assimilating a large volume of data, some measure of automated quality assessment must be employed. The methods can range from rudimentary—for example, the temporal behavior of data can be used to identify problems, such as blocked wind vanes or damaged cables; to more sophisticated methods to meet this demand as explained in the following and in Chapter 7, Section 7.7. Depending on how strict the screening parameters are and how their corresponding values are chosen, however, too many or too few events might be detected. A variety of factors—ranging from characteristics of the site and/or instruments to local weather conditions—can affect the data and the validity of screening tests; therefore, the results of the automatic screening always demand a manual check by an expert to ensure their validity. Finally, additional data issues potentially known by the station's supervisor must be included as comments or flags. Such information should be documented in the metadata (Section 3.4.2.3)

As a general rule, data for inspection should be aggregated to some degree, typically in daily sets (Wilcox and McCormack 2011). This is because individual data points might not lend well to definitive conclusions about quality without the context of many nearby measurements. For example, a sudden change in solar irradiance can often be correlated with the passage of weather fronts that bring clouds and wind. And those conditions might also show a rapid change in temperature, adding to a compelling conclusion.

Data inspection routines should be automated toward the end goal of presenting the quality analyst with on-demand visual plots to streamline the inspection process. This becomes particularly necessary for network operations with dozens of stations where hundreds of thousands of measurements could be generated each day. Background processes can run automated data quality assessment routines and then plot the data and flags in a report readied for the quality analyst to begin inspection. For example, Figure 3-26 holds multiple panels with data graphs from a single station, providing the expert analyst thousands of data

points that can be quickly scanned by eye and related with each other to spot inconsistencies.

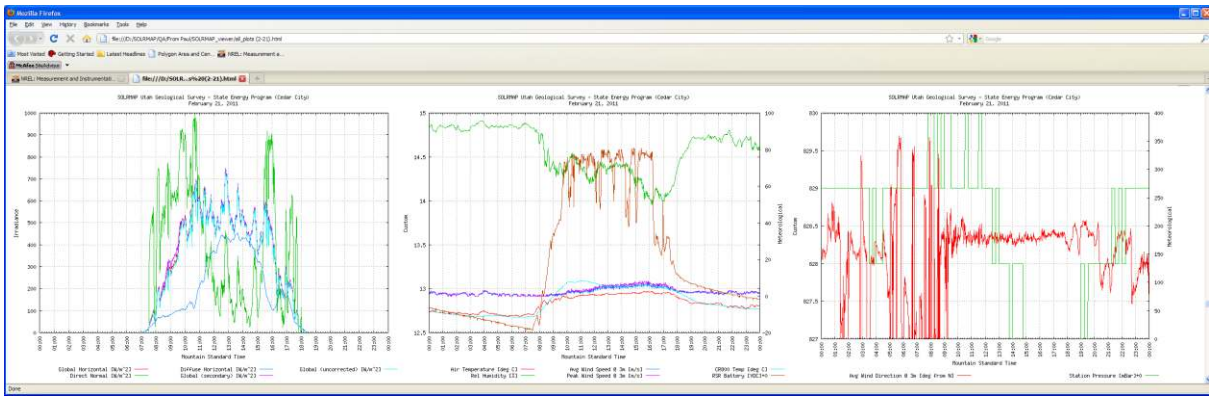

Figure 3-26. Multiple-grouped data plots for a single station for a single day: (left) three-component irradiance data; (center) wind speed, temperature, and battery voltage; and (right) wind direction and barometric pressure. ***Image from NREL***

The flags can be visualized next to the data, as shown in Figure 3-27. Here, a suspicious period in the morning was detected by the automatic quality control and marked with the orange background. Of great help is the visualization of the difference between the measured DNI and the DNI calculated from collocated GHI and DHI measurements. This difference plotted over time can help to identify, for example, pyranometer levelling issues, radiometer soiling/dew, or tracking errors.

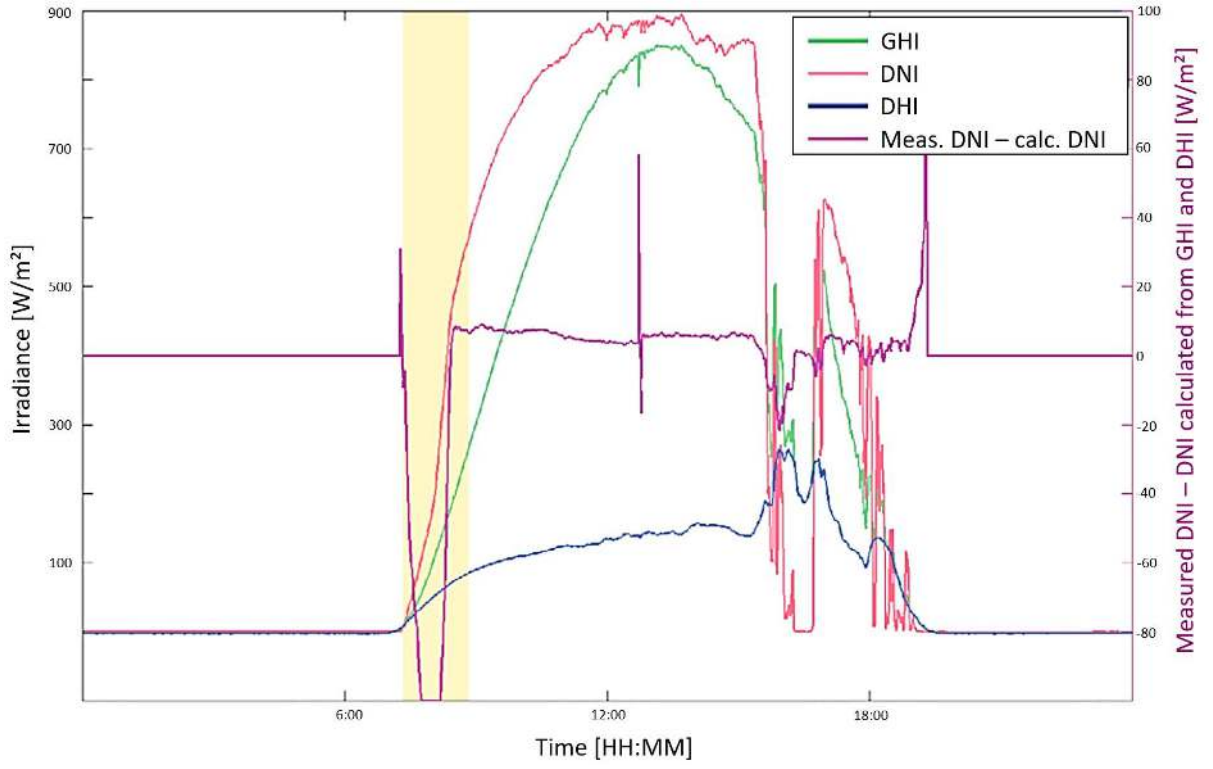

Figure 3-27 Time plot of the three irradiance components and the difference of measured and calculated DNI. Data marked by automatic quality control is marked with an orange background to guide the data analyst during the daily data control. ***Image from DLR, after Geuder et al. (2015)***

If redundant sensors are used, both measurements or their differences can be plotted and analyzed, which allows for detecting errors that affected only one of the instruments. Digital instruments and some ventilation units for pyranometers also provide additional useful information, such as the rotation speed of the ventilator, the sensor inclination, the sensor acceleration (shock sensor), or error codes. Such data are valuable for quality control and at times allow for corrections before the measurements are strongly affected by the error.

A time series of some measurements can reveal error conditions before they become a problem. Figure 3-28 shows a plot of the daily battery voltage for a remote RSI instrument and indicates a charging problem. In this case, a technician was dispatched, parts were obtained, and the charging circuit was repaired before the instrument lost power and data were lost.

The addition of data quality flags to the data files is an extremely important step in the quality assurance process. For example, the SERI QC software for irradiance measurements (Maxwell, Wilcox, and Rymes 1993) (see Chapter 7, Section 7.7.1) produces flags that can be plotted and included in the rapid visual inspection paradigm (see Figure 3-29). These flags are plotted in the left panel to show a gradation of flag severity from low (dark blue) to high (red) for each minute of a month. To aid the analysis, each solar measurement's *K*-space value is plotted in the right three panels, allowing the analyst to find measurement periods that correspond with periods of high flags. Although Figure 3-29 shows a plot for a calendar month, these reports can be generated daily in a moving window to show flagging from previous weeks that lead up to the current day. This allows the analyst to detect error trends early and to formulate a correction.

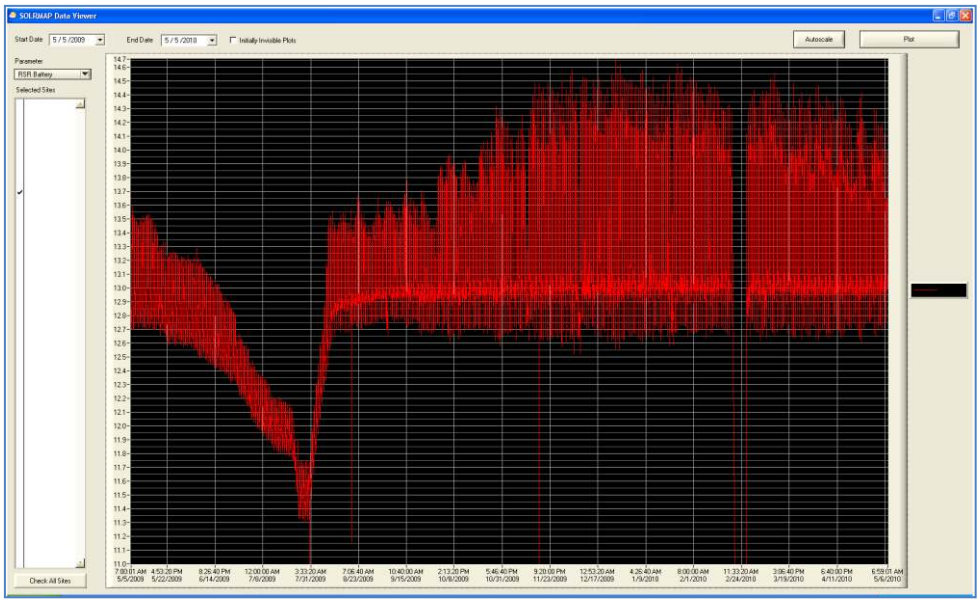

Figure 3-28. Time-series plot of battery voltage as a diagnostic tool. ***Figure from NREL***

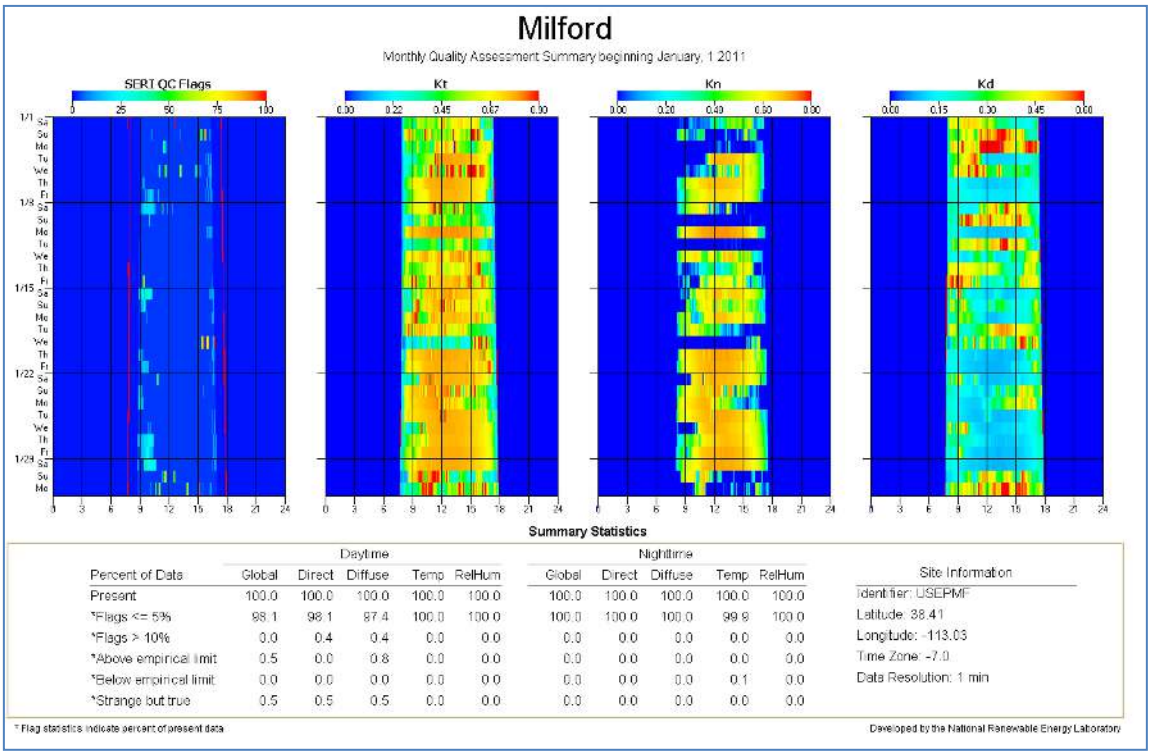

Figure 3-29. Plots of SERI QC flags (left panel) for 1 month (y-axis) by hour of day (x-axis). The three right panels plot associated K-space values. *Image from NREL*

In all these examples, the automated reports should be generated daily (or some other interval consistent with the end use of the data) in preparation for a scheduled session by the analyst, minimizing the amount of manpower required for a thorough data inspection.

Other automated procedures, usually implemented in the data ingest system, employ more rudimentary bounds checking, parameter coupling, and detection of missing data. These checks provide near-real-time triggers for automated email messages to alert operators that a potential error condition exists. These alerts are a first line of defense against serious failures in the system.

3.4.2.3 Metadata and Record-Keeping

The interpretation and application of solar resource measurements depend greatly on the efforts to record and include metadata relevant to the observations. This includes site location; quantitative local horizon surveys with a device visualizing the solar path during the year; data acquisition system(s); input signal channel assignments; radiometer types, models, serial numbers, calibration histories, and installation schemes; and information on eventual post processing of the data and maintenance records. For example, online metadata are available from NREL's Solar Radiation Research Laboratory.[8] Such metadata should be included with the archiving of the measured solar resource data. Examples of issues that need to be documented include damaged or misaligned sensors, maintenance works on the instruments, detection of soiled sensors and subsequent sensor cleaning, obstructed sensors, temporarily erroneous calibration constants in the program code, loose electrical connections, and data logger clock error. These events are frequently not detected automatically or sometimes not even detectable by automatic quality-control screening tools;

[8] See http://www.nrel.gov/midc/srrl_bms.

hence, manual on-site checks are required. The metadata should not necessarily be limited to error conditions and corrections. Information about unusual weather events, animal activity, or even significant flora blooms or vegetation die-off events could prove useful in future analyses that could benefit from knowledge of the measurement environment. Such supplementary information could convey to an auditor that the station operators were thorough in recording station details.

When deciding on a metadata archival method, some consideration should be given to the pros and cons of paper (physical) versus electronic storage. Paper, though not immune to peril, is a simple form that can be read for decades or even centuries. Electronic formats, which are invaluable for easy access and extraction for computer analyses, are too often subject to catastrophic loss through myriad electronic mishaps. Further, changes in the format of once commonplace electronic storage schemes might also render historic metadata unreadable or inaccessible. Using both methods simultaneously solves many of these problems, but it can create new issues with the additional labor for double entry or possible inconsistencies between the two methods.

Figure 3-30 shows a sample paper log that a maintenance technician is required to complete on-site during the maintenance visit. The log not only provides a checklist to ensure a complete inspection but also serves as permanent documentation for the station archive.

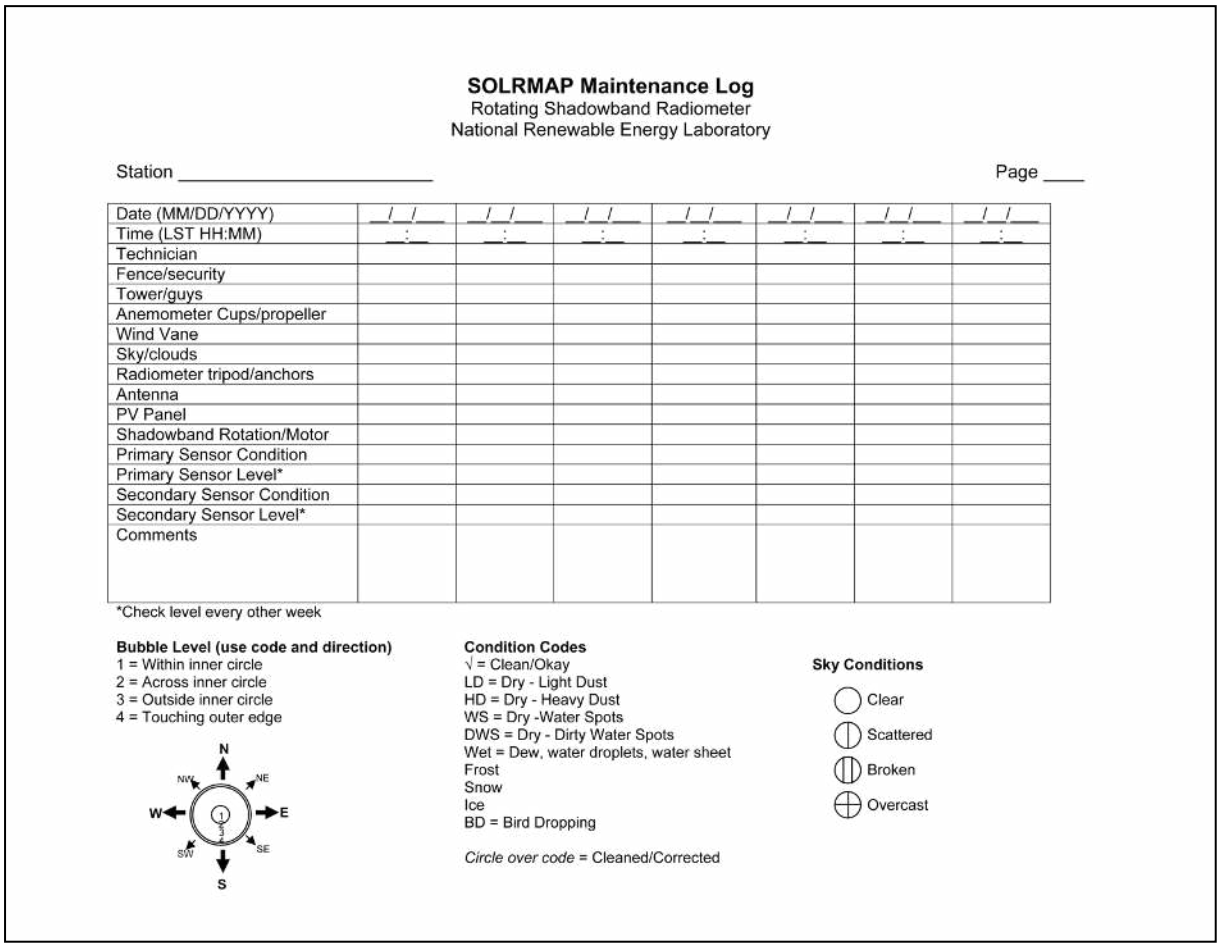

SOLRMAP Maintenance Log
Rotating Shadowband Radiometer
National Renewable Energy Laboratory

Station _____ Page ____

Date (MM/DD/YYYY)	__/__/____	__/__/____	__/__/____	__/__/____	__/__/____	__/__/____	__/__/____
Time (LST HH:MM)	__:__	__:__	__:__	__:__	__:__	__:__	__:__
Technician							
Fence/security							
Tower/guys							
Anemometer Cups/propeller							
Wind Vane							
Sky/clouds							
Radiometer tripod/anchors							
Antenna							
PV Panel							
Shadowband Rotation/Motor							
Primary Sensor Condition							
Primary Sensor Level*							
Secondary Sensor Condition							
Secondary Sensor Level*							
Comments							

*Check level every other week

Bubble Level (use code and direction)
1 = Within inner circle
2 = Across inner circle
3 = Outside inner circle
4 = Touching outer edge

N NW NE W E SW SE S

Condition Codes
√ = Clean/Okay
LD = Dry - Light Dust
HD = Dry - Heavy Dust
WS = Dry -Water Spots
DWS = Dry - Dirty Water Spots
Wet = Dew, water droplets, water sheet
Frost
Snow
Ice
BD = Bird Dropping

Circle over code = Cleaned/Corrected

Sky Conditions
Clear
Scattered
Broken
Overcast

Figure 3-30. Sample paper maintenance log sheet to be filled out by a technician on-site during a maintenance visit. *Image from NREL*

Figure 3-31 shows a (partial) online log form that allows the maintenance technician to remotely access a database interface. Each item in the prescribed maintenance checklist is reported to complete the documentation for the station visit. The log sheet streamlines much

of the documentation with codes and checkmarks, and it provides space for freehand comments to describe unusual conditions. For paper logs and online logs, protocols must be in place to ensure that the technician is actually performing the tasks that appear in the logs. At a minimum, station management must be aware of the possibility that a dishonest technician might develop creative ways to falsify a work product. There are ways to remotely verify that the maintenance protocol is being followed. In many cases, when instruments are cleaned, an anomaly appears in the data while the sky irradiance is blocked. The analyst can look at a data plot at the logged time of the visit, and if no disruption appears, further investigation could be warranted. Some systems provide a momentary switch or button that the technician is required to push when arriving on-site. This action places a flag in the data stream verifying that the technician was on-site for the inspection. Remote video cameras can also be a valuable means to verify a proper inspection.

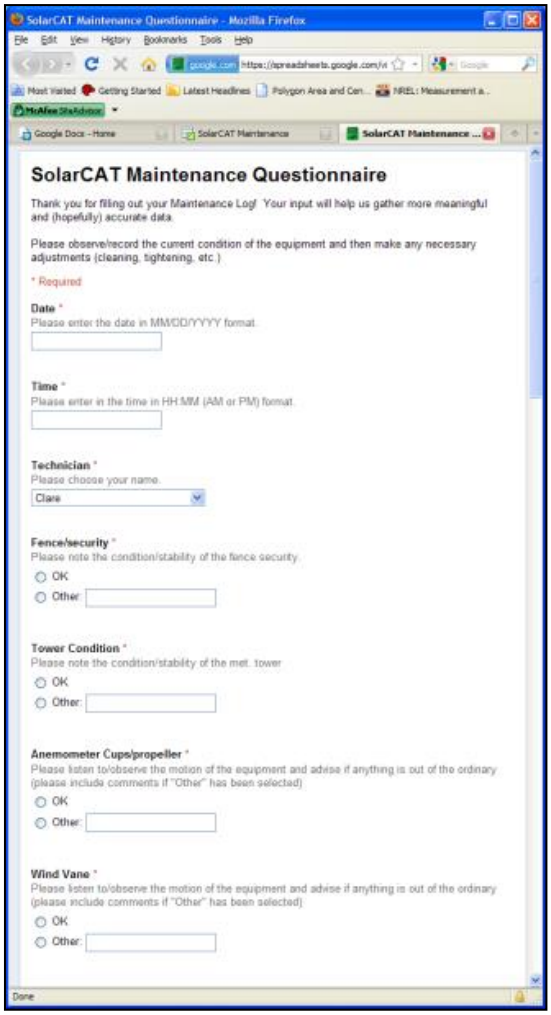

Figure 3-31. Sample online interface for documenting maintenance. ***Image from NREL***

Analysts—whether associated with station operations or employed in a later due diligence process—are immensely aided by ample documentation of station O&M. The documentation, in addition to providing the specific information contained, also indicates the extent of the maintenance protocol. This gives the analyst confidence that problems are discovered and corrected in a minimal amount of time. Further, the documents show that even at well-run stations with a few inevitable malfunctions, best practices and high-quality data govern operations.

Complete documentation includes thorough information in a dedicated metadata archive about the instruments, including manufacturer and model, serial number, calibrations (current and historical), deployment location and configuration, repairs, and inventory or storage details. Of particular importance is the record of instrument calibrations and the associated certificate, traceability, and statement of uncertainty. The calibration record is fundamental to the measurement itself and the assignment of uncertainties to the measured data. Absent a current calibration certificate, a knowledgeable analyst performing validation or due diligence on a data set will likely reject *any* statement of uncertainty, rendering the measurements highly questionable.

3.4.3 Data Aggregations and Summaries

Solar irradiance measurements for renewable energy applications are becoming more common, and in some electric utility applications, they are required. These measurements are also important for applications in energy-efficiency and climate research. Measurement station design includes data loggers and their configuration as described in Section 3.3.5. Ideally, the station designers will have knowledge in advance about the form (necessary parameters, time resolution, period of record, acceptable uncertainty limits, etc.) of the data required to complete the planned analyses to satisfy the project objectives. But this is not always the case. Further, it is quite common for data sets to be accessed for uses other than their original purpose; thus, the value of a data set could be significantly enhanced if it is in a more generic form that is easily adaptable or convertible to other more specific forms. This typically relates to the frequency of the measurements, which could range from 1 minute to monthly or even yearly.

As noted in Section 3.3.5, the time resolution of the measurements can be increased without significantly increasing the costs for data transfer and storage when compared with the overall costs of operating a station. Because data values can be easily converted to longer timescales, it is recommended that the station be designed to collect data at 1-minute intervals.[9] Many commercially available data loggers are capable of sampling the instruments near 1 Hz and then integrating the samples to a 1-minute value (or some other chosen time interval). These values are quite often represented with a unit of W/m^2, but the correct unit from this process is W-minute/m^2. Most solar analytical tools expect values in Wh/m^2, so the conversion must be made prior to further averaging to daily, monthly, or annual values. As a practical matter, the conversion to Wh/m^2 can be made by averaging the 1-minute values for 1 hour. The result is mathematically the same as the more descriptively correct method of adding the 60 values in W-minute/m^2 and dividing by 60 minutes to convert from the minute to the hourly unit.

Some analytical tools expect hourly values during the period of interest, often a full year. Other tools might expect daily total energy, and others monthly mean daily totals. The conversion from Wh/m^2 can then be made to the daily total in Wh/m^2 per day by simply adding the hourly values from a single day. From there, the conversion to monthly mean daily totals is accomplished by averaging the daily totals for the month. Examples of reporting monthly solar irradiance measurements are available from https://midcdmz.nrel.gov/apps/report.pl?site=BMS.

In addition to the statistics described, some applications (power plant load matching or building design) look for long-term values by hour of day, for example, the average energy

[9] Data recording at time intervals as short as 1 second has been needed for research applications requiring special attention to the radiometer performance specifications. (See https://dx.doi.org/10.5439/1052451.)

available throughout a month at 11:00. These slices are formed by sorting the hourly data by time stamp and then averaging the subsets during the desired period.

Aggregating solar irradiance and meteorological measurements over various timescales also requires careful attention to methods for estimating the associated measurement uncertainties. This is currently an active area of research that will be addressed in future editions of this handbook.

3.5 References

Alados-Arboledas, L., F. J. Batlles, and F. J. Olmo. 1995. "Solar Radiation Resource Assessment by Means of Silicon Cells." *Solar Energy* 54 (3): 183–91.

Apogee. 2019. *New ISO 9060Pyranometer Classifications*. Logan, UT. Accessed January 18, 2021. https://www.apogeeinstruments.com/content/ISO_9060_Apogee_Comparison.pdf.

Augustyn, J., T. Geer, T. Stoffel, R. Kessler, E. Kern, R. Little, and F. Vignola. 2002. "Improving the Accuracy of Low Cost Measurement of Direct Normal Solar Irradiance." *Solar 2002 Conference Proceedings*, Reno, Nevada, June 15–20, 2002.

Bachour, D., D. Perez-Astudillo, and L. M. Pomares. 2016. "Study of Soiling on Pyranometers in Desert Conditions." *Proceedings of Eurosun 2016 Conference*, Palma de Mallorca, Spain. International Solar Energy Society.

Badosa, J., J. Wood, P. Blanc, C. N. Long, L. Vuilleumier, D. Demengel, and M. Haeffelin. 2014. "Solar Irradiances Measured Using SPN1 Radiometers: Uncertainties and Clues for Development." *Atmospheric Measurement Techniques* 7 (12): 4,267–83. https://doi.org/10.5194/amt-7-4267-2014.

Bergholter, U., and K. Dehne. 1994. *SCAPP: A Compact Scanning Pyrheliometer/Pyranometer System for Direct, Diffuse, and Global Solar Radiation* (WMO-IOM No. 57). Geneva, Switzerland: World Meteorogolical Organizaion.

Driesse, A. 2018. "Radiometer Response Time and Irradiance Measurement Accuracy." *Proceedings of the European Photovoltaic Solar Energy Conference*, Brussels. https://doi.org/10.4229/35thEUPVSEC20182018-6DO.10.6.

Driesse, A., and J. Stein. 2017. "Site-Specific Evaluation of Errors and Uncertainty in Irradiance Measurements." Presented at the 33rd European Photovoltaic Solar Energy Conference, Amsterdam, The Netherlands. https://doi.org/10.13140/RG.2.2.14876.39044.

Driesse, A., W. Zaaiman, D. Riley, N. Taylor, and J. Stein. 2015. "Indoor and Outdoor Evaluation of Global Irradiance Sensors." Presented at the 31st European Photovoltaic Solar Energy Conference, Hamburg, Germany.

Dutton, E. G., J. J. Michalsky, T. Stoffel, B. W. Forgan, J. Hickey, D. W. Nelson, T. J. Alberta, and I. Reda. 2000. "Measurement of Broadband Diffuse Solar Irradiance Using Current Commercial Instrumentation with a Correction for Thermal Offset Errors." *Journal of Atmospheric and Oceanic Technology* 18 (3): 297–314.

Espinar, B., L. Wald, P. Blanc, C. Hoyer-Klick, M. Schroedter-Homscheidt, and T. Wanderer. 2011. *Report on the Harmonization and Qualification of Meteorological Data: Project ENDORSE—Energy Downstream Service: Providing Energy Components for GMES—Grant Agreement No. 262892*. Paris, France: Armines. Accessed November 11, 2014. http://www.endorse-fp7.eu/public_deliverables.

Finsterle, W. 2011. *WMO International Pyrheliometer Comparison: IPC-XI 27 September–15 October 2010: Final Report* (WMO IOM Report No. 108). Davos, Switzerland.

Forstinger, A., S. Wilbert, A. Driesse, N. Hanrieder, R. Affolter, S. Kumar, N. Goswami et al. 2020. "Physically Based Correction of Systematic Errors of Rotating Shadowband Irradiometers." *Meteorologische Zeitschrift*. https://doi.org/10.1127/metz/2019/0972.

Fröhlich, C. 1991. "History of Solar Radiometry and the World Radiation Reference." *Metrologia* 28: 111–15.

Geuder, N., and V. Quaschning. 2006. "Soiling of Irradiation Sensors and Methods for Soiling correction." *Solar Energy* 80 (11): 1,402–09.

Geuder, N., B. Pulvermüller, and O. Vorbrügg. 2008. "Corrections for Rotating Shadowband Pyranometers for Solar Resource Assessment." *Solar Energy Applications Conference Proceedings, Part of SPIE Optics + Photonics*, San Diego, California, August 10–14, 2008.

Geuder, N., B. Pulvermüller, O. Vorbrügg, J. T. Butrón, R. Kistner, K. Behrens, and R.-D. Grewe. 2006. "Examination of Different Irradiation Sensors: Operation Experiences and Comparative Study." *4th International Conference on Experiences with Automatic Weather Stations Proceedings*, Lisbon, Portugal, May 24–26, 2006.

Geuder, N., F. Wolfertstetter, S. Wilbert, D. Schüler, R. Affolter, B. Kraas, E. Lüpfert, and B. Espinar. 2015. "Screening and Flagging of Solar Irradiation and Ancillary Meteorological Data." *Energy Procedia* 69 (0): 1,989–98. http://dx.doi.org/10.1016/j.egypro.2015.03.20.

Geuder, N., M. Hanussek, J. Haller, R. Affolter, and S. Wilbert. 2011. "Comparison of Corrections and Calibration Procedures for Rotating Shadowband Irradiance Sensors." *Proceedings of the SolarPACES Conference*, Granada, Spain, September 20–23, 2011.

Geuder, N., R. Affolter, and B. Kraas. 2012. "Experiences on Radiation Measurements with Rotating Shadowband Irradiometers." *COST WIRE Workshop Payerne Proceedings*, Payerne, Switzerland, September 21, 2012.

Geuder, N., R. Affolter, B. Kraas, and S. Wilbert. 2014. "Long-Term Behavior, Accuracy and Drift of Li-200 Pyranometers as Radiation Sensors in Rotating Shadowband Irradiometers (RSI)." *Energy Procedia* 49: 2,330-39.

Geuder, N., R. Affolter, O. Goebel, B. Dahleh, M. Al Khawaja, S. Wilbert, B. Pape, and B. Pulvermüller. 2016. "Validation of Direct Beam Irradiance Measurements from Rotating Shadowband Irradiometers in a Region with Different Atmospheric Conditions." *Journal of Solar Energy Engineering* 138, 5: 051007-07.

Gueymard, C. A. 2017a. "Cloud and Albedo Enhancement Impacts on Solar Irradiance Using High Frequency Measurements from Thermopile and Photodiode Radiometers. Part 1: Impacts on Global Horizontal Irradiance." *Solar Energy*, 153: 755–65.

———. 2017b. "Cloud and Albedo Enhancement Impacts on Solar Irradiance Using High Frequency Measurements from Thermopile and Photodiode Radiometers. Part 2: Performance of Separation and Transposition Models for Global Tilted Irradiance." *Solar Energy*, 153: 766–79.

Gueymard, C. A., and D. R. Myers. 2009. "Evaluation of Conventional and High-Performance Routine Solar Radiation Measurements for Improved Solar Resource, Climatological Trends, and Radiative Modeling." *Solar Energy* 83: 171–85.

Gueymard, C. A., and J. A. Ruiz-Arias. 2015. "Validation of Direct Normal Irradiance Predictions under Arid Conditions: A Review of Radiative Models and their Turbidity-Dependent Performance." *Renewable and Sustainable Energy Reviews* 45: 379–96.

Habte, A., M. Sengupta, A. Andreas, S. Wilcox, and T. Stoffel. 2016. "Intercomparison of 51 Radiometers for Determining Global Horizontal and Direct Normal Irradiance Measurements. *Solar Energy* 133: 372–93. https://doi.org/10.1016/j.solener.2016.03.065.

Habte, A., M. Sengupta, Y. Xie, M. Dooraghi, I. Reda, A. Driesse, C. Gueymard, S. Wilbert, and Frank Vignola. 2018. *Developing a Framework for Reference Cell Standards for PV Resource Applications* (NREL/TP-5D00-72599). Golden, CO: National Renewable Energy Laboratory. https://www.nrel.gov/docs/fy19osti/72599.pdf.

Habte, A., S. Wilcox, and T. Stoffel. 2014. *Evaluation of Radiometers Deployed at the National Renewable Energy Laboratory's Solar Radiation Research Laboratory* (NREL/TP-5D00-60896). Golden, CO: National Renewable Energy Laboratory.

Harrison, L., J. Michalsky, and J. Berndt. 1994. "Automated Multi-Filter Rotating Shadowband Radiometer: An Instrument for Optical Depth and Radiation Measurements." *Applied Optics* 33 (22): 5,118–25.

Holben, B., T. Eck et al. 1998. "AERONET—A Federated Instrument Network and Data Archive for Aerosol Characterization." *Remote Sensing of Environment* 66 (1): 1–16.

Hoyer-Klick, C., F. Hustig, M. Schwandt, and R. Meyer. 2009. "Characteristic Meteorological Years from Ground and Satellite Data." *Proceedings of the SolarPACES Conference*, Berlin, Germany.

Ineichen, P., and R. Perez. 2002. "A New Airmass Independent Formulation for the Linke Turbidity Coefficient." *Solar Energy* 73 (3): 151–57.

International Electrotechnical Commission (IEC). 2009. *IEC 60891 Ed. 2.0:2009 Photovoltaic Devices - Procedures for Temperature and Irradiance Corrections to Measured I-V Characteristics*. Geneva, Switzerland. www.iec.ch.

———. 2015. *IEC 60904-2:2015, Photovoltaic Devices – Part 2: Requirements for Photovoltaic Reference Devices*. Geneva, Switzerland. www.iec.ch.

———. 2017. *IEC 61724-1:2017 Photovoltaic System Performance – Part 1: Monitoring*. Geneva, Switzerland. www.iec.ch.

———. 2019a. *IEC 60904-3 Ed. 4.0:2019 Photovoltaic Devices – Part 3: Measurement Principles for Terrestrial Photovoltaic (PV) Solar Devices with Reference Spectral Irradiance Data*. Geneva, Switzerland. www.iec.ch.

———. 2019b. *IEC 60904-4 Ed. 2.0:2019 Photovoltaic Devices – Part 4: Reference Solar Devices - Procedures for Establishing Calibration Traceability*. Geneva, Switzerland. www.iec.ch.

International Organization for Standardization (ISO). 1990a. *ISO 9060:1990. Solar Energy—Specification and Classification of Instruments for Measuring Hemispherical Solar and Direct Solar Radiation*. Geneva, Switzerland.

———. 1990b. *ISO 9059:1990. Solar Energy—Calibration of Field Pyrheliometers by Comparison to a Reference Pyrheliometer*. Geneva, Switzerland.

———. 1992. *ISO 9847: 1992 (E). Solar Energy—Calibration of Field Pyranometers by Comparison to a Reference Pyranometer*. Geneva, Switzerland.

———. 1993. *ISO 9846: 1993(E). Solar Energy—Calibration of a Pyranometer Using a Pyrheliometer*. Geneva, Switzerland.

———. 2018. *ISO 9060:2018. Solar Energy—Specification and Classification of Instruments for Measuring Hemispherical Solar and Direct Solar Radiation*. Geneva, Switzerland. www.iso.org/standard/67464.html.

Iqbal, M. 1983. *An Introduction to Solar Radiation*. Academic Press, New York.

Jessen, W., S. Wilbert, B. Nouri, N. Geuder, and H. Fritz. 2016. "Calibration Methods for Rotating Shadowband Irradiometers and Optimizing the Calibration Duration." *Atmospheric Measurement Technology* (4): 1,601–12. https://doi.org/10.5194/amt-9-1601-2016.

Jessen, W., S. Wilbert, L. Z. Tirado, L. R. Santigosa, R. V. Balderrama, J. Liria, B. Nouri, and N. Hanrieder. 2017. *Calibration Procedures for Rotating Shadowband Irradiometers*. Public Project Report EU FP 7 SFERA II. Deliverable 11.5.

Kern, E. C. 2010. "Calibration Methods for Silicon Photodiode Pyranometers Used in Rotating Shadowband Radiometers." *Proceedings of the SolarPACES Conference*, Perpignan, France.

King, D. L., and D. R. Myers. 1997. "Silicon Photodiode Pyranometers: Operational Characteristics, Historical Experiences, and New Calibration Procedures." *26th IEEE Photovoltaic Specialists Conference Proceedings*, Washington, D.C, May 13–17, 1997.

Kipp & Zonen. 2017. *Instruction Manual, SHP1 Smart Pyrheliometer*. https://www.kippzonen.com/Download/596/Manual-Smart-Pyrheliometer-SHP1-English.

Kurtz, B., and J. Kleissl. 2017. "Measuring Diffuse, Direct, and Global Irradiance Using a Sky Imager." *Solar Energy* 141: 311–22. http://dx.doi.org/10.1016/j.solener.2016.11.032.

LI-COR Biosciences. 2005. *LICOR Terrestrial Irradiation Sensors: Instruction Manual*. Lincoln, Nebraska. https://www.licor.com/documents/8yfdtw1rs27w93vemwp6.

Lindner, P. 1984. "A New Sunshine Duration Sensor." *Instruments and Observing Methods: WMO-IOM No. 15—Technical Conference on Instruments and Cost-Effective Meteorological Observations Proceedings*, Nordwijkerhout, The Netherlands, September 24–28, 1984.

Löf, G. O. G., J. A. Duffie, and C. O. Smith. 1966. "World Distribution of Solar Radiation." *Solar Energy* 10 (1): 27–37. http://doi.org/10.1016/0038-092X(66)90069-7.

Maxwell, E., et al. 1999. *Progress Report for Annex II – Assessment of Solar Radiation Resources in Saudi Arabia 1993 – 1997* (NREL /TP-560-25374). Golden, CO: National Renewable Energy Laboratory. https://digital.library.unt.edu/ark:/67531/metadc622174/.

Maxwell, E., S. Wilcox, and M. Rymes. 1993. *Users Manual for SERI QC Software: Assessing the Quality of Solar Radiation Data* (NREL/TP-463-5608 DE93018210). Golden, CO: National Renewable Energy Laboratory. Accessed September 26, 2014. http://www.nrel.gov/docs/legosti/old/5608.pdf.

McArthur, L. J. B. 2005. *Baseline Surface Radiation Network (BSRN) Operations Manual Version 2.1* (WCRP-121 WMO/TD-No. 1274). Geneva, Switzerland.

Michalsky, J., E. Dutton, M. Rubes, D. Nelson, T. Stoffel, M. Wesley, M. Splitt, and J. DeLuisi. 1999. "Optimal Measurement of Surface Shortwave Irradiance Using Current Instrumentation." *Journal of Atmospheric Oceanic Technology* 16: 55–69.

Michalsky, J., E. G. Dutton, D. Nelson, J. Wendell, S. Wilcox, A. Andreas, P. Gotseff, D. Myers, I. Reda, T. Stoffel, K. Behrens, T. Carlund, W. Finsterle, and D. Halliwell. 2011. "An Extensive Comparison of Commercial Pyrheliometers under a Wide Range of Routine Observing Conditions." *Journal of Atmospheric Oceanic Technology* 28: 752-66. https://doi.org/10.1175/2010JTECHA1518.1.

Michalsky, J., M. Kutchenreiter, and C. N. Long. 2019. "Significant Improvements in Pyranometer Nighttime Offsets Using High-Flow DC Ventilation." *Journal of Atmospheric Oceanicic Technology* 34: 1,323–32. https://dx.doi.org/10.1175/JTECH-D-16-0224.1.

Morrison, R. 1998. *Grounding and Shielding Techniques. 4th edition*. New York: John Wiley and Sons.

Müller, R., T. Behrendt, A. Hammer, and A. Kemper. 2012. "A New Algorithm for the Satellite-Based Retrieval of Solar Surface Irradiance in Spectral Bands." *Remote Sensing* 4: 622–47.

Myers, D. R. 2011. "Quantitative Analysis of Spectral Impacts on Silicon Photodiode Radiometers." *American Solar Energy Society Solar Conference Proceedings*, Raleigh, North Carolina, May 17–20. Boulder, CO: American Solar Energy Society.

Myers, D., and S. Wilcox. 2009. "Relative Accuracy of 1-Minute and Daily Total Solar Radiation Data for 12 Global and 4 Direct Beam Solar Radiometers" (NREL/CP-550-45734). *Proceedings of the American Solar Energy Society Annual Conference*, Buffalo, New York, May 11–16, 2009.

Myers, D., S. Wilcox, W. Marion, N. Al-Abbadi, M. Mahfoodh, and Z. Al-Otaibi. 2002. *Final Report for Annex II—Assessment of Solar Radiation Resources in Saudi Arabia 1998–2000* (NREL/TP-50-31546). Golden, CO: National Renewable Energy Laboratory.

Osterwald, C. R., S. Anevsky, A. K. Barua, P. Chaudhuri, J. Dubard, K. Emery et al. 1999. "The World Photovoltaic Scale: An International Reference Cell Calibration Program." *Progress in Photovoltaics Research and Applications* 7: 287–97.

Painter, H. E. 1981. "The Performance of a Campbell-Stokes Sunshine Recorder Compared with a Simultaneous Record of Normal Incidence Irradiance." *Meteorology Magazine* 110: 102–9.

Pape, B., J. Battles, N. Geuder, R. Zurita, F. Adan, and B. Pulvermüller. 2009. "Soiling Impact and Correction Formulas in Solar Measurements for CSP Projects." *Proceedings of the SolarPACES Conference*, Berlin, Germany, September 15–18, 2009.

Plag, F., I. Kröger, S. Riechelmann, and S. Winter. 2018. "Multidimensional Model to Correct PV Device Performance Measurements Taken under Diffuse Irradiation to Reference Conditions." *Solar Energy* 174: 431–44. https://doi.org/10.1016/j.solener.2018.08.072.

Reda, I. 1996. "Calibration of a Solar Absolute Cavity Radiometer with Traceability to the World Radiometric Reference" (NREL/TP-463-20619). Golden, CO: National Renewable Energy Laboratory.

Reda, I., T. Stoffel, and D. Myers. 2003. "A Method to Calibrate a Solar Pyranometer for Measuring Reference Diffuse Irradiance." *Solar Energy* 74: 103–12.

Roesch, A., M. Wild, A. Ohmura, E. G. Dutton, C. N. Long, and T. Zhang. 2011a. "Assessment of BSRN Radiation Records for the Computation of Monthly Means." *Atmospheric Measurement Techniques* 4: 339–54. https://doi.org/10.5194/amt-4-339-2011.

Roesch, A., M. Wild, A. Ohmura, E. G. Dutton, C. N. Long, and T. Zhang. 2011b. Corrigendum to "Assessment of BSRN Radiation Records for the Computation of Monthly Means." *Atmospheric Measurement Techniques* 4: 973. https://doi.org/10.5194/amt-4-973-2011.

Schüler, D., S. Wilbert, N. Geuder, R. Affolter, F. Wolfertstetter, C. Prahl, M. Röger, et al. 2016. "The Enermena Meteorological Network—Solar Radiation Measurements in the Mena Region." *AIP Conference Proceedings* 1734 (1): 150008. https://doi.org/doi:http://dx.doi.org/10.1063/1.4949240.

Schwandt, M., K. Chhatbar, R. Meyer, K. Fross, I. Mitra, R. Vashistha, G. Giridhar, S. Gomathinayagam, and A. Kumar. 2014. "Development and Test of Gap Filling Procedures for Solar Radiation Data of the Indian SRRA Measurement Network." *Energy Procedia* 57: 1100–9. http://dx.doi.org/10.1016/j.egyp.

Stanhill, G. 1998. "Estimation of Direct Solar Beam Irradiance from Measurements of the Duration of Bright Sunshine." *International Journal of Climatology* 18 (3): 347–54. https://doi.org/10.1002/(SICI)1097-0088(19980315)18:3<347::AID-JOC239>3.0.CO;2-O.

Vignola, F. 2006. "Removing Systematic Errors from Rotating Shadowband Pyranometer Data." *Solar 2006 Conference Proceedings*, Denver, Colorado, July 7–13, 2006.

Vignola, F., C. N. Long, and I. Reda. 2009. "Testing a Model of IR Radiative Losses" (NREL/CP- 3B0-46411). *Proceedings SPIE Solar Energy + Technology Conf.,* Volume 7410, Optical Modeling and Measurements for Solar Energy Systems III; 741003. https://doi.org/10.1117/12.826325.

Vignola, F., J. Michalsky, and T. Stoffel. 2020. "Solar and Infrared Radiation Measurements, Second Edition." Boca Raton, FL: CRC Press. ISBN-10: 1138096296.

Vignola, F., J. Peterson, F. Mavromatakis, S. Wilbert, A. Forstinger, M. Dooraghi, and M. Sengupta. 2019. "Removing Biases from Rotating Shadowband Radiometers." *AIP Conference Proceedings* 2126 (1): 190017. https://doi.org/10.1063/1.5117714.

Vignola, F., J. Peterson, R. Kessler, M. Dooraghi, M. Sengupta, and F. Mavromatakis. 2018. "Evaluation of Photodiode-Based Pyranometers and Reference Solar Cells on a Two-Axis Tracking System." *Proceedings of the 45th IEEE Photovoltaic Specialists Conference*. Waikoloa Village, HI. https://doi.org/10.1109/PVSC.2018.8547299.

Vignola, F., J. Peterson, S. Wilbert, P. Blanc, N. Geuder, and C. Kern. 2017. "New Methodology for Adjusting Rotating Shadowband Irradiometer Measurements." *AIP Conference Proceedings* 1850 (1): 140021. https://doi.org/10.1063/1.4984529.

Vuilleumier, L., M. Hauser, C. Félix, N. Sommer, D. Ruffieux, and B. Calpini. 2012. "Performance Evaluation of Radiation Sensors for the Solar Energy Sector" (TECO-2012). *WMO Technical Conference on Meteorological and Environmental Instruments and Methods of Observation*, Brussels, Belgium, October 16–18, 2012. https://www.wmo.int/pages/prog/www/IMOP/publications/IOM-109_TECO-2012/Session1/P1_25_Vuilleumier_performance_eval_radiation_sensors.pdf.

Wilbert, S. 2014. "Determination of Circumsolar Radiation and Its Effect on Concentrating Solar Power." Ph.D. diss., Rheinisch-Westfälische Technische Hochschule Aachen University (Aachen, Germany). urn:nbn:de:hbz:82-opus-51715. Accessed November 11, 2014. http://darwin.bth.rwth-aachen.de/opus3/volltexte/2014/5171/.

Wilbert, S., N. Geuder, M. Schwandt, B. Kraas, W. Jessen, R. Meyer, and B. Nouri. 2015. *Best Practices for Solar Irradiance Measurements with Rotating Shadowband Irradiometers: A Report of IEA SHC Task 46, Solar Resource Assessment and Forecasting, August 18th, 2015*. Paris, France. http://task46.iea-shc.org/data/sites/1/publications/INSRSI_IEA-Task46B1_BestPractices-RSI_150819.pdf.

Wilbert, S., S. Kleindiek, B. Nouri, N. Geuder, A. Habte, M. Schwandt, and F. Vignola. 2016. "Uncertainty of Rotating Shadowband Irradiometers and Si-Pyranometers Including the Spectral Irradiance Error." *AIP Conference Proceedings* 1734 (1): 150009. http://dx.doi.org/10.1063/1.4949241.

Wilbert, S., W. Jessen, A. Forstinger, A. Driesse, A. Habte, M. Sengupta, A. Marzo, F. Vignola, and L. F. Zarzalejo. 2020. "Application of the Clear Sky Spectral Error for Radiometer Classification in ISO 9060." *Proceedings of the Solar World Congress*, Santiago de Chile. DOI: 10.18086/swc.2019.44.08.

Wilcox, S., and D. Myers. 2008. *Evaluation of Radiometers in Full-Time Use at the National Renewable Energy Laboratory Solar Radiation Research Laboratory* (NREL/TP-550-44627). Golden, CO: National Renewable Energy Laboratory.

Wilcox, S., and P. McCormack. 2011. "Implementing Best Practices for Data Quality Assessment of the National Renewable Energy Laboratory's Solar Resource and Meteorological Assessment Project." *Proceedings of the 40th ASES National Solar Conference 2011 (Solar 2011)*, Raleigh, North Carolina, May 17–20, 2011, 471–78. Boulder, CO: American Solar Energy Society (ASES). https://www.nrel.gov/docs/fy11osti/50897.pdf.

World Meteorological Organization (WMO). 2018. *Guide to Instruments and Methods of Observation, Volume 1 – Measurement of Meteorological Variables* (WMO-No. 8), 2018 edition. https://library.wmo.int/index.php?lvl=categ_see&id=10586.

Xie, Y., and M. Sengupta. 2018. "A Fast All-sky Radiation Model for Solar applications with Narrowband Irradiances on Tilted surfaces (FARMS-NIT): Part I. The Clear-Sky Model." *Solar Energy* 174: 691–702.

4 MODELING SOLAR RADIATION: CURRENT PRACTICES

Manajit Sengupta,[1] Jesús Polo,[2] Christian Gueymard,[3] and Ping Wang[4]
[1] *National Renewable Energy Laboratory*
[2] *Centro de Investigaciones Energéticas, Medioambientales y Tecnológicas (CIEMAT)*
[3] *Solar Consulting Services*
[4] *The Royal Netherlands Meteorological Institute (KNMI)*

4.1 Introduction

High-quality solar resource assessment accelerates technology deployment by making a positive impact on decision making and by reducing uncertainty in investment decisions. Global horizontal irradiance (GHI), global tilted irradiance (GTI), and/or direct normal irradiance (DNI) are the quantities of interest for solar resource assessment and characterization at a particular location. Surface-based measurements of DNI and GHI can be made only on a relatively sparse network, given the costs of operation and maintenance. GTI is rarely measured in radiometric networks. Nevertheless, observations from ground networks have been used in conjunction with models to create maps of surface solar radiation (Gueymard 2008a). Another option is to use information from geostationary satellites to estimate GHI and DNI at the surface (Cano et al. 1986; Diabate et al. 1988; Pinker and Laszlo 1992; Beyer, Costanzo, and Heinemann 1996; Perez et al. 2002; Rigollier et al. 2004; Cebecauer and Suri 2010; Qu et al. 2016). Because different geostationary satellites are available at different longitudes around the world, radiation can be available for the entire globe (at least between latitudes from approximately -60° to +60°) at temporal and spatial resolutions representative of a particular satellite. For northern and southern high latitudes, a compilation of satellite-derived data based on observations from polar orbiters offers good spatial coverage but typically at a lower spatiotemporal resolution (Karlsson et al. 2017a, 2017b; Kato et al. 2018).

Solar radiation models that use only ground-measured input parameters were used in the past when satellite or weather-model-derived databases were not available. Examples of such models are briefly mentioned for historic reasons. One popular historic model type is based on data from the Campbell-Stokes sunshine duration recorder. The monthly mean GHI is derived using a regression fit to the number of sunshine hours measured by the sunshine recorder's burn marks when direct solar irradiance exceeds a threshold value of ≈120 W/m^2. The regression coefficients are calculated using existing GHI measurements at specific locations. The exact method to calculate GHI using sunshine recorder information is empirical and therefore specific to each geographic area. Moreover, the meteorological services of some countries, such as the United States and Canada, have stopped measuring sunshine duration because of the limited quality and significance of this measurement, which is not standardized and varies from one country to another.

In the absence of surface radiation measurements, estimates of surface radiation can be made using routine meteorological ground measurements and human observations of cloud cover in a radiative transfer model (Marion and Wilcox 1994). For instance, the METeorolgoical-STATistical (METSTAT) model (Maxwell 1998) used information about cloud cover, water vapor, ozone, and aerosol optical depth (AOD) to develop empirical correlations to compute atmospheric transmittance extinction during both clear- and cloudy-sky conditions. That model was used to create earlier versions of the U.S. National Solar Radiation Database (NSRDB) (1991–2005) (e.g., George et al. [2007]). Similar

developments have been carried out in Europe with successive versions of the European Solar Radiation Atlas (Page, Albuisson, and Wald 2001).

Long-term GHI data can also be obtained from various numerical weather prediction (NWP) models, either by operating them in reanalysis mode or from actual operational weather forecasts. Examples of reanalysis data include the ERA5 (Hersbach et al. 2019; Trolliet et al, 2018) from the European Center for Medium-Range Weather Forecasting (ECMWF) and the Modern Era Retrospective analysis for Research and Applications, Version 2 (MERRA-2) from the National Aeronautics and Space Administration (NASA) (Bosilovich, Lucchesi, and Suarez 2016; Trolliet et al. 2018). Weather forecasts such as those from the ECMWF's Integrated Forecasting System (IFS) and the National Oceanic and Atmospheric Administration's (NOAA's) Global Forecast System (GFS) can also provide estimates of GHI. Such estimates, however, are typically not as accurate as those derived from satellite-based models, and they require careful bias corrections (Boilley and Wald 2015, Urraca et al, 2018).

This chapter contains an introduction to satellite-based models, information about currently operational models that provide surface radiation data for current or recent periods, a summary of radiative transfer models used in the operational models, and a discussion of uncertainty in solar-based resource assessments. A short discussion on NWP-based solar radiation data is also included.

4.2 Estimating the Direct and Diffuse Components from Global Horizontal Irradiance

During clear and partly cloudy conditions, diffuse irradiance on a horizontal surface, DHI, is often only a relatively small part (<30%) of GHI. During dense overcast conditions, GHI and DHI should be identical. When no simultaneous DHI or DNI measurements exist and no alternate determinations are available—for example, from physical-based satellite-based models—DNI and DHI must be estimated from GHI data. Many models based on empirical correlations between GHI and either DHI or DNI data have been developed since Liu and Jordan (1960); Erbs, Klein, and Duffie (1982); Maxwell (1987); Perez et al. (1990); and Louche et al. (1991). More recently, Engerer (2015), Gueymard and Ruiz-Arias (2016), Aler et al. (2017), and Yang and Gueymard (2020) extended this empirical methodology to obtain DNI and DHI at a 1-minute resolution. These algorithms use empirical correlations between the global clearness index, K_t = GHI/[ETR cos(SZA)], and the diffuse fraction, K = DHI/GHI, the diffuse clearness index (i.e., the diffuse transmittance), K_d = DHI/[ETR cos(SZA)], or the direct clearness index (direct transmittance), K_n = DNI/ETR. All these separation models are derived empirically. There are reviews of substantial literature on this topic (e.g., see Gueymard [2008a], Gueymard and Ruiz-Arias [2016], and Tapakis et al. [2016]). Analysts should note that some hourly separation models, including the most popular ones, might not perform correctly if used with subhourly data (Gueymard and Ruiz-Arias 2016).

4.3 Estimating Irradiance on a Tilted Surface

Solar conversion systems, such as flat-plate collectors or non-concentrating photovoltaics (PV), are tilted toward the equator to increase their solar resource. Estimating or modeling the irradiance incident upon them is essential to predicting their performance and yield. This irradiance incident on the plane of array (POA) is usually called GTI, or sometimes simply POA. GTI can be measured directly by pyranometers that are tilted the same as the collector plane. Modeling GTI mainly requires data of the three main components on the horizontal surface (GHI, DNI, and DHI). GTI can be estimated as the sum of the incident beam, incident sky diffuse, and incident ground-reflected irradiances on the tilted surface; see Eq.

2-2b. The incident beam contribution is simply a straightforward geometric transformation of DNI, requiring only the angle of incidence of DNI on the tilted plane. The ground-reflected contribution is generally small for tilts less than 45°, unless the ground is covered with snow. A simple estimation is possible but requires several assumptions: the foreground is assumed infinite, horizontal, and of isotropic reflectance. In practice, however, the reflected irradiance incident on PV panels outside of the front row would be overestimated with this approach.

The main difficulty is the computation of the sky diffuse irradiance, which has been studied by many authors with different approaches ranging from the simplest isotropic model to more elaborate and complex formulations (Gueymard 1987; Kambezidis, Psiloglou, and Gueymard 1994; Khalil and Shaffie 2013; Liu and Jordan 1960; Loutzenhiser et al. 2007; Muneer and Saluja 1985; Olmo et al. 1999; Padovan and Del Col 2010; Ridley, Boland, and Lauret 2010; Wattan and Janjai 2016; Xie et al. 2016). See the recent review of these models in Yang (2016). Based on the existing studies of the literature, one of the most widely used and validated models is the Perez model (Perez et al. 1987, 1988, 1990). It is the result of a detailed analysis of the isotropic diffuse, circumsolar, and horizon brightening irradiances that are computed by using empirically derived parameters. This approach works well with hourly data, but recently it has been found to generate erroneous values with subhourly data when $K_t > 1$ (i.e., under cloud-enhancement conditions) (Gueymard 2017).

4.4 Introduction to Satellite-Based Models

The goal of satellite-based irradiance models is to use observed information about top-of-atmosphere (TOA) upwelling radiances and atmospheric and surface albedos to derive GHI and DNI at the surface of the Earth. During the last decades, satellite-based retrievals of GHI have been used, for example, for climate studies (Justus et al. 1986). A broad overview of these methods was published by Renné et al. (1999). These methods were originally divided into subjective, empirical/statistical, empirical/physical, and physical methods (Pinker, Frouin, and Li 1995; Schmetz 1989; Myers 2013). The empirical/statistical methods are based on developing relationships between satellite- and ground-based observations; the empirical/physical and theoretical methods estimate surface radiation directly from satellite information using retrieval schemes to determine the atmospheric properties important to radiative transfer. Most empirical/statistical and empirical/physical models are now classified as semiempirical because they involve the development of intermediate relationships either to relate satellite observations with surface radiation measurements or to convert satellite observations directly to solar radiation estimates. Empirical and semiempirical methods generally produce only GHI and require additional models (see Sections 4.2 and 4.4.3) to calculate DNI from GHI. Physical models, on the other hand, generally follow a two-step process that derives cloud optical properties using the satellite radiances in the first step and then computes GHI and DNI using these cloud properties in a radiative transfer model in the second step.

4.4.1 Geostationary Satellites

Geostationary satellites located above the equator that orbit at the same rate as the Earth's rotation provide continuous coverage of their field of view. Observations are usable up to latitudes 60° N and 60° S because of the Earth's curvature, as shown in Figure 4-1. The current Geostationary Operational Environmental Satellite (GOES) series covers North and South America (full disk) every 10–15 minutes and the Northern Hemisphere every 5 minutes. Two GOES satellites (GOES-East/GOES-16 and GOES-West/GOES-17) operate concurrently and provide 5-minute coverage for the entire United States. The Advanced Baseline Imager (ABI) on the current GOES satellites makes radiance observations in 16 wavelength bands, or spectral regions (see Table 1) (Schmit et al. 2005; Schmit 2018).

GOES-16 became operational in 2018, and GOES-17 became operational in 2019. The wavelengths in Table 1 are representative of the latest generation of geostationary satellite and are similar to those used on the Himawari series of satellites. The previous version of the GOES-East and GOES-West series provided data for five channels (one visible, four infrared) every 30 minutes for the Northern Hemisphere and every 3 hours at full disk.

Table 4-1. GOES-16 and GOES-17 ABI Bands

ABI Band	Central Wavelength (μm)	Type	Spatial Resolution at Nadir (km)
1	0.47	Visible	1
2	0.64	Visible	0.5
3	0.86	Near-infrared	1
4	1.37	Near-infrared	2
5	1.6	Infrared	1
6	2.2	Infrared	2
7	3.9	Infrared	2
8	6.2	Infrared	2
9	6.9	Infrared	2
10	7.3	Infrared	2
11	8.4	Infrared	2
12	9.6	Infrared	2
13	10.3	Infrared	2
14	11.2	Infrared	2
15	12.3	Infrared	2
16	13.3	Infrared	2

The European Organization for the Exploitation of Meteorological Satellites (EUMETSAT) owns the Meteosat series of satellites that covers Europe, Africa, Middle East, the Indian Ocean, and western Asia. The visible and infrared imager on the Meteosat First Generation (MFG) satellites (up to Meteosat-7) had three visible channels, water vapor (6.2 μm), and infrared. The visible channel produced a 5-km nadir resolution; the infrared channel's nadir resolution was also 5 km. Moreover, there were two channels with 2.5-km resolution, in interleaved format. Imagery had a repetition frequency of 30 minutes. The Spinning Enhanced Visible and InfraRed Imager (SEVIRI) on the Meteosat Second Generation (MSG) satellites (Meteosat-8 onward) provides satellite imagery every 15 minutes at a nominal 3-km resolution for 11 channels (Schmetz et al. 2002). The 12th channel, a high-resolution visible channel, has a nadir resolution of 1 km.

The Himawari-8 is a third-generation satellite similar to GOES-16 and the EUMETSAT's Meteosat Third Generation (MTG) satellites and covers East Asia and the Western Pacific. Himawari-8 was launched in October 2014 and harbors the Advanced Himawari Imager, which has characteristics similar to the ABI (Besho et al. 2016). Of the 16 bands, the visible and near-infrared bands measure at resolutions of 0.5 km or 1 km, whereas the infrared bands measure at 2 km. A full-disk image is produced every 10 minutes, and the sectors are generated every 2.5 minutes. Himawari-8 replaced the Multifunctional Transport Satellite series of satellites, which had been in operation since 2005.

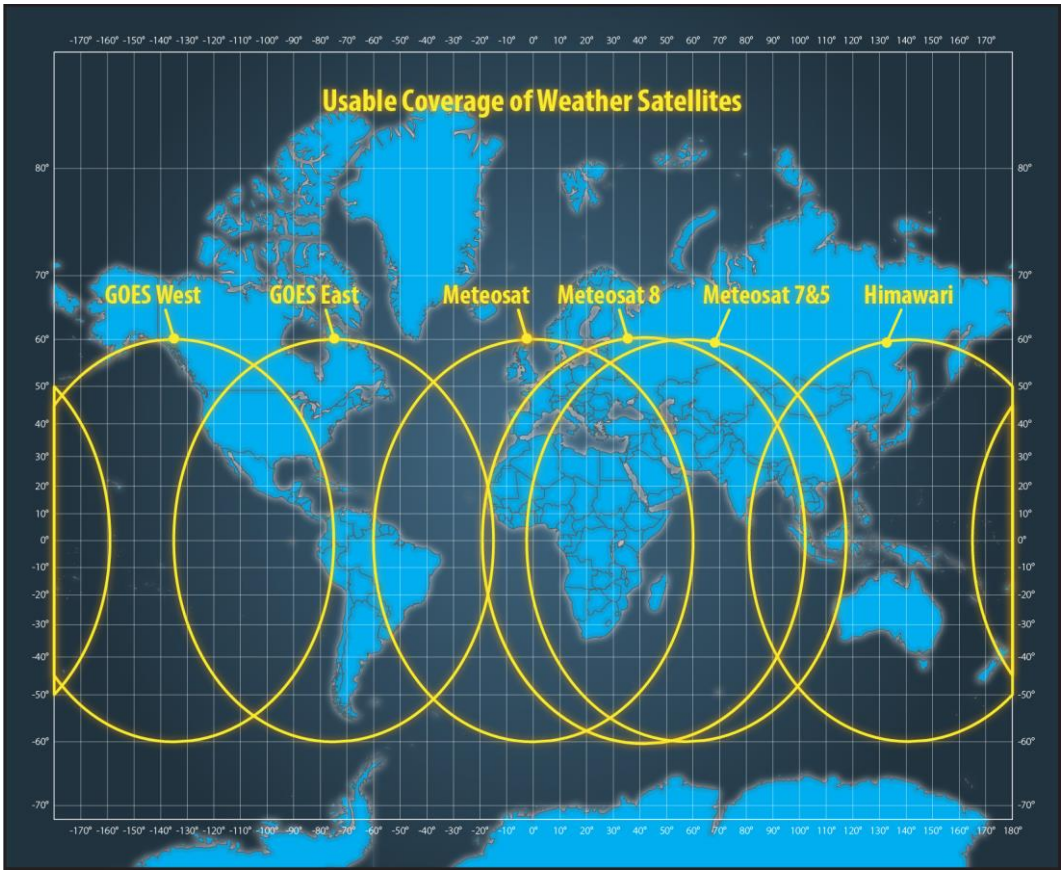

Figure 4-1. Location of the current geostationary satellites that provide coverage around the globe. *Image from NREL*

4.4.2 Polar-Orbiting Satellites

Polar-orbiting satellites are used to continuously sense the Earth and retrieve cloud properties and solar radiation at the surface. An example of one such instrument is the Advanced Very High Resolution Radiometer (AVHRR) on the NOAA series of polar-orbiting platforms. Other examples are the Moderate Resolution Imaging Spectroradiometer (MODIS) and the Clouds and the Earth's Radiant Energy System (CERES) instruments on NASA's Aqua and Terra satellites. The Joint Polar Satellite System (JPSS) series of satellites is expected to replace the legacy NOAA polar satellites. The first satellite in the JPSS series was launched in 2011 and is called the Suomi National Polar-Orbiting Partnership. The second satellite, NOAA-20, was launched in 2017. This next-generation series of satellites has multiple instruments, including the Visible Infrared Imaging Radiometer Suite, Cross-track Infrared Sounder, Advance Technology Microwave Sounder, Ozone Mapping and Profiler Suite, and CERES. Although polar orbiters provide global coverage, their temporal coverage is limited because of their orbit, in which they essentially cover a particular location only once per day at the lower latitudes. At higher latitudes, a combination of many polar-orbiting, satellite-based products is recommended to achieve a sufficient temporal resolution while also benefiting from better spatial resolution.

4.4.3 Satellite-Based Empirical and Semiempirical Methods

Satellite-based semiempirical methods consider a pseudo-linear correlation between the atmospheric transmittance and the radiance sensed by the satellite. Semiempirical models are classified as such because of their hybrid approach to retrieving surface radiation from satellite observations, in which the normalized satellite-observed reflectance is related to

GHI at the surface. Cloud-cover indices that use visible satellite imagery are first created with budget equations between TOA and surface radiation. Those indices are then used to modify the clear-sky GHI and estimate GHI at the ground consistent with the cloud scene. DNI can then be derived from GHI and the clear-sky DNI using one of the empirical methods discussed later in this subsection. The semiempirical approach was originally designed to create regression relationships between what is simultaneously observed by a satellite and ground-based instruments (Cano et al. 1986; Hay et al. 1978; Justus et al. 1986; Tarpley 1979). The method developed by Cano et al. (1986) is called the Heliosat method. It has been regularly updated and modified to rely on atmospheric transmittance properties of water vapor and aerosols to provide solar radiation estimates under clear-sky conditions rather than direct empirical relationships with ground data.

The original Heliosat method evaluates the clearness index, K_t, or the ratio of the radiative flux at the Earth's surface and the radiative flux at the TOA (which is known), using the relationship:

$$K_t = a\, n + b \tag{4-1}$$

where a and b are the slope and intercept of the assumed linear relation, and n is the so-called cloud index defined as:

$$n = [\rho - \rho_g] \,/\, [\rho_{cloud} - \rho_g] \tag{4-2}$$

where ρ, ρ_{cloud}, and ρ_g are the satellite-based reflectance observations of the current scene, of the brightest clouds, and of the ground, respectively. The cloud index is close to 0 when the observed reflectance is close to the ground reflectance (i.e., when the sky is clear). It can be negative if the sky is very clear, in which case ρ is smaller than ρ_g. The cloud index increases as clouds appear, and it can be greater than 1 for clouds that are optically very thick.

The parameters a and b in Eq. 4-1 can be derived empirically by comparison with coincident ground measurements or they can determined based on the physical principles of atmospheric transmittance, which include not only the cloud index but also the influence of aerosols, water vapor, and trace gases. Diabate et al. (1988) observed that three sets of parameters for the morning, noon, and afternoon were needed for Europe. The Heliosat method (and all cloud-index-based methods) requires the determination of cloud-free and extremely high cloud reflectivity instances to establish bounds to Eq. 4-1. Espinar et al. (2009) and Lefèvre, Wald, and Diabate (2007) found that a relative error in the ground albedo related to errors in determining the reflectivity from a cloud-free pixel leads to a relative error of the same magnitude in GHI under clear-sky conditions, which corresponds to approximately 10% of the GHI in clear cases. In cloudy cases, the error, which is caused by an error in the limit for the albedo of the brightest clouds, increases as cloud optical depth (COD) increases, and the relative error in the GHI can reach 60% (Espinar et al. 2009; Lefèvre, Wald, and Diabate 2007).

Beyer, Costanzo, and Heinemann (1996) developed an enhanced version of the Heliosat method called Heliosat-1. One major enhancement was the adoption of the clear-sky index, K_c (the ratio of the actual GHI to the GHI under ideal clear conditions), instead of the clearness index, K_t. This resulted in the relationship $K_c = 1 - n$, which simplified the method. Additional work was done to remove the dependence of the satellite radiance based on the sun-to-satellite geometry, thereby leading to a more spatially homogeneous cloud index. In addition, the determination of ground albedo and cloud albedo was improved by Beyer, Costanzo, and Heinemann (1996). Rigollier et al. (2004) developed Heliosat-2, which further enhanced Heliosat-1 by removing parameters that needed to be tuned and replacing them with either constants or values that can be computed automatically during the process. The

HelioClim-3 and Solar Energy Mining (SOLEMI) databases, produced by MINES ParisTech and DLR, respectively, use Heliosat-2. The Heliosat-3 version was designed collaboratively by the University of Oldenburg, MINES ParisTech, and DLR, among others, and it uses the SOLIS clear-sky model, which approximates radiative transfer equations for fast implementation (Müller et al. 2004). Centro de Investigaciones Energéticas, Medioambientales y Tecnológicas (CIEMAT) and its spin-off, IrSoLaV, performed remarkable modifications on the Heliosat-3 scheme. This resulted in a different model, which includes a clear-sky detection algorithm, different possible clear-sky models with atmospheric component data sets as input, and a dynamic model for estimating the ground albedo as a function of the scattering angle (Polo et al. 2012, 2013).

Hay et al. (1978) developed a regression model that relates the atmospheric transmittance to the ratio of incoming to outgoing radiation at the TOA. The transmittance was then used to derive GHI. In this method, the coefficients of the regression model change significantly based on location, and they need to be trained with surface observations (Nunez 1990) to produce accurate results. The Tarpley (1979) method also used the well-known relation between surface radiation, TOA radiation (both upwelling and downwelling), and atmospheric transmittance to create three separate regression equations. The regression equations were classified based on sky conditions labeled as clear, partly cloudy, and cloudy, and they were used accordingly.

Models such as those developed by Perez et al. (2002), Rigollier et al. (2004), and Cebecauer and Suri (2010) evolved from Cano et al. (1986) and included refinements to address albedo issues, when the surface is covered by snow, and the effects of sun-satellite geometry. Some of these models have since been modified to include the simplified SOLIS model (Ineichen 2008), and are used to estimate GHI first and then DNI after component separation (Section 4.2).

4.4.4 Satellite-Based Physical Models

Physical models generally use radiative transfer theory to directly estimate surface radiation based on first principles using cloud properties, water vapor, AOD, and ozone as inputs. The radiative transfer models can be classified as either broadband or spectral, depending on whether the radiative transfer calculations involve a single broadband calculation or multiple calculations in different wavelength bands.

The broadband method of Gautier et al. (1980) used thresholds depending on multiple days of satellite pixel measurements to determine clear and cloudy skies. Separate clear-sky and cloudy-sky models were then used to evaluate the surface DNI and GHI. The clear-sky model initially included water vapor and Rayleigh scattering but progressively added ozone (Diak and Gautier 1983) and aerosols (Gautier and Frouin 1984). Assuming that attenuation caused by the atmosphere does not vary from clear to cloudy conditions, Dedieu, Deschamps, and Kerr (1987) created a method that combines the impacts of clouds and the atmosphere. This method uses a time series of images to determine clear-sky periods for computing surface albedo. Darnell et al. (1988) created a parameterized model to calculate surface radiation using a product of the TOA irradiance, atmospheric transmittance, and cloud transmittance. Developed with data from polar-orbiting satellites, this model used collocated surface and satellite measurements to create relationships between cloud transmittance and planetary albedo.

Möser and Raschke (1983) created a model based on the premise that GHI is related to fractional cloud cover and used it with Meteosat data to estimate solar radiation over Europe (Möser and Raschke 1984). The fractional sky cover was determined to be a function of satellite measurements in the visible channel. This method uses radiative transfer modeling (Kerschgens et al. 1978) to determine the clear- and overcast-sky boundaries. Stuhlmann et

al. (1990) have since enhanced the model to include elevation dependence and additional constituents as well as multiple reflections in the all-sky model.

An important spectral model developed by Pinker and Ewing (1985) divided the solar spectrum into 12 intervals and applied the Delta-Eddington approximation for radiative transfer (Joseph et al. 1976) to a three-layer atmosphere. The primary input to the model is the COD, which can be provided from various sources. This model was enhanced by Pinker and Laszlo (1992) and used in conjunction with cloud information from the International Satellite Cloud Climatology Project (ISCCP) (Schiffer and Rossow 1983). Another physical method involves the use of satellite information from multiple channels to derive cloud properties (Stowe et al. 1999) and then evaluate DNI and GHI using the cloud properties in a radiative transfer model. This method, called CLOUDS, was originally developed using the polar-satellite data from the AVHRR instrument onboard NOAA satellites, and the processing system was called Clouds from AVHRR Extended System (CLAVR-x) (Heidinger 2003; Pavolonis et al. 2005). This method has been modified and enhanced to use cloud properties from the GOES satellites (Heidinger 2003; Pavlonis et al. 2005). In 2013, CLAVR-x was updated again to support the generation of higher spatial resolution output for the NOAA National Centers for Environmental Prediction and incorporated many algorithm improvements from the GOES-R Algorithm Working Group effort.

The cloud information produced from the CLAVR-x type of algorithms can then be input to a radiative transfer model, such as the Fast All-sky Radiation Model for Solar applications (FARMS) (Xie et al. 2016), to calculate GHI and DNI, as has been done for the development of the most recent versions of the National Renewable Energy Laboratory's (NREL's) gridded NSRDB (1998–2015).

Another cloud retrieval scheme, called AVHRR Processing scheme Over cLouds, Land, and Ocean (APOLLO), was developed by Kriebel et al. (1989, 2003) for the AVHRR instrument. APOLLO has been adapted for use with data obtained from the SEVIRI instrument on the MSG satellite. APOLLO-derived cloud products, including COD and cloud type, can be used in a radiative transfer model such as Heliosat-4 (Oumbe 2009; Qu et al. 2016), made operational by the Copernicus service (http://www.copernicus-atmosphere.eu).

The ISCCP (Schiffer and Rossow 1983) was established in 1982 as part of the World Climate Research Programme. The ISCCP cloud products include COD, cloud top temperature, cloud particle size, and other cloud properties that could be used to derive surface radiation.

Physical models are computationally more intensive than empirical and semiempirical models. Advantage of physical models, however, are that they can use additional channels from new satellites (such as MSG or GOES-16) to improve cloud property retrieval and can include physical properties of aerosols and other gaseous species, such as water vapor, explicitly.

4.5 Clear-Sky Models Used in Operational Models

4.5.1 Bird Clear-Sky Model

The Bird clear-sky model (Bird and Hulstrom 1981) is a broadband algorithm that produces estimates of clear-sky direct beam, hemispherical diffuse, and total hemispherical solar radiation on a horizontal surface. The model uses a parameterization based on radiative transfer computations and comprising simple algebraic expressions. Model results are expected to agree within ±10% with detailed high-resolution spectral or broadband physics-based radiative transfer models. The model can be used at resolutions of 1 minute or better and can duly accept inputs at that frequency, if available. In the absence of high-temporal-

resolution input parameters, however, climatological or annual average values can be used alternatively as inputs to the model. The Bird clear-sky model also forms the basis of the clear-sky part of METSTAT, with only minor modifications. The performance of these two models has been assessed rigorously and compared to other algorithms (Badescu et al. 2012; Gueymard 1993, 2003a, 2003b, 2004a, 2004b, 2012; Gueymard and Myers 2008; Gueymard and Ruiz-Arias 2015).

4.5.2 European Solar Radiation Atlas Model

The European Solar Radiation Atlas (ESRA) model is another example of a clear-sky model (Rigollier et al. 2000). Used in the Heliosat-2 model that retrieves GHI from satellites, this model computes DNI, GHI, and DHI using Rayleigh optical depth, elevation, and the Linke turbidity factor as its inputs. The performance of the model has been evaluated at various locations (Badescu et al. 2012; Gueymard and Myers 2008; Gueymard 2012; and Gueymard and Ruiz-Arias 2015).

4.5.3 SOLIS Model

The SOLIS model (Müller et al. 2004) is a relatively simple spectral clear-sky model that can calculate DNI, GHI, and diffuse radiation based on an approximation to the Lambert-Beer relation for computing DNI:

$$I = I_0 \, e^{(-M*\tau)} \tag{4-3}$$

where:

- τ is the atmospheric optical depth at a specific (monochromatic) wavelength
- M is the optical air mass
- I_0 is the TOA spectral direct irradiance for a monochromatic wavelength
- I is the DNI at the surface for a monochromatic wavelength.

This equation is modified to account for slant paths and adapted for global and diffuse radiation. The modified Lambert-Beer relation (Müller et al. 2004) is:

$$I(\mathrm{SZA}) = I_0 \, .\exp(-\tau_c / (\cos(\mathrm{SZA}))^c) \tag{4-4}$$

where:

- I(SZA) is one of the irradiance components GHI, DNI, or DHI
- c is the empirical exponent that depends on the radiation component DNI, DHI, or GHI
- τ_c is the vertical broadband optical depth of the atmosphere for the radiation component of interest
- SZA is the solar zenith angle.

The Beer-Lambert equation is a simple relationship because it accounts for monochromatic DNI and is impacted only by atmospheric attenuation. On the other hand, DHI and GHI are broadband values that contain energy that is scattered by the atmosphere. The empirical exponent c is used as an adjustment to compute either GHI or DHI, as explained in Müller et al. (2004). Ineichen (2008) developed a simplified (broadband) version of that clear-sky model by developing parameterizations to replace radiative transfer model runs, thereby increasing the speed of the model.

4.5.4 McClear Model

The fast clear-sky broadband model called McClear implements a fully physical model, replacing the empirical relations or simpler models used before, such as ESRA. It exploits the recent results on aerosol properties and total column content in water vapor and ozone produced by the European Copernicus Atmosphere Monitoring Service (CAMS) project. It is based on lookup tables precomputed with the radiative transfer model libRadtran (Gschwind et al. 2019). McClear irradiances were compared to 1-minute measurements made under clear-sky conditions at several Baseline Surface Radiation Network (BSRN) stations representative of various climates (Lefèvre et al. 2013). For GHI and DNI, the correlation coefficients range from 0.95–0.99 and from 0.86–0.99, respectively. The bias ranges from 14–25 W/m² and 49–33 W/m², respectively. The root mean square errors range from 20 W/m² (3% of the mean observed irradiance) to 36 W/m² (5%) and from 33 W/m² (5%) to 64 W/m² (10%), respectively.

4.5.5 REST2 Model

The high-performance REST2 model is based on transmittance parameterizations over two distinct spectral bands separated at 0.7 µm. The model's development and its benchmarking are described by Gueymard (2008b). REST2 has been thoroughly validated and compared to other irradiance models under varied atmospheric conditions, including extremely high aerosol loads (Antonanzas-Torres et al. 2016; Engerer and Mills 2015; Gueymard 2012, 2014; Gueymard and Myers 2008; Gueymard and Ruiz-Arias 2015; Sengupta and Gotseff 2013; Zhong and Kleissl 2015).

The model is used in solar-related applications, including the benchmarking of the radiative output of the Weather Research and Forecasting (WRF) model (Ruiz-Arias et al. 2012), the operational derivation of surface irradiance components using MODIS satellite observations (Chen et al. 2014), the improvement in GHI to DNI separation modeling (Vindel et al. 2013), and the development of future climate scenarios (Fatichi et al. 2011). REST2 is also being used at NREL (Xie et al. 2016) and is integrated into its suite of algorithms that produces the current version of the NSRDB (1998–2019).

4.6 All-Sky Models Used in Operational Models

4.6.1 Fast All-Sky Radiative Transfer Model

Radiative transfer models are capable of simulating atmospheric radiation under all-sky conditions and have been used in a broad range of applications, such as satellite remote sensing or climate studies. Compared to other applications, solar energy has unique requirements from radiative transfer models and thus has particular prerequisites in the model design. For instance, the study of solar energy demands more efficient simulations of solar irradiance than the conventional models used in weather or climate studies, such as the Rapid Radiation Transfer Model (RRTM) or its simplified two-stream version for inclusion in general circulation models (RRTMG). To provide a new option for efficiently computing solar radiation, NREL developed FARMS (Xie et al. 2016) using cloud transmittances and reflectances for direct and diffuse radiation computed by RRTM with the 16-stream discrete-ordinates radiative transfer method. To reduce the computing burden, the cloud transmittances and reflectances are parameterized as functions of SZA, cloud thermodynamic phase, optical thickness, and particle size. The all-sky GHI, DHI, and DNI are ultimately computed by coupling the cloud transmittances and reflectances with surface albedo and a fast clear-sky radiation model (REST2) to account for atmospheric absorption and scattering.

To understand the accuracy and efficiency of FARMS, GHI was simulated using the cloud microphysical and optical properties retrieved from GOES data during 2009–2012 with both FARMS and RRTMG and compared to measurements taken at the Southern Great Plains site of the U.S. Department of Energy's Atmospheric Radiation Measurement Climate Research Facility. Results indicate that the accuracy of FARMS is comparable to, if not better than, the two-stream approach; however, FARMS is approximately 1000 times more efficient and faster because it does not explicitly solve the radiative transfer equation for each individual cloud condition.

Note that FARMS, as well as the conventional radiative transfer models developed for weather and climate studies, outputs only broadband irradiance over horizontal surfaces. Recently, FARMS expanded its capabilities to incorporate tilted surfaces and spectral distributions (Xie and Sengupta 2018; Xie, Sengupta, and Wang 2019).

4.6.2 All-Sky Models Used in the Recent Heliosat Model

The CAMS radiation service uses a physical retrieval of cloud parameters and the fast parameterized radiative transfer method called Heliosat-4 (Qu et al. 2016). The new Heliosat-4 method computes GHI, DNI, and DHI under all-sky conditions as a broadband aggregation of spectrally resolved internal computations. It is a fast but accurate physical model that mimics a full radiative transfer model, and it is well suited for geostationary satellite retrievals. The method is based on the work of Oumbe et al. (2014), which proved that the surface solar irradiance can be approximated by the product of the irradiance under cloudless conditions and a modification index depending only on cloud properties and ground albedo. This is why Heliosat-4 contains two precomputed lookup-table-based models: the McClear model (Lefèvre et al. 2013; Gschwind et al. 2019) for clear-sky conditions and the McCloud model for cloudy conditions. The databases for both models were developed using the libRadtran radiative transfer model (Mayer and Kylling 2005). The main inputs to McClear are aerosol properties, total column water vapor, and ozone, whereas cloud properties, such as COD, are the main inputs to the McCloud part of Heliosat-4. With MSG satellite observations, cloud properties are derived at a 15-minute temporal resolution using an adapted APOLLO retrieval scheme. An easy-to-read summary can be found in the "User's Guide to the CAMS Radiation Service"[10] (Schroedter-Homscheidt et. al. 2016).

4.6.3 Cloud Physical Properties-Surface Insolation under Clear and Cloudy Skies Algorithm

The Cloud Physical Properties (CPP) retrieval algorithms have been developed in EUMETSAT's Satellite Application Facility on Climate Monitoring (CM SAF)[11] as well as other European and national (The Netherlands) projects (Roebeling et al. 2006; Stengel et al. 2014; Karlsson et al. 2017a, 2017b; Benas et al. 2017). The basic retrieved parameters are cloud mask, cloud-top height, cloud thermodynamic phase, COD, particle effective radius, and water path. From these parameters, surface downwelling shortwave radiation is derived, as well as precipitation.

---

[10] See http://www.soda-pro.com/documents/10157/326238/CAMS72_2015SC1_D72.11.3.1_201612_UserGuide_v2.pdf/ed54f8ec-e19e-4948-af14-d4c2a94083ac.

[11] See http://www.soda-pro.com/documents/10157/326332/CAMS72_2015SC3_D72.1.3.1_2018_UserGuide_v1_201812.pdf/95ca8325-71f6-49ea-b5a6-8ae4557242bd.

The CPP algorithm first identifies cloudy and cloud-contaminated pixels using a series of thresholds and spatial coherence tests imposed on the measured visible and infrared radiances (Roebeling et al. 2006; 2009). Depending on the tests, the sky can be classified as clear, contaminated, or overcast. Subsequently, cloud optical properties (COD and effective radius) are retrieved by matching observed reflectances at visible (0.6 µm) and near-infrared (1.6 µm) wavelengths to simulated reflectances of homogeneous clouds comprising either liquid or ice particles. The thermodynamic phase (liquid or ice) is determined as part of this procedure using a cloud-top temperature estimate as additional input.

Building on the retrieval of cloud physical properties, the Surface Insolation under Clear and Cloudy Skies (SICCS) algorithm was developed to estimate surface downwelling solar radiation using broadband radiative transfer simulations (Deneke et al. 2008; Greuell et al. 2013). GHI, DNI, and DHI are retrieved. The cloud properties are the main input for cloudy and cloud-contaminated (partly cloudy) pixels. Information about atmospheric aerosol from the Monitoring Atmospheric Composition and Climate (MACC) is used for cloud-free scenes. Other inputs for the CPP and SICCS algorithms include surface elevation from the ETOPO2v2-2006 database, monthly varying integrated atmospheric water vapor from the ECMWF ERA-Interim reanalysis, and 8-day varying surface albedo derived from MODIS data.

4.7 Numerical Weather Prediction-Based Solar Radiation Estimates

NWP models, run either in reanalysis mode or to generate weather forecasts, can provide GHI estimates for long periods of time. The accuracy of such estimates is known to be less than those provided by satellite-based models. Significant improvements, however, can be obtained by improving both the model physics and the assimilation of various observations. Some commonly available models and data sets are described in the following sections. Note that this is not a complete and comprehensive list. The goal is only to provide the user with initial information related to this potential source of data.

4.7.1 Reanalysis Models

ERA5 is a global atmospheric reanalysis that provides data starting in 1979. This data set is produced using the ECMWF's data assimilation system used in the IFS. This system uses four-dimensional variational analysis and provides analysis data with TOA and both GHI and direct horizontal irradiance (all-sky and clear-sky) in hourly time resolution on an approximate 0.25° x 0.25° grid. More information can be found on the Copernicus ERA5 website.[12]

NASA's MERRA-2 is another global atmospheric reanalysis data set that provides data starting in 1980 and comprises TOA and GHI (all-sky and clear-sky). It includes additional data sets from those assimilated into the original MERRA data set. The spatial resolution is 0.5° x 0.625°, and the temporal resolution is hourly.[13]

[12] See https://cds.climate.copernicus.eu/cdsapp#!/dataset/reanalysis-era5-single-levels?tab=overview/.
[13] See https://gmao.gsfc.nasa.gov/reanalysis/MERRA-2/.

Finally, the Climate Forecast System Reanalysis from NOAA provides reanalysis data from 1979. The GHI data are available hourly at a 0.5° resolution.[14]

4.7.2 Forecast Models

Various national meteorological agencies run operational weather forecasts both regionally and globally. Some data from these operational models might be available from archives. Some of the most popular examples of global data sets are from the ECMWF's IFS runs and from NOAA's GFS runs. There are various regional model runs by national meteorological agencies that produce forecasts for individual countries and regions. Because many data sets now exist, this type of data is mentioned without pointing to specific sources. See Chapter 8, Section 8.2.2, for additional information and some examples of such data sets.

Solar forecasting requires improved forecasting of clouds, which is generally a weakness in many NWP models, so there have been significant recent efforts to improve cloud and radiation modeling, especially within the WRF mesoscale model. This led to the development of the WRF-Solar model (Jimenez et al. 2016), which includes significant improvements in cloud modeling as well as the capability to compute surface radiation using FARMS.

4.8 Site Adaptation: Merging Measurements and Models

A major goal of solar resource assessments is to provide high-quality data to evaluate the financial viability of solar power plant projects (Moser et al., 2020). This essentially implies that accurate data over long time periods are available for conducting these studies. Normally, satellite-derived data time series fulfill the requirement for long-term data; however, they could be hampered by inherent biases and uncertainty because of the following:

- The information content, quality, and spatial and temporal resolution of the raw satellite data
- The approximations made by the models converting satellite observations into surface solar radiation estimates
- The uncertainty in ancillary information needed by these models
- The empirical process used to separate the direct and diffuse components.

As part of a resource assessment study for a new large solar power plant, ground-based solar measurements are conducted for a short period of time (nominally approximately 1 year) and used to validate the satellite data. The main goal is to remove some of the uncertainties and bias in modeled data sets. This process has been given various names, including "site adaptation," which is used here for simplification. A review paper by Polo et al. (2016) provides a summary of the various methods currently used.

Note, however, that the ground-based irradiance data need to be of high quality, otherwise the correction method could degrade the quality of the modeled time series. High-quality ground measurements can be achieved only by using well-calibrated, high-quality instruments that have been deployed at well-chosen locations using optimal installation methods and regular maintenance, per the best practices described in other sections.

[14] See https://www.ncdc.noaa.gov/data-access/model-data/model-datasets/climate-forecast-system-version2-cfsv2.

Site-adaptation methods can be separated into two broad categories. The first consists of physical methods that attempt to reduce the uncertainty and bias in the data by improving the satellite model inputs, such as AOD. The second approach develops statistical correction schemes directly comparing the satellite-based irradiance estimates with "unbiased" ground observations and uses those functions to correct the satellite-based radiation estimates.

Various site-adaptation methods have been benchmarked (Polo et al., 2020) within the International Energy Agency's Photovoltaic Power Systems Programme Task 16. In that study, 11 different site-adaptation techniques have been used to assess improvements in accuracy. Ten different data sets covering both satellite-derived and reanalysis solar radiation data were used. The effectiveness of these methods is not found to be universal or spatially homogeneous, but in general it can be stated that significant improvements can be achieved eventually for most sites and data sets.

4.8.1 Physical Methods

Because the highest uncertainty in satellite models is in DNI, the primary goal is to reduce errors in DNI by improving the quantification of AOD. Methods such as those proposed by Gueymard (2011, 2012) demonstrate how accurate AOD data obtained from ground sunphotometric measurements can indeed improve DNI. Nevertheless, the scarcity of such high-quality AOD observations implies that other sources should be used. Possible sources of AOD with global coverage include retrievals from the MODIS and MISR satellites, data assimilation output from CAMS, and NASA's MERRA-2 data (Gueymard and Yang 2020). In parallel, specific methods have been developed by Gueymard and Thevenard (2009) and Ruiz-Arias et al. (2013a, 2013b) to correct biases and uncertainties in the satellite- or model-based AOD data using ground observations. These adjusted AOD data sets have been shown to improve the satellite-based solar radiation estimates at various locations.

4.8.2 Statistical Methods

Various statistical methods have been developed to use short-term ground measurements to directly correct long-term satellite-based data sets. These bias correction methods range from linear methods (Cebecauer and Suri 2010; Vindel et al. 2013; Harmsen et al. 2014; Polo et al. 2015) to various nonlinear methods, including feature transformation (Schumann et al. 2011), polynomial-based corrections (Mieslinger et al. 2014), model output statistics corrections (Bender et al. 2011; Gueymard et al. 2012), measure-correlate-predict corrections (Thuman et al. 2012), and Fourier-decomposition-based corrections (Vernay et al. 2013). Other statistical methods include regional fusion methods of ground observations with satellite-based data (Journée et al. 2012; Ruiz-Arias et al. 2015) and improvements to the irradiance cumulative distribution function (Cebecauer and Suri 2012; Blanc et al. 2012).

4.9 Summary

This chapter provided a brief overview of solar radiation modeling methods with a focus on satellite-based models. Since the 1980s, both the technology of operational meteorological satellites and models to estimate surface radiation from these satellites have improved in their resolution and accuracy. With the recent launch of GOES-16, the world is now mostly covered at temporal resolutions of 15 minutes or better and spatial resolutions of 1 km. Improvements in computational capabilities have also contributed to improving our ability to use increasingly sophisticated models that can use higher volumes of satellite and ancillary data sets and ultimately deliver products of increasing resolution and accuracy.

This chapter also contained a short introduction to NWP modeling because improvements in that area can contribute to better irradiance estimates around the globe. This chapter has

been kept deliberately short while providing the interested readers with references for more detailed reading. Finally, the following appendix provides short descriptions of some commonly used satellite-based data sets.

Appendix: Currently Available Satellite-Based Data Sets

This section presents examples of currently available operational models. Only a selection of models is presented here. Further public, scientific, and commercial operational models exist and might also be of interest for solar resource analyses. See also Chapter 6 for additional details.

National Solar Radiation Database Physical Solar Model (2019 Update)

For many years, the National Renewable Energy Laboratory (NREL) has maintained a ground-based solar radiation data set known as the National Solar Radiation Database (NSRDB). This data set included both actual in situ ground measurements and the METeorolgoical-STATistical model (METSTAT) model (Maxwell et al. 1997) to convert U.S. National Weather Surface ground-based sky observations to solar radiation estimates. The original NSRDB (1961–1990) (NREL 1992) covered the period from 1961–1990 for 239 ground stations in the United States. That original version of the NSRDB was subsequently updated to cover an extended period (1991–2005), including many more ground stations and making use of satellite-based data to correct for some ground-based measurements (NREL 2007).

In collaboration with the University of Wisconsin and the National Oceanic and Atmospheric Administration, NREL produced a physics-based satellite-derived solar radiation data set as part of a new gridded NSRDB (1998–2019) (Xie and Sengupta 2018). This gridded NSRDB (1998–2019) uses the Physical Solar Model (PSM), which produces satellite-based data every 30 minutes for 4-km-resolution pixels for North American and South America and is freely available from the NSRDB website (https://nsrdb.nrel.gov). The data fields include solar radiation and meteorological data. With the availability of the next-generation Geostationary Operational Environmental Satellites (GOES-16 and GOES-17), the NSRDB is currently producing 5-minute data for most of the Northern Hemisphere and 10- to 15-minute data for both the Northern Hemisphere and Southern Hemisphere. These data are being produced at a 2-km spatial resolution.

The PSM (currently Version 3) consists of a two-stage scheme that retrieves cloud properties and uses those properties in a radiative transfer model to compute surface radiation. In the first stage, cloud properties are generated using the Advanced Very High Resolution Radiometer (AVHRR) Pathfinder Atmospheres-Extended (PATMOS-x) algorithms (Heidinger et al. 2014). In the second stage, global horizontal irradiance (GHI) and diffuse horizontal irradiance (DHI) are computed by the Fast All-sky Radiation Model for Solar applications (FARMS) model (Xie et al. 2016) using these cloud properties as well as additional meteorological parameters as inputs. The FARMS model uses the REST2 model (Section 4.5.5) for clear-sky calculations and a fast all-sky model for cloudy-sky calculations (Section 4.6.1). The aerosol optical depth (AOD) inputs required for clear-sky calculations are obtained from the hourly Modern Era Retrospective analysis for Research and Applications, Version 2 (MERRA-2) aerosol products from the National Aeronautics and Space Administration (NASA) after scaling and bias reduction using ground AOD measurements from the Aerosol Robotic Network (AERONET). Water vapor, temperature, wind speed, relative humidity, and dew point data are obtained from NASA's MERRA-2.

The NSRDB also provides spectral data sets for 2002 wavelengths. The spectral data are produced on demand and use the FARMS-Narrowband Irradiance on Tilted Surface (FARMS-NIT) model (Xie and Sengupta 2018; Xie et. al. 2019).

The time-series irradiance data for each pixel are quality-checked to ensure that they are within acceptable physical limits, that gaps are filled, and that the Coordinate Universal Time stamp is shifted to local standard time. Finally, the GOES-East and GOES-West data sets are blended to create a contiguous data set for the period from 1998–2019.

National Aeronautics and Space Administration/Global Energy and Water Cycle Experiment Surface Radiation Budget

To serve the needs of the World Climate Research Program, Whitlock et al. (1995) developed a global Surface Radiation Budget (SRB) data set using cloud information from the International Satellite Cloud Climatology Project (ISCCP) C1 data set at a resolution of 250 km by 250 km (approximately 2.5° x 2.5°) every 3 hours (Schiffer and Rossow 1983; Zhang et al. 2004). Information from the ISCCP C1 data set is used as an input into the Pinker and Laszlo (1992) model and the Darnell et al. (1988) model.

The currently available version is the NASA/Global Energy and Water Cycle Experiment SRB Release 3.0 data set that contains global 3-hour, daily, monthly/3-hour, and monthly averages of surface longwave and shortwave radiative parameters on a 1° x 1° grid. Primary inputs to the models include:

- Visible and infrared radiances and cloud and surface properties inferred from ISCCP pixel-level data
- Temperature and moisture profiles from the GEOS-4 reanalysis product obtained from NASA's Global Modeling and Assimilation Office
- Column ozone amounts constituted by assimilating various observations.

The SRB data set is available from multiple sources. The Surface meteorology and Solar Energy (SSE) website provided SRB data in a version that was more applicable to renewable energy. SSE has recently been replaced by an improved version called POWER.[15] SRB data sets are also available from the Clouds and the Earth's Radiant Energy System (CERES) project.[16] Additionally, the Fast Longwave and Shortwave Radiative Fluxes (FLASHFlux) project generates real-time SRB data.[17] All these projects use global observations from CERES and Moderate Resolution Imaging Spectroradiometer (MODIS) instruments onboard polar-orbiting satellites. Table 4-2 shows the estimated bias and root-mean-square (RMS) error between the original NASA SSE irradiation estimates and measured World Meteorological Organization (WMO) Baseline Surface Radiation Network (BSRN) monthly averages of the three usual solar radiation components. The NASA POWER accuracy and methodology are documented on its website.

[15] See https://power.larc.nasa.gov/data-access-viewer/.
[16] See https://asdc.larc.nasa.gov/project/CERES.
[17] See https://ceres.larc.nasa.gov/data/#fast-longwave-and-shortwave-flux-flashflux.

Table 4-2. Regression Analysis of NASA SSE Compared to BSRN Bias and RMS Error for Monthly Averaged Values from July 1983–June 2006

Parameter	Region	Bias (%)	RMS (%)
GHI	Global	-0.01	10.25
	60° poleward	-1.18	34.37
	60° equatorward	0.29	8.71
DHI	Global	7.49	29.34
	60° poleward	11.29	54.14
	60° equatorward	6.86	22.78
DNI	Global	-4.06	22.73
	60° poleward	-15.66	33.12
	60° equatorward	2.40	20.93

German Aerospace Center (DLR)-Irradiance at the Surface Derived from ISCCP Cloud Data (ISIS) Model (DLR-ISIS Model)

Similar to the NASA SSE and POWER data sets, the DLR-ISIS data set[18] is a 21-year direct normal irradiance (DNI) and GHI data set based on the ISCCP cloud product covering the period from July 1983–December 2004. The cloud products are used in a two-stream radiative transfer model (Kylling et al. 1995) to evaluate DNI and GHI. The correlated-k method from Kato et al. (1999) is used to compute atmospheric absorption in the solar spectrum. Scattering and absorption in water clouds are analyzed using the parameterization of Hu and Stamnes (1993); ice cloud properties are obtained from Yang et al. (2000) and Key et al. (2002). Fixed effective radii of 10 µm and 30 µm are used for water and ice clouds, respectively. The radiative transfer algorithm and parameterizations are included in the radiative transfer library libRadtran (Mayer and Kylling 2005).

The complete method for creating the DLR-ISIS data set using the ISCCP cloud products and the libRadtran library is outlined in Lohmann et al. (2006). The cloud data used for the derivation of the DLR-ISIS data set are taken from the ISCCP FD (global radiative flux data product) input data set (Zhang et al. 2004), which is based on ISCCP D1 cloud data. (See the ISCCP website for more information about cloud data sets.[19]) It provides 3-hour cloud observations on a 280-km by 280-km equal area grid, which is also the spatiotemporal resolution of the DLR-ISIS irradiance product. The whole data set comprises 6,596 grid boxes on 72 latitude steps of 2.5°. This grid is maintained for the DLR-ISIS data set.

ISCCP differentiates among 15 cloud types. The classification includes three intervals of optical thickness in three cloud levels: low, middle, and high clouds. Low and middle cloud types are further divided into water and ice clouds; high clouds are always ice clouds.

For DLR-ISIS, optical thickness, cloud top pressure, and cloud phase given in the ISCCP data set are processed to generate clouds for the radiative transfer calculations. One radiative transfer calculation is carried out for each occurring cloud type assuming 100% cloud coverage, plus one calculation for clear sky. For the final result, irradiances are weighted with the cloud amount for each cloud type and for clear-sky conditions, respectively.

[18] See http://www.pa.op.dlr.de/ISIS/.
[19] See http://isccp.giss.nasa.gov.

HelioClim

The Heliosat-2 method, which is based on Cano et al. (1986) and modified by Rigollier et al. (2004), is used to produce the HelioClim databases[20] using Meteosat data. The HelioClim databases cover Europe, Africa, the Mediterranean Basin, the Atlantic Ocean, and part of the Indian Ocean (latitude and longitude between ±66°). The freely available HelioClim-1 database established from the Meteosat First Generation (MFG) covers the period from 1985–2005 and provides daily values of GHI with a spatial resolution of 25 km. Some statistical comparison analyses with ground measurements have been provided by Blanc et al. (2011).

The two current versions of the HelioClim-3 database (versions 4 and 5) are based on Meteosat Second Generation (MSG) and provide, over its field of view, 15-minute surface solar irradiance estimates with a spatial resolution of 3 km at nadir. These databases are available for free for the period from February 2004–December 2006. Transvalor, the valorization company of MINES ParisTech, commercializes, through their website www.soda-pro.com, the two HelioClim-3 databases for 2007 onward. Version 4 of the database makes use of the European Solar Radiation Atlas (ESRA) clear-sky irradiance model with the climatological database of monthly values of Linke turbidity (Remund et al. 2003). This database provides surface solar irradiance estimates on a near-real-time basis, with a few minutes of delay after the last image acquisition by MSG every 15 minutes. Version 5 of HelioClim-3 makes use of the McClear clear-sky irradiance model.

Ineichen (2016) provided an independent validation of HelioClim-3 versions 4 and 5, using irradiance measurements from BSRN stations.

Solar Energy Mining

Solar Energy Mining (SOLEMI) is a service from DLR that provides irradiance data commercially and for scientific purposes. The data are based on global atmospheric data sets (aerosol, water vapor, ozone) from different earth observation sources and climate models as well as cloud data from Meteosat. GHI and DNI data sets are available every hour at a 2.5-km resolution and cover Europe and Africa (1991–2012) and Asia (1999–2012). SOLEMI basically uses the Heliosat-2 method of Rigollier et al. (2004).

Copernicus Atmosphere Monitoring Service-Radiation Services

Within the European Commission's Copernicus program, the European Copernicus Atmosphere Monitoring Service (CAMS) provides atmospheric composition as aerosols, water vapor, and ozone. By coupling with MSG satellite-based cloud physical parameters in the Heliosat-4 method, the CAMS radiation service provides clear-sky and all-sky global, direct, diffuse, and direct normal irradiation. The service is jointly provided by DLR, MINES ParisTech, and Transvalor with help of the SOlar radiation DAta service.[21]

In addition to all-sky irradiation, clear-sky (cloudless) irradiation is provided as the CAMS McClear service.[22] Both services provide time series with temporal resolutions of 1 minute, 15 minutes, 1 hour, 1 day, or 1 month at the latitude and longitude requested by the user. Time series can be accessed by an interactive user interface or automatically in a scripting environment. The data records start in 2004 and last until the present time. Data are continuously updated and provided with a delay up to 2 days. The coverage is on the global scale for CAMS McClear and limited to Europe, Africa, and the Middle East for the CAMS

[20] See http://www.soda-is.com/eng/helioclim/heliosat.html.
[21] See http://www.soda-pro.com/web-services/radiation/cams-radiation-service.
[22] See http://www.soda-pro.com/web-services/radiation/cams-mcclear.

all-sky radiation service. An "expert" mode allows access to all used atmospheric input parameters for clouds, aerosols, ozone, water vapor, and surface-reflective properties.

The European program Copernicus provides environmental information to support policymakers, public authorities, and both public and commercial users. Data are provided under the Copernicus data policy, which includes free availability for any use, including commercial use.

The preoperational atmosphere service of Copernicus was provided through the EU FP7 projects MACC and MACC-II. On January 1, 2016, the MACC Radiation Service was renamed CAMS Radiation Service once it went operational within CAMS.

The user's guide (Schroedter-Homscheidt et al. 2016) describes the data, methods, and operations used to deliver time series of solar radiation available at the ground surface in an easy-to-read manner. The Heliosat-4 method is based on the decoupling solution proposed by Oumbe et al. (2014) and further described in Qu et al. (2016). The clear-sky McClear model is described in Lefèvre et al. (2013) and Gschwind et al. (2019) (see Section 4.5.4). Table 4-3 shows an overview of the data used in the CAMS Radiation Service.

Table 4-3. Summary of Data Used in CAMS-RAD

Variable	Data Sources	Temporal Resolution	Spatial Resolution
Aerosol properties and type	CAMS	3 hours	40 km
Cloud properties and type	APOLLO (DLR)	15 minutes	3–10 km
Total column content in ozone	CAMS	3 hours	40 km
Total column content in water vapor	CAMS	3 hours	40 km
Ground albedo	MODIS (prepared by MINES/ ParisTech)	Climatology of monthly values	6 km

Perez/Clean Power Research

The Perez et al. (2002) method (herein referred to as the Perez State University of New York [Perez SUNY] model) evaluates GHI and DNI based on the concept that the atmospheric transmittance is directly proportional to the top-of-atmosphere planetary albedo (Schmetz 1989). This method is being applied to the GOES satellites and is currently available as the SolarAnywhere product from Clean Power Research.[23] The concept of using satellite-based measurements of radiance assumes that the visible imagery demonstrates cloud cover for high levels of brightness and lower levels for clearer conditions (e.g., dark ground cover). Readers are referred to Perez et al. (2002) for additional details.

Vaisala Solar Data Set

3Tier (now Vaisala) developed a global solar radiation data set for both GHI and DNI. It follows the method of Perez et al. (2002) using independently developed algorithms. The revised Vaisala algorithms currently use the REST2 clear-sky model and other refinements. This data set is available for global locations at a 3-km resolution from 1997.[24]

[23] See www.cleanpower.com.
[24] See http://www.vaisala.com/Vaisala%20Documents/Scientific%20papers/3TIER%20Solar%20Dataset%20Methodology%20and%20Validation.pdf.

Solargis

An advanced semi-empirical satellite model for the calculation of global and direct irradiances has been developed by Solargis (Cebecauer and Suri 2010) and implemented for the region covered by the Meteosat, GOES, and Himawari satellites covering land between latitudes 60° N and 50° S. The model philosophy is based on the principles of the Heliosat-2 calculation scheme (Hammer et al. 2003) and the model by Perez et al. (2002), and it is implemented to operationally process satellite data at a full spatial and temporal resolution. Compared to these earlier developments, the Solargis model includes various enhancements, such as a downscaling capability to take terrain effects and local variability into account.

EnMetSol Model

The EnMetSol method[25] is a technique for determining the global radiation at ground level by using data from a geostationary satellite (Beyer, Costanzo, and Heinemann 1996; Hammer et al. 2003). It is used in combination with a clear-sky model to evaluate the three usual irradiance components. The key parameter of the method is the cloud index, *n*, which is estimated from the satellite measurements and related to the transmissivity of the atmosphere. The method is used for MFG, MSG, and GOES data. The EnMetSol method uses the SOLIS model (Müller et al. 2004) in combination with monthly averages of AOD (Kinne et al. 2005) and water vapor (Kalnay et al. 1996) as input parameters to calculate DNI or spectrally resolved solar irradiance. The DNI and DHI for all-sky conditions are derived from GHI with a beam-fraction model (Hammer et al. 2009; Lorenz 2007).

The method uses the clear-sky model of Dumortier (1998; see also Fontoynont et al. 1998) with Remund's (2009) Meteonorm high-resolution database for the turbidity input. This model is also used to obtain near-real-time and forecasts of global tilted irradiance (GTI) as inputs for photovoltaic power prediction.

KNMI Cloud Physical Properties-Surface Insolation under Clear and Cloudy Skies and Solar Radiation Data Sets

KNMI operates a specific service, MSG-Cloud Physical Properties (CPP), by which near-real-time and historic satellite observations of cloud properties, surface radiation, and precipitation are provided to users. The data are retrieved from the Spinning Enhanced Visible and InfraRed Imager (SEVIRI) instrument onboard the EUMETSAT MSG satellite, and they are particularly attractive because of their high temporal frequency of 15 minutes combined with a 3-km by 3-km subsatellite spatial resolution. Retrieval algorithms have been developed in EUMETSAT's Satellite Application Facility on Climate Monitoring (CM SAF) as well as other European and national projects. The basic retrieved parameters are cloud mask, cloud-top height, cloud thermodynamic phase, COD, particle effective radius, and water path.

The MSG-SEVIRI Surface Insolation under Clear and Cloudy Skies (SICCS) algorithm derives surface solar radiation (direct, diffuse, and global irradiance) using cloud physical properties. The SICCS products are available since 2004 at a 15-minute time interval. The CPP-SICCS products are provided at the SEVIRI pixels for the MSG full disk. The images and data can be obtained from the MSG-CPP website in near real time (http://msgcpp.knmi.nl/).

[25] See https://www.uni-oldenburg.de/fileadmin/user_upload/physik/ag/ehf/enmet/download/EnMetSol.pdf.

Validation results of hourly mean SEVIRI CPP-SICCS retrievals with observations at eight European BSRN stations yield median biases of 7 W/m^2 (2%), 6 W/m^2 (5%), and 1 W/m^2 (1%) for global, direct, and diffuse irradiance, respectively; and median root mean square errors of 65 W/m^2 (18%), 69 W/m^2 (39%), and 52 W/m^2 (34%) for global, direct, and diffuse irradiance, respectively. More detailed validation results are presented by Greuell et al. (2013).

Satellite Application Facility on Climate Monitoring Surface Radiation Products

The EUMETSAT's CM SAF service and data portal provides various satellite-derived data records of cloud properties and surface solar radiation. The surface radiation products are part of the Cloud, Albedo, and surface RAdiation data set (CLARA) and the SARAH (Surface Radiation Data Set – Heliosat) data records. The global CLARA data record is based on polar-orbiting satellites, whereas the SARAH data record is based on geostationary Meteosat satellites. The CM SAF surface radiation data records are well documented and freely available as gridded netcdf data files; further information is available here: https://www.cmsaf.eu/EN/Overview/OurProducts/Surface_Radiation_Albedo/Surface_Radiation_Products_node.html.

The CM SAF Surface Solar Radiation Data Set - Heliosat Edition 2.1 (SARAH-2.1) includes 30-minute, daily, and monthly mean data for solar surface irradiance (SIS); two surface direct irradiance parameters (SID) (direct horizontal radiation and DNI); sunshine duration (SDU) (daily, monthly sum); the spectrally resolved global irradiance (SRI) (monthly mean); and the effective cloud albedo (CAL) from 1983–2017 (Pfeifroth et al. 2018). Data are provided with a spatial resolution of 0.05° for the full disc of the Meteosat satellites at 0°, i.e., they cover Africa, Europe, and parts of South America. An adjusted Heliosat approach and the SPECMAGIC clear-sky model are used to estimate the irradiance from the geostationary satellite measurements (Müller et al. 2012; 2015).

For the SARAH-2.1 data, the achieved accuracies of the monthly means as determined by comparison with reference measurements from the BSRN for the SIS, SID, and DNI parameters are 5.2 W/m^2, 7.7 W/m^2, and 16.4 W/m^2, respectively. The daily accuracies are 11.7 W/m² for GHI, 17.1 W/m^2 for SID, and 33.1 W/m^2 for DNI. All values are based on the mean absolute difference between the SARAH-2.1 and the BSRN reference data.

To temporally extend the SARAH-2.1 climate data records, the CM SAF service provides consistent surface radiation data (SIS, SID, DNI, SDU) from 2018 onward with a delay of 5 days as part of the Interim Climate Data Record SARAH ICDR.

For the SARAH-E climate data record, satellite measurements from the Meteosat satellites located at the Indian Ocean Data Coverage have been used to estimate 60-minute, daily, and monthly surface irradiance (global and direct) from 1999–2016 (Amillo et al., 2014). The data cover most parts of Asia, Africa, and the western part of Australia and are provided with a spatial resolution of 0.05°.

The CLARA-A2 climate data record provides global data of cloud coverage and various cloud properties, surface radiation, and surface albedo from 1982–2015 (soon to be extended to mid-2019) (Karlsson et al. 2017a, 2017b). The SIS data are derived from the AVHRR measurements using a lookup-table approach (Müller et al. 2009) and are provided as daily and monthly means with a spatial resolution of 0.25°. The accuracy of the monthly and daily surface irradiance has been determined to be 9 W/m^2 and 18 W/m^2, respectively, by comparison with surface reference measurements from the BSRN.

EUMETSAT's Satellite Application Facility on Climate Monitoring Cloud Property Data Sets

The CM SAF cloud products also include two records: one derived from the polar satellite instrument AVHRR and one from Meteosat. Details on the products, retrieval algorithms, and quality can be found in the Product User Manuals, the Algorithm Theoretical Basis Documents, and the Validation Reports (https://www.cmsaf.eu/EN/Overview/OurProducts/CloudProducts/Cloud_Products_node.html). The products can be ordered via the web user interface.

Reuniwatt SICLONE Cloud Property Data Set

Reuniwatt offers SICLONE (Système d'Information pour l'analyse et la prévision des Configurations spatio-temporelLes des Occurrences NuageusEs), a cloud property data set containing cloud retrieval properties calculated with the Nowcasting Satellite Application Facility (NWCSAF) software (http://reuniwatt.com/en/applications/atmospheric-sciences/).

A comparison of cloud product databases was presented in 2019 at the European Meteorological Society conference: https://hal-mines-paristech.archives-ouvertes.fr/hal-02418087. In that study, the Heliosat-4 method was applied to three different cloud properties databases for the estimation of the surface downwelling shortwave irradiance. The first is the AVHRR Processing scheme Over cLouds, Land, and Ocean (APOLLO) database from the German Aerospace Center (DLR), which is implemented in the framework of the CAMS Radiation service. The second is the MSG-CPP product issued by the Royal Netherlands Meteorological Institute. The third is the CLAAS-2 data set generated by the German DWD in the framework of CM SAF.

Meteotest's Meteonorm Satellite Irradiation Product

A model for the calculation of global irradiances was implemented for the region covered by the GOES-E, Meteosat, INDOEX, and Himawari satellites covering land between latitudes 65° N and 65° S. The model is based on the Heliomont method (Stöckli et al. 2013), which is itself based on the Heliosat approach. It is implemented to operationally process satellite data at a full spatial and temporal resolution. Data are adapted to ground sites with spatially interpolated linear regression functions. The model was further improved by Meteotest (Müller and Remund, 2018, Schmutz et al. 2020).

4.10 References

Aler, R., I. M Galván, J. A. Ruiz-Arias, and C. A. Gueymard. 2017. "Improving the Separation of Direct and Diffuse Solar Radiation Components Using Machine Learning by Gradient Boosting." *Solar Energy* 150: 558–69. https://doi.org/10.1016/j.solener.2017.05.018.

Amillo, A.G., T. Huld, R. Müller. 2014. "A New Database of Global and Direct Solar Radiation Using the Eastern Meteosat Satellite, Models and Validation." *Remote Sensing* 6: 8,165–89.

Antonanzas-Torres, F., J. Antonanzas, R. Urraca, M. Alia-Martinez, and F. J. Martinez-de-Pison. 2016. "Impact of Atmospheric Components on Solar Clear-Sky Models at Different Elevation: Case Study Canary Islands." *Energy Conversion and Management* 109 (2016): 122–29.

Badescu, V., C. A. Gueymard, S. Cheval, C. Oprea, M. Baciu, A. Dumitrescu, F. Iacobescua, I. Milso, and C. Rada. 2012. "Computing Global and Diffuse Solar Hourly Irradiation on Clear-Sky: Review and Testing of 54 Models." *Renewable and Sustainable Energy Reviews* 16: 1,636–56.

Benas, N., S. Finkensieper, M. Stengel, G.-J. van Zadelhoff, T. Hanschmann, R. Hollmann, and J. F. Meirink. 2017. "The MSG-SEVIRI-Based Cloud Property Data Record CLAAS-2." *Earth System Science Data* 9: 415–434. https://doi.org/10.5194/essd-9-415-2017.

Bender, G., F. Davidson, F. Eichelberger, and C. A. Gueymard. 2011. "The Road to Bankability: Improving Assessments for More Accurate Financial Planning." *Proceedings of: Solar 2011 Conference of American Solar Energy Society*, Raleigh, North Carolina.

Besho, K., K. Date, M. Hayashi, A. Ikeda, T. Imai, H. Inoue, Y. Kumagai, T. Miyakawa, H. Murata, T. Ohno, A. Okuyama, R. Oyama, Y. Sasaki, Y. Shimazu, K. Shimoji, and Y. Sumida. 2016. "An Introduction to Himawari-8/9—Japan's New-Generation Geostationary Meteorological Satellites." *Journal of the Meteorological Society of Japan* 94: 151–83. https://doi.org/10.2151/jmsj.2016-009.

Beyer, H., C. Costanzo, and D. Heinemann. 1996. "Modifications of the HELIOSAT Procedure for Irradiance Estimates from Satellite Images." *Solar Energy* 56 (3): 207–21.

Bird, R. E., and R. L. Hulstrom. 1981. *A Simplified Clear-Sky Model for Direct and Diffuse Insolation on Horizontal Surfaces* (SERI/TR-642-761). Golden, CO: Solar Energy Research Institute.

Blanc, P., A. Boilley, N. Killius, P. Massip, Marion Schroedter-Homscheidt, and L. Wald. 2012. "Methods for Data Fusion." Report of the Project ENDORSE, 7th Framework Programme EU.

Blanc, P., B. Gschwind, M. Lefèvre, and L. Wald. 2011. "The HelioClim Project: Surface Solar Irradiance Data for Climate Applications." *Remote Sensing* 3 (12): 343–61. https://doi.org/10.3390/rs3020343.

Boilley, A., and L. Wald. 2015. "Comparison Between Meteorological Re-Analyses from ERA-Interim and MERRA and Measurements of Daily Solar Irradiation at Surface." *Renewable Energy* 75: 135–43. https://doi.org/10.1016/j.renene.2014.09.042.

Bosilovich, M. G., R. Lucchesi, and M. Suarez. 2016. MERRA-2: File Specification. GMAO Office Note No. 9 (Version 1.1): 73 pp.

Cano, D., J. M. Monget, M. Albuisson, H. Guillard, N. Regas, and L. Wald. 1986. "A Method for the Determination of the Global Solar Radiation from Meteorological Satellite Data." *Solar Energy* 37 (1): 31–9.

Cebecauer, T., and M. Suri. 2010. "Accuracy Improvements of Satellite-Derived Solar Resource Based on GEMS Re-Analysis Aerosols." *Proceedings of SolarPACES 2010 Conference*, Perpignan, France.

Cebecauer, T., and M. Suri. 2012. "Correction of Satellite-Derived DNI Time Series Using Locally-Resolved Aerosol Data." *Proceedings of: SolarPACES 2012 Conference*, Marrakech, Morocco.

Darnell, W. L., W. F. Staylor, S. K. Gupta, and M. Denn. 1988. "Estimation of Surface Insolation Using Sun-Synchronous Satellite Data." *Journal of Climate* 1: 820–35.

Dedieu, G., P. Y. Deschamps, and Y. H. Kerr. 1987. "Satellite Estimation of Solar Irradiance at the Surface of the Earth and of Surface Albedo Using a Physical Model Applied to Meteosat Data." *Journal of Climate and Applied Meteorology* 26: 79–87.

Deneke, H. M., A. J. Feijt, and R. A. Roebeling. 2008. "Estimating Global Irradiance from METEOSAT SEVIRI-derived Cloud Properties." *Remote Sensing Environment* 112 (6): 3,131–41.

Diabate, L., H. Demarcq, N. Michaud-Regas, and L. Wald. 1988. "Estimating Incident Solar Radiation at the Surface from Images of the Earth Transmitted by Geostationary Satellites: The HELIOSAT Project." *International Journal of Solar Energy* 5: 261–78.

Diak G. R., and C. Gautier. 1983. "Improvements to a Simple Physical Model for Estimating Insolation from GOES Data." *Journal of Climate and Applied Meteorology* 22: 505–8.

Dumortier D. 1998. *The Satellite Model of Turbidity Variations in Europe* (Technical Report).

Engerer, N. A. 2015. "Minute Resolution Estimates of the Diffuse Fraction of Global Irradiance for Southeastern Australia." *Solar Energy* 116: 215–37.

Engerer, N. A., and F. P. Mills. 2015. "Validating Nine Clear Sky Radiation Models in Australia." *Solar Energy* 120: 9–24.

Erbs, D. G., S. A. Klein, and J. A. Duffie. 1982. Estimation of the Diffuse Radiation Fraction for Hourly, Daily, and Monthly-Average Global Radiation." *Solar Energy* 28(4): 293–302. ISSN 0038-092X. https://doi.org/10.1016/0038-092X(82)90302-4.

Espinar, B., L. Ramírez, J. Polo, L. F. Zarzalejo, and L. Wald. 2009. "Analysis of the Influences of Uncertainties in Input Variables on the Outcomes of the Heliosat-2 Method." *Solar Energy* 83: 1,731–41. https://doi.org/10.1016/j.solener.2009.06.010.

Fontoynont, M, D. Dumortier, D. Heinemann, A. Hammer, J. A. Olseth, Skartveit, P. Ineichen, C. Reise, J. Page, J. Roche, H. Beyer, L. Wald. 1998. "Satellight: A WWW server which provides high quality daylight and solar radiation data for Western and Central Europe." Presented at the 9th Conference on Satellite Meteorology and Oceanography. 434–37.

Gautier, C., and R. Frouin. 1984. "Satellite-Derived Ocean Surface Radiation Fluxes." *Proceedings of the Workshop on Advances in Remote Sensing Retrieval Methods,* Williamsburg, Virginia.

Gautier, C., G. Diak, and S. Masse. 1980. "A Simple Physical Model to Estimate Incident Solar Radiation at the Surface from GOES Satellite Data." *Journal of Applied Meteorology* 19: 1,005–12.

George, R., S. Wilcox, M. Anderberg, and R. Perez. 2007. "National Solar Radiation Database (NSRDB): 10 Km Gridded Hourly Solar Database." *Solar 2007 Conference Proceedings*, July 7–12, 2007, Cleveland, Ohio. NREL/CP-581-41599. Golden, CO: National Renewable Energy Laboratory.

Greuell, W., J. F. Meirink, and P. Wang. 2013. "Retrieval and Validation of Global, Direct, and Diffuse Irradiance Derived from SEVIRI Satellite Observations." *Journal of Geophysical Research Atmospheres* 118: 2,340–61. https://doi.org/10.1002/jgrd.50194.

Gschwind B., L. Wald, P. Blanc, M. Lefèvre, M. Schroedter-Homscheidt, and A. Arola. 2019. "Improving the McClear Model Estimating the Downwelling Solar Radiation at Ground Level in Cloud-Free Conditions – McClear-v3." *Meteorologische Zeitschrift* 28 (2): 147–63. DOI: 10.1127/metz/2019/0946.

Gueymard, C. 1987. "An Anisotropic Solar Irradiance Model for Tilted Surfaces and its Comparison With Selected Engineering Algorithms." *Solar Energy* 38: 367–86. https://doi.org/10.1016/0038-092X(87)90009-0. Erratum, *Solar Energy* 40: 175 (1988). https://doi.org/10.1016/0038-092X(88)90087-4.

———. 1993. "Critical Analysis and Performance Assessment of Clear-Sky Irradiance Models Using Theoretical and Measured Data." *Solar Energy* 51: 121–38.

———. 2003a. “Direct Solar Transmittance and Irradiance Predictions with Broadband Models: Part I—Detailed Theoretical Performance Assessment.” *Solar Energy* 74: 355–79.

———. 2003b. “Direct Solar Transmittance and Irradiance Predictions with Broadband Models: Part II—Validation with High-Quality Measurements.” *Solar Energy* 74: 381–95.

———. 2004a. “Direct Solar Transmittance and Irradiance Predictions with Broadband Models: Part I—Detailed Theoretical Performance Assessment.” Corrigendum *Solar Energy* 76: 513.

———. 2004b. “Direct Solar Transmittance and Irradiance Predictions with Broadband Models: Part II—Validation with High-Quality Measurements.” Corrigendum *Solar Energy* 76: 515.

———. 2008a. “From Global Horizontal to Global Tilted Irradiance: How Accurate are Solar Energy Engineering Predictions in Practice?” *Solar 2008 Conference Proceedings*, San Diego, California. American Solar Energy Society.

———. 2008b. “REST2: High-Performance Solar Radiation Model for Cloudless-Sky Irradiance, Illuminance and Photosynthetically Active Radiation—Validation with a Benchmark Dataset.” *Solar Energy* 82: 272–85.

———. 2011. “Uncertainties in Modeled Direct Irradiance Around the Sahara as Affected by Aerosols: Are Current Datasets of Bankable Quality?” *Journal of Solar Energy Engineering* 133: 031024.

———. 2012. “Clear-Sky Irradiance Predictions for Solar Resource Mapping and Large-Scale Applications: Improved Validation Methodology and Detailed Performance Analysis of 18 Broadband Radiative Models.” *Solar Energy* 86: 2,145–69.

———. 2014. “A Review of Validation Methodologies and Statistical Performance Indicators for Modeled Solar Radiation Data: Towards a Better Bankability of Solar Projects.” *Renewable and Sustainable Energy Reviews* 39: 1,024–34.

———. 2017. “Cloud and Albedo Enhancement Impacts on Solar Irradiance Using Highfrequency Measurements from Thermopile and Photodiode Radiometers. Part 2: Performance of Separation and Transposition Models for Global Tilted Irradiance.” *Solar Energy* 153: 766–79.

Gueymard C. A., W. T. Gustafson, G. Bender, A. Etringer, and P. Storck. 2012. “Evaluation of Procedures to Improve Solar Resource Assessments: Optimum Use of Short-Term Data from a Local Weather Station to Correct Bias in Long-Term Satellite-Derived Solar Radiaiton Time Series.” *Proceedings of the World Renewable Energy Forum*, Denver, Colorado, American Solar Energy Society.

Gueymard, C. A., and D. Myers. 2008. “Validation and Ranking Methodologies for Solar Radiation Models.” In *Modeling Solar Radiation at the Earth’s Surface*, edited by V. Badescu. Berlin, Germany: Springer.

Gueymard, C. A., and D. Thevenard, 2009. “Monthly Average Clear-Sky Broadband Irradiance Database for Worldwide Solar Heat Gain and Building Cooling Load Calculations.” *Solar Energy* 83: 1,998–2,018.

Gueymard, C. A., and J. A. Ruiz-Arias. 2015. “Validation of Direct Normal Irradiance Predictions Under Arid Conditions: A Review of Radiative Models and Their Turbidity-Dependent Performance.” *Renewable and Sustainable Energy Reviews* 45: 379–96.

———. 2016. “Extensive Worldwide Validation and Climate Sensitivity Analysis of Direct Irradiance Predictions from 1-Min Global Irradiance.” *Solar Energy* 128: 1–30. https://doi.org/10.1016/j.solener.2015.10.010.

Gueymard, C. A., and D. Yang. 2020. "Worldwide Validation of CAMS and MERRA-2 Reanalysis Aerosol Optical Depth Products Using 15 years of AERONET Observations." *Atmospheric Environment* 225: 117216. https://doi.org/10.1016/j.atmosenv.2019.117216.

Hammer, A., D. Heinemann, C. Hoyer, R. Kuhlemann, E. Lorenz, R. Müller, and H. G. Beyer. 2003. "Solar Energy Assessment Using Remote Sensing Technologies." *Remote Sensing of Environment* 86: 423–32.

Harmsen, E. W., P. Tosado-Cruz, and J. R. Mecikalski. 2014. "Calibration of Selected Pyranometers and Satellite Derived Solar Radiation in Puerto Rico." *International Journal Renewable Energy Technology* 5: 43–54.

Hay, J. E., K. Hanson, and J. Hanson. 1978. "A Satellite-Based Methodology for Determining Solar Irradiance at the Ocean Surface during GATE." *Bulletin of the American Meteorological Society* 59: 1,549.

Heidinger, A. K. 2003. "Rapid Daytime Estimation of Cloud Properties Over a Large Area from Radiance Distributions." *Journal of Atmospheric and Oceanic Technology* 20: 1,237–50.

Heidinger, A. K., M. J. Foster, A. Walther, and X. Zhao. 2014. "The Pathfinder Atmospheres—Extended (PATMOS-x) AVHRR Climate Data Set." *Bulletin of the American Meteorological Society* 95: 909–22. http://dx.doi.org/10.1175/BAMS-D-12-00246.1.

Hersbach, H., B. Bell, P. Berrisford, A. Horányi, J. M. Sabater, J. Nicolas, R. Radu, D. Schepers, A. Simmons, C. Soci, and D. Deeet. 2019. "Global Reanalysis: Goodbye ERA-Interim, Hello ERA5." *ECMWF Newsletter* 159: 17–24.

Hu, Y. X., and K. Stamnes. 1993. "An Accurate Parameterization of the Radiative Properties of Water Clouds Suitable for Use in Climate Models." *Journal of Climate* 6 (4): 728–42.

Ineichen, P. 2008. "A Broadband Simplified Version of the Solis Clear-Sky Model." *Solar Energy* 82 (8): 758–762. DOI: 10.1016/j.solener.2008.02.009. https://archive-ouverte.unige.ch/unige:17186.

———. 2016. "Long Term Helioclim-3 Global, Beam and Diffuse Irradiance Validation." Working paper with appendices. https://archive-ouverte.unige.ch/unige:81915.

Jimenez, P. A., J. P. Hacker, J. Dudhia, S. E. Haupt, J. A. Ruiz-Arias, C. A. Gueymard, G. Thompson, T. Eidhammer and A. Deng. 2016. "WRF-Solar: Description and Clear-Sky Assessment of an Augmented NWP Model for Solar Power Prediction." *Bulletin of the American Meteorological Society* 97: 1,249–64.

Joseph, J. H., W. J. Wiscombe, and J. A. Weinman. 1976. "The Delta-Eddington Approximation for Radiative Transfer." *Journal of Atmospheric Science* 33: 2,452–59.

Journée, M., R. Müller, and C. Bertrand. 2012. "Solar resource assessment in the Benelux by merging Meteosat-derived climate data and ground measurements." *Solar Energy* 86: 3,561–74.

Justus, C., M. V. Paris, and J. D. Tarpley. 1986. "Satellite-Measured Insolation in the United States, Mexico, and South America." *Remote Sensing of Environment* 20: 57–83.

Kalnay, E., M. Kanamitsu, R. E. Kistler, W. D. Collins, D. Deaven, L. S. Gandin, M. Iredell, S. Saha, G. H. White, J. S. Woollen, Y. Zhu, M. Chelliah, W. Ebisuzaki, W. Higgins, J. Janowiak, K. Mo, C. Ropelewski, J. Wang, A. Leetmaa, R. Reynolds, R. L. Jenne and D. Joseph. 1996. "The NCEP/NCAR 40-Year Reanalysis Project." *Bulletin of the American Meteorological Society* 77: 437–71.

Kambezidis, H. D., B. E. Psiloglou, and C. Gueymard. 1994. "Measurements and Models for Total Solar Irradiance on Inclined Surface in Athens, Greece." *Solar Energy* 53: 177–85. https://doi.org/10.1016/0038-092X(94)90479-0.

Karlsson, K.-G., K. Anttila, J. Trentmann, M. Stengel, J. F. Meirink, A. Devasthale, T. Hanschmann, S. Kothe, E. Jääskeläinen, J. Sedlar, N. Benas, G.-J. van Zadelhoff, C. Schlundt, D. Stein, S. Finkensieper, N. Håkansson, and R. Hollmann. 2017a. "CLARA-A2: The Second Edition of the CM SAF Cloud and Radiation Data Record from 34 Years of Global AVHRR Data." *Atmospheric Chemistry and Physics* 17: 5,809–28. https://doi.org/10.5194/acp-17-5809-2017.

Karlsson, K.-G., K. Anttila, J. Trentmann, M. Stengel, J.F. Meirink, A. Devasthale, T. Hanschmann, S. Kothe, E. Jääskeläinen, J. Sedlar, N. Benas, G.J. van Zadelhoff, C. Schlundt, D. Stein, S. Finkensieper, N. Håkansson, R. Hollmann, P. Fuchs, and M. Werscheck. 2017b. "CLARA-A2: CM SAF cLoud, Albedo and surface RAdiation dataset from AVHRR data - Edition 2." Satellite Application Facility on Climate Monitoring. https://doi.org/10.5676/EUM_SAF_CM/CLARA_AVHRR/V002.

Kato, S., T. Ackerman, J. H. Mather and E. Clothiaux. 1999. "The k-Distribution Method and Correlated-k Approximation for a Shortwave Radiative Transfer Model." *Journal of Quantitative Spectroscopy & Radiative Transfer* 62: 109–21.

Kato, S., F. G. Rose, D. A. Rutan, T. J. Thorsen, N. G. Loeb, D. R. Doelling, X. Huang, W. L. Smith, W. Su, and S. Ham. 2018. "Surface Irradiances of Edition 4.0 Clouds and the Earth's Radiant Energy System (CERES) Energy Balanced and Filled (EBAF) Data Product." Journal of Climate 31: 4501-27. https://doi.org/10.1175/JCLI-D-17-0523.1.

Kerschgens, M., U. Pilz, and E. Raschke. 1978. "A Modified Two-Stream Approximation for Computations of the Solar Radiation in a Cloudy Atmosphere." *Tellus* 30: 429–35.

Key, J. R., P. Yang, B. A. Baum, and S. L. Nasiri. 2002. "Parameterization of shortwave ice cloud optical properties for various particle habits." *Journal of Geophysical Research* 107 D13. DOI: 10.1029/2001JD000742.

Khalil, S. A., and A. M. Shaffie. 2013. "A Comparative Study of Total, Direct and Diffuse Solar Irradiance by Using Different Models on Horizontal and Inclined Surfaces for Cairo, Egypt." *Renewable and Sustainable Energy Reviews* 27: 853–63. https://doi.org/10.1016/j.rser.2013.06.038.

Kinne, S., M. Schulz, C. Textor, S. Guibert, Y. Balkanski, S. E. Bauer, T. Berntsen, T. F. Berglen, O. Boucher, M. Chin, W. Collins, F. Dentener, T. Diehl, R. Easter, J. Feichter, D. Fillmore, S. Ghan, P. Ginoux, S. Gong, A. Grini, J. Hendricks, M. Herzog, L. Horowitz, I. Isaksen, T. Iversen, A. Kirkevag, S. Kloster, D. Koch, J. E. Kristjansson, M. Krol, A. Lauer, J. F. Lamarque, G. Lesins, X. Liu, U. Lohmann, V. Montanaro, G. Myhre, J. Penner, G. Pitari, S. Reddy, O. Seland, P. Stier, T. Takemura, and X. Tie. 2005. "An AeroCom Initial Assessment – Optical Properties in Aerosol Component Modules of Global Models." *Atmospheric Chemistry and Physics Discussions* 5: 8,285–330.

Kriebel K. T., G. Gesell, M. Kästner, H. Mannstein. 2003. "The Cloud Analysis Tool APOLLO: Improvements and Validation. " *International Journal of Remote Sensing* 24: 2,389–408.

Kriebel, K. T., R. W. Saunders, and G. Gesell. 1989. "Optical Properties of Clouds Derived from Fully Cloudy AVHRR Pixels." *Beiträge zur Physik der Atmosphäre* 62 (3 August): 165–71.

Kylling A., K. Stamnes, and S.-C. Tsay. 1995. "A Reliable and Efficient Two-Stream Algorithm for Spherical Radiative Transfer: Documentation of Accuracy in Realistic Layered Media." *Journal of Atmospheric Chemistry* 21: 115–50.

Lefèvre, M., A. Oumbe, P. Blanc, B. Espinar, B. Gschwind, Z. Qu, L. Wald, M. Schroedter-Homscheidt, C. Hoyer-Klick, A. Arola, A. Benedetti, J.W. Kaiser, and J.-J. Morcrette. 2013. "McClear: A New Model Estimating Downwelling Solar Radiation at Ground Level in Clear-Sky Conditions" *Atmospheric Measurement Techniques* 6: 2,403–18. https://doi.org/10.5194/amt-6-2403-2013.

Lefèvre, M., L. Wald, and L. Diabate. 2007. "Using Reduced Datasets ISCCP-B2 from the Meteosat Satellites To Assess Surface Solar Irradiance." *Solar Energy* 81: 240–53.

Liu, B. Y. H., and R. C. Jordan. 1960. "The Interrelationship and Characteristic Distribution of Direct, Diffuse and Total Solar Radiation." *Solar Energy* 4: 1–19. https://doi.org/10.1016/0038-092X(60)90062-1.

Lohmann S., C. Schillings, B. Mayer, R. Meyer. 2006. "Long-Term Variability of Solar Direct and Global Radiation Derived from ISCCP Data and Comparison with Reanalysis Data." *Solar Energy* 80: 1,390–401.

Lorenz, E. 2007. *Improved Diffuse Radiation Model, MSG. Report for the EC-project PVSAT-2: Intelligent Performance Check of PV System Operation Based on Satellite Data* (NNE5-2001-0571, Deliverable D4.2b). Oldenburg, Germany: University of Oldenburg.

Louche, A., G. Notton, P. Poggi, and G. Simonnot. 1991. "Correlations for Direct Normal and Global Horizontal Irradiation on a French Mediterranean Site." *Solar Energy* 46: 261–6. https://doi.org/10.1016/0038-092X(91)90072-5.

Loutzenhiser, P. G., H. Manz, C. Felsmann, P. A. Strachan, T. Frank, and G. M. Maxwell. 2007. "Empirical Validation of Models to Compute Solar Irradiance on Inclined Surfaces for Building Energy Simulation." *Solar Energy* 81: 254–67. https://doi.org/10.1016/j.solener.2006.03.009.

Marion, W., and S. Wilcox. 1994. *Solar Radiation Data Manual for Flat-Plate and Concentrating Collectors* (NREL/TP-463-5607). Golden, CO: National Renewable Energy Laboratory.

Maxwell, E. L.1987. "Quasi-Physical Model for Converting Hourly Global Horizontal to Direct Normal Insolation." *Solar '87; Proceedings of Annual Meeting, American Solar Energy Society, Inc.*, Solar Energy Society of Canada, Inc., Portland, Oregon, July 12–16, 1987: 35–46. Boulder, CO: American Solar Energy Society, Inc.

———.1998. "METSTAT: The Solar Radiation Model Used in the Production of the National Solar Radiation Data Base (NSRDB)." *Solar Energy* 62: 263–79. https://dx.doi.org/10.1016/S0038-092X(98)00003-6.

Mayer B. and A. Kylling. 2005. "Technical Note: The libRadtran Software Package for Radiative Transfer Calculations - Description and Examples of Use." *Atmospheric Chemistry and Physics* 5: 1,855–77. DOI: 10.5194/acp-5-1855-2005.

Mieslinger T., A. Felix, C. Kaushal, and R. Meyer. 2014. "A New Method for Fusion of Measured and Model-derived Solar Radiation Time-series." *Energy Procedia* 48: 1,617–26. ISSN 1876-6102. https://doi.org/10.1016/j.egypro.2014.02.182.

Möser, W., and E. Raschke. 1983. "Mapping of Global Radiation and Cloudiness from METEOSAT Image Data." *Meteorologische Rundschau* 36: 33–41.

———. 1984. "Incident Solar Radiation over Europe Estimated from METEOSAT Data." *Journal of Climate and Applied Meteorology* 23: 166–70.

Mueller, R., T. Behrendt, A. Hammer, A. Kemper. 2012. "A New Algorithm for the Satellite-Based Retrieval of Solar Surface Irradiance in Spectral Bands." *Remote Sensing* 4: 622–47. https://doi.org/10.3390/rs4030622.

Müller, R. W., C. Matsoukas, A. Gratzki, H. D. Behr, and R. Hollmann. 2009. "The CM-SAF Operational Scheme for the Satellite Based Retrieval of Solar Surface Irradiance—A LUT Based Eigenvector Hybrid Approach." *Remote Sensing of Environment* 113 (5): 1,012–24. https://doi.org/10.1016/j.rse.2009.01.012.

Müller, R. W., K. F. Dagestad, P. Ineichen, M. Schroedter, S. Cros, D. Dumortier, R. Kuhlemann, J. A. Olseth, G. Piernavieja, C. Reise, L. Wald, and D. Heinnemann. 2004. "Rethinking Satellite Based Solar Irradiance Modelling: The SOLIS Clear Sky Module." *Remote Sensing of Environment* 90 (2): 160–74.

Müller, R., U. Pfeifroth, C. Träger-Chatterjee, J. Trentmann, and R. Cremer. 2015. "Digging the METEOSAT Treasure-3 Decades of Solar Surface Radiation." *Remote Sensing* 7 (6): 8,067–101. https://doi.org/10.3390/rs70608067.

Müller, S and J. Remund. 2018. "Validation of the Meteonorm Satellite Irradiation Dataset." *Proceedings of the European PV Solar Conference and Exhibition (EU PVSEC) 2018*, Brussels, Belgium, September 24–27, 2018.

Muneer, T., and G. S. Saluja. 1985. "A Brief Review of Models for Computing Solar Radiation on Inclined Surfaces." *Energy Conversion and Management* 25: 443–58. https://doi.org/10.1016/0196-8904(85)90009-3.

Myers, D. R. 2013. *Solar Radiation: Practical Modeling for Renewable Energy Applications*, edited by A. Ghassemi. New York: Energy and the Environment Series, CRC Press.

National Renewable Energy Laboratory (NREL). 1992. *User's Manual: National Solar Radiation Database, 1961–1990. Version 1.0.* Golden, CO: National Renewable Energy Laboratory.

———. 2007. *National Solar Radiation Database 1991–2005 Update: User's Manual* (NREL/TP-581-41364). Golden, CO: National Renewable Energy Laboratory. https://www.nrel.gov/docs/fy07osti/41364.pdf.

Nunez, M. 1990. "Solar Energy Statistics for Australian Capital Regions." *Solar Energy* 44: 343–54.

Olmo, F., J. Vida, I. Foyo, Y. Castro-Diez, and L. Alados-Arboledas. 1999. "Prediction of Global Irradiance on Inclined Surfaces from Horizontal Global Irradiance." *Energy* 24: 689–704. https://doi.org/10.1016/S0360-5442(99)00025-0.

Oumbe, A. 2009. "Exploitation Des Nouvelles Capacités D'observation De La Terre Pour Evaluer Le Rayonnement Solaire Incident Au Sol (Assessment of Solar Surface Radiation Using New Earth Observation Capabilities)." Ph.D. Diss., MINES ParisTech, Paris, France.

Oumbe, A., Z. Qu, P. Blanc, M. Lefèvre, L. Wald, and S. Cros. 2014. "Decoupling the Effects of Clear Atmosphere and Clouds to Simplify Calculations of the Broadband Solar Irradiance at Ground Level." *Geoscientific Model Development Discussions* 7 (2): 1,661–69. DOI: 10.5194/gmd-7-1661-2014. Corrigendum 7: 2,409. https://doi.org/10.5194/gmd-7-1661-2014.

Padovan, A., and D. Del Col. 2010. "Measurement and Modeling of Solar Irradiance Components on Horizontal and Tilted Planes." *Solar Energy* 84: 2,068–84. https://doi.org/10.1016/j.solener.2010.09.009.

Page, J. K., M. Albuisson, and L. Wald. 2001. "The European Solar Radiation Atlas: A Valuable Digital Tool." *Solar Energy* 71 (1): 81–3.

Pavolonis, M., A. Heidinger and T. Uttal. 2005. “Daytime Global Cloud Typing from AVHRR and VIIRS: Algorithm Description, Validation, and Comparisons.” *Journal of Applied Meteorology* 44 (6): 804–26.

Perez, R., P. Ineichen, K. Moore, M. Kmiecik, C. Chain, R. George, and F. Vignola. 2002. “A New Operational Satellite-to-Irradiance Model.” *Solar Energy* 73 (5): 307–17.

Perez, R., P. Ineichen, R. Seals, J. Michalsky, and R. Stewart. 1990. “Modeling Daylight Availability and Irradiance Components from Direct and Global Irradiance.” *Solar Energy* 44: 271–89. https://doi.org/10.1016/0038-092X(90)90055-H.

Perez, R., R. Seals, P. Ineichen, R. Stewart, and D. Menicucci. 1987. “A New Simplified Version of the Perez Diffuse Irradiance Model for Tilted Surfaces.” *Solar Energy* 39: 221–31. https://doi.org/10.1016/S0038-092X(87)80031-2.

Perez, R., R. Stewart, R. Seals, and T. Guertin. 1988. *The Development and Verification of the Perez Diffuse Radiation Model* (SAND 88-7030). Albuquerque, NM. http://prod.sandia.gov/techlib/access-control.cgi/1988/887030.pdf.

Pfeifroth, U., A. Sanchez-Lorenzo, V. Manara, J. Trentmann, and R. Hollmann. 2018. “Trends and Variability of Surface Solar Radiation in Europe based on Surface- and Satellite-based Data Records.” *Journal of Geophysical Research* 123: 1735–54. https://doi.org/10.1002/2017JD027418.

Pinker, R. T., and I. Laszlo 1992. “Modeling of Surface Solar Irradiance for Satellite Applications on a Global Scale.” *Journal of Applied Meteorology and Climatology* 31: 194–211.

Pinker, R. T., and J. A. Ewing. 1985. “Modeling Surface Solar Radiation: Model Formulation and Validation.” *Journal of Climate and Applied Meteorology* 24: 389–401.

Pinker, R. T., R. Frouin, and Z. Li. 1995. “A Review of Satellite Methods to Derive Surface Shortwave Irradiance.” *Remote Sensing of Environment* 51: 108–24.

Polo J., L. Martín, and J. M. Vindel. 2015. “Correcting Satellite Derived DNI with Systematic and Seasonal Deviations: Application to India.” *Renewable Energy* 80: 238–43. ISSN 0960-1481. https://doi.org/10.1016/j.renene.2015.02.031.

Polo, J., C. Fernández-Peruchena, V. Salamalikis, L. Mazorra-Aguiar, M. Turpin, L. Martín-Pomares, A. Kazantzidis, P. Blanc, and J. Remund. 2020. “Benchmarking on Improvement and Site-Adaptation Techniques for Modeled Solar Radiation Datasets.” *Solar Energy* 201: 469–79. https://doi.org/10.1016/J.SOLENER.2020.03.040.

Polo, J., J. M. Vindel, and L. Martín. 2013. “Angular Dependence of the Albedo Estimated in Models for Solar Radiation Derived from Geostationary Satellites.” *Solar Energy* 93: 256–66. https://doi.org/10.1016/j.solener.2013.04.019.

Polo, J., L. Martín, and M. Cony. 2012. “Revision of Ground Albedo Estimation in Heliosat Scheme for Deriving Solar Radiation from SEVIRI HRV Channel of Meteosat Satellite.” *Solar Energy* 86: 275–82. https://doi.org/10.1016/j.solener.2011.09.030.

Polo, J., S. Wilbert, J. A. Ruiz-Arias, R. Meyer, C. Gueymard, M. Súri, L. Martín, T. Mieslinger, P. Blanc, I. Grant, J. Boland, P. Ineichen, J. Remund, R. Escobar, A. Troccoli, M. Sengupta, K. P. Nielsen, D. Renne, N. Geuder, and T. Cebecauer. 2016. “Preliminary Survey on Site-Adaptation Techniques for Satellite-Derived and Reanalysis Solar Radiation Datasets.” *Solar Energy* 132: 25–37.

Qu, Z., A. Oumbe, P. Blanc, B. Espinar, G. Gesell, B. Gschwind, L. Klüser, M. Lefèvre, L. Saboret, M. Schroedter-Homscheidt, and L. Wald. 2016. “Fast Radiative Transfer

Parameterisation for Assessing the Surface Solar Irradiance: The Heliosat-4 Method." *Meteorologische Zeitschrift* 26 (1): 33–57.

Remund, J. 2009. *Aerosol Optical Depth and Linke Turbidity Climatology: Description for Final Report of IEA SHC Task 36*. Bern, Switzerland: Meteotest.

Remund, J., L. Wald, M. Lefèvre, T. Ranchin, and J. Page. 2003. "Worldwide Linke Turbidity Information." CD-ROM published by International Solar Energy Society, *Proceedings of ISES SolarWorld Congress*, Goteborg, Sweden, June 16–19.

Renné, D. S., R. Perez, A. Zelenka, C. Whitlock, and R. DiPasquale. 1999. "Use of Weather and Climate Research Satellites for Estimating Solar Resources." Chapter 5 in *Advances in Solar Energy: An Annual Review of Research and Development, Vol. 13.*, edited by D. Yogi Goswami and K. W. Boer. Boulder, CO: American Solar Energy Society, Boulder

Ridley, B., J. Boland, P. Lauret. 2010. "Modelling of Diffuse Solar Fraction with Multiple Predictors." *Renewable Energy* 35 (2): 478–83. https://doi.org/10.1016/j.renene.2009.07.018.

Rigollier, C., M. Lefèvre, and L. Wald. 2004. "The Method HELIOSAT-2 for Deriving Shortwave Solar Radiation Data from Satellite Images." *Solar Energy* 77: 159–69.

Rigollier, C., O. Bauer, and L. Wald. 2000. "On the Clear Sky Model of the ESRA European Solar Radiation Atlas with Respect to the Heliosat Method." *Solar Energy* 68 (1): 33–48. DOI: 10.1016/S0038-092X(99)00055-9.

Roebeling, R. A., A. J. Feijt, and P. Stammes. 2006. "Cloud Property Retrievals for Climate Monitoring: Implications of Differences between SEVIRI on METEOSAT-8 and AVHRR on NOAA-17." *Journal of Geophysical Research* 111 (D20210). https://doi.org/10.1029/2005JD006990.

Roebeling, R. A., and E. van Meijgaard. 2009. "Evaluation of the Diurnal Cycle of Model Predicted Cloud Amount and Liquid Water Path with Observations from MSG-SEVIRI." *Journal of Climate* 22: 1749–66. https://doi.org/10.1175/2008JCLI2391.1.

Ruiz-Arias, J. A., J. Dudhia, C. A. Gueymard, and D. Pozo-Vázquez. 2013a. "Assessment of the Level-3 MODIS Daily Aerosol Optical Depth in the Context of Surface Solar Radiation and Numerical Weather Modeling." *Atmospheric Chemistry and Physics* 13: 675–92. DOI: 10.5194/acp-13-675-2013.

Ruiz-Arias, J. A., J. Dudhia, F. J. Santos-Alamillos, and D. Pozo-Vázquez. 2013b. "Surface Clear-Sky Shortwave Radiative Closure Intercomparisons in the Weather Research and Forecasting Model." *Journal of Geophysical Research - Atmospheres* 118 (17): 9,901–13. DOI: 10.1002/jgrd.50778.

Ruiz-Arias, J. A., S. Quesada-Ruiz, E. F. Fernández, and C. A. Gueymard. 2015. "Optimal Combination of Gridded and Ground-Observed Solar Radiation Data for Regional Solar Resource Assessment." *Solar Energy* 112: 411–24. DOI: 10.1016/j.solener.2014.12.011.

Schiffer, R. A., and W. B. Rossow. 1983. "The International Satellite Cloud Climatology Project (ISCCP): The First Project of the World Climate Research Programme." *Bulletin of the American Meteorological Society* 64: 779–84.

Schmetz, J. 1989. "Towards a Surface Radiation Climatology: Retrieval of Downward Irradiances from Satellites." *Atmospheric Research* 23: 287–321.

Schmetz, J., P. Pili, S. Tjemkes, D. Just, J. Kerkmann, S. Rota, and A. Ratier. 2002. "An Introduction to Meteosat Second Generation (MSG)." *Bulletin of the American Meteorological Society* 83: 977–92.

Schmit, T. J., S. S. Lindstrom, J. J. Gerth, and M. M. Gunshor. 2018. "Applications of the 16 Spectral Bands on the Advanced Baseline Imager (ABI)." *Journal of Operational Meteorology* 6 (4): 33–46.

Schmit, T., M. M. Gunshor, W. Menzel, J. Gurka, J. Li and A. Bachmeier. 2005. "Introducing the Next-Generation Advanced Baseline Imager on GOES-R." *Bulletin of the American Meteorological Society* 86 (8): 1,079–96. https://doi.org/10.1175/BAMS-86-8-1079.

Schmutz, M., S.C. Müller, J. Remund. 2020. "Real-Time Global Coverage of Satellite Based Irradiation Data—Benchmark and Applications." *Proceedings of the European PV Solar Conference and Exhibition (EU PVSEC) 2020*, September 7–11.

Schroedter-Homscheidt, M., C. Hoyer-Klick, N. Killius, M. Lefèvre, L. Wald, E. Wey, and L. Saboret. 2016. *User's Guide to the CAMS Radiation Service*. http://www.soda-pro.com/documents/10157/326332/CAMS72_2015SC3_D72.1.3.1_2018_UserGuide_v1_201812.pdf/95ca8325-71f6-49ea-b5a6-8ae4557242bd

Schumann, K., Beyer, H. G., Chhatbar, K. and Meyer, R., 2011. "Improving Satellite-Derived Solar Resource Analysis with Parallel Ground-Based Measurements." *Proceedings of the ISES Solar World Congress*, Kasel, Germany.

Sengupta, M., and P. Gotseff. 2013. *Evaluation of Clear Sky Models for Satellite-Based Irradiance Estimates* (NREL/TP-5D00-60735). https://www.nrel.gov/docs/fy14osti/60735.pdf.

Stengel, M., A. Kniffka, J.F. Meirink, M. Lockhoff, J. Tan, and R. Hollmann. 2014. "CLAAS: The CM SAF Cloud Property Data Set Using SEVIRI." *Atmospheric Chemistry and Physics* 14: 4,297–311. https://doi.org/10.5194/acp-14-4297-2014.

Stowe, L. L., P. A. Davis, and E. P. McClain. 1999. "Scientific Basis and Initial Evaluation of the CLAVR-1 Global Clear/Cloud Classification Algorithm for the Advanced Very High Resolution Radiometer." *Journal of Atmospheric and Oceanic Technology* 16 (6): 656–81. https://journals.ametsoc.org/view/journals/atot/16/6/1520-0426_1999_016_0656_sbaieo_2_0_co_2.xml.

Stuhlmann, R., M. Rieland, and E. Raschke. 1990. "An Improvement of the IGMK Model to Derive Total and Diffuse Solar Radiation at the Surface from Satellite Data." *Journal of Applied Meteorology* 29: 586–603.

Tapakis, R., S. Michaelides, and A. G. Charalambides. 2016. "Computations of Diffuse Fraction of Global Irradiance: Part 1 – Analytical Modelling." *Solar Energy* 139: 711–22.

Tarpley, J. D. 1979. "Estimating Incident Solar Radiation at the Surface from Geostationary Satellite Data." *Journal of Applied Meteorology* 18: 1,172–81.

Thuman, C., M. Schitzer, and P. Johnson. 2012. "Quantifying the Accuracy of the Use of Measure-Correlate-Predict Methodology for Long-Term Solar Resource Estimates." *Proceedings of the American Solar Energy Society*, Denver, Colorado.

Trolliet, M., J. P. Walawender, B. Bourlès, A. Boilley, J. Trentmann, P. Blanc, M. Lefèvre, and L. Wald. 2018. "Estimating Downwelling Solar Irradiance at the Surface of the Tropical Atlantic Ocean: A Comparison of PIRATA Measurements Against Several Re-analyses and Satellite-Derived Data Sets." *Ocean Sciences* 14: 1,021–56. DOIi 10.5194/os-14-1021-2018.

Urraca, R., T. Huld, A. Gracia-Amillo, F. J. Martinez-de-Pison, F. Kaspar, and A. Sanz-Garcia. 2018. "Evaluation of Global Horizontal Irradiance Estimates from ERA5 and COSMO-REA6 Reanalyses Using Ground and Satellite-Based Data." *Solar Energy* 164: 339–54. https://doi.org/10.1016/j.solener.2018.02.059.

Vernay, C., P. Blanc, and S. Pitaval. 2013. "Characterizing Measurements Campaigns for an Innovative Calibration Approach of the Global Horizontal Irradiation Estimated by HelioClim-

3." *Renewable Energy* 57: 339–47. ISSN 0960-1481. https://doi.org/10.1016/j.renene.2013.01.049.

Vindel, J. M., J. Polo, and, F. Antonanzas-Torres. 2013. "Improving Daily Output of Global to Direct Solar Irradiance Models with Ground Measurements." *Journal of Renewable and Sustainable Energy* 5: 063123.

Wattan, R., and S. Janjai. 2016. "An Investigation of the Performance of 14 Models for Estimating Hourly Diffuse Irradiation on Inclined Surfaces at Tropical Sites." *Renewable Energy* 93: 667–74. https://doi.org/10.1016/j.renene.2016.02.076.

Whitlock, C. H., T. P. Charlock, W. F. Staylor, R. T. Pinker, I. Laszlo, A. Ohmura, H. Gilgen, T. Konzelman, R. C. DiPasquale, C. D. Moats, S. R. LeCroy, and N. A. Ritchey. 1995. "First Global WCRP Shortwave Surface Radiation Budget Data Set." *Bulletin of the American Meteorological Society* 76: 1–18.

Xie, Y., and M. Sengupta. 2018. "A Fast All-sky Radiation Model for Solar applications with Narrowband Irradiances on Tilted surfaces (FARMS-NIT): Part I. The Clear-Sky Model." *Solar Energy* 174: 691–702.

Xie, Y., M. Sengupta, and J. Dudhia. 2016 "Fast All-Sky Radiation Model for Solar applications (FARMS): Algorithm and Performance Evaluation." *Solar Energy* 135: 435–45. https://dx.doi.org/10.1016/j.solener.2016.06.003.

Xie, Y., M. Sengupta, and C. Wang. 2019. "A Fast All-sky Radiation Model for Solar applications with Narrowband Irradiances on Tilted surfaces (FARMS-NIT): Part II. The Cloudy-Sky Model." *Solar Energy* 188: 799–812. https://doi.org/10.1016/j.solener.2019.06.058.

Yang, D. 2016. "Solar Radiation on Inclined Surfaces: Corrections and Benchmarks." *Solar Energy* 136: 288–302.

Yang, D., and C. A. Gueymard. 2020. "Ensemble Model Output Statistics for the Separation of Direct and Diffuse Components from 1-min Global Irradiance." *Solar Energy* 208: 591–603. https://doi.org/10.1016/j.solener.2020.05.082.

Yang, P., K. N. Liou, K. Wyser, and D. Mitchell. 2000. "Parameterization of the Scattering and Absorption Properties of Individual Ice Crystals." *Journal of Geophysical Research* 105: 4,699–718. DOI: 10.1029/1999JD900755.

Zhang, Y.-C., W. B. Rossow, A. A. Lacis, V. Oinas, and M. I. Mishchenko. 2004. "Calculation of Radiative Fluxes from the Surface to Top of Atmosphere Based on ISCCP and Other Global Data Sets: Refinements of the Radiative Transfer Model and the Input Data." *Journal Geophysical Research* 109 (D19105). DOI: 10.1029/2003JD004457.

Zhong, X., and J. Kleissl. 2015. "Clear Sky Irradiances Using REST2 and MODIS." *Solar Energy* 116: 144–64.

5 FURTHER RELEVANT METEOROLOGICAL PARAMETERS

Stefan Wilbert,[1] Christian Gueymard,[2] Aron Habte,[3] Manajit Sengupta,[3] Yu Xie,[3] Tomas Landelius,[4] Jesús Polo,[5] Vicente Lara-Fanego,[6] and Frank Vignola[7]

[1] *German Aerospace Center (DLR)*
[2] *Solar Consulting Services*
[3] *National Renewable Energy Laboratory*
[4] *Swedish Meteorological and Hydrological Institute*
[5] *Centro de Investigaciones Energéticas, Medioambientales y Tecnológicas (CIEMAT)*
[6] *Solargis*
[7] *University of Oregon*

Solar irradiance is the most important meteorological input parameter for solar energy, but additional meteorological parameters are required for accurate performance analysis as well as for optimal plant and grid operation and design. The influence of ambient temperature and wind on photovoltaic (PV) efficiency is one example. A discussion of the influence of the different meteorological parameters on concentrating solar power (CSP) can be found in Chhatbar and Meyer (2011). Also for CSP, a guideline for yield assessment, including the proper selection and subsequent impact of key meteorological parameters, has been prepared by the International Energy Agency (IEA) Solar Power and Chemical Energy Systems program (Hirsch 2017). For PV, a similar study was presented in an IEA Photovoltaic Power Systems Programme report (Reise et al. 2018; Bonilla Castro 2020). Recently, parameters such as soiling have gained interest. Unless specified otherwise, modeled data for the duration of the long-term radiation time series and measured data accompanying the radiation measurements should be available for the parameters described in the following sections.

5.1 Wind

Wind speed, gust, and wind direction are important for the design and performance of solar power plants and electric grids. Wind speed and direction are often understood as the horizontal component of the wind velocity. The gust is the maximum wind speed in a given time interval. For many applications, an interval of 3 seconds is adequate (WMO 2018).

Wind loads, and in particular wind gusts, must be considered for the design of solar collectors and overhead lines. In tracked solar collectors, high wind gusts or speed might also require moving the collectors to their stow position. Cooling effects are strongly related to wind (convection)—they increase the efficiency of PV, but they decrease that of thermal collectors because their thermal losses are increased. For some specialized applications in CSP testing (e.g., convective receiver losses), the three-dimensional wind velocities are also of interest.

Wind speed and gust can be measured using *anemometers*. Cup anemometers and propeller anemometers consist of a rotor whose frequency of rotation corresponds to the wind velocity. Ultrasonic anemometers measure the wind speed, gust, and direction. Many ultrasonic anemometers emit an ultrasonic signal over a constant, short distance and measure the time the signal needs to reach a detector. Using several measurement paths, the wind direction or the three-dimensional wind vector can be derived.

Mechanical sensors used to determine the wind direction are called *wind vanes*. The vane's position is read by, e.g., a potentiometer setup. Propeller anemometers often include a wind vane. Recommendations on wind measurements can be found in the *Guide to Meteorological Instruments and Methods of Observation* (WMO 2018), also known as the "CIMO guide" (Commission for Instruments and Methods of Observation). In solar power applications, it is often impossible to measure the wind velocity solely by following the CIMO guide. Because wind measurements at an existing or potential solar power plant site must represent the conditions affecting the collectors, measurements might be taken much closer to obstacles (buildings, trees, etc.) than required for wind measurements for other purposes. For resource assessment, one measurement at 10-m height is considered sufficient, whereas in existing power plants with tracked collectors, it is common to monitor the wind at different heights and at more than one site in the solar field.

In addition to measurements, modeled wind data are available based on either historical time series or forecasts. Many numerical weather prediction (NWP) models and reanalysis data sets provide wind data. Examples are the Modern-Era Retrospective analysis for Research and Applications, Version 2 (MERRA-2) from the National Aeronautics and Space Administration (Bosilovich Lucchesi, and M. Suarez 2016); the North American Regional Reanalysis (Mesinger et al. 2006); the Climate Forecast System Reanalysis from the National Centers for Environmental Prediction; and ERA5 from the European Centre for Medium-Range Weather Forecasts (see also Chapter 4, Section 4.7.1). A global, albeit limited, validation of the wind speed predicted by five reanalyses has shown that their accuracy is highly variable and might not be sufficient for demanding applications (Ramon et al. 2019).

The MERRA-2 reanalysis wind data set (time-averaged two-dimensional data, tavg1_2d_slv_Nx) contains the U2M and V2M parameters, which represent wind speeds 2 m eastward and 2 m northward, respectively, in m s^{-1}. To obtain the wind speed magnitude, its two components are added in quadrature:

$$Wind\ speed = \sqrt{U2M^2 + V2M^2} \tag{5-1}$$

and the wind direction is calculated using:

$$Wind\ direction = artctan\left(\frac{U2M}{V2M}\right) \tag{5-2}$$

MERRA-2 is on a coarse grid of 0.5° latitude x 0.625° longitude (approximately 60 km x 60 km). In general, the spatial and temporal interpolation of reanalysis is coarse compared to satellite-derived irradiance data; therefore, upscaling methods are used to increase the spatial resolution. Sometimes such reanalysis data are available together with solar radiation data sets. The upscaled MERRA-2 wind data, for instance, is disseminated through https://nsrdb.nrel.gov, and it is also accessible through the National Renewable Energy Laboratory's (NREL's) System Advisor model (SAM), which is a techno-economic model (Blair et al. 2018). In the latter, wind information is a weather input.

Similar to MERRA2, ERA5 includes east- and northward components (U and V) of wind speed on a 0.25 x 0.25° grid spatial resolution.

5.2 Ambient Temperature and Relative Humidity

Air temperature is an important factor needed to calculate the efficiency of solar power plants and the maximum load of electric power transmission lines. High temperatures reduce the thermal losses of thermal collectors, reduce the efficiency of a thermal plant's cooling system, and reduce the efficiency (of many common types) of PV modules. Transmission

lines expand with increasing temperature, while their resistance increases. Temperature and temperature changes are also relevant for the selection of the appropriate materials to be used in a power plant, considering aging processes. Air temperature is often called dry-bulb temperature, and it is defined as the temperature of air when shielded from radiation and moisture.

Relative humidity has an impact on the cooling processes in thermal power plants and on the efficiency of thermal receivers, depending on receiver technology (e.g., air receivers). Relative humidity is also involved in soiling processes through the formation of dew and the accumulation of particles on solar collectors. Moreover, similarly to temperature, relative humidity influences aging processes. Relative humidity is the ratio (usually reported in percentage) between the observed vapor pressure and the saturation vapor pressure with respect to water at the same temperature and pressure (WMO 2018). The saturation vapor pressure is a sole function of ambient temperature, and it can be obtained using one of many empirical formulae; see Alduchov and Eskridge (1996) and Gueymard (1993).

Hygrometers and *thermometers* are used to measure relative humidity and dry-bulb temperature, respectively. Today, temperature-dependent resistors, or bandgap sensors, are used in the construction of thermometers. Capacity or resistance changes in the sensor material directly correspond to changes in humidity, thus providing the basis for measurement. Often, combined sensors (hygro-thermometers) are used. The sensors are placed in a radiation shield and can be optionally ventilated.

Higher accuracies can be reached with more sophisticated measurement methods, but these are usually not required in solar energy applications. Recommendations on temperature and relative humidity measurements can be found in the CIMO guide (WMO 2018).

As in the case of wind, temperature and relative humidity predictions are included in the output of many NWP or reanalysis models. Because the resolution of such data might be too coarse, upscaling is typically necessary to match that of the satellite radiation data. To that end, an elevation correction on temperature and humidity needs to be applied. As an example, the upscaling method used in the production of the National Solar Radiation Database (NSRDB) is presented. The correction for temperature uses a lapse rate of 6.5°C per kilometer, according to Hemond and Fechner (2015):

$$Air\ temperature = Coarse\ pixel\ air\ temperature + E * \left(\frac{6.5}{1000}\right) \quad (5\text{-}3)$$

where E is the location's elevation (in meters) relative to the upscaled grid.

To upscale the relative humidity data, a multistep procedure has been devised for the NSRDB: the specific humidity is first interpolated using a combination of nearest neighbor temporal interpolation and second-degree inverse distance weighting. Additional steps are taken to estimate relative humidity from the interpolated specific humidity. In particular, the saturation vapor pressure is calculated using the method described in Tetens (1930):

$$Saturation\ vapor\ pressure = 610.79 * exp\left(\frac{Air\ temperature}{Air\ temperature+238.3} * 17.2694\right) \quad (5\text{-}4)$$

where air temperature is in °C. Then the mixing ratio (w), which is the mass of water vapor per mass of dry air, is calculated using the method described in an online document by DeCaria26:

$$w = \frac{h}{(1-h)} \qquad (5\text{-}5)$$

where *h* is the 2-m specific humidity in kg kg^{-1}, a MERRA-2 output named QV2M. The next step is to estimate the saturation mixing ratio (*ws*) using a method described by DeCaria[27] and the National Weather Service[28]:

$$ws = 621.97 * \frac{\left(Saturation\ vapor\ pressure / 1000\right)}{Surface\ pressure - \left(Saturation\ vapor\ pressure / 1000\right)}. \qquad (5\text{-}6)$$

The surface pressure is also obtained from MERRA-2 and upscaled, as discussed in Section 5.3. Finally, relative humidity is calculated from[29]:

$$RH = \frac{w}{ws}. \qquad (5\text{-}7)$$

In general, it is advised to interpolate dew-point and ambient temperatures separately and then calculate relative humidity at the place of interest.

5.3 Atmospheric Pressure

Atmospheric pressure has a direct effect on some CSP receiver technologies, particularly on the power block efficiency, and on cooling processes in thermal plants. Pressure variations influence the aging processes of components with sealed volumes; however, pressure data are also used for intermediate calculations in solar resource assessments, such as for the accurate calculation of the solar position, atmospheric transmittance, dew point, or relative humidity.

The atmospheric pressure on a given surface is defined as the force per-unit area resulting from the weight of the atmosphere aloft (WMO 2018). Atmospheric pressure can be measured with mercury barometers, aneroid barometers, hypsometers, or electronic barometers. For solar energy applications, *electronic barometers* are of the most interest. Such barometers use piezoelectric materials, an aneroid capsule that changes its form or position depending on pressure, or a resonator whose mode of vibration depends on pressure. The displacement of the aneroid capsule can be detected using, e.g., capacity or resistance changes. The recommendations for pressure measurements made in the CIMO guide (WMO 2018) can be used in solar energy applications.

As mentioned in the previous section, surface pressure can be obtained from NWP and reanalysis data such as MERRA-2. Pressure data might also need to be upscaled. For example, to upscale the NSRDB data, a combination of linear temporal interpolation and second-degree inverse distance weighting is used, as for relative humidity. An elevation correction is carried out using the method described in McIntosh (1978) with elevation *E* in m:

---

[26] See http://snowball.millersville.edu/~adecaria/ESCI241/esci241_lesson06_humidity.pdf.
[27] See http://snowball.millersville.edu/~adecaria/ESCI241/esci241_lesson06_humidity.pdf.
[28] See https://www.weather.gov/media/epz/wxcalc/mixingRatio.pdf.
[29] See https://www.weather.gov/media/epz/wxcalc/mixingRatio.pdf.

$$Surface\ pressure = Coarse\ pixel\ surface\ pressure + \left[1013.25 * \left\{1 - \left(1 - \frac{E}{44307.69231}\right)^{5.25328}\right\}\right]. \quad (5\text{-}8)$$

5.4 Precipitation

Precipitation is a relevant quantity in solar energy applications. In the form of rain, precipitation can wash dirty collectors, but it can also cause efficiency loss resulting from droplets on exposed optical surfaces, especially in concentrating technologies. Rain-induced cooling effects tend to increase the efficiency of PV modules, but they reduce that of thermal plants. Moreover, precipitation can strongly influence aging processes. Hail could damage solar collectors and other plant components. If water enters the insulation material of hot pipes, a prolonged efficiency loss occurs until the wet insulation is replaced. The effect of rain on transmission lines is less important because its cooling effect and the weight increase mostly compensate each other. Ice loads on transmission lines can be of importance, however, and have even resulted in catastrophic failures in the recent past, such as during the January 1998 North American ice storm (Phillips 2002).

The presence of snow can have either positive or negative effects on solar energy production. Snow in the vicinity of a PV installation or flat-plate thermal collectors could increase production because of the higher albedo and increased reflected irradiance (Andrews, Pollard, and Pearce 2013; Burnham et al. 2019). In some cases, this increase in reflected irradiance can combine with cloud enhancement situations and lead to substantial spikes in incident irradiance (Gueymard 2017). In turn, these spikes can have negative impacts on the normal operation of PV plants (do Nascimento et al. 2019; Järvelä, Lappalainen, and Valkealahti 2020). On the other hand, it is more likely that accumulated snow on collectors will lead to losses, increased wear and tear, and even pose a danger because of the increased load on the supporting structure and snow sliding down onto underlying areas (Andenæs et al. 2018). In concentrating systems, no irradiance gains can exist because only direct radiation is used.

Rain is often measured with *tipping bucket rain gauges*. The raindrops are collected by a horizontal aperture of known small area, and they fall on a lever. When the droplets trickle on the lever, a signal is produced. Such rain gauges can measure only liquid precipitation (in areas where snow is common, heated systems must be considered). In parallel, optical pluviometers also exist. The lever of the tipping bucket's rain gauge can be replaced by a laser and an appropriate sensor to detect the droplets. Another optical measurement method for all types of precipitation uses an open measurement volume, which directly detects the falling raindrops or snowflakes in the air with an optical scattering method. A light source emits light, and a sensor detects the scattered light under a specific scattering angle. The number of pulses detected by the sensor corresponds to the number of particles, and the pulsing pattern helps to determine the size of the droplets and helps to distinguish between snow and rain. The CIMO guide (WMO 2018) contains recommendations for precipitation measurements that are of interest in solar applications. Precipitation data can also be obtained from NWP or reanalysis predictions but with much less accuracy.

In relation to precipitation, it is of practical importance to know how long raindrops, and even more so snow, can remain on the surface of solar collectors; hence, data about snow cover is of interest. Examples of global snow cover products include those from the Interactive Multisensor Snow and Ice Mapping System (produced by the U.S. National Ice Center), the Microwave Integrated Retrieval System, the National Oceanic and Atmospheric Administration's Microwave Surface and Precipitation Products System, and the JAXA Satellite Monitoring for Environmental Studies (produced by the Japan Aerospace Exploration Agency). Products with a European focus are available from the CryoLand

Copernicus Service. Some global snow products have been intercompared recently (Chiu et al. 2020). Other options are reanalysis data (e.g., ERA, Copernicus Atmosphere Monitoring Service (CAMS) or MERRA-2) and databases with snow depth information from in situ measurements, such as the European Climate Assessment & Dataset project.[30] More detailed data regarding snow conditions might be also available from the national weather service of each country.

When designing installations for snowy regions, precautions should be followed to optimize the solar system's performance—see Andenæs et al. (2018) for architectural considerations. In particular, it is recommended to use frameless PV modules and to ensure that there is enough clearance between them and the underlying surface so that snow can slide off easily (Bogenrieder 2018; Riley et al. 2019). It is good to increase the tilt angle to facilitate this process and to arrange the panels in landscape-oriented layouts to prevent the bypass diodes from becoming ineffective during periods of partial shading (Gwamuri et al. 2015). The possible benefit of mechanically removing snow accumulations depends on location or climate. In high-latitude regions characterized by long cloudy winters, snow clearing does not seem to be beneficial (Stridh 2012), but it might be of value in sunnier regions where the winter potential production is higher (Gwamuri et al. 2015).

How much loss can be expected because of snow? Existing studies based on a limited number of sites have reported annual production losses in the range from 0%–25% and monthly losses as high as 100% (Andrews, Pollard, and Pearce 2013; Becker et al. 2008; Sugiura et al. 2003; Townsend and Powers 2011). Many models have been developed to estimate the snow loss as a function of weather given information about the installation—e.g., Townsend and Powers (2011); Lorenz, Heinemann, and Kurz (2012); and Marion et al. (2013). Such results are site-specific, so little is known about their general validity; therefore, it is difficult to predict the potential impact of snow on the performance of future projects. Because of a lack of general snow-loss models, the major PV modeling software products on the market do not support such calculations beyond a simple scaling, such as in PVWatts® (Dobos 2014). Ryberg and Freeman (2017), however, incorporated the snow model from Marion et al. (2013) into NREL's SAM. In a 30-year simulation using NSRDB data for 239 locations across the United States, the modeled snow loss varied from 0%–4% in areas with only occasional snow to 15–25% in areas with abundant snow. These limited results can be considered today's best practice for snow-loss modeling.

5.5 Aerosols and Water Vapor

Some solar energy applications can benefit from the knowledge of spectral aerosol optical depth (AOD), single-scattering albedo, asymmetry factor, scattering phase functions, and total column water vapor. The latter is often referred to as precipitable water (PW) or integrated water vapor (IWV). These parameters can be used to simulate clear-sky broadband or spectral irradiance, as explained further in the following sections, and could aid in understanding the spatiotemporal variability of the radiation field. Precise knowledge of these variables at any site or instant can be used to improve modeled solar radiation data sets and to conduct site adaptations. For solar tower power plants, these variables are helpful to model the slant-path radiation attenuation between the heliostats and the receiver.

Sun photometers are typically used to determine these variables. One type of sun photometer measures spectral direct normal irradiance (DNI) and the spectral sky radiance at several wavelengths (Figure 5-1). Simpler sun photometers sense only the spectral DNI.

[30] See https://www.ecad.eu/.

Both instruments consist of one or more photodetectors positioned behind different spectral filters and a collimator system. Additional polarization filters are optionally used. Solid-state sensors, such as photodiodes, are used for signal detection. For sun photometers that measure only spectral DNI, a tracker is required. For sky radiance measurements, more elaborate tracking systems are used.

Figure 5-1. AERONET sun photometric station at CIEMAT's Plataforma Solar de Almería. *Photo from DLR*

Because these aerosol properties are highly wavelength dependent, it is necessary to make measurements at more than a single wavelength. Sun photometers are primarily used to monitor aerosol properties, but they normally have a dedicated channel (near 940 nm) to also determine PW.

The direct-sun irradiance measurements are used to derive basic information on aerosols. First, the total atmospheric optical depth is calculated. The AOD is then determined by subtracting the optical depths of all other atmospheric constituents, such as molecules, water vapor, ozone, or nitrogen dioxide. Most optical depths are obtained from separate sources (e.g., satellite retrievals or atmospheric models), whereas the water vapor optical depth is derived from the concomitant precipitable water measurement. The Ångström exponent can then be derived by fitting the spectral AOD data to the equation describing Ångström's law. In a separate step, the direct-sun measurements can be combined with the concomitant sky radiance measurements to derive the aerosol single-scattering albedo, asymmetry factor, aerosol phase function, and other parameters using inversion algorithms (NASA 2006).

Note the two main sun photometer networks in the world: the Aerosol Robotic Network (AERONET)[31] and SKYNET.[32] These networks are important for solar resource assessment because of the relatively large number of available observing stations and the applied quality assurance and calibration methods.

The proper determination of aerosol properties (most importantly AOD) and water vapor can be done only if the solar disk is not obscured by clouds; therefore, cloud-detection algorithms are used to post-process the raw data and generate usable data. With AERONET, for example, the spectral DNI measurements are taken in direct-sun triplets. In a triplet, three series of measurements are made in rapid succession. In each series, all different filters are

[31] See http://aeronet.gsfc.nasa.gov/new_web/index.html.
[32] See https://www.skynet-isdc.org/.

used. Cloud episodes can be detected by comparing the total optical depth derived from the spectral data of the three series to each other and to defined limits (Smirnov et al. 2000; Giles et al. 2019). This cloud screening process relies on the higher temporal variability and higher value of cloud optical depth compared to AOD.

Data from measurement networks are available in different levels of quality control. In addition to cloud screening, the quality-control procedures involve various other criteria. In AERONET, for instance, the best data quality (Level 2) includes manual outlier rejection and correction for the change of the calibration constants before and after a measurement period of approximately 1 year (Holben et al. 2006). Unfortunately, this regular calibration process, as well as other experimental difficulties that might arise in the field, result in data breaks of various duration (sometimes of many months) at all stations. Despite this important issue, the instrument's calibration is of central importance for overall data accuracy. When available, the highest quality data should be used.

In practice, it is rare that ground measurements of aerosols and water vapor are available for the site or period under scrutiny; hence, it is generally necessary to rely on other sources of data. Aerosol data can be retrieved from spaceborne observations, such as those sensed by the Moderate Resolution Imaging Spectroradiometer (MODIS) instrument onboard the Terra and Aqua satellites (Bright and Gueymard 2019; Wei et al. 2019). Another source of data is provided by reanalysis models, such as CAMS or MERRA-2 (Gueymard and Yang 2020; Kosmopoulos et al. 2018). Similarly, water vapor information can be retrieved from the Global Ozone Monitoring Experiment–2 (GOME-2), the Scanning Imaging Absorption Spectrometer for Atmospheric Cartography (SCIAMACHY), and MODIS spaceborne instruments (Beirle et al. 2018; Bright et al. 2018), or from reanalysis models (Mishra 2019). Although AOD and PW are derived mostly from polar-orbiting satellites, several retrievals are developed with geostationary satellites, such as Himawari-8, the Geostationary Operational Environmental Satellite (GOES), and Meteosat (Kaufman, Tanré, and Boucher 2002). For both aerosol and water vapor, more details about the available sources of data and their accuracy are provided by Gueymard (2019b).

For most solar energy projects, aerosol and water vapor data are required only for radiation modeling, i.e., as an intermediate step. No strict recommendation is given to systematically collect such modeled or measured data; however, aerosol and water vapor data can help to answer questions related to the quality of model-derived irradiance data, especially DNI data. Moreover, such data are linked to the solar spectrum, which is of interest in PV applications (see section 5.6). Further, aerosol data are related to soiling, circumsolar radiation, and beam attenuation between the heliostats and the receiver in solar tower power plants, as discussed next.

5.6 Spectral Irradiance

Most sections in this handbook relate to the solar resource in terms of *broadband* shortwave fluxes. Considering the rapid deployment of new solar technologies and the diversification of their physical principles, spectral solar irradiance data and models are sometimes necessary to address specific aspects of the solar resource in PV, photobiological, and photochemical processes; hence, the demand for spectral information has considerably increased in recent decades, at least at the level of high-end research and experimentation. New investigations (Lindsay et al. 2020) show that neglecting spectral and angular details can lead to significant deviations in PV power modeling.

Like with broadband irradiance, the need for spectral irradiance data can be fulfilled with either measurements or models. As mentioned in Section 2.7.5 (Chapter 2), there are also a few *reference* clear-sky spectra that have been standardized for a potentially large number

of applications—most importantly PV. Because cloudy conditions are highly variable and extremely difficult to characterize, no equivalent cloudy-sky reference standard spectrum exists.

For solar PV applications in particular, reference spectra are particularly useful to, for example, (1) obtain a performance rating following the industry's best practice, such as standard test conditions, which prescribe a reference spectrum (Emery et al. 2013; Taylor 2010); (2) determine PV spectral mismatch factors when the actual spectral conditions differ from the reference spectrum defined by ASTM G173-03 (ASTM 2020a) or the International Electrotechnical Commission (IEC) 60904-3 (Braga, do Nascimento, and Rüther 2019; Mambrini et al. 2015; Mullejans et al. 2005; Myers and Gueymard 2004); or (3) evaluate how well solar simulators agree with a reference spectrum, according to, e.g., IEC 60904-9 (Bliss, Betts, and Gottschalg 2010; Meng, Wang, and Zhan 2011; Sarwar et al. 2014). One issue with reference spectra is that they are developed for specific atmospheric conditions (Gueymard, Myers, and Emery 2002) and thus might not correspond to observable natural conditions at all locations of interest or during some periods of the year. To ease this, subordinate standard spectra have been proposed (Jessen et al. 2018). These spectra are referenced in ISO standard 9060:2018 (ISO 2018) to evaluate spectral mismatch factors or spectral errors in radiometers.

Under natural conditions, the solar spectrum continuously varies in both magnitude and relative distribution. It is mostly affected by solar zenith angle (and hence by air mass) and a few variable atmospheric constituents, most importantly AOD and PW. An increase in air mass or AOD modifies the shape of both direct and global spectra in a way referred to as "red shift" because short wavelengths are attenuated more than longer ones, whereas an increase in PW does the opposite and results in a "blue shift."

Obtaining outdoor accurate solar spectra for experimental PV research or for the validation of solar radiation models requires high-quality measurements obtained with carefully maintained spectroradiometers. Two different types of instruments now exist, depending on their detection method: (1) scanning monochromators and (2) charge-coupled device (CCD) arrays. In the field, CCD-array (solid-state) instruments are preferable because they are faster, lighter, more compact, and more reliable than scanning (optomechanical) instruments. The latter are normally more accurate; hence, they are typically considered laboratory instruments for indoor measurements. Like broadband radiometers, field spectroradiometers can be deployed for unattended operation because their casing is weatherproof. They can be mounted on a sun tracker and equipped with an appropriate collimating tube to sense the direct normal spectrum. If mounted horizontally or on a tilt, they sense the global horizontal or global tilted spectrum, respectively. Examples of such mounting options are shown in Figure 5-2. This figure displays a group of three instruments because they cover different spectral bands: one has a silicon-based detector and covers the typical spectral range from approximately 350–1100 nm, another covers the ultraviolet (UV) (300–400 nm), and the last covers near-infrared in the range from 900–1700 nm. The combination makes it possible to sense the spectrum in an extended range—approximately 300–1700 nm—which might be necessary to investigate some advanced solar cells, for instance.

Figure 5-2. (Left) Three field spectroradiometers mounted on a solar tracker to sense the direct normal spectrum. Photo by NREL. (Right) The same three spectroradiometers but mounted horizontally to sense the global horizontal spectrum. Photo by Christian Gueymard

Figure 5-3 displays the direct normal spectra observed (at regular intervals) by a field spectroradiometer during a clear summer morning at NREL's Solar Radiation Research Laboratory, in Golden, Colorado, at an elevation of 1829 m. When comparing spectra that are observed under contrasting sun positions (high sun versus low sun), the red shift mentioned earlier clearly appears. Two strong atmospheric absorption bands—caused by oxygen (near 760 nm) and water vapor (near 940 nm)—are also clearly visible.

Considering the significant costs associated with the deployment, calibration, and maintenance of spectroradiometers, only a few solar laboratories in the world can continuously operate such instruments for long periods. In most cases, the spectral databases thus collected are considered proprietary and can be difficult to obtain. A few exceptions exist, such as the public-domain databases offered by NREL[33] or the Solar Radiation Monitoring Laboratory of the University of Oregon.[34]

[33] See https://midcdmz.nrel.gov/apps/spectra.pl?BMS.
[34] See http://solardat.uoregon.edu/SelectSpectral.html.

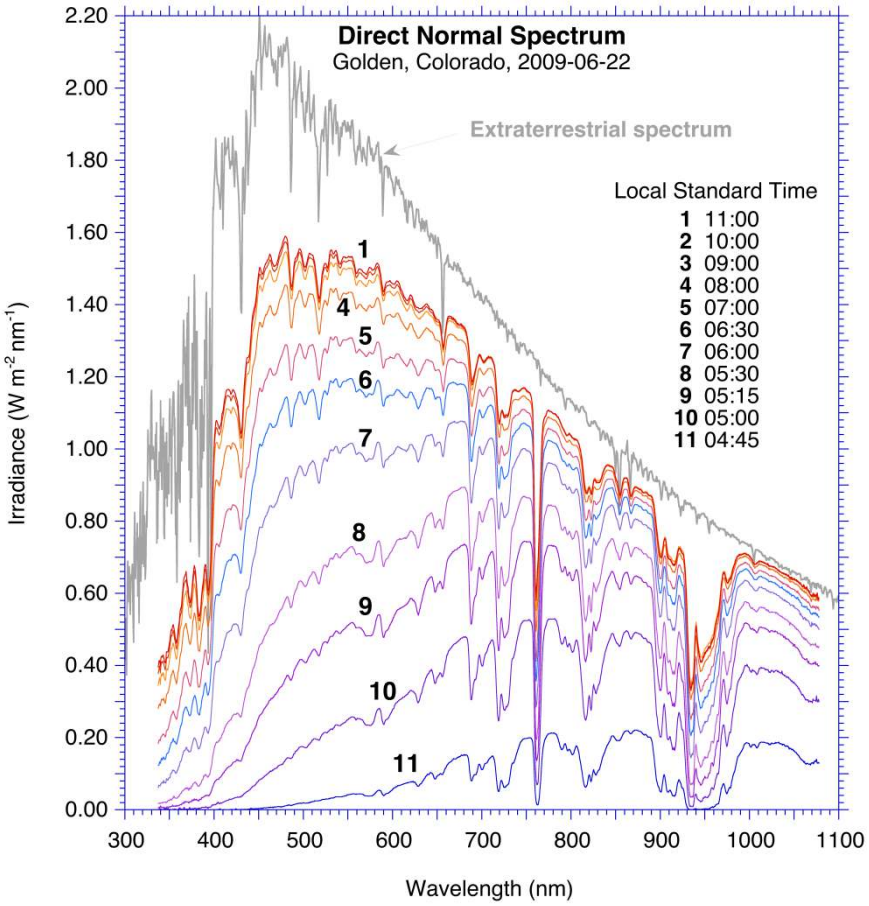

Figure 5-3. Series of DNI spectra measured during a clear summer morning by a field spectroradiometer mounted on a sun tracker at NREL. The extraterrestrial spectrum is also indicated to exacerbate some important atmospheric absorption bands.

Because of the lack of measured data, it is convenient to depend on radiative models and obtain the solar spectrum at any location and any instant. One early spectral model used in solar engineering was SPCTRAL2 (Bird 1984). Its limited resolution, capabilities, and performance prompted the development of the Simple Model of the Atmospheric Radiative Transfer of Sunshine (SMARTS) model (Gueymard 1995, 2001), which has been thoroughly validated (Gueymard 2008, 2019a). It has been used to develop the current reference spectra mentioned in Section 2.7.5 (Chapter 2). To operate a spectral radiation model such as SMARTS, precise information about atmospheric constituents is necessary, but this is essentially the same information as would be needed to obtain only broadband clear-sky irradiances with a simpler radiation model. The most accessible sources of data, particularly regarding aerosols, are discussed in detail by Gueymard (2019b).

Many spectral radiation models, such as SMARTS, are limited to the prediction of clear-sky spectra. Modeling the spectral radiation under all-sky conditions is a challenge because of the need to balance the computational burden and errors attributed to the resolution of the spectral bands. As a result, high-spectral-resolution models designed to solve spectral radiation based on fundamental physics—e.g., the line-by-line model (Clough et al. 2005)—are often time-consuming in computing the absorption coefficients of the molecular species in the atmosphere. Adding to the complexity of the radiative transfer calculations is the cloud scattering involving highly complex interactions between clouds, the over- and underlying atmosphere, and land surface. An efficient solution—implemented in the TMYSPEC model (Myers 2012)—is to empirically develop regressions that link numerically between long-term observations of broadband and spectral solar radiation. More rigorous

models based on the solution of the radiative transfer equation precompute cloud extinction, reflection, and emission for possible cloud conditions and incident and outgoing solar directions and then integrate the results with the clear-sky solution (Minnis et al. 2011). The computational efficiency of those models can be substantially improved when the precomputations are parameterized by plain functions of cloud optical and microphysical properties (Xie, Sengupta, and Dudhia 2016). On the other hand, the models can be extended to cover the computation of spectral irradiance—for example, the Fast All-sky Radiation Model for Solar applications with Narrowband Irradiances on Tilted surfaces (FARMS-NIT) (Xie and Sengupta 2018; Xie, Sengupta, and Wan 2019) precomputed a cloud lookup table using the 32-stream DIScrete Ordinates Radiative Transfer (DISORT) model (Stamnes et al. 1988) and the parameterization of cloud optical properties developed by Hu and Stamnes (1993) and Baum et al. (2011). The cloud bidirectional reflectance distribution function (BRDF) and bidirectional transmittance distribution function (BTDF) are stored in a lookup table containing data for 2002 wavelengths within the spectral range from 0.28–4.0 μm. Surface radiances in the spectral bands are analytically solved from the radiative transfer equation for five independent photon paths using the optical thickness of the clear-sky atmosphere provided by SMARTS and the cloud BRDF and BTDF.

Spectral data are required only for selected solar energy projects. For thermal collectors using current technology, spectral information does not need to be collected for each individual project, and the application of standard spectra suffices. For large PV plants, however, the site-specific spectral effects should be considered to increase accuracy. This can be done best if spectral data are available. Because of the high costs of spectral measurements, the state of the art is to introduce the spectral effects via modeling approaches, such as in PV simulation models. This procedure is generally empirical and can be improved; hence, related research is required. Additionally, spectral irradiance data are useful in related solar technology developments, and they are also relevant as an intermediate product to understand specific effects, such as soiling, beam attenuation near the ground, or measurement error of various radiometers.

5.7 Ultraviolet Irradiance

Although UV constitutes only a small portion of the solar spectrum, the high energy of the photons contained at wavelengths less than 400 nm can cause degradation of materials, such as those used in the construction of PV modules. More generally, UV irradiance information can be useful in many research-and-development applications, such as PV and CSP material degradation, service life prediction, monitoring of lamps in accelerated weathering chambers, aging tests in solar simulators, and climate-related research using predictions from appropriate models or actual data from weather stations; therefore, high-quality measured and modeled UV databases are often required for various locations with differing climatic conditions. Such data sources typically provide accurate inputs for these applications.

The UV spectral ranges of interest are defined in various standards and publications. ASTM G113-16 (ASTM 2016) defines UV irradiance for natural weathering applications as the amount of electromagnetic radiation greater than 295 nm and less than the visible electromagnetic radiation. According to ASTM G177 (ASTM 2020b), the total UV is defined from 280–400 nm, and it is subdivided into UV-A (320–400 nm) and UV-B (280–320 nm). The World Health Organization (WHO 2020), however, defines these ranges slightly differently, using 315–400 nm for UV-A and 280–315 nm for UV-B. Other definitions can be found in the literature or in the specifications of UV radiometers. In weathering and durability studies, for instance, radiant UV doses are reported in the ranges from 295–400 nm or 295–385 nm (Habte et al. 2019).

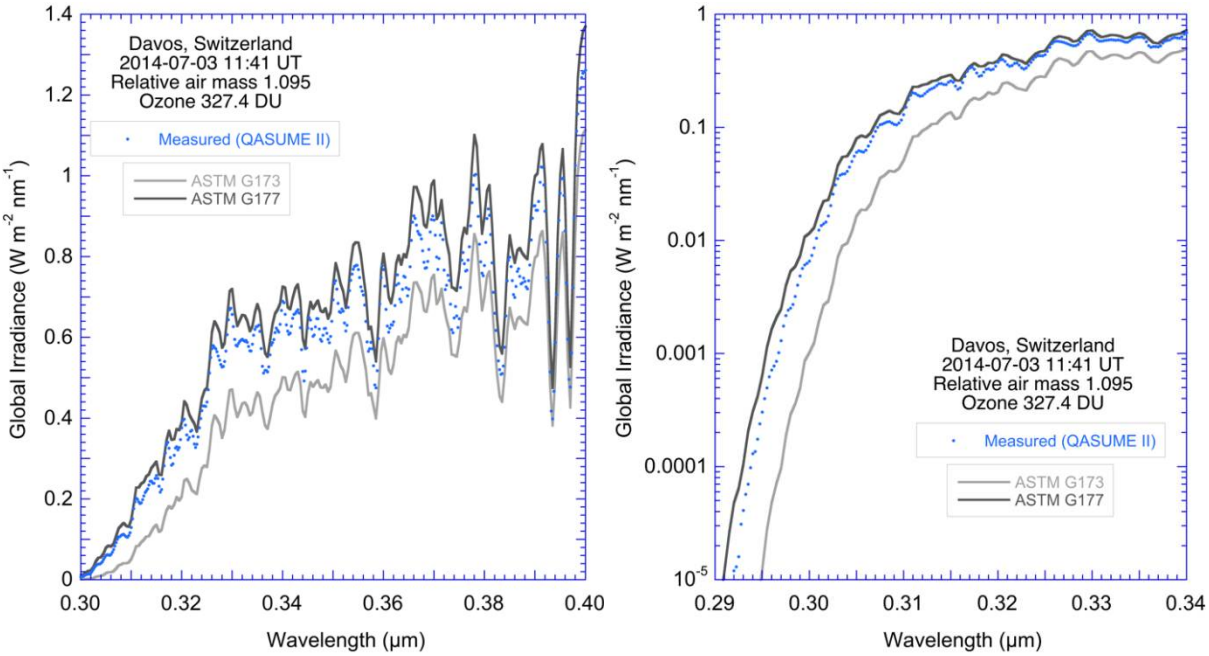

Figure 5-4. UV global spectrum measured with a QASUME II spectroradiometer at the PMOD/WRC laboratory under high-sun conditions compared with standards ASTM G173 (low UV) and G177 (high UV) in (left) linear scale and (right) logarithmic scale

The varying definitions that currently exist introduce confusion, especially because the UV irradiance magnitude is highly dependent on wavelength. This is shown in Figure 5-4, where actual measurements of spectral global horizontal irradiance (GHI) conducted at the Physikalisch-Meteorologisches Observatorium Davos/World Radiation Center (PMOD/WRC) with a QASUME II spectroradiometer are compared with the reference global tilted irradiance spectra promulgated in standards ASTM G173 (for moderate air mass, AM1.5) and G177 (for low air mass, AM1.05). As shown, at less than approximately 0.33 µm, the irradiance magnitude varies considerably for only small incremental changes in wavelength, hence the need for an excellent wavelength calibration of UV radiometers. A consensus on the range of UV irradiances applicable for solar energy conversion technologies is desirable, but it has not yet been reached.

Some information disseminated by WHO (WHO 2020) about the UV irradiance distribution is valuable because of its relevance to solar energy applications. In particular, note that clean snow reflects up to approximately 80% of UV irradiance and that more than approximately 90% of UV irradiance can be transmitted through thin clouds. Further, WHO emphasizes the relationship between site elevation and UV irradiance, stating an increase of 4% in UV irradiance for a 300-m increase in altitude. Additionally, most of the daily UV dose is said to be received during a 4-hour period centered on local solar noon.

As stated in Hülsen and Gröbner (2007), spectroradiometers are the best instruments to measure UV irradiance, but they are expensive and require high maintenance. High-end instruments, called double monochromators, are less sensitive to stray-light issues than simpler instruments based on CCD technology, and they are necessary to sense the UV accurately at less than approximately 320 nm, but they are also extremely delicate and expensive; therefore, in most cases, only broadband UV radiometers are used in applications that do not demand spectral information. All UV radiometers can be calibrated so that they are traceable to one of the existing National Metrological Institutes through a calibrated reference lamp. Further, some institutions, such as the World Meteorological Organization (WMO), assist in maintaining traceability through a commonly accepted calibration methodology and through regular intercomparisons using standard reference

spectroradiometers maintained and operated by the PMOD/WRC. In general, an annual calibration interval is recommended because UV radiometers are susceptible to atmospheric constituent changes, degradation and stability issues, and other uncertainties (Webb, Gröbner, and Blumthaler 2006).

There are many types of broadband UV radiometers, as described in Hülsen et al. (2020). There are also multiwavelength narrowband filter radiometers that measure solar irradiance at a few wavelengths in the UV spectrum, but they require an intricate absolute calibration process that involves model simulations (Kerr and Fioletov 2008).

Measuring UV is difficult because it is prone to high measurement uncertainty resulting from factors such as stray-light contamination, calibration error, or directional response deviation. On the other hand, measured and/or modeled GHI data of fairly low uncertainty is relatively abundant for many locations. Many studies have attempted to parameterize the global UV irradiance (UV-B and/or UV-A)—for example, by considering the empirical relationship between global UV irradiance and other readily available quantities, such as GHI (Krzyścin 1996; Fioletov, Kerr, and Wardle 1997; McArthur et al. 1999; Schwander et al. 2002; Habte et al. 2019). Some studies have used radiative transfer models (Madronich and Flocke 1997; Evans 1998; Ricchiazzi and Gautier 1998; Mayer and Kylling 2005; Koepke 2009); whereas others have used satellite instruments, such as the Ozone Monitoring Instrument (OMI), to estimate the surface UV irradiance (Krotkov et al. 1998; Peeters et al. 1998; Herman et al. 1999; Levelt et al. 2006; Tanskanen et al. 2006).

5.7.1 Soiling

Soiling can greatly reduce the efficiency of solar collectors because of the induced reduction of optical transmission through the collector's glass cover or entrance window or degradation of the specular reflectance of mirrors. The soiling loss ratio is defined as the ratio between the efficiency of the soiled component and that of the clean component for otherwise identical conditions. The soiling loss ratio is also called the "soiling ratio" or "cleanliness." The soiling rate describes the rate of change of cleanliness over time. For mirrors, average soiling rates of 2% per day have been reported at some CSP installations. For flat-plate panels, soiling rates are approximately 10 times less for the same conditions because the forward-scattered light still contributes to the PV or flat-plate collector yield (Bellmann et al. 2020). Reviews of actual soiling effects on solar power plants can be found in Sarver, Al-Qaraghuli, and Kazmerski (2013); Ilse et al. (2018); and Maghami et al. (2016).

The cleanliness can be measured using different techniques. For PV, the short-circuit current of soiled reference cells or modules can be compared to that of a clean cell or module. In the general case, modules comprise a large number of cells; hence, such a measurement can be inaccurate if the module's surface is not homogeneously soiled. In that configuration, either the IV curves of a clean and a soiled module need to be analyzed for an accurate estimation of the soiling ratio or the output powers of both modules obtained with maximum power point trackers need to be compared. Care must be taken if only one module or cell is used for the estimation of the cleanliness by comparing its performance before and after cleaning because the external conditions might have changed in the meantime. Moreover, the module or cell temperature can be affected by the cleaning process itself. The cleaning of the clean reference glass sheet or reference module/cell is of great importance. Automatic cleaning of the reference device is complex, whereas manual cleaning is time-consuming.

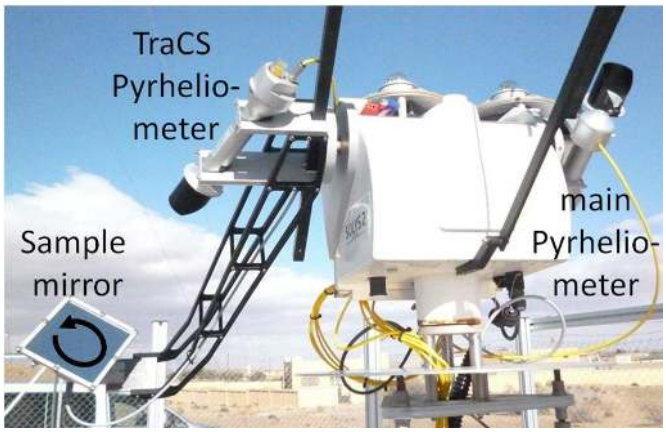

Figure 5-5. TraCS system for the measurement of mirror soiling. The reflected DNI is compared to the incident DNI to obtain the reflectance of the sample mirror. *Photo by DLR*

For CSP, one option is to use handheld reflectometers and measure the reflectance of working mirrors or sample mirrors before and after cleaning. Alternatively, transmissometers can be used to monitor soiling effects on CSP entrance windows. These measurements are time-consuming and expensive; therefore, automatic methods have been developed for reflectance (see Figure 5-5) (Wolfertstetter et al. 2014) and transmittance, respectively.

Another technique that can be applied to either PV or CSP uses a photodiode behind a glass sheet and a detector that senses the scattered radiation. Any soiling on the glass sheet increases the latter. The measured signal can be converted into transmittance or reflectance reduction. Further, methods based on the analysis of digital pictures of soiled collectors are under development.

Figure 5-6. Several cleanliness measurement options for PV and CSP. *Photo by DLR*

Some of the aforementioned measurement options are shown in Figure 5-6. For fixed-tilt and tracked reference cells, the orientation of the soiling sensors is crucial and should be as close as possible to that of the plant itself. Further, the test material must be similar—or ideally identical—to that in the power plant; therefore, two different types of reference cells are shown. The TraCS device shown in Figure 5-5 is used here to evaluate the cleanliness of four mirrors with different antisoiling coatings that are mounted on a rotating plate. The cleanliness thus obtained at regular intervals can be used to derive the soiling rate. Effects related to the incidence angle, for example, can cause the soiling rate to change strongly throughout the day. Even if the component is not cleaned, positive soiling rates (increase of cleanliness) occur, at least momentarily, if the time resolution is too high; therefore, soiling rates are reported most frequently at a daily resolution. To properly determine the soiling rate, it is important to compare data points collected under similar conditions. For instance, the cleanliness measured at noon under clear-sky conditions should not be compared to that of the next days if measured under cloudy conditions or at a different sun elevation.

Modeling the soiling rate is a potential solution to strongly reduce the costs associated with experimental soiling data and to rapidly provide long-term data sets at many sites. Soiling models are mainly based on particle concentration and precipitation, though other meteorological data are also required in general. Existing models (Picotti et al. 2018; Micheli and Muller 2017; Wolfertstetter et al. 2019) are currently further enhanced and adapted to create soiling maps and soiling forecasts based on atmospheric dust transportation models (Micheli, Deceglie, and Muller 2019).

Several systems are commercially available for the measurement of cleanliness and soiling rate. They can be used in feasibility studies or for the optimization of plant operation and cleaning intervals. Soiling measurements are recommended during the site selection process, especially if no soiling data are available from nearby sites, and they continue to be desirable during plant operation. Depending on the soiling levels at a PV plant and the peak power of a PV plant, for instance, IEC 61724-1 defines a certain number of required soiling measurements. Soiling rate results are typically not in the public domain, and only a few data sets are available from data portals—e.g., NREL (2020).

5.8 Circumsolar Radiation

As discussed in Chapter 2, Section 2.7.1, circumsolar radiation is the scattered radiation received from the angular region close to the sun. Most of the circumsolar radiation is included in DNI measurements, but typically only a smaller part of it can be used by focusing collectors; therefore, information on circumsolar radiation is important for CSP plant yield assessments and the design of any type of concentrating power plant. High circumsolar radiation contributions to DNI can reduce the efficiency by 10% or more compared to the efficiency for low circumsolar radiation levels, even for DNI greater than 200 W/m². Using typical estimates of the average circumsolar radiation conditions can lead to errors of several percent in the long-term plant yield—e.g., approximately 2% for an exemplary tower plant in the United Arab Emirates (Wilbert 2014).

Different techniques are available to measure circumsolar radiation. For instance, a method based on two commercial instruments exists: a camera-based “sun and aureole measurement system” and a sun photometer (Gueymard 2010; Wilbert et al. 2013). Another camera-based method is also used in Schrott et al. (2014). A different system uses two pyrheliometers with contrasting acceptance angles (Wilbert, Pitz-Paal, and Jaus 2013). Kalapatapu et al. (2012) presented a modified rotating shadowband irradiometer (RSI) with a slit aperture on top of the RSI sensor. Alternatively, circumsolar radiation can be measured with unmodified RSIs (Wilbert et al. 2018). The irradiance signal collected during the rotation of the shadowband is analyzed to obtain the circumsolar contribution.

Only camera-based systems can measure the sunshape. This quantity (not to be confused with the shape of the sun disk itself) is defined as the normalized radially averaged radiance profile as a function of the angular distance from the apparent sun center. The other radiometric systems can derive the circumsolar contribution to DNI, which can, in turn, be used to estimate the sunshape. Because of the high costs, maintenance and calibration constraints, and analysis difficulties, so far the existing camera-based systems have been limited to high-end scientific studies. In contrast, RSI- and pyrheliometer-based methods are already commercially available.

Obtaining long-term information on circumsolar radiation to help power plant project developments at an early stage would require substantial modeling effort. A model for the influence of thin ice clouds (cirrus), which considerably increase the circumsolar contribution, has been presented (Reinhardt et al. 2013). The effect of aerosols can also be modeled (Eissa et al. 2018). More recent work using specialized radiative models to evaluate the difference between the true and apparent DNI can be found in Räisänen and Lindfors (2019); Sun et al. (2020); and Xie et al. (2020); however, so far modeled circumsolar data are not routinely available for site assessment.

Circumsolar radiation measurements are available for several sites (Bendt and Rabl 1980; Noring, Grether, and Hunt 1991; Wilbert 2014; Wilbert, Pitz-Paal, and Guillot 2013). For nearby plant projects, or for projects in a similar climate, such measurements might be sufficient for plant yield calculations. For other regions and climates, measurement campaigns are recommended for site assessment, CSP technology selection, acceptance testing, or optimization of plant operation. More research would be necessary, however, before the circumsolar contribution can be easily determined by analysts at any location and any instant in their practice of solar resource assessments.

5.9 Beam Attenuation Between Heliostats and Receiver in Tower Power Plants

Among all CSP technologies, tower power plants present a specific challenge because atmospheric constituents tend to attenuate the radiation beams along their path from the heliostats to the solar receiver on the tower. This attenuation could have a significant impact on the efficiency of this technology (Figure 5-7). During clear days, the optical losses over a 1-km slant range can be less than approximately 5%. Under hazy, humid conditions, however, more than 50% can be lost; hence, attenuation data must be available for the plant design, plant yield analysis, and plant operation. Under extreme conditions, high extinction levels could prevent towers from being an economically feasible technology option.

Figure 5-7. (Left) CIEMAT's CESA 1 solar tower on a clear day and (right) on a hazy day. *Photo by DLR*

Beam attenuation along a slant path can be evaluated with scatterometers or transmissiometers (Hanrieder et al. 2015). Camera-based methods also exist (Ballestrín et al. 2018), and at least three such options are commercially available. Sengupta and Wagner (2012) and Hanrieder et al. (2016, 2020) presented models to derive the attenuation based on only conventional DNI measurements. Polo, Ballestrín, and Carra (2016) and Polo et al. (2017) estimated the attenuation based on AOD data. Mishra et al. (2020) assessed the sensitivity of three existing attenuation models for different atmospheric conditions and have evaluated the feasibility of using satellite data as additional inputs.

The main difficulty resides in the estimation of the vertical profile of the aerosol concentration. An overview of measurement and modeling methods and the effect of attenuation on CSP plants has been presented (Hanrieder et al. 2017).

For prefeasibility and feasibility studies, the existing attenuation models should be applied to obtain a first idea of the extinction levels at the site(s) of interest. The extinction varies over time, depending on aerosol and humidity conditions; hence, the frequencies of high AOD and high humidity values become relevant factors to consider. Under clear conditions, the existing models can provide sufficient accuracy. Under hazy conditions with insufficient local atmospheric data on AOD or humidity, the uncertainties can be quite high. In that case, measurements are recommended for reasonable plant yield estimates. For acceptance tests and plant operation, particularly at sites that are frequently impacted by hazy conditions, measurements are recommended.

5.10 Surface Albedo

The ratio of the total irradiance reflected to the total irradiance received by a surface is called the "bihemispherical reflectance," which is also customarily known as "albedo" (ρ). In contrast, the term *reflectance* is used whenever angular properties are significant—for instance, in the case of a surface exhibiting specular properties. More discussion on these definitions appear in Gueymard et al. (2019). For solar energy applications, the albedo definition can be mathematically expressed as the ratio of the reflected horizontal irradiance (RHI) emanating from a surface to the GHI that is incident onto it:

$$\rho = \mathrm{RHI/GHI}. \tag{5-9}$$

This definition holds for either *spectral* or *broadband* fluxes. Only the latter case is discussed further here because of its predominant interest in solar applications. The albedo's physical possible values range from 0–1 (sometimes expressed in percentage). In nature, most land areas not covered by ice or snow have an albedo in the approximate range from 0.15–0.35. Water bodies usually have a low albedo, typically near 0.05. At the other extreme, areas covered with fresh snow or clean ice have a very high albedo, which could exceed 0.85. One difficulty is that albedo is not merely a true constant surface property but rather a property of the coupled surface-atmosphere system. In particular, surface albedo is a function of the inherent surface characteristics, atmospheric state, and illuminating conditions (Wang et al. 2015). For that reason, in general albedo presents a high variability both in space (at scales from a few centimeters to hundreds of kilometers) and time (at scales from minutes to daily, seasonal, and even interannual); e.g., dry regions with sparse vegetation or spots of snow cover—see, e.g., Berg et al. (2020) and Gueymard et al. (2019, 2020).

Figure 5-8 shows an example of the temporal variability of the albedo of a specific site at different timescales. Under clear skies, the diurnal albedo evolution is a function of solar position because the reflection process is never purely isotropic (Lambertian) in the real world. Conversely, albedo tends to be constant under dense overcast conditions because

the direct beam component then vanishes and the incident illumination is nearly isotropic. Additionally, daily albedo time series vary on a daily, seasonal, and interannual basis.

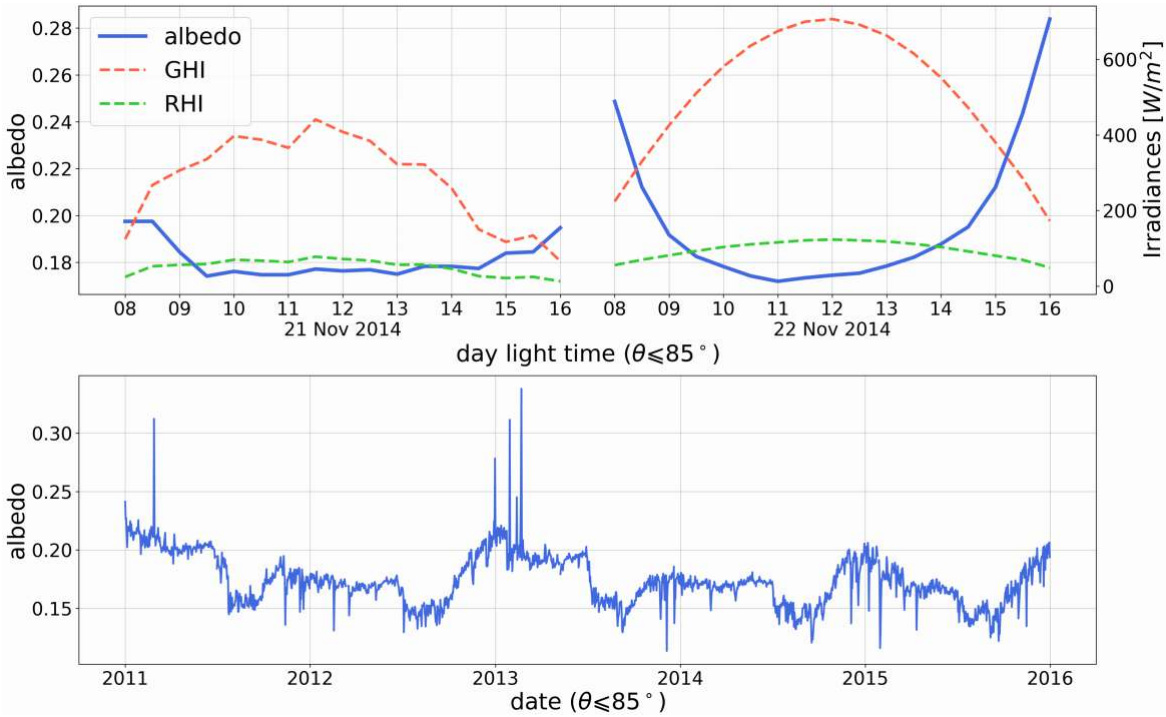

Figure 5-8. (Top) Example of diurnal variation of albedo (30-minute intervals) for (left) cloudy-sky conditions and (right) clear conditions derived from the total incident and reflected horizontal irradiances, GHI and RHI, measured at the AmeriFlux radiometric station of Walnut Gulch Kendall Grasslands in Arizona, United States. (Bottom) Five years of daily mean albedo recorded at the same station, illustrating its seasonal and interannual variability

These variations are typically related to the vegetation's phenological state, the surface's roughness and wetness, and the presence of snow or ice. Additionally, the albedo's spatiotemporal variability is impacted by both the atmospheric state and the ambient illumination conditions through the GHI's direct and diffuse components. In this respect, it is possible and convenient to define two theoretical illumination scenarios. The extreme situation in which there is only pure direct-beam illumination—resulting in an ideally black sky dome—corresponds to the conceptual case of "directional-hemispherical reflectance," also known as *black-sky albedo* (BSA). The opposite theoretical situation is that of a "bihemispherical reflectance" under purely isotropic diffuse illumination, referred to as *white-sky albedo* (WSA). Overall, RHI can be expressed as a combination of these individual components as:

$$\mathrm{RHI} = \mathrm{BSA}\cdot\mathrm{DIR} + \mathrm{WSA}\cdot\mathrm{DHI} \tag{5-10}$$

where DIR and DHI denote the direct and diffuse horizontal irradiances, respectively. Assuming that the diffuse illumination is purely isotropic, the actual surface albedo—sometimes referred to as *blue-sky albedo*—can be interpolated as a weighted linear combination of its components (Lewis and Barnsley 1994; Lucht, Schaaf, and Strahler 2000; Roman et al. 2010):

$$\rho = \mathrm{WSA}\cdot K + \mathrm{BSA}\cdot(1 - K) \tag{5-11}$$

where K is the diffuse fraction, DHI/GHI. Under overcast conditions, usually only the diffuse component is present ($K \approx 1$), hence $\rho \approx$ WSA. This approximation is convenient and typically

used in most solar energy applications because of practical constraints and lack of detailed data on BSA. Most often, WSA is considered a constant value over time, such as 0.2.

Both BSA and WSA can be determined by respective spatial integrations of the surface's BRDF. This is the conceptual foundation to determine the reflectance of the target surface according to the geometry of the source-surface-observer directions of radiation. It is a function of wavelength (λ) and of the structural and optical properties of the surface. The BRDF attempts to describe the behavior of the naturally anisotropic scattering of the solar radiation at the surface-air interface. Because of the complexity, diversity, and variability of BRDF distributions, mathematical models are used in practice to generate a parametric representation of it (Lucht, Schaaf, and Strahler 2000). In addition to the precise determination of the angular reflectance in any direction, the BRDF framework is used in a large range of applications related to satellite remote sensing.

In solar energy applications, determining surface albedo is fundamental for various reasons (Gueymard et al. 2019). First, radiative transfer models require albedo to account for the multiple reflections between the surface and the atmosphere (referred to as the backscattering effect) and to ultimately evaluate DHI and GHI (Ruiz-Arias and Gueymard 2018; Sun et al. 2019; Xie, Sengupta, and Dudhia 2016). Second, in the frequent case when the incoming solar irradiance is modeled based on satellite imagery, the surface albedo also constitutes a key independent variable to estimate the dynamic range of cloud reflectance (Perez, Cebecauer, and Suri 2013). Third, most solar applications involve planar solar thermal collectors or PV modules that are tilted with respect to the horizontal, in which case the ground-reflected irradiance that is incident on the tilted plane must be determined. This is particularly important in increasingly popular bifacial PV technology, which directly exploits the reflected irradiance as the primary source of energy for each module's rear side. This makes bifacial PV modules markedly more sensitive to the albedo magnitude and variations than monofacial modules; hence, reliable information about the surface albedo has become important to determine the most suitable PV technology at any site, to obtain reliable simulations of the envisioned system's energy output, and to assess the economic feasibility of any solar power project. Difficulties exist because the calculation of the reflected irradiance on a tilted surface is generally performed following several simplifying assumptions that do not apply in practice (Gueymard et al. 2019; Kamphuis et al. 2020).

There are three main sources of data on surface albedo: (1) ground measurements using albedometers (two pyranometers placed horizontally in opposite up and down directions, measuring GHI and RHI, respectively); (2) satellite estimates based on monitoring the reflected radiance emanating from the Earth's surface-atmosphere system; and (3) predictions based on a reanalysis model. All present distinct characteristics with advantages and limitations.

In bifacial PV plants, the in-plane rear-side irradiance (RPOA), must be measured or modeled according to IEC 61724-1. Models for the RPOA can use raytracing based on horizontal albedo measurements and can optionally also rely on diffuse irradiance measurements. The albedo measurement must be as representative for the site as possible. If different albedos are expected in a PV plant, several albedo measurements are needed. ISO TR 9901 and IEC 61724-1 provide recommendations on albedo measurements. Measuring the albedo on a steep slope is prone to error because the GHI measurement made with a pyranometer facing up and mounted horizontally then contains part of the radiation measured by the downward-facing pyranometer. This can lead to an underestimation of the albedo. In this situation, the GHI signal should be measured such that the radiation reflected by the ground does not affect it. The height of the albedo measurement should be high enough to achieve a sufficient measurement area with low shading losses but low enough to allow for easy maintenance access; therefore, heights

between 1.5 m and 2 m are recommended if the expected snow heights allow this. In contrast, heights of 10 m or more are necessary to evaluate the albedo over a larger ground area, with the goal of comparing such data with airborne or spaceborne observations, for instance. The area below the downward-facing pyranometer should not be shaded, and therefore the instrument's mounting structure should be oriented toward the nearest pole and minimized. Shadows affecting the area below the downward-facing pyranometer caused by fences, other instruments, or solar collectors should also be minimized to avoid errors. To avoid parasitic specular reflections caused by metallic surfaces around, glare screens might also be considered to protect the downward-facing pyranometer.

Various albedo products have been proposed and cover various geographic areas and periods at diverse spatiotemporal resolutions. An exhaustive table of openly accessible sources is available in Gueymard et al. (2019), along with their main characteristics. In addition, some specialized proprietary databases of surface albedo exist and are accessible through service providers.

When using such databases to evaluate the specific albedo at a site during the design phase of a projected solar energy system, some critical questions arise: (1) Will the historical albedo at hand be conserved in the future, considering possible changes in the surface characteristics caused by the system's construction (e.g., vegetation removal)? (2) How is the albedo of the specific site under scrutiny related to the albedo of the area (e.g., grid cell) for which information is available from these databases? The first question must be answered on a case-by-case basis by the designer. To address the second question, an analysis of the spatial variability of the albedo over the area around the site must be conducted. Analyses show that this spatial variability can be high in many cases (Gueymard et al. 2020; Wang et al. 2015), which complicates the matter because the use of spatial interpolation or extrapolation over inhomogeneous areas could result in incorrect results. When dealing with inhomogeneous surfaces at the small scale—for instance, near a solar power plant—methods have been proposed to evaluate the angular effects of composite surfaces (Ziar et al. 2019). Finally, methods of various complexity are being developed to determine the ground-reflected irradiance that is incident on the rear side of bifacial PV modules using either spectral or broadband albedo information (Berrian and Libal 2020; Chudinzow et al. 2019; Hansen et al. 2017; Monokroussos et al. 2020; Patel et al. 2019; Russell et al. 2017; Sun et al. 2018).

5.11 References

Alduchov, O. A., and R. E. Eskridge. 1996. "Improved Magnus Form Approximation of Saturation Vapor Pressure." *Journal of Applied Meteorology* 35: 601–9.

Andenæs, E., B. P. Jelle, K. Ramlo, T. Kolås, J. Selj, and S. E. Foss. 2018. "The Influence of Snow and Ice Coverage on the Energy Generation from Photovoltaic Solar Cells." *Solar Energy* 159: 318–28. https://doi.org/10.1016/j.solener.2017.10.078.

Andrews, R. W., A. Pollard, J. M. Pearce. 2013. "The Effects of Snowfall on Solar Photovoltaic Performance." *Solar Energy* 92: 84–97. https://doi.org/10.1016/j.solener.2013.02.014.

ASTM. 2016. *ASTM G113-16, Standard Terminology Relating to Natural and Artificial Weathering Tests of Nonmetallic Materials*. West Conshohocken, PA: , ASTM International. www.astm.org.

ASTM. 2020a. *ASTM G173-03(2020), Standard Tables for Reference Solar Spectral Irradiances: Direct Normal and Hemispherical on 37° Tilted Surface*. West Conshohocken, PA: ASTM International. www.astm.org.

ASTM. 2020b. *ASTM G177-03(2020), Standard Tables for Reference Solar Ultraviolet Spectral Distributions: Hemispherical on 37° Tilted Surface*. West Conshohocken, PA: ASTM International. www.astm.org.

Ballestrín, J., R. Monterreal, M. E. Carra, J. Fernández-Reche, J. Polo, R. Enrique, J. Rodríguez, M. Casanova, F. J. Barbero, J. Alonso-Montesinos, G. López, J. L. Bosch, F. J. Batlles, and A. Marzo. 2018. "Solar Extinction Measurement System Based on Digital Cameras: Application to Solar Tower Plants." *Renewable Energy* 125: 648–54. https://doi.org/10.1016/j.renene.2018.03.004.

Baum, B. A., P. Yang, A. J. Heymsfield, C. G. Schmitt, Y. Xie, A. Bansemer, Y. X. Hu, and Z. B. Zhang. 2011. "Improvements in Shortwave Bulk Scattering and Absorption Models for the Remote Sensing of Ice Clouds." *Journal Applied Meteorology and Climatology* 50: 1,037–56. https://doi.org/10.1175/2010JAMC2608.1.

Becker, G., B. Schiebelsberger, W. Weber, J. Schumacher, M. Zehner, G. Wotruba, and C. Vodermayer. 2008. "Energy Yields of PV Systems - Comparison of Simulation and Reality." *Proceedings of the 23rd European Photovoltaic Solar Energy Conference and Exhibition*, Valencia, Spain: 3,184–86. https://doi.org/10.4229/23rdEUPVSEC2008-4BV.1.57.

Beirle, S., J. Lampel, Y. Wang, K. Mies, S. Dörner, M. Grossi, D. Loyola, A. Dehn, A. Danielczok, M. Schröder, and T. Wagner. 2018. "The ESA GOME-Evolution 'Climate' Water Vapor Product: A Homogenized Time Series of H2O Columns from GOME, SCIAMACHY, and GOME-2." *Earth System Science Data* 10 (1): 449–68.

Bellmann, P., F. Wolfertstetter, R. Conceição, and H. G. Silva. 2020. "Comparative Modeling of Optical Soiling Losses for CSP and PV Energy Systems." *Solar Energy* 197: 229–37.

Bendt, P., and A. Rabl. 1980. *Effect of Circumsolar Radiation on Performance of Focusing Collectors* (SERI/TR-34-093). Golden, CO: Solar Energy Research Institute.

Berg, L. K., C. N. Long, E.I. Kassianov, D. Chand, S. L. Tai, Z. Yang et al. 2020. "Fine-Scale Variability of Observed and Simulated Surface Albedo Over the Southern Great Plains." *Journal of Geophysical Research: Atmospheres* 125: e2019JD030559.

Berrian, D. and J. Libal. 2020. "A Comparison of Ray Tracing and View Factor Simulations of Locally Resolved Rear Irradiance with the Experimental Values." *Progress in Photovoltaics: Research and Applications* 2020: 1–12. https://doi.org/10.1002/pip.3261.

Bird, R. E. 1984. "A Simple, Solar Spectral Model for Direct-Normal and Diffuse Horizontal Irradiance." *Solar Energy* 32: 461–71.

Blair, N., N. Diorio, J. Freeman, P. Gilman, S. Janzou, Ty. Neises, and M. Wagner. 2018. *System Advisor Model (SAM) General Description (Version 2017.9.5)* (NREL/TP-6A20-70414). Golden, CO: National Renewable Energy Laboratory. https://www.osti.gov/servlets/purl/1440404.

Bliss, M., T. R. Betts, and R. Gottschalg. 2010. "Indoor Measurement of Photovoltaic Device Characteristics at Varying Irradiance, Temperature and Spectrum for Energy Rating." *Measurement Science and Technology* 21: 115701.

Bogenrieder, J., C. Camus, M. Hüttner, P. Offermann, J. Hauch, and C. Brabec. 2018. "Technology-Dependent Analysis of the Snow Melting and Sliding Behavior on Photovoltaic Modules." *Journal of Renewable and Sustainable Energy* 10: 021005. https://doi.org/10.1063/1.5001556.

Bonilla Castro, J., M. Schweiger, D. Moser, T. Tanahashi, B. H. King, G. Friesen, L. Haitao, R. French, L.S. Bruckman, B. Müller, C. Reise, G. Eder, W. van Sark, Y. Sangpongsanon, F. Valencia, and J. Stein. 2020. *Climatic Rating of Photovoltaic Modules: Different*

Technologies for Various Operating Conditions (Report IEA PVPS T13 20:2020) (ISBN 978-3-907281-08-6).

Bosilovich, M. G., R. Lucchesi, and M. Suarez. 2016. MERRA-2: File Specification. GMAO Office Note No. 9 (Version 1.1): 73 pp. https://gmao.gsfc.nasa.gov/pubs/docs/Bosilovich785.pdf.

Braga M., L. R. do Nascimento, and R. Rüther. 2019. "Spectral Modeling and Spectral Impacts on the Performance of mc-Si and New Generation CdTe Photovoltaics in Warm and Sunny Climates." *Solar Energy* 188: 976–88.

Bright, J. M., and C. A. Gueymard. 2019. "Climate-Specific and Global Validation of MODIS Aqua and Terra Aerosol Optical Depth at 452 AERONET Stations." *Solar Energy* 183: 594–605.

Bright, J. M., C. A. Gueymard, S. Killinger, D. Lingfors, X. Sun, P. Wang, and N. A. Engerer. 2018. "Climatic and Global Validation of Daily MODIS Precipitable Water Data at AERONET Sites for Clear-sky Irradiance Modelling." *Proceedings of the EuroSun 2018 Conference*, Rapperswil, Switzerland. https://doi.org/10.18086/eurosun2018.09.07.

Burnham, L., D. Riley, B. Walker, and J. M. Pearce. 2019. "Performance of Bifacial Photovoltaic Modules on a Dual-Axis Tracker in a High-Latitude, High-Albedo Environment." *Proceedings of the 2019 IEEE 46th Photovoltaic Specialists Conference (PVSC)*: 1,320–27. DOI: 10.1109/PVSC40753.2019.8980964.

Chhatbar, K. and R. Meyer. 2011. "The Influence of Meteorological Parameters on the Energy Yield of Solar Thermal Power Plants." *Proceedings of SolarPACES Symposium*, Granada, Spain.

Chiu, J., S. Paredes-Mesa, T. Lakhankar, P. Romanov, N. Krakauer, R. Khanbilvardi, and R. Ferraro. 2020. "Intercomparison and Validation of MIRS, MSPPS, and IMS Snow Cover Products." *Advances in Meteorology*: 4532478. https://doi.org/10.1155/2020/4532478.

Chudinzow D., J. Haas, G. Díaz-Ferrán, S. Moreno-Leiva, and L. Eltrop. 2019. "Simulating the Energy Yield of a Bifacial Photovoltaic Power Plant." *Solar Energy* 183: 812–22.

Clough, S. A., M. W. Shephard, E. J. Mlawer, J. S. Delamere, M. J. Iacono, K. Cady-Pereira, S. Boukabara, and P. D. Brown. 2005. "Atmospheric Radiative Transfer Modeling: A Summary of the AER Codes." *Journal of Quantitative Spectroscopy and Radiative Transfer* 91 (2): 233–44.

do Nascimento, L., T. de Souza Viana, R. Antunes Campos, R. Rüther. 2019. "Extreme Solar Overirradiance Events: Occurrence and Impacts on Utility-Scale Photovoltaic Power Plants in Brazil." *Solar Energy* 186: 370–381. ISSN 0038-092X. https://doi.org/10.1016/j.solener.2019.05.008 .

Dobos, A. P. 2014. *PVWatts Version 5 Manual* (NREL/TP-6A20-62641). Golden, CO: National Renewable Energy Laboratory. https://www.nrel.gov/docs/fy14osti/62641.pdf.

Eissa, Y., P. Blanc, H. Ghedira, A. Oumbe, and L. Wald. 2018. "A Fast and Simple Model to Estimate the Contribution of the Circumsolar Irradiance to Measured Broadband Beam Irradiance Under Cloud-Free Conditions in Desert Environment." *Solar Energy* 163: 497–509. https://doi.org/10.1016/j.solener.2018.02.015.

Emery, K., A. Anderberg, M. Campanelli, P. Ciszek, C. Mack, T. Moriarty, C. Osterwald, L. Ottoson, S. Rummel, and R. Williams. 2013. "Rating Photovoltaics." *Proceedings of the 39th IEEE Photovoltaic Specialists Conference*, Tampa, Florida.

Evans, K. F. 1998. "The Spherical Harmonics Discrete Ordinate Method for Three-Dimensional Atmospheric Radiative Transfer." *Journal of the Atmospheric Sciences* 55: 429–46.

Fioletov, V. E., J. B. Kerr, and D. I. Wardle. 1997. "The Relationship between Total Ozone and Spectral UV Irradiance from Brewer Observations and Its Use for Derivation of Total Ozone from UV Measurements." *Geophysical Research Letters* 24: 2,997–3,000.

Giles, D. M., Sinyuk, A., Sorokin, M. G., Schafer, J. S., Smirnov, A., Slutsker, I., Eck, T. F., Holben, B. N., Lewis, J. R., Campbell, J. R., Welton, E. J., Korkin, S. V., and Lyapustin, A. I. 2019. "Advancements in the Aerosol Robotic Network (AERONET) Version 3 Database – Automated Near-Real-Time Quality Control Algorithm with Improved Cloud Screening for Sun Photometer Aerosol Optical Depth (AOD) Measurements." *Atmospheric Measurement Techniques* 12: 169–209.

Gueymard C. A., V. Lara-Fanego, M. Sengupta, and Y. Xie. 2019. "Surface Albedo and Reflectance: Review of Definitions, Angular and Spectral Effects, and Intercomparison of Major Data Sources in Support of Advanced Solar Irradiance Modeling over the Americas." *Solar Energy* 182: 194–212.

Gueymard, C. 1993. "Assessment of the Accuracy and Computing Speed of Simplified Saturation Vapor Equations Using a New Reference Dataset." *Journal of Applied Meteorology* 32: 1,294–1,300.

Gueymard, C. A. 1995. *Simple Model of the Atmospheric Radiative Transfer of Sunshine, version 2 (SMARTS2): Algorithms Description and Performance Assessment*. Cocoa, FL: Florida Solar Energy Center.

Gueymard, C. A. 2001. "Parameterized Transmittance Model for Direct Beam and Circumsolar Spectral Irradiance." *Solar Energy* 71: 325–46.

Gueymard, C. A. 2008. "Prediction and Validation of Cloudless Shortwave Solar Spectra Incident on Horizontal, Tilted, or Tracking Surfaces." *Solar Energy* 82: 260–71.

Gueymard, C. A. 2010. "Spectral Circumsolar Radiation Contribution To CPV." *AIP Conference Proceedings* 1277: 316. https://doi.org/10.1063/1.3509220.

Gueymard, C. A. 2017. "Cloud and Albedo Enhancement Impacts on Solar Irradiance Using Highfrequency Measurements from Thermopile and Photodiode Radiometers. Part 2: Performance of Separation and Transposition Models for Global Tilted Irradiance." *Solar Energy* 153: 766–79.

Gueymard, C. A., and D. Yang. 2020. "Worldwide Validation of CAMS and MERRA-2 Reanalysis Aerosol Optical Depth Products Using 15 Years of AERONET Observations." *Atmospheric Environment* 225: 117216.

Gueymard, C. A., D. Myers, and K. Emery. 2002. "Proposed Reference Irradiance Spectra for Solar Energy Systems Testing." *Solar Energy* 73: 443–467.

Gueymard, C. A., V. Lara-Fanego, M. Sengupta, and A. Habte. 2020. *Surface Albedo Spatial Variability: Local Measurements vs. Gridded Data* (NREL/TP-5D00-76686). Golden, CO: National Renewable Energy Laboratory.

Gueymard. C. A. 2019a. "The SMARTS Spectral Irradiance Model After 25 Years: New Developments and Validation of Reference Spectra." *Solar Energy* 187: 2,333–53.

Gueymard. C. A. 2019b. "Clear-Sky Radiation Models and Aerosol Effects." In *Solar Resources Mapping*, edited by J. Polo et al., 137–82. Springer.

Gwamuri, J., N. Heidari, T. Townsend, and J. Pearce. 2015. "Impact of Snow and Ground Interference on Photovoltaic Electric System Performance." *IEEE Journal of Photovoltaics* 5: 1–6. https://doi.org/10.1109/JPHOTOV.2015.2466448.

Habte, A., M. Sengupta, C.A. Gueymard, R. Narasappa, O. Rosseler, and D. M. Burns. 2019. "Estimating Ultraviolet Radiation from Global Horizontal Irradiance." *IEEE Journal of Photovoltaics* 9 (1): 139–46.

Hanrieder, N., A. Ghennioui, S. Wilbert, M. Sengupta, and L. Zarzalejo. 2020. "AATTENUATION-The Atmospheric Attenuation Model for CSP Tower Plants: A Look-Up Table for Operational Implementation." *Energies* 13: 5248. DOI: 10.3390/en13205248. ISSN 1996-1073.

Hanrieder, N., M. Sengupta, Y. Xie, S. Wilbert, and R. Pitz-Paal. 2016. "Modeling Beam Attenuation in Solar Tower Plants Using Common DNI Measurements." *Solar Energy* 129: 244–55. https://doi.org/10.1016/j.solener.2016.01.051.

Hanrieder, N., S. Wilbert, D. Mancera-Guevara, R. Buck, S. Giuliano, and R. Pitz-Paal. 2017. "Atmospheric Extinction in Solar Tower Plants – A Review." *Solar Energy* 152: 193–207. http://doi.org/10.1016/j.solener.2017.01.013.

Hanrieder, N., S. Wilbert, R. Pitz-Paal, C. Emde, J. Gasteiger, B. Mayer, and J. Polo. 2015. "Atmospheric Extinction in Solar Tower Plants: Absorption and Broadband Correction for MOR Measurements." *Atmospheric Measurement Techniques* 8: 3,467–80. https://doi.org/10.5194/amt-8-3467-2015.

Hansen, C. W., R. Gooding, N. Guay, D. M. Riley, J. Kallickal, D. Ellibee, A. Asgharzadeh, B. Marion, F. Toor, and J. S. Stein. 2017. "A Detailed Model of Rear-Side Irradiance for Bifacial PV Modules." *Proceedings of the IEEE 44th Photovoltaic Specialist Conference (PVSC)*, Washington, D.C.: 1,543–48.

Hemond, H. F. and E. J. Fechner. 2015. "Chapter 4 - The Atmosphere." In *Chemical Fate and Transport in the Environment (Third Edition)*, edited by H. F. Hemond and E. J. Fechner. Boston, 311–454. Academic Press.

Herman, J. R., N. Krotkov, E. Celarier, D. Larko and G. Labow. 1999. "Distribution of UV Radiation at the Earth's Surface from TOMS-Measured UV-Backscattered Radiances." *Journal of Geophysical Research: Atmospheres* 104 (D10): 12,059–76.

Hirsch, T. (Ed.) 2017. *SolarPACES Guideline for Bankable STE Yield Assessment, Version 2017*. http://www.solarpaces.org/csp-research-tasks/task-annexes-iea/task-i-solar-thermal-electric-systems/solarpaces-guideline-for-bankable-ste-yield-assessment/. Spain.

Holben, B. N., T. F. Eck, I. Slutsker, A. Smirnov, A. Sinyuk, J. Schafer, D. Giles, and O. Dubovik. 2006. "AERONET's Version 2.0 Quality Assurance Criteria." *SPIE Proceedings, Vol. 6408*, Remote Sensing of the Atmosphere and Clouds. https://doi.org/10.1117/12.706524.

Hu, Y. X., and K. Stamnes. 1993. "An Accurate Parameterization of the Radiative Properties of Water Clouds Suitable for Use in Climate Models." *Journal of Climate* 6: 728–42. https://doi.org/10.1175/1520-0442(1993)006<0728:AAPOTR>2.0.CO;2.

Hülsen, G. and J. Gröbner. 2007. "Characterization and Calibration of Ultraviolet Broadband Radiometers Measuring Erythemally Weighted Irradiance." *Applied Optics* 46: 5,877–86.

Hülsen, G., J. Gröbner, A. Bais, M. Blumthaler, H. Diémoz, D. Bolsée, A. Diaz, I. Fountoulakis, E. Naranen, and J. Schreder. 2020. "Second Solar Ultraviolet Radiometer Comparison Campaign UVC-II." *Metrologia* 57: 035001. https://doi.org/10.1088/1681-7575/ab74e5.

International Electrotechnical Commission (IEC). 2019. *IEC 60904-3:2019 Photovoltaic devices – Part 3: Measurement Principles for Terrestrial Photovoltaic (PV) Solar Devices with Reference Spectral Irradiance Data*. Geneva, Switzerland.

———. 2007. *IEC 60904-9:2007 Photovoltaic Devices – Part 9: Solar Simulator Performance Requirements*. Geneva, Switzerland.

———. 2017. IEC 61724-1:2017 Photovoltaic system performance – Part 1: Monitoring. Geneva, Switzerland.

Ilse, K. K., B. W. Figgis, V. Naumann, C. Hagendorf, and J. Bagdahn. 2018. "Fundamentals of Soiling Processes on Photovoltaic Modules." *Renewable and Sustainable Energy Reviews* 98: 239–54. https://doi.org/10.1016/j.rser.2018.09.015.

International Organization for Standardization (ISO). 1990. *ISO TR 9901:1990 Solar Energy — Field Pyranometers - Recommended Practice for Use*. Geneva, Switzerland.

———. 2018. *ISO 9060:2018 Solar Energy — Specification and Classification of Instruments for Measuring Hemispherical Solar and Direct Solar Radiation*. Geneva, Switzerland.

Järvelä, M., K. Lappalainen, and S. Valkealahti. 2020. "Characteristics of the Cloud Enhancement Phenomenon and PV Power Plants." *Solar Energy* 196: 137–45.

Jessen, W., S. Wilbert, C. A. Gueymard, J. Polo, Z. Bian, A. Driesse, A. Habte, P. R. Armstrong, F. Vignola, and L. Ramírez. 2018. "Proposal and Evaluation of Subordinate Standard Solar Irradiance Spectra for Applications in Solar Energy Systems." *Solar Energy* 168: 30–43.

Kalapatapu, R., M. Chiesa, P. Armstrong, and S. Wilbert. 2012. "Measurement of DNI Angular Distribution with a Sunshape Profiling Irradiometer." *Proceedings of the SolarPACES Conference*, Marakkesch, Morocco.

Kamphuis, N. R., C. A. Gueymard, M. T. Holtzapple, A. T. Duggleby, and K. Annamalai. 2020. "Perspectives on the Origin, Derivation, Meaning, and Significance of the Isotropic Model." *Solar Energy* 201: 8–12.

Kaufman Y. J., D. Tanré, and O. Boucher. 2002. "A Satellite View of Aerosols in the Climate System." *Nature* 419: 215–23. https://doi.org/10.1038/nature01091.

Kerr, J. B., and V. E. Fioletov. 2008. "Surface Ultraviolet Radiation." *Atmosphere-Ocean* 46 (1): 159–84.

Koepke, P. 2009. "Radiative Models for the Evaluation of the UV Radiation at the Ground." *Radiation Protection Dosimetry* 137: 188–92.

Kosmopoulos, P. G., S. Kazadzis, H. El-Askary, M. Taylor, A. Gkikas, E. Proestakis, C. Kontoes, and M. M. El-Khayat. 2018. "Earth-Observation-Based Estimation and Forecasting of Particulate Matter Impact on Solar Energy in Egypt." *Remote Sensing* 10: 1870. https://doi.org/10.3390/rs10121870.

Krotkov, N. A., P. K. Bhartia, J. R. Herman, V. Fioletov, and J. Kerr. 1998. "Satellite Estimation of Spectral Surface UV Irradiance in the Presence of Tropospheric Aerosols: 1. Cloud-Free Case." *Journal of Geophysical Research: Atmospheres* 103(D8): 8,779–93. https://doi.org/10.1029/98JD00233.

Krzyścin, J. W. 1996. "UV Controlling Factors and Trends Derived from the Ground-Based Measurements Taken at Belsk, Poland, 1976–1994." *Journal of Geophysical Research: Atmospheres* 101(D11): 16,797–805. https://doi.org/10.1029/96JD00217.

Levelt, P. F., E. Hilsenrath, G. W. Leppelmeier, G. H. J. van den Oord, P. K. Bhartia, J. Tamminen, J. F. de Haan, and J. P. Veefkind. 2006. "Science Objectives of the Ozone Monitoring Instrument." *IEEE Transactions on Geoscience and Remote Sensing* 44: 1,199–1,208. https://doi.org/10.1109/TGRS.2006.872336.

Lewis, P., and M. J. Barnsley. 1994. "Influence of the Sky Radiance Distribution on Various Formulations of the Earth Surface Albedo." *Proceedings of the 6th International Symposium on Physical Measurements and Signatures in Remote Sensing, ISPRS*, Val d'Isere, France: CNES, 707−15.

Lindsay, N., Libois, Q., Badosa, J., Migan-Dubois, A., & Bourdin, V. 2020. "Errors in PV Power Modelling Due to the Lack of Spectral and Angular Details of Solar Irradiance Inputs." *Solar Energy* 197(February): 266–278. https://doi.org/10.1016/j.solener.2019.12.042.

Lorenz, E., D. Heinemann, D., and C. Kurz. 2012. "Local and Regional Photovoltaic Power Prediction for Large-Scale Grid Integration: Assessment of a New Algorithm for Snow Detection." *Progress in Photovoltaics: Research Applications* 20: 760–69. https://doi.org/10.1002/pip.1224.

Lucht, W., C. B. Schaaf, and A. H. Strahler. 2000. "An Algorithm for the Retrieval of Albedo from Space Using Semiempirical BRDF Models." *IEEE Transactions on Geoscience and Remote Sensing* 38 (2): 977–98.

Madronich, S., and S. Flocke. 1997. *Theoretical Estimation of Biologically Effective UV Radiation at the Earth's Surface*. Springer.

Maghami, M. R., H. Hizam, C. Gomes, M. A. Radzi, M. I. Rezadad, and S. Hajighorbani. 2016. "Power Loss Due to Soiling on Solar Panel: A Review." *Renewable and Sustainable Energy Reviews* 59: 1,307–16. https://doi.org/10.1016/j.rser.2016.01.044.

Mambrini, T., A. M. Dubois, C. Longeaud, J. Badosa, M. Haeffelin, L. Prieur, and V. Radivoniuk. 2015. "Photovoltaic Yield: Correction Method for the Mismatch Between the Solar Spectrum and the Reference ASTMG AM1.5G Spectrum." *EPJ Photovoltaics* 6: 60701.

Marion, B., R. Schaefer, H. Caine, and G. Sanchez. 2013. "Measured and Modeled Photovoltaic System Energy Losses from Snow for Colorado and Wisconsin Locations." *Solar Energy* 97: 112–21.

Mayer, B., and A. Kylling. 2005. "Technical Note: The libRadtran Software Package for Radiative Transfer Calculations—Description and Examples of Use." *Atmospheric Chemistry and Physics* 5 (7): 1,855–77.

McArthur, L. J. B., V. E. Fioletov, J. B. Kerr, C. T. McElroy, and D. I. Wardle. 1999. "Derivation of UV-A Irradiance from Pyranometer Measurements." *Journal of Geophysical Research: Atmospheres* 104 (D23): 30,139–51. https://doi.org/10.1029/1999JD900808.

McIntosh, D. H. 1978. "Atmospheric Science: An Introductory Survey." By J. M. Wallace and P. V. Hobbs. Academic Press (New York), 1977." *Quarterly Journal of the Royal Meteorological Society*, 104: 534. https://doi.org/10.1002/qj.49710444024.

Meng, Q., Y. Wang, and L. Zhan. 2011. "Irradiance Characteristics and Optimization Design of a Large-Scale Solar Simulator." *Solar Energy* 85: 1,758–67.

Mesinger, F., G. Dimego, E. Kalnay, K. Mitchell, P. Shafran, W. Ebisuzaki, Dušan Jović, J. S. Woollen, E. Rogers, E. Berbery, M. Ek, Y. Fan, Robert W. Grumbine, W. Higgins, Hong Li, Y. Lin, G. Manikin, D. Parrish and Wei Shi. 2006. "North American Regional Reanalysis." *Bulletin of the American Meteorological Society* 87: 343–360.

Micheli, L., and M. Muller, 2017. "An Investigation of the Key Parameters for Predicting PV Soiling Losses." *Progress in Photovoltaics: Research and Applications* 25: 291–307. https://doi.org/10.1002/pip.2860.

Micheli, L., M. G. Deceglie, and M. Muller, 2019. "Mapping Photovoltaic Soiling Using Spatial Interpolation Techniques." *I*EEE Journal of Photovoltaics 9: 272–77. https://doi.org/10.1109/JPHOTOV.2018.2872548.

Minnis, P., B. Lin, L. Nguyen, and W. L. Smith, S. Sun-Mack, Y. Chen, M. M. Khaiyer, Y, Yi, J. K. Ayers, R. R. Brown, S.C. Gibson, M.L. Nordeen, R. Palikonda, D. A. Spangenberg, Q. Z. Trepte, P. W. Heck, X. Dong and B. Xi. 2011. "CERES Edition-2 Cloud Property Retrievals Using TRMM VIRS and Terra and Aqua MODIS Data—Part I: Algorithms." *IEEE Transactions on Geoscience and Remote Sensing* 49: 4,374–4,400. https://doi.org/10.1109/TGRS.2011.2144601.

Mishra, A. K. 2019. "Variability of Integrated Precipitable Water Over India in a Warming Climate." *Meteorological Applications* 27: e1869. https://doi.org/10.1002/met.1869.

Mishra, B. R., Hanrieder, N., Modi, A., and S. B. Kedare. 2020. "Comparison of Three Models to Estimate the Slant Path Atmospheric Attenuation in Central Receiver Solar Thermal Plants under Indian Climatic Conditions." *Solar Energy* 211: 1,042–52. https://doi.org/10.1016/j.solener.2020.10.049.

Monokroussos, C., Q. Gao, X. Y. Zhang, E. Lee, Y. Wang, C. Zou, L. Rimmelspacher, J. B. Castro, M. Schweiger, and W. Herrmann. 2020. "Rear-Side Spectral Irradiance at 1 Sun and Application to Bifacial Module Power Rating." *Progress in Photovoltaics: Research and Applications* 2020: 1–12. https://doi.org/10.1002/pip.3268.

Mullejans, H., A. Ioannides, R. Kenny, W. Zaaiman, H. A. Ossenbrink, and E. D. Dunlop. 2005. "Spectral Mismatch in Calibration of Photovoltaic Reference Devices by Global Sunlight Method." *Measurement Science and Technology* 16: 1,250–54.

Myers, D. R., and C. A. Gueymard. 2004. "Description and Availability of the SMARTS Spectral Model for Photovoltaic Applications." *Proceedings Vol. 5520, Organic Photovoltaics V, SPIE*. https://doi.org/10.1117/12.555943.

Myers, Daryl R. 2012. "Direct Beam and Hemispherical Terrestrial Solar Spectral Distributions Derived from Broadband Hourly Solar Radiation Data." *Solar Energy* 86 (9): 2,771–82.

National Aeronautics and Space Administration (NASA). 2006. "AERONET Inversion Products." https://aeronet.gsfc.nasa.gov/new_web/Documents/Inversion_products_V2.pdf.

National Renewable Energy Laboratory (NREL). 2020. "Photovoltaic Soiling Module Map." Accessed December 5, 2020. https://www.nrel.gov/pv/soiling.html.

Noring, J. E., D. F. Grether, and A. J. Hunt. 1991. *Circumsolar Radiation Data: The Lawrence Berkeley Laboratory Reduced Data Base* (NREL/TP-262-4429). Golden, CO: National Renewable Energy Laboratory. https://doi.org/10.2172/6125786.

Patel, M. T., M. R. Khan, X. Sun, and M. A. Alam. 2019. "A Worldwide Cost-Based Design and Optimization of Tilted Bifacial Solar Farms." *Applied Energy* 247: 467–79.

Peeters, P., J.-F. Müller, P. C. Simon, E. Celarier, and J. Herman. 1998. "Estimation of UV Flux at the Earth's Surface Using GOME Data." *Earth Observation Quarterly* 58: 39–40.

Perez, R., T. Cebecauer, and M. Suri. 2013. "Semi-Empirical Satellite Models." In *Solar Energy Forecasting and Resource Assessment*, edited by J. Kleissl. Elsevier.

Phillips, D. 2002. “A Closer Look at a Rare Situation. 1998 Ice Storm.” Meteorological Service of Canada.

Picotti, G., P. Borghesani, M. E. Cholette, and G. Manzolini. 2018. “Soiling of Solar Collectors—Modelling Approaches for Airborne Dust and Its Interactions with Surfaces.” *Renewable and Sustainable Energy Reviews* 81: 2,343–57.

Polo J., J. Ballestrín, and E. Carra. 2016. “Sensitivity Study for Modelling Atmospheric Attenuation of Solar Radiation with Radiative Transfer Models and the Impact in Solar Tower Plant Production.” *Solar Energy* 134: 219–27. https://doi.org/10.1016/j.solener.2016.04.050.

Polo, J., J. Ballestrín, J. Alonso-Montesinos, G. López-Rodriguez, J. Barbero, E. Carra, J. Fernández-Reche, J. L. Bosch, and F.J. Batlles. 2017. “Analysis of Solar Tower Plant Performance Influenced by Atmospheric Attenuation at Different Temporal Resolutions Related to Aerosol Optical Depth. *Solar Energy* 157: 803–10. https://doi.org/10.1016/j.solener.2017.09.003.

Räisänen, P., and A. V. Lindfors. 2019. “On the Computation of Apparent Direct Solar Radiation.” *Journal of Atmospheric Sciences* 76: 2,761–80.

Ramon, J., Lledó, L., Torralba, V., Soret, A., and Doblas-Reyes, F.J. 2019. “What Global Reanalysis Best Represents Near-Surface Winds?” *Quarterly Journal of the Royal Meteorological Society* 145: 3,236–51. https://doi.org/10.1002/qj.3616.

Reinhardt, B., R. Buras, L. Bugliaro, S. Wilbert, and B. Mayer. 2013. “Determination of Circumsolar Radiation from Meteosat Second Generation.” *Atmospheric Measurement Techniques* 6 (3): 5,835–79. https://doi.org/10.5194/amtd-6-5835-2013.

Reise, C., B. Müller, A. Driesse, G. Razongles, and M. Richter. 2018. *Uncertainties in PV System Yield Predictions and Assessments* (Rep. IEA-PVPS T13-12:2018).

Ricchiazzi, P., and C. Gautier. 1998. “Investigation of the Effect of Surface Heterogeneity and Topography on the Radiation Environment of Palmer Station, Antarctica, with a Hybrid 3D Radiative Rransfer Model.” *Journal of Geophysical Research: Atmospheres* 103 (D6): 6,161–76. https://doi.org/10.1029/97JD03629.

Riley, D., L. Burnham, B. Walker, and J. Pearce. 2019. “Differences in Snow Shedding in Photovoltaic Systems with Framed and Frameless Modules.” *Proceedings of 46th IEEE Photovoltaic Specialists Conference (PVSC)*. Chicago, Illinois. https://doi.org/10.1109/PVSC40753.2019.8981389.

Roman M. O., C. B. Schaaf, P. Lewis, F. Gao, G. P. Anderson, J. L. Privette, A. H. Strahler, C. E. Woodcock, and M. Barnsley. 2010. “Assessing the Coupling Between Surface Albedo Derived from MODIS and the Fraction of Diffuse Skylight Over Spatially-Characterized Landscapes.” *Remote Sensing of the Environment* 114 (4): 738–60.

Ruiz-Arias J. A., and C. A. Gueymard. 2018. “Worldwide Inter-Comparison of Clear-Sky Solar Radiation Models: Consensus-Based Review of Direct and Global Irradiance Components Simulated at the Earth Surface.” *Solar Energy* 168: 10–29.

Russell, T. C. R., R. Saive, A. Augusto, S. G. Bowden, and H. A. Atwater. 2017. “The Influence of Spectral Albedo on Bifacial Solar Cells: A Theoretical and Experimental Study.” *IEEE Journal of Photovoltaics* 7 (6): 1,611–18.

Ryberg, D., and J. Freeman. 2017. *Integration, Validation, and Application of a PV Snow Coverage Model in SAM* (NREL/TP-6A20-68705). Golden, CO: National Renewable Energy Laboratory.

Sarver, T., A. Al-Qaraghuli, and L. L. Kazmerski. 2013. “A Comprehensive Review of the Impact of Dust on the Use of Solar Energy: History, Investigations, Results, Literature, and

Mitigation Approaches." *Renewable and Sustainable Energy Reviews* 22: 698–733. http://dx.doi.org/10.1016/j.rser.2012.12.065.

Sarwar, J., G. Georgakis, R. LaChance, and N. Ozalp. 2014. "Description and Characterization of an Adjustable Flux Solar Simulator for Solar Thermal, Thermochemical, and Photovoltaic Applications." *Solar Energy* 100: 179–194.

Schrott, S., T. Schmidt, T. Hornung, P. Nitz, G. S. Kinsey, D. Riley, S. Kurtz, K. Araki, and M. Baudrit. 2014. "Scientific System for High-Resolution Measurement of the Circumsolar Radiation." *AIP Conference Proceedings* 1616: 88. https://doi.org/10.1063/1.4897035.

Schwander, H., P. Koepke, A. Kaifel, and G. Seckmeyer. 2002. "Modification of Spectral UV Irradiance by Clouds." *Journal of Geophysical Research: Atmospheres* 107 (D16): 4296. doi:10.1029/2001JD001297.

Sengupta, M., and M.J. Wagner. 2012. "Atmospheric Attenuation in Central Receiver Systems from DNI Measurements." *Proceedings of the World Renewable Energy Forum*, Denver, Colorado (NREL/CP-5500-54760).

Smirnov, A., B. N. Holben, T. F. Eck, O. Dubovik, and I. Slutsker. 2000. "Cloud-Screening and Quality Control Algorithms for the AERONET Database." *Remote Sensing of Environment* 73 (3): 337–49. https://doi.org/10.1016/S0034-4257(00)00109-7.

Stamnes, K., S.-C. Tsay, W. J. Wiscombe, and K. Jayaweera.1988. "An Improved, Numerically Stable Computer Code for Discrete Ordinate-Method Radiative Transfer in Scattering and Emitting Layered Media." National Aeronautics and Space Administration.

Stridh, B. 2012. "Evaluation of Economical Benefit of Cleaning of Soiling and Snow in PV Plants at Three European Locations." *Proc. 38th IEEE Photovoltaic Specialists Conference*. https://doi.org/10.1109/PVSC.2012.6317869.

Sugiura, T., T. Yamadaa, H. Nakamuraa, M. Umeyaa, K. Sakutab, and K. Kurokawa. 2003. "Measurements, Analyses and Evaluation of Residential PV Systems by Japanese Monitoring Program." *Solar Energy Materials and Solar Cells* 73 (3): 767–79.

Sun, X., J. M. Bright, C. A. Gueymard, B. Acord, P. Wang, and N. A. Engerer. 2019. "Worldwide Performance Assessment of 75 Global Clear-Sky Irradiance Models Using Principal Component Analysis." *Renewable and Sustainable Energy Reviews* 111: 550–70.

Sun, X., M. R. Khan, C. Deline, and M. A. Alam. 2018. "Optimization and Performance of Bifacial Solar Modules: A Global Perspective." *Applied Energy* 212: 1,601–10.

Sun, Z., J. Li, G. Shi, J. Manners, and J. Li. 2020. "Fast Scheme for Determination of Direct Normal Irradiance. Part II: Parameterization of Circumsolar Radiation." *Solar Energy* 199: 256–67.

Tanskanen, A., N. A. Krotkov, J. R. Herman, and A. Arola. 2006. "Surface Utraviolet Irradiance from OMI." *IEEE Transactions on Geoscience and Remote Sensing* 44: 1,267–71. https://doi.org/10.1109/TGRS.2005.862203.

Taylor, N. (Ed.). 2010. *Guidelines for PV Power Measurement in Industry* (EUR 24359 EN). Ispra, Italy: European Commission Joint Research Centre.

Tetens, O. 1930. Über einige Meteorologische Begriffe. *Zeitschrift für Geophysik* 6: 207–309.

Townsend, T., and L. Powers. 2011. "Photovoltaics and Snow: An Update from Two Winters of Measurements in the SIERRA." *Proceedings of the 37th IEEE Photovoltaic Specialists Conference*. https://doi.org/10.1109/PVSC.2011.6186627.

Wang, D., S. L. Liang, T. He, Y. Yu, C. Schaaf, and Z. Wang. 2015. "Estimating Daily Mean Land Surface Albedo from MODIS Data." *Journal of Geophysical Research: Atmospheres* 120: 4,825–41.

Webb, A., J. Gröbner, and M. Blumthaler. 2006. *A Practical Guide to Operating Broadband Instruments Measuring Erythemally Weighted Irradiance* (Rep. COST-726, EUR-OP).

Wei, J., Z. Li, Y. Peng, and L. Sun. 2019. "MODIS Collection 6.1 Aerosol Optical Depth Products Over Land and Ocean: Validation and Comparison." *Atmospheric Environment* 201: 428–40.

Wilbert, S. 2014. *Determination of Circumsolar Radiation and its Effect on Concentrating Solar Power*. Doktorarbeit, Maschinenwesen, RWTH Aachen. https://publications.rwth-aachen.de/record/444996.

Wilbert, S., B. Reinhardt, J. DeVore, M. Röger, R. Pitz-Paal, C. Gueymard, and R. Buras. 2013. "Measurement of Solar Radiance Profiles with the Sun and Aureole Measurement System." *Journal of Solar Energy Engineering* 135 (4): 041002-041002. https://doi.org/10.1115/1.4024244.

Wilbert, S., M. Röger, J. Csambor, M. Breitbach, F. Klinger, B. Nouri, N. Hanrieder, F. Wolfertstetter, D. Schüler, S. Shaswattam, N. Goswami, S. Kumar, A. Ghennioui, R. Affolter, N. Geuder, and B. Kraas. 2018. "Sunshape Measurements with Conventional Rotating Shadowband Irradiometers." *AIP Conference Proceedings* 2033 (1): 190016. https://doi.org/10.1063/1.5067201.

Wilbert, S., R. Pitz-Paal, and E. Guillot. 2013. *Database with Frequencies of Circumsolar ratio (CSR) Occurrence at Different Sites and Correlations of CSR with DNI and DHI Data* (SFERA EU FP7 project report). DLR, CNRS.

Wilbert, S., R. Pitz-Paal, and J. Jaus. 2013. "Comparison of Measurement Techniques for the Determination of Circumsolar Irradiance." *AIP Conference Proceedings* 1556 (1): 162–67. http://dx.doi.org/10.1063/1.4822222.

Wolfertstetter, F., K. Pottler, N. Geuder, R. Affolter, A. A. Merrouni, A. Mezrhab, and R. Pitz-Paal. 2014. "Monitoring of Mirror and Sensor Soiling with TraCS for Improved Quality of Ground based Irradiance Measurements." *Energy Procedia* 49:2422-2432. http://dx.doi.org/10.1016/j.egypro.2014.03.257.

Wolfertstetter, F., S. Wilbert, F. Terhag, N. Hanrieder, A. Fernandez-García, C. Sansom, P. King, L. Zarzalejo, and A. Ghennioui. 2019. "Modelling the Soiling Rate: Dependencies on Meteorological Parameters." *AIP Conference Proceedings* 2126 (1): 190018.

World Health Organization (WHO). 2020. "Ultraviolet Radiation (UV)." Geneva, Switzerland. https://www.who.int/uv/uv_and_health/en/.

World Meteorological Organization (WMO). 2018. *Guide to Meteorological Instruments and Methods of Observation. WMO-No. 8, 2018 Update*. Geneva, Switzerland.

Xie, Y., and M. Sengupta. 2018. "A Fast All-sky Radiation Model for Solar Applications with Narrowband Irradiances on Tilted surfaces (FARMS-NIT): Part I. The Clear-Sky Model." *Solar Energy* 174: 691–702.

Xie, Y., M. Sengupta, and C. Wan. 2019. "A Fast All-sky Radiation Model for Solar Applications with Narrowband Irradiances on Tilted Surfaces (FARMS-NIT): Part II. The Cloudy-Sky Model." *Solar Energy* 188: 799–812.

Xie, Y., M. Sengupta, and J. Dudhia. 2016. "A Fast All-sky Radiation Model for Solar applications (FARMS): Algorithm and Performance Evaluation." *Solar Energy* 135: 435–45.

Xie, Y., M. Sengupta, Y. Liu, C. Long, Q. Min, W. Liu, and A. Habte. 2020. "A Physics-Based DNI Model Assessing All-Sky Circumsolar Radiation." *iScience* 23: 100893. https://doi.org/10.1016/j.isci.2020.100893.

Ziar, H., F. F. Sönmez, O. Isabella, and M. Zeman. 2019. "A Comprehensive Albedo Model for Solar Energy Applications: Geometric Spectral Albedo." *Applied Energy* 255: 113867. https://doi.org/10.1016/j.apenergy.2019.113867.

6 SOLAR RESOURCE DATA

Manajit Sengupta,[1] Aron Habte,[1] and Christian Gueymard[2]
[1] *National Renewable Energy Laboratory*
[2] *Solar Consulting Services*

6.1 Introduction

Understanding the long-term spatial and temporal variability of available solar resources is fundamental to any assessment of solar energy potential. Information derived from historical solar resource data can be used to make energy policy decisions, to select optimum energy conversion technologies, to design systems for specific locations, and to operate and maintain installed solar energy conversion systems. Historical solar resource data can be the result of in situ measurement programs, satellite remote-sensing methods, or meteorological model outputs. As described in the previous chapters, each type of data has different information content and applicability.

This chapter summarizes historical solar resource data available around the world. It provides an inventory of representative sources of solar radiation data and a summary of important data characteristics associated with each data source (e.g., period of record, temporal and spatial resolutions, available data elements, and estimated uncertainties). Some data sets discussed in this chapter are commercial sources and might not be freely available. Additionally, some historical data sets that were listed in previous editions are not retained in this version because direct links to download them are not available. We recommend that users refer to previous versions of this handbook if they are interested in references to historical archives with no known direct source of download.

The authors and other participants in the International Energy Agency's Photovoltaic Power Systems Programme Task 16 have made every effort to make data products that are as useful, robust, and representative as possible; however, the responsibility for applying the data correctly resides with the user. A thorough understanding of the data sources, how they are created, and their limitations remain vital to proper application of the resource data to analyses and subsequent decision making. Discussions and examples of the use of several of these data sets for solar energy applications are presented here. Users are encouraged to read the pertinent sections of this chapter before applying solar resource and meteorological data.

Measured solar irradiance data can provide detailed temporal information for a specific site. Because solar radiation measurement stations are challenging to operate and because the data collected are not used for routine weather forecasts, their density is low, and they have limited data collection records. Some examples in the United States are the National Oceanic and Atmospheric Administration's (NOAA's) Surface Radiation Budget Network (SURFRAD) and SOLRAD networks, the University of Oregon network, stations from the U.S. Department of Energy's (DOE) Atmospheric Radiation Measurement (ARM) program, and the National Renewable Energy Laboratory (NREL). The total number of ground stations measuring solar irradiance in some form and with a wide range of data quality is now more than 3,000 in the United States alone. These stations are operated by several interests producing data for varied applications (including agriculture). Links to most of those stations are not presented here because there is limited confidence in the data quality. For other parts of the world, users are requested to refer to the Baseline Surface Radiation Network (BSRN) network (http://bsrn.awi.de/) for high-quality data (e.g., Gueymard and Myers 2008,

2009). Table 6.1 provides more details on sources of measured or partly measured databases. (The meteorological services of various countries might operate many radiometric stations, so Table 6.1 should not be considered exhaustive; furthermore, some of these national services do not release their data in the public domain.) An increasing number of photovoltaic (PV) and concentrating solar power installations now collect high-quality solar radiation data, but those data sets are not publicly available, so they are not listed in this chapter.

Satellite-based observations and mesoscale meteorological models address the needs for understanding the spatial variability of solar radiation resources throughout a range of distances. Present state-of-the-art models provide estimates for global horizontal irradiance (GHI) and direct normal irradiance (DNI) at spatial resolutions of 10 km or less for the United States and other parts of the world (see, e.g., CM SAF, the National Solar Radiation Database (NSRDB), SolarAnywhere, Meteonorm, PVGIS, and Solargis in Table 6.1). Numerical weather models can be used to produce long-term meteorological information when they are used by reanalysis models. These reanalysis models have spatially coarser resolutions and have higher uncertainty in estimating solar radiation than satellite models or ground measurements. Nevertheless, reanalysis data sets such as ERA5, which is the European Center for Medium-Range Weather Forecast's (ECMWF's) fifth-generation atmospheric reanalysis of the global climate,[35] or the National Aeronautics and Space Administration's (NASA's) Modern Era Retrospective analysis for Research and Applications, Version 2 (MERRA-2)[36] are useful sources of data because they are available globally and for periods longer than 30 years. The rapidly growing needs for more accurate solar resource information throughout shorter temporal and smaller spatial scales require the user to fully appreciate the characteristics of all available data, especially those from historical sources.

6.2 Solar Resource Data Characteristics

Characterizing the available solar resources for solar energy applications is important for all aspects of realizing the full potential of this utility-scale energy source. Energy policy decisions, engineering designs, and system deployment considerations require an accurate understanding of the relevant historical solar resource data, the ability to assess the accuracy of current solar measurement and modeling techniques, and forecasts of the levels of solar irradiance for various temporal and spatial scales.

Measured solar irradiance data can provide information about the temporal variability at a specific site. Practical radiometer designs were developed in the early 1900s to determine the sun's energy output based on high-altitude measurements of DNI made with pyrheliometers (Hulstrom 1989). To address the needs of agriculture for monitoring such quantities as evapotranspiration, in the 1950s the U.S. Weather Bureau (now National Weather Service) deployed a national radiometer network to collect GHI. Since then, both radiometer design and data acquisition system performance have advanced considerably.

The earliest records of solar flux measurements were based on thermopile-type pyranometer signals recorded and stored on analog strip charts to determine daily amounts of solar flux on a horizontal surface. Today, 1-minute (or shorter) digital recordings are available from fast-response silicon photodiodes and improved thermopile-type pyranometers and

[35] See http://climate.copernicus.eu/products/climate-reanalysis.
[36] See https://gmao.gsfc.nasa.gov/reanalysis/MERRA-2/.

pyrheliometers that are deployed in regional measurement networks to provide solar energy resource data for a variety of applications.

Historically, there have been four radiometer calibration reference scales: the Ångström scale (ÅS; created in 1905), the Smithsonian scale (SS; created in 1913), the international pyrheliometric scale (IPS; created in 1956), and the World Radiometric Reference (WRR; 1979). The relative differences among these scales can introduce a data bias on the order of 2%. The user should be aware of this potential bias in data measured before 1979. A correction is necessary to harmonize older data sets to the current scale, according to:

- WRR = 1.026 (ÅS 1905)
- WRR = 0.977 (SS 1913)
- WRR = 1.022 (IPS 1956).

Modeled solar resource data derived from available surface meteorological observations and satellite measurements provide estimates of solar resource potential for locations lacking actual measurements. These modeling methods address the needs for improved spatial resolution of the resource data. In the United States, the first national effort to model solar resources in the 1970s advanced the understanding of solar radiation distributions based on the then-available historical measurements at 26 locations to an additional 222 meteorological observing stations with detailed records of hourly cloud amounts and other relevant data (see the entry for SOLMET/ERSATZ in Table 6.1). Today, satellite-based observations of clouds are used to model subhourly surface solar fluxes with a 4-km spatial resolution over North America and part of South America (Sengupta et al. 2018). Similar efforts are conducted over other parts of the world.

6.3 Long-Term and Typical Meteorological Data Sets

Understanding the time frame, or period of record, associated with solar resource data and related meteorological information is important for conducting useful analyses. These weather-driven variables have fluctuations that can range from seconds to years and longer. Long-term data can be representative of the climate if the period of record is at least 30 years. By convention, the meteorological community has deemed that, according to the 1933 International Meteorological Conference in Warsaw, a 30-year interval is sufficient to reflect longer term climatic trends and filter the short-term interannual fluctuations and anomalies. Climate “normals” are recomputed each decade to address temperature, pressure, precipitation, and other surface meteorological variables. Note that the term *normal* is not equivalent to “average” and has a specific meaning in the meteorological and climatological community. Namely, *normal* refers to the 30-year average of an observed parameter that is updated every 10 years (Arguez and Vose 2011); thus, the averaging period shifts every 10 years.

Often, plant project developers require “typical” meteorological information related to a potential plant site for prefeasibility studies. A *typical meteorological year* (TMY) data set provides designers and other users with a small-size annual data set that holds 8,760 hourly meteorological values that typify conditions at a specific location throughout a longer period, such as the 30-year climatic normal. Different types of TMYs exist. Twelve typical meteorological months (TMMs) selected based on their similarity of individual cumulative frequency distributions for selected data elements comprise the TMY data set. The longer-term distributions are determined for that month using data from the full period of record. The TMMs are then concatenated, essentially without modification, to form a single year with a serially complete data record. The resulting TMY data set contains measured and/or modeled time series of solar radiation and surface meteorological data, though some hourly

records might contain filled or interpolated data for periods when original observations are missing from the data archive. Further, there are many methods used to develop TMMs, as reviewed in Nielsen et al. (2017) and García et al. (2020). Novel TMY approaches include a stochastic method (Remund et al. 2012), the generation of TMYs at high temporal resolution (Ernst and Gooday 2019), the preparation of TMYs specifically tailored for PV applications (Sengupta and Habte 2019), or even customized TMYs (Sengupta, Habte, and Freeman 2019).

TMY data sets are widely used by building designers and others for rough modeling of renewable energy conversion systems. Although the TMY data are not designed to provide meteorological extremes, they have natural diurnal and seasonal variations and represent a year of typical climatic conditions for a location. A TMY data set should not be used to predict weather or solar resources for a particular period of time, nor is it an appropriate basis for evaluating real-time energy production or detailed power plant design. Rather, a TMY data set represents conditions judged to be typical throughout a long period, such as 30 years. Because it represents typical rather than extreme conditions, it is not suited for designing systems and their components to meet the worst-case weather conditions that could occur at a location. Additionally, a TMY is not well suited to assess any probability of energy yield exceedances because the natural variability is most likely not fully described with its correct statistical distribution.

6.3.1 Key Considerations

Applying solar and meteorological data from different sources requires attention to these key considerations:

- **Period of record.** Influenced by many factors, solar resource data vary yearly, seasonally, monthly, weekly, daily, and on timescales down to 1 second or so. In contrast, the 30-year averaging period involved in the production of climate normals is updated (shifted) every 10 years. For instance, the current climate normals span the period from 1981–2010, but soon the 1991–2020 normals will become available from meteorological services around the world. The normal for one period will not likely be the same as a normal for previous or successive periods. Another popular approach is to determine a TMY data set from a statistical analysis of multiyear data and eventually derive a single year of data that is deemed representative of a longer-term record. Comparative analyses must account for any natural differences that result from the periods when the data were acquired.
- **Temporal resolution.** Solar resource data can range from annually averaged daily irradiation, typically used for mapping resource distributions, to 1-second samples of irradiance for operational time-series analyses. Other considerations depend on the data type.
- **Units.** The unit of irradiance is W/m^2. The most common unit of irradiation, or integrated power, is kWh/m^2. The actual Système International unit for irradiation, J/m^2, is rarely used anymore. The conversion is 1 kWh/m^2 = 3.6 MJ/m^2. Note that daily average irradiation data produced by or for climatologists are most often incorrectly reported with a unit of W/m^2. Here, a daily irradiation of 1 W/m^2 means an average irradiance of 1 W/m^2 over 24 hours, or 24 Wh/m^2. Unfortunately, this can create confusion. A daily irradiation should be expressed in kWh/m^2, not kWh/m^2/day, even though this is a frequent mistake.
- **Spatial coverage.** The area represented by the data can range from a single station, to a sample geographic region, to a global (world) perspective.

- **Spatial resolution.** Ground-based measurements are site specific. Current satellite remote-sensing estimates are representative of areas typically spanning 3 km by 3 km to 10 km by 10 km. The “pixel” size of reanalysis data is significantly larger, at least 30 km by 30 km with current products.
- **Data elements and sources of the data.** The usefulness of solar resource data might depend on the available data elements (e.g., DNI or GHI) and whether the data were measured, modeled, or produced from a combination of measurement and models.
- **Time stamp.** There are three possible time references: Local Apparent Time (LAT, also known as Apparent Solar Time), Local Standard Time (LST), and Universal Time (UT). The former is rarely used anymore. Global databases tend to use UT, but there is no general rule. Moreover, for comparative purposes, it is also important to consider what each time stamp specifically refers to. Depending on database, it can be the start, the mid-point, or the end of the time period (for subdaily data). In climatology, the latter is standard. For more details, see Polo et al. (2019).
- **Availability.** Data are distributed in the public domain, for purchase, or by license.

Table 6-1. Inventory of Solar Resource Data Sources, Presented in Alphabetical Order

Database	Period of Record	Temporal Resolution	Spatial Coverage	Spatial Resolution	Data Elements and Sources	Availability
U.S. Department of Energy (DOE) Atmospheric Radiation Measurement (ARM) Program	1997–present	20-second instantaneous samples and 1-minute averages of 2-second scans	Southern Great Plains, North Slope of Alaska, and tropical western Pacific	32 (active and inactive) 11 stations inactive (7 at Southern Great Plains, 1 at North Slope of Alaska, and 3 at tropical western Pacific)	GHI, DNI, DHI, DIR, UIR, and upwelling (reflected) shortwave irradiance. Measurements from the Eppley Laboratory, Inc., Model PSP (GHI, DHI, and upwelling shortwave irradiance), Model 8-48 (DHI after 2000), Model NIP (DNI), and Model PIR (DIR and UIR) radiometers	DOE, ARM Climate Research Facility: http://www.arm.gov Data sets are labeled SIRS, SKYRAD, and GNDRAD. SIRS data form the Billings and E13 locations are also submitted to the WRMC-BSRN archives: http://www.bsrn.awi.de/.
Baseline Surface Radiation Network (BSRN)	1992–present	1 minute (3 minute for SURFRAD stations before 2009)	Global	76 (active and inactive) radiometric stations, 17 of 76 are either decommissioned or candidates to become BSRN stations (as of 4/17/2020)	The number and type of measurements vary by station. Basic radiation measurements include GHI, DNI, DHI, downwelling infrared irradiance, upwelling infrared irradiance, and upwelling (reflected) shortwave irradiance. Measurements are from radiometers of various manufacturers. Synoptic meteorological observations, upper air measurements, and numerous expanded and supporting measurements are available.	The World Radiation Monitoring Center (WRMC) provides web-based and FTP data access: http://www.bsrn.awi.de/en/home/
Australian Bureau of Meteorology (BOM) One-Minute Solar Data	Varies	1 minute	Australia	21 radiometric stations	GHI, DNI, DHI, DIR, longwave, sunshine	http://www.bom.gov.au/climate/data/oneminsolar/stations.shtml

Database	Period of Record	Temporal Resolution	Spatial Coverage	Spatial Resolution	Data Elements and Sources	Availability
Copernicus Atmospheric Monitoring Service (CAMS) McClear	2004–present	1 minute, 15 minute, 1 hour, 1 day, 1 month	Global	Various input data sources with different spatial resolutions are interpolated to the location of interest.	Clear-sky global, direct, direct normal, diffuse irradiances; inputs describe atmospheric conditions (aerosols, water vapor, trace gases, surface reflectivity parameters).	http://www.soda-pro.com/web-services/radiation/cams-mcclear
CAMS Radiation Service	2004–present	1 minute, 15 minute, 1 hour, 1 day, 1 month	Europe/Africa/Middle East/Atlantic Ocean/eastern part of South America (-66° to 66° in both latitudes and longitudes)	Various input data sources with different spatial resolutions are interpolated to the location of interest.	All-sky GHI, DNI, DIR, DHI, and corresponding clear-sky irradiances; inputs describe atmospheric conditions (aerosols, clouds, water vapor, trace gases, surface reflectivity parameters); bias-corrected, and non-bias-corrected irradiances.	http://www.soda-pro.com/web-services/radiation/cams-radiation-service
Clean Power Research—Solar Anywhere	1998–present	1 hour, 30 minute, 15 minute, options for high-resolution data	Continental United States, Hawaii, Canada up to 60° N, South America India, parts of the Middle East, parts of Europe	1 km 2.5 km, 3 km 2.5 km, 1 km	GHI, DNI, wind speed, and ambient air temperature	https://www.solaranywhere.com/solutions/solaranywhere-data/

Database	Period of Record	Temporal Resolution	Spatial Coverage	Spatial Resolution	Data Elements and Sources	Availability
Clouds and the Earth's Radiant Energy System (CERES) SYN1deg	2000–2019	1 hour 3 hour	Global	1°x1°	GHI, DHI, and DNI based on physical modeling and satellite-based cloud observations	https://ceres.larc.nasa.gov/data/
CM SAF Cloud, Albedo and Surface Radiation Data Set from AVHRR Data, Edition 2 (CLARA-A2)	1982–2015	Daily, monthly averages	Global	0.25°x0.25°	Cloud properties, surface albedo, and surface radiation parameters derived from the AVHRR sensor onboard polar-orbiting NOAA and MetOp satellites GHI	https://wui.cmsaf.eu/
CM SAF Surface Solar Radiation Data Set - Heliosat (SARAH), Edition 2.1	1983–2017	30 minute, daily, monthly	Europe, Africa, parts of South America	0.05°	Based on MVIRI/SEVIRI instruments onboard the Meteosat satellites; GHI, DNI, DIR	https://wui.cmsaf.eu/
CM SAF SARAH-2 ICDR	2018–present	15 minute, 30 minute, daily, monthly	Europe, Africa, parts of South America	0.05°	Based on SEVIRI instruments onboard the MSG satellite; GHI, DNI, DIR	https://wui.cmsaf.eu/
CM SAF Surface Solar Radiation Data Set - Heliosat - East (SARAH-E), Edition 1.1	1999–2016	1 hour, daily, monthly	Most parts of Asia, Africa; western part of Australia	0.05°	Based on MVIRI instruments onboard the Meteosat IODC satellites GHI, DNI, DIR	https://wui.cmsaf.eu/

Database	Period of Record	Temporal Resolution	Spatial Coverage	Spatial Resolution	Data Elements and Sources	Availability
Daymet	1980–2019	Daily	Continental United States	1 km	GHI, air temperature (minimum and maximum), vapor pressure, and snow water equivalent	https://daymet.ornl.gov
DLR ISIS	July 1983–December 2004	3 hour	Global	280 km by 280 km	DNI and GHI from a radiative transfer model using cloud and aerosol inputs	http://www.pa.op.dlr.de/ISIS/
European Center for Medium-Range Weather Forecasts (ECMWF) ERA5 Reanalysis	1979–present	1 hour	Global	31 km	Clear-sky and all-sky GHI and DIR UV irradiance, longwave irradiance, surface albedo	https://cds.climate.copernicus.eu/cdsapp - !/dataset/reanalysis-era5-single-levels?tab=form
EnMetSol	1995–2019 (1995–2004 based on Meteosat First Generation (MFG); 2005–present based on Meteosat Second Generation (MSG)	30 minute for MFG, 15 minute for MSG	Continental Europe, Canary Islands, Turkey, and Israel	2.5 km for MFG, 1 km for MSG	GHI, DHI, and DNI	University of Oldenburg: http://www.energiemeteorologie.de, available on request
European Solar Radiation Atlas (ESRA)	1981–1990	Monthly and annual average daily totals (kWh/m^2)	Europe	10 km	GHI, DNI, and DHI, sunshine duration, air temperatures, precipitation, water vapor pressure, and air pressure at several stations	Les Presses MINES ParisTech: http://www.mines-paristech.fr/Ecole/Culture-scientifique/Presses-des-mines/#54. See also http://www.soda-pro.com/home.

Database	Period of Record	Temporal Resolution	Spatial Coverage	Spatial Resolution	Data Elements and Sources	Availability
Green Power Labs: SolarSatData	1995–present (Americas) 2000–present (Europe) 2005–present (Asia, Australia)	30 minute	Americas, Asia, Australia, Europe	1–4 km	GHI, DNI, DHI, GTI, temperature, pressure, wind speed, ozone, water vapor, total cloud fraction Irradiance time series for P10, P50, P90, and P95 exceedance probabilities	https://greenpowerlabs.com/
HelioClim V2–V5	2004–present	15 minute	Europe and Africa	5 km	Hourly and daily GHI from satellite remote-sensing mode	MINES ParisTech Armines Center for Energy and Processes: http://www.soda-pro.com/home
Historically Black Colleges and Universities Solar Measurement Network	1985–1996	5 minute	Southeastern United States: Daytona Beach, Florida; Savannah, Georgia; Itta Bena, Mississippi; Elizabeth City, North Carolina; Orangeburg, South Carolina; and Bluefield, West Virginia	Six radiometric stations	GHI, DNI (at three stations), DHI (shadowband) from measurements by the Eppley Laboratory, Inc., Model PSP pyranometers and Model NIP pyrheliometers mounted in automatic solar trackers (LI-COR Model 2020)	NREL: https://www.nrel.gov/grid/solar-resource/hbcu.html (includes quality-assessed monthly data files, monthly summary reports, and monthly irradiance plots)
LSA SAF	2005–present	15 minute	Europe, Africa, parts of Asia and South America (no geographic subsetting offered)	≈5 km	GHI, diffuse fraction, albedo, snow cover, vegetation cover	https://landsaf.ipma.pt/en/data/catalogue/

Database	Period of Record	Temporal Resolution	Spatial Coverage	Spatial Resolution	Data Elements and Sources	Availability
Meteonorm	1996–2015	1-minute and 1-hour modeled data,	Global	Data from 8,350 meteorological stations are interpolated using satellite data to establish weather data at any specified point. Ultimate resolution: 0.0625° x 0.0625°	Measured: monthly means of GHI, temperature, humidity, precipitation, wind speed and direction, and bright sunshine duration. Modeled typical years: 1-minute and hourly typical year radiation parameters (GHI, DNI, DHI, GTI, downwelling infrared, luminance, and UVA and UVB), precipitation, and humidity parameters (dew point, relative humidity, mixing ratio, psychrometric temperature). Radiation data from ground measurements blended with satellite-based long-term averages.	Meteotest https://meteonorm.com/
Meteonorm time series	2010 (depending on region) – current	1-hour measured data	Global (62°S to 62°N)	0.0625° x 0.0625°	Measured time series: GHI from satellite, temperature, wind speed, humidity, precipitation, and wind speed from ERA5T and Swissmetnet	Meteotest https://meteonorm.com/
National Aeronautics and Space Administration's (NASA's) Modern-Era Retrospective Analysis for Research and Applications, Version 2 (MERRA-	1980–present	1 hour	Global	0.5°x0.625°	Clear-sky and all-sky GHI, detailed information on clouds, atmospheric constituents (aerosols, water vapor…), weather variables (temperature, wind…), and surface albedo	https://gmao.gsfc.nasa.gov/reanalysis/MERRA-2/data_access/

Database	Period of Record	Temporal Resolution	Spatial Coverage	Spatial Resolution	Data Elements and Sources	Availability
2)						
National Aeronautics and Space Administration's (NASA's) Prediction of Worldwide Energy Resources (POWER)	July 1983–June 2005	Monthly and annual average daily totals (kWh/m^2)	Global	0.5x0.5°	GHI, DNI, and DHI from a satellite remote-sensing model. Also available: estimates of clear-sky GHI, DNI, and DHI and tilted surface irradiance, temperature, pressure, humidity, precipitation, and wind speed	https://power.larc.nasa.gov/
National Center for Environmental Protection (NCEP)/ National Center for Atmospheric Research Global Reanalysis Products	1948–current	6 hour (W/m2)	Global	2.5° (nominal)	GHI and more than 80 variables, including geopotential height, temperature, relative humidity, and U and V wind components, in several coordinate systems, such as a 17-pressure-level stack on 2.5 x 2.5° grids, 28 sigma-level stacks on 192 x 94 Gaussian grids, and 11 isentropic-level stacks on a 2.5 x 2.5° grid	University Center for Atmospheric Research, Computational and Information Systems Laboratory Research Data Archive: http://rda.ucar.edu/datasets/ds090.0/
National Oceanic and Atmospheric Administration's (NOAA) Global Monitoring Laboratory (GML)/Earth System Research Laboratory (ESRL) Baseline Network	Varies	1 minute	Global	Five stations: Hawaii, Alaska, California, Greenland, American Samoa	GHI, DNI, DHI, downwelling infrared irradiance	https://esrl.noaa.gov/gmd/dv/site/index.php?program=grad

Database	Period of Record	Temporal Resolution	Spatial Coverage	Spatial Resolution	Data Elements and Sources	Availability
National Oceanic and Atmospheric Administration's (NOAA) SOLRAD Network	1995–present	1 minute (15 minute before 2001)	Continental United States	Nine stations: New Mexico, North Dakota, California, Wisconsin, Tennessee, Washington, Utah, Virginia, and Florida	GHI, DNI, DHI, and global UVB	NOAA, Earth Systems Research Laboratory, Global Monitoring Division, Boulder, Colorado: https://www.esrl.noaa.gov/gmd/grad/solrad/index.html Data available from: ftp://aftp.cmdl.noaa.gov/data/radiation/solrad
National Oceanic and Atmospheric Administration's (NOAA) Surface Radiation Budget Network (SURFRAD)	1993–present	Data are reported as 3-minute averages of 1-second samples before January 1, 2009, and 1-minute averages on and after January 1, 2009.	Continental United States	Seven permanent stations: Montana, Colorado, Illinois, Mississippi, Pennsylvania, Nevada, and South Dakota Four temporary stations: Arizona, Colorado, Oregon, and Vermont	GHI, DNI, DHI, downwelling infrared irradiance, upwelling infrared irradiance, and upwelling (reflected) shortwave irradiance. Photosynthetically active radiation, solar net radiation, infrared net radiation, air temperature, relative humidity, wind speed and direction (10-m AGL), and all-sky images	NOAA, Earth Systems Research Laboratory, Global Monitoring Division, in Boulder, Colorado: https://www.esrl.noaa.gov/gmd/grad/surfrad/sitepage.html Data available from: ftp://aftp.cmdl.noaa.gov/data/radiation/surfrad/ SURFRAD data from permanent stations are also submitted to the BSRN archives: www.bsrn.awi.de/.

Database	Period of Record	Temporal Resolution	Spatial Coverage	Spatial Resolution	Data Elements and Sources	Availability
National Renewable Energy Laboratory (NREL) Solar Radiation Research Laboratory (SRRL) Measurement and Instrumentation Data Center (MIDC)	1981–present	5 minute (beginning July 15, 1981), 1 minute (beginning January 13, 1999)	Golden, Colorado	One radiometric station	GHI, DNI, DHI (from shadowband and tracking disk), global on tilted surfaces, reflected solar irradiance, UV, infrared (upwelling and downwelling), photometric and spectral radiometers, sky imagery, and surface meteorological conditions (temperature, relative humidity, barometric pressure, precipitation, snow cover, and wind speed and direction at multiple levels)	http://www.nrel.gov/midc/srrl_bms/
National Solar Radiation Database (NSRDB) 1961–1990	1961–1990	1 hour	United States and territories	239 stations (56 stations have some radiation measurements)	Hourly GHI, DNI, DHI, ETR, direct normal ETR, total sky cover, opaque sky cover, ceiling height, dry-bulb temperature, dew-point temperature, relative humidity, atmospheric pressure, horizontal visibility, wind speed, wind direction, present weather, AOD, total precipitable water, snow depth, and number of days since last snowfall	NREL: https://nsrdb.nrel.gov/data-sets/archives.html
National Solar Radiation Database (NSRDB) 1991–2005	1991–2005	1 hour	United States	1,454 locations and 10-km by 10-km grid (1998–2005)	Computed or modeled data: ETR on surfaces horizontal and normal to the sun, GHI, DNI, and DHI. Measured or observed data: total sky cover, opaque sky cover, dry-bulb temperature, dew-point temperature, relative humidity, station pressure, wind speed and direction, horizontal visibility, ceiling height, precipitable water, AOD, surface albedo, and precipitation	NSRDB: https://www.ncdc.noaa.gov/data-access/land-based-station-data/land-based-datasets/solar-radiation Data available from: ftp://ftp.ncdc.noaa.gov/pub/data/nsrdb-solar/ and https://nsrdb.nrel.gov/data-sets/archives.html.

Database	Period of Record	Temporal Resolution	Spatial Coverage	Spatial Resolution	Data Elements and Sources	Availability
National Solar Radiation Database (NSRDB) 1991–2010	1991–2010	1 hour	United States	1,454 locations and 10-km by 10-km grid (1998–2009)	Computed or modeled data: ETR on surfaces horizontal and normal to the sun, GHI, DNI, and DHI. Measured or observed data: total sky cover, opaque sky cover, dry-bulb temperature, dew-point temperature, relative humidity, station pressure, wind speed and direction, horizontal visibility, ceiling height, precipitable water, AOD, surface albedo, and precipitation	*NSRDB User's Manual*: http://www.nrel.gov/docs/fy12osti/54824.pdf Data available upon request from NREL.
National Solar Radiation Database (NSRDB)	1998–2019 (updated annually)	5 minute from 2018 Half-hourly	Southern Canada, United States, and parts of South America (longitude: -25° E to -175° W, latitude: -21° S to 60° N). India 2000–2014	4 km; 2 km from 2018	GHI, DNI, DHI, clear-sky DHI, clear-sky DNI, clear-sky GHI, cloud type, dew point, surface air temperature, surface pressure, surface relative humidity, solar zenith angle, total precipitable water, wind direction, wind speed, surface albedo	https://nsrdb.nrel.gov
European Organisation for the Exploitation of Meteorological Satellites (EUMETSAT) Ocean and Sea Ice Satellite Application Facility (OSI-SAF)	2001–present	1 hour	Africa, Americas, Europe, western Asia	0.05°x0.05°	GHI, longwave infrared irradiance	http://www.osi-saf.org/?q=content/radiative-fluxes-products

Database	Period of Record	Temporal Resolution	Spatial Coverage	Spatial Resolution	Data Elements and Sources	Availability
Pacific Northwest Solar Radiation Data Network	1975–present	1 minute to 1 hour, depending on station and date	Oregon, Idaho, Washington, Utah, Wyoming, Montana	39 stations	Varies by site and date—GHI, DNI, DHI, GTI, spectral irradiance, surface meteorological data (temperature, relative humidity barometric pressure, precipitation, precipitable water vapor), PV output	http://solardat.uoregon.edu/SolarData.html
Photovoltaic Geographical Information System (PVGIS)	2005–2016	1 hour	Europe, Africa and most parts of Asia and America	1-km aggregated to 3 arc-minutes (~5 km)	GHI, DNI, DHI, and GTI, based on the CM-SAF, COSMO, NREL, and ECMWF databases, optional terrain shadowing. Also TMY data sets	European Commission Joint Research Centre, Directorate for Energy, Transport and Climate; Energy Efficiency and Renewables Unit: https://ec.europa.eu/jrc/en/pvgis
Reuniwatt—SunSat	2004 (depending on region)–present	10/15 minute, 1 hour	Worldwide between latitudes 60° N and 60° S	500 m to 3 km depending on location	GHI, DNI, DHI, BHI, GTI and corresponding clear-sky irradiance, cloud index, meteorological conditions (temperature, relative humidity, wind speed, pressure, aerosol optical depth, precipitable water, total column water vapor, etc.)	https://reuniwatt.com
Southern African Universities Radiometric Network (SAURAN)	Varies	1 minute	Botswana, Namibia, and South Africa	23 radiometric stations	GHI, DNI, and DHI; meteorological data	https://sauran.ac.za/
Solar Data Warehouse	Varies from 5–25 years ago to the present	1 hour and daily	Continental United States	More than 3,000 radiometric stations	GHI	http://www.solardatawarehouse.net
Solar Energy and Meteorological	1979–1983	1 minute	Fairbanks, Alaska; Atlanta, Georgia;	Four radiometric stations	GHI, DNI, and DHI; GTI on various surfaces, infrared irradiances, UV and other spectral	NREL: https://www.nrel.gov/grid/solar-

Database	Period of Record	Temporal Resolution	Spatial Coverage	Spatial Resolution	Data Elements and Sources	Availability
Research Training Sites			Albany, New York; San Antonio, Texas		irradiance (varies), and surface meteorological conditions (temperature, relative humidity, pressure, visibility, wind speed, and direction at 10 m, precipitation, etc.)	resource/semrts.html
Solcast	2007–present	1, 5, 10, 15, or 30 minute and 1 hour	Global, except polar areas	1–2 km cloud index, scaled to 150 m using DEM	GHI, DNI, EBH, DIF/DHI, GTI, cloud opacity, solar zenith angle, solar azimuth angle, temperature, wind speed, wind direction, relative humidity, surface pressure, precipitable water, snow depth, dew point, albedo. Data available as time series, typical year with P50, P75, P90, P95, or Pxx exceedance probabilities, and monthly and annual averages	https://solcast.com/
Solargis	1994, 1999, 2007 - present (depends on satellite region)	1, 5, 10, 15, 30 and 60 minute	Global, land and coastal waters, between latitudes 65° N and 55° S	Solar parameters at 2 to 3 km (at the Equator) enhanced to ~90 m and ~250 m using SRTM-3 DEM; Meteo parameters at 1 km and coarser	DNI, GHI, DHI (DIF), GTI, UVA, UVB, air temperature, dew point and wet bulb temperature, wind speed and direction, wind gust, relative humidity, air pressure, ground albedo, precipitable water, precipitation, snow depth, snow fall rate. Accessible as time series, TMY Pxx and long-term statistics	https://solargis.com
Solar Energy Mining (SOLEMI)	1991–present	30 minute	Europe, Africa, South America, Western Asia, Western Australia	2.5 km	GHI, DNI	DLR: http://www.dlr.de/tt/en/desktopdefault.aspx/tabid-2885/4422_read-6581/ Data available upon request.

Database	Period of Record	Temporal Resolution	Spatial Coverage	Spatial Resolution	Data Elements and Sources	Availability
TMY 98-19	1998–2019	1 hour	Southern Canada, United States, and parts of South America (longitude: -25° E to -175° W, latitude: -20° S to 60° N)	4 km	GHI, DNI, DHI, cloud type, dew point, surface air temperature, surface pressure, wind direction, wind speed	https://nsrdb.nrel.gov
TMY2	One year representative of the 1961–1990 NSRDB data period	1 hour	United States and territories	239 stations representing the 1961–1990 NSRDB	Same as NSRDB 1961–1991	NREL: https://nsrdb.nrel.gov/data-sets/archives.html
TMY3	1991–2005	1 hour	United States and territories	1,020 locations	Computed or modeled data: ETR on surfaces horizontal and normal to the sun, GHI and illuminance, DNI and illuminance, DHI and illuminance, zenith luminance. Measured or observed data: total sky cover, opaque sky cover, dry-bulb temperature, dew-point temperature, relative humidity, station pressure, wind speed and direction, horizontal visibility, ceiling height, precipitable water, AOD, surface albedo, and precipitation	NREL: https://nsrdb.nrel.gov/data-sets/archives.html
Vaisala (formerly 3Tier) Solar Time Series	January 1997–present	Approx. 30-minute instantaneous and 1-hour averages	Global	2 arc-min (~3 km)	GHI, DNI, and DHI from model estimates based on satellite remote-sensing input data, temperature, wind speed and direction, atmospheric pressure, precipitable water or relative humidity	https://www.vaisala.com/en/digital-and-data-services/renewable-energy

Database	Period of Record	Temporal Resolution	Spatial Coverage	Spatial Resolution	Data Elements and Sources	Availability
Vortex	Two periods:		Americas	4–5 km	Only GHI, DNI derived from GHI	
	2010–present;	1 hour	Europe, Africa,			
GOES	1995–2015		Middle East-East Europe-West		GHI, DNI, DHI	
SARAH				4–5 km		https://vortexfdc.com/
SARAH-E	1999–2015;		Asia	4–5 km	GHI, DNI, DHI	
		1 hour				
Himawari	2012–2018		Asia-Oceania	2 km	GHI, DNI, DHI	
Western Energy Supply and Transmission (WEST) Associates Solar Monitoring Network	1976–1980	15 minute	Arizona, California, Colorado, Nevada, New Mexico, and Wyoming	52 radiometric stations	GHI, DNI, and dry-bulb temperature measured with pyranometers (Eppley Black and White, Eppley PSP, and the Spectrolab Spectrosun SR75) and pyrheliometers (Eppley NIP) in automatic solar trackers	NREL: https://www.nrel.gov/grid/solar-resource/west-manual.html
World Meteorological Organization (WMO) World Radiation Data Center (WRDC)	1964–present	Daily totals with some 1-hour measurements at a few sites	Global	More than 1,000 radiometric stations	Primarily daily total GHI, radiation balance, and sunshine duration, but some DHI and DNI. Some hourly measurements are available from a few sites.	http://wrdc.mgo.rssi.ru

6.4 References

Arguez, A., and R. S. Vose. 2011. "The Definition of the Standard WMO Climate Normal: The Key to Deriving Alternative Climate Normals." *Bulletin of the American Meteorological Society* 92: 699–704.

Ernst, M., and J. Gooday. 2019. "Methodology for Generating High Time Resolution Typical Meteorological Year Data for Accurate Photovoltaic Energy Yield Modelling." *Solar Energy* 189: 299–306. https://doi.org/10.1016/j.solener.2019.07.069.

García, I., M. de Blas, J., and L. Torres. 2020. "Proposal and Evaluation of Typical Illuminance Year (TIY) Generation Procedures from Illuminance or Irradiance Data for Daylight Assessment in the Long Term." *Solar Energy* 205: 496–511. https://doi.org/10.1016/j.solener.2020.05.083.

Gueymard, C. A., and D. R. Myers. 2008. "Solar Radiation Measurement: Progress in Radiometry for Improved Modeling." In *Modeling Solar Radiation at the Earth Surface*, edited by V. Badescu, 1–27. Springer.

Gueymard, C. A., and D. R. Myers. 2009. "Evaluation of Conventional and High-Performance Routine Solar Radiation Measurements for Improved Solar Resource, Climatological Trends, and Radiative Modeling." *Solar Energy* 83: 171–85. https://doi.org/10.1016/j.solener.2008.07.015.

Hulstrom, R. L., ed. 1989. *Solar Resources.* Cambridge, MA: MIT Press.

Nielsen, K. P., Blanc, P., Vignola, F., Ramírez, L., Blanco, M., and R. Meyer. 2017. *Discussion of Currently Used Practices for: Creation of Meteorological Data Sets for CSP/STE Performance Simulations.* SolarPACES. http://www.solarpaces.org/wp-content/uploads/BeyondTMY_Discussion_of_current_methods_v3_0-1.pdf.

Polo, J., L. Martin-Pomares, C. A. Gueymard, J. L. Balenzategui, F. Fabero, and J. P. Silva. 2019. "Fundamentals, Quantities, Definitions, and Units." In *Solar Resources Mapping Fundamentals and Applications*, edited by J. Polo, L. Martin-Pomares, and A. Sanfilippo. Springer.

Remund, J., Mueller, S., Kunz, S., and Schilter, C. 2012. *METEONORM Handbook Part II : Theory*. Bern: Meteotest. https://www.energiehaus.es/wp-content/uploads/2015/06/manual-usuario-part-2-meteonorm.pdf.

Sengupta, M., and A. Habte. 2019. "The Impact of Plane-of-Array-Based TMYs on Solar Resource for PV Applications." *2019 European Photovoltaic Specialists Conference (EU PVSEC)*, Marseille, France. https://www.eupvsec-proceedings.com/proceedings/checkout.html?paper=48572.

Sengupta, M., Habte, A., and J. M. Freeman. 2019. "The Case for Custom TMY's: Examples Using the NSRDB." *2019 IEEE 46th Photovoltaic Specialists Conference (PVSC)*, Chicago, Illinois, 2,287–92. https://doi.org/10.1109/PVSC40753.2019.8980811.

Sengupta, M., Y. Xie, A. Lopez, A. Habte, G. Maclaurin, and J. Shelby. 2018. "The National Solar Radiation Data Base (NSRDB)." *Renewable and Sustainable Energy Reviews* 89: 51–60. https://doi.org/10.1016/j.rser.2018.03.003.

7 SOLAR IRRADIANCE UNCERTAINTY AND DATA QUALITY ASSESSMENT

Aron Habte,[1] Daryl Myers,[2] Stephen Wilcox,[3] Stefan Wilbert,[4] Christian Gueymard,[5] Marcel Šúri,[6] Manajit Sengupta,[1] Thomas Stoffel,[3] and Frank Vignola[7]
[1] *National Renewable Energy Laboratory*
[2] *National Renewable Energy Laboratory, retired*
[3] *Solar Resource Solutions, LLC*
[4] *German Aerospace Center (DLR)*
[5] *Solar Consulting Services*
[6] *Solargis*
[7] *University of Oregon*

7.1 Introduction

A clear statement of uncertainty should accompany any comprehensive measured or modeled solar radiation data set to provide the necessary context to understand the reliability of the analysis performed using the data.

For example, a full characterization of uncertainty provides a basis to assess confidence in the predicted output of a planned solar conversion system and is thus a key factor when determining the bankability of the project. Uncertainty is a way to specify the confidence in the data. It is important to determine the uncertainty using a standard methodology to provide authoritative results that can be relied on for analysis and comparisons. The *Guide to the Expression of Uncertainty in Measurements* (GUM) (ISO 2008) is an example of how to determine the uncertainty in measurements. GUM has been formalized by several organizations, including the International Bureau of Weights and Measurements (French acronym: BIPM), and published by the International Standards Organization (ISO).

This chapter discusses the uncertainties associated with the measured or modeled solar resource data along with the limits on the validation of physical or empirical models that use such data. Precise measurement or modeling of the solar resource is complicated by the rapidity with which the solar irradiance can change, the changing spectral composition of the irradiance, and the varied environment conditions experienced during measurements.

Even with improving instrumentation and radiation models, the measurement or modeling of incident irradiance can have large uncertainties, depending on circumstances. The uncertainty in modeled values is typically obtained by comparison with reference measurements and is affected by the uncertainty in the measurements. Section 7.1 summarizes the GUM methodology for quantifying the uncertainty for measured irradiance. Afterward, the uncertainty of modeled data is discussed in sections 7.2 to 7.5. Note that the uncertainty in the modeled data is typically obtained by comparison with reference measurements, which is why the section on measurements comes first. Section 7.6 addresses the automatic irradiance data quality assessment.

7.2 Measurement Uncertainty

To characterize a quantity, referred to in the GUM terminology as the *measurand*, it is necessary to provide a measure of the quantity. This characterization of the measurand is incomplete without supplying a quantitative statement of the associated uncertainty. This uncertainty provides an estimate of how well the value of the measurand is known and

provides a range of values that will result from measurements taken under similar circumstances with similar instruments. In general, the measurand has four general sources of uncertainty: the act of measurement, the instrument doing the measurement, the device recording the measurement, and the environment in which the measurements take place.

Any measurement only approximates the quantity being measured. Each element of a measurement system contributes to the final uncertainty of the data. The accuracy of solar radiation measurements made at ground stations depends on the radiometer specifications, proper installation and maintenance, data acquisition method and accuracy, calibration method and frequency, location, environmental conditions, and possible real-time or a posteriori adjustments to the data. A large portion of this overview of uncertainty in measurements of solar radiation made at ground stations is based on Habte et al. (2014, 2016b), Reda et al. (2011), Wilcox and Myers (2008), Myers et al. (2002), Stoffel et al. (2000), and Gueymard and Myers (2008a).

7.2.1 Estimation of Calibration and Field Measurement Uncertainty

The method to estimate uncertainty has changed significantly during the last few decades. The general adaptation to the current methodology takes time; hence, some outdated terminology and methods still appear in the literature and might be in use. Even though using the outdated methodologies are discouraged, short descriptions are provided to help users understand and correctly use uncertainty data based on older methodologies.

Historically, uncertainty analysis treated sources of uncertainty in terms of *random* and *bias* error types. Random sources were related to the standard deviation or variance of measured data sets. Biases were estimates of deviations from a "true value" primarily based on engineering judgments of the measurement system performance. Total uncertainty (UT_{old}) was computed as the square root of the sum of the squares for these two error types:

$$UT_{old} = [\Sigma\,(Bias)^2 + \Sigma(2\cdot Random)^2]^{1/2} \qquad (7\text{-}1)$$

Factor 2 in the random term was necessary to "inflate" the random component and ultimately provide an approximate 95% confidence interval for the computed value of UT_{old}. Factor 2 is equivalent to the coverage factor k in the current GUM terminology, where $k \approx 2$ for an infinite degree of freedom. This value assumes that the data points are normally distributed. Based on advancement in metrology science, the more comprehensive GUM model replaces this simple method.

GUM is currently the accepted guide for measurement uncertainty (ISO 2008). Similarly, the method provides the expanded uncertainty for an approximate 95% confidence interval by multiplying the combined uncertainty by the coverage factor k (k = 1.96 for a Gaussian distribution for infinite degrees of freedom; it is often approximated as 2). GUM defines Type A uncertainty values as derived from statistical methods and Type B sources as evaluated by other means, such as scientific judgment, experience, specifications, comparisons, and calibration data. GUM defines the concept of a standard uncertainty (u_{std}) for each uncertainty type, which is an estimate of an equivalent standard deviation (of a specified distribution) of the source of uncertainty. To appropriately combine the various uncertainties, the GUM methodology uses a sensitivity coefficient (c) that is calculated from the measurement equation using partial derivatives with respect to each input variable in the equation. The combined uncertainty (u_c) is computed from the Type A and Type B standard uncertainties summed under quadrature—the square root of the sum of the squares. GUM removes the historical factor of 2 and introduces the coverage factor k (which depends on

the known or assumed statistical distribution of uncertainties),[37] which is applied to both types of uncertainty to compute the *expanded uncertainty* (U_E) as:

$$U_E = k \cdot u_c = k \cdot [\Sigma (\text{Type B})^2 + \Sigma (\text{Type A})^2]^{1/2} \quad (7\text{-}2)$$

As shown in Figure 7-1, the GUM procedure can be summarized in six steps (Habte et al. 2016b; Reda 2011):

1. Define the measurement equation for the calibration and/or measurement system. This consists of a mathematical description of the relation between sensor voltage as well as any other independent variables and the desired output (calibration response or engineering units for measurements). The two example equations used to quantify radiometric measurement are:

$$E = \frac{(V - R_{net} * W_{net})}{R} \quad \text{or} \quad E = \frac{V}{R} \quad (7\text{-}3)$$

where:

- E = irradiance, in W m^{-2} (global horizontal irradiance [GHI], global tilted irradiance [GTI], diffuse horizontal irradiance [DHI], or direct normal irradiance [DNI]); for DNI, $R_{net} \approx 0$, resulting in the simplified equation on the right.
- R = responsivity of the radiometer in μV/ (W m^{-2})
- V = sensor output voltage of the radiometer in μV
- R_{net} = net infrared responsivity of the radiometer in μV/(W m^{-2})
- W_{net} = effective net infrared irradiance measured by a collocated pyrgeometer in W m^{-2}.

In the case of GHI, the closure equation applies: $E = \text{DNI} * \cos(Z) + \text{DHI}$, where:

- DNI = beam irradiance measured by a primary or standard reference standard pyrheliometer in W m^{-2}
- Z = solar zenith angle (SZA), in degrees or radians
- DHI = diffuse horizontal irradiance, measured by a shaded pyranometer (W m^{-2}).

2. Determine the sources of uncertainty. Most sources of uncertainty are obtained from statistical calculations, specifications from manufacturers, and previously published reports on radiometric data uncertainty or professional experience. Some common sources of uncertainty are associated with SZA response, spectral response, nonlinearity, temperature response, thermal loss, data logger accuracy, soiling, and calibration, including the drift of the calibration constant(s).

[37] k is 1.96 for a Gaussian distribution for a 95% confidence level. Generally, a 95% confidence level means that 95% of the values will be within the statistical limits defined by the uncertainty.

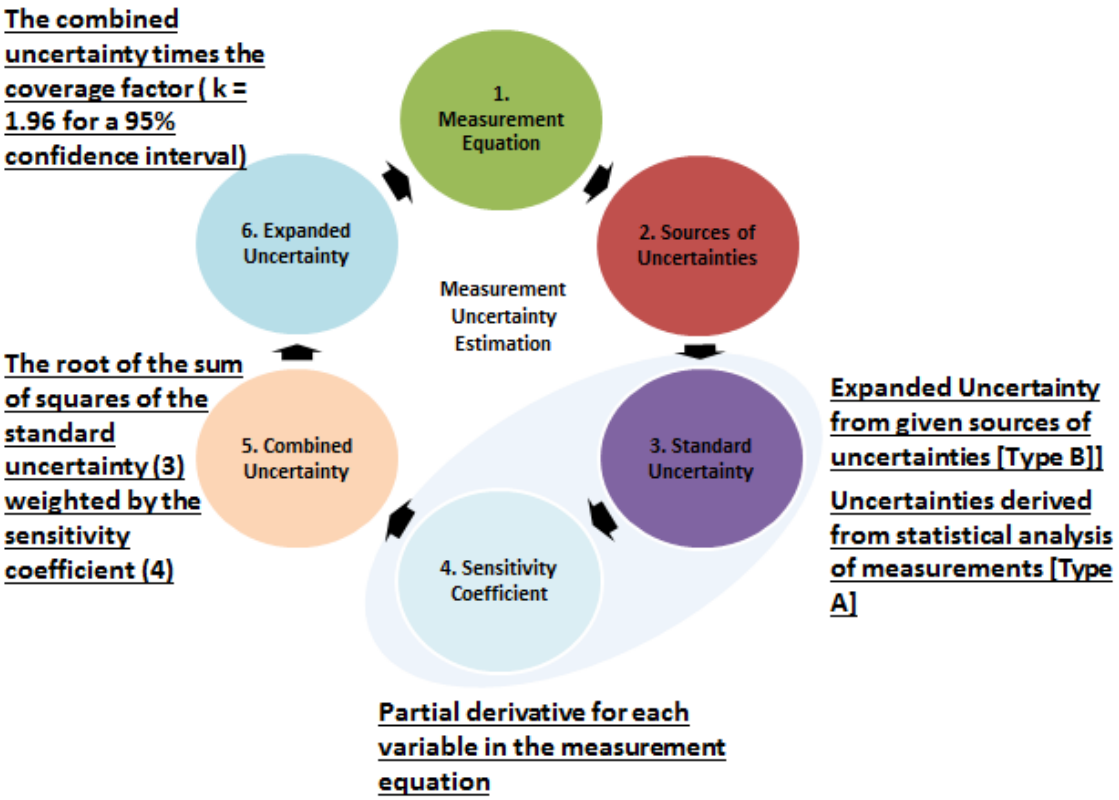

Figure 7-1. Measurement uncertainty estimation flowchart. ***Image from Habte et al. (2016b)***

3. Calculate the standard uncertainty, u. In this step, an individual u for each variable in the measurement equation is calculated using either a statistical method (Type A uncertainty component) or other methods (Type B uncertainty component, such as manufacturer specifications, calibration results, and experimental or engineering experience). In the GUM method, the standard uncertainties are calculated by dividing the expanded uncertainty of each source by the corresponding statistical distribution (ASTM 2017).

    A. Type A uncertainty:

        i. Type A standard uncertainty is calculated by taking repeated measurements of the input quantity value, from which the sample mean and sample standard deviation (SD) can be calculated. The Type A standard uncertainty (u) can then be estimated by:

$$\mathrm{SD} = \sqrt{\frac{\sum_{i=1}^{n}(X_i - \overline{X})^2}{n-1}} \tag{7-4}$$

        where n is the number of measurements, X_i is the measured value, and $\overline{X}$ is the average.

    B. Type B uncertainty:

        Type B uncertainties are often provided as an expanded uncertainty (U). To be consistent with Type A uncertainties, the standard Type B uncertainties, u, are calculated from the expanded uncertainties, U.

        i. Equation for unknown statistical distribution (common assumption: rectangular distribution): $u = U/\sqrt{3}$, where U is the expanded uncertainty of a variable

ii. Normal distribution: $u = U/k$, where k is a coverage factor of 2 or, more exactly, 1.96 (ISO 2008)
iii. For other statistical distributions, the applicable values for k are used.

4. Compute the sensitivity coefficient, c. To appropriately combine the various uncertainties in the next step, the uncertainties must be weighed. The GUM method does this by calculating the sensitivity coefficients (c) of the variables in a measurement equation. These coefficients affect the contribution of each input factor to the combined uncertainty of the irradiance value; therefore, the sensitivity coefficient for each input is calculated by partial differentiation with respect to each input variable in the measurement equation. Table 7-1 shows the sensitivity coefficients applicable to radiation measurements.

   The sensitivity equations given in Table 7-1 are for two distinct situations. The calibration sensitivity is for calibrations when the reference GHI is calculated from reference DNI and DHI measurements. The second column is for GHI measurements in the field. The calibration sensitivities are related to the inverse of the GHI value, whereas the field sensitivities are related to the inverse of the responsivity.

Table 7-1. Example of Computing Sensitivity Coefficients for GHI Pyranometer Calibration and Measurement Using Partial Derivatives

Calibration Sensitivity Equations	Field Measurement Sensitivity Equations
$c_V = \frac{\partial R}{\partial V} = \frac{1}{\mathrm{DNI}\cos(Z) + \mathrm{DHI}}$	$c_R = \frac{\partial \mathrm{GHI}}{\partial R} = \frac{-(V - R_{net} W_{net})}{R^2}$
$c_{Rnet} = \frac{\partial R}{\partial R_{net}} = \frac{-W_{net}}{\mathrm{DNI}\cos(Z) + \mathrm{DHI}}$	$c_{R_{net}} = \frac{\partial \mathrm{GHI}}{\partial R_{net}} = \frac{-W_{net}}{R}$
$c_{Wnet} = \frac{\partial R}{\partial W_{net}} = \frac{-\mathrm{R_{net}}}{\mathrm{DNI}\cos(Z) + \mathrm{DHI}}$	$c_{W_{net}} = \frac{\partial \mathrm{GHI}}{\partial W_{net}} = \frac{-R_{net}}{R}$
$c_{DNI} = \frac{\partial R}{\partial \mathrm{DNI}} = \frac{-(V - R_{net} W_{net})\cos(Z)}{(\mathrm{DNI}\cos(Z) + \mathrm{DHI})^2}$	$c_V = \frac{\partial \mathrm{GHI}}{\partial V} = \frac{1}{R}$
$c_{SZA} = \frac{\partial R}{\partial Z} = \frac{\mathrm{DNI}\sin(Z)\,(V - R_{net} W_{net})}{(\mathrm{DNI}\cos(Z) + \mathrm{DHI})^2}$	
$c_D = \frac{\partial R}{\partial \mathrm{DHI}} = \frac{-(V - Rnet\, W_{net})}{(\mathrm{DNI}\cos(Z) + \mathrm{DHI})^2}$	

5. Calculate the combined standard uncertainty, uc. This is the combined standard uncertainty using the propagation of errors formula and quadrature (square root sum of squares) method. It is applicable to both Type A and Type B sources of uncertainty. Standard uncertainties (u) in Step 3 multiplied by their sensitivity factors (c) in Step 4 are combined in quadrature to give the combined standard uncertainty, uc:

$$u_c = \sqrt{\sum_{j=0}^{n-1} (u * c)^2} \tag{7-5}$$

where n is the number of uncertain variables that are used to calculate the combined uncertainty.

6. Calculate the expanded uncertainty (U95). The expanded uncertainty is calculated by multiplying the combined standard uncertainty by the coverage factor, typically by applying the Student's t-analysis to determine the appropriate value of k (typically 1.96 for 95% and 3 for 98% confidence, respectively, for large data sets assuming a Gaussian distribution):

$$U_{95} = k * u_c. \tag{7-6}$$

These six steps, also described in Figure 7-1, demonstrate that the uncertainty quantification is a cycle. This means that one can use the expanded uncertainty in Step 6 as an input to a measurement equation. This would be the case, for example, in calculations of the performance ratio of solar conversion systems: to calculate the ratio of *system output/solar input*, the expanded uncertainty in Step 6 is used as an input to evaluate the denominator (*solar input*), and the cycle continues to ultimately quantify the expanded uncertainty of the performance ratio.

Further, these steps are applicable to the quantification of the uncertainty in both calibration and field measurements. Uncertainty in measurements begins with the uncertainty in calibration references, calibration processes, and sensor design characteristics. For example, for thermopile sensors, a calibration constant is required to convert the output voltage to the required irradiance, as discussed in Chapter 3. The resulting uncertainty in calibration factors must then be combined with the influence of additional sources of uncertainty in the field measurement instrumentation, installation methods, data acquisition, and operation-and-maintenance processes (Reda 2011). Overall, note that estimates of uncertainties for the magnitudes of values (e.g., voltage, *Rnet*) need some (documented) experimental, theoretical, or other (specifications) source. These are the magnitudes adjusted in these steps—for example, in the sensitivity coefficients calculation. Such example data are presented in several references (Reda 2011; Habte et al. 2014; Jörgen and Habte 2016; ASTM 2017). Further, users need to pay close attention to the source of uncertainties. For instance, the SZA uncertainty includes sources of error such as accuracy in latitude and longitude, air pressure (for refraction corrections), or timekeeping (clock accuracy). The units of these variables must be treated carefully and consistently, whether they are percentages (such as of full scale or reading) or absolute units (such as volts, degrees, or Watts per square meter). Additionally, it is essential to consider the symmetry of the sources of uncertainty. In this section, all sources of uncertainty are considered symmetric (+/-); however, some other sources could be asymmetric or one-sided. For example, Jörgen and Habte (2016) considered nonstability and zero offset as two one-sided sources of uncertainty.

The measurement of terrestrial solar radiation is traceable to the internationally accepted World Radiometric Reference (WRR) (ISO 2018), discussed in Chapter 3. This internationally recognized measurement reference is a detector-based standard maintained by a group of electrically self-calibrating absolute cavity radiometers. The present accepted inherent expanded uncertainty in the WRR is ±0.30% (Finsterle 2011). Reference cavity radiometers used as national and institutional standards are calibrated by comparison to the World Standard Group of absolute cavity pyrheliometers. The transfer of calibrations from the WRR to national standards results in an expanded uncertainty for these measurement standards of ±0.45% (Reda, Dooraghi, and Habte 2013).

Applying the GUM procedure to the case of pyrheliometer and pyranometer calibration, Table 7-2 summarizes the estimated uncertainties that are typically found in practice. In addition, Table 7-2 identifies the typical sources of uncertainty considered for the overall uncertainty analysis of irradiance measurements from two types of radiometers: radiometers with thermopile detector and photodiode radiometers with silicon detector before the

application of correction functions for systematic errors. Note that the contribution to uncertainty caused by insufficient maintenance (alignment, leveling, cleaning, etc.) can be much greater than the combined uncertainties for well-maintained instruments. As explained in Chapter 3, instruments with clear optics (such as most thermopile radiometers) are more strongly affected by soiling; hence, the uncertainty related to their operation in the field depends on the regularity and quality of their maintenance over time.

Table 7-2. Example of Estimated Expanded Uncertainties of Responsivities of Field Pyranometers and Pyrheliometers. *Modified from Reda (2011)*

Type B Uncertainty Source	Thermopile Pyranometer (%)	Photodiode Pyranometer (%)	Thermopile Pyrheliometer (%)	Photodiode Pyrheliometer (%)
Calibration[a]	3	5	2	3
Zenith response[b]	2	2	0.5	1
Azimuth response	1	1	0	0
Spectral response	1	5	1.5	8
Tilt[c]	0.2	0.2	0	0
Nonlinearity	0.5	1	0.5	1
Temperature response	1	1	1	1
Aging per year	0.2	0.5	0.1	0.5
U_{95}	4.1	8.0	2.7	8.9

[a] Includes zenith angle responses from 30° to 60°
[b] Includes zenith angle responses from 0° to 30° and from 60° to 90°
[c] This uncertainty is set to zero for untilted radiometers.

Detailed uncertainty analyses for high-quality field pyrheliometers can be found in Michalsky et al. (2011); the study in Vuilleumier et al. (2014) is similar, but it also includes field pyranometers. These studies show that the uncertainty of the calibration is the most important contribution to the overall uncertainty for well-maintained high-quality instruments. The calibration stability of the present commercially available pyrheliometers and pyranometers is generally satisfactory, as revealed by only a slight change in responsivity (*Rs*)—less than 0.1% and 0.2% per year, respectively. When finally deployed in the field, factors such as accuracy of solar tracking and/or leveling, data logger accuracy, cleanliness of the windows, and frequency of recalibration could contribute more sources of uncertainty. Even if these effects are kept low by following measurement best practices, expanded uncertainties of ±2.0%–±2.5% in field DNI measurements and ±3.0%–±5% in field GHI measurements have been found from a high-quality measurement system (Reda 2011).

For rotating shadowband irradiometers (RSI) and photodiode pyranometers, one of the most crucial impacts on uncertainty is the spectral irradiance error. This is because silicon photodiode sensors detect only visible and near-infrared radiation in a limited range, 300–1200 nm at most, and have a spectral response that varies strongly within this wavelength interval. Further, the role of using algorithms to reduce systematic effects and the uncertainty introduced by imperfect shading must be considered. A more detailed uncertainty analysis for RSIs following GUM can be found in Wilbert et al. (2016). The study defines a method for the derivation of the spectral error and spectral uncertainties and presents quantitative values of the spectral and overall uncertainties. The results of this detailed analysis and other studies such as (Wilcox and Myers 2008) indicated lower overall uncertainties than those presented in Table 7-2 for silicon photodiode pyranometers because the uncertainty for the silicon pyranometer described in Table 7-2 does not include any rigorous adjustment

methodology. The expanded measurement uncertainty for subhourly DNI measurements is approximately ±5% for a photodiode radiometer with state-of-the-art correction functions for systematic errors. For RSIs, GHI was found to be affected by slightly lower uncertainties than DNI (4%, k = 2, after application of state-of-the-art adjustment functions). Moreover, advanced adjustment functions were found to significantly reduce the uncertainty.

The typical shade/unshade calibration uncertainty for any thermopile pyranometer with respect to a WRR reference cavity radiometer is ≈0.5% at any very narrow range (±2°–±5°) of SZA (Reda, Myers, and Stoffel 2008). Typically, *Rs* is selected as an average responsivity for a specified SZA (usually 45°); however, the irradiance is collected for a wide range of SZAs (0°–90°), and the measurement uncertainty over the whole range is larger. As shown in Chapter 3, for some pyranometers, *Rs* can vary by ±3%–±10% or even more over this zenith angle interval. These effects then need to be combined with the field measurement influences, the same as with the DNI measurement uncertainty estimate (e.g., including pyranometer installation, data logger accuracy, cleanliness, spectral dependency, or temperature sensitivity).

If only one *Rs* is used for a wide range of solar angles, that value is often derived for relatively low SZAs. The variation of responsivity with SZA and azimuth angles is typically greater for high SZAs; hence, large uncertainties usually occur at high SZAs. These high-SZA-related uncertainties occur throughout parts of the day (early morning and late afternoon) when the available solar resource is much smaller than typical midday values and/or when SZAs are smaller. Because the minimum SZAs vary throughout the year (except close to the equator), the uncertainty in hemispherical radiation data will vary as well. This effect is especially important for latitudes beyond ±45°, when SZA is rarely greater than or equal to the SZA at which the responsivity of the pyranometer was determined.

Even when good measurement conditions exist, such as near midday under clear-sky conditions, the uncertainty in hemispherical field measurements is typically two to three times that of direct-beam measurements, or ±4%–±5% throughout a year, primarily because of seasonal variations in uncertainty. Better instrumentation design and careful applications of correction factors as a function of SZA are ways to improve (reduce) the uncertainty in GHI measurements. The alternative is to use high-quality DNI and DHI measurements using a tracking shading disk/ball to derive GHI from the closure equation (Michalsky et al. 1999). The expanded uncertainty for this calculated GHI then approaches that of DNI (±2%) for clear-sky measurements. One limitation of this method, however, is that it assumes “perfect” operating condition such as tracking for both DNI and DHI. Slight misalignment of tracking and complete tracker failures do happen in practice, and large errors in all three components result, unless they are properly detected during the quality control procedure—which is difficult in practice.

Figure 7-2 shows the calibration traceability for pyrheliometers used to measure DNI and for pyranometers used to measure GHI or DHI. The figure indicates how uncertainties accumulate from calibration to field deployment. Broad arrow boxes show the accumulated expanded uncertainty at each phase of the process. The resulting uncertainty in field deployment for pyrheliometers is ±2.0%–±2.5% in this example, assuming regular and high-quality maintenance. Measurement uncertainties for pyranometers used to measure GHI in the field range from ±3.0%–±5% for SZAs between 30° and 60° but are higher for angles greater than 60°, again assuming regular and high-quality maintenance.

Calibrations of pyranometers are normally performed on the horizontal (GHI) but can also be performed at tilt (GTI). Pyranometers measuring GHI are calibrated on the horizontal using either a reference GHI or from DNI and DHI measurements. Calibration of a tilted pyranometer is done using a reference pyranometer under the same tilt. Tilting a pyranometer for GTI measurements typically alters its responsivity because of, for example, changes in convection patterns inside the dome or changes in thermal offset. This typically affects the calibration

uncertainty of GTI measurements. Some thermopile pyranometers are not designed for tilted measurements, and at certain times of day, direct sunlight can strike their unshaded body, affecting measurements. Proper shielding of the instrument's body can reduce or eliminate this problem. To help evaluate the uncertainty in GTI data, the metadata of such data sets should include shielding information. This caveat also holds for the measurement of upwelling irradiance using a down-facing pyranometer. (This measurement is necessary to obtain the surface albedo by dividing it by GHI.)

The calibration and assessment of calibration and field uncertainties for pyrheliometers and pyranometers are described in detail in national and international standards, including the ASTM International G167-15,[38] ASTM E816-15,[39] ASTM E824 - 10(2018)e1,[40] ASTM G183-15,[41] ISO 9059,[42] ISO 9846,[43] and ISO 9847.[44]

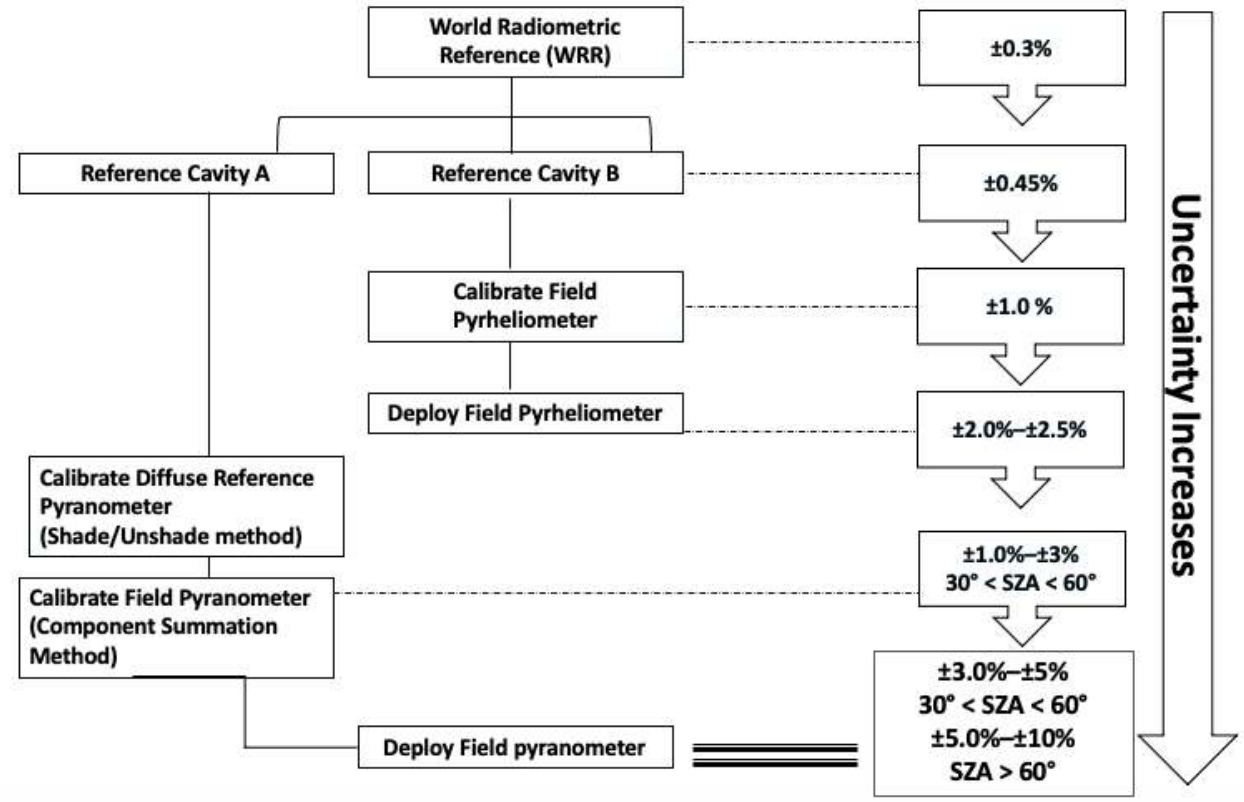

Figure 7-2. Calibration traceability and accumulation of measurement uncertainty for pyrheliometers and pyranometers (coverage factor *k* = 2). *Image by NREL*

[38] See https://www.astm.org/Standards/G167.htm.
[39] See https://www.astm.org/Standards/E816.htm.
[40] See https://www.astm.org/Standards/E824.htm.
[41] See https://www.astm.org/Standards/G183.htm.
[42] See https://www.iso.org/standard/16628.html?browse=tc.
[43] See https://www.iso.org/standard/17724.html?browse=tc.
[44] See https://www.iso.org/standard/17725.html?browse=tc.

7.3 Uncertainty Quantification of Solar Resource Estimates

Solar radiation can be modeled in many different ways, depending on the available inputs, origin (ground-based or satellite-based), application requirements (e.g., clear-sky or all-sky conditions), and degree of detail (broadband or spectral irradiance).

Satellite-based models estimating solar radiation can use a physics-based approach relying on radiative transfer modeling, an empirical or semiempirical approach relating the reflected radiance sensed by the satellite sensor directly to surface radiation, or a mix of both.

Models derived using empirical or semiempirical correlations between ground-based irradiance measurements and reflected radiance observations from satellite sensors inherently carry the uncertainty of all these measurements. This uncertainty is embedded in the ultimate model accuracy, along with the uncertainties associated with the satellite sensors and the modeling process. Models based on ground-based irradiance measurements with 2%, 5%, or 10% uncertainty cannot have a lower uncertainty than the data used to derive and/or validate the model. Similarly, models based on the first principles of physics and radiation transfer cannot be validated or verified to a level of accuracy greater than that of the ground-based irradiance measurements. A thoroughly documented uncertainty analysis of these measurements (Gueymard and Myers 2008b, 2009; Habte et al. 2016a; Vuilleumier et al. 2014) is necessary to ascertain the validity of model accuracy claims. The effect of biases in ground-based irradiance measurements should be part of any model analysis.

An understanding of the differences between the perspectives of satellite-derived irradiance values and ground-based measurements is essential when ground-based data are used to derive and validate satellite-derived irradiance values. Observations of a specific pixel (or grid cell) by a spaceborne radiometer ultimately provide (after substantial modeling) an estimate of surface radiation based on the estimated properties of those clouds and other atmospheric constituents spread throughout that pixel or a larger area. In contrast, surface irradiance observations are made by an instrument viewing the sky from a specific point. If the satellite pixel size is small enough, parallax errors enter into the comparison. Conversely, if it is too large, the radiation field over the pixel might not be homogenous enough for a correct comparison. Terrain effects could also influence a comparison in which cloudiness, elevation, and/or topographic shading could vary within a short distance. Often the data available for satellite modeling lack the exactitude for differentiating fine variations seen by ground-based measurements. This can be compounded by the fact that ground measurements represent an *average* irradiance value calculated over a fixed time interval (e.g., 1 min or 10 min), whereas satellite-based model predictions solely rely on *snapshots* (instantaneous observations) taken at different intervals (e.g., every 30 min).

7.4 Historical Uncertainty Quantification Approach of Solar Resource Estimates from Models

This section presents the historical uncertainty quantification approach of radiation models. This provides an overview of progress in satellite-based data quality. To alleviate the absence of any standardized method for accuracy assessment, many possible statistical metrics used in the literature have been reviewed (Gueymard 2014). Still, most authors report only the root-mean-square deviation and bias (absolute or relative). As an example, the model of Darnell et al. (1988) was used to evaluate surface radiation using cloud information from the International Satellite Cloud Climatology Project C1 cloud database. The results were then compared to surface observations collected by the World Radiation Data Center by Darnell and Staylor (1992). The root-mean-square error (RMSE) from this comparison was approximately 16 W m^{-2}, and the bias (also known as mean bias error,

MBE) was ≈4 W m^{-2}. Note that the interpretation of the reported source of uncertainties depends on the spatial and temporal resolution of the data being compared (random errors tend to decrease rapidly with increasing averaging period) and that the relative uncertainties in the modeled DNI are always greater than in GHI—opposite to what occurs with high-quality measurements.

According to Perez et al. (1987), satellite-based retrievals of hourly DNI were "accurate" to 10%–12%. Later, Renné et al. (1999) and Zelenka et al. (1999) found that the target-specific comparison to ground-based observations had a relative RMSE of at least 20%; the time-specific pixel-wide accuracy was 10%–12% on an hourly basis at the sites under scrutiny. Most uncertainties contain values that are proportional to the measured values (percentage), given that the measured values are within a certain range and specifications are related to a fixed value in W m^{-2}. The validation of satellite-based irradiance predictions is sometimes performed on a daily (instead of hourly or subhourly) timescale. This might not always be appropriate, particularly in areas where strong morning/afternoon cloudiness asymmetries exist (Salazar et al. 2019).

7.5 Current Uncertainty Quantification Approach of Solar Resource Estimates from Models

To improve modeled data integrity, a comprehensive representation of the model uncertainty method is required. The assessment of model uncertainty attempts to replicate the developments made for measurement uncertainty, as detailed in Section 7.1, with the caveat that an equivalent of the GUM, specifically addressing modeled estimates, does not exist yet. It is essential to use measurements of solar radiation made at ground stations from regions in various climates (or even microclimates) with the goal to perform a detailed evaluation of the modeled data set; however, measurements of solar radiation made at ground stations are temporally and spatially sparse, and they are expensive to operate and maintain. Further, to perform an accurate evaluation of the model's predictions, it is critical that these ground-based irradiance measurements be of high quality and rely on low-uncertainty radiometers that follow the best practices for collection, operation, maintenance, and quality assurance.

An important distinction between measurements and model estimates is that the latter actually include two separate sources of uncertainty, which in principle would need to be decoupled. These sources are (1) the intrinsic model's uncertainty (caused by inadequacies in the model's functions, which do not perfectly describe the physical radiation transport processes in the atmosphere) and (2) the error propagation uncertainty (caused by unavoidable imperfections in the model's inputs, which make their way to the model's outputs)]. The model *itself* is perfectly *repeatable*, but its inputs are not—all the more that a specific model can be used with different sets of inputs, depending on availability, location, period, model operator, etc. Additionally, the distinction introduced above clearly indicates that the term *model uncertainty* should not be confused with *prediction uncertainty* because the latter includes the two sources of uncertainty just described. (Hence, the prediction uncertainty is necessarily larger than the intrinsic model uncertainty.) Whereas the former can be evaluated using a reproducible theoretical approach (ideally by comparison with a "perfect" physical model), the latter is more difficult to establish.

The error propagation effects can be evaluated by analyzing the model's sensitivity to variations in its inputs (of supposedly known uncertainty), with an approach that has already been demonstrated for clear-sky radiation models (Gueymard 2003). In practice, however, the quality of irradiance predictions is evaluated against ground measurements that are not perfect and have uncertainty themselves, as discussed in Section 7.1. Hence, the prediction

uncertainty needs to take the measurement uncertainty into account, resulting in what could be called *effective prediction uncertainty*, which is necessarily larger than the raw prediction uncertainty just described. It is important to consider that the latter is not necessarily independent from the measurement uncertainty, which complicates the picture, as demonstrated by the following example. Suppose that the predictions from two models, M1 and M2, are compared against GHI measurements obtained with a high-quality pyranometer of assumed 5% uncertainty (from Section 7.1). Unbeknownst to the analyst, however, that specific instrument is incorrectly calibrated, resulting in a systematic bias of +3% in the measurements. Unbeknownst to the analyst as well, M1 and M2 behave the same in terms of introducing randomness in their outputs, but M1 happens to be perfectly centered (no bias), whereas M2 is biased +3% for the specific inputs used at that specific location. The comparison with ground measurements would lead the analyst to the incorrect conclusion that M2 is better than M1 and that the latter's uncertainty is larger than the former's.

Studies such as those by Habte, Sengupta, and Lopez (2017); Šúri and Cebecauer (2014); Wilcox (2012); Gueymard (2014); Thevenard and Pelland (2013); and Cebecauer, Perez, and Šúri (2011) discussed quantification methods aimed at a comprehensive representation of prediction uncertainty using different interpretations of the GUM method. Various error statistics (bias, random error metrics) can be used to evaluate the effective uncertainty of modeled data when also considering the uncertainty in the ground-based irradiance measurements.

In the absence of a specific standard for the evaluation of prediction uncertainty, the National Renewable Energy Laboratory (NREL) developed a way to include these sources and derive the uncertainty estimate for a 95% confidence interval representing two standard deviations (coverage factor of ≈2):

$$U_{95} = k * \sqrt{\left(\frac{U_{meas}}{k}\right)^2 + \left(\frac{bias}{k}\right)^2 + \left(\frac{\mathrm{RMSE}}{k}\right)^2} \tag{7-7}$$

where U_{meas} is the expanded (95% level of confidence) estimated uncertainty in ground-based irradiance measurements ("ground truth"), and both *bias* and RMSE are derived from the model's validation analyses. As described in Section 7.1.1, these three statistics are divided by k (≈2 assuming normal distribution). In this conservative approach, the resulting U_{95} might be pessimistic because RMSE includes the bias error, which is thus counted twice; therefore, the authors of this handbook are investigating to find statistic metrics that assist in quantifying the overall uncertainty, which they will report in the next edition.

Habte, Sengupta, and Lopez (2017) determined the method of estimating the overall uncertainty of the modeled irradiance data in the National Solar Radiation Database (NSRDB) Physical Solar Model (PSM) Version 2 (1998–2015). This method was applicable for hourly averages, daily totals, monthly means of daily totals, and annual differences. Varying the time interval helps capture the temporal uncertainty of the specific modeled solar resource data required for each phase of a solar energy project. For instance, the annual (or seasonal) data uncertainty estimate is important for financial analysts during the conceptual phase of a project, whereas the uncertainty in hourly data is essential during the engineering design phase and due-diligence studies. Using the same method, Figure 7-3 shows the overall uncertainty of the NSRDB PSM Version 3 (1998–2017).

As shown in Figure 7-3, an uncertainty of 5% was assumed for the measurements (red dashed line) and kept constant throughout the averaging time because, for radiometers, the main source of uncertainty does not normally change with averaging time (Habte, Sengupta, and Lopez 2017; Reda 2011); however, one can substitute the estimated 5% with any other measurement uncertainty value that would be specifically determined using the GUM method. It is also essential to estimate any possible systematic bias in the measurements

because this would directly affect the model validation process, as discussed above. Systematic biases can be caused by the lack of repeatability of a radiometer, calibration error, data logger issues, etc. Such systematic errors are assumed negligible in the following results.

The relative GHI bias and RMSE associated with Figure 7-3 are shown in Figure 7-4. It is obvious that both bias and RMSE might vary depending on the radiative climate of the location, among other factors.

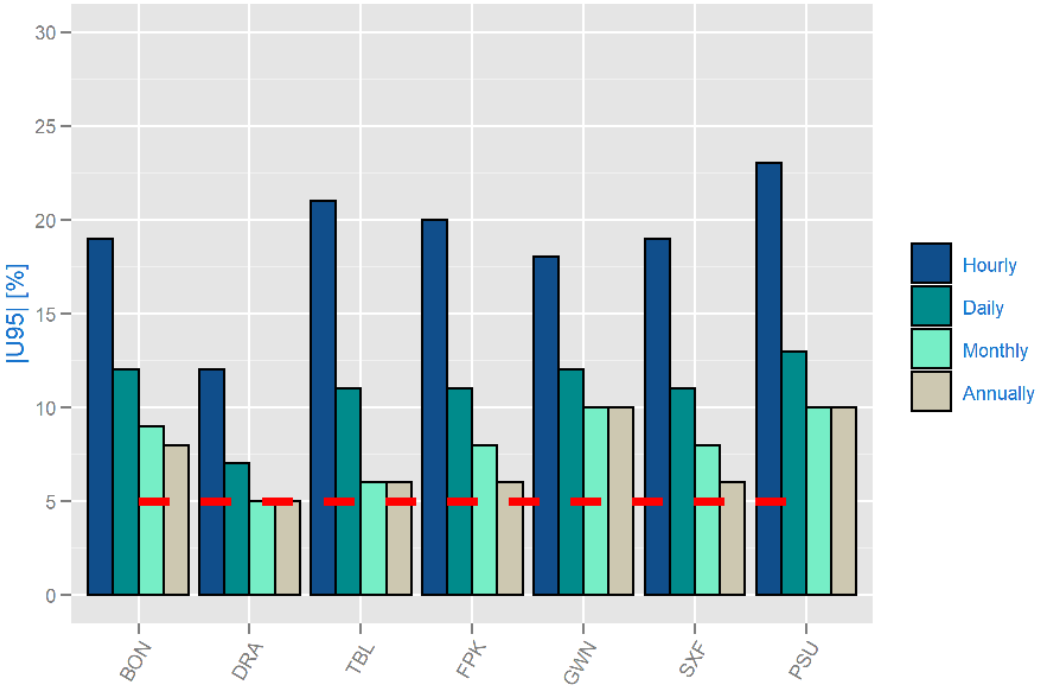

Figure 7-3. Overall uncertainty estimation at the 95% confidence interval (CI; *k*≈2) for the modeled GHI for NSRDB PSM Version 3 and under various time averages at seven NOAA SURFRAD locations. The Version 3 data used in this figure are from 1998–2017. Note: The red dashed line is the assumed uncertainty in the measurement data. *Image by NREL*

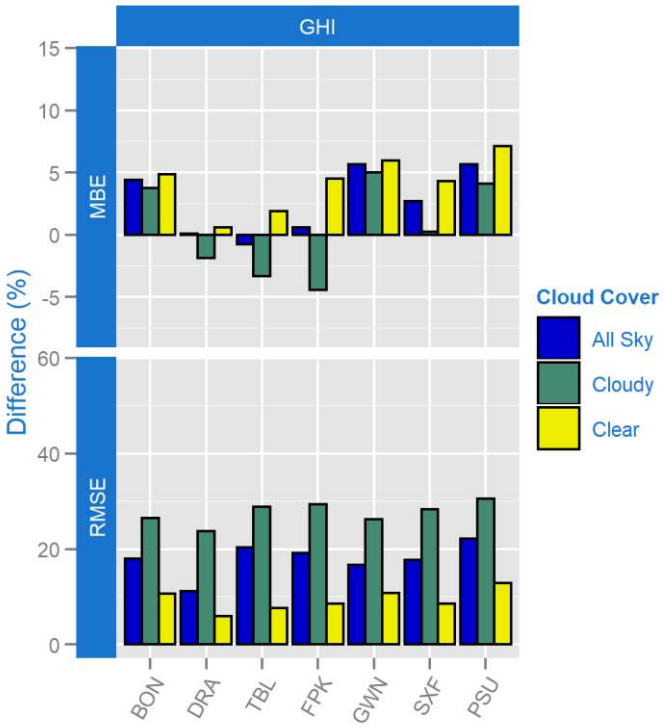

Figure 7-4. (Top) Relative GHI bias and (bottom) RMSE comparison results of hourly modeled data from the NSRDB PSM Version 3 (1998–2017) relative to irradiance measurements made at seven stations from the NOAA SURFRAD network

In contrast with NREL's Eq. 7-7, Solargis implemented a slightly different approach to determine uncertainty in their satellite-derived data sets by incorporating the model uncertainty, the uncertainty of the ground-based irradiance measurements, and the interannual irradiance variability:

$$u_{\text{combined}} = \pm\sqrt{(U_{meas})^2 + (U_{model})^2 + (U_{interannual\ variability})^2} \tag{7-8}$$

The annual solar resource is thus allowed to vary from the long-term averages. A detailed discussion about the relative importance of these uncertainties is provided in Cebecauer, Perez, and Šúri (2011).

Following Gueymard and Wilcox (2011), Habte, Sengupta, and Lopez (2017) formalized an interannual variability metric as follows:

$$\text{SD} = \sqrt{\left(\frac{1}{n}\sum_{i=1}^{n}\ (a_i - \hat{a})^2\right)} \tag{7-9}$$

$$U_{inter-annual\ variability}(\%) = \text{COV}(\%) = \frac{\text{SD}}{\hat{a}} * 100 \tag{7-10}$$

where SD is the standard deviation, and a_i is the average irradiance of the *i*th year of the considered period of *n* years. The mean irradiance during the selected long-term period is represented by â.

In parallel, the accuracy of satellite-derived modeled data can be determined using various other statistical indicators, such as the mean absolute error or the Kolmogorov-Smirnov test (Massey 1951). The Kolmogorov-Smirnov test is a rigorous nonparametric method that is used for benchmarking satellite-retrieved GHI and DNI against ground-based observations (Espinar et al. 2009; Gueymard 2014). Many methods are described in Beyer et al. (2009),

such as the Kolmogorov-Smirnov integral (KSI), which calculates the area differences between two Cumulative Distribution Frequencies to determine the deviation, for example, between satellite-derived data and ground measurement data. Another is the OVER method, which assimilates the original KSI and attempts to find values that are above a critical value. Unlike MBE and RMSE, OVER provides a relative frequency of exceedance situations when the normalized distribution of predictions exceeds the critical limit that would make it statistically undistinguishable from the reference distribution (Gueymard 2014). This test has the advantage of being nonparametric and is therefore not distribution dependent. It compares the two distributions of irradiance to evaluate their resemblance. In the future, it can be expected that more elaborate methods, such as those used in the meteorological community to quantify the performance of weather forecasts (Murphy 1993), will be adopted more often in large-scale solar resource assessment studies.

7.6 Modeled Data Uncertainty Estimation Challenges

Satellite-derived irradiance data sets have various embedded sources of uncertainty (Cebecauer, Perez, and Šúri 2011; Cebecauer, Šúri, and Gueymard 2011; Perez, Cebecauer, and Šúri 2013). Most importantly, irradiance values obtained from satellite-based models use satellite observations of clouds. The satellite pixel represents a certain area, typically 1–100 km^2. Depending on that size, some subpixel variability and cloud-induced parallax effects could contribute to higher random errors in both GHI and DNI, as suggested by previous studies, e.g., Habte, Sengupta, and Lopez (2017); Cebecauer, Perez, and Šúri (2011); and Zelenka et al. (1999). In intermittent cloud situations, the resolution of satellite images has limited ability to adequately describe properties of small and scattered clouds. This problem can be exacerbated when a physical retrieval method is used to first characterize the cloud optical properties for a given pixel, which can result in actual partly cloudy periods being classified as cloudless, thus yielding significant positive bias in DNI, for instance (Salazar et al. 2019).

In tropical rainforest climates, it is often challenging to find cloudless situations for characterizing the surface albedo, which is often used as a reference based on which the pixel's overall cloudiness characteristics can be eventually quantified. For geostationary satellites at high latitudes, the low satellite viewing angles introduce errors in the detection of cloud position and properties (the satellite sensor most often sees clouds from the side rather than from the top). For intermittent cloud situations, the major part of the observed random errors (evaluated by RMSE statistics) is driven by inadequacies in the cloud-related portions of the radiative transfer algorithms.

Adequate specification of aerosols is another area of concern (Cebecauer, Šúri, and Gueymard 2011). Aerosols tend to affect DNI three to four times more than GHI, depending on the relative proportions of absorption and scattering for the specific aerosol mixture of the moment and location (Gueymard 2012). For example, mineral dust is mostly scattering, whereas black carbon is partly absorbing. At any instant, the aerosol optical depth (AOD) varies spectrally, so the common use of a single broadband AOD could result in additional uncertainties. (See Section 5.5 in Chapter 5 for more information on AOD.) When monthly (or "climatological") AOD averages are used, they could introduce significant errors in long-term DNI estimates (Ruiz-Arias et al. 2016). This is more likely to happen over areas of biomass burning, urban air pollution, and dust storms, where an aerosol climatology tends to smooth out episodic high-AOD events; therefore, it is advantageous to use AOD data with daily or subdaily resolution in advanced modeling approaches (Cebecauer, Šúri, and Gueymard 2011; Gueymard, Habte, and Sengupta 2018).

In regions with variable or complex landscape patterns (e.g., high spatial variability caused by land/water mosaics, complex urbanization, or mountains), the surface reflectance

properties change rapidly, both over the space and time domains and even over distances that are shorter than the satellite's spatial resolution. (See Chapter 5, Section 5.11, for more information on this topic.) Compared to neighboring rural or natural landscapes, large urban or industrial areas have much higher and temporarily changing concentrations of aerosols and water vapor. Over mountains, rapid changes in elevation also induce rapid changes in the concentration of key atmospheric constituents and in cloud properties. In addition, 3D effects and terrain shading are local complexities that need to be considered and approximated by the solar radiation models.

Another difficulty inherent to satellite-derived data sets is the poor discrimination between clouds and snow-covered surfaces when using only the visible imagery. This is because both situations have a high reflectance in the visible spectrum; hence, a clear-sky scene over snowy ground might look like an overcast sky, resulting in a strong overestimation or underestimation of both GHI and DNI, depending on the situation (Vignola and Perez 2002; Perez et al. 2002). One such adverse situation is known as the "Eugene syndrome" (Gueymard and Wilcox 2011). The use of multiple channels in the visible and infrared can solve this issue.

Finally, specular reflections of significant intensity, especially from sandy deserts or snowy/icy surfaces during certain times of the day, could result in interpreting the satellite image as temporarily cloudy and thus in an underestimation of both GHI and DNI. Theoretically, this issue can be resolved by estimating the probability of specular reflection for such areas and factoring that into the calculation of surface radiation.

7.6.1 Indicative Uncertainty of Modern Satellite-Based Models

As an example, experience based on more than 200 validation sites shows that state-of the-art semiempirical satellite models can estimate the annual GHI with bias ranging from ±4% when normalized to daytime irradiation (Cebecauer and Šúri 2012). This bias value depends on topography and climate. It can be higher (up to at least ±8%) in complex tropical regions; in areas with high atmospheric pollution, high latitudes, high mountains, and complex terrain; and in regions with low sun angles and the occurrence of snow. Typical bias for DNI estimates at a specific site is approximately twice that of GHI.

Regarding random errors, the main sources of increased uncertainty are clouds and, to a lesser extent, changes in snow cover and increased dynamics of aerosols. Over arid and semiarid areas or during sunny seasons, the RMSE of hourly GHI values normally range from 7%–20%. In more cloudy regions with more intricate weather patterns, higher dynamics of atmospheric constituents, complex landscapes, or middle latitudes, the hourly RMSE increases to 15%–30%. Over high mountains, high latitudes, or during seasons with low sun angles and frequent occurrences of snow, the relative RMSE for GHI can be 25%–35% or more. Similar patterns of RMSE exist for the hourly DNI but with approximately twice the errors mentioned for GHI. In arid and semiarid zones, which are of the highest interest for concentrating solar energy technologies, RMSE for the hourly DNI ranging from 18%–30% is typical. In more cloudy regions, with significant dynamics exhibited by aerosols, RMSE can reach 25%–45%. Finally, at high latitudes and over mountains, RMSE could exceed 45%.

With continuous progress in satellite sensors and radiation models, it can be expected that the accuracy in satellite-derived databases will continue to improve, as suggested by recent validation results (Babar, Gaversen, and Boström 2018, 2019; Bright 2019; Kamath and Srinivasan 2020; Shi et al. 2018; Urraca et al. 2018). In Urraca et al. (2017), satellite data are used to test ground measurements using the positive-quality aspects of satellite-based irradiance data.

7.7 Methods of Automated Data Quality Evaluation

Data quality assessment is a method by which data quality can be judged based on criteria for a particular application. Several particular errors of meteorological data can be detected by automatic screening algorithms. Corresponding tests for radiation data are documented in a number of publications, including Espinar et al. (2011); Journée and Bertrand (2011); Long and Shi (2008); Longman, Giambelluca, and Nulle 2013; Maxwell, Wilcox, and Rymes (1993); Perez-Astudillo, Bachour, and Pomares (2016); Urraca et al. (2017); and Wilcox and McCormack (2011). Auxiliary data of direct interest can also be tested, as explained in Geuder et al. (2015). The main parameters discussed there are data logger and battery voltage; logger temperature; speed of ventilation units; and meteorological measurands, such as wind speed and pressure. Data can be compared to certain physical limits that have been determined to be reasonable, with redundant or complementary measurements, or with physical or empirical models—all of which will provide some degree of independent measure for a quality judgment.

Moreover, one common method for evaluating the quality of DNI, GHI, and DHI is a three-component closure test. The measurements of DNI and DHI can be combined mathematically to derive GHI, as described in Eq. 2-2a. When all three components are measured, measurement redundancy is apparent because any one component can be derived from the other two; hence, in the context of quality assurance, the expected values of each component can be calculated from any other two. This method helps quantify the relative deviation among the three components, although it does not automatically determine strictly which specific measurement—or measurements—increases the deviation. Even though one, two, or all three value(s) could be responsible for the mismatch, the magnitude of the mismatch could indicate the presence of a problem in the data. Moreover, operational knowledge of the instruments and trackers can provide valuable insight into likely problems. A frequent problem is caused by malfunction of the tracker. If the pyrheliometer does not point at the sun, DNI is ≈0 and DHI≈GHI. This situation could last for hours and can be incorrectly interpreted as the signature of an overcast sky. Similarly, a slightly misaligned tracker would cause a too low DNI and too high DHI. With this information, combined with the visual detection of trends in the magnitude of flagging, a data quality expert can quickly spot common operational problems. For example, one can visually inspect the data by plotting the difference between the measured and derived GHI as a function of SZA. Any deviation from the true cosine response of the pyranometer would become apparent and would be cause for concern. Based on this discussion, it is clear that the *independent* measurement of the three redundant components is a significant and important tool for data quality analysis, which should be strongly considered when specifying instrumentation for a station.[45]

The three-component method is generally more reliable than a simple clear-sky data analysis in which some conclusions are drawn based on modeled or other expected values of clear-sky data. Significant day-to-day variations in clear-sky data can occur because of variations in atmospheric constituents, such as aerosols or water vapor; thus, such natural variations can make it difficult to draw conclusions about possible instrument problems without specific information regarding other critical atmospheric components.

The following sections summarize two methods of automated quality checks for solar measurement data. In addition to the quality-control checks described here, partly similar

[45] Note that even though RSIs provide three components, they measure only two of them per se—hence preventing them access to this procedure.

checks must be applied during the data acquisition of measured radiation data. These checks are described in Chapter 3, Section 3.4.2.

There are many other data quality-control and assessment methods as well, such as the Baseline Surface Radiation Network (BSRN), Management and Exploitation of Solar Resource Knowledge (MESOR), ENergy DOwnstReam Services (ENDORSE), Meteorological Data Management System (MDMS), and Copernicus Atmosphere Monitoring System (CAMS). It is anticipated that the next editions of this handbook will include detailed discussions of these and other methods.

7.7.1 SERI QC

The SERI QC software package was developed by the Solar Energy Research Institute (SERI, now NREL) to address the need for performing quality assessment on large sets of solar measurement data (Maxwell, Wilcox, and Rymes 1993). SERI QC and associated programs are available from https://www.osti.gov/biblio/1231498-seri-qc-solar-data-quality-assessment-software.

At the time of development, in the late 1980s, measured solar data were not common, although some entities recognized the need for conducting solar resource assessments, and some significant measurement programs were underway. SERI QC was developed largely using hourly measurement data from the SOLMET network established by the U.S. National Weather Service and the National Oceanic and Atmospheric Administration (NOAA). SOLMET data were collected with an hourly time step, and other smaller data sets of 5-minute and 1-minute time steps were also used during the SERI QC development.

SERI QC was envisioned to provide data quality assessment for one-, two-, or three-component solar data with time resolutions from 1 minute to 1 hour. That software is not a stand-alone program but rather a function in the C programming language (and earlier, the Fortran language) that evaluates only one record of data at a single point in time (e.g., a single set of one-, two- or three-component measurements). The function is provided for users to write an analytic program that ingests the data, calls the SERI QC function, and then reports or otherwise uses the flags returned from the function. The SERI QC software package includes a sample program and a benchmarking data file.

For three-component data, SERI QC performs the three-component closure test in the realm of normalized indices (i.e., K_t, K_n, and K_d). This analysis is performed in K-space to remove the SZA effect. Thus, in K-space, Eq. 2-2a translates into:

$$K_t = K_n + K_d \tag{7-11}$$

Or, rearranged, the deviation from this equation of component closure can be quantified as the residual error and represented by:

$$\mathcal{E} = K_t - K_n - K_d \tag{7-12}$$

Perfect component closure would result in $K_t - K_n - K_d = 0$; hence, any nonzero value indicates some disagreement among the instruments, and a flag is assigned based on the magnitude of the disagreement. This method does not reveal which component or components have problems, however; it reveals only that there is some disagreement. Further, compensations of random deviations or systematic biases can result in a “false” zero value. This is the case when, for instance, the tracker is completely misaligned.

To achieve a quality test for two-component data, a scheme was developed to exploit the relationship between K_n and K_t. The two values are not independent; in fact, they correlate to some degree because K_n is a subset of K_t (Eq. 7-11). Figure 7-5 shows this relationship by plotting K_n against K_t. For every value of K_t (x axis), there exists a range of valid values for K_n

(y axis). This scheme significantly narrows the range of valid combinations of K_t and K_n. (In the figure, three subsets of data are evaluated based on air mass.) When two measured components include K_d rather than either K_t or K_n, the missing value is calculated for this K_t-K_n analysis using Eq. 7-11.

Thus, by determining the range boundaries on the relationship, *which is site specific*, suspect data can be identified, although not with the same precision as three-component closure, where there is only one zero-residual solution to the equation.

The SERI QC package includes a stand-alone executable for the Windows operating system called QCFIT (Figure 7-5), which uses historic data from a site to fit the bounds on expected values for two-component data. The QCFIT program also includes various analytic capabilities to investigate errant or anomalous data.

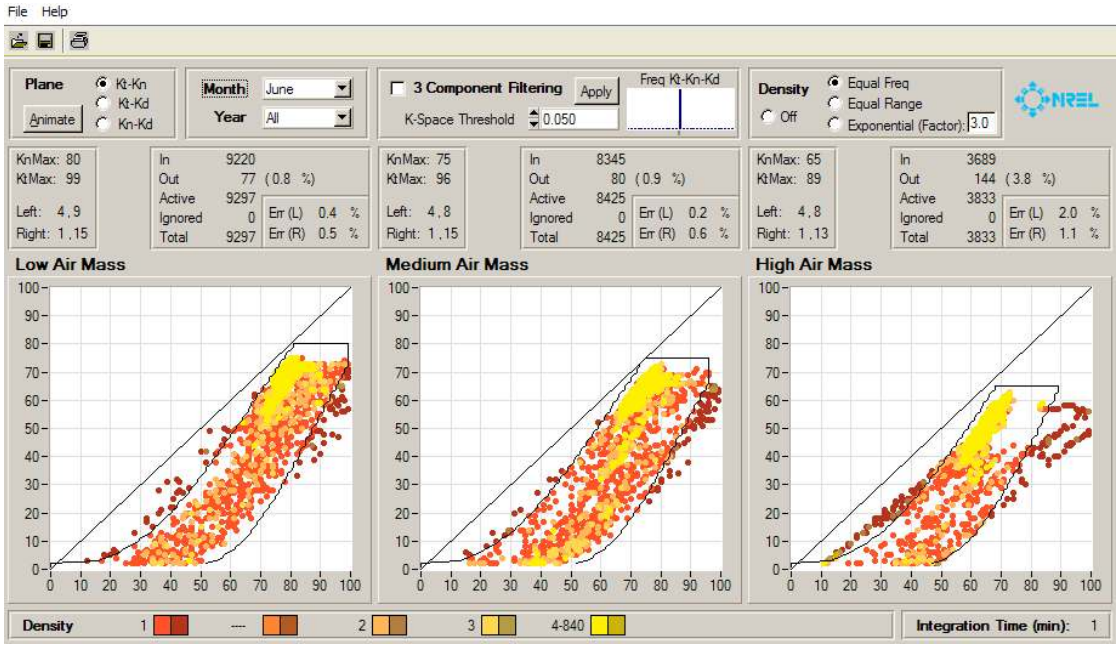

Figure 7-5. Display from QCFIT program to aid in the setting boundaries for SERI QC.
Image from NREL

SERI QC can also perform rudimentary quality checks on one-component data by virtue of maximum and minimum limits set according to historical data.

The SERI QC flagging scheme provides information about the magnitude of the error, the direction of the error (high or low), and what test (one-, two-, or three-component) produced the flag. With this information, a program that calls the SERI QC function can generate a report with enough information for an expert, or data quality analyst, to formulate a likely failure mode in the equipment (Wilcox and McCormack, 2011). Figure 7-6 shows SERI QC flags in the leftmost panel in gradation by severity from dark blue (low error) to red (high error). Plots have hour of day on the x-axis and day of month on the y-axis, allowing for an inspection of an entire month of data. The right three panels show the corresponding *K*-space solar values for global (K_t), direct (K_n), and diffuse (K_d) to aid in identifying periods corresponding with the flags.

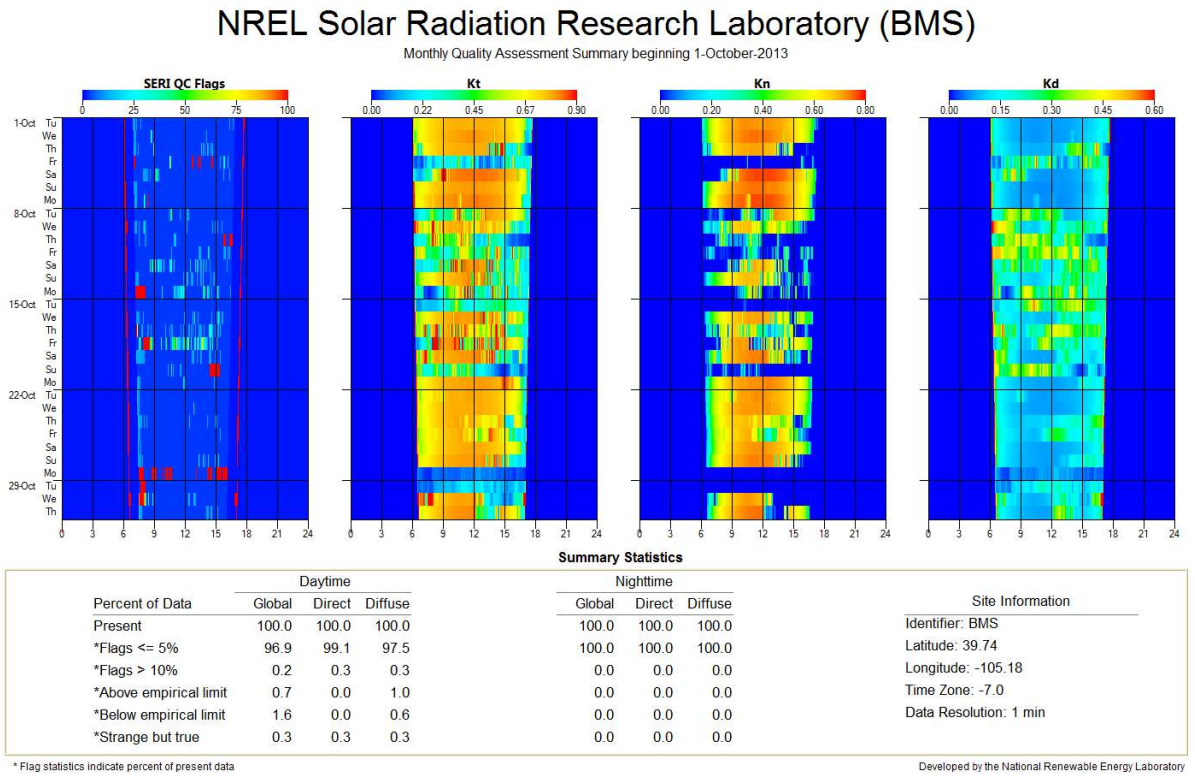

Figure 7-6. Example of data quality-assurance reporting using SERI-QC flags. *Image by NREL*

7.7.2 QCRad

The QCRad data quality software (Long and Shi 2006, 2008) aids the data quality assessment of large amounts of solar data from the U.S. Department of Energy's Atmospheric Radiation Measurement (ARM) program. The measurements support climate research, and in addition to a comprehensive complement of meteorological parameters, they include a superset of radiation measurements beyond those typically used in renewable energy solar resource assessment. With many other collocated measurements available, the method can establish more refined physical limits for measurements. In some cases, the results provide diagnostics beyond the ambiguous results from the three-component closure test described above (which cannot determine the exact cause of disagreement).

QCRad uses surface climate analyses and historic data to establish the probable maximum and minimum limits on a measurement. These tests include limits established for quality checks for the BSRN data (Long and Dutton 2002), and other tests rely on site-specific parameters that can be fine-tuned for each station. Each measurement might undergo a series of preliminary tests before being used in a multiple-parameter test. Different limits for GHI are established based on historical preponderance, physically possible, and a modeled clear-sky value. The diffuse measurement (DIF in ARM nomenclature) is checked for values less than theoretical limits, and if necessary, a correction is applied to both the diffuse and global measurements. If these and other tests are passed, then QCRad applies a modified three-component closure test. Using Eq. 7-11 to calculate $K_t = K_n + K_d$, the K_t derived from the global measurement is ratioed with the calculated K_t. A ratio of 1.0 represents perfect agreement among the instruments, and any other value indicates some disagreement. Long and Shi (2008) established boundaries for that closure ratio.

Some tests comparing global and diffuse can give information indicating the likelihood of a tracker failure that allows part or all the direct beam component to bypass the diffuse

shading apparatus and irradiate the diffuse instrument. Moreover, a few tests typically require a preliminary climatological analysis to establish the site-dependent coefficients to define reasonable limits and to identify incorrect and/or suspect reading.

QCRad can be run at the end of each day. The program scans the whole daily time series and makes adjustments to the initial clear-sky irradiance estimates to account for the specific atmospheric conditions of that day. ARM runs QCRad in a batch processing mode on a daily interval once the complete data set is available from the previous day. Many QCRad tests produce two-tiered flag results, providing not only a qualification of severity but also in some cases an indication of high or low values. In the ARM processes, the flags are used to generate reports for the entire network, allowing an analyst to quickly scan the results and direct attention to stations with malfunctioning equipment. Other reports with a longer timescale can be used to identify errors from instrument drift or other slowly developing failure conditions.

QCRad is not available by software distribution, but the algorithms and inputs are summarized in Long and Shi (2006, 2008).

7.8 References

ASTM International. 2015a. ASTM E816-15 - Standard Test Method for Calibration of Pyrheliometers by Comparison to Reference Pyrheliometers. West Conshohocken, PA. www.astm.org.

———. 2015b. ASTM G167-15 - Standard Test Method for Calibration of a Pyranometer Using a Pyrheliometer. West Conshohocken, PA. www.astm.org.

———. 2015c. ASTM G183-15 - Standard Practice for Field Use of Pyranometers, Pyrheliometers and UV Radiometers. West Conshohocken, PA. www.astm.org.

———. 2017. ASTM G213-17 - Standard Guide for Evaluating Uncertainty in Calibration and Field Measurements of Broadband Irradiance with Pyranometers and Pyrheliometers. West Conshohocken, PA. www.astm.org.

———. 2018. ASTM E824-10(2018)e1 - Standard Test Method for Transfer of Calibration From Reference to Field Radiometers. West Conshohocken, PA. www.astm.org.

Babar, B., R. Graversen, and T. Boström. 2018. “Evaluating CM-SAF Solar Radiation CLARA-A1 and CLARA-A2 Datasets in Scandinavia.” Solar Energy 170: 76–85.

———. 2019. “Solar Radiation Estimation at High Latitudes: Assessment of the CMSAF Databases, ASR and ERA5.” Solar Energy 182: 397–411.

Beyer, H. G., J. Polo Martinez, M. Šúri, J. L. Torres, E. Lorenz, S. C. Müller, C. Hoyer-Klick, and P. Ineichen. 2009. D 1.1. 3 Report on Benchmarking of Radiation Products (Technical Report 038665). Management and Exploitation of Solar Resource Knowledge. http://www.mesor.org/docs/MESoR_Benchmarking_of_radiation_products.pdf.

Bright, J. M. 2019. “Solcast: Validation of a Satellite-Derived Solar Irradiance Dataset.” Solar Energy 189: 435–49.

Cebecauer T., R. Perez, and M. Šúri. 2011. “Comparing Performance of Solargis and SUNY Satellite Models Using Monthly and Daily Aerosol Data.” Proceedings of the ISES Solar World Congress, Kassel, Germany.

Cebecauer, T., M. Šúri, and C. A. Gueymard. 2011. “Uncertainty Sources in Satellite-Derived Direct Normal Irradiance: How Can Prediction Accuracy Be Improved Globally?” Proceedings of the SolarPACES Conference.

Darnell, W. L., and W. F. Staylor. 1992. "Seasonal Variation of Surface Radiation Budget Derived From International Satellite Cloud Climatology Project C1 Data." Journal of Geophysical Research 97 (15): 741–60.

Darnell, W. L., W. F. Staylor, S. K. Gupta, and M. Denn. 1988. "Estimation of Surface Insolation Using Sun-Synchronous Satellite Data." Journal of Climate 1: 820–35.

Espinar, B., L. Ramirez, A. Drews, H. G. Beyer, L. F. Zarzalejo, J. Polo, and L. Martin. 2009. "Analysis of Different Error Parameters Applied to Solar Radiation Data from Satellite and German Radiometric Stations." Solar Energy 83 (1): 118–25.

Espinar, B., L. Wald, P. Blanc, C. Hoyer-Klick, M. Schroedter-Homscheidt, and T. Wanderer. 2011. Project ENDORSE—Excerpt of the Report on the Harmonization and Qualification of Meteorological Data: Procedures for Quality Check of Meteorological Data (hal-01493608, D3.2). Paris, France: MINES ParisTech.

Finsterle, W. 2011. WMO International Pyrheliometer Comparison: IPC-XI 27 Sept.–15 Oct. 2010 (Rep. WMO IOM No. 108). Davos, Switzerland: World Meteorological Organization.

Geuder, N., F. Wolfertstetter, S. Wilbert, D. Schüler, R. Affolter, B. Kraas, E. Lüpfert, and B. Espinar. 2015. "Screening and Flagging of Solar Irradiation and Ancillary Meteorological Data." Energy Procedia 69 (0): 1989–98. https://doi.org/10.1016/j.egypro.2015.03.205.

Gueymard, C. A. 2003. "Direct Solar Transmittance and Irradiance Predictions with Broadband Models. Part II: Validation with High-Quality Measurements." Solar Energy 74: 381–95. Corrigendum, Solar Energy 76: 515 (2004).

———. 2012. "Temporal Variability in Direct and Global Irradiance at Various Timescales as Affected by Aerosols." Solar Energy 86: 3544–53.

———. 2014. "A Review of Validation Methodologies and Statistical Performance Indicators for Modeled Solar Radiation Data: Towards a Better Bankability of Solar Projects." Renewable and Sustainable Energy Reviews 39: 1024–34.

Gueymard, C. A., A. Habte, and M. Sengupta. 2018. "Reducing Uncertainties in Large-Scale Solar Resource Data: The Impact of Aerosols." IEEE Journal of Photovoltaics 8 (6): 1732–37. https://doi.org/10.1109/JPHOTOV.2018.2869554.

Gueymard, C. A., and D. R. Myers. 2008a. "Solar Radiation Measurement: Progress in Radiometry for Improved Modeling." In Modeling Solar radiation at the Earth Surface, edited by V. Badescu, 1–27. Springer.

———. 2008b. "Validation and Ranking Methodologies for Solar Radiation Models." In Modeling Solar Radiation at the Earth Surface, edited by V. Badescu, 479–509. Springer.

———. 2009. "Evaluation of Conventional and High-Performance Routine Solar Radiation Measurements for Improved Solar Resource, Climatological Trends, and Radiative Modeling." Solar Energy 83: 171–85.

Gueymard, C. A., and S. M. Wilcox. 2011. "Assessment of Spatial and Temporal Variability in the U.S. Solar Resource from Radiometric Measurements and Predictions From Models Using Ground-Based or Satellite Data." Solar Energy 85: 1068–84.

Habte, A., M. Sengupta, A. Andreas, I. Reda, and J. Robinson. 2016b. "The Impact of Indoor and Outdoor Radiometer Calibration on Solar Measurements" (NREL/PO-5D00-66668). Proceedings of the European Photovoltaic Solar Energy Conference and Exhibition, Munich, Germany, June 20–24, 2016. http://www.nrel.gov/docs/fy17osti/66668.pdf.

Habte, A., M. Sengupta, A. Andreas, S. Wilcox, and T. Stoffel. 2016a. "Intercomparison of 51 Radiometers for Determining Global Horizontal Irradiance and Direct Normal Irradiance Measurements." Solar Energy 133: 372–93.

Habte, A., M. Sengupta, and A. Lopez. 2017. *Evaluation of the National Solar Radiation Database (NSRDB): 1998–2015* (NREL/TP-5D00-67722). Golden, CO: National Renewable Energy Laboratory. http://www.nrel.gov/docs/fy17osti/67722.pdf.

Habte, A., M. Sengupta, I. Reda, A. Andreas, and J. Konings. 2014. "Calibration and Measurement Uncertainty Estimation of Radiometric Data." Proceedings of Solar 2014 Conference, San Francisco, California, American Solar Energy Society.

International Organization for Standardization (ISO). 2008. ISO/IEC Guide 98-3:2008(E): Uncertainty of measurement – Part 3: Guide to the expression of uncertainty in measurement (GUM: 1995). Geneva, Switzerland.

———. 1990. ISO 9059:1990: Calibration of Field Pyrheliometers by Comparison to a Reference Pyrheliometer. Geneva, Switzerland.

———. 1992. ISO 9847: 1992 (E): Solar Energy—Calibration of Field Pyranometers by Comparison to a Reference Pyranometer. Geneva, Switzerland; 20 pp.

———. 1993. ISO 9846: 1993(E): Solar Energy—Calibration of a Pyranometer Using a Pyrheliometer. Geneva, Switzerland; 24 pp.

Journée, M., and C. Bertrand. 2011. "Quality Control of Solar Radiation Data within the RMIB Solar Measurements Network." Solar Energy 85: 72–86.

Kamath, H. G., and J. Srinivasan. 2020. "Validation of Global Irradiance Derived from INSAT-3D over India." Solar Energy 202: 45–54.

Konings, J., and A. Habte. 2016. "Uncertainty Evaluation of Measurements with Pyranometers and Pyrheliometers." Proceedings of SWC 2015: ISES Solar World Congress, Daegu, Korea. https://proceedings.ises.org/paper/swc2015/swc2015-0030-Konings.pdf.

Long, C. N., and E. G. Dutton. 2002. "BSRN Global Network recommended QCtests, V2.0." Baseline Surface Radiation Network. https://bsrn.awi.de/fileadmin/user_upload/bsrn.awi.de/Publications/BSRN_recommended_QC_tests_V2.pdf.

Long, C. N., and Y. Shi. 2006. The QCRad Value Added Product: Surface Radiation Measurement Quality Control Testing, Including Climatology Configurable Limits (Rep. DOE/SC-ARM/TR-074). Washington, D.C.: U.S. Department of Energy. https://www.osti.gov/servlets/purl/1019540.

———. 2008. "An Automated Quality Assessment and Control Algorithm for Surface Radiation Measurements." The Open Atmospheric Science Journal 2: 23–37.

Longman, R. J., T. W. Giambelluca, and M. A. Nulle. 2013. "Use of a Clear-Day Solar Radiation Model to Homogenize Solar Radiation Measurements in Hawai'i." Solar Energy 91: 102–10.

Massey, F. J. 1951. "The Kolmogorov-Smirnov Test of Goodness of Fit." Journal of the American Statistical Association 46: 68–78.

Maxwell, E., S. Wilcox, and M. Rymes. 1993. Users Manual for SERI_QC Software: Assessing the Quality of Solar Radiation Data (NREL/TP-463-5608). Golden, CO: National Renewable Energy Laboratory. https://www.nrel.gov/docs/legosti/old/5608.pdf.

Michalsky, J., E. Dutton, M. Rubes, D. Nelson, T. Stoffel, M. Wesley, M. Splitt, and J. DeLuisi. 1999. "Optimal Measurement of Surface Shortwave Irradiance Using Current Instrumentation." Journal of Atmospheric and Oceanic Technology 16: 55–69.

Michalsky, J., E. G. Dutton, D. Nelson, J. Wendell, S. Wilcox, A. Andreas, P. Gotseff, D. Myers, I. Reda, T. Stoffel, K. Behrens, T. Carlund, W. Finsterle, and D. Halliwell. 2011. "An Extensive Comparison of Commercial Pyrheliometers under a Wide Range of Routine Observing Conditions." Journal of Atmospheric and Oceanic Technology 28: 752–66.

Murphy, A. H. 1993. "What Is a Good Forecast? An Essay on the Nature of Goodness in Weather Forecasting." Weather Forecasting 8: 281–93. https://doi.org/10.1175/1520-0434(1993)008<0281:WIAGFA>2.0.CO;2.

Myers, D. R., T. L. Stoffel, S. Wilcox, I. Reda, and A. Andreas. 2002. "Recent Progress in Reducing the Uncertainty in and Improving Pyranometer Calibrations." Journal of Solar Energy Engineering 124: 44–50.

Perez, R., P. Ineichen, K. Moore, M. Kmiecik, C. Chain, R. George, and F. Vignola, 2002. "A New Operational Model for Satellite-Derived Irradiances Description and Validation." Solar Energy 73: 307–17.

Perez, R., R. Seals, P. Ineichen, P. Stewart, and D. Menicucci. 1987. "A New Simplified Version of the Perez Diffuse Irradiance Model for Tilted Surfaces: Description Performance Validation." Solar Energy 39: 221–32.

Perez, R., T. Cebecauer, and M. Šúri. 2013. "Semi-Empirical Satellite Models." In Solar Energy Forecasting and Resource Assessment, edited by J. Kleissl J. Academic Press.

Perez-Astudillo, D., D. Bachour, and L. M. Pomares. 2016. "Improved Quality Control Protocols on Solar Radiation Measurements." Proceedings of the Eurosun 2016 Conference, Palma de Mallorca, Spain, International Solar Energy Society.

Reda, I. 2011. Method to Calculate Uncertainties in Measuring Shortwave Solar Irradiance Using Thermopile and Semiconductor Solar Radiometers (NREL/TP-3B10-52194). Golden, CO: National Renewable Energy Laboratory. http://www.nrel.gov/docs/fy11osti/52194.pdf.

Reda, I., D. Myers, and T. Stoffel. 2008. "Uncertainty Estimate for the Outdoor Calibration of Solar Pyranometers: A Metrologist Perspective." Measure 3 (4): 58–66.

Reda, I., M. Dooraghi, and A. Habte. 2013. NREL Pyrheliometer Comparison: September 16 to 27, 2013 (NPC-2013) (NREL/TP-3B10-60749). Golden, CO: National Renewable Energy Laboratory.

Renné, D. S., R. Perez, A. Zelenka, C. Whitlock, and R. DiPasquale. 1999. Advances in Solar Energy: An Annual Review of Research and Development: Volume 13, edited by D. Y. Goswami, and K. W. Böer. Boulder, CO: American Solar Energy Society.

Ruiz-Arias, J. A., C. A. Gueymard, F. J. Santos-Alamillos, and D. Pozo-Vázquez. 2016. "Worldwide Impact of Aerosol's Time Scale on the Predicted Long-Term Concentrating Solar Power Potential." Nature Scientific Reports 6: 30546. https://doi.org/10.1038/srep30546.

Salazar, G., C. A. Gueymard, J. B. Galdino, and O. C. Vilela. 2019. "Solar Irradiance Time Series Derived from High-Quality Measurements, Satellite-Based Models, and Reanalyses at a Near-Equatorial Site in Brazil." Renewable and Sustainable Energy Reviews 117: 109478.

Shi, H., W. Li, X. Fan, J. Zhang, B. Hu, L. Husi, H. Shang, X. Han, Z. Song, Y. Zhang, S. Wang, H. Chen, and X. Xia. 2018. "First Assessment of Surface Solar Irradiance Derived from Himawari-8 across China." Solar Energy 174: 164–70.

Stoffel, T. L., I. Reda, D. R. Myers, D. Renné, S. Wilcox, and J. Treadwell. 2000. "Current Issues in Terrestrial Solar Radiation Instrumentation for Energy, Climate, and Space Applications." Metrologia 37 (5): 399–401.

Šúri, M., and T. Cebecauer. 2014. "Satellite-Based Solar Resource Data: Model Validation Statistics Versus User's Uncertainty." Proceedings of the 43th ASES National Solar Conference.

Thevenard, D., and S. Pelland. 2013. "Estimating the Uncertainty in Long-Term Photovoltaic Yield Predictions." Solar Energy 91: 432–45.

Urraca, R., A. M. Gracia-Amillo, T. Huld, F. J. Martinez-de-Pison, J. Trentmann, A.V. Lindfors, A. Riihelä, and A. Sanz-Garcia. 2017. "Quality Control of Global Solar Radiation Data with Satellite-Based Products." Solar Energy 158: 49–62. https://doi.org/10.1016/j.solener.2017.09.032.

Urraca, R., T. Huld, A. Gracia-Amillo, F.J. Martinez-de-Pison, F. Kaspar, and A. Sanz-Garcia. 2018. "Evaluation of Global Horizontal Irradiance Estimates from ERA5 and COSMO-REA6 Reanalyses Using Ground and Satellite-Based Data." Solar Energy 164: 339–54. https://doi.org/10.1016/j.solener.2018.02.059.

Vignola, F., and R. Perez. 2004. Solar Resource GIS Data Base for the Pacific Northwest using Satellite Data: Final Report (DOE DE-PS36-0036-00GO10499). Eugene, OR.

Vuilleumier, L., M. Hauser, C. Flix, F. Vignola, P. Blanc, A. Kazantzidis, and B. Calpini. 2014. "Accuracy of Ground Surface Broadband Shortwave Radiation Monitoring." Journal of Geophysical Research Atmospheres, 119 (24): 838–60.

Wilbert, S., S. Kleindiek, B. Nouri, N. Geuder, A. Habte, M. Schwandt, and F. Vignola. 2016. "Uncertainty of Rotating Shadowband Irradiometers and Si-Pyranometers Including the Spectral Irradiance Error." AIP Conference Proceedings 1734 (1): 150009. https://doi.org/10.1063/1.4949241

Wilcox, S. M. 2012. National Solar Radiation Database 1991–2010 Update: User's Manual (NREL/TP-5500-54824). Golden, CO: National Renewable Energy Laboratory. http://www.nrel.gov/docs/fy12osti/54824.pdf.

Wilcox, S. M., and D. Myers. 2008. Evaluation of Radiometers in Full-Time Use at the National Renewable Energy Laboratory Solar Radiation Research Laboratory (NREL/TP-550-44627). Golden, CO: National Renewable Energy Laboratory. http://www.nrel.gov/docs/fy09osti/44627.pdf.

Wilcox, S., and P. McCormack. 2011. "Implementing Best Practices for Data Quality Assessment of the National Renewable Energy Laboratory's Solar Resource and Meteorological Assessment Project." Proceedings of the 40th ASES National Solar Conference 2011 (Solar 2011), May 17–20, 2011, Raleigh, North Carolina, 471–78. Boulder, CO: American Solar Energy Society (ASES). 2011. https://www.nrel.gov/docs/fy11osti/50897.pdf.

Zelenka, A., R. Perez, R. Seals, and Renné, D. 1999. "Effective Accuracy of Satellite-Derived Irradiance." Theoretical and Applied Climatology 62: 199–207.

8 FORECASTING SOLAR RADIATION AND PHOTOVOLTAIC POWER

Elke Lorenz,[1] Jose Antonio Ruiz-Arias,[2] Luis Martin,[3] Stefan Wilbert,[4] Carmen Köhler,[5] Rafael Fritz,[6] Alessandro Betti,[7] Philippe Lauret,[8] Mathieu David,[8] Jing Huang,[9] Richard Perez,[10] Andreas Kazantzidis,[11] Ping Wang,[12] and Yves-Marie Saint-Drenan[13]

[1] *Fraunhofer Institute for Solar Energy Systems*
[2] *Solargis*
[3] *Qatar Environment and Energy Research Institute (QEERI), Hamad Bin Khalifa University*
[4] *German Aerospace Center (DLR)*
[5] *P3R*
[6] *Fraunhofer Institute for Energy Economics and Energy System Technology*
[7] *Intelligence in Energy Management (i-EM)*
[8] *Laboratory of Physics and Mathematical Engineering for Energy and the Environment (PIMENT), University of La Réunion*
[9] *Oceans and Atmosphere, CSIRO*
[10] *State University of New York at Albany (SUNY)*
[11] *University of Patras*
[12] *The Royal Netherlands Meteorological Institute (KNMI)*
[13] *MINES ParisTech*

8.1 Introduction

Solar resource forecasting is critical for the operation and management of solar power plants and electric grids. Solar radiation is highly variable because it is driven mainly by synoptic and local weather patterns. This high variability presents challenges to meeting power production and demand curves, notably in the case of solar photovoltaic (PV) power plants, which have little or no storage capacity. For concentrating solar power (CSP) plants, variability issues are partially mitigated by the thermal inertia of the plant, including its heat transfer fluid, heat exchangers, turbines, and potentially coupling with a heat storage facility; however, temporally and spatially varying irradiance introduces thermal stress in critical system components and plant management issues that can result in the degradation of the overall system's performance and reduction of the plant's lifetime. The variability can also result in lower plant efficiencies than those that occur under operation in stable conditions because optimally operating the plant under variable conditions is significantly more challenging. For PV power plants that have battery storage, forecasts are helpful for scheduling the charging process of the batteries at the most appropriate time, optimizing the fractions of electricity delivered and stored at any instant, and thus avoiding the loss of usable energy.

Solar radiation forecasting anticipates the solar radiation transients and the power production of solar energy systems, allowing for the setup of contingency mechanisms to mitigate any deviation from the required production.

With the expected integration of increasing shares of solar power into the electric grid, reliable predictions of solar power production are becoming increasingly important. PV power represents one of the main shares of the total renewable energy, along with wind power generation (IRENA 2019). High penetrations of PV power generation pose several challenges for the stability of the electric grid because of the stochastic variability of the residual electric load (i.e., the difference between the energy need—or load—and the

distributed PV power generation, depending on meteorological conditions and sun position); therefore, accurate forecasting of PV power generation is required for energy scheduling and for balancing demand and supply. This information is essential for distribution system operators and transmission system operators (TSOs) as well as for aggregators and energy traders (Pierro et al. 2017).

Today, PV power prediction systems are an essential part of electric grid management in countries that have substantial shares of solar power generation, among which Germany is a paradigmatic case. For example, in 2020, Germany had an installed PV power capacity of more than 50 GW_{peak}, supplying more than 50% of the total load on sunny summer days at noon. In this context, and according to the German Renewable Energy Sources Act,[46] TSOs are in charge of marketing and balancing the overall fluctuating PV power feed-in, which requires the use of regional forecasts for the designated control areas. Additionally, optional direct marketing of PV power is based on forecasts for the PV power plant's output. PV power is first offered on the day-ahead auction at the European Power Exchange. Subsequently, amendments based on updated forecasts can be made on the intraday market, when electricity can be traded until 30 minutes before delivery begins. Remaining deviations between scheduled and needed power are adjusted using balancing power. A similar procedure for California's electricity market was described by Mathiesen, Kleissl, and Collier (2013). Also, Kleissl (2013) described the stakeholder needs from the perspective of independent system operators and energy traders. Hence, accurate PV power forecasts at different spatial and temporal scales are extremely important for cost-efficient grid integration because large errors in the day-ahead forecast can cause either very high or negative prices on the intraday market, and intraday forecast errors determine the need for costly balancing power.

Several studies have evaluated the added value of solar irradiance forecasting for solar energy applications. For example, Dumortier (2009) gave a preliminary overview of such applications. Many other authors have detailed specific use cases and benefits of solar power forecasting. The following is a nonexhaustive list:

- In the realm of electric grids, Perez et al. (2007) evaluated the operational accuracy of end-use forecasts and their ability to predict the effective capacity of grid-connected PV power plants.
- Kaur et al. (2016) described the benefits of solar forecasting for energy imbalance markets.
- The specific needs of solar forecasting for the real-time electricity market and forecasting requirements from the California Independent System Operator have been examined by Yang, Wu, and Kleissl (2019), showing that hourly forecasts could be appropriately downscaled to the contemplated 15-minute resolution.
- Rikos et al. (2008), Diagné et al. (2013), and Simoglou et al. (2014) examined the solar power forecasting requirements to support microgrid and island systems with respect to stability and power quality. More specifically, Martinez-Anido et al. (2016) evaluated the value of solar forecast improvements for the Independent System Operator – New England.

[46] The German Renewable Energy Sources Act is a set of laws aimed at promoting renewable energy in Germany See "Renewable Energy," Federal Ministry for Economic Affairs and Energy, https://www.bmwi.de/Redaktion/EN/Dossier/renewable-energy.html, accessed May 2017.

- At the power plant level, Marcos et al. (2013) described the benefits of power prediction to optimize a storage system that attenuates power fluctuations in large PV power plants.
- Almeida, Perpiñán, and Narvarte (2015) explored the skill of a nonparametric method to predict the AC power output of PV power plants.
- Wittmann et al. (2008) and Kraas, Schroedter-Homscheidt, and Madlener et al. (2013) used case studies to show the economic benefit of supplying direct normal irradiance (DNI) forecasts for the optimized operation strategies of CSP plants.
- Schroedter-Homscheidt et al. (2013) evaluated the aerosol forecasting requirements for forecasts of concentrating solar electricity production.
- Law et al. (2014) reviewed different DNI forecasting methods and their applications to yield forecasting of CSP plants. In a later publication, Law, Kay, and Taylor (2016) reviewed the benefits of short-term DNI forecasts for the CSP technology.
- Hirsch et al. (2014) specifically evaluated the use of 6-hour forecasts (nowcasting) to operate CSP plants.

In a broader context, different solar radiation forecasting approaches, targeted at various time horizons, have been developed using different input data and data processing methods. In the IEA PVPS context, the state of the art of solar forecasting has been addressed in a report for Task 14 (Pelland et al. 2013). A nonexhaustive list includes methods based on:

- Statistical inference on ground-observed time-series (Huang et al. 2013; Lonij et al. 2013; Voyant et al. 2014; Boland and Soubdhan 2015; Graditi, Ferlito, and Adinolfi 2016)
- Use of cloud motion vectors (CMVs) and other cloud advection techniques on data from all-sky cameras and satellite imagery (Hammer et al. 1999; Perez et al. 2010; Chow et al. 2011; Marquez and Coimbra 2013; Quesada-Ruiz et al. 2014; Schmidt et al. 2016; Lee et al. 2017; Arbizu-Barrena et al. 2017; Miller et al. 2018)
- Forecasts based on numerical weather prediction (NWP) models (Mathiesen and Kleissl 2011; Lara-Fanego et al. 2012; Pelland, Galanis, and Kallos 2013; Ohtake et al. 2013; Perez et al. 2013; Jimenez et al. 2016a; Jimenez et al. 2016b) or even hybrid techniques (Marquez and Coimbra 2011; Marquez, Pedro, and Coimbra 2013; Perez et al. 2014; Dambreville et al. 2014; Wolff et al. 2016; Mazorra Aguiar et al. 2016).

This chapter provides an overview of basic concepts of solar irradiance forecasting by referring to selected examples and operational models rather than reviewing the state of the art because such reviews can be found elsewhere, including in Lorenz and Heinemann (2012); Inman, Pedro, and Coimbra (2013); Kleissl, Schroedter-Homscheidt, and Madlener (2013), and, for PV applications, in Antonanzas et al. (2016). The evaluations and comparisons of different irradiance forecasting approaches focus on global horizontal irradiance (GHI), with DNI being discussed in less detail. Nevertheless, forecasting and, in particular, evaluation methods apply to DNI to some extent. A focus on DNI forecasting can be found in Schroedter-Homscheidt and Wilbert (2017). The selected examples presented below have been investigated in the context of the International Energy Agency (IEA) Solar Heating and Cooling Programme (SHC) Task 36 and Task 46, and Photovoltaic Power Systems Programme (PVPS) Task 16.

Irradiance is a key driver for solar power output, but other environmental factors—including ambient temperature, air humidity, wind speed, and wind direction—have a nonnegligible impact on the final power yield of the plant. Ambient temperature, for instance, affects the PV efficiency and the thermal regime of CST plants. Humidity might also have some impact on CSP systems. Similarly, wind speed and especially wind gust prediction are important for preventing strong mechanical loads in tracking systems; therefore, the forecasting of such

other ancillary factors will provide tangible benefits for the effective operation of power plants. Forecasts of these ancillary variables, however, are not discussed here.

8.1.1 Overview of Solar Irradiance Forecasting Methods

Depending on the specific application and requirements regarding forecast horizon and spatiotemporal resolution, different forecasting methods are customarily used. From short to long forecasting horizons, the most important solar forecasting methods are the following:

- **Intrahour forecasts with high spatial and temporal resolution:** These require on-site observations of irradiance and/or cloud conditions that are processed using statistical methods and, more recently, artificial intelligence and machine learning models, such as neural networks, as discussed in Section 8.3. Those that are based on solar irradiance measurements and, for instance, conventional autoregressive techniques might provide meaningful forecasts even up to a few hours ahead under relatively stable sky conditions; however, these methods rarely have good skill under variable sky conditions, given the chaotic behavior of the cloud system and the limited information contained in point-wise observations. In these cases, the local distribution of clouds, as gathered by one or more ground-based sky imagers, might enhance the forecast skill. This cloud-related information allows for the generation of solar irradiance forecasts with a temporal resolution on the order of a few minutes and a spatial resolution from 10–100 m covering a few square kilometers around the sky imagers. The typical forecast horizon of these systems is from 10–20 minutes, depending on the cloud height and speed.
- **Forecasts up to 4 hours ahead:** These are conventionally derived by extrapolating the cloud locations into the future using CMV techniques based on satellite imagery, and they are often referred to as *nowcasts*. The typical spatial resolution is from 1–5 km for the current generation of geostationary satellites, with forecast updates every 10–30 minutes; see Section 8.2.1.
- **Intraday and day-ahead forecasts:** These are based on NWP models, which typically offer higher performance for forecast horizons more than several hours and up to several days ahead. These models predict the evolution of the atmospheric system, including the formation, advection, diffusion, and dissipation of clouds. They are based on a physical description of the dynamic processes occurring in the atmosphere by solving and parameterizing the governing system of equations, and they depend on an observed set of initial conditions; see Section 8.2.2 for details. Current global NWP models cover the Earth with a spatial resolution from approximately 0.1–0.5° and a temporal resolution from 1–3 hours. Regional models, which are sometimes referred to as limited area models or mesoscale models, have a spatial resolution of a few kilometers and an intrahour temporal resolution in the area of interest.

An illustration of these different forecasting methods for various spatial and and temporal scales is given in Figure 8-1.

In addition to this broad classification, when historical or near-real-time on-site solar irradiance or PV yield observations are available, these methods can be further improved by combination with machine learning (hybrid methods). For NWP-based methods, particularly, model output statistics (MOS) techniques are often applied; see, e.g., Yang (2019a) and Yagli, Yang and Srinivasan (2020). These techniques are sometimes referred to as

statistical downscaling techniques.[47] These methods learn error patterns by comparing forecasts and observations and use them to reduce the error of the final prediction.

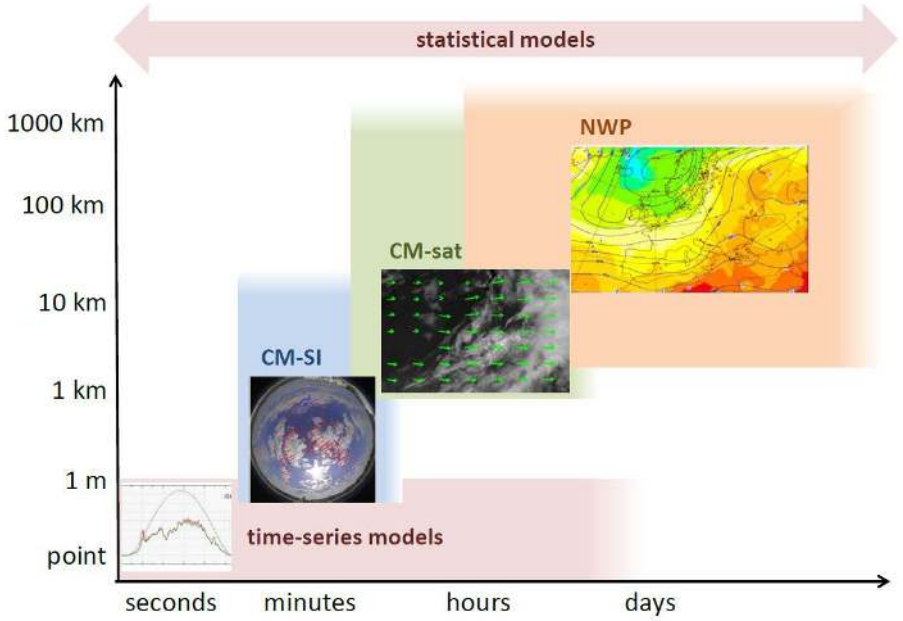

Figure 8-1. Illustration of different forecasting methods for various spatial and temporal scales. The y-axis shows the spatial resolution, and the x-axis shows the forecast horizon intended for the different forecasting techniques. CM-SI: cloud motion forecast based on sky imagers; CM-sat: cloud motion forecast based on satellite imagery. Statistical models apply to all forecast horizons.

8.2 Empirical and Physical Solar Irradiance Forecasting Methods

This section presents empirical and physical solar forecasting methods. Solar irradiance forecasting methods using statistical approaches and machine learning are described in Section 8.3. The empirical methods introduced here rely on the correlation between the cloud structures, atmospheric conditions, and solar irradiance. When using satellite data to calculate solar irradiance with radiative transfer models, wind fields from NWP models are used for cloud advection. For physical solar irradiance forecasting methods, various NWP models are discussed.

8.2.1 Irradiance Forecasting with Cloud Motion Vectors

At timescales from a few minutes to a few hours, horizontal advection has a strong influence on the temporal evolution of cloud patterns, with the shape of clouds often remaining quite stable. Here, the spatial scale is also extremely important because small-scale cloud structures change faster than larger structures. In these situations, techniques for detecting clouds and their motion trajectories, referred to as CMV techniques, are used to provide valuable information for irradiance forecasting. Obviously, the performance of these forecasting methods degrades as the importance of local processes of cloud formation and dissipation, such as strong thermally driven convection, increases.

CMV-based techniques consist of the following basic steps:

[47] The application of regional NWP models to global model output is known as a dynamic downscaling technique.

- Images with cloud information are derived from satellite- or ground-based sky-imager measurements.
- Assuming stable cloud structures and optical properties, the CMVs are determined by identifying matching cloud structures in consecutive cloud images.
- To predict future cloud conditions, the CMVs are applied to the latest available cloud image assuming cloud speed persistence.
- Solar irradiance forecasts are calculated from the predicted cloud structures.

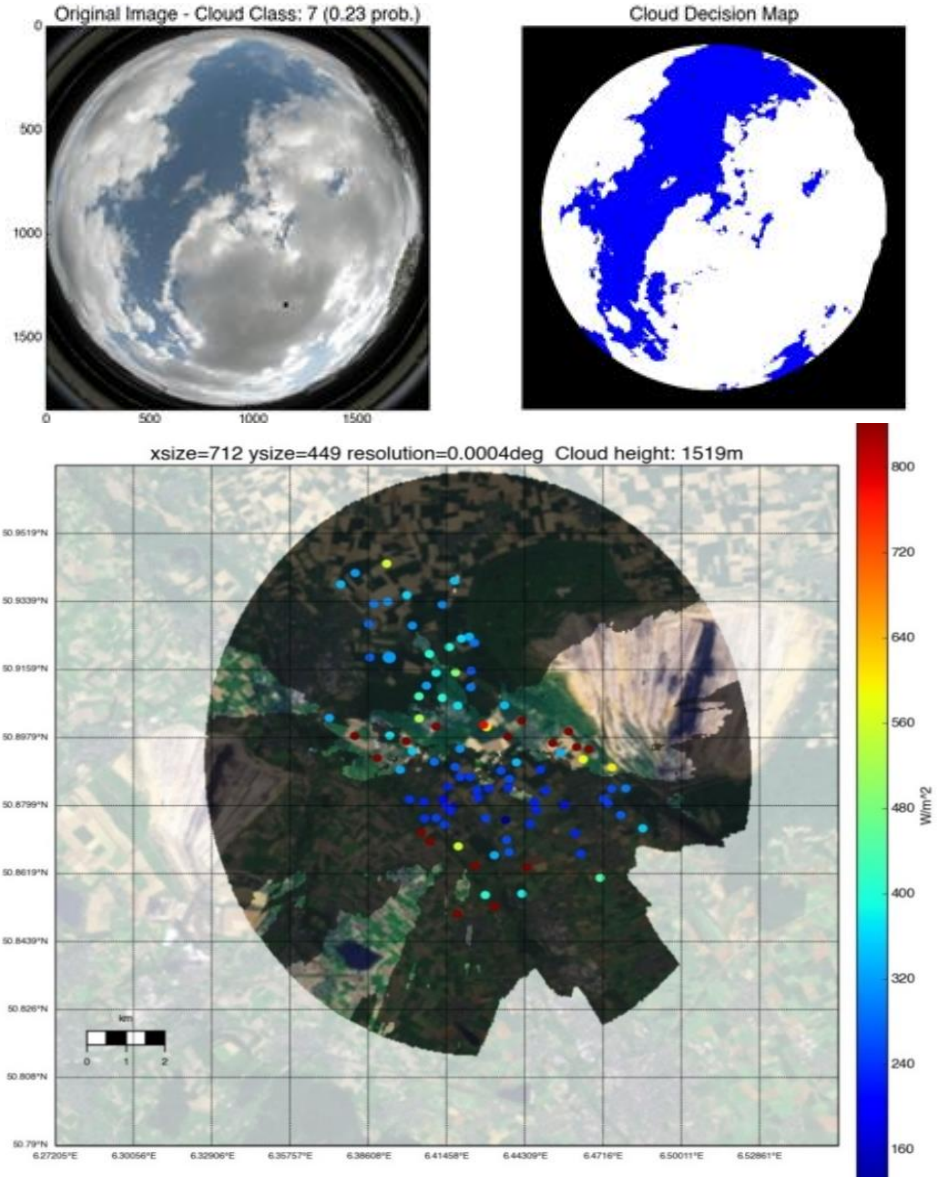

Figure 8-2. Cloud information from ASI: (upper left) original image; (upper right), cloud decision map; and (bottom), shadow map with irradiance measurements. Sky image and irradiance measurements were taken in Jülich, Germany, on April 9, 2013, at 12:59 UTC in the framework of the HD(CP)^2 Observational Prototype Experiment (HOPE) campaign (Macke and HOPE-Team 2014). *Images from the University of Oldenburg*

8.2.1.1 Forecasting Using Ground-Based All-Sky Imagers

Solar irradiance forecasts at subhourly scales with high temporal and spatial resolutions can be derived from ground-based all-sky imagers (ASIs). Such cameras are installed horizontally and photograph the whole sky above them (see Figure 8-2, upper left image). ASIs are at times also called whole-sky imagers or sky imagers. The word *imager* is sometimes replaced by the term *camera*, even though they are not strictly identical. In the IEA PVPS Task 16, the term *ASI* is normally used.

ASIs can capture sudden changes in irradiance, which are often referred to as *ramps*, at temporal scales from seconds to minutes (Figure 8-3). Cloud fields sensed from ASIs or from an assembly of ASIs can be resolved in high detail (e.g., 10 x 10-m resolution), allowing the partial cloud cover on large PV installations to be modeled and forecasted (see Figure 8-2). The maximum predictable horizon strongly depends on cloud conditions (i.e., cloud height and velocity), and it is constrained by the cloud speed and the field of view of the ASIs. This forecast horizon is typically in the range of 10 minutes, but it can reach 30 minutes in some cases.

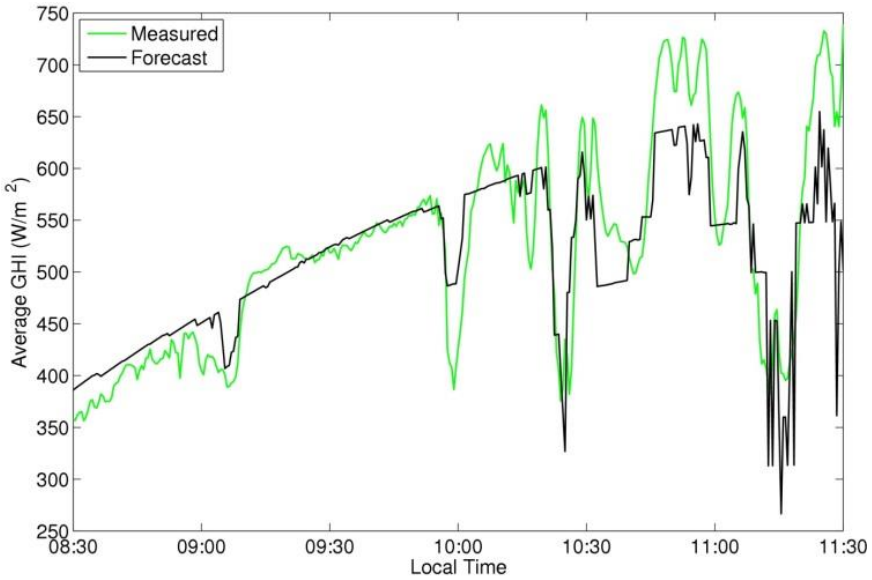

Figure 8-3. Example of 5-minute-ahead GHI forecast using a sky imager. Location: University of California, San Diego, November 14, 2012. *Image from the University of California, San Diego, Center for Energy Research*

Currently, there is no defined standard for sky-imaging hardware, camera calibration, or image-processing techniques. Systems in use include commercially available, low-cost, webcams or surveillance cameras and systems developed specifically for sky imaging; e.g., Urquhart et al. (2015). Most systems use digital RGB (red-green-blue) cameras with fish-eye lenses and therefore consider visible radiation, although some systems rather work with infrared cameras, which are more expensive. In particular, older RGB systems and some infrared cameras use a downward-looking camera that takes photos of an image of the sky that appears on a roughly spherical upward-looking mirror. (This is where the term *imager* comes from.) This concept—unlike the smaller lens or dome of fish-eye cameras—has the disadvantage that the *whole* mirror must be cleaned. Moreover, some older systems use sun-tracked “shadowbands” to prevent the direct sunlight from reaching the camera. This can reduce lens flare-induced saturated areas in the photos, but the shadowband also covers a noticeable part of the image. Because the required tracking of the shadowband entails higher costs and can lead to system failures, shaded devices have been uncommon in recent years.

The operation of all ASI-based forecasts typically involves these five steps:

1. Take images of the sky and detect which pixels show clouds and which do not.
2. Detect the cloud motion in image series.
3. Geolocate the clouds, including cloud height (if irradiance maps are forecasted).
4. Project the shadow on the ground or determine whether a shadow is at the location of the sky imager (for the current and future cloud positions).
5. Estimate the radiative effect of the clouds on the ideal cloudless DNI, GHI, or GTI (global tilted irradiance).

Machine learning methods are used in some ASI systems for these individual tasks. Some ASI systems do not follow these steps and instead use machine learning methods to directly connect image series to the current and future GHI at the site of the camera (Pierer and Remund 2019).

Cloud detection (which is often also referred to as cloud segmentation) from ASI observations is performed by evaluating different image properties. The red-to-blue ratio (RBR) or multicolor criteria (Kazantzidis et al. 2012) have been used as a main indicator for clouds because of their different spectral-scattering properties (high RBR) compared to clear-sky (low RBR) conditions (Shields, Johnson, and Koehler 1993; Long and DeLuisi 1998). Binary cloud decision maps (Figure 8-2, top right) can be derived based on threshold procedures. Evaluating the RBR in relation to a clear-sky library (Chow et al. 2011; Shaffery et al. 2020) has proven helpful to account for a nonuniform clear-sky signal over the sky hemisphere that depends on the position of the sun and the turbidity of the atmosphere (Ghonima et al. 2012). Cloud detection is particularly difficult in the circumsolar and solar disk regions because of saturated pixel information that have high RBR values for not only cloudy but also clear-sky conditions. High potential has been seen in machine learning-based segmentation (Hasenbalg et al. 2020).

Detecting cloud motion is the next step to derive irradiance forecasts. For instance, Chow et al. (2011) identified cloud motion based on a normalized cross-correlation procedure—in other words, by maximizing the cross-correlation between shifted areas in two consecutive images. In contrast, Quesada-Ruiz et al. (2014) proposed a discretization method (the sector method) of the cloud image that helps to derive both the direction and speed of clouds. Alternatively, cloud movement can be analyzed by applying optical flow techniques to subsequent images (Lucas and Kanade 1981; Wood-Bradley, Zapata, and Pye 2012). The derived CMVs are then used to cast the observed cloud scenes into the future. For point-wise forecasts at the sky-imager location, information about cloud height is not required because the cloud movement can be parameterized in terms of “pixels per second.” In contrast, for applications requiring mapping cloud shadows, the cloud speed derived using CMVs needs to be expressed in meters per second; this requires knowing the cloud height, which cannot be derived using a single ASI.

The multiple options to determine cloud height include the application of two or more ASIs, ceilometers, distributed radiometers, satellite methods, and NWP data. In particular, the most accurate information on cloud-base height directly above the instrument is currently obtained using ceilometers (Arbizu-Barrena et al. 2015), which are typically employed at airport weather stations; however, the different clouds seen in a sky image can have different cloud heights, and the ceilometer measures only the cloud height directly above it. Thus, the applicability of ceilometers for this purpose strongly depends on the particular cloud arrangement. Retrieving the cloud-top height from satellite images gives spatially continuous information but shows large uncertainties. Different methods to determine cloud height using combined information from more than one ASI are described by Nguyen and

Kleissl (2014) and Wang, Kurtz, and Kleissl (2016). Some of these methods allow deriving different cloud heights for the individual clouds seen in the sky image (Peng et al. 2015). Additionally, the combination of one ASI's CMV in pixels per second with another device's absolute CMV in meters per second can be used to determine the cloud height. Spatially distributed radiometers can be used to derive CMVs in meters per second, as described by Wang, Kurtz, and Kleissl (2016) and Kuhn et al. (2017a). A system using two ASIs can achieve higher accuracy than the application of NWP and distributed radiometers (Kuhn et al. 2018).

Cloud shadow maps at the surface (see Figure 8-2, bottom) are produced by projecting the forecasted cloud scenes with their assigned height using information about the position of the sun and a digital elevation model. The impact of the projection method on solar forecast accuracy can be large. Local irradiance or PV power measurements can be used to estimate the effect of the clouds on irradiance or PV power. Urquhart et al. (2013) analyzed the frequency distributions of PV power normalized to clear-sky conditions to determine a clear and a cloudy mode and to assign them to shaded and unshaded cells, respectively. Schmidt et al. (2016) used the clear-sky index derived from pyranometer measurements to determine the forecasted all-sky GHI. Similarly, Blanc et al. (2017) used the beam clear-sky index determined from the last 30 minutes of pyrheliometer measurements to derive the cloud transmittance. Additional information on cloud type in the monitored scene indicates cloud optical thickness and cloud height and can be obtained with cloud classification algorithms or by using infrared and thermographic sky imagers. Ghonima et al. (2012) proposed a method to differentiate thin and thick clouds for various atmospheric conditions using a clear-sky library. Gauchet et al. (2012) proposed using a regression model in combination with a clear-sky model to estimate the surface solar irradiance from segmented sky images with information about clear-sky areas; bright and dark clouds; circumsolar area; and solar disk. This specific segmentation is made to optimally accommodate various luminance thresholds.

Instead of using only one or a few ASI systems, networks of approximately 10 or more ASIs can be created to increase the spatial coverage, the forecast horizon, and the accuracy of observations. The combination of several ASIs can provide a more accurate 3D reconstruction of the cloud field (Mejia et al. 2018). Also, the combination of several ASI-derived irradiance maps or intermediate results (e.g., segmentation and cloud height) can be used to improve the nowcasts (Blum et al. 2019). In addition to irradiance nowcasting, ASIs have many other applications that are relevant to meteorology and solar energy. Deriving GHI and/or DNI from sky images is discussed by Schmidt et al. (2016), Chauvin et al. (2018), Kurtz and Kleissl (2017), and Gauchet et al. (2012). Estimating the sky radiance distribution is also possible (Chauvin et al. 2015). Further, the aerosol optical depth (AOD) can be retrieved from ASIs as well (e.g., Olmo et al. 2008 and Kazantzidis et al. 2017).

Another camera-based nowcasting method uses so-called shadow cameras installed at elevated positions, such as on towers or mountains, that take images of the ground around their position (Kuhn et al. 2017a). In such photos, cloud shadows can be detected, and the brightness of the pixels contains information on the irradiance at the pixel of interest. Unlike ASIs, these systems have the advantage that no modeling of the clouds is required to obtain irradiance maps; however, the development of shadow-camera systems is still in an early phase compared to ASI systems.

8.2.1.2 Satellite-Based Forecasts

Forecasts up to approximately 6 hours ahead require wide-area observations of cloud fields. For example, assuming a maximum cloud velocity of 160 km/h, a region of approximately 2,000 km by 2,000 km would need to be monitored if the goal is to track any arriving cloud 6 hours ahead. Satellite data with broad coverage are appropriate sources for these horizons.

Cloud and irradiance information from satellite images can be derived by a variety of methods (see Chapter 4). In principle, all of them can be applied to cloud predictions using CMVs to obtain forecasts of solar irradiance. In addition, multiple methods exist to derive CMVs, as described in Section 8.2.1.1 for ASIs. Methods to calculate CMVs from satellite images have also been developed and are routinely used in operational weather forecasting, where CMVs are used to describe wind fields at upper levels in the atmosphere in NWP models.

Satellite-based nowcasting schemes for solar irradiance forecasts have been developed mostly in the past decade based on CMVs or sectoral cloud tracking (Hammer et al. 2003; Schroedter-Homscheidt and Pulvermüller 2011). The satellite-based forecasting scheme from the University of Oldenburg in Germany (Lorenz, Hammer, and Heinemann 2004; Kühnert, Lorenz, and Heineman 2013) is introduced here as an example of such a system. It uses images of the geostationary Meteosat Second Generation (MSG) satellites (see Chapter 4). The semiempirical HELIOSAT method (Hammer et al. 2003) is applied to obtain information about clouds and irradiance. A characteristic feature of the method is the dimensionless cloud index, which provides information about cloud transmittance.

CMVs are derived by identifying corresponding cloud patterns in two consecutive images (Figure 8-4). Rectangular areas—the "target areas"—are defined with an approximate size of 90 km by 90 km. This is large enough to contain information about temporally stable cloud structures and small enough that cloud motion for this area can be described by a single vector. Mean square pixel differences among target areas in consecutive images (n_0 and n_{-1}) are calculated for displacements in all directions (Figure 8-4, a–c). The maximum possible displacement ("search area") is determined by the maximum wind speeds at typical cloud heights. The displacement that yields the minimum mean square pixel difference for a given target area is assigned as a motion vector (Figure 8-4, d). The derived motion vectors are applied to the cloud index image, n_0, to predict future cloud conditions. A smoothing filter is applied to the predicted cloud index image to eliminate randomly varying small-scale structures that are hardly predictable. Finally, solar irradiance is derived from the predicted cloud index images using the HELIOSAT method (see Chapter 4).

The SolarAnywhere short-term forecasting scheme (Perez and Hoff 2013) for the United States is based on Geostationary Operational Environmental Satellite (GOES) imagery and follows a similar approach to detect cloud motion. It is also based on a semiempirical cloud index method (see Chapter 4). In parallel, Solargis has developed a CMV short-term forecasting scheme that is run under the principles just described but incorporates a multiresolution treatment of cloud structures. Another method—presented by Schroedter-Homscheidt and Pulvermüller (2011)—discriminates between tracking optically thin cirrus and tracking optically thick cumulus or stratus with respect to the need for increased accuracy in direct irradiance nowcasting aimed at concentrating technologies.

Müller and Remund (2014) proposed a method that combines cloud index values retrieved from MSG satellites with wind fields from a NWP model. The wind fields are predicted with the Weather Research and Forecasting (WRF) model (Skamarock et al. 2005) with hourly resolution and are applied to the forward propagation of the observed cloud patterns from the satellite imagery. Information about the height of the monitored clouds is needed to determine the corresponding NWP model's pressure level. Müller and Remund (2014) assumed fixed cloud heights for this purpose. An advantage of the application of NWP wind fields over satellite-derived CMVs is the potential to describe changes in the direction and speed of cloud movement during the extrapolation process.

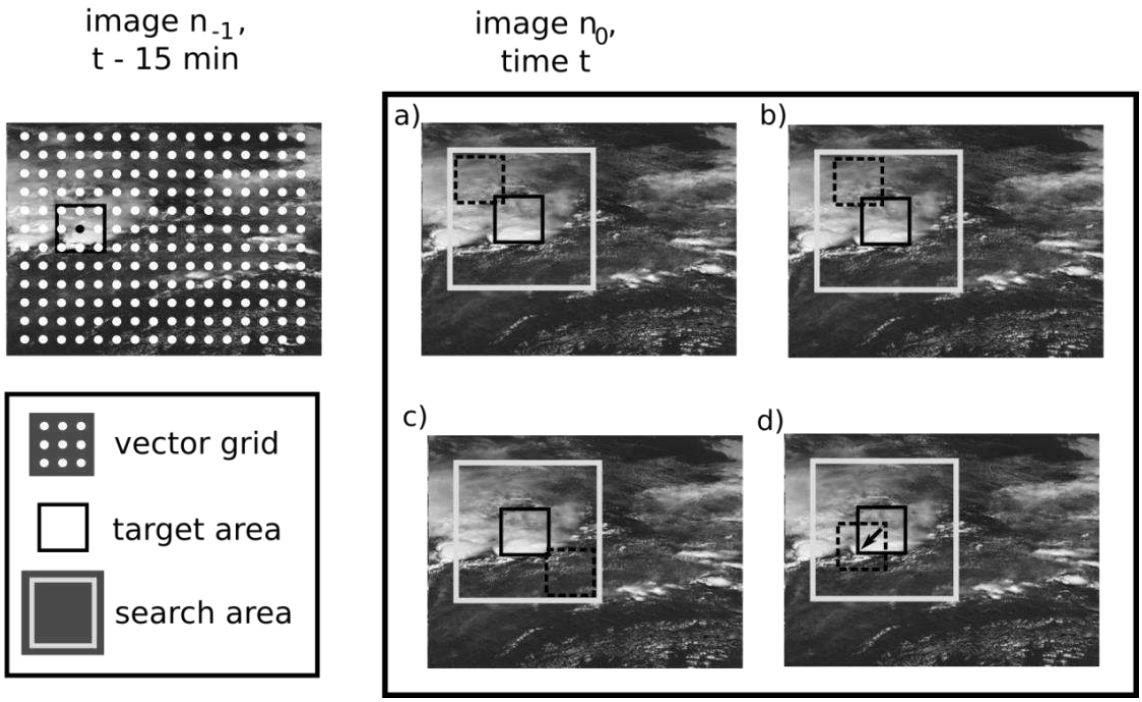

Figure 8-4. Schematic representation of the CMV derivation using satellite images.
Images reproduced from Kühnert et al. (2013)

A method for satellite-based short-term forecasting using a physical cloud and irradiance retrieval scheme was introduced by Miller, Heidinger, and Sengupta (2013) and Miller et al. (2018). The method processes GOES satellite observations with the National Oceanic and Atmospheric Administration (NOAA) Pathfinder Atmospheres Extended (PATMOS-x) retrieval package (Heidinger et al. 2014), which is a stand-alone radiative transfer code, and combines them with wind field data from the Global Forecast System (GFS) model. Cloud properties are retrieved with PATMOS-x in a first step. Next, the cloud fields are advected using GFS winds at the vertical level matching the cloud-top height as retrieved from PATMOS-x. Finally, solar irradiance at the surface is calculated with radiative transfer calculations using predicted cloud properties and additional atmospheric parameters.

Another satellite-based irradiance scheme that is based on cloud physical properties (CPPs) is the Spinning Enhanced Visible and InfraRed Imager (SEVIRI) CPP method, which uses the SEVIRI instrument onboard the MSG satellites. The method is based on advecting the cloud properties and is used to forecast both GHI and DNI. Details about the CPP surface solar forecasting algorithm and its evaluation are presented by Wang et al. (2019). The forecast horizon of this method is from 0–4 hours at a 15-minute temporal resolution. The forecast has been tested over the Netherlands at a spatial resolution of approximately 4 km by 6 km. CMVs are derived from three cloud properties (cloud top height, cloud optical thickness, and particle effective radius) with a method adapted from the weather radar precipitation forecast system of the Royal Netherlands Meteorological Institute (KNMI). The advected cloud properties are used as input for the CPP-SICCS (Surface Insolation under Clear and Cloudy skies derived from SEVIRI imagery) algorithm to calculate the surface solar irradiance.

8.2.2 Irradiance Forecasting with Numerical Weather Prediction

NWP models are routinely operated by weather services to forecast the state of the atmosphere. Starting from initial conditions that are derived from routine Earth observations from worldwide networks of ground, airborne, and spaceborne sensors, the temporal evolution of the atmosphere is simulated by solving the equations that describe the physical

processes occurring in the atmosphere. Such physical modeling is the only feasible approach when there is little correlation between the actual observations and the forecasted values, which is typically the case for time horizons longer than approximately 5 hours ahead. A comprehensive overview of NWP modeling was given by Kalnay (2003).

Global NWP models predict the future state of the atmosphere worldwide. To determine the initial state from which an NWP model is run, data assimilation techniques are applied to make efficient use of worldwide meteorological observations (Jones and Fletcher 2013). These include observations from ground-based weather stations, buoys, and spaceborne sensors (i.e., satellites). The simulation with NWP models involves spatial and temporal discretization, and the resolution of this discretization determines the computational cost of the simulation. In addition, many physical processes occur on spatial scales much smaller than the grid size—including, for example, condensation, convection, turbulence, as well as scattering and absorption of shortwave and longwave radiation. The effect of these unresolved processes on the mean flow at the model's grid size is evaluated with the so-called parameterizations of atmospheric physics. They include interactions of the land and ocean with the atmosphere, vertical and temporal development of the planetary boundary layer, cumulus triggering and cloud microphysics, as well as shortwave and longwave radiation. The physical parameterizations are a key component of the prediction with NWP models. They bridge the small-scale and large-scale processes, and they make possible the convergence of the numerical routines that solve the physical equations. Today, global NWP models are run by approximately 15 national and international weather services, and their resolutions range from approximately 10 km to approximately 50 km. The temporal resolution of the global model outputs is typically 1 or 3 hours, and their forecasts are normally updated every 6 or 12 hours.

Mesoscale or regional models cover only a limited area of the Earth. They take the initial and lateral boundary conditions from a previous global NWP model run and bring the spatial and temporal grid of the global NWP model down to a finer resolution. Weather services typically operate mesoscale models with a spatial resolution ranging from 1–10 km, and they provide hourly forecasts, though higher resolutions are feasible. Compared to global models, the higher spatial resolution of mesoscale models allows for explicit modeling of small-scale atmospheric phenomena.

For irradiance forecasting, the parameterizations of radiation transfer and cloud properties are of special importance. Larson (2013) compared the respective model configurations with respect to GHI for four operational NWP models, including the Integrated Forecast System (IFS) of the European Center for Medium-Range Weather Forecasts (ECMWF) and the Global Forecast System (GFS) run by NOAA. In particular, Larson (2013) discussed deep and shallow cumulus parameterizations, turbulent transport, stratiform microphysics and prognosed hydrometeors, cloud fraction and overlap assumptions, aerosols, and the shortwave radiative transfer schemes. But Larson (2013) emphasized that "because of the strong feedback and interactions of physical processes in the atmosphere," other processes might have a significant impact on irradiance forecasting.

Today, most NWP models offer GHI as direct model output, and some also provide forecasts of direct and diffuse irradiance. Although in principle direct model output can be used for solar energy applications, in practice additional post-processing is customarily applied to improve forecast accuracy.

8.2.2.1 Examples of Operational Numerical Weather Prediction Models

This section describes some examples of NWP models enumerated together with their spatial resolutions and output time intervals. In particular, it highlights cloud fraction parameterizations and radiation schemes. Additionally, specific references are provided with

respect to the application and evaluation of irradiance forecasts in the context of solar energy applications. A comparison of GHI forecasts based on these models was described by Lorenz et al. (2016) for Europe and by Perez et al. (2013) for the United States, Canada, and Europe. It should be emphasized that the sample of operational models and applications given here is non-exhaustive; it simply summarizes the research experience and lessons learned from some research completed within the frameworks of the IEA SHC Task 36 and Task 46 and the IEA PVPS Task 16.

The IFS of the ECMWF is a global model currently being operated with a horizontal grid spacing of approximately 12 km and 137 vertical levels for high-resolution deterministic forecasts. Operational output is available with a temporal resolution of 3 hours and up to 6 days ahead, with a higher resolution of 1 hour being accessible in the framework of research projects. The model is cycled every 12 hours. The radiation code is based on a version of the Rapid Radiation Transfer Model for General Circulation Models (RRTMG) that has been specially developed for use in NWP models (Mlawer et al. 1997; Iacono et al. 2008). Cloud-radiation interactions are taken into account in detail by using the values of cloud fraction and liquid, ice, and snow water content from the cloud scheme using the Monte Carlo Independent Column Approximation (McICA) method (Pincus, Barker, and Morcrette 2003; Morcrette et al. 2008). McICA uses a stochastic approach to infer the cloud extinction of shortwave and longwave solar radiation from only a random selection of calculations. The prognostic scheme for clouds and large-scale precipitation is based on Tiedtke (1993). The ECMWF irradiance forecasts were analyzed by Lorenz et al. (2009) with respect to different relevant properties for PV power prediction applications. In addition, Lorenz et al. (2011) proposed and evaluated an approach based on the ECMWF forecasts for regional PV power prediction for improved electric grid integration.

NOAA's GFS is currently being operated at a spatial resolution of approximately 13 km and 64 vertical levels; however, the outputs are provided in a regular latitude/longitude grid with a resolution of 0.25º and 46 levels, with hourly resolution up to 120 hours ahead and 3-hour resolution up to 240 hours ahead. The model is cycled every 6 hours. Model physics related to clouds and radiation were summarized by Larson (2013). Note that cloud fraction is a diagnostic variable in the GFS model in contrast to the IFS model. Mathiesen and Kleissl (2011) compared intraday GHI forecasts of the GFS and IFS forecasts from the ECMWF and the North American Model.

Environment Canada's Canadian Meteorological Centre operates the Global Environmental Multiscale (GEM) model. It is run in different configurations, including a regional deterministic configuration (Mailhot et al. 2006) that generates forecasts up to 48 hours ahead at a 7.5-minute time step and with a spatial resolution of approximately 15 km centered at the grid. Pelland, Galanis, and Kallos (2013) investigated solar irradiance and PV power forecasting with post-processing applied to the high-resolution GEM forecasts.

The mesoscale (or regional) WRF model (Skamarock et al. 2005) was developed in the framework of a long-term collaborative effort of several institutes led by the National Center for Atmospheric Research (NCAR) in the United States. Now it is a community model, meaning it is publicly and freely available and can receive contributions from all participants. The WRF model is nonhydrostatic, has multiple nesting capabilities, and offers several schemes for each different parameterization of the atmospheric physical processes. This allows the WRF model to be adapted to widely different climate conditions and different applications over virtually any region of interest. The shortwave radiation parameterization usually runs the Dudhia (1989) scheme; however, the latest version of the WRF model includes up to eight different shortwave parameterization schemes (v. 3.9, 2017). This includes the RRTMG radiative scheme already mentioned for the ECMWF's IFS model but also other advanced and research-class radiative models, such as the New Goddard

shortwave radiation scheme of the WRF model (Chou and Suarez 1999), the NCAR Community Atmosphere Model (Collins et al. 2004), the Fu-Liou-Gu model (Gu et al. 2011), and the Fast All-sky Radiation Model for Solar applications (FARMS) model (Xie, Sengupta, and Dudhia 2016). The user can select any of these schemes. The current WRF model's cloud fraction schemes are diagnostic. The impact of the resolved topography on the downward solar radiation can be optionally included in the computations. The direct aerosol impact can also be modeled using built-in climatologies or inputs from the user.

The ability of the WRF model and its precursor, the fifth generation of the Penn State University/NCAR Mesoscale Model (MM5), to produce solar radiation forecasts have been evaluated (Guichard et al. 2003; Zamora et al. 2003; Zamora et al. 2005; Ruiz-Arias et al. 2008; Wen et al. 2011). More recently, and mostly toward solar energy applications, the WRF model has been extensively evaluated. For instance, within the framework of the IEA SHC Task 36 and Task 46, Lara-Fanego et al. (2012) evaluated 3-day-ahead hourly and 10-minute WRF model forecasts of GHI and DNI in Spain. Perez and Hoff (2013) conducted a benchmarking study of multiple NWP models, including the WRF model, at a number of European and North American radiometric sites. Lorenz et al. (2016) compared the GHI predictions of multiple models, including the WRF model, and various model configurations against irradiance measurements in Europe. Many other studies from the last few years have evaluated the model over different worldwide regions, including Isvoranu and Badescu (2015) in Romania; Zempila et al. (2016) in Greece; Aryaputera, Yang, and Walsh (2015) in Singapore; He, Yuan, and Yang (2016) in China; Lima et al. (2016) in Brazil; Gueymard and Jimenez (2018) in Kuwait; and Sosa-Tinoco et al. (2016) in Mexico.

Other studies have analyzed the causes of model errors, and some studies have proposed improvements. For instance, Mathiesen, Collier, and Kleissl (2013) proposed a direct cloud assimilation technique tailored for the WRF model to improve its representation of clouds along the California coastline for improved solar radiation forecasts. Ruiz-Arias et al. (2013) performed surface clear-sky shortwave radiative closure intercomparisons of various shortwave radiation schemes, including the RRTMG, Goddard, and Dudhia models, in which RRTMG showed the highest performance, whereas some deficiencies were found in the Goddard radiative scheme. A correction for these deficiencies was proposed by Zhong, Ruiz-Arias, and Kleissl (2016). Ruiz-Arias, Dudhia, and Gueymard (2014) proposed a parameterization of the shortwave aerosol optical properties for surface direct and diffuse irradiances assessment. And Ruiz-Arias et al. (2015) described problems with WRF when simulating convective clouds in the Iberian Peninsula and highlighted the need for a dedicated shallow cumulus scheme to reduce model biases.

An important milestone in the use of the WRF model for solar radiation applications has been the recent development of WRF-Solar, a dedicated suite of WRF model parameterizations for solar radiation forecasting (Deng et al. 2014; Ruiz-Arias, Dudhia, and Gueymard 2014; Thompson and Eidhammer 2014) within the U.S. Department of Energy's Sun4Cast project (Haupt et al. 2016). Some of these improvements, and others, have been summarized by Jimenez et al. (2016b). Moreover, the Sun4Cast project has contributed to the development of the Multisensor Advection Diffusion nowCast (MADCast) system (Descombes et al. 2014), which is a particular configuration of the WRF model for fast assimilation of satellite reflectance images. That configuration can be used to obtain a proxy field to cloud fraction that can be subsequently advected in WRF and used to compute solar radiation nowcasts. Lee et al. (2017) presented a comparative evaluation of WRF-Solar, MADCast, and satellite-based forecasts and found that WRF-Solar performed generally well at predicting GHI under challenging situations in California.

The WRF model is operated for solar irradiance forecasting at several public and private entities, including Solargis (Slovakia); Meteotest (Switzerland); GL-Garrad Hassan

(Mathiesen, Kleissl, and Collier 2013); the Atmospheric Sciences Research Center of the University of Albany as part of the operational air quality forecasting program; and AWS Truepower, a UL company in the United States.

The High Resolution Limited Area Model (HIRLAM)[48] is a hydrostatic regional NWP model operated by several national meteorological services in Europe, including the Spanish National Weather Service and the Danish Meteorological Institute. The Spanish National Weather Service runs HIRLAM four times daily in three spatial configurations (one covering Europe at a resolution of 16 km and two covering Spain and the Canary Islands at a resolution of 5 km) with 40 vertical levels. The Danish Meteorological Institute runs its highest-resolution HIRLAM model, "SKA," for an area covering Northwestern Europe with a grid size of 0.03° (≈3 km) and 65 vertical levels. HIRLAM uses the clear-sky irradiance scheme of Savijärvi (1990) and the cloud scheme of Wyser, Rontu, and Savijärvi (1999). The nonhydrostatic HIRLAM ALADIN Regional Mesoscale Operational NWP In Europe (HARMONIE) regional model is being run experimentally by the Spanish National Weather Service daily over Spain and the Balearic Islands at a resolution of 2.5 km, with 65 vertical levels. Closely related to HARMONIE and HIRLAM is the STRÅNG mesoscale model,[49] which provides hourly nowcasts of GHI, DNI, erythemal ultraviolet, photosynthetically active radiation, and sunshine over Scandinavia at 2.5-km resolution.

The German Weather Service (Deutscher Wetterdienst, or DWD) has an operational model chain consisting of the global model ICON (ICOsahedral Nonhydrostatic); the ICON-EU, which is the nested European regional model; and the regional model for Germany called COSMO-D2. The horizontal resolution of the ICON model is 13 km, and it has 90 model layers extending to 75 km (Zängl et al. 2014). The ICON-EU is nested via a two-way interaction. It has a horizontal model resolution of approximately 7 km and 60 model layers up to a height of 22.5 km. The third model is the regional nonhydrostatic COSMO-D2 model, which has a horizontal resolution of 2.2 km and 65 vertical levels. The COSMO model was developed by the Consortium for Small-scale Modeling (COSMO), which consists of the national meteorological services of Germany, Greece, Italy, Poland, Romania, Russia, and Switzerland. The COSMO-D2 (Baldauf et al. 2011) is a model for short-term forecasts of +27 hours, except for the 03:00 UTC run, which has a forecast length of +45 hours. The radiation scheme in the ICON and ICON-EU is currently called once per hour; however, the radiative transfer scheme of Ritter and Geleyn (1992) is called every 15 minutes within COSMO-D2. Thus, the direct and diffuse radiation predictions are available every 15 minutes via direct model output. Using the regional COSMO model, DWD performed a statistical analysis to detect those days with the highest forecast error in Germany, and they identified that NWP forecasts have frequent errors in the presence of low stratus. To address those situations, they proposed a low stratus-detection method that operationally uses post-production.

Another example is NOAA's High-Resolution Rapid Refresh (HRRR) model for the United States, which provides forecasts at 3-km by 3-km resolution with hourly updates.

Finally, the "SKIRON" regional weather forecasting system (Kallos 1997) is operated for solar energy applications at the National Renewable Energy Centre of Spain (Gastón et al. 2009).

[48] See http://www.hirlam.org.
[49] See http://strang.smhi.se/.

8.3 Irradiance Forecasting Based on Irradiance Time Series and Post-Processing with Statistical and Machine Learning Methods

Statistical learning models are widely used for solar irradiance and power forecasting. The dependence between input variables (predictors) and forecast values (predictands) is established in a training phase by learning from historical data, assuming that patterns in the historical data sets are repeated in the future and thus might be exploited for forecasting. Statistical methods include classical regression methods, such as autoregressive and autoregressive integrated moving average models as well as machine learning or artificial intelligence techniques, such as artificial neural networks (ANNs), k-nearest neighbors, or support vector regression. Coimbra and Pedro (2013a), Diagné et al. (2013), and Yang et al. (2018) provided an overview of different statistical approaches used for solar irradiance forecasting. Voyant et al. (2017) and Sobri et al. (2018) reviewed the topic with a heavy focus on the use of machine learning methods for solar radiation or power forecasting as well as for post-processing.

Statistical and machine leaning models are applied for different purposes in irradiance and PV power forecasting. Pure time-series approaches aim to derive solar irradiance or power forecasts based solely on local measurements without involving any physical modeling (i.e., *time-series approaches with no exogenous input*). They are suitable for forecast horizons from several minutes to several hours ahead.

Statistical and machine learning methods also play an important role in enhancing the output of NWP models and CMV forecasts. Regardless of the physics-based forecasting model used, errors that are partly stochastic and partly systematic will always remain. These errors can be reduced with statistical learning based on historical data sets of predicted and measured irradiance or PV power. Further, statistical learning methods can be employed to derive quantities not included in the native model output. Different terminology is used for this combination of statistical and physical forecasting methods, depending on the perspective of the researchers. The community of statistical modeling and artificial intelligence refers to these models as *statistical models with exogenous input*. Meteorologists commonly use the terms *statistical post-processing* or, more specifically, model output statistics (MOS) in the context of NWP, which is the terminology adopted here.

Section 8.3.1 provides an overview of selected machine learning models, and Section 8.3.2 addresses pure time-series models based on irradiance measurements. Finally, Section 8.3.3 describes the application of statistical and machine learning models for post-processing.

8.3.1 Examples of Machine Learning Models Applied for Forecasting

The use of state-of-the-art machine learning models is popular in irradiance as well as in PV power forecasting. This section lists several approaches discussed by Winter et al. (2019).

8.3.1.1 Artificial Neural Networks

ANNs constitute one of the most versatile machine learning methods and are known for their use in complex tasks such as image or speech recognition (LeCun et al. 1989; Sak and Beaufays 2014).

As described by Bishop (1995), an ANN consists of a fixed number of nodes, called units, that can take on numerical values and are arranged in several layers. The input layer contains one unit for each feature of the data set, whereas the output layer, in case of a single regression problem, is only one unit. The layers between the input and output layers

are referred to as hidden layers. The key task is to establish a connection between the nodes by assigning to each unit in one layer the weighted sum of the previous layer's units, and to then apply a nonlinear activation function. In the case of a regression problem, a linear activation function is applied to the weighted sum of the output unit.

By training an ANN on a given set of input and output data, all its weights are adjusted to minimize an error function, typically the mean square error (MSE). This is usually done by back-propagation, an iterative process for calculating the gradient of the error function with respect to each weight (Rumelhart, Hinton, and Williams 1986). In each step, the weights get updated by using a gradient descent optimization algorithm. An alternative option is the method of adaptive moment estimation, or "Adam," as described by Kingma and Ba (2015). Instead of calculating the gradient of the error function with respect to the full data set, in each step the weights can be updated only with respect to a subset of the data set (see Bottou 1998; Ruder 2016). The weights can be initialized using a common heuristic described by Glorot and Bengio (2010).

To enable an ANN to learn nonlinear relationships between input and output, a nonlinear activation function must be chosen. For example, the leaky rectified linear unit activation function can be used (Maas, Hannun, and Ng 2013).

8.3.1.2 Extreme Learning Machines

An extreme learning machine, as proposed by Huang, Zhu, and Siew (2006), is an ANN with a single hidden layer between the input and output layers. Its learning method does not rely on gradient descent. Instead, the weights between the input and hidden layers are chosen randomly. In this way, only the weights between the hidden and output layers need to be determined. Because this is just a linear regression problem, an analytic solution exists, which can be calculated directly without an iterative optimization algorithm. Hence, training the model is considerably faster while maintaining good performance of the model.

8.3.1.3 Gradient Boosted Regression Trees

Gradient boosted regression trees are an ensemble technique using multiple classification and regression trees (CART) (Breiman et al. 1984). The CART algorithm creates binary decision trees, which means that at each new node the data is split into two parts according to a threshold value. Starting with a root node, which in general contains all training data, the tree grows until some stop condition is reached. The last nodes form the tree's leaves. Each splitting leads to either another node or a leaf. The leaf contains the class to be predicted. In the case of regression, a leaf returns the mean value of the training samples it contains.

The principle of boosting is described by Friedman (2001). Starting with a single CART tree that is fit to minimize the MSE on the training data, the following trees are trained consecutively so that each new tree predicts the residual error. This residual error is proportional to the gradient of the MSE. By scaling the new tree's prediction with a step size between 0 and 1 and by adding it to the current ensemble, every new tree aims to further reduce the MSE of the ensemble's prediction.

8.3.1.4 Random Forest

A random forest is another technique based on ensembles of CARTs and is presented by Breiman (2001). The ensemble's prediction is the average over all single tree predictions. Each tree is trained on a bootstrap data set generated by randomly drawn samples with replacement from the original data set (Efron 1979). Further, for each node split, only a random subset of features is considered. By omitting data randomly, the resulting trees become less correlated. This lowered correlation of single trees has been observed to reduce the model error.

8.3.2 Time-Series Models Based on Measurements

Intrahour or hours-ahead solar irradiance and PV power forecasting with time-series models use recent measurements of irradiance or PV power as a basic input, possibly complemented by measurements of other variables. Examples are the application of a coupled autoregressive and dynamic system model for forecasting solar radiation on an hourly timescale, as described by Huang et al. (2013); the comparison of ANN and classical time-series models. as described by Reikard (2009); and the short-term PV power prediction approach of Bacher, Madsen, and Nielsen (2009). Through their review of machine learning methods, Voyant et al. (2017) concluded that although ANN and autoregression-style methods still dominate statistical forecasting, other methods (e.g., support vector regression, regression tree, random forest, and gradient boosting) are increasingly being used. Although the ranking of such methods is complicated by many factors, it generally holds that a multi-model approach results in improvement in forecasting performance (Zemouri, Bouzgou, and Gueymard 2019).

For any statistical model, the selection and availability of appropriate input variables as well as the optimized preprocessing of the data is of critical importance for good forecast performance. Also, the choice of the model configuration (e.g., the ANN architecture or the selection of hyperparameters in machine learning models) is essential. Finally, the setup of the training sample (e.g., the number of days and sites used for the training) has a noteworthy influence on the forecast accuracy. Coimbra and Pedro (2013a) showed the benefits of the application of a generic algorithm to identify the most suitable ANN architecture, preprocessing scheme, and training data.

The advantages and limits of purely statistical approaches are discussed next. High-quality measurements of the actual surface solar irradiance or PV power are the best possible starting point for any forecast. In comparison, the assessment of the initial irradiance conditions (i.e., the irradiance analysis) with an empirical or physical forecasting model shows considerably higher uncertainties. Any physics-based forecasting model has an inherent uncertainty, regardless of the forecast horizon, that is caused by limits in spatial and temporal resolution, uncertainty in input parameters, and simplifying assumptions within the model. Time-series models exploit the autocorrelation in time series of solar irradiance, cloud cover and, possibly, other explanatory variables. For very short-term forecast horizons, forecasts based on accurate on-site measurements and statistical methods reach forecast errors that are smaller than even the NWP analysis errors or the initial errors of irradiances derived from satellite images.

Given the inherent chaotic nature of weather phenomena, any existing autocorrelation decreases as the time lag between time-series instances increases. Hence, the performance of these models is (1) strongly determined by the underlying autocorrelation of each particular weather condition and (2) decreases as forecast lead time increases. For longer forecast horizons, wide-area observations (e.g., those from satellites) or physical models (e.g., NWP models) are required to meet the forecast skill requirements.

Pure time-series approaches are typically applied to forecast horizons ranging from several minutes to a few hours ahead. Evidently, their performance in comparison to other methods strongly depends on the prevailing climate and weather conditions (e.g., the stability of the sky situation), the spatiotemporal resolution of the forecasts, and the models to which they are compared.

In this context, Bacher, Madsen, and Nielsen (2009) compared an autoregressive model for hourly solar power forecasting combined with and without exogenous inputs from a diverse origin. The study was based on PV plants in Denmark, and the authors found that ground-observed data are the most important class of inputs up to approximately 2 hours ahead,

whereas the NWP forecast parameters are adequate for next-day horizons. A comparison of pure time-series models with satellite-based CMV forecasts was given by Wolff et al. (2016) for PV systems in Germany. The authors found that CMV forecasts outperformed the time-series approach for forecast horizons more than 30 minutes ahead for single sites and for forecast horizons of more than 2 hours ahead for the German average.

Further, sky camera imagery-based forecasting methods were demonstrated to be valuable for short-term high-resolution forecasting. Pedro et al. (2018) and Huang et al. (2019) assessed intrahour hybrid forecasting models that combine statistical (or machine learning) methods with information extracted from sky imagery and found substantial improvements. Huang et al. (2019) proposed the conditional autoregressive method of clear-sky index, which can separate and model characteristic weather events through the identification of key condition variables. Based on high-frequency data measured in Australia, it was shown that by adding exogenous forecasts derived from sky imagery, their hybrid model could produce accurate forecasts seamlessly across timescales from 10 seconds to 10 minutes ahead.

8.3.3 Statistical Post-Processing Methods

Statistical post-processing (or machine learning with exogenous input) plays an important role in irradiance and PV power forecasting. Post-processing methods are applied to:

- Reduce model errors by considering unaccounted or partially accounted local and regional effects (e.g., topography and aerosols)
- Combine the outputs of different models
- Derive quantities that are not direct model outputs.

In what follows, various statistical post-processing methods are summarized for the possible applications enumerated.

8.3.3.1 Model Output Statistics to Reduce Forecast Errors

MOS are widely used to refine the output of NWP models, primarily to account for local variations in weather and surface conditions (Glahn and Lowry 1972). They use measurements and/or climatology for specific locations as a basis to adapt the forecasts. For example, MOS techniques constitute a powerful tool to adapt the results from NWP or satellite-based models to site-specific conditions (Gueymard et al. 2012). For solar irradiance forecasting, satellite-derived values might be used in lieu of ground measurements. The set of predictors consists of NWP output and might be extended by including any relevant information—for example, prior observations or climatological values.

Originally, the term *model output statistics* was associated with the use of regression equations; however, a generalization of this concept now involves other statistical approaches. Lorenz et al. (2009) applied a bias correction MOS based on solar elevation and clear-sky index to ECMWF irradiance forecasts. Kalman filters have also been proposed by Pelland, Galanis, and Kallos (2013) to improve irradiance forecasts of the Canadian GEM model and by Diagné et al. (2014) in the case of WRF model solar irradiance forecasts. Marquez and Coimbra (2011) investigated the application of ANNs to predicted variables from a weather forecasting database, and Gastón et al. (2009) used a machine learning algorithm to enhance SKIRON solar irradiance forecasts. Pierro et al. (2015) proposed a MOS technique to correct WRF-based GHI forecasts by coupling two intermediate MOS consisting of correlations with relative humidity and ANNs, respectively. Other powerful post-processing approaches have been thoroughly reviewed by Yang and van der Meer (2021).

8.3.3.2 Combination of Forecast Model Outputs

Combining the output of different models can considerably increase the forecast accuracy. First, simple averaging is beneficial for models with similar accuracy, exploiting the fact that forecast errors of different models are usually not perfectly correlated (Perez et al. 2013; Lorenz et al. 2016).

Combining methods using more advanced techniques might also account for strengths and weaknesses of the different models for certain situations—for example, by adapting the contribution of each model depending on the weather situation. In particular, they might be applied to establish a forecast consensus covering horizons from several minutes to several days ahead by integrating measurements, climate monitoring, and NWP forecasts. Various approaches to this aim have been proposed. For instance, Lorenz and Heinemann (2012) used a weighted average with weights optimized for each forecast horizon. Sanfilippo et al. (2016) applied a multi-model approach to solar forecasting that uses supervised classification of forecasting evaluation results to select the best predictions from persistence, support vector regression, and diverse stochastic models. Wolff et al. (2016) and Mazorra Aguiar et al. (2016) combined forecasts based on support vector regression machines and ANNs respectively. Yang et al. (2017) used a hierarchical scheme and minimization of the trace of the forecast error covariance matrix. Within the context of the Sun4Cast project, NCAR's DICast system (Myers et al. 2011, 2012) has been applied to blend multiple solar radiation forecasts. This system—which has already been applied in other forecasting areas, such as transportation, agriculture, and wind energy—consists of a two-step process: (1) a statistical bias correction process using a dynamic MOS and (2) optimization of the model blending weights for each lead time (Haupt et al. 2016).

8.3.3.3 Post-Processing to Derive Additional Quantities

Not all quantities of interest in the context of irradiance forecasting (i.e., GTI, DNI or PV power) are always available as direct NWP output or as a result of CMV forecasts. Post-processing can be applied to derive these quantities. To that aim, statistical or machine learning methods are typically employed, but empirical or physical models are also frequently used to derive the desired quantity from the direct output of the forecasting model.

Although GHI has become a standard output of most NWP models, this was not the case when the field of solar forecasting started to emerge. For example, Perez et al. (2007) proposed an empirical solar radiation forecast model relating sky-cover predictions from the National Digital Forecast Database to the clear-sky index to derive GHI forecasts.

The irradiance components (DHI and DNI) are still not provided as direct output from many irradiance forecasting systems. To derive them from GHI forecasts, several empirical diffuse or direct fraction models can be used, many of which were originally developed for application to measurements or satellite data (see also Section 4.2 in Chapter 4). These models are also being used in DNI forecasting systems that are based on a GHI forecast (e.g., Schroedter-Homscheidt, Benedetti, and Killius 2016). For DNI forecasts, several physical post-processing approaches have also been proposed, specifically for better consideration of aerosols. Breitkreuz et al. (2009) proposed a forecasting approach for direct and diffuse irradiance based on the combination of a chemistry transport model and an NWP model in which forecasts of AOD are directly collected from the chemistry transport model outputs. Similarly, Gueymard and Jimenez (2018) used WRF-Solar with hourly inputs of aerosol forecasts from NASA's Goddard Earth Observing System Model 5 (GEOS-5) atmospheric analysis model. Such aerosol forecasts, together with other remote sensing data (ground albedo and ozone) and NWP parameters (water vapor and clouds), are used as input to radiation transfer calculations to derive the irradiance forecasts. A similar approach was used by Lara-Fanego et al. (2012) to derive DNI from WRF output using

aerosol observations from the Moderate Resolution Imaging Spectroradiometer (MODIS) onboard the Terra satellite.

In the context of PV applications, deriving GTI (or plane-of-array [POA]) forecasts is also of interest (see Section 8.4.1.1).

8.4 PV Power Forecasting and Regional Upscaling

PV power forecasts for a given location or region are important for plant operators, grid operators, and the marketing of produced energy. They are derived from irradiance predictions with physics-based or statistical methods or a combination of both (see Figure 8-5). The exceptions are time-series approaches for very short-term forecast horizons that are solely based on PV power measurements.

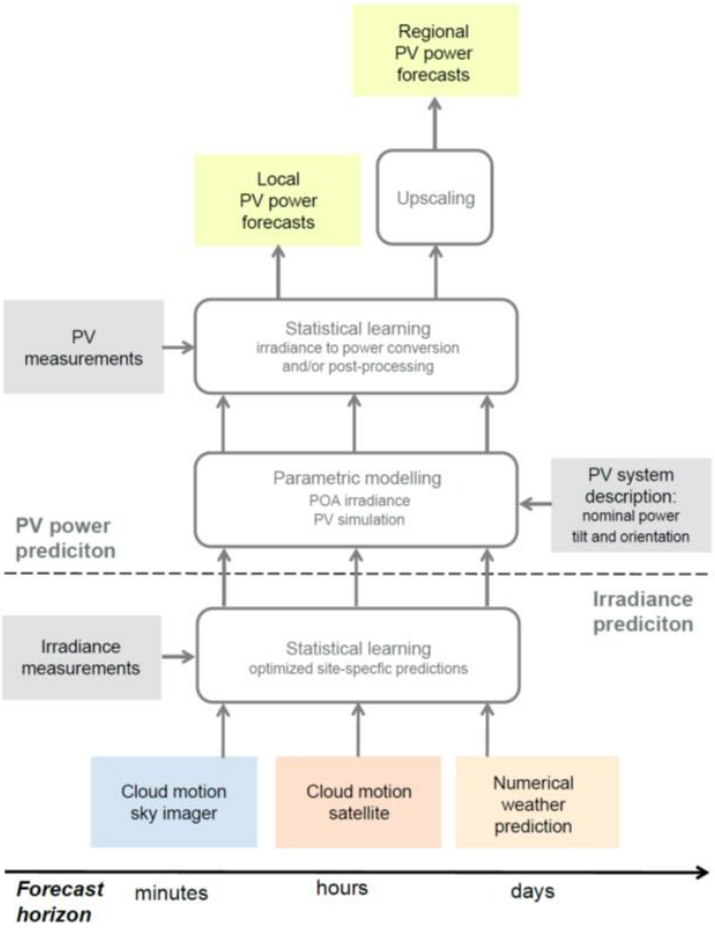

Figure 8-5. Overview of basic modeling steps in PV power prediction. Irradiance prediction: Different forecasting models for different forecast horizons (e.g., cloud-motion sky imager and satellite data, NWP) and combination with statistical learning approaches for optimized site-specific predictions. PV power prediction: Conversion of irradiance to PV power with parametric PV simulation models and/or statistical learning approaches; regional PV power prediction requires upscaling as a last step. ***Image reproduced from Lorenz (2018)***

Physics-based parametric modeling involves transposing GHI to GTI (POA) irradiance (Section 8.4.1.1) and then applying a PV simulation model (Section 8.4.1.2). For this, information on the characteristics of the PV system configuration is required in addition to the meteorological input data; this includes information on nominal power, tilt, and

orientation of a PV system as well as characterization of the module efficiency as a function of irradiance and temperature. Alternatively, the relationship between PV power output and irradiance forecasts and other input variables can be directly established with statistical or machine learning on the basis of historical data sets including measured PV power. In practice, the approaches are often combined, and statistical post-processing using measured PV power data is applied to improve predictions with parametric simulation models (Section 8.4.1.3). PV power prediction for grid operators requires forecasts of the aggregated PV power generation for a specified area (i.e., regional forecasts instead of single-site forecasts). These regional predictions are typically obtained by upscaling methods (see Section 8.4.2).

8.4.1 Simulation of PV Power Plant Production

The simplest way to forecast the production of a PV power plant is to apply a PV power simulation model to the forecast of the relevant predicting variables (primarily irradiance, but also environmental temperature and wind speed). Physics-based models explicitly require specific inputs. ANNs or other machine learning models might be more flexible and benefit from a more extensive set of input variables.

8.4.1.1 Estimating Plane-of-Array or PV Power from Irradiance Forecast

Because empirical PV simulation models use irradiance or the POA as key inputs, the transposition of GHI into GTI to obtain the POA irradiance (see also Chapter 4, Section 4.2) is the first modeling step. For example, the PV power forecasting approaches presented by Lorenz et al. (2011) and Pelland, Galanis, and Kallos (2013) involve empirical models to derive the POA irradiance as input for PV simulation models. Unless DNI and DHI are explicitly provided by the forecast model, this first step requires splitting GHI into its direct and diffuse irradiance components. For that purpose, many empirical diffuse or direct fraction models that were originally developed for application to measurements or satellite data can be used (see also Section 4.2). Gueymard and Ruiz-Arias (2015) and Aler et al. (2017) presented an unprecedented worldwide evaluation of 140 of these separation models proposed during the last 60 years.

Next, the direct and diffuse components are projected or “transposed” to the POA (see Chapter 4, Section 4.3). The transposition of the direct irradiance is straightforward, subject only to geometric considerations. The transposition of the diffuse irradiance requires, again, an empirical model for the directional distribution of radiance over the sky, describing anisotropic effects such as horizon brightening and circumsolar irradiance (Perez et al. 1987; Gueymard 1987; Hay 1979). Validation studies of these transposition models are provided by Behr (1997); David, Lauret, and Boland (2013); Gueymard (2009); Ineichen (2011); and Kambezidis et al. (1994). The validation of combined separation and transposition models has been undertaken by Gueymard (2009); Orehounig, Dervishi, and Mahdavi (2014); Lave et al. (2015); and Yang (2016).

8.4.1.2 PV Power Simulation

In the next step, the POA irradiance is converted to PV output power. Most simple PV simulation models use only the global tilted irradiance on the POA as input and scale it with the PV module array area and efficiency:

$$P_{PV}\,[kW] = I_{POA}\left[\frac{kW}{m^2}\right] * A_{PV}[m^2] * \frac{\eta_{mod}[\%]}{100} * f_{Loss} \qquad (8\text{-}1)$$

with:

- $I_{POA}\left[\frac{kW}{m^2}\right]$, irradiance on the module’s POA

- $A_{PV}[m^2]$, the PV array module area
- $\eta_{mod}[\%]$, the efficiency of the PV modules
- f_{Loss}, a factor accounting for additional deviations (e.g., deviations that are due to electrical, optical, or thermal losses).

State-of-the-art PV simulation models consider additional influencing factors. Because of optical losses on the module surface, the effective irradiance is lower than the incoming POA irradiance (e.g., Martin and Ruiz 2001). The DC module efficiency depends on the POA irradiance and decreases with increasing temperature. It is secondarily also affected by wind speed and direction (e.g., Beyer et al. 2004). The spectral distribution of irradiance is another influencing factor. Moreover, the conversion efficiency of DC-to-AC inverters is not constant and should be also modeled (e.g., Schmidt and Sauer 1996).

A deeper insight into the modeling of PV power and corresponding variables can be achieved with the tools provided by *pvlib*, a software package for modeling PV systems (Andrews et al. 2014) (see also Section 9.4). The choice of input parameters is an issue for using such a model. A natural approach is to use the metadata available for the PV system (e.g., module and inverter specifications, orientation, and peak power); however, this information is frequently missing or erroneous, especially for smaller PV systems. An alternative is learning the parameters from historical data. Here, it is emphasized that measurement issues, plant outages, or shading can impact the estimation of these parameters. Failures of technical components are likely to have large impacts, but the same is true with grid codes, consumption, and curtailments, which are caused by grid operation or electricity market price. To overcome these issues, a robust training method has been proposed by Saint-Drenan et al. (2015).

8.4.1.3 Statistical and Machine Learning Methods for PV Power Forecasting Based on PV Power or Irradiance Measurements

When PV power measurements are available, the output of a forecast derived with PV power simulation is often adapted to PV power measurements with statistical or machine learning methods to improve the predictions (e.g., Kühnert 2015). When aiming to fit a time series of measured PV power plant feed-in, one needs to account for external effects reducing the production, as described in Section 8.4.2.

Recently, the direct simulation of PV power with statistical or machine learning models (see Section 8.3.1) has also gained popularity. This forecasting technique is based on historical data, either by means of a statistical analysis of the different input variables (e.g., autoregressive moving average or autoregressive integrated moving average) or by using machine learning algorithms that can also handle nonlinear and nonstationary data patterns (Das, Tey and Seydmahmoudia 2018; Ulbricht 2013).

8.4.2 Estimation and Forecasting of Regional PV Power Feed-In

A very large number of PV systems contribute to the overall PV power generation in a control area or a country. TSOs and utilities require forecasts and estimates of this overall PV power (e.g., as a basis for energy trading).

For many small PV systems, which contribute a large share of the overall feed-in, PV power is not measured with sufficient resolution (e.g., 15-minute or hourly) in many countries; only annual energy totals are available. Consequently, the actual overall PV power feed-in must be estimated using other available data. These estimates of regionally aggregated PV power are important as a starting point for the shortest-term forecasting in real time and as a reference for the statistical training of regional forecasts as well as for evaluations.

Regional PV power feed-in can be estimated using the following data:

- Measurements of the output of PV plants
- Meteorological data (irradiance and temperature)
- Information on the fleet of PV system: coordinates and installed capacity (along with tilt and orientation if available).

An approach frequently applied for both the estimation and the forecasting of regional PV power feed-in is upscaling from a representative set of PV systems in combination with information on the PV fleet. Another approach combines meteorological information (e.g., real-time irradiance from satellite data or irradiance forecasts) with PV simulation using information of the characteristics of the PV fleet. This information is available at different levels in various countries but remains difficult to obtain on a regular basis. Killinger et al. (2018) addressed this issue by collecting the data and applying the method at several thousands of PV system characteristics. As a first step, this approach does not rely on PV measurements, but in practice some-post processing is often applied.

With respect to forecasting of regional PV power, there are additional options. In principle, it would be possible to predict the PV power output for each PV plant in a region (even if PV power measurements were unavailable), and subsequently aggregating the predictions for the whole area (i.e., a “bottom-up” or accumulation approach). This method, however, is characterized by a high computational burden and requires a detailed knowledge of every plant in the area; therefore, it is difficult to achieve, especially for large areas. Nonetheless, two examples of PV-system-based forecasts have been published (Vaz et al. 2016; Carillo et al. 2020).

Finally, if an estimated time series of regional PV power time series is given, forecast providers can also train their models directly to this PV power time series without requiring detailed information of the PV fleet (i.e., a “models input average” approach).

These approaches are introduced in sections 8.4.2.1, 8.4.2.1, and 8.4.2.3.

8.4.2.1 Upscaling Based on Representative PV Systems

One option for upscaling is to rescale the output of the reference plants to the overall installed capacity in a given region (Lorenz et al. 2011; Kühnert 2015). This approach exploits the strong correlation of the power output of nearby PV systems and allows for the estimation and the prediction of PV power with good accuracy given a sufficient number of reference plants and given that the representative set reflects the basic properties of the total data set (Kühnert 2015; Saint-Drenan et al. 2016). Representation of the spatial distribution of the nominal power and of the PV systems’ tilt and orientation is most important in this approach. In operational PV power prediction systems based on this approach, the upscaling is typically performed for small subregions (e.g., down to postal codes) and potentially also for different classes of PV system size in a first step. Then, the estimates for the different subregions and classes are aggregated to the region of interest.

Another approach for upscaling based on representative PV systems uses spatial interpolation methods. Starting with a set of reference power plants, one can interpolate the (measured or predicted) power to any other power plant, assuming that at least the exact coordinates of reference as well as target locations are known. Geosciences offer several methods to conduct that task; see the review by Li and Heap (2014). The most popular of these methods are the simple but robust inverse distance weighting (IDW), and some authors apply the more complex kriging method, at least to interpolate irradiation data (Jamaly and Kleissl 2017; Yang et al. 2013). Because irradiance is the most important

variable for PV power production, methods are likely to apply to both measured and predicted power.

One key difference of the two mentioned methods is the feature of convexity: the IDW method is convex and therefore generates interpolated values only in the range from the min to the max input values; on the other hand, kriging is a nonconvex method that can produce results outside the range of input measurements. Considering the aim to estimate many local PV power production values based on a set of measurements from different locations, it seems reasonable to rely on a set of references that is as large as possible when using the IDW method.

Because this robust method is one of the most commonly implemented methods, as exemplified by Saint-Drenan (2011) and Bright et al. (2018), it is briefly described here. The PV power, P_j, for power plant, *j*, is the weighted sum of *n* surrounding power plants, *i,* where the weights, w_{ij}, are calculated based on the inverse of distance, *d*, between *j* and *i*, so that the sum of all weights equals one. The exponent, *u*, is typically optimized and found to be approximately 1.7–2.0.

$$P_j(t) = \sum_{i=1}^{n} w_{ij}\, P_i(t) \tag{8-2}$$

$$w_{ij} = \frac{d(i,j)^{-u}}{\sum_{k=1}^{n} d(k,j)^{-u}}, u > 0 \tag{8-3}$$

The targets, *j*, can alternatively be seen as the center of all installed capacity of an area of interest; however, assuming similar characteristics (e.g., orientation angles) between references and targets is needed for this. Improvements have been observed by accounting for known orientations (e.g., Killinger et al. 2016). Last, an important step is the aggregation of all relevant targets (power plants or areas) for a region of interest. When it comes to unknown or dynamically changing electric grid connections, a new source of uncertainty becomes important. An extensive investigation of more general uncertainties can be found in Saint-Drenan et al. (2016).

8.4.2.2 Regional Model Based on Statistical Analysis of the Fleet of PV Systems

As mentioned, simulating each single plant installed in a region is not realistic because of the very high computational costs. As shown by Saint-Drenan, Good, and Braun (2017), a realistic alternative is to group all plants with similar characteristics (i.e., orientation angles) and simulate this limited number of groups. It can easily be shown that this computational technique allows for speeding up the calculation without losing information, making this approach viable. This type of implementation requires determining the share of each group of plants—in other words, the share of installed capacity for each class of orientation must be assessed. Several approaches can be followed to obtain this information.

The first approach, which is described by Saint-Drenan et al. (2017), involves conducting a statistical analysis on a subset of the installed PV plants (see Figure 8-6). The risk here is that the selected samples are not representative of the actual PV system. To address this issue, it is possible to train the distribution of the different classes of PV plants; this option was demonstrated by Saint-Drenan et al. (2019), where a Bayesian approach was used to regularize the training approach. This statistical approach has also been employed in the Copernicus Climate Change Service to generate regional PV power for each region in Europe using the ERA5 reanalysis data set. As described by Saint-Drenan et al. (2018), the parameters of the statistical regional model have been derived from the optimal tilt angle, allowing this model to be implemented anywhere in Europe without the need for a training data set. A comparison of the model output with the European Network of TSOs for Electricity data showed that this approach is well accepted. Note that estimates of the

regional power production for each European Union country is calculated operationally each month with this method. The data can be found on the Copernicus Data Store.[50]

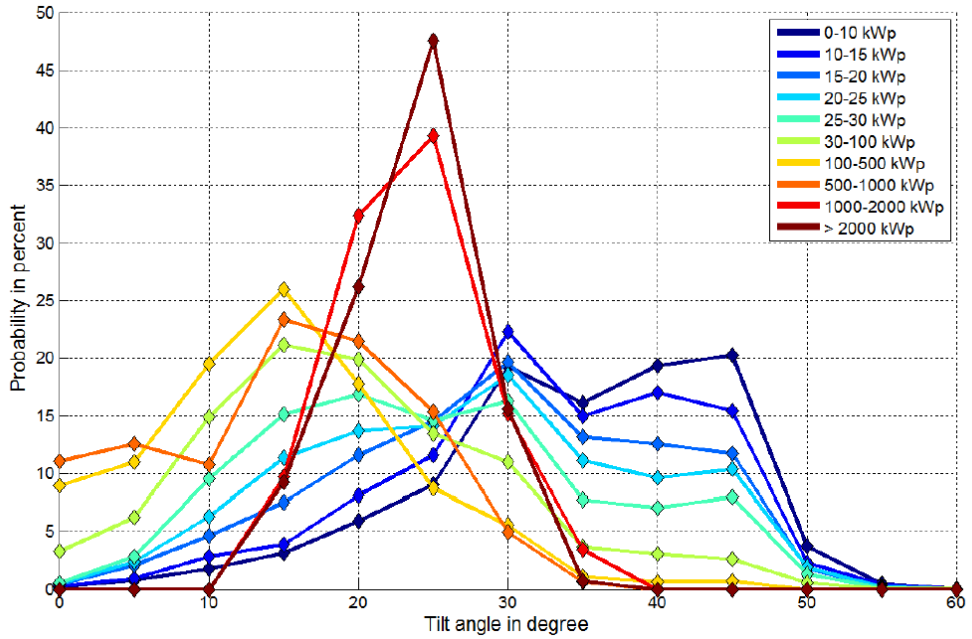

Figure 8-6. Distribution of the tilt angle of German PV systems for different classes of peak power. ***Image from Saint-Drenan et al. (2017)***

8.4.2.3 Forecasting Regional PV Power Based on Averaged Model Inputs

The direct approach, called "model inputs average," is based on the spatial smoothing of the input features. In this case, the PV power generation of the area is considered to be a virtual power plant, and prediction is made directly at the regional level by using a historical data set of regional PV power (measured or estimated) and input meteorological forecasts aggregated at a smaller spatial scale than the region of interest. The main advantage of this approach is the possibility of obtaining a reliable power forecast without additional details about the installations beyond the total installed capacity of the whole area. The relationship between meteorological forecasts and PV power time series is typically established with machine learning approaches. An overview of the relationship is given by Betti et al. (2020). A prerequisite of this approach is the availability of a time series of actual PV power feed-in, which can be estimated by the upscaling models described in Section 8.4.2.1. In many countries, estimates of the regional PV power feed-in are published, for example, by grid operators, and they are available to forecast data providers as a basis for training.

8.5 Evaluation of Irradiance and PV Power Forecasts

The evaluation of solar irradiance forecasts provides users with the necessary information about forecast accuracy and helps them choose different forecasting products or assess the risk when using a particular forecast as a basis for decisions. An extensive overview of forecast verification methods was given by Jolliffe and Stephenson (2011). This section addresses the evaluation of deterministic irradiance forecasts that provides an overall indication of the uncertainty of a specific forecast model. Probabilistic solar forecasts

[50] See https://cds.climate.copernicus.eu/#!/home.

assigning uncertainty estimates to each individual forecast value are described in Section 8.6.

The quality of forecasts is evaluated by assessing their similarity to reference data. Most often, irradiance measurements are used as reference data, which are commonly referred to as ground truth data. Nevertheless, reference data are always affected by a certain degree of uncertainty (see Chapter 7). Alternatively, satellite-retrieved irradiance values or the output of a detailed physical model might serve as a reference.

The choice of appropriate metrics and concepts for the evaluation of solar irradiance and power forecasts is the subject of ongoing discussions within the solar forecasting community; see, e.g., Hoff et al. (2012a) and Marquez and Coimbra (2013). Recently, Yang et al. (2020) proposed applying the well-established Murphy-Winkler framework for distribution-oriented forecast verification as a standard practice to analyze and compare solar forecasts.

Here, the most standard evaluation methods are outlined, including (1) statistical error measures (Section 8.5.1.1); (2) comparison to reference models using the skill score parameter (Section 8.5.1.2); and (3) other important considerations, such as the representation of the observed frequency distribution and the forecast "goodness" as a function of solar position, hour of the day, cloud variability, or even spatiotemporal averaging (Sections 8.5.2–8.5.4). These concepts are introduced using examples from an observational data set of hourly pyranometer measurements from 18 weather stations of the German Weather Service from March 2013 to February 2014 (Lorenz et al. 2016) and forecasts from two NWP models, including the:

- High-resolution deterministic global IFS model, operated at the ECMWF, with spatial resolution of 0.125°, 3-hourly outputs, and forecast horizon of 24 hours issued every day at 00:00 UTC
- High-resolution regional HIRLAM SKA model, operated at the Danish Meteorological Institute, with spatial resolution of 3 km, hourly outputs, and forecast horizons from 4–9 hours ahead, issued daily at 00:00 UTC, 06:00 UTC, 12:00 UTC, and 18:00 UTC.

In addition, Section 8.5.5 addresses the evaluation of regional PV power forecasts in a case study in Italy. Finally, Section 8.5.6 introduces the concept of "firm power forecasts" as an effective model validation metric to account for the economic value of solar forecasts.

8.5.1 Error Measures

Statistical error measures and skill scores are applied for quantitative forecast evaluation.

8.5.1.1 Statistical Error Measures

Here, the most commonly used error measures based on first-order statistics are presented. The error of a single measurement is given as:

$$\varepsilon_i = I_{pred,i} - I_{meas,i}\,, \tag{8-4}$$

where $I_{pred,i}$ denotes a predicted irradiance value (GHI or DNI), and $I_{meas,i}$ is the corresponding measured value.

To evaluate the forecast accuracy of the solar power predictions, the root mean square error (RMSE) is commonly used:

$$\mathrm{RMSE} = \frac{1}{\sqrt{N}} \sqrt{\sum_{i=1}^{N} \varepsilon_i^2} \tag{8-5}$$

where *N* is the number of data pairs. The mean square error, MSE = RMSE^2, is also commonly used. Typically, only daytime values are considered for the evaluation. Relative errors for the irradiance forecast are generally derived by normalization with respect to mean measured irradiance of a given time interval. In contrast, relative errors of PV power forecasts for utility applications are often normalized to the installed power rather than the mean measured value (e.g., Lorenz et al. 2011).

The RMSE can be split into two components: systematic (1) or bias error and (2) stochastic error or standard deviation. The bias is the difference between the mean of the predicted and measured values (systematic error):

$$bias = \bar{\varepsilon} = \frac{1}{N}\sum_{i=1}^{N}\varepsilon_i \tag{8-6}$$

A positive bias means the predicted values exceed the measurements on average.

The standard deviation of the errors, *stderr*, is defined as:

$$stderr = \sigma(\varepsilon) = \frac{1}{\sqrt{N}}\sqrt{\sum_{i=1}^{N}(\varepsilon_i - \bar{\varepsilon})^2} \tag{8-7}$$

The *stderr* provides information on the spread of the errors around their mean value and might be further decomposed into one part related to the error amplitude [$\sigma(I_{pred}) - \sigma(I_{meas})$] and another part related to the correlation coefficient, *r*, of the time series, which is defined as:

$$r = \frac{\sum_{i=1}^{n}\left(I_{pred,i} - \overline{I_{pred}}\right)\cdot\left(I_{meas,i} - \overline{I_{meas}}\right)}{\sigma(I_{pred})\sigma(I_{meas})}. \tag{8-8}$$

Overall, the complete decomposition of RMSE yields:

$$\mathrm{RMSE}^2 = bias^2 + (\sigma(I_{pred}) - \sigma(I_{meas}))^2 + 2\sigma(I_{meas})\,\sigma(I_{pred})\,(1 - r) \tag{8-9a}$$

or, equivalently, and more simply:

$$\mathrm{RMSE}^2 = bias^2 + stderr^2. \tag{8-9b}$$

Another common measure to assess forecast accuracy is the mean absolute error (MAE):

$$\mathrm{MAE} = \frac{1}{N}\sum_{i=1}^{N}|\,\varepsilon_i\,| \tag{8-10}$$

which is recommended by Hoff et al. (2012a) as a preferred measure, in particular for reporting relative errors.

From a user's point of view, the choice of the most suitable error measure will be based on the impact of forecast errors on their application. MAE is appropriate for applications with linear cost functions (i.e., when the costs caused by inaccurate forecast are proportional to the forecast error). The RMSE is more sensitive to large forecast errors and hence suitable when small errors are more tolerable and larger errors cause disproportionately high costs, which is the case for many applications in the energy market and for grid management issues.

In addition to the computation of these error measures, at least some basic visual analysis is strongly recommended. A direct comparison of measurements and forecasts in scatter plots

or 2D histograms and time series is helpful to develop a better understanding of forecast performance.

8.5.1.2 Skill Score and Persistence Forecast Model

Skill score (also referred to as forecast skill) is used to quantify the forecast performance relative to a reference model. The RMSE is normally used for this comparison; other scores such as MAE or MSE are also often used. The skill score is defined as the difference between the score of the reference model and the forecast model divided by the difference between the score of the reference model and a perfect model; note that a perfect model yields zero RMSE. For RMSE, the skill score, ss_{RMSE}, is calculated as:

$$ss_{\mathrm{RMSE}} = \frac{\mathrm{RMSE}_{\mathrm{ref}} - \mathrm{RMSE}}{\mathrm{RMSE}_{\mathrm{ref}}}, \tag{8-11}$$

where $\mathrm{RMSE}_{\mathrm{ref}}$ refers to the reference model, and RMSE refers to the investigated forecasting algorithm (Coimbra and Pedro 2013a). The skill score's value of 1 hence indicates a perfect forecast, and a skill score of 0 means that the investigated algorithm has the same RMSE as the reference forecast. A negative value indicates performance that is worse than the reference. Skill scores might be applied for comparisons to a simple reference model and also for intercomparisons of different forecasting approaches (i.e., improvement scores).

In solar radiation forecasting, *persistence* is the simplest and most widely used forecast reference model. The persistence model is a trivial model that assumes that the current situation does not change during the forecasted lead time. Several definitions of persistence exist, including *simple* persistence; *scaled* persistence, which accounts for solar geometry changes; and more-advanced concepts, such as *smart* persistence. The most widely used definitions are presented next.

For day-ahead forecasts, the simplest approach is to assume that irradiance, *I* (GHI or DNI), persists during a period of 24 hours, that is:

$$I_{\mathrm{per,24h}}(t) = I_{\mathrm{meas}}(t - 24\mathrm{h}). \tag{8-12}$$

A more elaborate option for GHI, which produces higher accuracy forecasts, is to separate the clear and cloudy contributions to solar radiation and assume that only the cloudy component (i.e., the random component of GHI) persists during the forecast lead time. The clear component is strongly influenced by the deterministic solar geometry and can be described with reasonable accuracy using a clear-sky radiation model. In such a modeling approach, the persisting magnitude is the clear-sky index, K_c, calculated from the measured GHI. For forecast horizons of several hours (Δt) ahead, persistence $\mathrm{GHI}_{\mathrm{per},\Delta t}$ for time *t* is then defined as:

$$\mathrm{GHI}_{\mathrm{per\ Kc},\Delta t}(t) = \mathrm{GHI}_{\mathrm{clear}}(t)\, K_c(t - \Delta t). \tag{8-13}$$

For DNI, a similar approach can be used based on the beam clear-sky index or the Linke turbidity factor (Kuhn et al. 2017b).

In the context of the IEA Task 46 (IEA 2015), the so-called "smart persistence" has been proposed. It consists of increasing the integration time that defines the current conditions commensurately to the forecast time horizon Δt:

$$GHI_{per\ smart,\Delta t}(\mathrm{t}) = GHI_{clear}(\mathrm{t}) \frac{1}{\Delta t} \int_{t-2*\Delta t}^{t-\Delta t} K_c(t')dt' \tag{8-14}$$

Or, for measurements available in discrete time interval Δt_{meas} :

$$GHI_{per\ smart,\Delta t}(\mathrm{t}) = GHI_{clear}(\mathrm{t})\frac{1}{N}\sum_{i=1}^{N} K_c(t - \Delta t\left(1 + \frac{i}{N}\right)), \quad (8\text{-}15)$$

with $N = \frac{\Delta t}{\Delta t_{meas}}$.

Another less-used reference model is based on climatological mean values. Alternatively, combinations of climatology and persistence can be applied as a reference, as recommended by Yang et al. (2020). Further discussion on forecast benchmarking using the skill score and clear-sky persistence is provided by Yang (2019b).

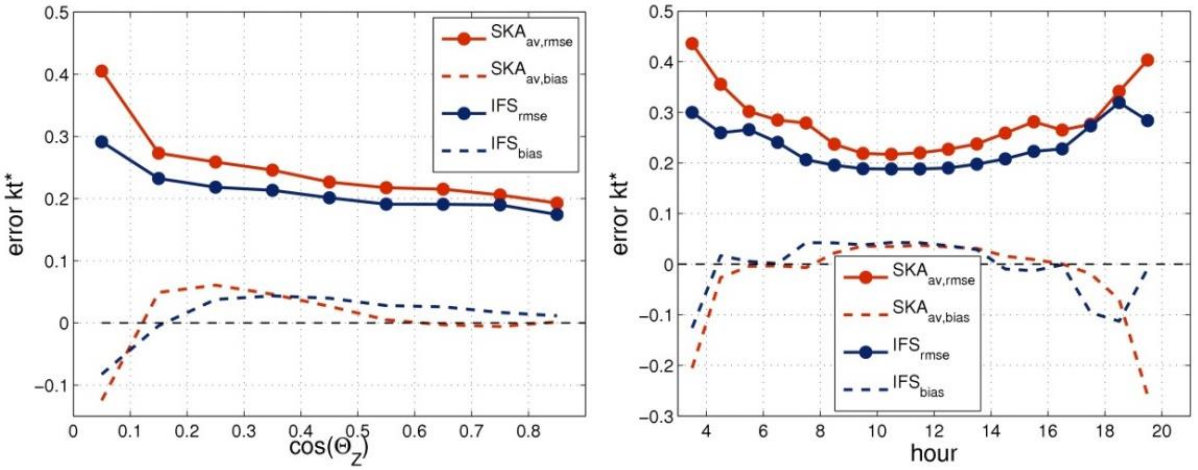

Figure 8-7. Clear-sky index (here noted as kt*) forecast error as a function of (left) cosine of solar zenith angle and (right) hour of the day for the forecasts issued by the IFS and SKA NWP models (blue and red lines, respectively). Solid lines show RMSE, and dashed lines show mean bias error. The evaluated period is from March 1, 2013–February 28, 2014.

8.5.2 Analysis of Forecast Error with Respect to Solar Elevation

A special feature of solar irradiance is its very strong deterministic component, which results from the daily and seasonal course of the sun. This deterministic signal strongly influences the forecast error signal. Hence, to investigate the solar irradiance forecast errors, it is sometimes advisable to evaluate only the nondeterministic part of solar radiation, which is primarily caused by errors in the representation of clouds. To this aim, the analyzed variable is often the clear-sky index forecast error instead of GHI forecast errors.

Figure 8-7 shows the RMSE and bias of the clear-sky index, K_c, as a function of the cosine of the solar zenith angle (Figure 8-7, left) and the time of day (Figure 8-7, right) for two different NWP model forecasts (IFS and SKA). The two models show similar behavior: RMSE increases with low SZA or, equivalently, during morning and evening hours, as is also the case with the magnitude of bias. This error pattern is very often caused by deficient modeling of the atmospheric transport of radiation for low solar altitudes. This limitation is a well-known flaw of the two-stream schemes used in most NWP models. Other model limitations also exist, such as 3D effects and atmospheric refraction issues whose impact is enhanced for low solar altitudes.

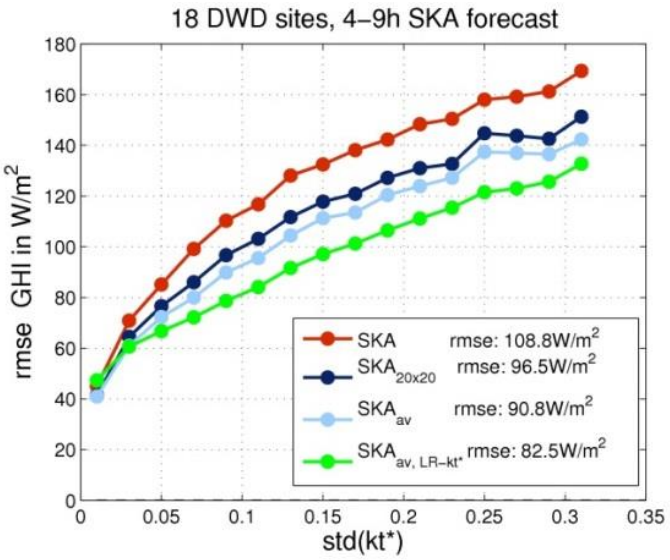

Figure 8-8. RMSE of various versions of the SKA forecasts as a function of the standard deviation of measurement-based clear-sky index (here noted as kt*) (red) SKA.
Dark blue: Nearest grid point, SKA20 x 20 averaged throughout 20 by 20 grid points. Light blue: SKAav 5-hour sliding mean of the clear-sky index of the forecasts of the average throughout 20 by 20 grid points. Green: SKAav, LR.kt*: linear regression of the clear-sky index of the forecasts applied to SKAav. The evaluated period is from April 3, 2013–February 28, 2014. Training set: Last 30 days, all 18 DWD sites

8.5.3 Analysis of Forecast Error with Respect to Cloud Variability and Spatiotemporal Averaging

Forecasts generally show good agreement with measurements for clear-sky periods or even completely overcast days, which basically have a quasi-constant clear-sky index; however, cloud variability strongly impacts solar forecasting accuracy. Hence, considerable deviations from the measurements are typically observed for days with variable cloudiness. An evaluation of the SKA forecast errors as a function of the measurement-derived K_c variability, here represented by the standard deviation of K_c throughout 5 hours, is shown in Figure 8-8. The evaluation also shows this dependence for multiple spatial and temporal averaging configurations of the SKA forecasts. Overall, Figure 8-8 shows:

1. The forecast error increases with enhanced cloud variability.
2. Spatial and temporal forecast averages result in reduced RMSE values, going from negligible reductions for very stable conditions to large reductions for highly variable conditions.

Regarding the first point, the solar radiation forecast error shows a clear dependency with respect to cloud variability and, more generally, with respect to the cloud conditions. Combining the error trend in the dependence of cloud conditions and the solar elevation has been proposed as an efficient method to reduce the systematic error in NWP model forecasts using a post-processing MOS. In particular, Lorenz et al. (2009) used a polynomial function with cos(SZA) and K_c as independent variables to parameterize the forecast bias error from historical forecasts relative to observations and ultimately to subtract the parameterized error from operational forecasts. This approach has also been adapted and evaluated for other NWP models and different climates. Mathiesen and Kleissl (2011) found improved accuracies when applying that approach to three different NWP models—GFS, North American Model, and IFS—for stations in the continental United States. Pelland,

Galanis, and Kallos (2013) did the same for the Canadian GEM model, and Müller and Remund (2010) for the WRF model forecasts in Switzerland.

Regarding the second point, the rationale of the RMSE decreases when an averaging scheme is applied, and this is explained by the existence of small correlations among the pixels over which the averaging scheme is applied. This leads to random error cancellations during the averaging process. In contrast, for stable conditions, when the correlation among neighboring pixels is very high, the cancellation of random errors is small.

The optimal region size and time interval for RMSE reduction using averaging depends on the correlation structure among neighboring forecasts, both in time and space. Multiple studies have been conducted on this topic. For instance, a detailed evaluation of irradiance forecasts from the Canadian GEM model resulted in a reduction of forecast errors in the range from 10% to 15% when the model outputs were averaged throughout several hundred kilometers (Pelland, Galanis, and Kallos 2013). A similar improvement was achieved with WRF forecasts provided by Meteotest using averages over an area of 50 km by 50 km (Müller and Remund 2010). In parallel, Mathiesen and Kleissl (2011) reported an averaging area of 100 km by 100 km as suitable for irradiance forecasts using the GFS and North American Mesoscale forecast system models. The benefit of horizon-dependent smoothing filters for CMV forecasts was also shown by Lorenz, Hammer, and Heinemann (2004) and by Kühnert, Lorenz, and Heineman (2013).

The reduction of RMSE by spatial and temporal averaging can be extrapolated to the particular case in which the forecasting model performance is evaluated throughout multiple sites across a wide region (also referred to as *regional* forecast) or for coarser temporal granularities, such as monthly or yearly. In these cases, there is a reduction of random errors with respect to point-wise evaluations that make regional forecasting more accurate than point-wise forecasting. Again, the extent of the reduction depends on the particular correlation levels among the aggregated values in each case. An analysis of regional forecast errors for different region sizes and different forecast models was given by Lorenz et al. (2009); Kühnert, Lorenz, and Heineman (2013); and Lorenz and Heinemann (2012).

Temporal and spatial averaging can be also considered for ASI-based forecasts. It has been found that in a nowcasting system with four sky imagers during days with many transient clouds, the DNI RMSE for forecasts that are 10 minutes ahead is reduced from 13.0% to 6.5% using averages of 4 km^2 and 15 minutes with respect to pixel-wise forecasts (Kuhn et al. 2017c).

Despite the positive impact of spatiotemporal averaging on reducing the RMSE of a forecast, there is a negative effect that adversely impacts the frequency distribution of forecasted data because averaging reduces extreme forecasted values and distorts the original frequency distribution of the forecast data. Consequently, forecast averages should be used only when the forecast frequency distribution is not critical.

8.5.4 Analysis of the Frequency Distributions of Forecasted Values

The ability of a model to reproduce the observed frequency distribution of both solar irradiance and clear-sky index is a required property for some applications. In addition, it can provide insights about potential problems in the forecast model.

Figure 8-9 shows the probability density function (PDF) of the clear-sky index, K_c, for forecasts issued by the SKA and IFS NWP models, as in Figure 8-7, and the actual PDF obtained from observations. These plots show that the SKA model systematically overpredicts clear-sky situations and underpredicts overcast conditions. Consequently, intermediate situations are underrepresented. On the other hand, the IFS model underrepresents very clear and very cloudy conditions and overrepresents intermediate

situations. Although this gives insightful information about the forecast performance, the similarity of the distribution functions of measurements and forecasts does not guarantee an accurate forecast because it does not include information regarding the correct timing of the modeled events.

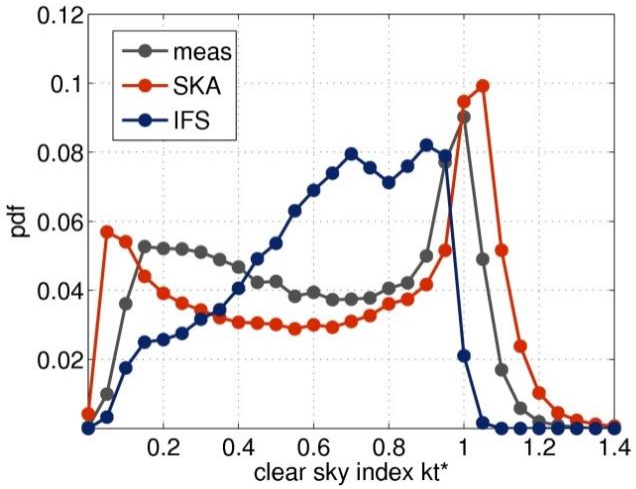

Figure 8-9. PDF of the clear-sky index (here noted as kt*) derived from measurements (gray), SKA model forecasts (red), and IFS model forecasts (blue). The evaluated period is from March 1, 2013–February 28, 2014; cos(SZA) > 0.1.

A quantitative evaluation of the agreement between the observed and forecasted distribution functions can be done using the Kolmogorov-Smirnov integral (Espinar et al. 2008; Gueymard 2014), which is usually applied to distribution functions of GHI or DNI rather than to K_c (Beyer et al. 2009; Perez and Hoff 2013).

8.5.5 Analysis of Regional Forecasts

Regionally aggregated forecasts of PV power, typically derived through upscaling (see Section 8.4.2), are required by grid operators. Regional forecasts show much lower uncertainties than single-site forecasts. By enlarging the footprint of the forecast region of interest, forecast errors are reduced (Hoff and Perez 2012; Lorenz et al. 2009, 2011; Fonseca et al. 2014; David et al. 2016; Saint-Drenan et al. 2016). This phenomenon, which is called the smoothing effect, is related to the correlation between the forecast errors at different locations. The larger the region, the more locations with different irradiance variability are included, and thus solar forecast errors of the different sites are less correlated. This subsequently leads to a higher accuracy of the regional PV power forecasts.

An example is shown in Figure 8-10, which depicts the day-ahead forecast accuracy that can be reached in Italy by predicting the PV generation of different control areas: The adopted model corresponds to an upscaling method using averaged model inputs and forecasting the power generation at market zone level directly (Betti et al. 2020).

In addition, a measure of PV power variability is displayed in Figure 8-10. With $P(t)$ denoting the PV power output at time *t,* the change in PV power for a given time step, Δt, is defined as:

$$\Delta P_{\Delta t} = P(t) - P(t - \Delta t). \tag{8-16}$$

Hourly values and a time step Δt of 24 hours are specifically considered in Figure 8-10.

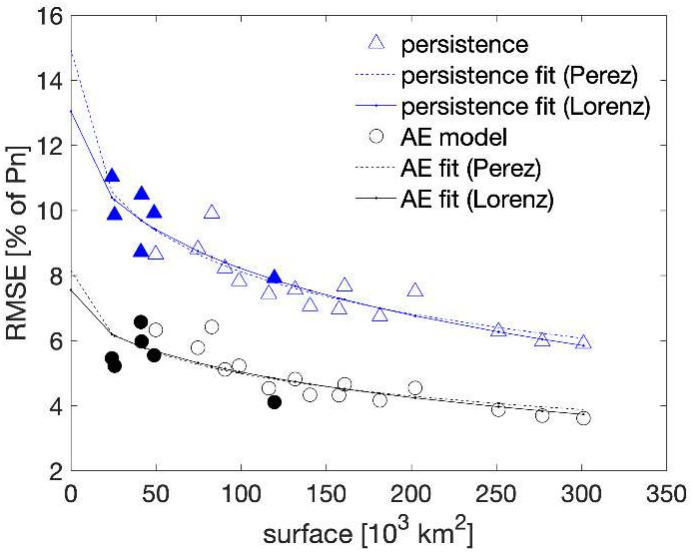

Figure 8-10. Smoothing effect over Italy: RMSE of regional forecasts (circles) and persistence (triangles) as a function of the area size for the market zones in Italy (full circles/triangles) and for areas merging several adjacent market zones (empty circles/triangles).

PV power variability in each zone is defined as the standard deviation, $\sigma(\Delta P_{\Delta t})$, as proposed by Perez et al. (2016), which is equivalent to the RMSE of the persistence of PV power (see also equations 8.5 and 8.12)

$$RMSE_{per} = \frac{1}{\sqrt{N}}\sqrt{\sum_{i=1}^{N}(\Delta P_{\Delta t})^2} = \sigma(\Delta P_{\Delta t}). \quad (8\text{-}17)$$

Here, it is commonly assumed that the average of $\Delta P_{\Delta t}$ should be zero.

Both the variability and the forecast errors decrease with an increase in the size of the region and the number of PV systems considered. They can be well fitted either by a hyperbolic function, similar to one proposed by Perez et al. (2016), or by an exponential function, similar to the one proposed by Lorenz et al. (2009). As shown in Figure 8-10, by enlarging the footprint of the forecast region from the prediction of the PV generation in each market zone in Italy to the prediction of the PV generation over all of Italy, the RMSE can decrease from 5.5% (market zones average) to 3.6% (countrywide).

To summarize, expanding the transmission grid to manage the power generation in large areas (e.g., entire countries instead of market zones) not only reduces congestion and constraints on production capacity but also increases the forecast accuracy, as shown with the Italy example.

8.5.6 Effective Model Validation Benchmarking: Operationally Firm Solar Forecasts

When validating solar forecasts, the classical error metrics (e.g., RMSE and MAE) introduced in Section 8.5.1 are commonly used. With continuous development in technology and changes in the energy market, the need arises for new validation measures that account for the economic value of solar forecasts. Thus, the firm power forecast (FPF or “perfect forecast”) concept was developed and introduced in a recent series of publications by Perez et al. (2019a, 2019b) and Pierro et al. (2020a). This forecast is both an effective model validation metric and an operational strategy to integrate increasing amounts of variable solar generation on electric grids (see also Section 9.7.3). The costs incurred in transforming imperfect forecasts into firm predictions define the new metric: These include the costs of

energy storage and output curtailment needed to make up for any over- or underprediction situations. It was shown by Perez et al. (2019a, 2019b) and Pierro et al. (2020a) that delivering firm predictions (i.e., fully eliminating grid operator renewable supply-side uncertainty and, incidentally, the need to characterize forecasts probabilistically) could be achieved at a modest operational cost.

Although other recent publications have focused on standardizing error metrics and forecast model validation practice (e.g., Hoff et al. 2012a; Yang et al. 2020), the choice of possible references as well as the possible definitions of persistence constitute sources of ambiguity when evaluating results from different studies, particularly reports emanating from the industry. In addition, the standard metrics, however "standardized," are not directly exploitable by grid operators for estimating operational costs incurred by forecast errors.

The FPF metric is defined as the optimum (i.e., minimum possible) capital cost of PV plant oversizing and storage that is sufficient to make up for all instances of over- and underforecasts. This minimum is a function of the assumed capital costs for PV and storage and, of course, of the quality of the forecast. This metric bypasses both the ambiguity of standard metrics and their exploitability by grid operators because the metric is (1) a tangible hardware cost and (2) an indirect measure of operational costs resulting from solar supply-side uncertainty, because applying firm forecasts would entirely eliminate the said uncertainty.

Figure 8-11 compares the MAE and FPF metrics for GHI forecasts at 1-, 3-, and 24-hour forecast horizons. Results stem from the analysis of time series at the seven NOAA Surface Radiation Budget Network (SURFRAD) sites for a period of 1 year. The forecast models include smart persistence (Section 8.5.1.2), SUNY (also known as SolarAnywhere; SolarAnywhere 2019), and its underlying NWP components: IFS, GFS, National Digital Forecast Database, and the HRRR. In this example, the hardware costs quantifying the FPF metric amount to $1,200 per kW for PV oversizing and $200 per kWh for storage.

A noticeable difference between the two metrics is the performance of smart persistence relative to the other models, especially for short-term horizons. Persistence turns out to be operationally more robust than generally assumed because, whereas its dispersion can be large (i.e., large MAE and RMSE), this dispersion tends to be well balanced around the 1:1 diagonal, with fewer instances of the prolonged over/underestimations that are operationally costly.

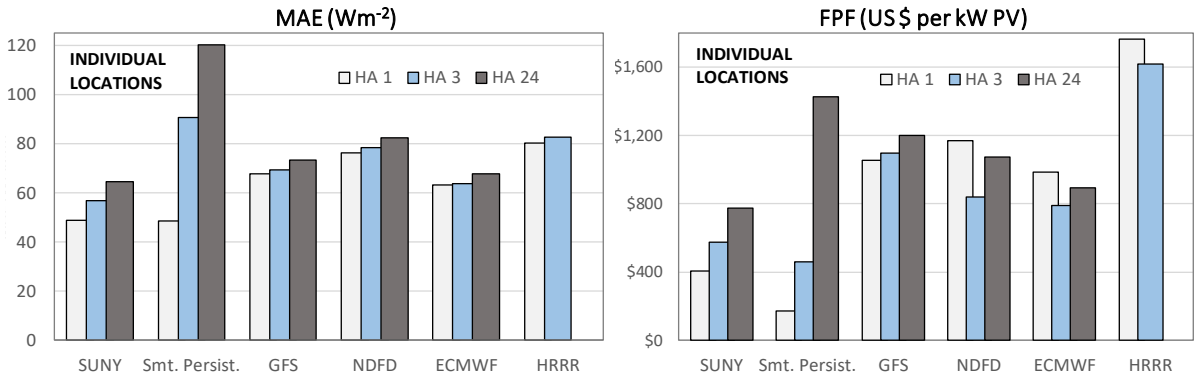

Figure 8-11. Comparison of forecast model performance at 1-, 3-, and 24-hour horizons for all SURFRAD stations using (left) the MAE metric and (right) the FPF metric.

8.6 Probabilistic Solar Forecasts

A forecast is inherently uncertain and a proper assessment of its associated uncertainty offers the grid operator a more informed decision-making framework. For example, a deterministic forecast that includes predictions intervals is of genuine added value and, if appropriately incorporated in grid operations, might permit an increase in the value of solar power generation (Morales et al. 2014).

This section is restricted to the univariate[51] context that corresponds to probabilistic forecasts that do not consider the spatiotemporal dependencies generated by stochastic processes such as solar power generation. Two types of solar[52] probabilistic forecasts are considered here: *quantile forecasts* and *ensemble forecasts* (i.e., those using the Ensemble Prediction System, or EPS). Quantile forecasts are quite versatile probabilistic models and as such might address different forecasting time horizons, whereas EPS forecasts generally provide day-ahead probabilistic forecasts. Further, a verification framework is considered for evaluating the quality of solar probabilistic forecasts. The evaluation framework is based on visual diagnostic tools and a set of scores mostly originating from the weather forecast verification community (Wilks 2014). What follows provides an overview of the basic concepts related to solar probabilistic forecasting methods with an emphasis on the specific associated verification metrics. Comprehensive overviews regarding forecasting methods and the verification of solar probabilistic forecasts metrics can be found in van der Meer, Widén, and Munkhammar (2018); Antonanzas et al. (2016); and Lauret, David, and Pinson (2019).

8.6.1 Nature of Probabilistic Forecasts of Continuous Variables

In contrast to deterministic forecasts, probabilistic forecasts provide additional information about the inherent uncertainty embodied in NWP. The probabilistic forecast of a continuous variable, such as solar power generation or solar irradiance, takes the form of either a cumulative distribution function (CDF), $F(Y)$, or a PDF, $f(Y)$, of the random variable of interest, Y (e.g., GHI).

The CDF of a random variable *Y* is given as:

$$F(y) = P(Y \leq y) \tag{8-18}$$

where $P(Y \leq y)$ represents the probability that this random variable is less or equal to y.

The predictive distribution can be summarized by a set of quantiles. The quantile, q_τ, at probability level $\tau \in [0,1]$ is defined as follows:

$$q_\tau = F^{-1}(\tau), \tag{8.19}$$

where F^{-1} is the so-called *quantile function*. A quantile, q_τ, corresponds to the threshold value below which an event, *y*, materializes with a probability level, τ.

Prediction intervals (also called interval forecasts) can be inferred from the set of quantiles. Prediction intervals define the range of values within which the observation is expected to be with a certain probability (i.e., its nominal coverage rate) (Pinson et al. 2007). For example, a central prediction interval with a coverage rate of 95% is estimated by using the quantile

[51] Future work (see Chapter 10) will be devoted to multivariate probabilistic models capable of capturing the spatiotemporal correlations present in irradiance and PV forecasts.
[52] The term *solar forecast* encompasses solar irradiance forecasts and PV power forecasts.

$q_{\tau=0.025}$ as the lower bound and $q_{\tau=0.975}$ as the upper bound. Figure 8-12 shows an example of the probabilistic forecasts of solar irradiance where prediction intervals have been computed for nominal coverage rates ranging from 20% to 80%.

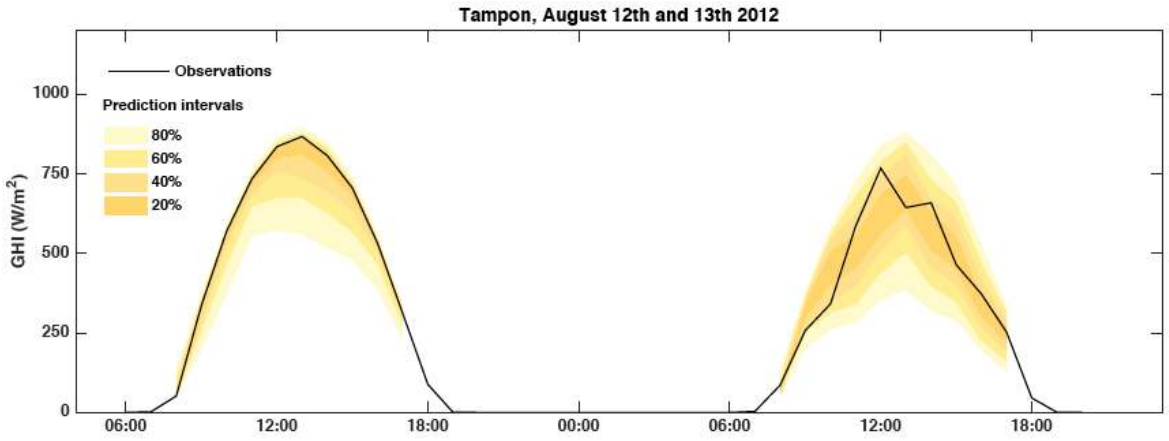

Figure 8-12. Example of probabilistic solar irradiance forecasts: two days of measured GHI at Le Tampon, France, and associated 1-hour ahead forecasts with prediction intervals (yellow) generated with the quantile regression forest model.

8.6.2 Quantile Forecasts

Two approaches are commonly used in the community to generate quantile forecasts (see Figure 8-13) addressing different forecast horizons. As input, they use past ground observations and satellite images for intraday forecasting or NWP deterministic forecasts that are more effective for day-ahead forecasting. The first approach (Bacher, Madsen, and Nielsen 2009; Pedro et al. 2018) involves directly generating the quantiles of the predictive distribution of the variable of interest (e.g., GHI, DNI, or PV power). The second approach (Lorenz et al. 2009; David et al. 2016; Grantham, Gel, and Boland 2016; Pierro et al. 2020b) produces the interval forecasts from the combination of a deterministic (point) forecast and quantiles of the prediction error.

For both approaches, quantiles can be estimated either by assuming a parametric law for the predictive distribution or by nonparametric methods, which make no assumptions about the shape of the predictive distribution.

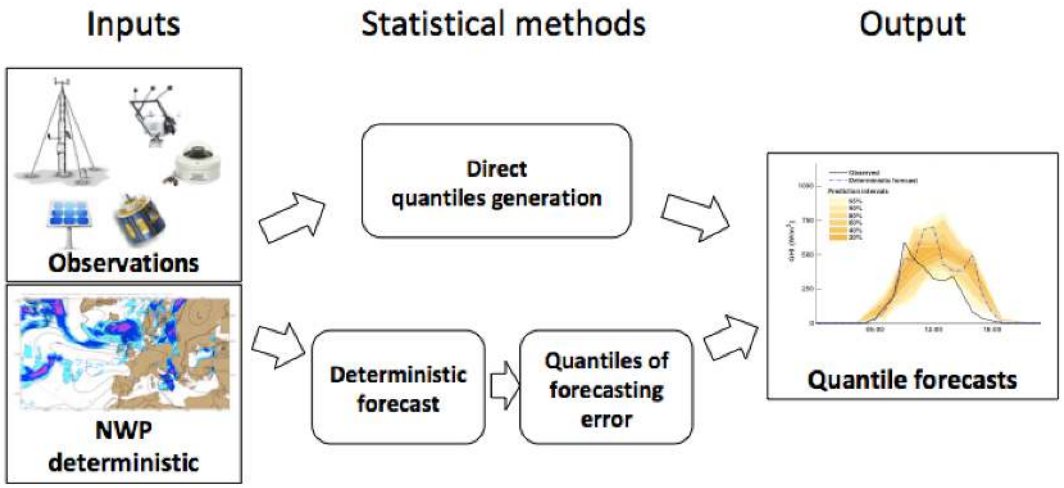

Figure 8-13. The two typical workflows used to generate quantile forecasts from recent past observations and/or deterministic NWP forecasts

8.6.2.1 Parametric Methods

Parametric models assume that the variable of interest or the prediction error follows a known law of distribution (e.g., a doubly truncated Gaussian for GHI or a Gaussian for the error distribution). Only a few parameters (e.g., mean and variance) are needed to fully characterize the predictive distribution. Consequently, this approach is particularly interesting in an operational context because it requires a low computational effort.

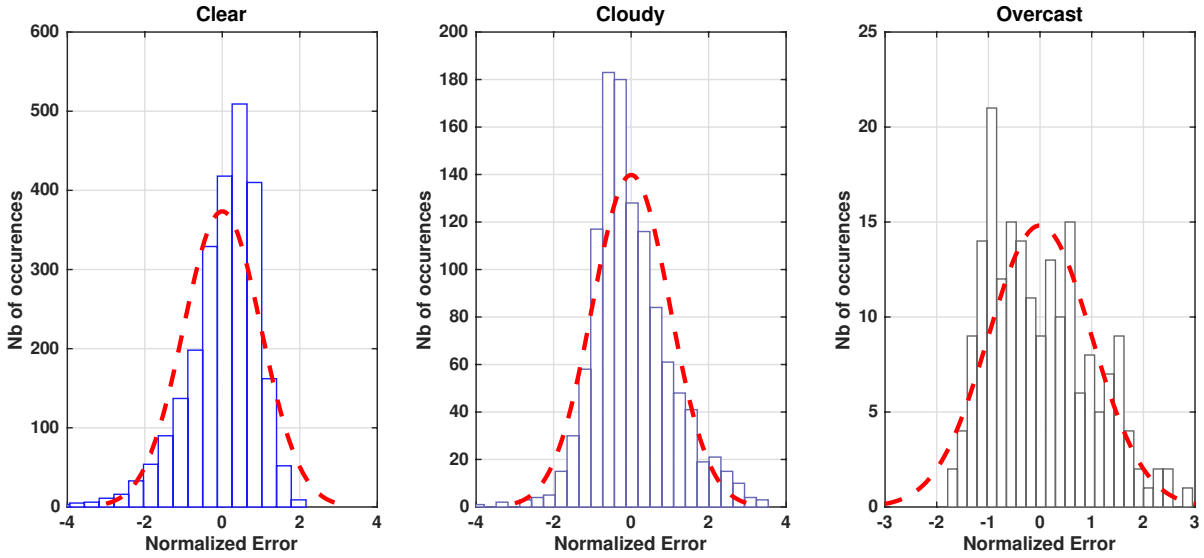

Figure 8-14. PDF of the normalized error (zero mean and unit variance) of the hourly profile of day-ahead forecasts of the clear-sky index provided by ECMWF-HRES for three different sky conditions and for the site of Saint-Pierre (21.34°S, 55.49°E), Reunion, France, in 2012. The red dashed line represents the fitted standard normal PDF. *Image from David and Lauret (2018)*

In the solar forecasting community, it is very common to fit a Gaussian distribution to the errors even though errors derived from deterministic forecasts of solar irradiance and of clear-sky index do not follow a Gaussian distribution (see Figure 8-14). For instance, Lorenz et al. (2009) developed the first operational PV forecasting model in Germany by assuming a Gaussian distribution of the error of the deterministic GHI forecasts generated by the IFS. More precisely, the predictive CDF was a Gaussian distribution with a mean corresponding to the point forecast and a standard deviation derived from a fourth-degree polynomial function for different classes of cloud index and solar elevation. For intrahour and intraday solar irradiance probabilistic forecasts, David et al. (2016) assumed a Gaussian error distribution of the deterministic forecast to generate a predictive CDF with a Generalized AutoRegressive Conditional Heteroskedasticity (GARCH) model. Instead of fitting a parametric PDF to the error distribution, Fatemi et al. (2018) proposed a framework for parametric probabilistic forecast of solar irradiance using the beta distribution and standard two-sided power distribution.

8.6.2.2 Nonparametric Methods

To avoid making assumptions about the shape of the predictive distribution, numerous nonparametric methods have been proposed in the literature (van der Meer, Widén, and Munkhammar 2018). Examples are techniques such as bootstrapping (Efron 1979; Grantham, Gel, and Boland 2016), kernel density estimation (Parzen 1962), or k-nearest neighbor (Pedro et al. 2018). Here, two prominent and simple nonparametric methods are discussed briefly: the quantile regression and analog ensemble techniques.

Quantile regression models relate quantiles of the variable of interest (predictand) to a set of explanatory variables (predictors). Statistical or machine learning techniques—such as linear quantile regression, quantile regression forest, or gradient boosting (David and Lauret 2018; van der Meer, Widén, and Munkhammar 2018)—are commonly used to produce the set of quantiles with probability levels spanning the unit interval.

The following summarizes the linear quantile regression method first proposed by Koenker and Bassett (1978). See David, Luis, and Lauret (2018) for details about the implementation of other regression methods, including other variants of the linear quantile regression, quantile regression forest, quantile regression neural network, or boosting.

The linear quantile regression technique estimates a set of quantiles of the cumulative distribution function, F, of some response variable, Y (the predictand), by assuming a linear relationship between the quantiles of Y (q_τ) and a set of explanatory variables, X (the predictors):

$$q_\tau = \beta_\tau X + \epsilon, \tag{8-20}$$

where β_τ is a vector of the parameters to be optimized at each probability level, τ, and ϵ represents a random error term (Koenker and Bassett 1978).

Numerous implementations of the linear quantile regression technique (and of its related variants) have been proposed in the literature to generate quantile forecasts for different forecast horizons and using different types of predictors, X. See, e.g., Bacher, Madsen, and Nielsen (2009); Zamo et al. (2014); Lauret, David, and Pedro (2017); van der Meer, Widén, and Munkhammar 2018; and Bakker et al. (2019).

The analog ensemble (AnEn) method (Delle Monache et al. 2013) is a simple nonparametric technique used to build the predictive distributions. The aim is to search for similar forecasted conditions in the historical data and to create a probability distribution with the corresponding observations. Alessandrini et al. (2015) applied an AnEn approach to a set of predicted meteorological variables (e.g., GHI, cloud cover, and air temperature) generated by the Regional Atmospheric Modeling System (RAMS). Note that the AnEn technique is mostly employed for day-ahead forecasts and generates the predictive distribution using NWP deterministic forecasts.

8.6.3 Ensemble Prediction System

8.6.3.1 Definition

The EPS corresponds to a perturbed set of forecasts generated by slightly changing the initial conditions of the control run and of the modeling of unresolved phenomena (Leutbecher and Palmer 2008). Figure 8-15 shows a schematic representation of an ensemble forecast generated by an NWP model. The trajectories of the perturbed forecasts (blue lines) can differ strongly from the control run (red line). The spread of the resulting members (blue stain) represents the forecast uncertainty. For example, the ECMWF provides an ensemble forecast from the IFS model. It consists of 1 control run and 50 “perturbed” members.

Though members of the ensemble are not directly linked to the notion of quantiles, they can be seen as discrete estimates of a CDF when they are sorted in ascending order. Lauret, David, and Pinson (2019) proposed different ways to associate these sorted members to a CDF.

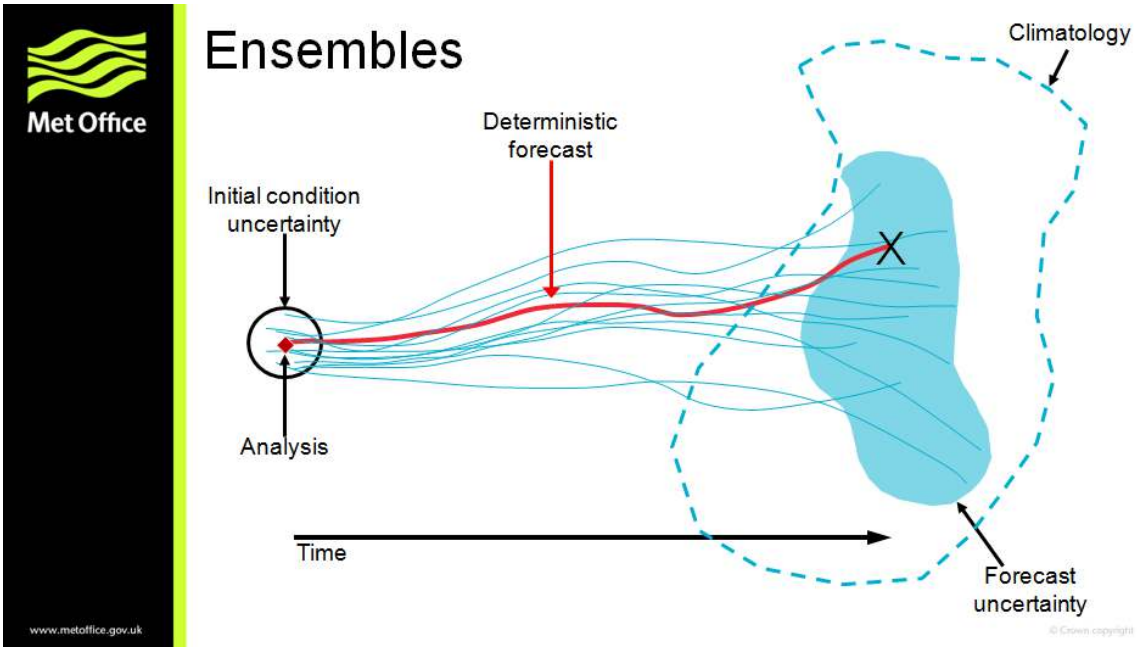

Figure 8-15. A schematic illustration of an ensemble forecast generated with an NWP model. *Image from Met Office, © British Crown copyright (2021)*

8.6.3.2 Post-Processing of the Ensemble Prediction System

Global and regional NWPs are designed to forecast a large variety of meteorological variables (but mainly precipitation and temperature) and have not previously focused on the accurate generation of the different components of solar radiation. Consequently, raw ensembles provided by meteorological centers suffer from a lack of accuracy, a lack of calibration, or both (Leutbecher and Palmer 2008). Additionally, see, e.g., Yang et al. (2020) for definitions and discussions about the specific meaning of accuracy, calibration, and other specialized terms in the field of forecasting—some of which appearing in the following. Overall, raw ensemble forecasts are systematically refined by post-processing techniques (also called calibration techniques) to further improve their quality.

The aim of post-processing is to apply a statistical calibration to the PDF drawn by the raw initial ensemble forecasts to optimize a specific metric (e.g., the continuous ranked probability score [CRPS] described in Section 8.6.4) used to assess the quality of probabilistic forecasts. Indeed, as well as having a coarse spatial resolution, the ensemble forecasts from NWPs are known to be underdispersive; in other words, they exhibit a lack of spread (Leutbecher and Palmer 2008). To address this, Sperati, Alessandrini, and Delle Monache (2016) proposed two different methods already used in the realm of wind forecasting: The variance deficit method designed by Buizza et al. (2003) and the ensemble model output statistic (MOS) method proposed by Gneiting et al. (2005). Even if these methods cannot be considered to be parametric, they are based on the characteristics of a normal distribution. Indeed, such a distribution is appealing because it can be assessed with only two parameters: the mean and the standard deviation, which are related to the average bias and the spread of the ensemble, respectively.

Another method of calibration is based on the rank histogram (see Section 8.6.4); it was initially proposed by Hamill and Colucci (1997) for precipitation forecasts. Zamo et al. (2014) applied this method to the Météo France's EPS, called PEARP, to generate probabilistic solar forecasts. The aim of this method is to build a calibrated CDF from the rank histogram derived from past forecasts and observations. Other techniques of EPS calibration exist, but they have not been used for solar forecasting. For example, Pinson (2012) and Pinson and

Madsen (2009) suggested a framework for the calibration of wind ensemble forecasts. Junk, Delle Monache, and Alessandrini (2015) proposed an original calibration model for wind-speed forecasting applied to ECMWF-EPS based on the combination of nonhomogeneous Gaussian regression and AnEn models. Likewise, Hamill and Whitaker (2006) suggested an adaptation of the AnEn technique for the calibration of ensemble precipitation forecasts using the statistical moments of the distribution, such as the mean and spread of the members as predictors. See Wilks (2018) for a thorough review of univariate ensemble postprocessing methods.

8.6.4 Verification of Solar Probabilistic Forecasts

8.6.4.1 Properties Required for a Skillful Probabilistic System

Several attributes characterize the quality[53] of probabilistic forecasts (Jolliffe and Stephenson 2011; Wilks 2014), but two main properties (reliability and resolution) are used to assess the quality of the forecasts.

The *reliability* or calibration refers to the statistical consistency between forecasts and observations; in other words, a forecast system has a high reliability if the forecast probability and observed frequency agree. The reliability property is an important prerequisite because nonreliable forecasts would lead to a systematic bias in subsequent decision-making processes (Pinson et al. 2007).

The *resolution* measures the ability of a forecasting model to generate predictive distributions that depend on forecast conditions. Put differently, the more distinct the observed frequency distributions for various forecast situations are from the full climatological distribution, the more resolution the forecast system has. Climatological forecasts are perfectly reliable but have no resolution. Consequently, a skillful probabilistic forecasting system should issue reliable forecasts and should exhibit high resolution.

Sharpness, which refers to the concentration of predictive distributions, can be measured by the average width of the prediction intervals. Unlike reliability and resolution, sharpness is a function of only the forecasts and does not depend on the observations. Consequently, a forecasting system can produce sharp forecasts yet be useless if the probabilistic forecasts are unreliable.

8.6.4.2 Probabilistic Verification Tools

The evaluation framework is based on visual diagnostic tools and numerical scores.

8.6.4.2.1 Visual Diagnostic Tools

Table 8-1 lists the diagnostic tools for which Lauret, David, and Pinson (2019) provided pros and cons as well as detailed information about their implementation. Note that some tools were initially designed for a specific type of forecast (i.e., an ensemble or quantile forecast) and that there is apparently no visual diagnostic tool to assess the resolution property.

[53] *Quality* refers to the correspondence between forecasts and the observations.

Table 8-1. Visual Diagnostic Tools

Diagnostic Tool	Remarks
Reliability diagram	Initially designed for the reliability assessment of quantile forecasts Can be used for ensemble forecasts if members are assigned specific probability levels (see Lauret, David, and Pinson [2019])
Rank histogram	Initially designed for the reliability assessment of ensemble forecasts Can be extended to quantile forecasts if quantiles are evenly spaced
Probability integral transform histogram	Represents a reliability assessment of quantile forecasts
Sharpness diagram	Plots the average width of the prediction intervals for different nominal coverage rates Sharpness can only contribute to a qualitative evaluation of the probabilistic forecasts. Even if narrow prediction intervals are preferred, sharpness cannot be seen as a property to verify the quality of probabilistic forecasts but is more like the consequence of a high resolution.

Table 8-2. Forecast Metrics

Forecast Metric	Remarks
Continuous ranked probability score (CRPS)	Can be normalized to define a skill score (CRPS skill score) Can be further partitioned into the two main attributes: reliability and resolution
Ignorance score	Local score (i.e., the score depends only on the value of the predictive distribution at the observation) Cannot be normalized
Interval score	Specifically designed for interval forecasts
Quantile score	Forecast performance of specific quantiles

8.6.4.2.2 Numerical Scores

Numerical scores provide summary measures for the evaluation of the quality of probabilistic forecasts. Table 8-2 enumerates the main scoring rules for evaluating the quality of probabilistic forecasts of a continuous variable. All the scores listed in the table are proper scoring rules (Gneiting and Raftery 2007), hence ensuring that perfect forecasts are given the best score value. Lauret, David, and Pinson (2019) gave a detailed definition of each score.

8.6.4.3 Presentation of Some Tools and Scores

This section describes in detail some diagnostic tools and numerical scores. See Lauret, David, and Pinson (2019) and Yang et al. (2020) for descriptions of other metrics.

8.6.4.3.1 Reliability Diagram

A reliability diagram is a graphical verification display used to assess the reliability attribute of quantile forecasts. Quantile forecasts are evaluated one by one, and their observed frequencies are reported versus their forecast probabilities (see Figure 8-16). Such a representation is appealing because the deviations from perfect reliability (the diagonal) can be visually assessed (Pinson, McSharry, and Madsen 2010); however, because of both the finite number of pairs of observation/forecast and also possible serial correlation in the sequence of forecast-verification pairs, observed proportions are not expected to lie exactly along the diagonal, even if the density forecasts are perfectly reliable. Pinson, McSharry, and Madsen (2010) proposed a method to add consistency bars to the reliability diagram. This adding of consistency bars to the reliability diagrams can help users gain more confidence in their (possibly subjective) judgment regarding the reliability of the different models. Figure 8-16 shows an example of reliability diagram with consistency bars. In this example, the forecasts cannot be considered reliable because the line corresponding to the forecasts falls outside the consistency bars. More elaborate reliability diagrams are proposed by Yang (2019a, 2019c).

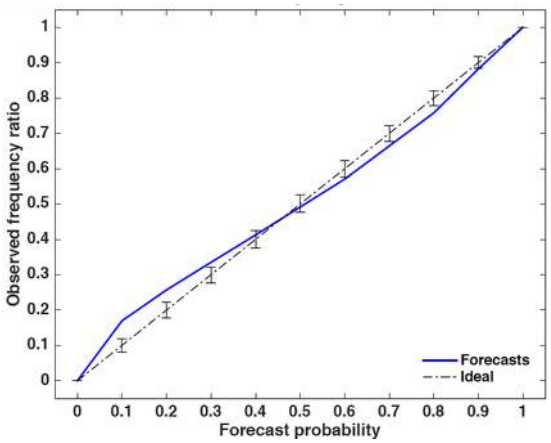

Figure 8-16. Example of a reliability diagram. Consistency bars for a 90% confidence level around the ideal line are individually computed for each nominal forecast probability.

8.6.4.3.2 Rank Histogram

A rank histogram is a graphical display initially designed for assessing the reliability of ensemble forecasts (Wilks 2014). Rank histograms permit users to visually assess the statistical consistency of the ensemble—that is, if the observation can be seen statistically like another member of the ensemble (Wilks 2014). A flat rank histogram is a necessary condition for ensemble consistency and shows an appropriate degree of dispersion of the ensemble. An underdispersed or overdispersed ensemble leads to U-shaped or hump-shaped rank histogram; see Figure 8-17.

In addition, some unconditional biases can be revealed by asymmetric (triangle-shaped) rank histograms. It must be stressed that one should be cautious when analyzing rank histograms. As shown by Hamill (2001), a perfectly flat rank histogram does not mean that the corresponding forecast is reliable. Further, when the number of observations is limited, consistency bars can also be calculated with the procedure proposed by Bröcker and Smith (2007).

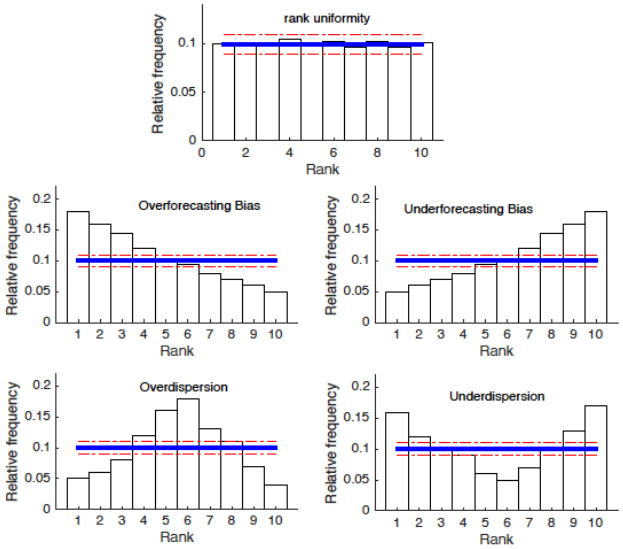

Figure 8-17. Illustrative examples of rank histograms for an ensemble of *M* = 9 members. The horizontal solid blue line denotes the statistical consistency of the ensemble. The dashed-dotted lines represent the consistency bars. *Figure inspired from Wilks (2014)*

8.6.4.3.3 Overall Skill Assessment with the Continuous Ranked Probability Score

The most common skill score for evaluating the quality of predictive densities of continuous variable is the CRPS, whose formulation is:

$$CRPS = \frac{1}{N}\sum_{i=1}^{N}\int_{-\infty}^{+\infty}\left[\hat{F}^{i}_{fcst}(y) - F^{i}_{yobs}(y)\right]^{2} dy, \tag{8-21}$$

where $\hat{F}^{i}_{fcst}(y)$ is the predictive CDF of the variable of interest, *x* (e.g., GHI), and $F^{i}_{yobs}(y)$ is a CDF of the observation (i.e., a step function that jumps from 0 to 1 at the point where the forecast variable, y, equals the observation, y_{obs}). The squared difference between the two CDFs is averaged over the *N* forecast/observation pairs. Note that the CRPS is negatively oriented (smaller values are better) and has the same dimension as the forecasted variable.

Figure 8-18(a) shows three hypothetical predictive PDFs, and Figure 8-18(b) plots the corresponding predictive CDFs. The black thick line in Figure 8-18(b) represents the CDF of the observation, $F^{i}_{yobs}(y)$. Because CRPS represents the integrated squared difference between the two CDFs, the pair of observation/forecast indicated by 1 will be assigned the best score. Conversely, forecasts indicated by 2 and 3 will lead to a higher CRPS. Indeed, although it has the same degree of sharpness as Forecast 1, Forecast 2 is not centered on the observation (i.e., this is a biased forecast). Regarding Forecast 3, even though it is centered on the observation, it is less sharp than forecasts 1 and 2. In summary, CRPS rewards the concentration of probability around the step function located at the observed value (Hersbach 2000).

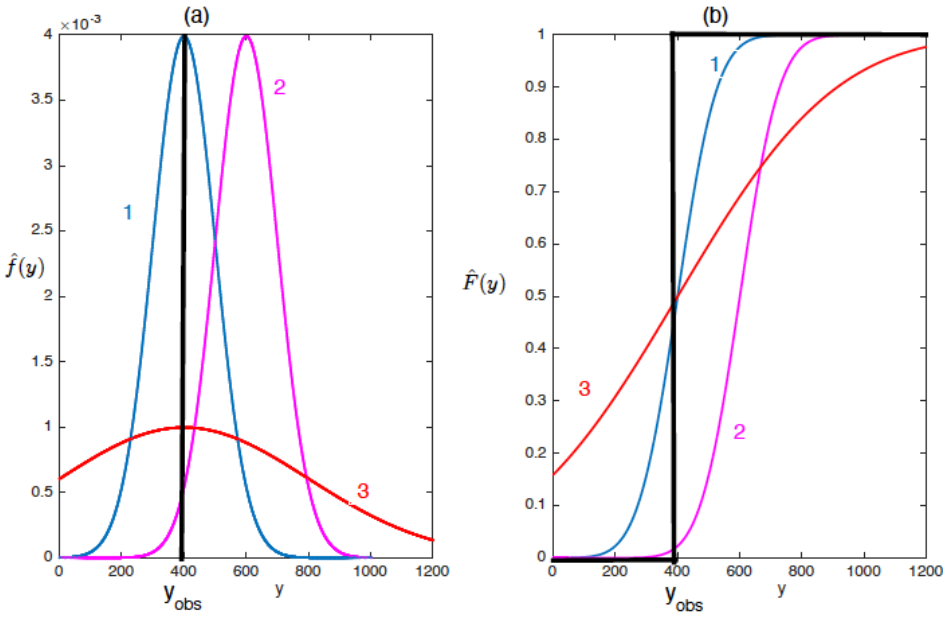

Figure 8-18. Schematic of the CRPS skill score. Three forecast PDFs are shown in relation to the observed variable in (a). The corresponding CDFs are shown in (b), together with the step function CDF for the observation (black heavy line). Forecast PDF 1 would produce a small (i.e., good) CRPS. This would not be the case for Forecast 2 or Forecast 3. *Illustration inspired from Wilks (2014)*

The CRPS can be further partitioned into the two main attributes of probabilistic forecasts described: reliability and resolution. The decomposition of the CRPS leads to:

$$CRPS = \text{RELIABILITY} - \text{RESOLUTION} + \text{UNCERTAINTY}. \quad (8\text{-}22)$$

The uncertainty[54] term cannot be modified by the forecast system and depends only on the observation's variability (Wilks 2014). Because the CRPS is negatively oriented, the goal of a forecast system is to minimize the reliability term and maximize the resolution term as much as possible. Hersbach (2000) and Lauret, David, and Pinson (2019) detail the procedures for calculating the different terms (reliability and resolution, respectively) for ensemble and quantile forecasts.

It must be stressed that the decomposition of the CRPS provides quantitative overall measures of reliability and resolution, hence providing additional and valuable insight into the performance of a forecasting system.

Similarly, to obtain skill scores used for evaluating deterministic forecasts (Coimbra et al. 2013b), a CRPS skill score (CRPSS) can be derived to quantify the improvement brought by a new method over a reference easy-to-implement (or "baseline") model, such as:

$$CRPSS = 1 - \frac{CRPS_{new\ method}}{CRPS_{Reference}}. \quad (8\text{-}23)$$

Negative values of CRPSS indicate that the new proposed method fails to outperform the reference baseline model, and positive values of CRPSS mean that the new method outperforms the reference model. Further, the higher the CRPSS, the better the

[54] Note that the term *uncertainty* defined in this framework is not the same as the "uncertainty for measurements and models" defined in Chapter 7.

improvement. Note that the uncertainty part of the decomposition of the CRPS (which corresponds to the score of the climatology) can be used as a reference baseline model. CRPSS and a mean-normalized CRPS are also discussed by Yang (2020).

8.6.4.3.4 Interval Score

The interval score (IS) specifically assesses the quality of interval forecasts. As shown by Eq. 8-24 the interval score rewards narrow prediction intervals but penalizes (with a penalty term that increases with increasing nominal coverage rate) the forecasts for which the observation, x_{obs}, is outside the interval. For a $(1-\alpha)\times 100\%$ nominal coverage rate, the interval score reads as:

$$\mathrm{IS}_{\alpha} = \frac{1}{N}\sum_{i=1}^{N}\left(U^i - L^i\right) + \frac{2}{\alpha}\left(L^i - x_{obs}^i\right)I_{x_{obs}^i < L^i} + \frac{2}{\alpha}\left(x_{obs}^i - U^i\right)I_{x_{obs}^i > U^i} \tag{8-24}$$

where I_u is the indicator function (I_u=1 if U is true and 0 otherwise). U^i and L^i represent the upper $\left(\tau = 1-\frac{\alpha}{2}\right)$ and lower $\left(\tau = \frac{\alpha}{2}\right)$ quantiles, respectively.

A plot of interval scores for different nominal coverage rates might offer a consistent evaluation of the quality of interval forecasts. Consequently, such a plot could advantageously replace the sharpness diagram.

8.6.4.4 Benchmark Probabilistic Models

This section describes the benchmark probabilistic models used to gauge the performance of new proposed probabilistic methods using skill scores such as the CRPSS. By analogy with the deterministic approach, persistence ensemble (PeEn) models based on GHI (Alessandrini et al. 2015) and on clear-sky index (David et al. 2016) have been proposed. The empirical CDF of a PeEn forecast is simply built with the most recent k past measurements of solar irradiance. Considering an infinite number of past measurements, the PeEn turns to be the climatology. In numerous other fields of meteorology, climatology is often considered to be a reference that can be used to test the performance of probabilistic models (Wilks 2014). Indeed, the climatology is perfectly reliable, but it has no resolution. Also, an advanced climatology, called the complete-history persistence ensemble, was proposed by Yang (2019b); this reference model corresponds to a conditional climatology where the time of the day is used as a predictor. In addition, for ensemble forecasts, the CRPS of the raw ensemble can serve as a benchmark.

8.7 Summary and Recommendations for Irradiance Forecasting

Solar power forecasting is essential for the reliable and cost-effective system integration of solar energy. It is used for a variety of applications with their specific requirements with respect to forecast horizon and spatiotemporal resolution. To meet these needs, different solar irradiance and power forecasting methods have been developed, including physical and empirical models as well as statistical and machine learning approaches. Based on these developments, a number of forecasting services of good quality is available for users today. In the following, a summary of different forecasting methods and their applicability for different tasks is given, along with criteria that determine model performance as well as recommendations for forecast evaluation.

- Different empirical and physical models are suitable for different forecast horizons. Generally, the spatiotemporal resolution of irradiance forecasts decreases with increasing forecast horizon.

- Short-term irradiance forecasts from 10–20 minutes ahead resolving irradiance ramps with a temporal resolution of minutes or even less can be derived from ASIs using cloud motion-based methodologies.
- Irradiance forecasts up to several hours ahead with typical resolutions from 10–15 minutes can be derived from satellite data covering large areas, also using cloud motion-based methodologies.
- Irradiance forecasting from several hours to days ahead essentially relies on NWP models, with their capability to describe complex atmospheric dynamics, including advection as well as the formation and dissipation of clouds.

The performance of the different forecast models depends on multiple factors that have different impacts depending on the forecast horizons:

- The capability of the models to predict changes in clouds and irradiance
- The performance of the models for irradiance retrieval/analysis
- The capability of the models to predict AOD, especially for DNI forecasting in arid regions
- Input data to the model (parameters as well as the area covered by the input data)
- Time for a model run (run-time determines a lower limit for the delay of observations at the time of forecast delivery)
- Spatiotemporal resolution.

Complementing empirical and physical models, statistical and machine learning methods are widely used in solar irradiance and power forecasting:

- For time-series models and post-processing, which require reference values for training, the availability of irradiance and/or PV power measurements is crucial, as is proper quality control of the data. Satellite-derived data can also be used for training on irradiance.
- Short-term forecasting up to approximately 1 hour ahead benefits greatly from the use of local online irradiance or PV power measurements as input; however, pure time-series approaches based on local measurements only are outperformed by approaches integrating empirical and/or physical model forecasts from a few minutes to hours onward, depending on the spatiotemporal scale of the forecasts and the climatic conditions of the forecast location.
- Statistical and machine learning approaches are applied effectively for improving forecasts with empirical or physical models (post-processing). They can reduce systematic meteorological forecast errors. Training to PV power measurements in addition allows adaptation to the specifics of a given PV plant or to replace PV simulation models.
- Machine learning models are increasingly applied to replace parts of empirical models, e.g., algorithms to compute optical flow in cloud motion approaches.

State-of-the-art solar irradiance or PV power forecasting services do not rely on a single forecasting model but integrate and optimize different tools and data, with prominent examples given here:

- High-resolution intrahour forecasting systems combine the use of local measurements and ASI data with empirical and machine learning approaches.

- Forecasting systems for the intraday energy market up to several hours ahead integrate online measurements, satellite-based forecasts, and NWP model-based forecasts with statistical and/or machine learning approaches.
- Forecasting systems from several hours to several days ahead use different NWP models as input in combination with statistical and/or machine learning approaches.

Besides forecasting for single PV power plants, the estimation and forecasting of regionally aggregated PV power is important for grid operators. It involves the same modeling approaches described. Here, an additional challenge is that information on all the PV power plants contributing to the overall feed-in is often incomplete. Also, PV power is not measured at a sufficient resolution for most plants in many countries; therefore, upscaling approaches have been developed and are applied effectively to derive and forecast regionally aggregated PV power. Because of spatial smoothing effects, forecast errors of regionally aggregated PV power (normalized to the installed power) are much smaller than for single PV plants, depending on the size of the region and the set of PV plants contributing.

Forecast evaluations provide users with necessary information on forecast accuracy, assisting them in choosing between different forecasting services or assessing the risk when a forecast is used as a basis for decisions. The assessment of forecast accuracy should combine visual diagnostics (e.g., scatter plots or 2D histograms of forecasts and observations) and quantitative error measures (e.g., RMSE and skill in comparison to persistence). In addition to the model used, forecast accuracy depends on different factors, including the climatic conditions and the spatiotemporal scale; therefore, specific evaluation for a given application considering these factors is recommended—i.e., an evaluation for sites in a similar climate and with similar spatiotemporal resolutions.

Beyond general information on the overall accuracy of a deterministic forecast, probabilistic forecasts provide specific uncertainty information for each forecast value, depending on the weather conditions. Probabilistic forecasts take the form of CDFs or PDFs. They are summarized by quantiles from which prediction intervals can be inferred. Quantiles can be estimated using either a parametric or a nonparametric approach. In the latter case, statistical or machine learning techniques can be used to estimate the quantiles. Although NWP ensemble members are not directly linked to the notion of quantiles, different propositions exist to infer a CDF from an ensemble. As an example, for deterministic forecasting, the assessment of the quality of the probabilistic forecasts is based on visual diagnostic and proper scoring rules. In particular, the CRPS seems to have all the features needed to evaluate a probabilistic forecasting system and, as such, could become a standard for verifying probabilistic forecasts of solar irradiance and power.

Finally, forecasting solar irradiance should be evaluated in the context of strategies for the system integration of solar power, which aim to provide the necessary power to cover demand at any time. These strategies include spatial smoothing for grid-integrated PV and increasingly also the use of storage (batteries) and curtailment as well as in combination with other variable renewable energy sources, especially wind power. Applying these strategies reduces the variability of solar power as well as forecast errors.

8.8 References

Aler, R., I. M. Galván, J. A. Ruiz-Arias, and C. A. Gueymard. 2017. “Improving the Separation of Direct and Diffuse Solar Radiation Components Using Machine Learning by Gradient Boosting.” *Solar Energy* 150: 558–69. http://dx.doi.org/10.1016/j.solener.2017.05.018.

Alessandrini, S., L. Delle Monache, S. Sperati, and G. Cervone. 2015. "An Analog Ensemble for Short-Term Probabilistic Solar Power Forecast." *Applied Energy* 157: 95–110. https://doi.org/10.1016/j.apenergy.2015.08.011.

Almeida, M.P., O. Perpiñán, and L. Narvarte. 2015. "PV Power Forecast Using a Nonparametric PV Model." *Solar Energy* 115: 354–68. https://doi.org/10.1016/j.solener.2015.03.006 .

Andrews, R. W., J. S. Stein, C. Hansen, and Daniel Riley. 2014. "Introduction to the Open Source PV LIB for Python Photovoltaic System Modelling Package." In *Proceedings of the 2014 IEEE 40th Photovoltaic Specialist Conference (PVSC)*, 2014, S. 0170–74.

Antonanzas, J., N. Osorio, R. Escobar, R. Urraca, F.-J. Martinez-de-Pison, and F. Antonanzas-Torres. 2016. "Review of Photovoltaic Power Forecasting." *Solar Energy* 136: 78–111. http://dx.doi.org/10.1016/j.solener.2016.06.069.

Arbizu-Barrena, C., D. Pozo-Vázquez, J.A. Ruiz-Arias, and J. Tovar-Pescador. 2015. "Macroscopic Cloud Properties in the WRF NWP Model: An Assessment Using Sky Camera and Ceilometer Data." *Journal of Geophyscal Research: Atmospheres* 120: 1–16. https://doi.org/10.1002/2015JD023502.

Arbizu-Barrena, C., J. A. Ruiz-Arias, F. J. Rodríguez-Benítez, D. Pozo-Vázquez, and J. Tovar-Pescador. 2017. "Short-Term Solar Radiation Forecasting by Advecting and Diffusing MSG Cloud Index." *Solar Energy* 155: 1092–103. https://doi.org/10.1016/j.solener.2017.07.045.

Aryaputera, A. W., D. Yang, and W. M. Walsh. 2015. "Day-Ahead Solar Irradiance Forecasting in a Tropical Environment." *Journal of Solar Energy Engineering: Transactions of the ASME* 137 (5): 051009. https://doi.org/10.1115/1.4030231.

Bacher, P., H. Madsen, and H.A. Nielsen. 2009. "Online Short-Term Solar Power Forecasting." *Solar Energy* 83: 1772–83. https://doi.org/10.1016/j.solener.2009.05.016.

Bakker, K., K. Whan, W. Knap, and M. Schmeits. 2019. "Comparison of Statistical Post-Processing Methods for Probabilistic NWP Forecasts of Solar Radiation." *Solar Energy* 191: 138–50. https://doi.org/10.1016/j.solener.2019.08.044.

Baldauf M., A. Seifert, J. Förstner, D. Majewski, M. Raschendorfer, and T. Reinhardt. 2011. "Operational Convective-Scale Numerical Weather Prediction with the COSMO Model Description and Sensitivities." Monthly Weather Review 139 (12). 3887e3905. http://dx.doi.org/10.1175/MWR-D-10-05013.1.

Behr, H. D. 1997. "Solar Radiation on Tilted South Oriented Surfaces: Validation of Transfer Models." *Solar Energy* 61: 399–413. https://doi.org/10.1016/S0038-092X(97)00081-9.

Betti, A., M. Pierro, C. Cornaro, D. Moser, M. Moschella, E. Collino, D. Ronzio et al. 2020. Regional Solar Power Forecasting (IEA-PVPS T16-01:2020). May 2020. ISBN 978-3-906042-88-6.

Beyer, H. G., J. Bethke, A. Drews, D. Heinemann, E. Lorenz, G. Heilscher, and S. Bofinger. 2004. "Identification of a General Model for the MPP Performance of PV-Modules for the Application in a Procedure for the Performance Check of Grid Connected Systems." Presented at the European Photovoltaic Solar Energy Conference (19). https://www.researchgate.net/publication/228894566.

Beyer, H. G., J. P. Martinez, M. Suri, J. L. Torres, E. Lorenz, S. C. Müller, C. Hoyer-Klick, and P. Ineichen. 2009. *Management and Exploitation of Solar Resource Knowledge: Ca–Contract No. 038665—D 1.1.3. Report on Benchmarking of Radiation Products*. http://www.mesor.org/docs/MESoR_Benchmarking_of_radiation_products.pdf.

Bishop C. M. 1995. *Neural Networks for Pattern Recognition*. Oxford: Clarendon Press.

Blanc, P., P. Massip, A. Kazantzidis, P. Tzoumanikas, P. Kuhn, S. Wilbert, D. Schüler, and C. Prahl. 2017. "Short-Term Forecasting of High Resolution Local DNI Maps with Multiple Fish-Eye Cameras in Stereoscopic Mode." *AIP Conference Proceedings* 1850: 140004. https://doi.org/10.1063/1.4984512.

Blum, N., T. Schmidt, B. Nouri, S. Wilbert, E. Peerlings, D. Heinemann, T. Schmidt et al. 2019. "Nowcasting of Irradiance Using a Network of All-Sky-Imagers." *Proceedings of the EUPVSEC Conference*, Marseille, France.

Boland, J., and T. Soubdhan. 2015. "Spatial-Temporal Forecasting of Solar Radiation." *Renewable Energy* 75: 607–16. http://dx.doi.org/10.1016/j.renene.2014.10.035.

Bottou L. 1998. "Online Algorithms and Stochastic Approximations" In *Online Learning and Neural Networks*, edited by D. Saad. Cambridge, UK: Cambridge University Press.

Breiman L. 2001. "Random Forests." *Machine Learning* 45 (1): 5–32.

Breiman L., J. Friedman, C. Stone, and R. Olshen. 1984. *Classification and Regression Trees*. Belmont, CA: Wadsworth, Inc.

Breitkreuz, H., M. Schroedter-Homscheidt, T. Holzer-Popp, and S. Dech. 2009. "Short-Range Direct and Diffuse Irradiance Forecasts for Solar Energy Applications Based on Aerosol Chemical Transport and Numerical Weather Modeling." *Journal of Applied Meteorology and Climatology* 48: 1766. https://doi.org/10.1175/2009JAMC2090.1.

Bright, J. M., S. Killinger, D. Lingfors, and N. A. Engerer. 2018. "Improved Satellite-Derived PV Power Nowcasting Using Real-Time Power Data from Reference PV Systems." *Solar Energy 168* (August 2017): 118–39. https://doi.org/10.1016/j.solener.2017.10.091.

Bröcker, J., and L. A. Smith. 2007. "Increasing the Reliability of Reliability Diagrams." *Weather and Forecasting* 22: 651–61. https://doi.org/10.1175/WAF993.1

Buizza, R., D. S. Richardson, and T. N. Palmer. 2003. "Benefits of Increased Resolution in the ECMWF Ensemble System and Comparison with Poor-Man's Ensembles." *Quarterly Journal of the Royal Meteorological Society* 129: 1269–88. https://doi.org/10.1256/qj.02.92.

Carillo, R. E., M. Leblanc, B. Schubnel, R. Langou, C. Topfel, and P. Alet. 2020. High-Resolution PV Forecasting from Imperfect Data : A Graph-Based Solution." *Energies* 1–17. https://doi.org/10.3390/en13215763.

Chauvin, R., J. Nou, J. Eynard, S. Thil, and S. Grieu. 2018. "A New Approach to the Real-Time Assessment and Intraday Forecasting of Clear-Sky Direct Normal Irradiance." *Solar Energy* 119: 1–17.

Chauvin, R., J. Nou, S. Thil, and S. Grieu. 2015. "Modelling the Clear-Sky Intensity Distribution Using a Sky Imager." *Solar Energy* 119: 1–17.

Chou, M.-D., and M. J. Suarez. 1999. *A Solar Radiation Parameterization for Atmospheric Studies* (Vol. 15: Technical Report Series on Global Modeling and Data Assimilation). Greenbelt, MD: National Aeronautics and Space Administration Goddard Space Flight Center. NASA/TM-1999-104606.

Chow, C. W., B. Urquhart, M. Lave, A. Dominguez, J. Kleissl. J. Shields, and B. Washom. 2011. "Intra-Hour Forecasting with a Total Sky Imager at the UC San Diego Solar Energy Testbed." *Solar Energy* 85 (11): 2881–93. http://dx.doi.org/10.1016/j.solener.2011.08.025.

Coimbra, C. F. M., and H. T. C. Pedro. 2013a. "Stochastic-Learning Methods." In *Solar Energy Forecasting and Resource Assessment*, edited by J. Kleissl, 383–406. Boston: Academic Press. http://dx.doi.org/10.1016/B978-0-12-397177-7.00015-2.

Coimbra, C. F. M., J. Kleissl, and R. Marquez. 2013b. "Overview of Solar-Forecasting Methods and a Metric for Accuracy Evaluation." *Solar Energy Forecasting and Resource Assessment* 2013: 171–94.

Collins, W. D., P. J. Rasch, B. A. Boville, J. J. Hack, J. R. McCaa, D. L. Williamson, J. T. Kiehl et al. 2004. *Description of the NCAR Community Atmosphere Model (CAM 3.0)* (NCAR/TN-464+ STR, 226). Boulder, CO: National Center for Atmospheric Research.

Dambreville, R., P. Blanc, J. Chanussot, and D. Boldo. 2014. "Very Short-Term Forecasting of the Global Horizontal Irradiance Using a Spatio-Temporal Autoregressive Model." *Renewable Energy* 72: 291–300. http://dx.doi.org/10.1016/j.renene.2014.07.012.

Das U., K. Tey, and M. Seydmahmoudia. 2018. "Forecasting of Photovoltaic Power Generation and Model Optimization: A Review." *Renewable and Sustainable Energy Reviews* 81: 912–28.

David, M., and P. Lauret. 2018. "Solar Radiation Probabilistic Forecasting." In *Wind Field and Solar Radiation Characterization and Forecasting*, edited by R. Perez, 201–27. Springer International Publishing. https://doi.org/10.1007/978-3-319-76876-2_9.

David, M., F. Ramahatana, P. J. Trombe, and P. Lauret. 2016. "Probabilistic Forecasting of the Solar Irradiance with Recursive ARMA and GARCH Models." *Solar Energy* 133: 55–72. https://doi.org/10.1016/j.solener.2016.03.064.

David, M., M. A. Luis, and P. Lauret. 2018. "Comparison of Intraday Probabilistic Forecasting of Solar Irradiance Using Only Endogenous Data." *International Journal of Forecasting* 34: 529–47. https://doi.org/10.1016/j.ijforecast.2018.02.003.

David, M., P. Lauret, and J. Boland. 2013. "Evaluating Tilted Plane Models for Solar Radiation Using Comprehensive Testing Procedures at a Southern Hemisphere Location." *Renewable Energy* 51: 124–31.

Delle Monache, L., F. A. Eckel, D. L. Rife, B. Nagarajan, and K. Searight. 2013. "Probabilistic Weather Prediction with an Analog Ensemble." *Monthly Weather Review* 141: 3498–516. https://doi.org/10.1175/MWR-D-12-00281.1.

Deng, A., B. Gaudet, J. Dudhia, and K. Alapaty. 2014. "Implementation and Evaluation of a New Shallow Convection Scheme." Presented at the WRF: 94th American Meteorological Society Annual Meeting, 26th Conference on Weather Analysis and Forecasting/22nd conference on Numerical Weather Prediction, Atlanta, Georgia, February 2–6, 2014.

Descombes, G., T. Auligné, H.-C. Lin, D. Xu, C. Schwartz, and F. Vandenberghe. 2014. *Multisensor Advection Diffusion nowCast (MADCast) for Cloud Analysis and Short-Term Prediction* (NCAR/TN-509+STR). Boulder, CO: National Center for Atmospheric Research. http://dx.doi.org/10.5065/D62V2D37.

Diagné, H. M., D. Mathieu, P. Lauret, J. Boland, and N. Schmutz. 2013. "Review of Solar Irradiance Forecasting Methods and a Proposition for Small-Scale Insular Grids." *Renewable and Sustainable Energy Reviews* 27: 65–76. http://dx.doi.org/10.1016/j.rser.2013.06.042.

Diagné, M., M. David, J. Boland, N. Schmutz, and P. Lauret. 2014. "Post-Processing of Solar Irradiance Forecasts from WRF Model at Reunion Island." *Solar Energy* 105: 99–108. https://doi.org/10.1016/j.solener.2014.03.016.

Dudhia, J. 1989. "Numerical Study of Convection Observed During the Winter Monsoon Experiment Using a Mesoscale Two-Dimensional Model." *Journal of Atmospheric Science* 46 (20): 3077–107. https://doi.org/10.1175/1520-0469(1989)046%3C3077:NSOCOD%3E2.0.CO;2.

Dumortier, D. 2009. *Management and Exploitation of Solar Resource Knowledge: Contract No. 038665—D 1.2.1 & D1.2.2 Description of Solar Resource Products: Summary of Benchmarking Results and Examples of Use*. http://www.mesor.org/docs/MESoR_Handbook_on_best_practices.pdf.

Efron B. 1979. "Bootstrap Methods: Another Look at the Jackknife." *The Annals of Statistics* 7 (1): 1–26.

Espinar, B., L. Ramirez, A. Drews, H. G. Beyer, L. F. Zarzalejo, J. Polo, and L. Martin. 2008. "Analysis of Different Error Parameters Applied to Solar Radiation Data from Satellite and German Radiometric Stations." *Solar Energy* 83 (1).

Fatemi, S. A., A. Kuh, and M. Fripp. 2018. "Parametric Methods for Probabilistic Forecasting of Solar Irradiance." *Renewable Energy* 129: 666–76. https://doi.org/10.1016/j.renene.2018.06.022.

Fonseca, J. G., T. Oozeki, H. Ohtake, K. Ichi Shimose, T. Takashima, and K. Ogimoto. 2014. "Regional Forecasts and Smoothing Effect of Photovoltaic Power Generation in Japan: An Approach with Principal Component Analysis." *Renewable Energy* 68: 403–13.

Friedman, J. 2001. "Greedy Function Approximation: A Gradient Boosting Machine." *The Annals of Statistics* 29 (5): 1189–232. https://doi.org/10.1214/aos/1013203451.

Gastón, M., E. Lorenz, S. Lozano, D. Heinemann, M. Blanco, and L. Ramírez. 2009. "Comparison of Global Irradiance Forecasting Approaches." Presented at the SolarPACES Conference, Berlin, Germany, September 15–18, 2009.

Gauchet C., P. Blanc, B. Espinar, B. Charbonnier, and D. Demengel. 2012. "Surface Solar Irradiance Estimation with Low-Cost Fish-Eye Camera." Presented at COST WIRE Workshop on Remote Sensing Measurements for Renewable Energy, DTU Risoe, Denmark.

Ghonima, M. S., B. Urquhart, C. W. Chow, J. E. Shields, A. Cazorla, and J. Kleissl. 2012. "A Method for Cloud Detection and Opacity Classification Based on Ground-Based Sky Imagery." *Atmospheric Measurement Techniques* 5 (2): 2881–92. http://dx.doi.org/10.5194/amt-5-2881-2012.

Glahn, H. R., and D. A. Lowry. 1972. "The Use of Model Output Statistics (MOS) in Objective Weather Forecasting." *Journal of Applied Meteorology and Climatology* 11: 1203–11. https://doi.org/10.1175/1520-0450(1972)011<1203:TUOMOS>2.0.CO;2.

Glorot, X., and Y. Bengio. 2010. "Understanding the Difficulty of Training Deep Feedforward Neural Networks." *Journal of Machine Learning Research: Proceedings Track* 9: 249–56. http://dblp.uni-trier.de/db/journals/jmlr/jmlrp9.html#GlorotB10.

Gneiting, T., A. E. Raftery, A. H. Westveld, and T. Goldman. 2005. "Calibrated Probabilistic Forecasting Using Ensemble Model Output Statistics and Minimum CRPS Estimation." *Monthly Weather Review* 133: 1098–118. https://doi.org/10.1175/MWR2904.1.

Gneiting, T., and A. E. Raftery. 2007. "Strictly Proper Scoring Rules, Prediction, and Estimation." *Journal of the American Statistical Association* 102: 359–78. https://doi.org/10.1198/016214506000001437.

Graditi, G., S. Ferlito, and G. Adinolfi. 2016. "Comparison of Photovoltaic Plant Power Production Prediction Methods Using a Large Measured Dataset." *Renewable Energy* 90: 513–19. http://dx.doi.org/10.1016/j.renene.2016.01.027.

Grantham, A., Y. R. Gel, and J. Boland. 2016. "Nonparametric Short-Term Probabilistic Forecasting for Solar Radiation." *Solar Energy* 133: 465–75. https://doi.org/10.1016/j.solener.2016.04.011.

Gu, Y., K. N. Liou, S. C. Ou, and R. Fovell. 2011. "Cirrus Cloud Simulations Using WRF with Improved Radiation Parameterization and Increased Vertical Resolution." *Journal of Geophysical Research* 116 (D06119). http://dx.doi.org/10.1029/2010JD014574.

Gueymard, C. A. 2014. "A Review of Validation Methodologies and Statistical Performance Indicators for Modeled Solar Radiation Data: Towards a Better Bankability of Solar Projects." *Renewable and Sustainable Energy Reviews* 39: 1024–34. http://dx.doi.org/10.1016/j.rser.2014.07.117.

———. 1987. "An Anisotropic Solar Irradiance Model for Tilted Surfaces and Its Comparison with Selected Engineering Algorithms." *Solar Energy* 38: 367–86. https://doi.org/10.1016/0038-092X(87)90009-0. Erratum, *Solar Energy* 40: 175 (1988). https://doi.org/10.1016/0038-092X(88)90087-4.

———. 2009. "Direct and Indirect Uncertainties in the Prediction of Tilted Irradiance for Solar Engineering Applications." *Solar Energy* 83(3): 432–44. https://doi.org/10.1016/0038-092X(87)90009-0.

Gueymard, C. A., and J. A. Ruiz-Arias. 2015. "Extensive Worldwide Validation and Climate Sensitivity Analysis of Direct Irradiance Predictions from 1-Min Global Irradiance." *Solar Energy* 128: 1–30. http://dx.doi.org/10.1016/j.solener.2015.10.010.

Gueymard, C. A., and P. A. Jimenez. 2018. "Validation of Real-Time Solar Irradiance Simulations over Kuwait Using WRF-Solar." *Proceedings of the EuroSun Conference,* Rapperswil, Switzerland. http://dx.doi.org/10.18086/eurosun2018.09.14.

Gueymard, C. A., W. T. Gustafson, G. Bender, A. Etringer, and P. Storck. 2012. "Evaluation of Procedures to Improve Solar Resource Assessments: Optimum Use of Short-Term Data from a Local Weather Station to Correct Bias in Long-Term Satellite Derived Solar Radiation Time Series." Presented at the ASES-WREF Conference, Denver, Colorado.

Guichard, F., D. B. Parsons, J. Dudhia, and J. Bresch. 2003. "Evaluating Mesoscale Model Predictions of Clouds and Radiation with SGP ARM Data Over a Seasonal Timescale." *Monthly Weather Review* 131: 926–44.

Hamill, T. M. 2001. "Interpretation of Rank Histograms for Verifying Ensemble Forecasts." *Monthly Weather Review* 129: 550–60. https://doi.org/10.1175/1520-0493(2001)129<0550:IORHFV>2.0.CO;2.

Hamill, T. M., and J. S. Whitaker. 2006. "Probabilistic Quantitative Precipitation Forecasts Based on Reforecast Analogs: Theory and Application." *Monthly Weather Review* 134: 3209–29. https://doi.org/10.1175/MWR3237.1.

Hamill, T. M., and S. J. Colucci. 1997. "Verification of Eta–RSM Short-Range Ensemble Forecasts." *Monthly Weather Review* 125: 1312–27. https://doi.org/10.1175/1520-0493(1997)125<1312:VOERSR>2.0.CO;2.

Hammer, A., D. Heinemann, C. Hoyer, R. Kuhlemann, E. Lorenz, R. Müller, and H. G. Beyer. 2003. "Solar Energy Assessment Using Remote Sensing Technologies." *Remote Sensing of Environment* 86 (3): 423–32. http://dx.doi.org/10.1016/S0034-4257(03)00083-X.

Hammer, A., D. Heinemann, E. Lorenz, and B. Lückehe. 1999. "Short-Term Forecasting of Solar Radiation: A Statistical Approach Using Satellite Data." *Solar Energy* 67 (1–3): 139–50. http://dx.doi.org/10.1016/S0038-092X(00)00038-4.

Hasenbalg, M., P. Kuhn, S. Wilbert, B. Nouri, and A. Kazantzidis. 2020. "Benchmarking of Six Cloud Segmentation Algorithms for Ground-Based All-Sky Imagers." *Solar Energy* 201: 596–14. https://doi.org/10.1016/j.solener.2020.02.042.

Haupt, S. E., B. Kosovic, T. Jensen, J. L. Pedro Jimenez, J. Lazo, J. Cowie, T. McCandless et al. 2016. *The Sun4Cast Solar Power Forecasting System: The Result of the Public-Private-Academic Partnership to Advance Solar Power Forecasting* (NCAR/TN-526+STR). Boulder, CO: National Center for Atmospheric Research. http://dx.doi.org/10.5065/D6N58JR2.

Hay, J. E. 1979. *Study of Shortwave Radiation on Non-horizontal Surfaces* (Technical Report 79-12). Downsview, Ontario: Atmospheric Environment Service.

He, X., C. Yuan, and Z. Yang. 2016. "Performance Evaluation of Chinese Solar Radiation Forecast Based on Three Global Forecast Back Ground Fields." *Taiyangneng Xuebao/Acta Energiae Solaris Sinica* 37 (4): 897–904.

Heidinger, A. K., M. J. Foster, A. Walther, and X. Zhao. 2014. "The Pathfinder Atmospheres: Extended AVHRR Climate Dataset." *Bulletin of the American Meteorological Society* 95: 909–22. http://dx.doi.org/10.1175/BAMS-D-12-00246.1.

Hersbach, H. 2000. "Decomposition of the Continuous Ranked Probability Score for Ensemble Prediction Systems." *Weather and Forecasting* 15: 559–70.

Hirsch, T., N. Martin, L. Gonzalez, M. Biencinto, S. Wilbert, M. Schroedter-Homscheidt, F. Chenlo, and J. F. Feldhoff. 2014. *Technical Report on the Functional Requirements for the Nowcasting Method*. Cologne, Germany: DLR Institute of Solar Research, CIEMAT.

Hoff, T., and R. Perez. 2012. "Modeling PV Fleet Output Variability." *Solar Energy* 86: 2177–89. https://doi.org/10.1016/j.solener.2011.11.005.

Hoff, T. E., R. Perez, J. Kleissl, D. Renné, and J. Stein. 2012. "Reporting of Irradiance Modeling Relative Prediction Errors." *Progress in Photovoltaics: Research and Applications* 21: 1514–19. http://dx.doi.org/10.1002/pip.2225.

Huang, G., Q. Zhu, and C. K. Siew. 2006. "Extreme Learning Machine: Theory and Applications." *Neurocomputing* 70: 489–501. https://doi.org/10.1016/j.neucom.2005.12.126.

Huang, J., M. Korolkiewicz, M. Agrawal, and J. Boland. 2013. "Forecasting Solar Radiation on an Hourly Time Scale Using a Coupled AutoRegressive and Dynamical System (CARDS) Model." *Solar Energy* 87: 136–49. http://dx.doi.org/10.1016/j.solener.2012.10.012.

Huang, J., M. M. Khan, Y. Qin, and S. West. 2019. Hybrid Intra-Hour Solar PV Power Forecasting Using Statistical and Skycam-Based Methods. *Proceedings of the 46th IEEE Photovoltaic Specialists Conference*. https://doi.org/10.1109/PVSC40753.2019.8980732.

Iacono, M. J., J. S. Delamere, E. J. Mlawer, M. W. Shephard, S. A. Clough, and W. D. Collins. 2008. "Radiative Forcing by Long-Lived Greenhouse Gases: Calculations with the AER Radiative Transfer Models." *Journal of Geophysical Research* 113 (D13103). http://dx.doi.org/10.1029/2008JD009944.

Ineichen, P. 2011. *Global Irradiance on Tilted and Oriented Planes: Model Validations*. Geneva, Switzerland: University of Geneva. http://archive-ouverte.unige.ch/unige:23519.

Inman R. H., H. T. C. Pedro, and C. F. M. Coimbra. 2013. "Solar Forecasting Methods for Renewable Energy Integration." *Progress in Energy and Combustion Science* 39: 535–76. http://dx.doi.org/10.1016/j.pecs.2013.06.002.

International Energy Agency (IEA). 2015. "International Energy Agency, Solar Heating & Cooling Program, Task 46, Subtask C-1: Short-Term Solar."

International Renewable Energy Agency (IRENA). 2019. *Global Energy Transformation: A Roadmap to 2050*. 2019 Edition.

Isvoranu, D., and V. Badescu. 2015. "Comparison Between Measurements and WRF Numerical Simulation of Global Solar Irradiation in Romania." *Analele Universitatii de Vest din Timisoara, Seria Fizica* LVII: 24–33. https://doi.org/10.1515/awutp-2015-0103.

Jamaly, M., and J. Kleissl. 2017. Spatiotemporal Interpolation and Forecast of Irradiance Data Using Kriging. *Solar Energy* 158: 407–23. https://doi.org/10.1016/j.solener.2017.09.057.

Jimenez, P. A., J. P. Hacker, J. Dudhia, S. E. Haupt, J. A. Ruiz-Arias, C. A. Gueymard, G. Thompson, T. Eidhammer, and A. Deng. 2016a. "WRF-Solar: An Augmented NWP Model for Solar Power Prediction. Model Description and Clear-Sky Assessment." *Bulletin of the American Meteorological Society* 97: 1249–64. http://dx.doi.org/10.1175/BAMS-D-14-00279.1.

Jimenez, P. A., S. Alessandrini, S. E. Haupt, A. Deng, B. Kosovic, J. A. Lee, and L. D. Monache. 2016b. "The Role of Unresolved Clouds on Short-Range Global Horizontal Irradiance Predictability." *Monthly Weather Review* 144 (9): 3099–107. http://dx.doi.org/10.1175/MWR-D-16-0104.1.

Jolliffe I. T., and D. B. Stephenson, eds. 2011. *Forecast Verification: A Practitioner's Guide in Atmospheric Science: Second Edition*. New York: Wiley.

Jones, A. S., and S. J. Fletcher. 2013. "Data Assimilation in Numerical Weather Prediction and Sample Applications." In *Solar Energy Forecasting and Resource Assessment*, edited by J. Kleissl, 319–55. Boston, MA: Academic Press. http://dx.doi.org/10.1016/B978-0-12-397177-7.00013-9.

Junk, C., L. Delle Monache, and S. Alessandrini. 2015. "Analog-Based Ensemble Model Output Statistics." *Monthly Weather Review* 143: 2909–17. https://doi.org/10.1175/MWR-D-15-0095.1.

Kallos, G. 1997. "The Regional Weather Forecasting System SKIRON." Presented at the Symposium on Regional Weather Prediction on Parallel Computer Environments, Athens, Greece, October 15–17, 1997.

Kalnay, E. 2003. *Atmospheric Modeling, Data Assimilation and Predictability*. New York: Cambridge University Press.

Kambezidis, H. D., B. E. Psiloglou, and C. A. Gueymard. 1994. "Measurements and Models for Total Solar Irradiance on Inclined Surface in Athens, Greece." *Solar Energy* 53 (2): 177–185. https://doi.org/10.1016/0038-092X(94)90479-0.

Kaur, A., L. Nonnenmacher, H. T. C. Pedro, and C. F. M. Coimbra. 2016. "Benefits of Solar Forecasting for Energy Imbalance Markets." *Renewable Energy* 86: 819–30. http://dx.doi.org/10.1016/j.renene.2015.09.011.

Kazantzidis A., P. Tzoumanikas, A. F. Bais, S. Fotopoulos, and G. Economou. 2012. "Cloud Detection and Classification with the Use of Whole-Sky Ground-Based Images." *Atmospheric Research* 113: 80–88.

Kazantzidis, A., P. Tzoumanikas, E. Nikitidou, V. Salamalikis, S. Wilbert, and C. Prahl. 2017. "Application of Simple All-Sky Imagers for the Estimation of Aerosol Optical Depth." *AIP Conference Proceedings* 1850 (1): 140012.

Killinger, S., D. Lingfors, Y.-M. Saint-Drenan, P. Moraitis, W. van Sark, J. Taylor, N. A. Engerer, and J. M. Bright. 2018."On the Search for Representative Characteristics of PV Systems: Data Collection and Analysis of PV System Azimuth, Tilt, Capacity, Yield and Shading." *Solar Energy* 173: 1087–106. https://dx.doi.org/10.1016/j.solener.2018.08.051.

Killinger, S., F. Braam, B. Müller, B. Wille-Haussmann, and R. McKenna. 2016. "Projection of Power Generation between Differently-Oriented PV Systems." *Solar Energy* 136: 153–65. https://doi.org/10.1016/j.solener.2016.06.075.

Kingma D., and J. Ba. 2015. "Adam: A Method for Stochastic Optimization." *Proceedings of the International Conference on Learning Representations*, 1–13.

Kleissl, J. 2013. *Solar Energy Forecasting and Resource Assessment*. Boston, MA: Academic Press. http://dx.doi.org/10.1016/B978-0-12-397177-7.01001-9.

Koenker, R., and G. Bassett. 1978. "Regression Quantiles." *Econometrica* 46: 33–50. https://doi.org/10.2307/1913643.

Kraas, B., M. Schroedter-Homscheidt, and R. Madlener. 2013. "Economic Merits of a State-of-the-Art Concentrating Solar Power Forecasting System for Participation in the Spanish Electricity Market." *Solar Energy* 93: 244–55. https://doi.org/10.1016/j.solener.2013.04.012.

Kuhn, P. M., M. Wirtz, N. Killius, S. Wilbert, J. L. Bosch, N. Hanrieder, B. Nouri et al. 2018. "Benchmarking Three Low-Cost, Low-Maintenance Cloud Height Measurement Systems and ECMWF Cloud Heights Against a Ceilometer." *Solar Energy* 168: 140–52. https://doi.org/10.1016/j.solener.2018.02.050.

Kuhn, P., S. Wilbert, C. Prahl, A. Kazantzidis, L. Ramirez, L. Zarzalejo, L. Vuilleumier, P. Blanc, and R. Pitz-Paal. 2017c. "Shadow Camera System for the Validation of Nowcasted Plant-Size Irradiance Maps." Presented at the European Meteorological Society Annual Meeting, Dublin, Ireland, September 4–8, 2017.

Kuhn, P., S. Wilbert, C. Prahl, D. Schüler, T. Haase, T. Hirsch, M. Wittmann et al. 2017a. "Shadow Camera System for the Generation of Solar Irradiance Maps." *Solar Energy* 157: 157–70. https://doi.org/10.1016/j.solener.2017.05.074.

Kuhn, P., S. Wilbert, D. Schüler, C. Prahl, T. Haase, L. Ramirez, L. Zarzalejo et al. 2017b. "Validation of Spatially Resolved All Sky Imager Derived DNI Nowcasts." *Proceedings of the SolarPACES Conference*.

Kühnert J. 2015. "Development of a Photovoltaic Power Prediction System for Forecast Horizons of Several Hours." Ph.D diss. Oldenburg University.

Kühnert, J., E. Lorenz, and D. Heineman. 2013. "Satellite-Based Irradiance and Power Forecasting for the German Energy Market." In *Solar Energy Forecasting and Resource Assessment*, edited by J. Kleissl, 267–97. Boston, MA: Academic Press. http://dx.doi.org/10.1016/B978-0-12-397177-7.00011-5.

Kurtz, B., and J. Kleissl. 2017. "Measuring Diffuse, Direct, and Global Irradiance Using a Sky Imager." *Solar Energy* 141: 311–22. https://doi.org/10.1016/j.solener.2016.11.032.

Lara-Fanego, V., J. A. Ruiz-Arias, D. Pozo-Vázquez, F. J. Santos-Alamillos, and J. Tovar-Pescador. 2012. "Evaluation of the WRF Model Solar Irradiance Forecasts in Andalusia (Southern Spain)." *Solar Energy* 86 (8): 2200–17. http://dx.doi.org/10.1016/j.solener.2011.02.014.

Larson V. E. 2013. "Forecasting Solar Irradiance with Numerical Weather Prediction Models." In *Solar Energy Forecasting and Resource Assessment*, edited by J. Kleissl, 299–318. Boston, MA: Academic Press.

Lauret, P., M. David, and H. Pedro. 2017. "Probabilistic Solar Forecasting Using Quantile Regression Models." *Energies* 10: 1591. https://doi.org/10.3390/en10101591.

Lauret, P., M. David, and P. Pinson. 2019. "Verification of Solar Irradiance Probabilistic Forecasts." *Solar Energy* 194: 254–71. https://doi.org/10.1016/j.solener.2019.10.041.

Lave, M., W. Hayes, A. Pohl, and C. W. Hansen. 2015. "Evaluation of Global Horizontal Irradiance to Plane of Array Irradiance Models at Locations across the United States." *IEEE Journal of Photovoltaics* 99: 1–10.

Law, E. W., A. A. Prasad, M. Kay, and R. A. Taylor. 2014. "Direct Normal Irradiance Forecasting and Its Application to Concentrated Solar Thermal Output Forecasting: A Review." *Solar Energy* 108: 287–307. http://dx.doi.org/10.1016/j.solener.2014.07.008.

Law, E. W., M. Kay, and R. A. Taylor. 2016. "Evaluating the Benefits of Using Short-Term Direct Normal Irradiance Forecasts to Operate a Concentrated Solar Thermal Plant." *Solar Energy* 140: 93–108. http://dx.doi.org/10.1016/j.solener.2016.10.037.

LeCun Y., B. Boser, J. S. Denker, D. Henderson, R. E. Howard, W. Hubbard, and L. D. Jackel. 1989. "Backpropagation Applied to Handwritten ZIP Code Recognition." *Neural Computation* 1(4): 541–51. DOI: 10.1162/neco.1989.1.4.541.

Lee, J. A., S. E. Haupt, P. A. Jimenez, M. A. Rogers, S. D. Miller, and T. C. McCandless. 2017. "Solar Irradiance Nowcasting Case Studies Near Sacramento." *Journal of Applied Meteorology and Climatology* 56 (1): 85–108. http://dx.doi.org/10.1175/JAMC-D-16-0183.1.

Leutbecher, M., and T. N. Palmer. 2008. "Ensemble Forecasting." *Journal of Computational Physics* 227 (7): 3515–39. https://doi.org/10.1016/j.jcp.2007.02.014.

Li, J., and A. D. Heap. 2014. "Spatial Interpolation Methods Applied in the Environmental Sciences: A Review." *Environmental Modelling and Software* 53: 173–89. https://doi.org/10.1016/j.envsoft.2013.12.008.

Lima, F. J. L., F. R. Martins, E. B. Pereira, E. Lorenz, and D. Heinemann. 2016. "Forecast for Surface Solar Irradiance at the Brazilian Northeastern Region Using NWP Model and Artificial Neural Networks." *Renewable Energy* 87: 807–18. https://doi.org/10.1016/j.renene.2015.11.005.

Long, C. N., and J. J. DeLuisi. 1998. "Development of an Automated Hemispheric Sky Imager for Cloud Fraction Retrievals." *Proceedings of the 10th Symposium on Meteorological Observations and Instrumentation*, Phoenix, Arizona, January 11–16, 171–74.

Lonij, V. P. A., A. E. Brooks, A. D. Cronin, M. Leuthold, and K. Koch. 2013. "Intra-Hour Forecasts of Solar Power Production Using Measurements from a Network of Irradiance Sensors." *Solar Energy* 97: 58–66. http://dx.doi.org/10.1016/j.solener.2013.08.002.

Lorenz, E. 2018: *Solar Irradiance Forecasting for System Integration of Solar Energy*. Habilitation Thesis, Oldenburg University.

Lorenz, E., A. Hammer, and D. Heinemann. 2004. "Short-Term Forecasting of Solar Radiation Based on Satellite Data." *Proceedings of the EuroSun 2004, ISES Europe Solar Congress*, Freiburg, Germany.

Lorenz, E., and D. Heinemann. 2012. "Prediction of Solar Irradiance and Photovoltaic Power." *Comprehensive Renewable Energy* 1: 239–92. http://dx.doi.org/10.1016/B978-0-08-087872-0.00114-1.

Lorenz, E., J. Hurka, D. Heinemann, and H. G. Beyer. 2009. "Irradiance Forecasting for the Power Prediction of Grid-Connected Photovoltaic Systems." *IEEE Journal of Selected Topics in Applied Earth Observations and Remote Sensing* 2 (1): 2–10. DOI: 10.1109/JSTARS.2009.2020300.

Lorenz, E., J. Kühnert, D. Heinemann, K. P. Nielsen, J. Remund, and S. C. Müller. 2016. "Comparison of Global Horizontal Irradiance Forecasts Based on Numerical Weather

Prediction Models with Different Spatio-Temporal Resolutions." *Progress in Photovoltaics: Research and Applications* 24 (12): 1626–40. DOI: 10.1002/pip.2799.

Lorenz, E., J. Remund, S. C. Müller, W. Traunmüller, G. Steinmaurer, D. Pozo, J. A. Ruiz-Arias et al. 2009. "Benchmarking of Different Approaches to Forecast Solar Irradiance." Presented at the 24th European Photovoltaic Solar Energy Conference, Hamburg, Germany, September 21–25, 2009.

Lorenz, E., T. Scheidsteger, J. Hurka, D. Heinemann, and C. Kurz. 2011. "Regional PV Power Prediction for Improved Grid Integration." *Progress in Photovoltaics: Research and Applications* 19: 757–71. http://dx.doi.org/10.1002/pip.1033.

Lucas, B., and T. Kanade. 1981. "An Iterative Image Registration Technique with an Application to Stereovision." Presented at the Imaging Understanding Workshop, Pittsburgh, Pennsylvania.

Maas A. L., A. Y. Hannun, and A. Y. Ng. 2013. "Rectifier Nonlinearities Improve Neural Network Acoustic Models." *Proceedings of the 30th International Conference on Machine Learning* 28.

Macke, A., and HOPE-Team. 2014. "The HD(CP)² Observational Prototype Experiment HOPE: An Overview." *ACP Special Issue: HD(CP)² Observational Prototype Experiment*.

Mailhot, J., S. Belair, L. Lefaivre, B. Bilodeau, M. Desgagne, C. Girard, A. Glazer, A.M. Leduc, A. Methot, A. Patoine, A. Plante, A. Rahill, T. Robinson, D. Talbot, A. Tremblay, P.A. Vaillancourt, and A. Zadra. 2006. "The 15-km Version of the Canadian Regional Forecast System." *Atmosphere-Ocean* 44: 133–49. https://doi.org/10.3137/ao.440202.

Marcos, J., L. Narvarte Fernández, I. Berazaluce, R. González, and J. Samuel. 2013. "Attenuation of Power Fluctuations in Large PV Power Plants: The Use of Prediction to Optimize the Storage System." Presented at the 28th European Photovoltaic Solar Energy Conference (PVSEC), Paris, France, September 30–October 4, 2013.

Marquez, R., and C. F. M. Coimbra. 2011. "Forecasting of Global and Direct Solar Irradiance Using Stochastic Learning Methods, Ground Experiments and the NWS Database." *Solar Energy* 85 (5): 746–56. http://dx.doi.org/10.1016/j.solener.2011.01.007.

Marquez, R., and C. F. M. Coimbra. 2013. "Proposed Metric for Evaluation of Solar Forecasting Models." *Journal of Solar Energy Engineering* 135 (1): 11016. http://dx.doi.org/10.1115/1.4007496.

———. 2013. "Intra-Hour DNI Forecasting Based on Cloud Tracking Image Analysis." *Solar Energy* 91: 327–36. http://dx.doi.org/10.1016/j.solener.2012.09.018.

Marquez, R., H. T. C. Pedro, and C. F. M. Coimbra. 2013. "Hybrid Solar Forecasting Method Uses Satellite Imaging and Ground Telemetry as Inputs to ANNs." *Solar Energy* 92: 176–88. http://dx.doi.org/10.1016/j.solener.2013.02.023.

Martin, N., and J. M. Ruiz. 2001. "Calculation of the PV Modules Angular Losses Under Field Conditions by Means of an Analytical Model." *Solar Energy Materials and Solar Cells* 70 (1): 25–38. https://doi.org/10.1016/S0927-0248(00)00408-6.

Martinez-Anido, C. B., B. Botor, A. R. Florita, C. Draxl, S. Lu, H.F. Hamann, and B.-M. Hodge. 2016. "The Value of Day-Ahead Solar Power Forecasting Improvement." *Solar Energy* 129: 192–203. https://doi.org/10.1016/j.solener.2016.01.049.

Mathiesen, P., and J. Kleissl. 2011. "Evaluation of Numerical Weather Prediction for Intra-Day Solar Forecasting in the Continental United States." *Solar Energy* 85 (5): 967–77. http://dx.doi.org/10.1016/j.solener.2011.02.013.

Mathiesen, P., C. Collier, and J. Kleissl. 2013. "A High-Resolution, Cloud-Assimilating Numerical Weather Prediction Model for Solar Irradiance Forecasting." *Solar Energy* 92: 47–61. https://doi.org/10.1016/j.solener.2013.02.018.

Mathiesen, P., J. Kleissl, and C. Collier. 2013. "Case Studies of Solar Forecasting with the Weather Research and Forecasting Model at GL-Garrad Hassan." In *Solar Energy Forecasting and Resource Assessment*, edited by J. Kleissl, 357–82. Boston, MA: Academic Press. http://dx.doi.org/10.1016/B978-0-12-397177-7.00014-0.

Mazorra Aguiar, L., B. Pereira, P. Lauret, F. Díaz, and M. David. 2016. "Combining Solar Irradiance Measurements, Satellite-Derived Data and a Numerical Weather Prediction Model to Improve Intra-Day Solar Forecasting." *Renewable Energy* 97: 599–610. http://dx.doi.org/10.1016/j.renene.2016.06.018.

Met Office. 2021. "What Is an Ensemble Forecast?" https://www.metoffice.gov.uk/research/weather/ensemble-forecasting/what-is-an-ensemble-forecast.

Mejia, F. A., B. Kurtz, A. Levis, Í. de la Parra and J. Kleissl. 2018. "Cloud Tomography Applied to Sky Images: A Virtual Testbed." *Solar Energy* 176: 287–300.

Mejia, F.A., B. Kurtz, K. Murray, L. M. Hinkelman, M. Sengupta, Y. Xie, and J. Kleissl. 2016. "Coupling Sky Images with Radiative Transfer Models: A New Method to Estimate Cloud Optical Depth." *Atmospheric Measurement Techniques* 9 (4): 4151–65. http://dx.doi.org/10.5194/amt-9-4151-2016.

Miller, S. D., A. K. Heidinger, and M. Sengupta. 2013. "Physically Based Satellite Methods." In *Solar Energy Forecasting and Resource Assessment*, edited by J. Kleissl, 49–79. Boston, MA: Academic Press. http://dx.doi.org/10.1016/B978-0-12-397177-7.00003-6.

Miller, S. D., M. A. Rogers, J. M. Haynes, M. Sengupta, and A. K. Heidinger. 2018. "Short-Term Solar Irradiance Forecasting via Satellite/Model Coupling." *Solar Energy* 168: 102–117. https://doi.org/10.1016/j.solener.2017.11.049.

Mlawer, E. J., S. J. Taubman, P. D. Brown, M. J. Iacono, and S. A. Clough. 1997. "Radiative Transfer for Inhomogeneous Atmospheres: RRTM, a Validated Correlated-k Model for the Longwave." *Journal of Geophysical Research* 102: 16663–82. http://dx.doi.org/10.1029/97JD00237.

Morales, J. M., A. J. Conejo, H. Madsen, P. Pinson, and M. Zugno. 2014. *Integrating Renewables in Electricity Markets, International Series in Operations Research and Management Science*. Springer, Boston, MA.

Morcrette, J., H. W. Barker, J. N. Cole, M. J. Iacono, and R. Pincus. 2008. "Impact of a New Radiation Package, McRad, in the ECMWF Integrated Forecasting System." *Monthly Weather Review* 136: 4773–98. http://dx.doi.org/10.1175/2008MWR2363.1.

Müller S. C., and J. Remund. 2010. "Advances in Radiation Forecast Based on Regional Weather Models MM5 and WRF." Presented at the 25th European Photovoltaic Solar Energy Conference, Valencia, Spain, September 6–10, 2010.

———. 2014. "Satellite Based Shortest Term Solar Energy Forecast System for Entire Europe for the Next Hours." *Proceedings of the 29th European Photovoltaic Solar Energy Conference and Exhibition*, September 22–26, Amsterdam, The Netherlands. http://dx.doi.org/10.4229/EUPVSEC20142014-5BV.1.6.

Myers, W., G. Wiener, S. Linden, and S. E. Haupt. 2011. "A Consensus Forecasting Approach for Improved Turbine Hub Height Wind Speed Predictions." Presented at WindPower 2011, Anaheim, California, May 24, 2011.

Myers, W., S. Linden, G. Wiener, and S. E. Haupt. 2012. "A Consensus Wind Forecasting System." *Proceedings of the World Renewable Energy Forum*, Denver, Colorado, May 17.

Nguyen, D., and J. Kleissl. 2014. "Stereographic Methods for Cloud Base Height Determination Using Two Sky Imagers." *Solar Energy* 107: 495–509. https://doi.org/10.1016/j.solener.2014.05.005.

Oberländer, D., C. Prahl, S. Wilbert, S. Müller, B. Stanicki, and N. Hanrieder. 2015. "Cloud Shadow Maps from Whole Sky Imagers and Voxel Carving." Presented at the ICEM Conference, Boulder, Colorado, June 23–26, 2015.

Ohtake, H., K. Shimose, J. Gari da Silva Fonseca Jr., T. Takashima, T. Oozeki, and Y. Yamada. 2013. "Accuracy of the Solar Irradiance Forecasts of the Japan Meteorological Agency Mesoscale Model for the Kanto Region, Japan." *Solar Energy* 98 (Part B): 138–52. http://dx.doi.org/10.1016/j.solener.2012.10.007.

Olmo, F. J., A. Cazorla, L. Alados-Arboledas, M. A. López-Álvarez, J. Hernández-Andrés, and J. Romero. 2008. "Retrieval of the Optical Depth Using an All-Sky CCD Camera." *Applied Optics* 47 (34). https://doi.org/10.1364/AO.47.00H182.

Orehounig, K., S. Dervishi, and A. Mahdavi. 2014. "Computational Derivation of Irradiance on Building Surfaces: An Empirically-Based Model Comparison." *Renewable Energy* 71: 185–92. https://doi.org/10.1016/j.renene.2014.05.015.

Parzen E. 1962. "On Estimation of a Probability Density Function and Mode." *Annals of Mathematical Statistics* 33 (3): 1065–76. http://dx.doi.org/10.1214/aoms/1177704472.

Pedro, H. T. C., C. F. M. Coimbra, M. David, M., and P. Lauret. 2018. "Assessment of Machine Learning Techniques for Deterministic and Probabilistic Intra-Hour Solar Forecasts." *Renewable Energy* 123: 191–203. https://doi.org/10.1016/j.renene.2018.02.006.

Pelland, S., G. Galanis, and G. Kallos. 2013. "Solar and Photovoltaic Forecasting through Post-Processing of the Global Environmental Multiscale Numerical Weather Prediction Model." *Progress in Photovoltaics: Research and Applications* 21: 284–96. http://dx.doi.org/10.1002/pip.1180.

Pelland, S., J. Remund, J. Kleissl, T. Oozeki, and K. De Brabandere. 2013. *Photovoltaic and Solar Forecasting: State of the Art*. (IEA-PVPS T14-01:2013). October 2013. ISBN 978-3-906042-13-8. https://iea-pvps.org/wp-content/uploads/2013/10/Photovoltaic_and_Solar_Forecasting_State_of_the_Art_REPORT_PVPS_T14_01_2013.pdf

Peng, Z., D. Yu, D. Huang, J. Heiser, S. Yoo, and P. Kalb. 2015. "3D Cloud Detection and Tracking System for Solar Forecast Using Multiple Sky Imagers." *Solar Energy* 118: 496–519. http://dx.doi.org/10.1016/j.solener.2015.05.037.

Perez, R., M. Perez, M. Pierro, J. Schlemmer, S. Kivalov, J. Dise, P. Keelin et al. 2019a. "Operationally Perfect Solar Power Forecasts: A Scalable Strategy to Lowest-Cost Firm Solar Power Generation." *Proceedings of the 46th IEEE PV Specialists Conference*, Chicago, Illinois.

———. 2019b. "Perfect Operational Solar Forecasts: A Scalable Strategy Toward Firm Power Generation." *Proceedings of the ISES Solar World Congress*, Santiago, Chile.

Perez, R., A. Kankiewicz, J. Schlemmer, K. Hemker, and S. Kivalov. 2014. "A New Operational Solar Resource Forecast Model Service for PV Fleet Simulation." *Proceedings of the IEEE 40th Photovoltaic Specialist Conference (PVSC)*, June 8–13, Denver, Colorado. http://dx.doi.org/10.1109/PVSC.2014.6925204.

Perez, R., and T. Hoff. 2013. "SolarAnywhere Forecasting." In Solar Energy Forecasting and Resource Assessment, edited by J. Kleissl, 233–65. Boston, MA: Academic Press. http://dx.doi.org/10.1016/B978-0-12-397177-7.00010-3.

Perez, R., E. Lorenz, S. Pelland, M. Beauharnois, G. Van Knowe, K. Hemker Jr., D. Heinemann et al. 2013. "Comparison of Numerical Weather Prediction Solar Irradiance Forecasts in the U.S., Canada and Europe." *Solar Energy* 94: 305–26. http://dx.doi.org/10.1016/j.solener.2013.05.005.

Perez, R., K. Moore, S. Wilcox, D. Renné, and A. Zelenka. 2007. "Forecasting Solar Radiation: Preliminary Evaluation of an Approach Based Upon the National Forecast Database." *Solar Energy* 81 (6): 809–12. http://dx.doi.org/10.1016/j.solener.2006.09.009.

Perez, R., M. David, T. Hoff, M. Jamaly, S. Kivalov, J. Kleissl, P. Lauret, and M. Perez. 2016. "Spatial and Temporal Variability of Solar Energy." *Foundations and Trends in Renewable Energy* 1: 144. http://dx.doi.org/10.1561/2700000006.

Perez, R., R. Seals, P. Ineichen, R. Stewart, and D. Menicucci. 1987. "A New Simplified Version of the Perez Diffuse Irradiance Model for Tilted Surfaces." *Solar Energy* 39 (3): 221–31. http://dx.doi.org/10.1016/S0038-092X(87)80031-2.

Perez, R., S. Kivalov, J. Schlemmer, K. Hemker Jr., D. Renné, and T.E. Hoff. 2010. "Validation of Short and Medium Term Operational Solar Radiation Forecasts in the U.S." *Solar Energy* 84 (12): 2161–72. http://dx.doi.org/10.1016/j.solener.2010.08.014.

Pierer, R., and J. Remund 2019. *SKYCAM: Lokale Vorhersage der Sonneneinstrahlung* (BFE project report). https://www.aramis.admin.ch/Default.aspx?DocumentID=50306&Load=true .

Pierro M., R. Perez, M. Perez, D. Moser, M. Giacomo, and Cristina Cornaro. 2020a. Italian Protocol for Massive Solar Integration: Imbalance Mitigation Strategies. *Renewable Energy Journal* 153: 725–39. https://doi.org/10.1016/j.renene.2020.01.145.

Pierro, M., F. Bucci, C. Cornaro, F. Maggioni, A. Perotto, M. Pravettoni, and F. Spada. 2015. "Model Output Statistics Cascade to Improve Day Ahead Solar Irradiance Forecast." *Solar Energy* 117: 99–113. https://doi.org/10.1016/j.solener.2015.04.033.

Pierro, M., M. De Felice, E. Maggioni, D. Moser, A. Perotto, F. Spada and C. Cornaro. 2017. "Data-Driven Upscaling Methods for Regional Photovoltaic Power Estimation and Forecast Using Satellite and Numerical Weather Prediction Data." *Solar Energy* 158: 1026–38.

Pierro, M., M. De Felice, E. Maggioni, D. Moser, A. Perotto, F. Spada, and C. Cornaro. 2020b. "Residual Load Probabilistic Forecast for Reserve Assessment: A Real Case Study." *Renewable Energy* 149: 508–22. https://doi.org/10.1016/j.renene.2019.12.056.

Pincus, R., H. W. Barker, and J.-J. Morcrette. 2003. "A Fast, Flexible, Approximate Technique for Computing Radiative Transfer in Inhomogeneous Cloud Fields." *Journal of Geophysical Research* 108 (D13): 4376. http://dx.doi.org/10.1029/2002JD003322.

Pinson, P. 2012. "Adaptive Calibration of (u,v)-Wind Ensemble Forecasts." *Quarterly Journal of the Royal Meteorological Society* 138: 1273–84. https://doi.org/10.1002/qj.1873.

Pinson, P., and H. Madsen. 2009. "Ensemble-Based Probabilistic Forecasting at Horns Rev." *Wind Energy* 12: 137–55. https://doi.org/10.1002/we.309.

Pinson, P., H. A.Nielsen, J. K. Møller, H. Madsen, and G. N. Kariniotakis. 2007. "Non-Parametric Probabilistic Forecasts of Wind Power: Required Properties and Evaluation." *Wind Energy* 10: 497–516. https://doi.org/10.1002/we.230.

Pinson, P., P. McSharry, and H. Madsen. 2010. "Reliability Diagrams for Non-Parametric Density Forecasts of Continuous Variables: Accounting for Serial Correlation." *Quarterly Journal of the Royal Meteorological Society* 136: 77–90. https://doi.org/10.1002/qj.559.

Quesada-Ruiz, S., Y. Chu, J. Tovar-Pescador, H. T. C. Pedro, and C. F. M. Coimbra. 2014. "Cloud-Tracking Methodology for Intra-Hour DNI Forecasting." *Solar Energy* 102: 267–75. http://dx.doi.org/10.1016/j.solener.2014.01.030.

Ranchin, T., S. Wilbert, M. Schroedter-Homscheidt, and Y.-M. Saint-Drénan. 2017. *Best Practice Guideline for DNI Nowcasting* (DNICast Project Report).

Reikard, G. 2009. "Predicting Solar Radiation at High Resolutions: A Comparison of Time Series Forecasts." *Solar Energy* 83 (3): 342–49. http://dx.doi.org/10.1016/j.solener.2008.08.007.

Rikos, E., S. Tselepis, C. Hoyer-Klick, and M. Schroedter-Homscheidt. 2008. "Stability and Power Quality Issues in Microgrids Under Weather Disturbances: An Implementation to the Kythnos Island Power System." *IEEE Journal of Special Topics in Earth Observations and Remote Sensing* 1: 170–79. http://dx.doi.org/10.1109/JSTARS.2008.2010557.

Ritter, B., and J.-F. Geleyn. 1992. "A Comprehensive Radiation Scheme for Numerical Weather Prediction Models with Potential Applications in Climate Simulations." *Monthly Weather Review* 120: 303–25. https://doi.org/10.1175/1520-0493(1992)120<0303:ACRSFN>2.0.CO;2.

Ruder, S. 2016. "An Overview of Gradient Descent Optimization Algorithms." arXiv: 1609.04747v2.

Ruiz-Arias, J. A., C. Arbizu-Barrena, F.J. Santos-Alamillos, J. Tovar-Pescador, and D. Pozo-Vazquez. 2015. "Assessing the Surface Solar Radiation Budget in the WRF Model: A Spatio-Temporal Analysis of the Bias and its Causes." *Monthly Weather Review* 144: 703–11. http://dx.doi.org/10.1175/MWR-D-15-0262.1.

Ruiz-Arias, J. A., D. Pozo-Vázquez, N. Sánchez-Sánchez, J. P. Montávez, A. Hayas-Barrú, and J. Tovar-Pescador. 2008. "Evaluation of Two MM5-PBL Parameterizations for Solar Radiation and Temperature Estimation in the South-Eastern Area of the Iberian Peninsula." *Il Nuovo Cimento C* 31 (5–6): 825–42. http://dx.doi.org/10.1393/ncc/i2009-10343-6.

Ruiz-Arias, J. A., J. Dudhia, and C. A. Gueymard. 2014. "A Simple Parameterization of the Short-Wave Aerosol Optical Properties for Surface Direct and Diffuse Irradiances Assessment in a Numerical Weather Model." *Geoscientific Model Development* 7: 593–29. http://dx.doi.org/10.5194/gmd-7-1159-2014.

Ruiz-Arias, J. A., J. Dudhia, F. J. Santos-Alamillos, and D. Pozo-Vázquez. 2013. "Surface Clear-Sky Shortwave Radiative Closure Intercomparisons in the Weather Research and Forecasting Model." *Journal of Geophysical Research: Atmospheres* 118. http://dx.doi.org/10.1002/jgrd.50778.

Rumelhart D. E., G. E. Hinton, and R. J. Williams. 1986. "Learning Internal Representations by Error Propagation." In *Parallel Distributed Processing: Explorations in the Microstructure of Cognition*, edited by D. E. Rumelhart, J. L. McClelland, and the PDP Research Group. MIT Press.

Saint-Drenan Y.-M., L. Wald, T. Ranchin, L. Dubus, and A. Troccoli. 2018. "An Approach for the Estimation of the Aggregated Photovoltaic Power Generated in Several European Countries from Meteorological Data." *Advances in Science and Research* 15: 51–62. https://dx.doi.org/10.5194/asr-15-51-2018. ⟨hal-01782565⟩.

Saint-Drenan Y.-M., S. Vogt, S. Killinger, J. Bright, R., R. Fritz, and R. Potthast. 2019. "Bayesian Parameterisation of a Regional Photovoltaic Model: Application to Forecasting." *Solar Energy* 188: 760–74. https://dx.doi.org/10.1016/j.solener.2019.06.053. ⟨hal-02174688⟩.

Saint-Drenan, Y. M., G. H. Good, and M. Braun. 2017. "A Probabilistic Approach to the Estimation of Regional Photovoltaic Power Production." *Solar Energy* 147: 257–76. https://doi.org/10.1016/j.solener.2017.03.007.

Saint-Drenan, Y. M., G. H. Good, M. Braun, and T. Freisinger. 2016. "Analysis of the Uncertainty in the Estimates of Regional PV Power Generation Evaluated with the Upscaling Method." *Solar Energy* 135: 536–50. https://doi.org/10.1016/j.solener.2016.05.052.

Saint-Drenan, Y., S. Bofinger, K. Rohrig and B. Ernst. 2011. "Regional Nowcasting of the Solar Power Production with PV-Plant Measurements and Satellite Images." *Proceedings ISES Solar World Congress*, Kassel, Germany.

Saint-Drenan, Y. M. 2015. A Probabilistic Approach to the Estimation of Regional Photovoltaic Power Generation using Meteorological Data Application of the Approach to the German Case. Ph.D. thesis. University of Kassel.

Sak, H., A. Senior, and F. Beaufays. 2014. "Long Short-Term Memory Recurrent Neural Network Architectures for Large Scale Acoustic Modeling." *Proceedings of the Annual Conference of the International Speech Communication Association*, INTERSPEECH, 338–342: 01.

Sanfilippo, A., L. Martin-Pomares, N. Mohandes, D. Perez-Astudillo, and D. Bachour. 2016. "An Adaptive Multi-Modeling Approach to Solar Nowcasting." *Solar Energy* 125: 77–85. ISSN 0038-092X. https://doi.org/10.1016/j.solener.2015.11.041.

Savijärvi, H. 1990. "Fast Radiation Parameterization Schemes for Mesoscale and Short-Range Forecast Models." *Journal of Applied Meteorology* 29: 437–47. http://dx.doi.org/10.1175/1520-0450(1990)029<0437:FRPSFM>2.0.CO;2.

Schmidt, H., and D. Sauer. 1996. "Wechselrichter-Wirkungsgrade. Praxisgerechte Modellierung und Abschätzung." *Sonnenenergie* 4: 43–47.

Schmidt, T., J. Kalisch, E. Lorenz, and D. Heinemann. 2016. "Evaluating the Spatio-Temporal Performance of Sky-Imager-Based Solar Irradiance Analysis and Forecasts." *Atmospheric Chemistry and Physics* 16: 3399–412. http://dx.doi.org/10.5194/acp-16-3399-2016.

Schroedter-Homscheidt, M., A. Benedetti, and N. Killius. 2016. "Verification of ECMWF and ECMWF/MACC's Global and Direct Irradiance Forecasts with Respect to Solar Electricity Production Forecasts." *Meteorologische Zeitschrift* 26: 1–19. http://dx.doi.org/10.1127/metz/2016/0676.

Schroedter-Homscheidt, M., A. Oumbe, A. Benedetti, and J.-J. Morcrette. 2013. "Aerosols for Concentrating Solar Electricity Production Forecasts: Requirement Quantification and ECMWF/MACC Aerosol Forecast Assessment." *Bulletin of the American Meteorological Society* 94 (6): 903–14. http://dx.doi.org/10.1175/BAMS-D-11-00259.1.

Schroedter-Homscheidt, M., and B. Pulvermüller. 2011. "Verification of Direct Normal Irradiance Forecasts for the Concentrating Solar Thermal Power Plant Andasol-3 Location." *Proceedings of the SolarPACES Conference*, September 20–23, Granada, Spain.

Schroedter-Homscheidt, M., and S. Wilbert. 2017. "Methods to Provide Meteorological Forecasts for Optimum CSP Systems Operations." In *The Performance of Concentrated Solar Power (CSP) Systems: Analysis, Measurement and Assessment—1st Edition*, edited

by Peter Heller. Woodhead Publishing, 253–81. https://doi.org/10.1016/B978-0-08-100447-0.00008-0.

Shaffery, P., A. Habte, M. Netto, A. Andreas, and V. Krishnan. 2020. "Automated Construction of Clear-Sky Dictionary from All-Sky Imager Data." *Solar Energy* 212: 73–83. https://doi.org/10.1016/j.solener.2020.10.052.

Shields, J. E., R. W. Johnson, and T. L. Koehler. 1993. "Automated Whole Sky Imaging Systems for Cloud Field Assessment." Presented at the Fourth Symposium on Global Change Studies, American Meteorological Society, Boston, Massachusetts, January 17–22, 1993.

Simoglou, C. K., E. G. Kardakos, E. A. Bakirtzis, D. I. Chatzigiannis, S. I. Vagropoulos, A. V. Ntomaris, P. N. Biskas et al. 2014. "An Advanced Model for the Efficient and Reliable Short-Term Operation of Insular Electricity Networks with High Renewable Energy Sources Penetration." *Renewable and Sustainable Energy Reviews* 38: 415–27. http://dx.doi.org/10.1016/j.rser.2014.06.015.

Skamarock, W. C., J. B. Klemp, J. Dudhia, D. O. Gill, D. M. Barker, W. Wang, and J. G. Powers. 2005. *A Description of the Advanced Research WRF Version 2* (NCAR/TN-468+STR). Boulder, CO: National Center for Atmospheric Research.

Sobri, S., S. Koohi-Kamali, and N. A. Rahim. 2018. "Solar Photovoltaic Generation Forecasting Methods: A Review." *Energy Conversion and Management* 156 (C): 459–97. https://doi.org/10.1016/j.enconman.2017.11.019.

SolarAnywhere. 2019. https://www.solaranywhere.com/.

Sosa-Tinoco, I., J. Peralta-Jaramillo, C. Otero-Casal, A. López-Agüera, G. Miguez-Macho, and I. Rodríguez-Cabo. 2016. "Validation of a Global Horizontal Irradiation Assessment from a Numerical Weather Prediction Model in the South of Sonora-Mexico." *Renewable Energy* 90: 105–13.

Sperati, S., S. Alessandrini, and L. Delle Monache. 2016. "An Application of the ECMWF Ensemble Prediction System for Short-Term Solar Power Forecasting." *Solar Energy* 133: 437–50. https://doi.org/10.1016/j.solener.2016.04.016.

Thompson, G., and T. Eidhammer. 2014. "A Study of Aerosol Impact on Clouds and Precipitation Development in a Large Winter Cyclone." *Journal of Atmospheric Sciences* 71: 3636–58. https://doi.org/10.1175/JAS-D-13-0305.1.

Tiedtke, M. 1993. "Representation of Clouds in Large-Scale Models." *Monthly Weather Review* 121: 3040–61. https://doi.org/10.1175/1520-0493(1993)121<3040:ROCILS>2.0.CO;2.

Ulbricht R., U. Fischer, W. Lehner, and H. Donker, 2013. "First Steps Towards a Systematical Optimized Strategy for Solar Energy Supply Forecasting." In *Proceedings of the European Conference on Machine Learning and Principles and Practice of Knowledge Discovery in Databases*, Prague.

Urquhart, B., B. Kurtz, E. Dahlin, M. Ghonima, J. E. Shields, and J. Kleissl. 2015. "Development of a Sky Imaging System for Short-Term Solar Power Forecasting." *Atmospheric Measurement Techniques* 8 (2): 875–90. http://dx.doi.org/10.5194/amt-8-875-2015.

Urquhart, B., M. Ghonima, D. Nguyen, B. Kurtz, C. W. Chow, and J. Kleissl. 2013. "Sky-Imaging Systems for Short-Term Forecasting." In *Solar Energy Forecasting and Resource Assessment*, edited by J. Kleissl, 195–232. Boston, MA: Academic Press. http://dx.doi.org/10.1016/B978-0-12-397177-7.00009-7.

van der Meer, D. W., J. Widén, and J. Munkhammar. 2018. "Review on Probabilistic Forecasting of Photovoltaic Power Production and Electricity Consumption." *Renewable and Sustainable Energy Reviews* 81: 1484–512. https://doi.org/10.1016/j.rser.2017.05.212.

Vaz, A. G. R., B. Elsinga, W. G. J. H. M. van Sark, and M. C. Brito. 2016. "An Artificial Neural Network to Assess the Impact of Neighbouring Photovoltaic Systems in Power Forecasting in Utrecht, the Netherlands." *Renewable Energy* 85: 631–41. https://doi.org/10.1016/j.renene.2015.06.061.

Voyant, C., C. Darras, M. Muselli, C. Paoli, M.-L. Nivet, and P. Poggi. 2014. "Bayesian Rules and Stochastic Models for High Accuracy Prediction of Solar Radiation." *Applied Energy* 114: 218–26. http://dx.doi.org/10.1016/j.apenergy.2013.09.051.

Voyant, C., G. Nottona, S. Kalogirou, M.-L. Nivet, C. Paoli, F. Motte, and A. Fouilloy. 2017. "Machine Learning Methods for Solar Radiation Forecasting: A Review." *Renewable Energy* 105: 569–82. https://doi.org/10.1016/j.renene.2016.12.095.

Wang, G., B. Kurtz, and J. Kleissl. 2016. "Cloud Base Height from Sky Imager and Cloud Speed Sensor." *Solar Energy* 131: 208–21. https://doi.org/10.1016/j.solener.2016.02.027.

Wang, P., R. M. van Westrhenen, J. F. Meirink, S. H. van der Veen, and W. H. Knap. 2019. "Surface Solar Radiation Forecasts by Advecting Cloud Physical Properties Derived from Meteosat Second Generation Observations." *Solar Energy* 177: 47–58. https://doi.org/10.1016/j.solener.2018.10.073.

Wen, X., S. Lu, L. Shang, Y. Ao, Y. Bao, and W. Li. 2011. "Numerical Simulations of Radiation Budget Using WRF Model over the Jinta Oasis-Gobi." *Taiyangneng Xuebao/Acta Energiae Solaris Sinica* 32 (3): 346–53.

Wilks, D. S. 2014. *Statistical Methods in the Atmospheric Sciences: An Introduction.* Elsevier.

———. 2018. Univariate Ensemble Postprocessing. In *Statistical Postprocessing of Ensemble Forecasts* 2018: 49–89. https://doi.org/10.1016/B978-0-12-812372-0.00003-0.

Winter, K., D. Beinert, S. Vogt, and R. Fritz. 2019. "PV Power Forecast Comparison of Physical and Machine Learning Models." Presented at the 9th Solar & Storage Integration Workshop, Dublin, Ireland, October 2019.

Wittmann, M., H. Breitkreuz, M. Schroedter-Homscheidt, and M. Eck. 2008. "Case Studies on the Use of Solar Irradiance Forecast for Optimized Operation Strategies of Solar Thermal Power Plants." *IEEE Journal of Selected Topics in Applied Earth Observations and Remote Sensing* 1 (1): 18–27. http://dx.doi.org/10.1109/JSTARS.2008.2001152.

Wolff, B., J. Kühnert, E. Lorenz, O. Kramer, and D. Heinemann. 2016. "Comparing Support Vector Regression for PV Power Forecasting to a Physical Modeling Approach Using Measurement, Numerical Weather Prediction and Cloud Motion Data." *Solar Energy* 135: 197–208. http://dx.doi.org/10.1016/j.solener.2016.05.051.

Wood-Bradley, P., J. Zapata, and J. Pye. 2012. "Cloud Tracking with Optical Flow for Short-Term Solar Forecasting." Presented at the 50th Conference of the Australian Solar Energy Society, Melbourne, December.

Wyser, K., L. Rontu, and H. Savijärvi. 1999. "Introducing the Effective Radius into a Fast Radiation Scheme of a Mesoscale Model." *Contributions to Atmospheric Physics* 72 (3): 205–18.

Xie, Y., M. Sengupta, and J. Dudhia. 2016. "A Fast All-sky Radiation Model for Solar Applications (FARMS): Algorithm and Performance Evaluation." *Solar Energy* 135: 435–45.

Yagli, G. M., D. Yang, and D. Srinivasan. 2020. "Ensemble Solar Forecasting Using Data-Driven Models with Probabilistic Post-Processing through GAMLSS." *Solar Energy* 208: 612–22.

Yang, D. 2016. "Solar Radiation on Inclined Surfaces: Corrections and Benchmarks." *Solar Energy* 136: 288–302. http://dx.doi.org/10.1016/j.solener.2016.06.062.

———. 2019a. "On Post-Processing Day-Ahead NWP Forecasts Using Kalman Filtering." *Solar Energy* 182: 179–81. https://doi.org/10.1016/j.solener.2019.02.044.

———. 2019b. "A Universal Benchmarking Method for Probabilistic Solar Irradiance Forecasting." *Solar Energy* 184: 410–16. https://doi.org/10.1016/j.solener.2019.04.018.

———. 2019c. "Standard of Reference in Operational Day-Ahead Deterministic Solar Forecasting." *Journal of Renewable and Sustainable Energy* 11: 053702.

———. 2020. "Reconciling Solar Forecasts: Probabilistic Forecast Reconciliation in a Nonparametric Framework." *Solar Energy* 210: 49–58. https://doi.org/10.1016/j.solener.2020.03.095.

Yang, D., C. Gu, Z. Dong, P. Jirutitijaroen, N. Chen, and W. M. Walsh. 2013. "Solar Irradiance Forecasting Using Spatial-Temporal Covariance Structures and Time-Forward Kriging." *Renewable Energy* 60: 235–45. https://doi.org/10.1016/j.renene.2013.05.030.

Yang, D., J. Kleissl, C. A. Gueymard, H. T. C. Pedro, and C. F. M. Coimbra. 2018. "History and Trends in Solar Irradiance and PV Power Forecasting: A Preliminary Assessment and Review Using Text Mining. *Solar Energy* 168: 60–101. https://doi.org/10.1016/j.solener.2017.11.023.

Yang, D., and D. van der Meer. 2021. "Post-Processing in Solar Forecasting: Ten Overarching Thinking Tools." *Renewable and Sustainable Energy Reviews* 140: 110735. https://doi.org/10.1016/j.rser.2021.110735.

Yang, D., E. Wu, and J. Kleissl. 2019. "Operational Solar Forecasting for the Real-Time Market." *International Journal of Forecasting* 35: 1499–519. https://doi.org/10.1016/j.ijforecast.2019.03.009.

Yang, D., H. Quan, V. R. Disfani, and L. Liu. 2017. "Reconciling Solar Forecasts: Geographical Hierarchy." *Solar Energy* 146: 276–86. https://doi.org/10.1016/j.solener.2017.02.010.

Yang, D., S. Alessandrini , J. Antonanzas, F. Antonanzas-Torres, V. Badescu., H. G. Beyer, R. Blaga et al. 2020. "Verification of Deterministic Solar Forecasts." *Solar Energy* 210: 20–37. https://doi.org/10.1016/j.solener.2020.04.019.

Zamo, M., O. Mestre, P. Arbogast, and O. Pannekoucke. 2014. "A Benchmark of Statistical Regression Methods for Short-Term Forecasting of Photovoltaic Electricity Production. Part II: Probabilistic Forecast of Daily Production." *Solar Energy* 105: 804–16. https://doi.org/10.1016/j.solener.2014.03.026.

Zamora, R. J., E. G. Dutton, M. Trainer, S. A. McKeen, J. M. Wilczak, and Y.-T. Hou. 2005. "The Accuracy of Solar Irradiance Calculations Used in Mesoscale Numerical Weather Prediction." *Monthly Weather Review* 133: 783–92.

Zamora, R., S. Solomon, E. Dutton, J. Bao, M. Trainer, R. Portmann, A. White, D. Nelson, and R. McNider. 2003. "Comparing MM5 Radiative Fluxes with Observations Gathered During the 1995 and 1999 Nashville Southern Oxidants Studies." *Journal of Geophysical Research* 108: 4050. http://dx.doi.org/10.1029/2002JD002122.

Zängl G., D. Reinert, P. Ripodas, and M. Baldauf. 2014. "The ICON (ICOsahedral Non-Hydrostatic) Modelling Framework of DWD and MPI-M: Description of the Non-Hydrostatic Dynamical Core." *Quarterly Journal of the Royal Meteorological* Society 141(687): 563–79. https://doi.org/10.1002/qj.2378.

Zemouri, N., H. Bouzgou, and C. A. Gueymard. 2019. "Multimodel Ensemble Approach for Hourly Global Solar Irradiation Forecasting." *European Physical Journal Plus* 134: 594. https://doi.org/10.1140/epjp/i2019-12966-5.

Zempila, M.-M., T. M. Giannaros, A. Bais, D. Melas, and A. Kazantzidis. 2016. "Evaluation of WRF Shortwave Radiation Parameterizations in Predicting Global Horizontal Irradiance in Greece." *Renewable Energy* 86: 831–40. https://doi.org/10.1016/j.renene.2015.08.057.

Zhong, X., J.A. Ruiz-Arias, and J. Kleissl. 2016. "Dissecting Surface Clear-Sky Irradiance Bias in Numerical Weather Prediction: Application and Corrections to the New Goddard Shortwave Scheme." *Solar Energy* 132: 103–13. https://doi.org/10.1016/j.solener.2016.03.009.

9 APPLYING SOLAR RESOURCE DATA TO SOLAR ENERGY PROJECTS

Robert Höller,[1] Kristian Pagh Nielsen,[2] Luis F. Zarzalejo,[3] Janine Freeman,[4] Christian Gueymard,[5] Stefan Wilbert,[6] Manuel Silva,[7] Dave Renné,[8] Lourdes Ramírez,[9] David Spieldenner,[10] Rafael Fritz,[11] Mark Mehos,[4] Richard Perez,[12] and Aron Habte[4]

[1] *University of Applied Sciences Upper Austria*
[2] *Danish Meteorological Institute, Copenhagen*
[3] *Centro de Investigaciones Energéticas, Medioambientales y Tecnológicas (CIEMAT)*
[4] *National Renewable Energy Laboratory*
[5] *Solar Consulting Services*
[6] *German Aerospace Center (DLR)*
[7] *Universidad de Sevilla*
[8] *Dave Renné Renewables, LLC*
[9] *Universidad Carlos III de Madrid*
[10] *First Solar*
[11] *Fraunhofer Institute for Energy Economics and Energy System Technology*
[12] *University at Albany, The State University of New York*

9.1 Introduction and Background

As discussed in previous chapters, solar resource evaluation covers a wide range of topics and applications. Most applications are related to projects involving solar radiation energy conversion. In this section, these are referred to as “solar energy projects,” and they include electricity production applications (photovoltaics [PV], solar thermal electricity), solar heating applications (central solar heating for district heating, local domestic heating and cooling), water and air applications (disinfection, desalination, decontamination), and energy conservation (for building applications).

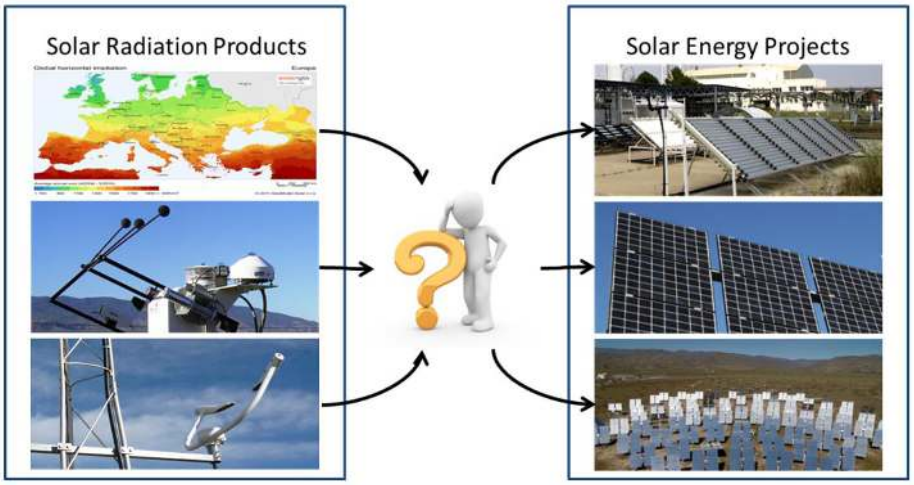

Figure 9-1. (Left) Different solar radiation products or evaluation methodologies described in previous chapters can be applied to (right) solar energy projects. *Image by L. Ramirez*

The overall goal in applying solar resource data to solar energy projects is to help the project developer or investor identify the best estimates or methodologies to obtain the optimal solar

resource and weather information to address each project stage; hence, this chapter summarizes available information and provides guidance on the types and uses of solar resource data that are relevant at various stages in the project development. In addition, some information about how to generate data sets for energy simulations is also provided. Sections 9.2–9.5 discuss an idealized project development pathway, corresponding to what is shown in Figure 9-2. Section 9.6 includes special needs of solar resource data for different types of solar projects. Finally, Section 9.7 provides a summary for further reference.

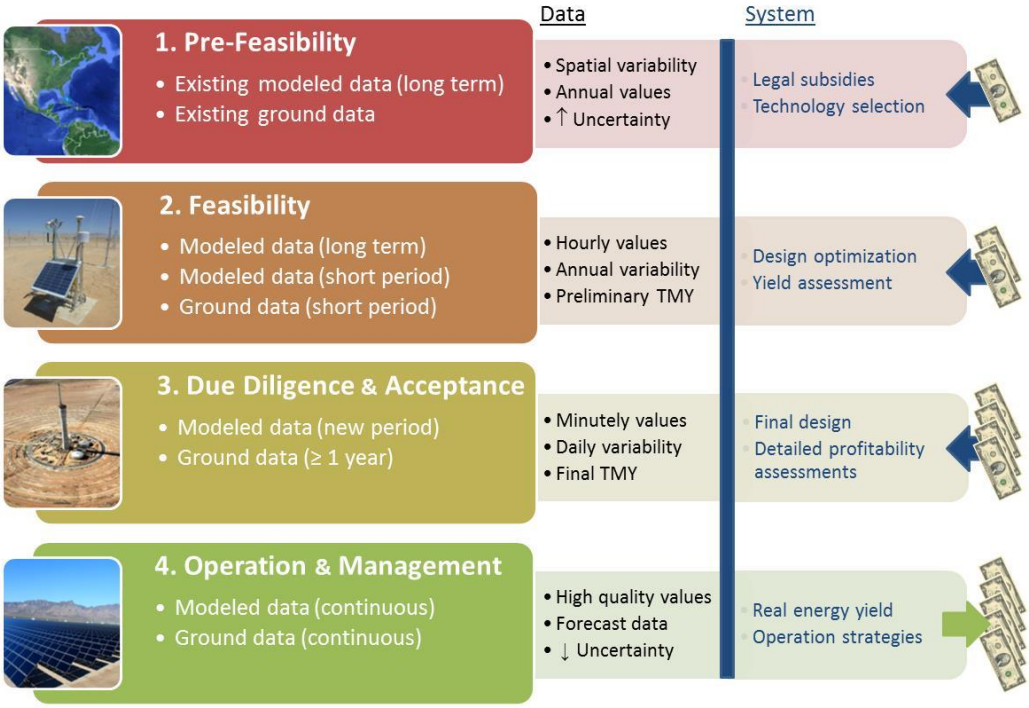

Figure 9-2. Solar radiation needs at four typical stages of a hypothetical solar power project: (1) Google Earth view; (2) CSP Services measurement station of low-maintenance requirements; (3) Gemasolar concentrating solar power (CSP), 20 MW, 15 hours of storage capacity, under construction; (4) Copper Mountain PV, 552 MW. *Image by L. Ramirez*

The exact needs for solar resource data for a project depend on the project characteristics and how it is financed. Typically, a large solar power project requires several years of high-quality modeled data and at least 1 year of on-site measured data during the final stages of the project execution. The on-site data need to be collected using the measurement procedures described in Chapter 3 and in formats directly relevant to the type of technology being considered. The modeled radiation data can be obtained from the methodologies described in Chapter 4, and further meteorological parameters can be obtained as described in Chapter 5.

For the first stages of the project execution, project developers can rely on several information sources. In most countries, solar radiation data sources include limited on-site information of varying quality, such as:

- Nearby measurements that might or might not be precisely applicable to the site because of spatial and temporal variability
- Satellite-derived irradiance estimates
- Estimations from reanalysis of numerical weather prediction (NWP) models.

Assuming that no high-quality on-site data are available during the site screening and prefeasibility stages, energy estimates must be derived from these three sources or from improved data sets from commercial vendors. During feasibility assessments, including engineering analysis and due diligence, some period (1 year or more) of high-quality measurements are assumed to be available at the site; however, these relative short-term measurements must be used by the solar resource provider and combined with long-term modeled data to ultimately derive a long-term record that removes the bias in the original modeled time series while capturing seasonal trends and the interannual variability of solar resources for the site. This merging process is usually referred to as "site adaptation," and it is described in Chapter 4, Section 4.8. During the project's operation, on-site, high-quality, ground-based measurements are normally necessary to evaluate how well the system is performing in real time compared with its theoretical output. These on-site measurements can be supplemented to some extent, or in some cases replaced, by ongoing estimations, such as satellite-derived data sets for the region or for the specific site.

Figure 9-3 provides a generalized view of solar radiation data requirements throughout various conceptual stages of a project's life cycle. In a solar power project, some questions must be addressed at each stage, as presented in the following sections. Sections 9.1.1–9.1.4 provide some specific information that could help in the interpretation of Figure 9-3**Fehler! Verweisquelle konnte nicht gefunden werden.** and also present topics that are addressed in sections 9.2–9.5.

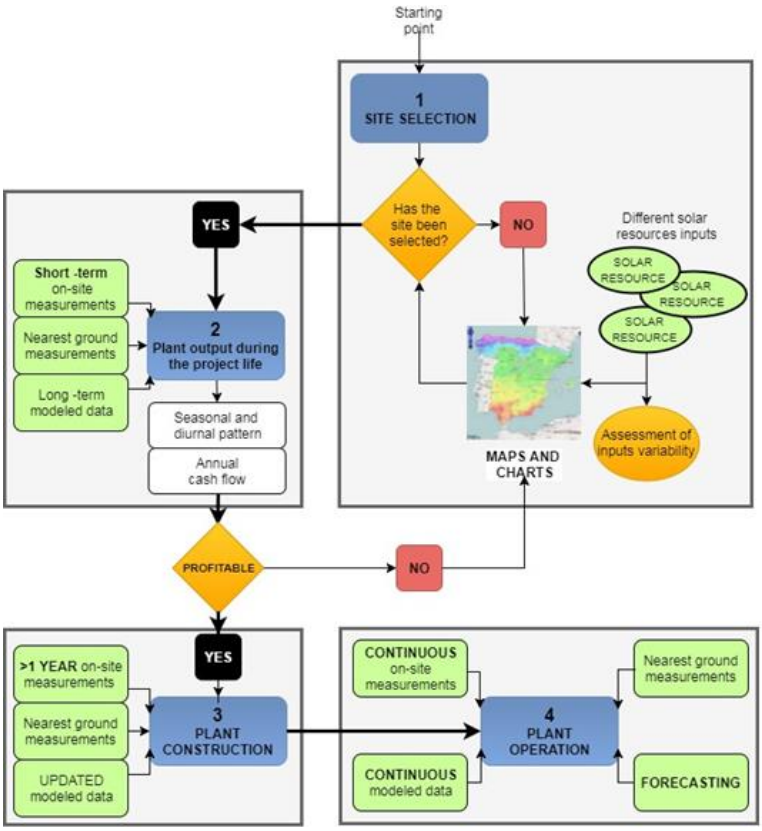

Figure 9-3. Flowchart of the solar radiation data needs (in green) for a hypothetical (large) solar power project. *Image by L. Ramirez*

9.1.1 Site Selection for Solar Energy Projects

During the first stages of a project, some questions related to its exact location might still be open:

- What proposed site location(s) need(s) to be evaluated?

- Has a single site been chosen?
- Is the developer making a choice from among two or more sites or still "prospecting" from a wider area?

If choosing from among multiple sites, the developer would benefit from using a geographic information system (GIS), maps, and other graphic techniques to evaluate the estimated resource as well as its variability and uncertainty.

- What temporal and spatial characteristics of the data sources are available to the developer, and how do these characteristics influence the evaluation of system performance?

Regarding temporal characteristics, measured solar data apply to a specific location and are usually recorded at short time intervals (1–10 minutes); then they are averaged to the desired time interval (often hourly in the early project phase). Modeled data, such as satellite-derived data, usually represent snapshots in time because of the scanning characteristics of spaceborne radiometers, and they are typically considered to represent averages from 5–60 minutes.

For most modeled gridded databases derived from geosynchronous satellite imagery, the individual pixel (or cell) size ranges from 1–10 km, but it depends on the specific model configuration, the specific instrument, and the pixel's geographic location. In some cases, data providers might aggregate several pixels into one grid cell, so the user needs to determine the exact spatial resolution based on the information associated with the chosen data set.

9.1.2 Predicted Plant Output Throughout the Project Life

Important questions that need to be addressed throughout the plant's operational phase include the following:

- What will be the energy produced during specified time periods (based on the project's financing and revenue generation schemes) throughout the project's life?
- How is the appropriate time series of solar radiation data generated to address the required energy simulation of a specific project?
- How can data sets provide the required projections throughout the next 20–30 years so that the cash flow (revenue minus expenses) can be evaluated throughout the life of the project?

Use of a typical meteorological year (TMY) (Wilcox and Marion 2008; Cebecauer and Šúri 2015) has traditionally been a popular method for solar system simulation. Much of the energy simulation software in the commercial and public domain still relies on TMYs to describe the hourly characteristics of the local solar resource. By design, however, a TMY represents only average or median (P50) conditions, and thus it does not provide information about the real variability or possible extremes throughout the system lifetime. Moreover, the degree of interannual variability can differ at different locations (Habte et al. 2020). Also, decadal variability of the solar resource occurs, and since the last half of the 20th century at least, it has been dominated by variations in man-made aerosol emissions (Wild 2016). In regions where such pollution is being reduced, TMY data based on data from the previous decades will underestimate the future solar resource—and vice versa in regions with increasing pollution. Typically, on-site measured data are not available for more than 1 year at the final stage of project preparation. Time series of satellite-derived modeled data covering the last 15–25 years are available from various (mostly commercial) providers. Longer term (up to 55 years) modeled irradiance data sets might be available from specific sites, such as from the earlier versions of the National Solar Radiation Database (NSRDB) in

the United States.[55] Long measured time series covering many decades also exist but for only a few stations around the world (Wild et al. 2017). Various aspects of variability are discussed in sections 9.2.5, 9.2.6, 9.3.2, and 9.6.

9.1.3 Solar Radiation Needs During Plant Financing, Construction, and Due Diligence Processes

Solar radiation information is necessary to answer key questions relevant to financing solar projects:

- How reliable is the plant output prediction? (This is important for addressing financing risks.)
- What is the expected uncertainty of the solar radiation estimations?
- What is the margin of error in the annual (or monthly) cash flow estimate?

Once the plant is under construction, different situations can occur. For example, in cases where the developer is not the final owner or is not in charge of the operation and maintenance, an independent due diligence of expected project performance is included in the evaluation process. Independent solar energy consulting services will likely be requested by financial investors to perform due diligence. Previous predictions of plant output should be updated as new solar radiation data (measurements or modeled estimates) become available through these due diligence activities. Even if the developer is the final owner, the uncertainty in the production results should be updated as improved data become available. All solar resource predictions that were obtained from different sources must be compared, and the corresponding uncertainties must be reconciled.

9.1.4 Data Requirements for System Operations and Performance Evaluations

During system operations, the following questions must be addressed:

- What kind of irradiance data are required to conduct studies on grid integration, load matching, or system intermittency?

In this case, daily, hourly, or subhourly data are typically needed for a specific time period, which cannot be provided by TMY data.

- How does the temporal variability and intermittency in the solar resource affect the plant's performance?

Most large solar energy projects are designed to provide electricity to the electric grid. In many cases, utilities buy electricity from producers at different rates during the day, depending on their load pattern, which can also vary seasonally; thus, it is in the interest of the solar power plant owners and operators to maximize electricity production when its value is largest and to minimize curtailment, which can occur during times of low load and high solar output. Maximizing output at times of high prices and minimizing curtailment is made possible by using energy storage systems. Optimizing the revenue from solar power plants under these conditions requires much more information than the estimate of the annual average production based on a TMY. For example, if a solar power plant includes significant storage capacity, a complex daily analysis—including measured on-site irradiance and forecasts—is needed to determine when the system will fill storage, and to which level, versus when it will provide power directly to the grid during daylight hours. Storage greatly mitigates the effect of system intermittency, but accurate, real-time, on-site measurements

[55] See https://nsrdb.nrel.gov.

are needed to make the best decisions under these operating conditions. Further, to anticipate how solar output can best match projected load in ways that optimize revenue, accurate solar forecasts up to 1 day ahead, continuously improved by real-time data, constitute the main tool to guide system operations. Forecasts for more than 1 day ahead are also required for electricity market participation and maintenance scheduling. Case by case, the system operator or local electric utility might need to disrupt the normal production schedule of solar power plants and ask their operators to increase (if the plant is equipped with storage) or decrease (curtail) production to avoid grid instability. Again, this situation requires high-quality, real-time irradiance measurements and solar forecasts.

9.2 Data Applications for Site Screening and Performance Assessment

9.2.1 Site Screening

In the early stages of project development, a prefeasibility assessment of possible sites is typically undertaken. A desired outcome at this stage is the estimated annual energy production that could be expected from the solar energy system in various proposed locations. Historical solar resource data sets are generally used at this stage, often in the form of maps or from publicly available or commercial gridded data, such as those discussed in Chapter 4 and Chapter 6. These data sets use a fairly consistent methodology to reliably identify the regions of highest solar potential. Depending on the type of technology used for the solar installation, this potential can refer to global horizontal irradiance (GHI), global tilted irradiance (GTI), or direct normal irradiance (DNI). The maps should be used to make a preliminary assessment of the solar resource, assuming a relatively large potential for error (up to approximately 10%–12 % for GHI or GTI and significantly larger for DNI), depending on the data provider and region; thus, if a desirable level of solar resource for a solar power plant project is a daily mean of 7.0 kWh/m^2, sites with mapped resource values down to approximately 6.0 kWh/m^2 should be considered. In some cases, a project developer could first attempt to build a plant based on concentrating solar technologies (CST); if the DNI resource turns out to be insufficient, a PV project could be considered instead and still be profitable.

A “first-order” prefeasibility assessment includes the analysis of potential for various technologies. For example, studies were conducted for the southwestern United States by the National Renewable Energy Laboratory’s (NREL’s) Concentrating Solar Power (CSP) Program (Mehos and Perez 2005)[56] to identify the most optimal sites for CSP installations. Using GIS screening techniques, resource maps were developed that highlighted regions potentially suitable for project development after considering various land-use constraints, such as protected land areas, sloping terrain, and distance from transmission lines (Figure 9-4). The results of these studies show that even with these constraints, vast areas in the southwestern United States are potentially suitable for CSP development. Maps such as these are valuable to project developers to highlight specific regions where various levels of site prospecting and prefeasibility analysis can take place.

Other studies are being done by various groups to evaluate the solar potential of PV installations on building roofs at the scale of a specific city. Such studies require GIS data at a very high resolution (better than 1 m), which are usually provided by lidar techniques and sophisticated shading analyses (Huang et al. 2015; Jakubiec and Reinhart 2013; Le et al.

[56] See www.nrel.gov/csp/data-tools.html.

2016; Martínez-Rubio et al. 2016; Mohajeri et al. 2016; Santos et al. 2014; Tooke et al. 2012).

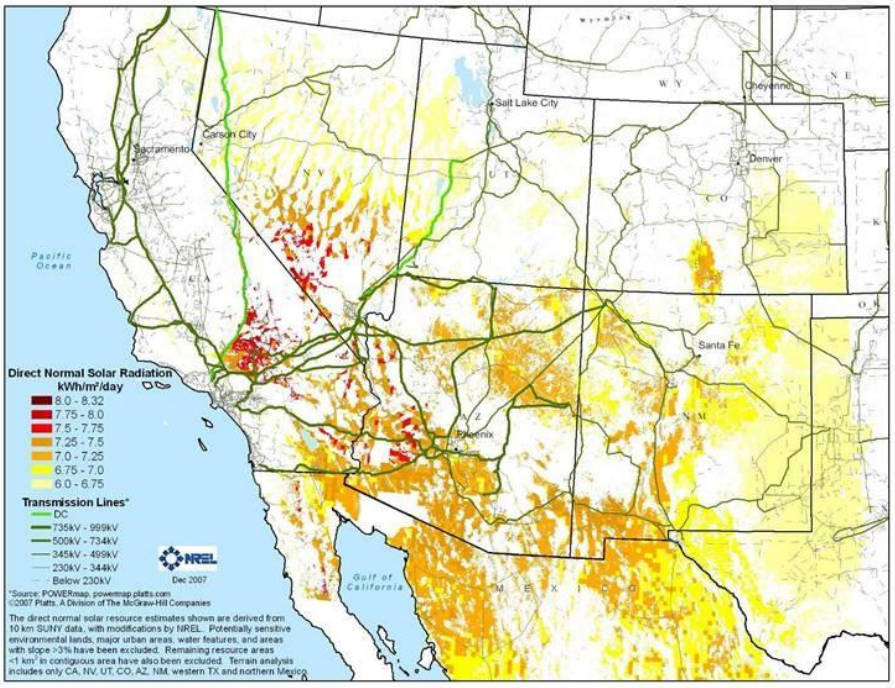

Figure 9-4. CSP prospects of the southwestern United States. GIS analysis for available site selection using the DNI resource, land use, and 3% terrain slope. *Image by NREL (Mehos and Perez 2005)*

Navarro et al. (2016) compared CSP potential assessment methodologies and showed the need for providing intercomparable results while also noting the importance of constraints such as terrain slope. A methodology called land constraints, radiation, and slope (LRS) considerations was proposed, harmonizing the treatment of these three main inputs. Figure 9-5 shows how the slope consideration (1%, 2%, or 3% of maximum slope) affects the site selection for what became a real CSP power plant in Spain. Only after accepting a maximum slope of 3%, the whole power plant was developed in a suitable area.

With the introduction of powerful, easy-to-use software tools and web pages—such as the System Advisor Model (SAM),[57] Greenius,[58] RETScreen,[59] or Global Atlas for Renewable Energy[60]—many analysts now expect to use maps and time-dependent modeling of their prospective solar systems as part of the preliminary analysis. Considerable care must be taken to choose the correct irradiance data sets for input to the model. Experts recommend multiple years of at least hourly input data, rather than data from only 1 year or from TMYs, to assess the effects of interannual variability of the solar resource on year-to-year system performance. Each hourly data set should be evaluated at a minimum to determine whether the monthly mean values from hourly data match the best estimate of the monthly mean values at the proposed site (Meyer et al. 2008). In most cases, the bankability of large projects requires on-site measurements during at least 1 year to validate the long-term

[57] See https://sam.nrel.gov/.
[58] See http://freegreenius.dlr.de/.
[59] See http://www.nrcan.gc.ca/energy/software-tools/7465.
[60] See https://irena.masdar.ac.ae/gallery/#gallery.

modeled time series and to correct them, if needed, using an appropriate site adaptation technique (see Chapter 4, Section 4.8).

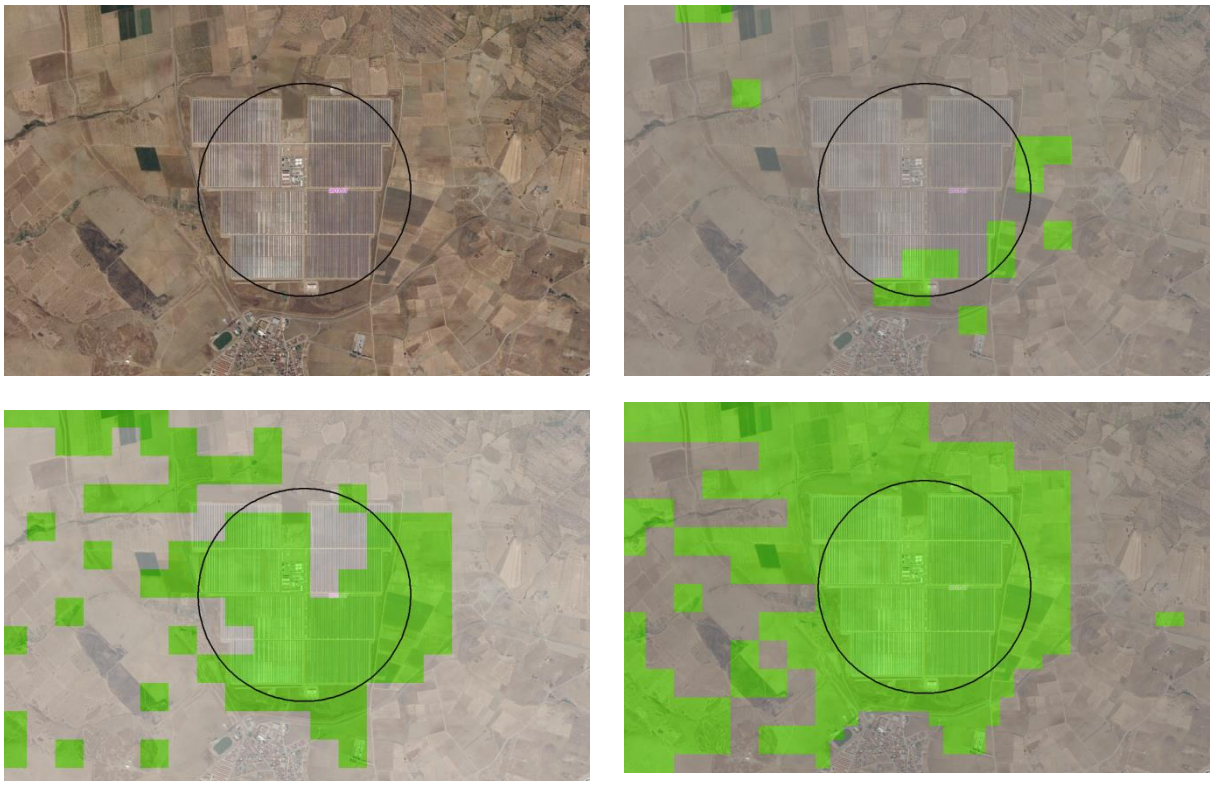

Figure 9-5. Buffer around the Orellana solar thermal energy plant (Spain) (upper left) and the suitable areas by the (upper right) LRS1, (bottom left) LRS2, and (bottom right) LRS3 methodologies with maximum slopes of 1%, 2%, and 3%, respectively. Suitable zones are shown in green. *Images from Navarro et al. (2016)*

9.2.2 Influence of Aerosols

For solar energy projects, a key step in site screening is to implement a concept called *clean air prospecting*. This is of special importance for CST, including solar thermal energy and other concentrating technology options, such as concentrating PV, because DNI is more strongly affected by the aerosol optical depth (AOD) than GHI or GTI are. AOD is a unitless optical characteristic of particles that summarizes their potential attenuation effect through scattering and absorption along a vertical atmospheric column. It is most usually reported at a wavelength of 550 nm, but it is sometimes also reported at 500 nm or 1000 nm, depending on the data source. Converting AOD from one wavelength to another is possible if the Ångström wavelength exponent is known (Gueymard 2019; Sun et al. 2021). Under an ideal aerosol-free atmosphere, AOD would be 0. At the other extreme, the sun disc would be obscured behind a thick aerosol layer when its AOD reaches approximately 5–7. In deserts and other areas with high solar resource, most sites have low annual average cloud cover, but dry conditions might favor a somewhat permanent suspension of dust in the air; thus, over these areas, the annual average DNI is strongly influenced by AOD. Understanding the AOD characteristics is vital to assessing the solar resource and the performance of CST installations.

AOD is a measure of the optical attenuation effects caused by various types of particles in the atmosphere, collectively called “aerosols.” These include vegetation exudates, dust and sand particulates, air pollution, smoke from wildfires or agricultural burning, and sea salt (near coastlines). Over arid or desert areas, the average AOD could be sufficiently low for

CST plants, even if dust events occur on an infrequent basis. Note, however, that the higher the annual average AOD, the higher its temporal variability (Gueymard 2012), which can be an issue for CST projects.

The analyst should consider the following questions about the site:

- What are the sources of potential aerosols? These could include:
  - Dust storms
  - Air pollution
  - Fires
  - Proximity to urban areas
  - Proximity to dirt roads with heavy traffic or to areas where biomass burning is frequent
  - Proximity to fossil fuel power plants, mining facilities, etc.
- Does the area have good visibility most of the time? Are distant hills or features visible without the effects of haze?
  - No visible haze would indicate that the AOD is low, and therefore the irradiance is likely to be well represented by modeled map values.
  - If the area is known to frequently have some form of visible haze, aerosols are likely to have an influence on the irradiation at the site. Further research or measurements might be necessary.

Typically, higher uncertainty in AOD can exist over mountainous areas, coastlines, deserts, or near urban areas. Because such areas could be good candidates for solar energy for economic and infrastructure reasons, additional measurements (of AOD and/or irradiance) might be necessary to resolve whether a site is sufficiently protected from sources of aerosols. In addition to decreasing the solar resource, aerosols can also deposit on solar collectors or mirrors and negatively impact the production of solar power. In such cases, a soiling analysis might be necessary.

Aerosol data sources are varied and have been reviewed (Gueymard 2019; Gueymard et al. 2018). In summary, the best source of data is from a local ground-based sunphotometer, but stations equipped with such instrumentation are scarce in many areas of the world. Gridded sources of data at the continental or global scale are provided by spaceborne sensors or reanalysis databases. The downside is that their AOD retrievals or predictions are typically biased (Bright and Gueymard 2019; Gueymard and Yang 2020; Petrenko and Ichoku 2013; Ruiz-Arias et al. 2015). When using AOD as an input to a radiation model to evaluate DNI, a simple rule of thumb is that an error of 0.1 AOD unit in the input induces an error of approximately 10% of opposite sign in the DNI output (Gueymard 2012). This can explain the bias that is sometimes found in DNI modeled databases (Gueymard 2011). Reducing the AOD bias is a technique used for the effective site adaptation of modeled DNI data (Gueymard et al. 2012; Polo et al. 2016); see also Chapter 5.

9.2.3 Volcanic Aerosols in the Stratosphere

Debris from volcanic eruptions affect the solar resource over large areas (at the country, continental, or global scale) and have radiative effects that can last up to a few years, depending on the eruption's strength and location. The main impact of volcanic aerosols on the solar resource arises when significant amounts of sulfur dioxide (SO_2) are ejected into the stably stratified stratosphere. Smaller volcanic eruptions do not reach the stratosphere, and thus they have only short-lived, local effects. SO_2 is converted into sulfuric acid aerosol droplets that scatter solar irradiance very efficiently. These droplets turn into aerosols, thus

increasing the total AOD and affecting DNI more than GHI. The AOD of the droplets decays exponentially with a decay time from 1–2 years (Crowley and Unterman 2013; Robock 2000). Overall, the droplets and volcanic aerosols can stay in suspension for several years after an eruption. For instance, El Chichón (1982) and Pinatubo (1991) impacted the solar resource globally for up to approximately 3 years.

Most solar resource data sets do not extend that far in the past and thus do not cover any large volcanic event. One exception is the NSRDB (Wilcox 2007), whose data can be used to estimate the effect the Pinatubo eruption had on the solar resource (Vignola et al. 2013). The reduction in DNI reached up to approximately 20% at midlatitude sites in the Northern Hemisphere a few months after the eruption, which in turn had an even larger negative impact on the electricity production of CST plants (Michalsky et al. 1994). The probability of a volcanic eruption as strong or stronger than Pinatubo (stratospheric AOD ≥0.2) is significant on a decadal basis (Hyde and Crowley 2000).

9.2.4 Choosing Modeled Irradiation Resource Data

During the first stages of a solar project, solar radiation information might be available from different sources, as discussed in Chapter 4 and Chapter 6. Having many sources of irradiance data is better than having none, but the question of selecting the best possible source then arises. This can be done through detailed comparisons between them and validations against high-quality ground measurements. Some concepts related to such tasks are stated in the following. The proposed definitions of *variability* and *error* can aid in better understanding the observed differences among databases, though these definitions are not always agreed upon by all analysts or applicable to all possible applications. In addition to these concepts, detailed discussions on uncertainty definition, characterization, and calculation are provided in Chapter 7.

9.2.4.1 Variability

Variability is the expected or actual dispersion of a variable during a specific period of time (temporal variability) or over a specific area (spatial variability). It is often expressed as the coefficient of variation (COV) for variables having a normal distribution (Calif and Soubdhan 2016), as the variance for any other known statistical distribution, or as the interquartile range when the distribution is unknown. COV is obtained by dividing the standard deviation by the mean of the population or sample. Temporal variability can be analyzed at various timescales (Bengulescu et al. 2018).

Variability relates to the analyzed time period (e.g., yearly variability of daily GHI, long-term variability of DNI) or to a given geographic area (e.g., spatial variability of DNI over an area of 50 km by 50 km). See detailed information in Section 9.2.5.

9.2.4.2 Error

Error is the difference (or deviation) between a measured or estimated value versus the "true" value of the measurand/quantity. Because the latter value cannot be determined, in practice a true conventional value must be measured or estimated by an adequate procedure using specialized and well-maintained instruments, harmonized protocols, or international standards. The individual error at instant *i* can be expressed as:

$$e_{y_i} = y_i - x_i \tag{9-1}$$

where e_{y_i} is the error of the estimate y_i, and x_i is the value of the quantity.

Common error expressions are mean bias error, mean absolute error, mean square error, and root mean square error. When the most probable value is uncertain itself (which is the

most general case), the error should be referred to as a difference or a deviation; then the letter *e* is replaced by *d* without any change in the calculation (Gueymard 2014).

Typically, some individual errors or differences are of a higher magnitude than all uncertainties. (See detailed information in Chapter 7.) In general, the accuracy of modeled data is reported in terms of the conventional error statistics mentioned. In addition, Espinar et al. (2009) proposed a new statistical indicator, called the Kolmogorov-Smirnov integral. It evaluates the area between the distribution functions from the two tested samples. Gueymard (2014) reviewed this and many other statistical indicators for solar radiation series comparisons and applied them to the performance evaluation of a variety of clear-sky radiation models.

A study conducted by the Management and Exploitation of Solar Resource Knowledge project in Europe (Beyer et al. 2008) provided insights into the spatial distribution of irradiance variability by cross-comparing five different data sources. Inherent differences were found between databases based on in situ (ground) measurement interpolations and those based on satellite observations as well as in the methods used to process such data. The databases relying on the interpolation of ground observations were sensitive to the quality and completeness of ground measurements and to the density of the measurement network. Terrain effects (e.g., shadowing by surrounding terrain) played a role in solar radiation modeling over hilly and mountainous regions. The spatial resolution of the input data and the selected digital elevation model were identified as factors with direct impact on the accuracy of the estimates. Finally, to compare modeled data properly, particularly under clear-sky conditions, it is important to consider how each model deals with cloud identification and AOD characterization (Ruiz-Arias et al. 2016). This is particularly important for DNI because of its higher sensitivity to AOD than GHI (Ruiz-Arias et al. 2019).

The quality and spatial detail of satellite-derived or numerical databases are determined by the specific input data used in the models. As can be expected, the main parameters describe the cloud properties and the optical transparency of the atmosphere in relation to aerosols and water vapor (Ineichen and Perez 2002; Ruiz-Arias et al. 2016). Regarding DNI more specifically, AOD is the most important variable under clear-sky conditions (Gueymard and George 2005). (See also Section 9.2.2.) Cebecauer, Šúri, and Gueymard (2011) provided a comprehensive and qualitative review of the different factors (including terrain) affecting the accuracy of DNI modeling.

The studies conducted so far provide only a preliminary outline of the state of the art of current knowledge in irradiance modeling. These studies still do not fully address the needs of the solar energy industry, so further work is needed to improve knowledge and decrease uncertainties. In most cases, similar studies must be performed for the sites of interest within an individual project. (See Section 9.1.1 and Section 9.2.1.)

9.2.5 Variability of the Solar Resource

Variability is a wide-ranging term that can characterize the solar resource in many ways, either from a spatial or temporal perspective. In the latter case, all temporal scales can be considered, depending on context, from the subsecond to multiyear scales. Temporal variability, if well characterized for a climate region, can be useful to determine the suitability of a short-term data set to produce valid long-term statistics. For instance, the term can be applied to refer to the interannual variability of the resource. The example in Figure 9-6 shows the interannual variability in monthly DNI at Daggett, California, in terms of monthly average daily total irradiation.

As mentioned above, the long-term dispersion of the solar resource is often characterized by the COV, which is the unitless ratio between the standard deviation and mean (Habte et al. 2020; Calif and Soubdhan 2016; Gueymard and Wilcox 2011):

$$\sigma_t = \sqrt{\left[\frac{1}{n}\sum_{i=1}^{i=n}\left(Yr_{irr_n} - \overline{Yr_{irr}}\right)^2\right]} \tag{9-2}$$

$$\mathrm{COV} = \frac{\sigma_t}{\overline{Yr_{irr}}}. \tag{9-3}$$

where Yr_{irr_n} is the annual irradiance of the individual n years, and $\overline{Yr_{irr}}$ is the mean of irradiance of all years.

Long-term oscillations in GHI and DNI are also important because of the succession of periods known as “dimming” and “brightening” that affect both climate change and the extrapolation of the historical solar resource into the future (Müller et al. 2014; Wild et al. 2015). Further, it is important to consider these sources of variability in the context of solar performance forecasting.

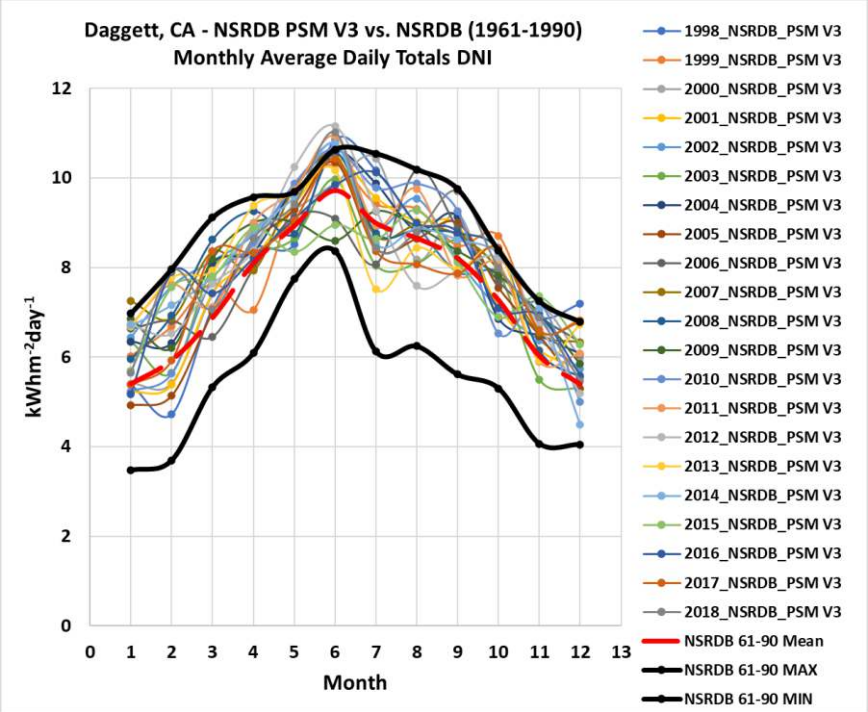

Figure 9-6. Example of direct-beam monthly average daily total (kWh/m^2) illustrating interannual and seasonal variability from 1961–2018 in Daggett, California. *Image by NREL*

The term *variability* is also used to describe the spatial variability of the resource in a climatological context. Spatial variability can help determine the applicability of a particular data set for a nearby location, possibly saving the need for additional measurements. In this case, variability characterizes microclimatic features and regional resource gradients. An example is provided in Figure 9-7, which shows the climatological GHI resource distribution over the Island of Oahu, Hawaii. Similarly, Figure 9-8 shows the spatial variability of DNI and

GTI over areas 50 by 50 km throughout the United States in terms of COV (Gueymard and Wilcox 2011).[61]

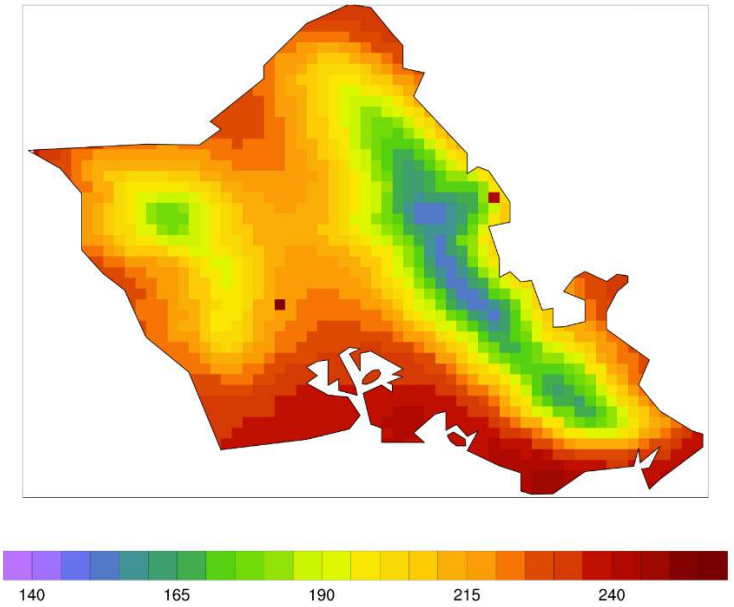

Figure 9-7. Example of microclimatic spatial variability for the Island of Oahu. The 1-km resolution map displays mean hourly GHI in W/m^2. *Image from SolarAnywhere V3.0 (2015)*

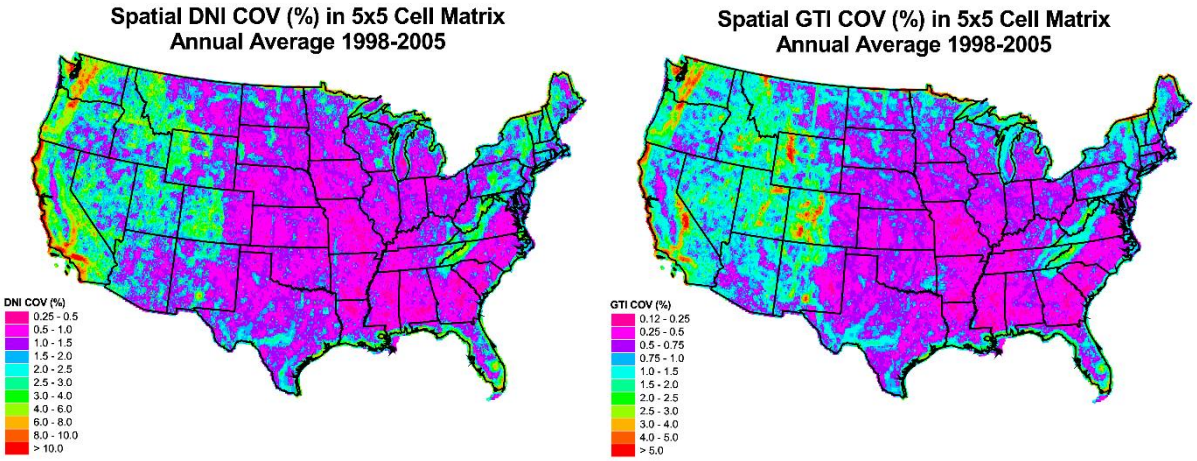

Figure 9-8. Spatial variability in (left) DNI and (right) GTI over the continental United States in terms of percentage of COV. *Images from NREL*

From a resource assessment perspective, the term *variability* is associated with the time/space impact of weather and with the cycle of days and seasons on the output of solar systems. This output can vary from zero to full power, and it is outside the control of plant operators. Understanding the solar resource's variability is key to optimally integrating the power output of solar electric systems into electric grids. This is discussed further in Section 9.6.

[61] Such spatial and temporal variability maps are available from https://www.nrel.gov/grid/solar-resource/variability.html.

Space/time variability has two causes: one is fully predictable and is the result of the apparent seasonal and daily motion of the sun in the sky and the sun-Earth distance; and the other results from the motion of clouds and, to a lesser extent, of aerosols in relation to weather systems. It is useful to first consider the temporal and spatial scales involved and how they impact the available solar resource.

9.2.5.1 Temporal Scale

Beginning with an intuitive example (Figure 9-9), a single location on a partly cloudy day will experience a high degree of temporal variability because of changes in the sun's position and the motion of clouds; however, the solar energy accumulated during several days at that same location exhibits less variability. Variability in GHI becomes small as the temporal integration increases to 1 year and more, but that in DNI or even GTI can still be significant (Gueymard and Wilcox 2011). In addition, investigating intra-seasonal variability can provide insightful information. In some areas, for example, summers might exhibit less variability than winters, e.g., if there are typically only a few cloudy days in summer and not-too-dissimilar numbers of cloudy and sunny days in winter. Adding or subtracting a sunny day during the summer does not significantly affect the monthly average in this case, contrary to what can happen in winter. In many temperate areas, on the other hand, low variability caused by consistently cloudy conditions is typical in winter, whereas a succession of clear and cloudy days is typical in summer (high variability).

Figure 9-10 shows a representation of interannual variability over the Americas, demonstrating some geographic dependence as a result of microclimate or long-term climatic fluctuations. Studies of GHI and DNI distributions in the United States show that GHI's interannual variability typically ranges from 2%–6% in terms of COV, whereas the variability of DNI is between 5% and 15%, about twice as much (Habte et al., 2020; Gueymard and Wilcox 2011). A single year can deviate much more from the long-term average. Gueymard and Wilcox (2009) analyzed the long-term data from four stations with continuous high-quality measurements spanning more than approximately 25 years to examine how many individual years would be required to converge to the long-term mean and whether the interannual irradiance variability changes significantly from one site to another. Sorting the data from the most exceptional years (largest anomalies) to the most typical years (smallest anomalies), the results showed that, first, there is much lower interannual variability in GHI than in DNI. In the examined stations in the United States, GHI is almost always within ±5% of the true long-term mean after only 1 year of measurements (see Fig. 9-11). The situation is quite different for DNI. After only 1 year of measurements, the study showed that the estimate of the average DNI is no better than ±10%–±20% of the true long-term mean. Note, however, that the worst years were associated with strong volcanic activity, which significantly impacts DNI.

Another interesting question is whether it is likely that good years with high irradiation occur in groups or are independent from the previous year's irradiation. Tomson, Russak, and Kallis (2008) showed that the mean annual GHI in any year is virtually independent from that of the previous year.

9.2.5.2 Spatial Scale

Increasing the solar generation footprint from a single location to a region, and even to a continent, considerably reduces intermittency. Increasing this footprint to the entire planet eliminates it almost entirely (Figure 9-12). This spatial integration effect is often referred to as the (geographic) "smoothing effect," which is discussed next.

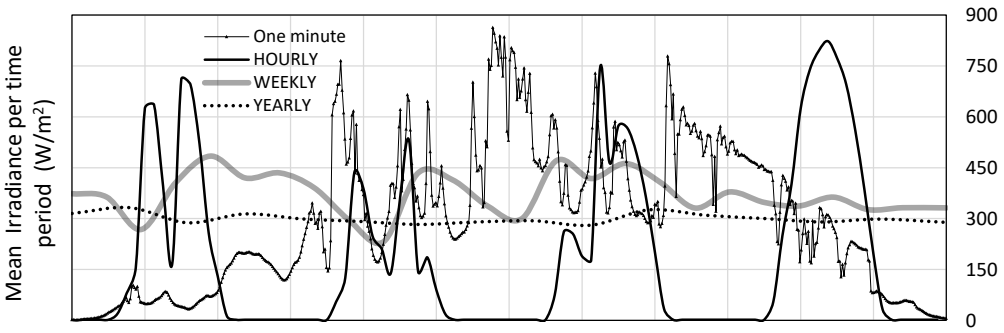

Figure 9-9. Variability of global irradiance time series at a North American location shown as a function of integration time. The figure includes 1 day of 1-minute data, 4 days of hourly data, 26 weeks of weekly data, and 16 years of yearly integrated data. ***Image from Perez et al. (2016)***

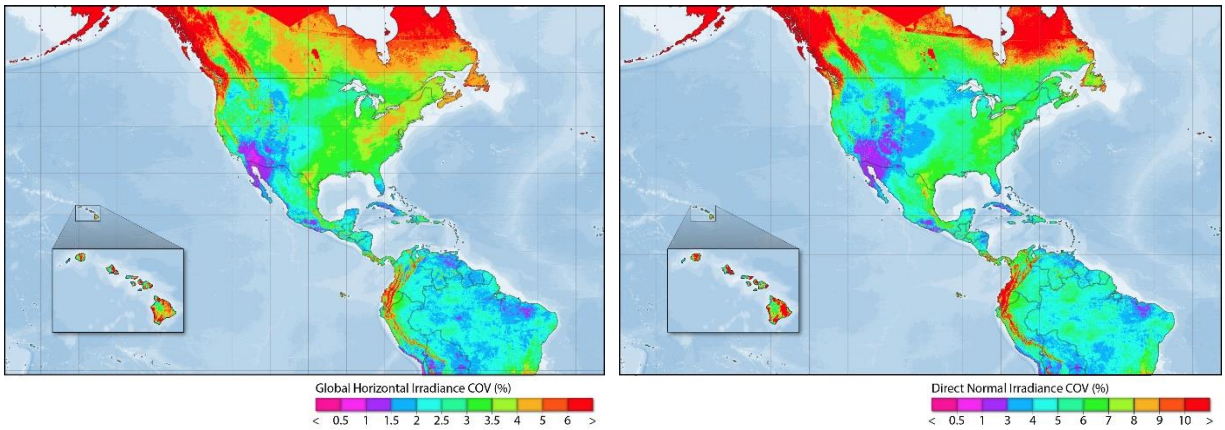

Figure 9-10. Interannual variability in (left) GHI and (right) DNI using the 1998–2017 NSRDB data expressed in terms of percentage of COV. ***Images from NREL***

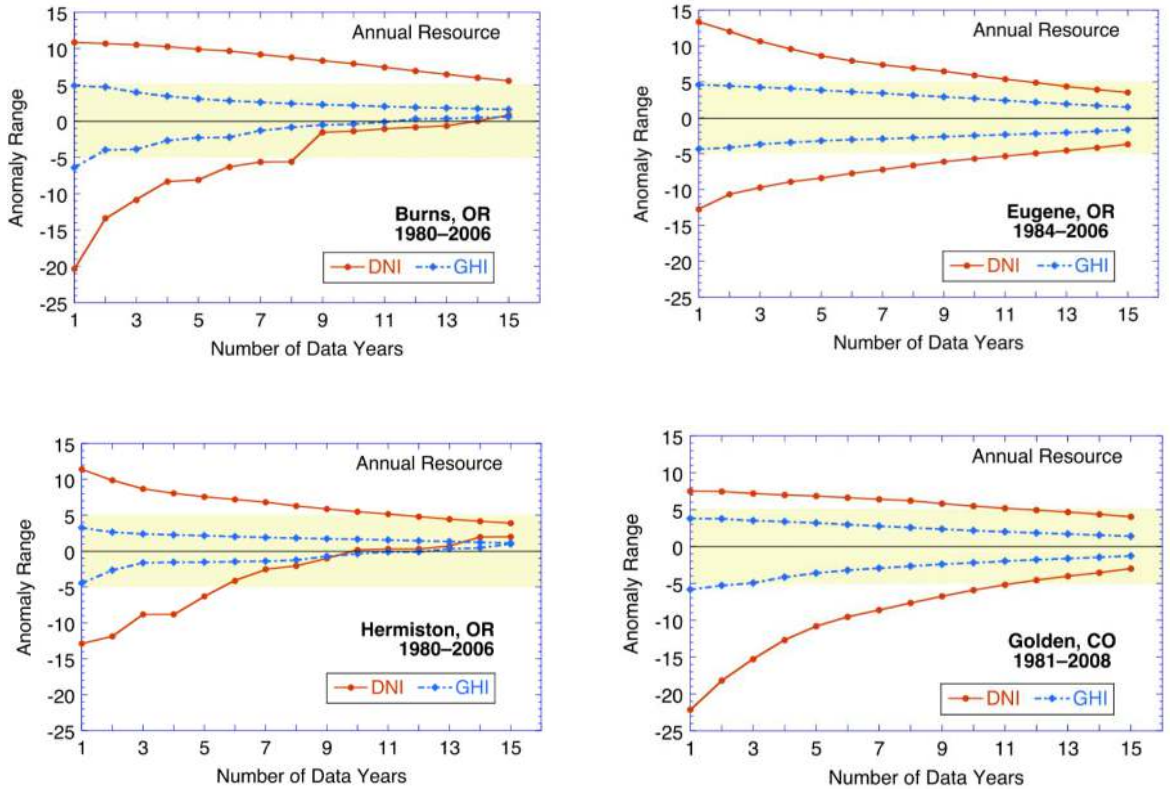

Figure 9-11. Number of years to stabilize DNI and GHI at (clockwise from upper left) Burns, Oregon; Eugene, Oregon; Hermiston, Oregon; and Golden, Colorado. Specific sorting (along the X-axis) from the most exceptional years (largest anomalies) to the most typical years (smallest anomalies). *Images from Gueymard and Wilcox (2009)*

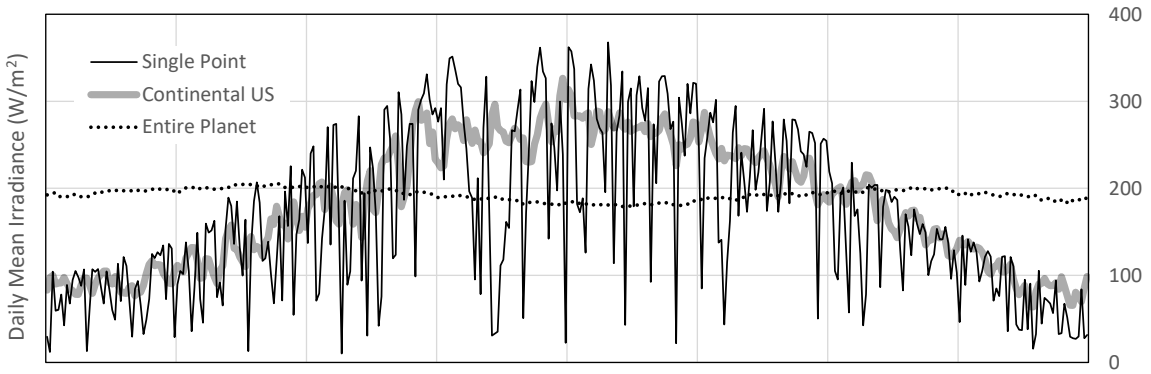

Figure 9-12. Variability of daily global irradiance time series for 1 year as a function of the considered footprint. *Image from Perez et al. (2016)*

Variability Impacts

Both the temporal variability and the spatial variability are specific to a site (or area) and period. Temporal variability could change seasonally, as mentioned. The two types of variability directly affect solar resource analyses for various reasons, including:

- Measured data sets often contain data gaps due to instrument failure or various problems, such as dew or snow on instruments. To avoid any discontinuity in the time series, analysts are typically tempted to use some form of temporal interpolation to fill the gaps. This is convenient but can significantly increase the overall uncertainty. The

magnitude of the overall uncertainty depends on the time period, the method used to fill the gaps, and the data used to fill the gaps. Moreover, replacing extended data breaks with climatological average values tends to underestimate the actual temporal variability.

- If no on-site measurements exist at the project's site but some exist at one or more "nearby" sites some distance away, analysts are tempted to extrapolate or average the data from those alternate sites. Depending on the distance and spatial variability over that region, this might or might not introduce significant errors.

Interannual and long-term variability (decadal oscillations) need to be considered to correctly project the measurements or modeled data of the past into the future for design and bankability purposes. These considerations explain why an evaluation of variability is an important step for accurate solar resource assessment at any location of interest. Further, the expected variability in the very near future (minutes to days) is also essential information for the correct operation and profitability of existing solar power plants. This can be estimated with appropriate solar forecasts (see Section 9.5.3).

Various studies have analyzed the spatial or temporal variability of the solar resource at the country or continental scale—e.g., Habte et al. (2020), Castillejo-Cuberos and Escobar (2020), Badosa et al. (2013), Davy and Troccoli (2012), Gueymard and Wilcox (2011), Lohmann et al. (2006), and Perez-Astudillo and Bachour (2015). A general finding is that the spatiotemporal variability of DNI is larger than that of GHI for a given location.

From an application perspective, the solar resource variability translates into power production variability, which could impact the stability of electric grids or the economics of the facility. One important question that has received specific attention is: How much is the temporal variability at one power plant site correlated with that of another site some distance away? This is discussed further in Section 9.6.

Predicting the behavior of existing or future solar systems assumes that the temporal and spatial irradiance variability can be adequately characterized with measurements and/or modeled data. It is easy to take care of the deterministic variability caused by location, date, and time of day. What matters most is the variability (temporal or spatial) in weather and climate.

With some knowledge about the interannual irradiance variability at a specific site, users can, in principle, select a particular experimental period to adequately characterize the solar resource. Ideally, such on-site measurement campaigns should last many years; however, in most cases, practical reasons limit them to 1 year or less, which increases the uncertainty in the long-term estimates. Likewise, with knowledge of the spatial variability over the area around a measurement station, users can evaluate the applicability of those measurements to a location some distance away using the appropriate extrapolation or interpolation methods. Knowledge of variability then becomes valuable when deciding how long to make measurements at a particular location and whether the characteristics of the solar resource at that location can be extrapolated to other nearby locations.

With such variability maps or statistics, users can better understand the extent of measurements required to best characterize the solar resource for a particular application. In areas with low interannual variability, a shorter measurement period could suffice. In areas with low spatial variability, a measurement station could represent the solar resource at nearby locations (e.g., within 10–50 km), avoiding the need for additional measurements. An analyst can use this information to build better confidence in a data set as being sufficient for an analysis and can use these data to understand the consistency of future solar power plant performance and how that relates to the economic viability of a particular location.

One remaining question is whether solar resource data of past decades can represent that of the future, considering that the power production of solar installations needs to be predicted up to 20 years into the future. To that end, the long-term trends in GHI and DNI need to be investigated in relation with climate cycles known as dimming and brightening (Müller et al. 2014; Pfeifroth et al. 2018) because of their impact on the yield predictions of solar installations (Müller et al. 2015).

Some statistics that are commonly used to describe the temporal variability of irradiance components assume that their distribution is Gaussian, which is a typical assumption (Cebecauer and Šúri 2015). Fernández-Peruchena et al. (2016) tested that assumption in annual GHI and in DNI time series. Regarding GHI, results from two normality tests indicated that the Gaussian assumption cannot be rejected at all 10 tested locations. In the case of DNI, five tests were applied to the annual DNI series for evaluating the Weibull goodness of fit at six locations, and the results suggested that such a distribution is more appropriate than a Gaussian distribution. Considering all these results, the temporal variability needs to be further analyzed to be able to clarify whether annual, monthly, or seasonal solar radiation values can be properly assumed (1) as independent; (2) as only random samples of the same population; or, conversely, (3) as representative of different probabilistic models having, for example, a stationary behavior.

As mentioned in Section 9.1.2, TMYs eliminate all interannual variability by design. Nevertheless, they can be used to investigate the spatial variability of the solar resource wherever gridded TMY databases are available (Habte et al. 2014).

9.3 Solar Radiation Data Requirements for Feasibility Assessments

In addition to selecting one or more candidate sites for an engineering feasibility assessment, solar power plant project developers need to ensure that they have meteorological data sets, including solar radiation and other meteorological variables, that can guarantee a reliable estimate of the system performance during the project life. There are different possible situations depending on the availability of measured data sets and/or of other modeled data sources. Because long-term, high quality ground measurements of solar radiation are rarely available, at least one whole year of local ground measurements and 10 years of modeled data are required to guarantee the bankability of large solar energy projects (Ramírez et al. 2012).

Solar system simulations often use an annual meteorological data set intended to be representative of the long-term average meteorological conditions of the project site, usually referred to as TMY or typical reference year (TRY). Such TMYs are discussed in Section 6.3. Additionally, it is common practice to use other meteorological annual series representing adverse conditions (e.g., P90; see Section 9.3.2) to test the project's revenue and financial stress under quasi-worst-case scenario conditions. The following sections provide a review of the current methodologies and possible improvements for the generation of these data sets. Section 9.3.3 provides a view of post-processing and site adaptation methodologies for reducing uncertainty in the data sets used for generating the series for simulation.

9.3.1 Utilization of Typical Meteorological Data for Solar Energy System Simulations

Typical meteorological data sets are used as the standard input to a wide range of solar energy system simulation software to obtain estimates of the average annual solar energy system yield during the project lifetime. Such data sets consist of annual time series of hourly or subhourly values of solar radiation and other meteorological variables specifically

constructed to be representative of the long-term time-series (usually 10–30 years) typical values.

TMY data sets are still widely used by building designers and solar energy engineers for basic modeling of renewable energy conversion systems and their preliminary design. These data have natural diurnal and seasonal variations and represent a year of typical climatic conditions for a location and can be useful for such basic tasks. TMYs do not, however, provide all solar resource data needed for solar energy, as discussed in more detail in Section 6.3. For example, TMYs do not contain information on interannual variability or meteorological extremes; therefore, TMYs should not be used to predict weather or solar resources for a particular time, for preparing the project's final design, or for evaluating real-time energy production. Because a TMY represents "typical" conditions over a long period, such as 30 years, it is not suited to analyze the system's response to worst-case weather conditions that could occur in the future.

9.3.2 Interannual Variability and Probabilities of Exceedance

In the case of large solar energy projects, bankability requirements are stringent; hence, reliable profitability and annual payback assessments need to be performed, and thus probabilistic information about the energy output is needed. This must be based on probabilistic solar resource time series that correctly account for extreme situations, which obviously require the statistical examination of long-term time series.

A preliminary step is to first determine the minimum duration of the radiation data set that is needed to capture the true long-term mean. The interannual variabilities, as discussed in Section 9.2.5.1, and trends in the resource must be considered. A consequence of the high interannual variability of DNI is that CST projects necessarily require scrutiny about the risk of bias in the DNI resource, which can be addressed by using long-term satellite data sets and site adaptation techniques. In general, PV projects are less at risk of bias in the GTI resource. Exceptions can occur over regions where the uncertainty in satellite-derived irradiance data is significant and/or in the case of PV installations using tracking systems, which attempt to maximize the DNI fraction of GTI.

Because long-term on-site measurements are the exception more than the rule, these results underline the importance of relying on an independent long-term data set, which, in practice, means a modeled data set derived from satellite images or reanalysis of NWP results. This is necessary to reduce the uncertainty in the long-term average DNI estimates for a proposed CST site, most particularly, and to provide reasonable due diligence of a plant's estimated performance throughout the life of the project. This and additional concepts related to the development of specialized TMYs or annual series for energy simulation are described by Vignola et al. (2012).

A common way to address the risks associated with the uncertainty of the long-term estimates of the mean annual GHI or DNI values is to consider the annual probability of exceedance (POE). POE, which is also denoted by "P," is the complementary value of a percentile value. In the case of P50, its value matches the 50th percentile and is the result of achieving an annual energy production based on the long-term median resource value. For this value, the probability of reaching a higher energy value is 50%. For example, TMYs are meant to represent the P50 value. In contrast, for P90, the risk that an annual energy value is not reached is 10% (90% of all values in a distribution exceed the P90 value). P90 corresponds to the 10th percentile. Depending on a project's size and the practices of the financial institution involved, the solar resource's "bad years" can be examined using various Ps—from relatively lax (P75), to stringent (P90 or P95), to very stringent (P99).

Although irradiance is the largest source of uncertainty in P estimates, the estimates must also include other sources of uncertainty, including modeling uncertainty, uncertainty in the system parameters, and reliability uncertainty. High uncertainty is always an issue, even if the P results appear favorable. The combination of probabilistic performance modeling and the uncertainty inherent in various components of the system (including the solar resource) requires specialized developments (Ho, Khalsa, and Kolb 2011; Ho and Kolb 2010).

Figure 9-13, taken from a study by Moody's Investors Services (2010) and reproduced in Renné (2016), demonstrates conceptually how improving our knowledge of the true long-term solar resource at a site serves to reduce financial risk. By assuming that a long-term annual data set follows a Gaussian or normal distribution (which is not necessarily the case), Figure 9-13 shows that the standard deviation of the true long-term mean based on only 1 year of data is expected to be much higher than that with 10 years of data because a 10-year data set contains much more actual information regarding the interannual variability at the site. Assuming that the median value (P50) of the distributions is the same for both the 1-year and the 10-year distribution curves, the P90 value increases with the additional knowledge (higher confidence) associated with having a 10-year data set. A 10-year P90 value reduces the financial risk of the project (or, in other words, is more bankable) because the yield estimates will be higher when more data are available. In addition to the uncertainty due to interannual variability, the uncertainty in the irradiance estimates (from modeling or measurement) must also be considered and corrected, if necessary, to evaluate the uncertainty in P.

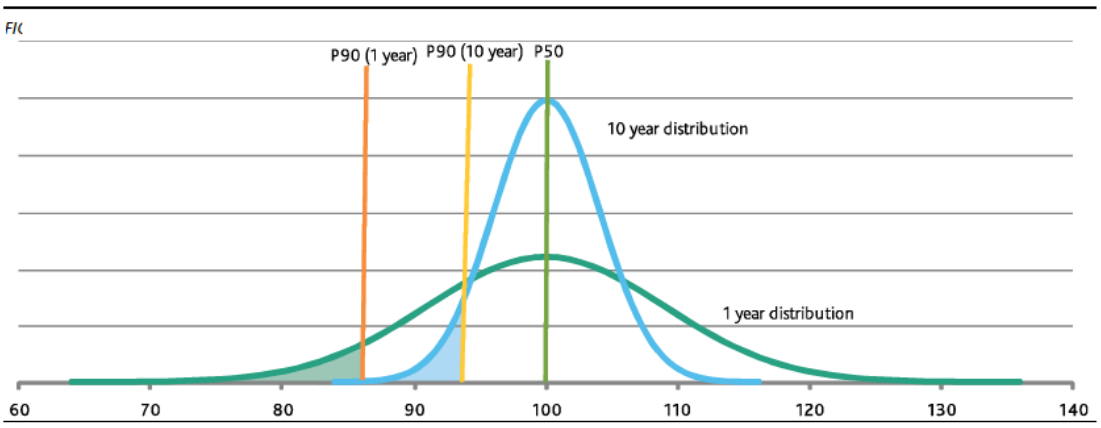

Figure 9-13. The uncertainty of the value of the true long-term mean is much higher with only 1 year of data (green curve) than with 10 years of data (blue curve). *Image from Moody's Investors Services (2010) as presented in Renné (2016)*

The statistical calculations of P values often assume that long-term irradiance data follow a normal (or Gaussian) distribution. As mentioned earlier, however, this assumption might not be correct. For example, Dobos, Gilman, and Kasberg (2012) considered long-term measured and modeled updated NSRDB GHI and DNI data for Phoenix, Arizona (Wilcox 2007), and produced cumulative distribution functions (CDFs) based on 30 separate annual data sets to illustrate the concept of P50 and P90. Figure 9-14 shows that if the annual Phoenix data were fit to a normal distribution (solid line) at CDF = 0.1 (which corresponds to the P90 value), an annual GHI of 1.96 MWh/m^2 would be exceeded 90% of the years (or, conversely, the solar resource would fall below this value 10% of the years). Similarly, for DNI, the annual solar resource exceeds 2.2 MWh/m^2 for 90% of the years. For Phoenix, however, the long-term solar data do not appear to follow a normal distribution, but other types of distribution (such as Weibull) have not been assessed for the study. Figure 9-14 shows that the P90 value is somewhat less in Phoenix when determined from an empirical

instead of a normal distribution. Further discussion on these points can be found in Section 9.2.6 and in Renné (2016; 2017).

As discussed by Pavón et al. (2016) and Ramírez et al. (2017), there are several issues related to a P estimate. The first is the assumption that, for instance, an irradiance at the P90 level is proportional to the P90 of the solar system energy output, or yield, which constitutes only an approximation. Additional elements are thus needed (1) to identify the most appropriate P value and (2) to construct a specific time series for that P using hourly or subhourly data during a year whose sum is that specified P value. A statistically based estimation of the P value depends on the assumed probability distribution. This probability distribution can be approximated with the normal distribution in the case of annual GHI. For DNI, however, there is no evidence that a normal, a log-normal, or a Weibull distribution would always be the best choice. When 10 (or preferably more than 20) whole years of local measurements or modeled estimates are available, methodologies based on the cumulative distribution function should be used, such as those proposed by Peruchena et al. (2016). In addition, new techniques are developed to construct meteorological years for bankability scenarios that correspond to P90—for example, Cebecauer and Šúri (2015), Lara-Fanego et al. (2016), and Fernández-Peruchena et al. (2018).

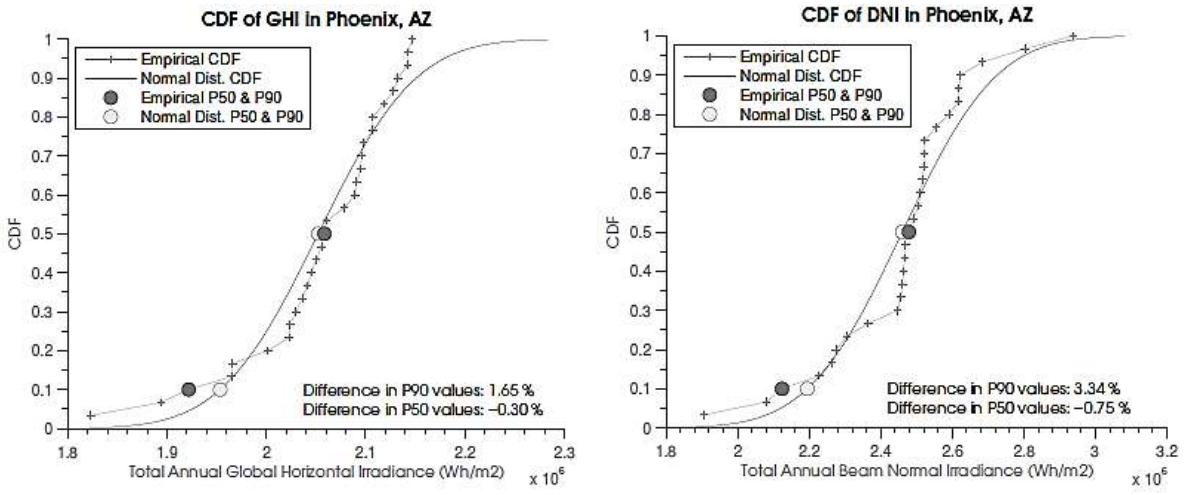

Figure 9-14. Annual (left) GHI and (right) DNI data fitted to a normal distribution (solid line) for Phoenix, Arizona. Note that each gray circle covers a marker (+).

An additional issue is the resolution of the data time series used for energy simulations. For CST projects, for instance, the yield and probabilistic predictions obtained with hourly data could differ substantially from those using 1-minute or 5-minute data (Hirsch et al. 2010; Meybodi et al. 2017). Satellite-derived irradiance time series are typically not available at a temporal resolution better than 15 minutes. Some stochastic methods have been proposed to derive 1-minute or 5-minute irradiance from data at a coarser resolution (Buster et al. 2021; Grantham et al. 2017; Hofmann et al. 2014), which can be helpful.

Instead of using a limited number of yearly data sets for simulation, Nielsen et al. (2017) proposed using Monte Carlo methodologies to generate an unlimited number of yearly series. This methodology allows the solar resource assessment—and thus the energy output calculation—to be performed in a way that is similar to that currently used for estimating other essential variables in the economic assessment of solar power plants. The generation of hundreds of such plausible years has been demonstrated by Larrañeta et al. (2019), Fernández-Peruchena et al. (2015), and Meybodi et al. (2017). Other authors—e.g., Ho, Khalsa, Kolb (2011) and Ho and Kolb (2010)—have found issues with the Monte Carlo approach and suggested the Latin hypercube sampling method instead.

Note that including long-term trends derived from the effect of climate change and other local or regional singularities (such as the increase of atmospheric aerosols derived from pollution) on solar radiation could improve the value of the solar power plant yield prediction (i.e., during the complete solar facility lifetime). For instance, the Meteonorm[62] software includes the effect of climate change estimated from the Intergovernmental Panel on Climate Change models for three different scenarios. Aerosol pollution scenarios are also important for the future GHI and DNI resource. For instance, a decrease in the solar resource has occurred in many Asian countries during the recent past, and this trend could continue into the foreseeable future.

9.3.3 Combining Data Sets: Site Adaptation to Improve Data Quality and Completeness

Long-term solar resource data sets always have uncertainty. If its magnitude can be precisely evaluated, investors can derive the risk of the project and evaluate whether the performance of the system could be lower than desired. Reducing uncertainty in solar resource data is thus a key step toward bankable projects. Combining modeled data sets with site observations are called post-processing techniques (Janotte et al. 2017). These cover a wide variety of methodologies that are applied to improve direct model or retrieval outputs and reduce uncertainty. A detailed description of these methods is given in Chapter 4, Section 4.8.

9.4 Solar Radiation Data Requirements for Yield Estimation

This section provides a summary of general approaches to using solar resource data (as described in chapters 1–5) to estimate the yield of solar energy systems. The used resource data include not only solar radiation but also other meteorological parameters (such as wind speed and temperature) that were discussed in Chapter 5. First, PV systems are discussed, followed by CST systems.

9.4.1 Yield Estimation of Nonconcentrating Photovoltaic Projects

The value of electricity generated by a PV plant depends on the amount of electricity generated and on the grid's need for that electricity at the time it is generated (i.e., its load curve). A quantitative understanding of the specific solar resource for the intended location and orientation of the PV array is essential to evaluate the first quantity. The relevant solar input for yield calculation is the irradiance incident on the plane of array (POA) (i.e., GTI), although other parameters (particularly ambient temperature, wind, and soiling) also impact the system's output. This section provides a high-level overview; more detailed descriptions of PV system modeling can be found in Ellis, Behnke, and Barker (2011). Three general approaches exist to estimating a PV system's yield. These are presented in order of increasing accuracy.

9.4.1.1 Performance Ratio Method

The output of a PV plant can be characterized by the performance ratio (PR) metric, which is the ratio of the electricity generated by the plant relative to its theoretical output during the same period.

When using this method, the first step is to determine the theoretical annual output of the system. The nameplate rating for PV systems refers to the system power output evaluated

[62] See http://www.meteonorm.com/.

under standard test conditions (GTI of 1000 W/m^2 at 25°C), and it is primarily a function of the efficiency, η, and area, A, of the PV module to convert incoming solar radiation to DC power output. The rated power, P_0, of the system is given by:

$$P_0\,[\mathrm{kW_p}] = A\,[\mathrm{m^2}] \cdot 1000\,[\mathrm{W/m^2}] \cdot \eta. \tag{9-4}$$

The reference yield, Y_R, of the module is then determined from the actual annual GTI [kWh/m^2-yr] at the site:

$$Y_R\,[\mathrm{kWh}] = P_0\,[\mathrm{kW}] \cdot \mathrm{GTI}\,[\mathrm{kWh/m^2\text{-}yr}] \,/\, 1000\,[\mathrm{W/m^2}]. \tag{9-5}$$

The performance ratio is then applied to Eq. (9-5) to determine the actual energy produced by the solar system, also called the final yield, Y_F, which is typically less than its theoretical energy because of a variety of factors, as described in the following:

$$Y_F\,[\mathrm{kWh}] = \mathrm{PR} \cdot Y_R\,[\mathrm{kWh}] \tag{9-6}$$

where the PV plant size is derived from the sum of each module's nameplate rating. The specific yield, y_F [kWh/kW$_p$] = Y_F / P_0, is the normalized final yield of the system. In practice, deviations from this estimate can be expected because of the interannual variability of the solar resource and the variability of the performance ratio (van Sark et al. 2012).

Typically, for most recent solar power plants, PR ranges from 0.8–0.9. Factors contributing to lower performance ratios include:

- Shading losses
- Soiling or snow-coverage losses
- Nonideal system orientation
- Wiring losses
- Lower module efficiencies under high-temperature operations
- Undersized inverters, making them "clip" the plant's output part of the time
- Older plants that have experienced module degradation
- Modules whose performance is less than expected because of incorrect nameplate information. (Many manufacturers now bin modules so that the actual performance is equal to or greater than the nameplate value. In past years, however, manufacturers often placed modules in the bin with the larger nameplate value.) Only measurements of the PV module power corrected to standard test conditions can provide correct values of the performance ratio.

Some factors that contribute to high observed performance ratios include:

- Operation in a cold climate
- Modules with low temperature coefficients. (Typically, CdTe, CIGS, and high-efficiency silicon modules tend to have the lowest temperature coefficients.) In the case of PV modules with low temperature coefficients, the power output degrades less when temperature rises; hence, the modules will produce a higher energy yield. Such modules are the preferred option at high-temperature locations.
- Modules that generate power above the nameplate rating (based on 1000 W/m²) as a result of high atmospheric transparency, cloud enhancement, and/or high ground reflection.

- Soiling or miscalibration of the radiation sensor, making it underestimate the incident irradiance and overestimate the performance ratio; therefore, regular cleaning and maintenance of the sensor is very important.

Other impacts on the performance ratio are the choice of the irradiation sensor (pyranometer versus reference cell) and the methodology of how the PV system power is determined (nameplate power, manufacturer flasher measurement, and/or on-site measurements).

The performance ratio method is simple, but it might not be accurate in all cases. For instance, van Sark et al. (2012) found a few older PV systems with performance ratios surprisingly less than 50%. The method is particularly useful, however, to compare the performance of existing systems or to quickly use solar resource data that might not be available to the alternate performance models, which are presented in the next sections. Otherwise, using a more sophisticated performance model is most likely the better approach.

9.4.1.2 Simple Photovoltaic Performance Models

Among other simple models, NREL's PVWatts® or the European Commission's Joint Research Centre Photovoltaic Geographical Information System (PVGIS) are free online tools that provide estimates of the electric energy production of roof- or ground-mounted PV systems based on a few simple inputs.[63, 64] The user needs to enter a street address or the geographic coordinates of the system's location and specify the main characteristics, such as installed power (kWp), array inclination and orientation, or the module technology type. Both tools also allow modeling of tracking PV systems, and PVGIS also provides estimates for off-grid systems. As output, both tools provide hourly and yearly estimates of energy incident on the PV installation and of the corresponding electricity production. The monetary value of the produced electricity can also be calculated, for which the user needs to provide information about the system's cost and the grid electricity consumer price.

By default, for locations in the United States, PVWatts uses a TMY created from the NREL NSRDB Physical Solar Model Version 3 data set (e.g., labeled "tmy-2018," where the year corresponds to the latest year in the data set); TMY2, which was created from NSRDB Meteorological Statistical Model (MTS) 1 (1961–1990); or TMY3, which was created from NSRDB MTS 2 (1991–2005 data). Other solar resource data options are available for world locations, but in most cases some spatial extrapolation is implied. Advanced users can change the default assumptions for losses caused by shading, soiling, and other factors. Full details about the underlying PVWatts algorithms can be found in Dobos (2014).

PVGIS provides hourly values of solar resource data and PV performance estimates for different technologies and system configurations based on averages of hourly calculations for time periods of more than 10 years. The effects of the irradiance spectral content, angle-of-incidence reflectance, and PV efficiency at low-irradiance or high-temperature conditions are considered, as are other general losses.[65] PVGIS uses automatically derived horizon profiles by default, which can be adapted by the user to the case of interest. PVGIS was originally developed for Europe, but it has been extended to Africa, and at present it offers data for most of Asia and America as well, thanks to the Joint Research Centre's collaboration with EUMETSTAT's Satellite Application Facility on Climate Monitoring and NREL. PVGIS also offers TMY data following the International Organization for Standardization 15927-4 methodology.

---

[63] See http://pvwatts.nrel.gov.
[64] See https://ec.europa.eu/jrc/en/pvgis .
[65] See https://ec.europa.eu/jrc/en/PVGIS/docs/methods.

These simple tools provide a very convenient and more accurate analysis method than the performance ratio described in the previous section, so they are recommended when a quick estimate is needed.

9.4.1.3 Detailed Photovoltaic System Performance Models

More accurate estimates of PV system performance can be obtained by setting up a detailed model of the PV plant that includes choosing specific modules and inverters, an array layout, detailed losses, and shading analysis. An increasing number of public and commercial tools are available to perform these detailed analyses. These elaborate models allow the user to have more control over the many submodels necessary to go from irradiance to power output. These tools usually include options for:

- Specifying irradiance and meteorological data sources
- Transposing the irradiance data from horizontal to the POA
- Modeling the impact of shading from both external objects and interrow (self-) shading
- Modeling or specifying loss percentages for soiling and snow cover
- Modeling the impact of the irradiance's spectral distribution on PV technologies
- Modeling reflections from the cover of the PV module
- Modeling the temperature of the PV module
- Modeling the power output from the PV module based on the effective irradiance reaching the PV cells and the module temperature
- Modeling or specifying losses resulting from a mismatch between modules and DC wiring
- Modeling the inverter's conversion of power from DC to AC
- Modeling or specifying AC wiring losses and transformer losses
- Specifying losses for planned or unplanned system maintenance and outages.

Examples of freely available programs that include such detailed PV performance models are NREL's SAM,[66] First Solar's PlantPredict,[67] RETScreen,[68] and Greenius.[69] Some popular commercially available options include PVsyst,[70] PV*SOL,[71] Aurora Solar,[72] HelioScope,[73] and archelios Pro.[74] Some programs are desktop tools, whereas others are web tools performing cloud-based applications. For software programmers, SAM, PlantPredict, and PVWatts include options for accessing calculations from various programming languages via an application programming interface, and SAM's code is open source, allowing interested parties to examine the underlying algorithms in great detail.

---

[66] See https://sam.nrel.gov/.
[67] See https://plantpredict.com/.
[68] See https://www.nrcan.gc.ca/maps-tools-publications/tools/data-analysis-software-modelling/retscreen/7465.
[69] See https://www.dlr.de/sf/en/desktopdefault.aspx/tabid-11688/20442_read-44865/.
[70] See https://www.pvsyst.com/.
[71] See https://valentin-software.com/en/products/pvsol-premium/.
[72] See https://www.aurorasolar.com/.
[73] See https://www.helioscope.com/.
[74] See https://www.trace-software.com/archelios-pro/solar-pv-design-software/.

As described in Chapter 5, all detailed PV modeling tools require not only irradiance but also meteorological parameters (most importantly ambient temperature and wind speed) to evaluate the power output. Because irradiance uncertainty is one of the biggest sources of uncertainty in the final modeled power output, care should be taken to minimize uncertainty in the irradiance resource data selected for PV modeling. Additional considerations for choosing the most appropriate input irradiance data can depend on the PV technology. For example, thin-film PV modules respond to a different (and smaller) part of the irradiance spectrum than crystalline modules (see Figure 3-22), making spectral corrections important for accurately modeling thin-film technologies.

Evolving module technologies make it hard for modeling software to keep up with technological advancements. For example, when modeling thin-film CdTe modules, optimal results might not be obtained from conventional modeling software packages. PlantPredict has specifically focused on properly modeling thin-film CdTe modules, but it is not limited to the CdTe technology; it can also be used to model mono-passivated emitter and rear cell, bifacial, and other thin-film module technologies.

The accuracy of predictions from these detailed PV modeling tools is very important to system feasibility and financing. Freeman et al. (2014) compared predicted outputs from multiple PV modeling tools to measured outputs for nine different systems. In parallel, Axaopoulos, Fylladitakis, and Gkarakis (2014) performed the same kind of comparison—but using a different set of modeling tools and measured data—for only one PV system.

9.4.2 Yield Estimation of Concentrating Solar Technology Projects

Yield estimation models for CST plants cover the calculation of the concentrating optics performance; the conversion of concentrated light to electricity, process heat, or chemical energy; and the management of the storage systems, if included.

In general, DNI is by far the most critical solar input for yield calculation in concentrating technologies. Other meteorological variables are also usually required: dry air temperature, relative humidity (or, alternatively, wet-bulb temperature), and wind speed. Wind direction, precipitation, and snow height are also recommended to better characterize local conditions (Hirsch et al. 2017).

Following are brief descriptions of the available types of optical performance models oriented to yield calculation. Some models are integrated with others for conversion into electricity, including storage, or with additional specialized modules for cost calculations (e.g., SAM, Greenius). Optical performance models can be separated into different categories: ray-tracing tools, analytical optical performance models, and models that determine the optical performance with lookup tables.

9.4.2.1 Monte Carlo Ray-Tracing Tools

The incident solar irradiance can be described as a multitude of solar rays transmitted from the sun to the concentrators and finally to the receiver. Although ray-tracing tools *can* provide highly accurate results, they are also highly demanding in terms of computing resources; thus, their use is usually limited to detailed design calculations (for example, calculation of the flux distribution on the receiver surfaces in central receiver systems) or to the elaboration of lookup tables or incidence angle modifiers for line-concentrating technologies.

Ray-tracing tools—such as STRAL (Belhomme et al. 2009), SolTRACE (Wendelin 2003), MIRVAL (Leary and Hankins 1979), SPRAY (Buck 2010), Tonatiuh (Blanco et al. 2009), and Heliosim (Potter et al. 2018)— calculate the path of the sun's rays from the sun's disk and

the circumsolar region to the target by application of physical laws. Monte Carlo techniques are often implemented to allow for reasonable calculation times.

For illustration, one method of ray tracing that is available in SPRAY is explained here. The method selects one concentrator element after another and traces a given number of rays from the current element. After calculating the vector to the center of the sun, the appropriate *sunshape* is included. (For details, see Chapter 2, Section 2.7.1, and Chapter 5, Section 5.9, respectively.) The specific ray under scrutiny is then related to a power calculated as the product of the incident DNI and the projected area of the current concentrator element divided by the number of rays per element. Then the path of the ray is followed until it reaches the receiver. This ray-tracing method can be based on actual measurements of the concentrator geometry or on its design geometry affected by typical optical errors.

9.4.2.2 Analytical Optical Performance Models

Analytical optical performance models are generally based on cone optics convolution methods. One example of a calculation method that uses an analytical approach is the Bendt-Rabl model (Bendt et al. 1979; Bendt and Rabl 1981). To accelerate calculations, analytical equations are derived and solved to describe the ray's path throughout the optical system. For example, the model can be used for parabolic troughs and solar dishes. In a first step, an angular acceptance function is determined from the design geometry. The angular acceptance function is defined by the fraction of rays incident on the aperture at a specific angle that ultimately reach the receiver. The second step consists of determining an effective source that includes both the user-defined sunshape and any possible deviation from the design geometry. The optical errors of concentrators are described as Gaussian-distributed independent uncertainties. Their combination is also a Gaussian distribution with a standard deviation, which is often called an optical error. The function that describes the optical errors is then combined with the sunshape using convolution. For line-focusing systems, such as parabolic troughs, a further integration step is required because the effect of circumsolar radiation on the incident irradiance depends strongly on angle. Finally, the intercepted radiation can be determined by summing the product of the effective source and the acceptance function over all angles. Similar analytical methods are used in HELIOS (Vittitoe and Biggs 1981), DELSOL (Kistler 1986), HFLCAL (Schwarzbözl et al. 2009), and SolarPILOT (Wagner and Wendelin 2018).

9.4.2.3 Lookup Table-Based Optical Performance Models

The fastest way to determine the optical performance of a CST collector uses only parameterizations or lookup tables that describe the change in the optical performance with solar position. The necessary parameters can be derived from experimental data, analytical performance models, or ray-tracing tools. Such lookup tables or parameterizations are used in some SAM submodels (Blair et al. 2014) and in Greenius (Dersch, Schwarzbözl, and Richert 2011; Quaschning et al. 2001).

9.5 Solar Resource Data for Plant Operations

This section discusses a variety of approaches for monitoring the solar resource at an existing solar power plant to better understand its performance. The performance of a solar energy system is directly linked to the meteorological conditions. For flat-plate thermal collectors and PV, the production is roughly proportional to the incident GTI; for concentrating technologies, the incident DNI is the driving input. In all cases, additional meteorological variables need to be monitored because they play a modulating role. In summary, the real-time monitoring of meteorological conditions at the system's location is important to:

- Evaluate a performance guarantee (acceptance testing)
- Assess the power plant's performance to improve yield predictions and to gain knowledge toward improvements in future plants
- Identify conditions of poor performance, including evidence of soiling, shading, hardware malfunction, or degradation, which could lead to warranty replacement, etc.

9.5.1 Performance Guarantee

Different methods exist to evaluate a plant's performance guarantee. In all cases, data recorded from on-site measurements of the solar resource are necessary. In the case of concentrating technologies, data sets derived from good-quality, on-site DNI measurements are usually required as inputs to the models used for performance guarantee. For flat-plate thermal collectors and PV, the yield prediction is generally based on GHI (even though the actual resource corresponds to GTI); hence, it is also common for a performance guarantee to use GHI as the basis for determining whether a plant has performed as promised. Some companies, however, have noted that the performance characterization of a PV plant can be accomplished with a lower uncertainty by using GTI instead. (That is because this approach reduces the uncertainty inherent to the approximate transposition procedure that transforms GHI into GTI.) Moreover, specific irradiance sensors (such as reference cells or reference modules that closely match the PV module response) can be chosen to match the expected response of the PV modules (thus reducing angle-of-incidence and spectral effects). Specifying GHI remains the best option if, for instance, a PV system comprises different sections with POAs of different tilts or azimuths, which might be the case over complex terrain. If the performance guarantee is specified in terms of GTI, the plant efficiency characterized during the performance guarantee evaluation could differ from the efficiency estimated in an earlier step with a model rather than using historical GHI data. Also, the placement of all sensors must (1) be in the correct plane (which is easy to confirm when the sensor is in the horizontal plane but not as easy for other orientations) and (2) experience the expected local conditions (ground albedo and shading) if the sensor is not in the horizontal plane (Kurtz et al. 2014).

Additional meteorological variables must be measured (see also Chapter 5), as discussed for yield predictions. Depending on the size of the solar system, more than one measurement point must be considered if the evaluation takes place during partly cloudy conditions. Acceptance tests for CST systems are discussed in Janotte, Lüpfert, and Pitz-Paal (2012) and Kearney (2009, 2014).

9.5.2 Power Plant Performance Monitoring

During power plant operation, knowledge of the current meteorological conditions and of the real-time status of the plant are of high importance. In addition, the future meteorological conditions are useful; therefore, both solar resource measurements and forecasts are essential parts of many large solar systems. Real-time DNI, wind, and temperature data are essential for the operation of CST plants, and thus they need to be continuously monitored. Although many PV plants can operate successfully with only episodic intervention, measurements and forecasts can also be advantageous. Cleaning a PV array as a function of meteorological conditions (e.g., frequency of recent precipitation) has benefits. Moreover, equipment malfunctions can be detected more quickly if the PV plant output is being continually compared to the expected output based on actual meteorological conditions. There is wide agreement that a well-maintained reference cell in the POA is the best choice when the goal is to identify the need for power plant maintenance. For a thorough PV power plant performance assessment, a calibrated, well-maintained, and regularly cleaned POA

pyranometer is required. More details about solar radiation measurement and maintenance of instrumentation are provided in Chapter 3.

9.5.3 Solar Radiation Forecasting Needs for Solar Power Project Operations and Maintenance

Forecasting the production of a solar power plant can considerably improve its profitability (Ramírez and Vindel 2017). Accurate predictions of the plant's average solar resource are needed for both solar thermal and PV power plants. The most important parameter to forecast is GHI in the case of flat PV plants and DNI in the case of concentrating systems.

Detailed explanations on solar radiation forecasting methodologies and the current state of the art are provided in Chapter 8. The specific forecasting needs depend on the intended application. Essentially, solar radiation forecasts can be used for either planning maintenance downtime or for optimizing operations.

9.5.3.1 Planning Maintenance

Maintenance work is needed in all types of solar power plants. Examples include technical closure, replacing defective components, cleaning modules or mirrors, or even conducting characterization tests. Depending on the expected duration of the maintenance work, the required forecasts correspond to different time horizons. Usually, a technical plant closure must be planned ahead of time and occurs on a fixed date based on the long-term forecasting on a monthly basis, whereas minor maintenance work is decided based on day-ahead forecasts.

9.5.3.2 Optimizing Operation and Revenue

To optimize operation, forecasting knowledge will help improve electricity sales by better matching production with demand if the plant is equipped with storage, particularly in the case of CST projects. In that case, the plant's annual revenue is conditioned by the quality of the solar forecasts (Ferretti et al. 2016); thus, especially when subject to a fluctuating electricity market, the plant's revenue can be maximized if production can be predicted appropriately. If there are ramp rate limitations defined by the grid operator, the yield of a PV plant with batteries can be improved by storing excess PV energy during positive ramps and using energy from the batteries during negative ramps. Forecasts can help manage the battery storage for this application and help limit the required storage capacity. Figure 9-15 shows the role of meteorological variables in demand and energy generation.

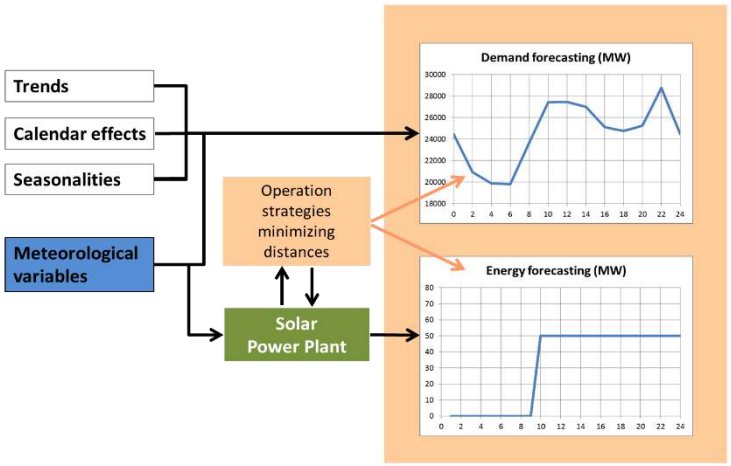

Figure 9-15. Importance of weather variables in forecasted demand and energy production. Image from Ramirez and Vindel (2017)

9.6 Variability of Solar Energy Production

From an application perspective, the solar resource variability (see Section 9.2.6) translates into power production variability, which could impact the stability of electric grids or the economics of the facility. One important question that has received specific attention is: How much is the temporal variability at one solar power plant site correlated with that of another site some distance away? A high correlation would tend to destabilize the grid and thus needs to be addressed in detail.

9.6.1 Photovoltaic Applications

Based on extensive studies (Hoff and Perez 2012a), it appears that the output's variability of a fleet of N PV plants over a given region will be reduced by the inverse of the square root of N if the plants' output variability is uncorrelated and if the plants experience similar natural variability. This is a consequence of the *spatial smoothing effect* noted by many (e.g., Marcos et al. 2012; Murata, Yamaguchi, and Otani 2009; Woyte et al. 2007; Wiemken et al. 2001). This result means that nearby locations are highly correlated, experiencing the same ramp rates at nearly the same time and varying in sync. In contrast, the time series from distant locations are uncorrelated. Partial correlation exists between these two extremes. Hoff and Perez (2012b) used 10-km, hourly, satellite-derived irradiances over the continental United States. They observed a similar asymptotic decay with distance and a predictable dependence of this decay upon Δt for time intervals of 1, 2, and 3 hours. They also noted that the rate of decrease of correlation with distance was different for various U.S. regions and attributed these differences to prevailing regional cloud speeds, as confirmed by Hoff and Norris (2010). Perez, Hoff, and Kivalov (2011) analyzed high-resolution, high-frequency, satellite-derived irradiances (1 km, 1 minute) in climatically distinct regions of North America and Hawaii to investigate the site-pair correlation decay as a function of distance, timescale, and mean monthly regional cloud speed (see Figure 9-16), itself independently derived from satellite cloud-motion vectors. Interestingly, as shown in Figure 9-16 for various areas and periods, the rate of decrease of this correlation with distance is a strong function of the data's temporal resolution. A distance of approximately 5 km might be sufficient to smooth out fluctuations on a 1-minute timescale, whereas distances greater than 50 km would be needed to smooth out hourly fluctuations. See also Remund et al. (2015) for examples pertaining to other regions in the world.

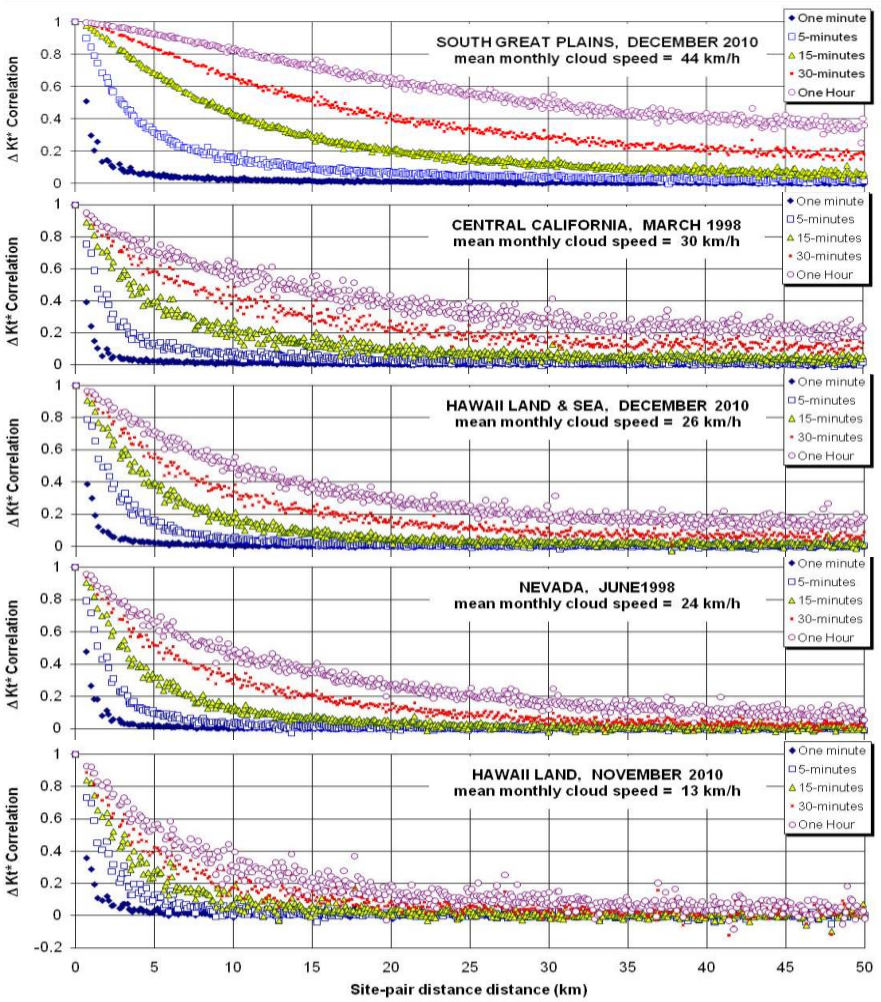

Figure 9-16. Site-pair correlations as a function of time and distance for sample regions in North America and Hawaii. Mean monthly cloud speed was estimated from satellite-derived cloud motion vectors computed for each data point. *Image from Perez, Hoff, and Kivalov (2011)*

9.6.2 Quantifying Photovoltaic Output Variability

The variability quantifying metric should adapt to a wide range of temporal and spatial scales and embed (1) the *physical quantity* that varies, (2) the variability *timescale*, and (3) the *time span* during which variability is assessed.

9.6.2.1 Physical Quantity

For energy producers and grid operators, the pertinent quantity is the power output, ***p***, of a power plant or of a fleet of power plants at a given point in time. The power output variability reflects the underlying variability of irradiance impinging on the plant(s); therefore, understanding and quantifying the variability of irradiance amounts to quantifying and understanding the variability of ***p***. DNI's variability is relevant for concentrating technologies, whereas the variability in GHI or GTI is representative of flat-plate technologies. This section focuses on the latter.

The solar geometry-induced variability is fully predictable. Here, the focus is on cloud/weather-induced variability that is stochastic in nature. To better understand this variability component, it is useful to first remove the solar geometry effects. The *clearness index*, *Kt* (ratio between GHI and its extraterrestrial counterpart), or *the clear-sky index*, *Kc*

(ratio between GHI and its clear-sky counterpart), both embed the stochastic variability of irradiance but are largely independent of solar geometry. The use of *Kc* is preferable in general because it more effectively removes solar geometry effects at low solar elevations (Perez et al. 1990). Nevertheless, its use implies that the clear-sky irradiance can be accurately estimated, which represents an additional step that many analysts try to avoid.

9.6.2.2 Timescale

The intuitive temporal example presented suggests that the temporal scale of the selected physical quantity's time series, Δt, is a fundamental factor. Depending on the application, Δt can range from 1 second or less to hours and more. A variation in *Kc* corresponding to the selected timescale Δt is noted $\Delta Kc_{\Delta t}$. On short scales (milliseconds to minutes), this change is often referred to as the *ramp rate*.

9.6.2.3 Time Span

A proper measure of variability should include ramp events covering a statistically significant *time span*. This time span should be a large multiple of Δt.

9.6.2.4 Nominal Variability Metric

Nominal variability refers to the variability of the selected dimensionless clear-sky index. The maximum or mean $\Delta Kc_{\Delta t}$ ramp rate over a given time span has been proposed as such a measure (Hoff and Perez 2010); however, most authors have recently settled on the ramp rate's variance, or its square root—the ramp rate's standard deviation—over a given time span as the preferred metric for variability.

$$\text{Nominal variability} = \sigma(\Delta Kc_{\Delta t}) = \sqrt{Var[\Delta Kc_{\Delta t}]} \tag{9-7}$$

9.6.2.5 Power Output (Absolute) Variability Metric

Eq. 9-7 describes a nominal dimensionless metric. When dealing with power generation, it is necessary to scale up the nominal metric and to quantify the power variability in absolute terms. This is expressed by Eq. 9-8:

$$\text{Power variability} = \sigma(\Delta \boldsymbol{p}_{\Delta t}) = \sqrt{Var[\Delta \boldsymbol{p}_{\Delta t}]} \tag{9-8}$$

Recall that $\boldsymbol{p}$ can be modeled from *Kc* via extraction of GHI, extrapolation to POA irradiance (GTI), and inclusion of PV specifications (i.e., without changing the inherent cause of variability); hence, Eq. 9-8 does not include additional intrinsic variability information relative to Eq. 9-7.

9.7 Applying Solar Resource Data to Other Types of Solar Energy Projects

9.7.1 Projects Using Flat-Plate Thermal Collectors

Energy simulation tools for flat-plate thermal collector systems usually include a suite of modules describing the thermal receiver and the thermal losses of the piping, parasitic losses, and thermal storage. Some typical tools for these simulations are Polysun[75] and

[75] See http://www.velasolaris.com/.

T*Sol[76]; however, some of the aforementioned general software tools also include these types of systems. For example, this is the case with RETScreen, SAM, and Greenius. Although the irradiance in the flat-plate collector plane (GTI) is the physically relevant irradiance, the separate specification of DNI and DHI can be of interest. Individual incidence angle modifiers can be used to determine the efficiency of the DNI and DHI energy conversion, respectively, for a given solar position.

9.7.2 Solar Heating and Cooling in Buildings

Solar heating and cooling in buildings (SDHtake-off Project 2012), smart cities, and smart grids are projects that include solar systems among other energy systems or energy conservation measures. Solar radiation data are still needed for sizing, simulation, and evaluation. Note, in particular, that TMY and Test Reference Year (TRY)/ Design Reference Years (DRY) (Crawley 1998; Hall et al. 1978; Lund 1974) were originally developed for building applications. The TRNSYS simulation software (University of Wisconsin) has also traditionally been applied to buildings.

9.7.3 Smart Electric Grids

Electric grids benefit from high-quality solar radiation data in both grid operation (now, today, and the next days) and grid planning (the next months to years). For example, solar radiation and forecasting data are used in grid operation for:

- Power system state estimation
- Unit commitment and scheduling of power plants and storage units
- Congestion forecasting and management
- Forward coordination between various stakeholders (e.g., transmission and distribution grid operators, plant operators, and other market players).

The further the integration of solar PV into the grid proceeds, the more important it is to integrate information about current and upcoming electrical power production and feed-in into operation processes. Regulations such as the European System Operation Guideline[77] define the need for data. Grid-connected PV power plants of a relevant size (e.g., more than 1 MWp) provide real-time measurement data and a regular schedule of the planned feed-in. Further, for a detailed congestion forecast in grid operation, one needs an additional estimate for the possibly large number of small grid-connected installations. Because even smart meters do not always provide real-time data to the grid operators, those not receiving the data need to generate or buy an estimation of regional feed-in, typically based on some upscaling method. To do so, radiation data from NWP and satellite observations are a valuable source of information. Forecasting providers, making use of sophisticated statistical or even machine learning models, usually process these inputs. For this, they rely on detailed master data about the individual plant or the large number of plants behind the meter. An extensive database (per grid and/or per nation) collecting and providing such master data should be available.[78] In contrast to grid operation, where individual estimates and forecasts are permanently integrated into the processes, grid planning is based on a

[76] See http://www.valentin-software.com/.
[77] See https://www.europex.org/eu-legislation/sogl/.
[78] See, for example, https://www.bundesnetzagentur.de/EN/Areas/Energy/Companies/CoreEnergyMarketDataRegister/CoreDataReg_node.html.

historical radiation data set, and simultaneity factors within a portfolio of installed or expected power plants are assumed.

As an alternative to operational approaches intended to blend with standard transmission system operator (TSO) practice, such as those just described, another avenue is currently explored in the International Energy Agency's Photovoltaic Power Systems Programme (PVPS) Task 16: *entirely eliminating supply-side forecast uncertainty and its impact on load imbalances via operationally firm solar forecasts*. This is achieved by adding and operating dedicated hardware and controls to PV plants or fleets of plants so that the output seen by the grid operator exactly amounts to the forecast output. The hardware consists of optimized storage and plant oversizing to make up for all instances of forecast over- or underestimation as well as controls to equate actuals and predictions in real time. In addition to being a prospectively cost-effective operational forecast strategy for TSOs, the real value of this strategy lies in opening the door to least-cost firm power generation, hence the possibility of ultrahigh solar penetration at the lowest possible cost.

- *A prospectively cost-effective operational forecast strategy for TSOs*: Firm forecast operations have been analyzed for individual Surface Radiation Budget Network (SURFRAD) locations in the United States as well as for a simulated fleet in California comprising 16 power plants—one in each state's climatic region (Perez et al. 2019a, 2019b). Applying the State University of New York forecast model to the California fleet would result in achieving a firm forecast cost less than $150/kWp today (i.e., an approximate 10% premium on current large-scale turnkey PV costs) for firm day-ahead forecasts. Future PV and storage costs anticipated in 10–15 years should reduce the cost of entirely eliminating solar supply-side imbalances to less than $50 per PV kWp. Pierro et al. (2020) recently showed that such a firm forecast strategy could already be cost-effective for ratepayers today in Italy, compared to the existing market for load imbalance corrections.
- *A least-cost ultrahigh penetration transition strategy*: The same operational strategy—optimized storage plus overbuilding—applied on a larger scale has been shown to be the key to achieving firm, effectively dispatchable PV production at the least possible cost. A series of recent publications (Perez et al. 2019c, 2019d) showed that 2040-targeted, firm, 24/7 electricity production levelized cost of energy (LCOE) of the order or less than 5 U.S. cents per kWh were realistic targets in the central United States, Italy, and the island grid of La Reunion, France. Figure 9-17 illustrates how PV overbuilding can sufficiently reduce storage requirements to achieve an acceptably low firm power generation LCOE. Pierro et al. (2021) showed that the entry-level firm forecast strategy can be gradually expanded over time, following technology costs and TSO practice learning curves to transition from low-level firmness requirements—meeting forecast production—to more stringent requirements, until meeting demand 24/7/365 becomes economically achievable with only minimal reliance on conventional resources.

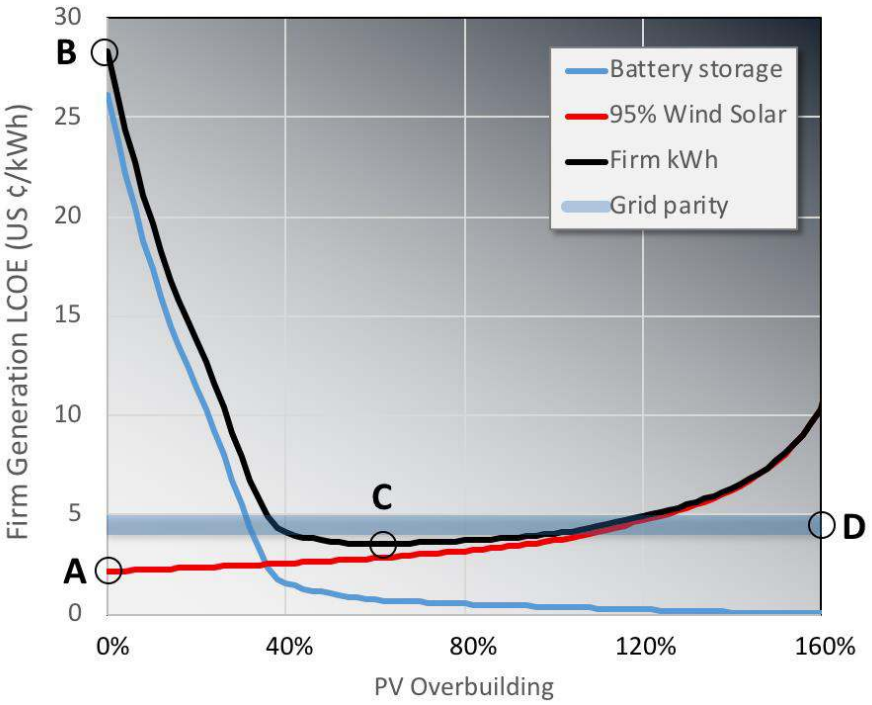

Figure 9-17. Impact of PV overbuilding on firm power generation LCOE. Although unconstrained PV (A) is inexpensive (apparently below grid parity), firming PV to meet demand 24/365 with storage alone (B) is unrealistically expensive. Overbuilding PV fleets reduces storage requirements to the point (C) where firm PV power generation can achieve true grid parity (D). ***Image from Perez et al. (2019c)***

9.7.4 Chemical Applications

Solar resource data are required for several chemical applications. These can be divided into two main topics because of their different use of the solar resource: desalination and photochemical applications.

9.7.4.1 Solar Desalination

Global demand for freshwater is continuously increasing because of population growth and economic development. To meet this increasing demand, desalination has become the most important source of freshwater for drinking and agriculture in some world regions with huge solar energy potential, such as the Middle East and North Africa (Isaka 2012).

Seawater solar thermal desalination via multistage flash or multi-effect distillation uses solar heat as the energy input. This methodology is the most promising desalination process based on renewable energy. As previously discussed, the CST part of the desalination project needs several years of high-quality, on-site data for simulation and design optimization or site-adapted data time series that are similar to the required data for CST plants.

Many small PV-based membrane desalination systems have been installed worldwide, especially in remote areas and islands. As in the case of a standard PV plant, GHI and/or GTI data are needed as the most relevant solar input for these systems.

9.7.4.2 Solar Photocatalysis: Detoxification and Disinfection of Fluids

Solar photocatalytic detoxification and disinfection processes constitute a solution for the treatment of contaminated groundwater, industrial wastewater, air, or soil (Malato 2004). The development of these processes has reached a point where the solar technology can be competitive with conventional treatment methods, particularly at isolated locations with high solar potential, which can be the case with many agricultural farms.

Solar photochemistry can be defined as the technology that collects solar photons and introduces them in an adequate reactor volume to promote specific chemical reactions (Blanco and Malato 2010). The equipment that performs this function is a solar collector—specifically, a compound parabolic collector with a relatively large acceptance angle; hence, they can use DNI and the part of DHI that emanates from the circumsolar region. The requirements for solar photochemical reactors are similar to any other photochemical reactor, with the particularity that their light input comes from the sun rather than from a lamp. For this reason, and according to the working temperature, the collector must be tilted or mounted on a tracking system with one or two axes; Figure 9-18 illustrates two different photo reactors installed at Plataforma Solar de Almería (CIEMAT), Spain.[79] Depending on the type of solar collector, tilted or direct ultraviolet solar irradiance data will be needed. In the most general case that ultraviolet radiation is not measured locally, these variables must be empirically derived from DNI and/or GHI data (e.g., Habte et al. 2019).

Figure 9-18. Compound parabolic collector photo reactors installed at Platforma Solar de Almería for solar water disinfection applications: (left) compund parabolic collector-SODIS and (right) FITOSOL-2 . ***Photos from Platforma Solar de Almería, CIEMAT***

9.8 Summary of Applications of Solar Resource Data

This chapter summarized available information as well as guidance on the type of solar resource relevant to various stages of a solar project, and attempted to inform readers about their specific needs relative to solar radiation data and how these needs depend on the type of solar project and on the project's stage.

Figure 9-19 displays a summary of the solar radiation needs at different steps of a hypothetical project. The information provided here is applicable to the case of large solar

[79] See http://www.psa.es/en/instalaciones/aguas.php.

energy projects, mainly PV and CST, and to the case of building energy performance evaluations.

System Size →

Phase ↓

	Small	Medium	Large
1. Prefeasibility and planning	• Long-term averages • Monthly data • Solar cadastres/ maps • Simple shading analysis	• TMY • Hourly data • Shading analysis	• Long-term satellite data • Hourly data
2. Feasibility			• Satellite data • Time series (>10 year) • Ground meas. (> 1 year) • Shading analysis • Further site- and technology- specific meteo. parameters (e.g., albedo, soiling)
3. Due diligence and finance		• Satellite data • Time series (>10 y) • Minute data • Shading • Further site- and technology- specific meteo. parameters (e.g., albedo, soiling)	• Satellite data • Time series (>10 y) • Ground meas. (> 1 year) • Minute data • Shading analysis • Further site- and technology- specific meteo. parameters (e.g., albedo, soiling)
4. Operation and maintenance	• Simple monitoring	• Local measurements • Forecasts	• Local measurements • Forecasts

Figure 9-19. Data application techniques for the various stages of project development

Maps (from, e.g., the Global Solar Atlas[80] or the Global Atlas for Renewable Energy[81]) should be used to make a preliminary assessment of the solar resource, cautiously assuming a fairly large potential for error. GIS tools and resources are commonly used at this step for convenience. Various spatial resolutions need to be used when addressing projects at the regional or national scale—compared to the case of the neighborhood or city scale. Using these tools, maps of solar radiation, and simple energy production models, the potential of the energy output from different technologies can be evaluated and compared. Using GIS tools for potential assessment, terrain slopes and additional land constraints must be considered for large projects. During this screening process, the nature of local aerosols and their spatiotemporal variability might need to be considered. Because widely different sources of information might be available at that stage, it is important to define appropriate comparison parameters among the solar resource data sources and to clarify the definition of variability, error, and uncertainty; thus, variability needs to be identified, mainly at the interannual level, and distinguished from the uncertainty of the model. Ideally, considering the uncertainties from each data source, a common “most probable” range should be obtained, which should include the expected or “true” value. Temporal and spatial variability

[80] See https://globalsolaratlas.info/map.
[81] See https://irena.masdar.ac.ae/gallery/#gallery.

is addressed in this chapter through the COV statistic, which can be determined by using long time series of measured or modeled data for the site and its surroundings.

In the feasibility assessment stage, typical solar radiation series are needed for plant simulation and for economic/profitability analysis. Typical annual time series are provided by a TMY, TRY, DRY, Typical global horizontal irradiance year (TGY), or Typical direct normal irradiance year (TDY). In addition to the review of typical meteorological data series generation for solar energy simulation, this chapter reviewed the proposed procedures for the analysis of the interannual variability and the generation of series of a specific POE, such as P90; thus, to evaluate the profitability and payback of a project, simulations of its behavior during bad years are needed. Section 4.8 specifically deals with the issues of combining data sets and reducing their uncertainty through site adaptation processes. These steps are very important for a precise feasibility assessment and to guarantee bankability, particularly for projects with large associated investments.

During and before the plant's construction phase, solar radiation data are needed to refine the yield estimation and to minimize the expected profitability uncertainties; thus, the value of the energy generated by a solar installation depends on the system's output and on the price offered for that energy at the time it is generated. Methods for the yield estimation of non-concentrating PV projects and of CST projects have been discussed. Additional meteorological inputs that are necessary for yield estimation, as well as solar radiation characteristics, such as its spectral and angular distribution, were also discussed.

For power plant operation, the solar resource information must include high-quality, on-site measurements to qualify the plant's performance as well as accurate irradiance forecasts for operation and revenue optimization. This chapter's final section discussed the type of solar radiation data needed for different types of solar projects, such as flat-plate thermal collectors, solar heating and cooling in buildings, smart electric grids, solar desalination, and other chemical applications.

9.9 References

Axaopoulos, P. J., E. D. Fylladitakis, and K. Gkarakis. 2014. "Accuracy Analysis of Software for the Estimation and Planning of Photovoltaic Installations." *International Journal of Energy and Environmental Engineering* 5 (71).

Badosa, J., M. Haeffelin, and H. Chepfer. 2013. "Scales of Spatial and Temporal Variation of Solar Irradiance on Reunion Tropical Island." *Solar Energy* 88: 42–56. https://doi.org/10.1016/j.solener.2012.11.007.

Belhomme, B., R. Pitz-Paal, P. Schwarzbozl, and S. Ulmer. 2009. "A New Fast Ray Tracing Tool for High-Precision Simulation of Heliostat Fields." *Journal of Solar Energy Engineering* 131 (31002). https://doi.org/10.1115/1.3139139.

Bendt, P., A. Rabl, H. W. Gaul, and K. A. Reed. 1979. *Optical Analysis and Optimization of Line Focus Solar Collectors* (SERI/TR-34-09). Golden, CO: Solar Energy Research Institute.

Bendt, P., and A. Rabl. 1981. "Optical Analysis of Point Focus Parabolic Radiation Concentrators." *Applied Optics* 20 (674). https://doi.org/10.1364/AO.20.000674.

Bengulescu, M., P. Blanc, and L. Wald. 2018. "On the Intrinsic Timescales of Temporal Variability in Measurements of the Surface Solar Radiation." *Nonlinear Processes in Geophysics* 25: 19–37. https://doi.org/10.5194/npg-25-19-2018.

Beyer, H. G., D. Dumortier, L. Wald, M. Martinoli, C. Schilings, B. Gschwind, L. Menard, E. Gaboardi, L. Ramirez-Santigosa, J. Polo, T. Cebecauer, T. Huld, M. Šúri, M. de Blas, E. Lorenz, R., Pfatischer, J. Remund, P. Ineichen, A. Tsvetkov, and J. Hofierka. 2008.

"Management and Exploitation of Solar Resource Knowledge." *Proceedings of the EUROSUN Conference*, Lisbon, Portugal.

Blair, N., A. P. Dobos, J. Freeman, T. Neises, M. Wagner, T. Ferguson, P. Gilman, and S. Janzou. 2014. *System Advisor Model, SAM 2014.1. 14: General Description* (NREL/TP-6A20-61019). Golden, CO: National Renewable Energy Laboratory.

Blanco, J., and S. Malato. 2010. *Solar Energy Conversion and Photoenergy System: Thermal Systems and Desalination Plants: v.3*. EOLSS Publishers Co Ltd.

Blanco, M. J., A. Mutuberria, P. Garcia, R. Gastesi, and V. Martin. 2009. "Preliminary Validation of Tonatiuh." *Proceedings of the 15th International Symposium on Solar Power and Chemical Energy Systems Conference (SolarPACES)*, Berlin, Germany.

Bright, J. M., C. A. Gueymard. 2019. "Climate-Specific and Global Validation of MODIS Aqua and Terra Aerosol Optical Depth at 452 AERONET Stations." *Solar Energy* 183: 594–605. https://doi.org/10.1016/j.solener.2019.03.043.

Buck, R. 2010. *Solar Power Raytracing Tool, SPRAY, User Manual, Version 2.6*, *20.3.2010*. DLR.

Buster, G., M. Rossol, G. MacLaurin, Y. Xie, and M. Sengupta. "A Physical Downscaling Algorithm for the Generation of High-Resolution Spatiotemporal Solar Irradiance Data." *Solar Energy* 216: 508–517. https://doi.org/10.1016/j.solener.2021.01.036.

Calif, R., and T. Soubdhan. 2016. "On the Use of the Coefficient of Variation to Measure Spatial and Temporal Correlation of Global Solar Radiation." *Renewable Energy* 88: 192–99. https://doi.org/10.1016/j.renene.2015.10.049.

Castillejo-Cuberos, A., and R. Escobar. 2020. "Understanding Solar Resource Variability: An In-Depth Analysis, Using Chile as a Case of Study." *Renewable and Sustainable Energy Reviews* 120: 109664. https://doi.org/10.1016/j.rser.2019.109664.

Cebecauer, T., and M. Šúri. 2015. "Typical Meteorological Year Data: SolarGIS Approach." *Energy Procedia* 69: 1958–69. https://doi.org/10.1016/j.egypro.2015.03.195.

Cebecauer, T., M. Šúri, and C. A. Gueymard. 2011. "Uncertainty Sources in Satellite-Derived Direct Normal Irradiance: How Can Prediction Accuracy Be Improved Globally?" *Proceedings of the SolarPACES Conference*, Granada, Spain.

Crawley, D. B. 1998. "Which Weather Data Should You Use for Energy Simulations of Commercial Buildings? *ASHRAE Transactions* 104 (2): 18.

Crowley, T. J., and M. B. Unterman. 2013. "Technical Details Concerning Development of a 1200 yr Proxy Index for Global Volcanism." *Earth System Science Data*, 5: 187–97. https://doi.org/10.5194/essd-5-187-2013.

Davy, R. J., and A. Troccoli. 2012. "Interannual Variability of Solar Energy Generation in Australia." *Solar Energy* 86 (12): 3554–60.

Dersch, J., P. Schwarzbözl, and T. Richert. 2011. "Annual Yield Analysis of Solar Tower Power Plants With GREENIUS." *Journal of Solar Energy Engineering* 133: 31017. https://doi.org/10.1115/1.4004355.

Dobos, A. P. 2014. *PVWatts Version 5 Manual* (NREL/TP-6A20-62641). Golden, CO: National Renewable Energy Laboratory.

Dobos, A., P. Gilman, and M. Kasberg. 2012. "P50/P90 Analysis for Solar Energy Systems Using the System Advisor Model (NREL/CP-6A20-54488)." Presented at the World Renewable Energy Congress, Denver, Colorado, May 13–17, 2012.

Ellis, A., M. Behnke, and C. Barker. 2011. "PV System Models for Grid Planning Studies." *Proceedings of the 37th IEEE Photovoltaic Specialists Conference*, Seattle.

Espinar, B., L. Ramírez, A. Drews, H. G. Beyer, L. F. Zarzalejo, J. Polo, and L. Martín. 2009. "Analysis of Different Comparison Parameters Applied to Solar Radiation Data from Satellite and German Radiometric Stations." *Solar Energy* 83: 118–25. https://doi.org/10.1016/j.solener.2008.07.009.

Fernández Peruchena, C. M., L. Ramírez, M. A. Silva-Pérez, V. Lara, D. Bermejo, M. Gastón, S. Moreno-Tejera, J. Pulgar, J. Liria, S. Macías, R. Gonzalez, A. Bernardos, N. Castillo, B. Bolinaga, R. X. Valenzuela, and L. F. Zarzalejo. 2016. "A Statistical Characterization of the Long-Term Solar Resource: Towards Risk Assessment for Solar Power Projects." *Solar Energy* 123: 29–39. https://doi.org/10.1016/j.solener.2015.10.051.

Fernández-Peruchena, C. M., F. Vignola, M. Gastón, V. Lara-Fanego, L. Ramírez, L. Zarzalejo, M. Silva, M. Pavón, S. Moreno, D. Bermejo, J. Pulgar, S. Macías, and R. X. Valenzuela. 2018. "Probabilistic Assessment of Concentrated Solar Power Plants Yield: The EVA Methodology." *Renewable and Sustainable Energy Reviews* 91: 802–11. https://doi.org/10.1016/j.rser.2018.03.018.

Fernández-Peruchena, C. M., M. Gastón, M. Sánchez, J. García-Barberena, M. Blanco, and A. Bernardos. 2015. "MUS: A Multiscale Stochastic Model for Generating Plausible Meteorological Years Designed for Multiyear Solar Energy Yield Simulations." *Solar Energy* 120: 244–56. https://doi.org/10.1016/j.solener.2015.07.037.

Ferretti, F., C. Hogendijk, V. Aga, and A. Ehrsam. 2016. "Addressing Forecast Uncertainty Impact on CSP Annual Performance." *Proceedings of the SolarPACES Conference*, Abu Dhabi, UAE.

Freeman, J., J. Whitmore, N. Blair, and A. P. Dobos. 2014. *Validation of Multiple Tools for Flat Plate Photovoltaic Modeling Against Measured Data* (NREL/TP-6A20-61497). Golden, CO: National Renewable Energy Laboratory.

Grantham, A. P., P. J. Pudney, L. A. Ward, M. Belusko, and J. W. Boland. 2017. "Generating Synthetic Five-Minute Solar Irradiance Values from Hourly Observations." *Solar Energy* 147: 209–21. https://doi.org/10.1063/1.5110785.

Gueymard, C. A. 2011. "Irradiance Variability and its Dependence on Aerosols." *Proceedings of the SolarPACES Conference*, Granada, Spain.

Gueymard, C. A. 2012. "Temporal Variability in Direct and Global Irradiance at Various Time Scales as Affected by Aerosols." *Solar Energy* 86: 3544–53. https://doi.org/10.1016/j.solener.2012.01.013.

Gueymard, C. A. 2014. "A Review of Validation Methodologies and Statistical Performance Indicators for Modeled Solar Radiation Data: Towards a Better Bankability of Solar Projects." *Renewable and Sustainable Energy Reviews* 39: 1024–34. https://doi.org/10.1016/j.rser.2014.07.117.

Gueymard, C. A. 2019. "Clear-Sky Radiation Models and Aerosol Effects." *Solar Resources Mapping Fundamentals and Applications*, edited by J. Polo, L. Martin-Pomares, and A. Sanfilippo. Springer, 137–82. https://doi.org/10.1007/978-3-319-97484-2.

Gueymard, C. A., and R. George. 2005. "Gridded Aerosol Optical Depth Climatological Datasets Over Continents for Solar Radiation Modeling." *Proceedings of the ISES Solar World Congress*, Orlando, Florida.

Gueymard, C. A., and S. M. Wilcox. 2011. "Assessment of Spatial and Temporal Variability in the US Solar Resource from Radiometric Measurements and Predictions from Models

Using Ground-Based or Satellite Data." *Solar Energy* 85: 1068–84. https://doi.org/10.1016/j.solener.2011.02.030.

Gueymard, C. A., W. T. Gustafson, G. Bender, A. Etringer, and P. Storck. 2012. "Evaluation of Procedures to Improve Solar Resource Assessments: Optimum Use of Short-Term Data from a Local Weather Station to Correct Bias in Long-Term Satellite-Derived Solar Radiation Time Series." *Proceedings of the World Renewable Energy Forum*, Denver, Colorado, American Solar Energy Society.

Gueymard, C., A. Habte and M. Sengupta. 2018 "Reducing Uncertainties in Large-Scale Solar Resource Data: The Impact of Aerosols." *IEEE Journal of Photovoltaics* 8: 1732-37. DOI: 10.1109/JPHOTOV.2018.2869554.

Gueymard, C., and S. Wilcox. 2009. "Spatial and Temporal Variability in the Solar Resource: Assessing the Value of Short-Term Measurements at Potential Solar Power Plant Sites." *Proceedings of the ASES National Solar Conference*, Buffalo, New York.

Gueymard, C. A. 2012. "Visibility, Aerosol Conditions, and Irradiance Attenuation Close to the Ground-Comments on "Solar radiation attenuation in solar tower plants" by J. Ballestrin and A. Marzo, Solar Energy (2012)." *Solar Energy* 86 (5): 1667–68.

Habte, A., A. Lopez, M. Sengupta, and S. Wilcox. 2014. *Temporal and Spatial Comparison of Gridded TMY, TDY, and TGY Data Sets* (NREL/TP-5D00-60886). Golden, CO: National Renewable Energy Laboratory.

Habte, A., M. Sengupta, C. A. Gueymard, R. Narasappa, O. Rosseler, and D. M. Burns. 2019. "Estimating Ultraviolet Radiation from Global Horizontal Irradiance." *IEEE Journal of Photovoltaics* 9: 139–46. https://doi.org/10.1109/JPHOTOV.2018.2871780.

Habte, A., M. Sengupta, C. Gueymard, A. Golnas, and Y. Xie. 2020. "Long-Term Spatial and Temporal Solar Resource Variability over America Using the NSRDB Version 3 (1998–2017)." *Renewable and Sustainable Energy Reviews* 134. https://doi.org/10.1016/j.rser.2020.110285.

Hall, I. J. R., R. R. Prairie, H. E. Anderson, and E. C. Boes. 1978. *Generation of Typical Meteorological Years for 26 SOLMET Stations* (SAND78-1601). Albuquerque, NM: Sandia National Laboratories.

Hirsch, T., et al. 2017. *SolarPACES Guideline for Bankable STE Yield Assessment* (IEA Technology Collaboration Programme SolarPACES Report).

Hirsch, T., H. Schenk, N. Schmidt, and R. Meyer. 2010. "Dynamics of Oil-Based Parabolic Trough Plants—Impact of Transient Behaviour on Energy Yield." *Proceedings of the SolarPACES Conference*, Perpignan, France.

Ho, C. K., and G. J. Kolb. 2010. "Incorporating Uncertainty into Probabilistic Performance Models of Concentrating Solar Power Plants." *Journal of Solar Energy Engineering* 132: 31012. https://doi.org/10.1115/1.4001468.

Ho, C. K., S. S. Khalsa, and G. J. Kolb. 2011. "Methods for Probabilistic Modeling of Concentrating Solar Power Plants." *Solar Energy* 85: 669–75. https://doi.org/10.1016/j.solener.2010.05.004/.

Hoff, T. E., and B. Norris. 2010. "Mobile High-Density Irradiance Sensor Network: Cordelia Junction Results." Personal communication.

Hoff, T. E., and R. Perez. 2010. "Quantifying PV power Output Variability." *Solar Energy* 84: 1782–93.

Hoff, T., and R. Perez. 2012a. "Modeling PV Fleet Output Variability." *Solar Energy* 86 (8): 2177–89. https://doi.org/doi:10.1016/j.solener.2011.11.005.

Hoff, T.E. and R. Perez. 2012b. "Predicting short-term variability of high-penetration PV." *Proceedings of the World Renewable Energy Forum* (ASES Annual Conference), Denver, Colorado.

Hofmann, M., S. Riechelmann, C. Crisosto, R. Mubarak, and G. Seckmeyer. 2014. "Improved Synthesis of Global Irradiance with One-Minute Resolution for PV System Simulations." *International Journal of Photoenergy*: 1–10. https://doi.org/10.1155/2014/808509.

Huang, Y., Z. Chen, B. Wu, L. Chen, W. Mao, F. Zhao, J. Wu, J. Wu, and B. Yu. 2015. "Estimating Roof Solar Energy Potential in the Downtown Area Using a GPU-Accelerated Solar Radiation Model and Airborne LiDAR Data." *Remote Sensing* 7: 17212–33. https://doi.org/10.3390/rs71215877.

Hyde, W. T., and T. J. Crowley. 2000. "Probability of Future Climatically Significant Volcanic Eruptions." *Journal of Climate* 13: 1445–50.

Ineichen, P., and R. Perez. 2002. "A New Airmass Independent Formulation for the Linke Turbidity Coefficient." *Solar Energy* 73: 151–57. https://doi.org/10.1016/S0038-092X(02)00045-2.

Isaka, M. 2012. "Water Desalination Using Renewable Energy." Technology brief. IEA-ETSAP and IRENA.

Jakubiec, J. A., and C. F. Reinhart. 2013. "A Method for Predicting City-Wide Electricity Gains from Photovoltaic Panels Based on LiDAR and GIS Data Combined with Hourly Daysim Simulations." *Solar Energy* 93: 127–43. https://doi.org/10.1016/j.solener.2013.03.022.

Janotte, N., E. Lüpfert, and R. Pitz-Paal. 2012. „Acceptance Testing and Advanced Evaluation Strategies for Commercial Parabolic Trough Solar Fields." *Proceedings of the SolarPACES Conference*, Marrakesch, Morocco.

Janotte, N., S. Wilbert, F. Sallaberry, M. Schroedter-Homscheidt, and L. Ramirez. 2017. "2 – Principles of CSP Performance Assessment." In *The Performance of Concentrated Solar Power (CSP) Systems*, 31–64. https://doi.org/10.1016/B978-0-08-100447-0.00002-X.

Kearney, D. 2009. *Utility-Scale Parabolic Trough Solar Systems: Performance Acceptance Test Guidelines: April 2009–December 2010* (NREL/SR-5500-48895). Golden, CO: National Renewable Energy Laboratory.

Kearney, D. 2014. "Utility-Scale Power Tower Solar Systems: Performance Acceptance Test Guidelines." *Energy Procedia* 49: 1784–91.

Kistler, B. L. 1986. *A User's Manual for DELSOL3: A Computer Code for Calculating the Optical Performance and Optimal System Design for Solar Thermal Central Receiver Plants* (SAND86-8018). Albuquerque, New Mexico: Sandia National Laboratories.

Kurtz, S., P. Krishnani, J. Freeman, R. Flottemesch, E. Riley, T. Dierauf, J. Newmiller, L. Ngan, D. Jordan, and A. Kimber. 2014. "PV System Energy Test." *Proceedings of the 2014 IEEE 40th Photovoltaic Specialist Conference (PVSC)*, 0879–84. https://doi.org/10.1109/PVSC.2014.6925055.

Lara-Fanego, V., J. Pulgar, C. M. Fernández-Peruchena, M. Gastón, S. Moreno, L. Ramírez, R. X. Valenzuela, D. Bermejo, M. Silva, M. Pavón, A. Bernardos, L. F. Zarzalejo, and S. Macías. 2016. "A Novel Procedure for Generating Solar Irradiance TSYs." *Proceedings of the SolarPACES Conference*, Abu Dhabi, UAE.

Larrañeta, M., C. Fernandez-Peruchena, M. A. Silva-Pérez, I. Lillo-bravo, A. Grantham, and J. Boland. 2019. "Generation of Synthetic Solar Datasets for Risk Analysis." *Solar Energy* 187: 212–25.

Le, T., D. Kholdi, H. Xie, B. Dong, and R. Vega. 2016. « LiDAR-Based Solar Mapping for Distributed Solar Plant Design and Grid Integration in San Antonio, Texas." *Remote Sensing* 8: 247. https://doi.org/10.3390/rs8030247.

Leary, P. L., and J. D. Hankins. 1979. *User's Guide for MIRVAL: A Computer Code for Comparing Designs of Heliostat-Receiver Optics for Central Receiver Solar Power Plants* (SAND-77-8280). Livermore, CA: Sandia National Laboratories.

Lohmann, S., C. Schillings, B. Mayer, and R. Meyer. 2006. "Long-term variability of solar direct and global radiation derived from ISCCP data and comparison with reanalysis data." *Solar Energy* 80 (11): 1390–1401.

Lund, H. 1974. "The 'Reference Year', a Set of Climatic Data for Environmental Engineering." Also published as "Report no. 32, Thermal Insulation Laboratory, Technical University of Denmark." *Proceedings of the Second Symposium on the Use of Computers for Environmental Engineering Related to Building*, Paris, France.

Malato, S. 2004. "Photocatalitic Reactors for the Treatment of Liquid Wastewater in the Presence of Solar Radiation." *Proceedings of the 1st Seminar of Advanced Oxidation Methods of the Treatment of Liquid and Air Waste*, Thessaloniki , Greece.

Marcos, J., L. Morroyo, E. Lorenzo, and M. Garcia. 2012. "Smoothing of PV Power Fluctuations by Geographical Dispersion." *Progress in Photovoltaic: Research and Applications* 20: 226–37.

Martínez-Rubio, A., F. Sanz-Adan, J. Santamaría-Peña, and A. Martínez. 2016. "Evaluating Solar Irradiance Over Facades in High Building Cities, Based on LiDAR Technology." *Applied Energy* 183: 133–47. https://doi.org/10.1016/j.apenergy.2016.08.163.

Mehos, M., and R. Perez. 2005. "Mining for Solar Resources: U.S. Southwest Provides Vast Potential." (NREL/JA-550-37799) *Imaging Notes* 20 (2): 12–15.

Meybodi, M. A., L. Ramírez-Santigosa, and A. C. Beath. 2017. "A Study on the Impact of Time Resolution in Solar Data on the Performance CSP Plants." *Renewable Energy*. https://doi.org/10.1016/j.renene.2017.03.024.

Meyer, R., J. Torres Butron, G. Marquard, M. Schwandt, N. Geuder, C. Hoyer-Klick, E. Lorenz, A. Hammer, and H. G. Beyer. 2008. "Combining Solar Irradiance Measurements and Various Satellite-Derived Products to a Site-Specific Best Estimate." *Proceedings of the SolarPACES Conference*.

Michalsky, J.J., R. Perez, R. Seals, P. Ineichen. 1994. "Degradation of solar concentrator performance in the aftermath of Mount Pinatubo." *Solar Energy* 52 (2): 205–13. https://doi.org/10.1016/0038-092X(94)90070-1.

Mohajeri, N., G. Upadhyay, A. Gudmundsson, D. Assouline, J. Kämpf, and J. L. Scartezzini. 2016. "Effects of Urban Compactness on Solar Energy Potential." *Renewable Energy* 93: 469–82. https://doi.org/10.1016/j.renene.2016.02.053.

Moody's Investors Services. 2010. "PV Solar Power Generation Projects. Special Comment." July 28, 2010.

Müller, B., L. Hardt, A., Armbruster, K., Kiefer, and C. Reise, C. 2015. "Yield Predictions for Photovoltaic Power Plants: Empirical Validation, Recent Advances and Remaining Uncertainties." *Progress in Photovoltaics: Research and Applications* 24 (4): 570–83. https://doi.org/10.1002/pip.2616.

Müller, B., M. Wild, A. Driesse, and K. Behrens. 2014. "Rethinking Solar Resource Assessments in the Context of Global Dimming and Brightening." *Solar Energy* 99: 272–82. DOI: 10.1016/j.solener.2013.11.013.

Murata, A., H. Yamaguchi, and K. Otani. 2009. "A Method of Estimating the Output Fluctuation of Many Photovoltaic Power Generation Systems Dispersed in a Wide Area." *Electrical Engineering in Japan* 166 (4): 9–19.

Navarro, A. A., L. Ramírez, P. Domínguez, M. Blanco, J. Polo, and E. Zarza. 2016. "Review and Validation of Solar Thermal Electricity potential methodologies." *Energy Conversion Management* 126: 42–50. https://doi.org/10.1016/j.enconman.2016.07.070.

Nielsen, K. P., P. Blanc, F. Vignola, L. Ramírez, M. Blanco, and R. Meyer. 2017. "Discussion of currently used practices for: 'Creation of Meteorological Data Sets for CSP/STE Performance Simulations.'" *Proceedings of the SolarPACES Conference*. http://www.solarpaces.org/images/BeyondTMY_Discussion_of_current_methods_v3_0.pdf.

Pavón, M., C. M. Fernández, M. Silva, S. Moreno, M. V. Guisado, and A. Bernardos. 2016. "Statistical Analysis of CSP Plants by Simulating Extensive Meteorological Series." *Proceedings of the SolarPACES Conference*, Abu Dhabi, UAE.

Perez R., M. Perez, M. Pierro, J. Schlemmer, S. Kivalov, J. Dise, P. Keelin, M. Grammatico, A. Swierc, J. Ferreira, A. Foster, M. Putnam, and T. Hoff. 2019a. "Operationally Perfect Solar Power Forecasts: A Scalable Strategy to Lowest-Cost Firm Solar Power Generation." *Proceedings of the 46th IEEE PV Specialists Conference* (oral), Chicago, Illinois.

Perez, M., R. Perez, K. Rabago, and M. Putnam. 2019c. "Overbuilding and Curtailment: The Cost-Effective Enablers of Firm PV Generation." *Solar Energy* 180: 412–22.

Perez, M., R. Perez, K. Rabago, and M. Putnam. 2019d. "Achieving 100% Renewables: Supply-Shaping Through Curtailment." *PVTECH Power* 19 (May). www.pv-tech.org.

Perez, R., M. David, T. Hoff, S. Kivalov, J. Kleissl, M. Jamaly, P. Lauret, and M. Perez. 2016. "Spatial and Temporal Variability of Solar Energy." *Foundations and Trends in Renewable Energy* 1 (1): 1–44.

Perez, R., M. Perez, M. Pierro, J. Schlemmer, S. Kivalov, J. Dise, P. Keelin, M. Grammatico, A. Swierc, J. Ferreira, A. Foster, M. Putnam, and T. Hoff. 2019b. "Perfect Operational Solar Forecasts – A Scalable Strategy Toward Firm Power Generation." *Proceedings of the International Energy Agency Solar World Congress*, Santiago, Chile.

Perez, R., P. Ineichen, R. Seals, and A. Zelenka. 1990. "Making Full Use of the Clearness Index for Parameterizing Hourly Insolation Conditions." *Solar Energy* 45: 111–14.

Perez, R., T. Hoff, and S. Kivalov. 2011. "Spatial & Temporal Characteristics of Solar Radiation Variability." *Proceedings of the International Solar Energy (ISES) World Congress*, Kassel, Germany.

Perez-Astudillo, D. and Bachour, D. 2015. "Variability of Measured global horizontal irradiation throughout Qatar. *Solar Energy* 119: 169–78.

Peruchena, C. M. F., L. Ramírez, M. Silva, V. Lara, D. Bermejo, M. Gastón, S. Moreno, J. Pulgar, J. Liria, S. Macías, R. Gonzalez, A. Bernardos, N. Castillo, B. Bolinaga, R. X. Valenzuela, and L. Zarzalejo. 2016. "A Methodology for Calculating Percentile Values of Annual Direct Normal Solar Irradiation Series." *Proeedings of the SolarPACES Conference*. https://doi.org/10.1063/1.4949237.

Petrenko, M., and C. Ichoku. 2013. "Coherent Uncertainty Analysis of Aerosol Measurements from Multiple Satellite Sensors." *Atmospheric Chemistry and Physics* 13: 6777–805. https://doi.org/10.5194/acp-13-6777-2013.

Pfeifroth, U., A. Sanchez-Lorenzo, V., Manara, J. Trentmann, and R. Hollmann. 2018. "Trends and Variability of Surface Solar Radiation in Europe Based on Surface- and Satellite-Based Data Records." *Journal of Geophysical Research: Atmospheres* 123 (3): 1735–54.

Pierro M., R. Perez, M. Perez, D. Moser, M. Giacomo, and C. Cornaro. 2020. "Italian Protocol for Massive Solar Integration: Imbalance Mitigation Strategies." *Renewable Energy* 153: 725–39.

Pierro, M., R. Perez, M. Perez, D. Moser, M. Giacomo, and C. Cornaro. 2021. "Italian Protocol for Massive Solar Integration: from Solar Imbalance Regulation to Firm 24/365 Solar Generation." *Renewable Energy* 69 (May): 425–36. https://doi.org/10.1016/j.renene.2021.01.023.

Polo, J., S. Wilbert, J. A. Ruiz-Arias, R. Meyer, C. Gueymard, M. Súri, L. Martín, T. Mieslinger, P. Blanc, I. Grant, J. Boland, P. Ineichen, J. Remund, R. Escobar, A. Troccoli, M. Sengupta, K. P. Nielsen, D. Renne, N. Geuder, and T. Cebecauer. 2016. "Preliminary Survey on Site-Adaptation Techniques for Satellite-Derived and Reanalysis Solar Radiation Datasets." *Solar Energy* 132: 25–37. https://doi.org/10.1016/j.solener.2016.03.001.

Potter, D., J.-S. Kim, A. Khassapov, R. Pascual, L. Hetherton, and Z. Zhang. 2018. "Heliosim: An Integrated Model for the Optimisation and Simulation of Central Receiver CSP Facilities." *AIP Conference Proceedings* 2033: 210011.

Quaschning, V., W. Ortmanns, R. Kistner, and M. Geyer. 2001. "Greenius: A New Simulation Environment for Technical and Economical Analysis of Renewable Independent Power Projects." *Solar Forum*: 413–18.

Ramírez, L., B. Barnechea, A. Bernardos, B. Bolinaga, M. Cony, S. Moreno, R. Orive, J. Polo, C. Redondo, I. B. Salbidegoitia, L. Serrano, J. Tovar, and L. F. Zarzalejo. 2012. "Towards the Standardization of Procedures for Solar Radiation Data Series Generation." *Proceedings of the SolarPACES Conference*.

Ramírez, L., K. Pagh, F. Vignola, M. Blanco, P. Blanc, R. Meyer, and S. Wilbert. 2017. "Road Map for Creation of Advanced Meteorological Data Sets for CSP Performance Simulations." *Proceedings of the SolarPACES Conference*. http://www.solarpaces.org/images/SolarPACES-T5_BeyondTMY_Road_Map.pdf .

Ramírez, L., Vindel, J.M., 2017. "Forecasting and Nowcasting of DNI for Concentrating Solar Thermal Systems." In *Advances in Concentrating Solar Thermal Research and Technology*, edited by M. Blanco and L. Ramirez Santigosa, 293–310. Elsevier. DOI: 10.1016/B978-0-08-100516-3.00013-7

Remund, J., C. Calhau, L. Perret, and D. Marcel. 2015. *Characterization of the Spatio-Temporal Variations and Ramp Rates of Solar Radiation PV* (IEA PVPS Task 14 Report: T14-05:2015, ISBN: 978-3-906042-35-0). https://iea-pvps.org/key-topics/characterization-of-the-spatio-temporal-variations-and-ramp-rates-of-solar-radiation-and-pv-2015/.

Renné, D. S. 2016. "Resource Assessment and Site Selection for Solar Heating and Cooling Systems." In *Advances in Solar Heating and Cooling*, edited by R. Wang and T. Ge. Elsevier, 13–41. https://doi.org/10.1016/B978-0-08-100301-5.00002-3.

Renné, D. S. 2017. "Effective Solar Resource Methodologies for Sustainable PV Applications." In *Photovoltaics for Sustainable Electricity and Buildings*, edited by A. Sayigh. Springer International Publishing, 25–53. https://doi.org/10.1007/978-3-319-39280-6_3.

Robock, A. 2000. "Volcanic Eruptions and Climate." *Review in Geophysics* 38: 191–219. https://doi.org/10.1029/1998RG000054.

Ruiz-Arias, J. A., C. A. Gueymard, S. Quesada-Ruiz, F. J. Santos-Alamillos, and D. Pozo-Vázquez. 2016. "Bias Induced by the AOD Representation Time Scale in Long-Term Solar Radiation Calculations. Part 1: Sensitivity of the AOD Distribution to the Representation Time Scale." *Solar Energy* 137: 608–20. https://doi.org/doi:10.1016/j.solener.2016.06.026.

Ruiz-Arias, J. A., S. Quesada-Ruiz, E. F. Fernández, and C. A. Gueymard. 2015. "Optimal Combination of Gridded and Ground-Observed Solar Radiation Data for Regional Solar Resource Assessment." *Solar Energy* 112: 411–24. https://doi.org/10.1016/j.solener.2014.12.011.

Ruiz-Arias, J.A., C. A. Gueymard, and T. Cebecauer. 2019. "Direct Normal Irradiance Modeling: Evaluating the Impact on Accuracy of Worldwide Gridded Aerosol Databases." *AIP Conference Proceedings* 2126 (1): 190013. https://doi.org/10.1063/1.5117710.

Santos, T., N. Gomes, S. Freire, M. C. Brito, L. Santos, and J. A. Tenedório. 2014. "Applications of Solar Mapping in the Urban Environment." *Applied Geography* 51: 48–57. https://doi.org/10.1016/j.apgeog.2014.03.008.

Schwarzbözl, P., R. Pitz-Paal, and M. Schmitz. 2009. "Visual HFLCAL - A Software Tool for Layout and Optimisation of Heliostat Fields." *Proceedings of the SolarPACES Conference*, Berlin, Germany.

SDHtake-off Project. 2012. *Solar District Heating Guidelines: Collection of Fact sheets WP3 – D3.1 and D3.2*. Europe: Intelligent Energy.

Sun, X., J. M. Bright, C. A. Gueymard, X. Bai, B. Acord, P. Wang. 2021. "Worldwide Performance Assessment of 95 Direct and Diffuse Clear-Sky Irradiance Models Using Principal Component Analysis." *Renewable and Sustainable Energy Reviews* 135: 110087. https://doi.org/10.1016/j.rser.2020.110087.

Tomson, T., V. Russak, and A. Kallis. 2008. "Dynamic Behavior of Solar Radiation." In *Modeling Solar Radiation at the Earth's Surface*, edited by V. Badescu. Berlin, Heidelberg: Springer Berlin, 257–81. https://doi.org/10.1007/978-3-540-77455-6_10.

Tooke, T. R., N. C. Coops, A. Christen, O. Gurtuna, and A. Prévot. 2012. "Integrated Irradiance Modelling in the Urban Environment Based on Remotely Sensed Data." *Solar Energy* 86: 2923–34. https://doi.org/10.1016/j.solener.2012.06.026.

van Sark, W., N. H. Reich, B. Müller, and A. Armbruster. 2012. "Review of PV Performance Ratio Development." *Proceedings of the World Renewable Energy Congress*, Denver, Colorado. https://doi.org/10.13140/2.1.2138.7204.

Vignola, F. E., A. C. McMahan, and C. N. Grover. 2013. "Bankable Solar-Radiation Datasets." In *Solar Energy Forecasting and Resource Assessment*, 97–131. Elsevier. https://doi.org/10.1016/B978-0-12-397177-7.00005-X.

Vignola, F., C. Grover, N. Lemon, and A. McMahan. 2012. "Building a Bankable Solar Radiation Dataset." *Solar Energy* 86: 2218–29. https://doi.org/10.1016/j.solener.2012.05.013.

Vittitoe, C. N., and F. Biggs. 1981. *User's Guide to HELIOS: A Computer Program for Modeling the Optical Behavior of Reflecting Solar Concentrators. Part 1: Introduction and Code Input* (NASA STI/Recon Technical Report N). NASA Astrophysics Data System.

Wagner, M. J., and T. Wendelin. 2018. "SolarPILOT: A Power Tower Solar Field Layout and Characterization Tool." *Solar Energy* 171: 185–96.

Wendelin, T. 2003. "SolTRACE: A New Optical Modeling Tool for Concentrating Solar Optics." *Solar Energy*: 253–60. https://doi.org/10.1115/ISEC2003-44090.

Wiemken, E., H. G. Beyer, W. Heydenreich, and K. Kiefer. 2001. "Power Characteristics of PV Ensembles: Experience from the Combined Power Productivity of 100 Grid-Connected Systems Distributed Over Germany." *Solar Energy* 70: 513–19.

Wilcox, S. 2007. *National Solar Radiation Database 1991-2005 Update: User's Manual* (NREL/TP-581-41364). Golden, CO: National Renewable Energy Laboratory. https://doi.org/10.2172/901864.

Wilcox, S., and W. Marion. 2008. *Users Manual for TMY3 Data Sets* (NREL/TP-581-43156). Golden, CO: National Renewable Energy Laboratory.

Wild, M. 2016. "Decadal Changes in Radiative Fluxes at Land and Ocean Surfaces and Their Relevance for Global Warming." *WIREs Climate Change* 7: 91–107.

Wild, M., A. Ohmura, C. Schär, G. Müller, D. Folini, D., Schwarz, D., Zyta Hakuba, M., and A. Sanchez-Lorenzo. 2017. "The Global Energy Balance Archive (GEBA) Version 2017: A Database for Worldwide Measured Surface Energy Fluxes." *Earth System Science Data* 9: 601–613. https://doi.org/10.5194/essd-9-601-2017.

Wild, M., D. Folini, F. Henschel, N. Fischer, and B. Müller. 2015. "Projections of Long-Term Changes in Solar Radiation Based on CMIP5 Climate Models and Their Influence on Energy Yields of Photovoltaic Systems." *Solar Energy* 11: 12–24. DOI: 10.1016/j.solener.2015.03.039.

Woyte, A., R. Belmans, and J. Nijs. 2007. "Fluctuations in Instantaneous Clearness Index: Analysis and Statistics." *Solar Energy* 81 (2): 195–206.

10 FUTURE WORK

Jan Remund,[1] Carlos Fernandez Peruchena,[2] Jan Kleissl,[3] and Stefan Wilbert[4]
[1] *Meteotest AG*
[2] *National Renewable Energy Centre of Spain (CENER)*
[3] *University of California, San Diego*
[4] *German Aerospace Center (DLR)*

10.1 Introduction

Advancing renewable energy technologies will require improvements in our understanding of solar radiation resources. This chapter briefly describes areas of research and development identified as emerging technology needs. The International Energy Agency (IEA) Photovoltaic Power System (PVPS) Task 16 work plan for the second phase (2020–2023) on "solar resource for high penetration and large-scale applications" seeks to address significant parts of the research-and-development needs presented in this chapter.

10.2 Application, Evaluation, and Standardization of Solar Resource Data

With the increasing diversity and complexity of solar resource data, it is necessary to invest significant effort in the application, evaluation, and standardization of these data. Users need to know which data sets are most suitable for their applications, and this requires readily available evaluations of existing products. As examples, such evaluations are planned within the IEA PVPS Task 16 related to satellite and numerical weather prediction-based (NWP-based) radiation data as well as ASI-based radiation nowcasts.

To create an efficient market, best practices and standards for the creation, documentation, and application of the resource data are needed. Task 16 contributes to relevant work in international standardization bodies, such as the International Organization for Standardization, International Electrotechnical Commission, and ASTM International. The standardization activities are related to solar spectra, radiation measurements, calibration and test methods, radiation forecasts, data formats, meteorological measurements for power plant performance measurement, and even to fundamental issues such as vocabulary. Some resource products are currently not used to their full extent. The potential benefits of their full applications might be understood by most stakeholders, but methods to use the data are yet to be developed or implemented. Examples of such resource products include meteorological parameters, such as time series of soiling rates; spectral mismatch factors; or circumsolar radiation data that are often included only as an approximation in power plant models. Other examples are probabilistic forecasts or ASI-based highly resolved spatial forecasts. Users and data providers must collaborate closely to create the best data sets and to fully exploit the potential of such resource data.

10.2.1 Improvement in Irradiance Quality Control Procedures

PVPS Task 16 is actively engaged in developing better and more stringent methods of evaluating the quality of irradiance measurements based on time series of experimental data. The primary objective is to produce a high-quality irradiance database for the validation of satellite-derived irradiance data sets at hundreds of sites worldwide. The new developments consist of improving and augmenting the few existing quality-control

algorithms in the literature, such as those discussed in Section 7.7, which follow Long and Shi (2008) and Maxwell, Wilcox, and Rymes (1993).

The improved methodology includes the implementation of new tests to check many difficult-to-detect and small perturbations, such as time stamp errors, mistracking, morning/afternoon asymmetry, soiling, shading, or calibration drift. The quality-control algorithm will allow for an easy visualization of the results for further inspection by trained observers. The overall applicability and repeatability of the process are being evaluated by having a group of experts separately quality-control several common data sets and comparing their results in a kind of round-robin experiment.

It is expected that a user-friendly and public-domain fully functional code will be released at the conclusion of this effort. Its wide adoption should eventually reduce the uncertainty in measured data sets, simplify the practice of solar resource assessments, and ultimately benefit the whole solar industry.

10.2.2 Evaluation of Solar Cadasters

As noted by the International Renewable Energy Agency (IRENA 2019), to face the challenges of supplying renewable energy in steadily growing cities, there will be a new focus on photovoltaics (PV) at the urban scale. The PV potential of rooftops—as well as parking shades, roads, etc.—can be modeled with high-spatial-resolution solar mapping techniques in the form of *solar cadasters*. Today, such cadasters are emerging as products for many urban areas, notably in North America and Europe.[82] Some solar cadasters even cover a whole country.[83]

Nevertheless, the methodology and the quality of such products are generally not well known. For example, Walch et al. (2020) compared several solar cadasters existing over the same regions and reported large discrepancies. These discrepancies and quality shortcomings could be caused by methodology differences in various aspects, such as (1) the nature (vector, raster) and the spatial resolution of the digital surface model used for the 3D modeling; (2) the source (satellite, network of radiation sensors, NWP, etc.), the model (all-sky, clear-sky, etc.), and the interpolation method used for the solar radiation data; or (3) the simplifications/approximations in the physical layout or in the PV yield simulations (tilted or horizontal planes, partial shadowing of PV modules, etc.). Task 16 of the IEA PVPS will assess some of these models and provide advice for best practices when using solar cadasters.

Additionally, the use of solar cadaster methodologies based on high-resolution solar modeling in urban-scale cadasters will be assessed for extended purposes, such as modeling and forecasting solar energy in cities, grid planning, or congestion management.

10.3 Forecasting Solar Radiation and Solar Power

Solar power forecasting will be an essential component of the future energy supply system, which will use large amounts of variable solar power. Solar power forecasting systems already contribute to the successful integration of considerable amounts of solar power to the electric grid, and solar power forecasting is receiving unprecedented attention from various scientific communities because the solar resource variability must be managed to

[82] See Google Project Sunroof (https://www.google.com/get/sunroof) or In Sun We Trust (http://www.insunwetrust.solar/).
[83] See Switzerland (http://www.sonnendach.ch).

maintain the stability of the grid and to enable optimal unit commitment and economic dispatch. Consequently, new techniques and approaches are being proposed to improve the accuracy of the models to provide solar radiation and power forecasts.

The earlier chapters of this handbook covered the different approaches being used in current research on irradiance forecasting and solar power forecasting; for convenience, these two tightly related topics are referred to collectively as "solar forecasting" (Yang et al. 2018). Improvements in NWP-based irradiance forecasting could emerge from improvements in resolution, data assimilation, and parameterizations of clouds and radiation. Specific forecasting products would need to be developed for areas where dust storms or smoke episodes can result in adverse situations and to prepare an optimal schedule for post-episode cleaning operations, especially where water is scarce. Moreover, to overcome NWP limitations, which lead to unavoidable errors in the estimation of the possible future atmospheric states (and are amplified at both higher forecast horizons and spatiotemporal resolutions), probabilistic forecast approaches are being proposed. In addition, the development and application of rapid-update-cycle models[84] has high potential to improve intraday forecasting. Such models need to be properly initialized; hence, satellite detection of cloud height and cloud optical depth as well as other atmospheric states remain research priorities. A further opportunity emerges from the expansion of large-eddy simulation approaches to increasingly larger domain sizes that could soon bring operational mesoscale forecasting within reach (Schalkwijk et al. 2015). Large-eddy simulation will reduce the need for cloud parameterization approaches that are challenged by the disparity between grid resolution and cloud turbulence scales in standard NWP methods, and it is expected to bring a new level of accuracy to NWP.

Forecasting techniques based on cloud motion will benefit from enhancements in cloud-detection approaches for both satellite-based and ASI-based methods. Improved update cycles of satellite imagery (e.g., 5-minute updates in the United States through the Geostationary Operational Environmental Satellite - R Series) will provide information that could so far be derived only from sky imagers for very short-term forecasting. It has become increasingly clear that accurate physics-based forecasting with sky imagers requires 3D reconstruction of the cloud field (Kurtz, Mejia, and Kleissl, 2017), and further research in this area is required.

With respect to statistical methods, apart from model development, the availability of high-quality, current measurement data of solar irradiance and solar power will be of critical importance. Increasingly, powerful artificial intelligence techniques are being developed that should lead to substantial progress. Finally, an optimized combination (or hybridization) of different physical and statistical models will be an advantage for any solar power prediction system (Guermoui et al. 2020; Marquez, Pedro, and Coimbra 2013).

10.3.1 Probabilistic Solar Forecasting

The specification of the expected uncertainty of solar irradiance or power predictions for different weather situations provide valuable additional information to forecast users and serve as a decision aid; therefore, users are increasingly demanding that probabilistic forecasts replace traditional deterministic ones.

Probabilistic forecasting—through the quantification of probabilities of future outcomes and information about uncertainty in addition to the commonly provided single-valued (best-estimate) prediction—has gained interest as an approach to providing a more

[84] See https://ruc.noaa.gov/.

comprehensive view than the traditional deterministic paradigm. This can be done for a specific site, or it could be extended over a geographic region from gridded deterministic NWP forecasts (Davò et al. 2016). Nevertheless, despite these advantages, a relevant way of quantifying the benefits of probabilistic forecasting is to assess its potential economic value.

Probabilistic forecasting could be based on the use of NWP ensemble prediction systems as well as on the statistical analysis of the distributions (or quantiles of distributions) of historic predictions and measurements. In this regard, several post-processing techniques have been explored to generate probabilistic forecasts (Antonanzas et al. 2016; Van der Meer, Widén, and Munkhammar 2018), and more effort can be devoted to evaluate multiple methods on the same data set to compare their performance. In addition to pursuing these promising strategies, new frameworks could be explored for generating probabilistic forecasts. As an example, the generation of multiple plausible weather scenarios along with current weather prediction and real-time data from ground measurements and satellite images can be used together to estimate the probability of occurrence of different atmospheric states and the associated solar resource.

In addition to exploring probabilistic generation schemes, key areas of investigation that can produce rich dividends are post-processing methods to improve forecasts by removing systematic biases and providing spatial and temporal downscaling. New techniques and the analysis of a variety of potential target variables (such as the ensemble mean or variance of forecasts) can be investigated (Gastón et al. 2018).

The following upcoming challenges have been identified for ongoing research on probabilistic solar forecasting.

10.3.1.1 Standardized Framework for the Evaluation of Solar Probabilistic Forecasts

Although it is less mature than wind probabilistic forecasting, in recent years the topic of solar probabilistic forecasting has seen a surge in landmark publications (Bakker et al. 2019; Doubleday, Hernandez, and Hodge 2020; Li and Zhang 2020; Van der Meer, Widén, and Munkhammar 2018; von Loeper et al. 2020; Yagli, Yang, and Srinivasan 2020; Yang 2019). Unfortunately, Lauret, David, and Pinson (2019) noted that the solar forecasting community uses diverse verification tools and sometimes even improper scoring rules for evaluating the quality of the forecasts. This fact does not facilitate forecast analysis and performance comparisons of the different probabilistic forecasting techniques and therefore hampers the dissemination of probabilistic forecasts among forecast users and developers. The challenge is to provide the forecasting solar community with a comprehensive, standardized, rigorous, and well-accepted verification framework. This should comprise a set of diagnostic tools, proper scoring rules, and skill scores mostly originating from the weather forecast verification community. Further, specific scoring rules (e.g., energy score or Variogram score) should be used to assess the quality of the multivariate forecasts (see Chapter 8, Section 8.6). The objective will be also to clearly define the different reference/benchmark models used to gauge the performance of any newly proposed methods. In addition, the verification framework should benefit from standardized publicly available data sets.

10.3.1.2 Generate Multivariate Probabilistic Forecasts

Until now, most work related to solar probabilistic forecasts has been restricted to the univariate context. This corresponds to probabilistic forecasts that do not consider spatiotemporal dependencies. Because of complex mechanisms such as cloud passage, however, solar power generation behaves as a random variable distributed in space and time (Golestaneh, Gooi, and Pinson 2016). The next challenge will be to design multivariate probabilistic models that can capture the spatiotemporal correlations present in solar

forecasts. The scenarios or the space-time trajectories generated by this type of model will provide better inputs than univariate forecasts in grid power optimization problems, such as unit commitment or optimal power flow.

10.3.1.3 Establish a Link Between Quality and Value of Probabilistic Forecasts[85]

In solar forecasting, most studies concentrate on the evaluation of the quality of the probabilistic forecasts. In contrast, very few publications are devoted to the assessment of their value. Recall that *quality* refers to the correspondence between forecasts and the observations, whereas *value* is linked to the benefit (economic or otherwise) gained from the use of these probabilistic forecasts in an operational context. As noted by Pinson (2013) for wind probabilistic forecasts, however, it is not clear how improving the quality of these forecasts—in terms of improved skill scores or increased probabilistic reliability—could lead to added value for decision makers. Hence, in the context of decision making, more work is needed to link the probabilistic metrics used by the forecasters and the utility functions defined by the decision makers.

10.3.2 Solar Forecast Based on All-Sky Imagers

ASI-based solar forecasting is a recent forecasting method, and many options to improve these forecasts can still be explored. The selection of the most promising development directions will be enabled by comparisons of different ASI forecasts, such as the one organized within the IEA PVPS Task 16. Future research on both the hardware and software sides can be expected. The first results of a common benchmark of different ASI systems will also be published.

Related to the hardware, the investigation of different camera types (infrared/visible, high dynamic range) is ongoing. Also, the combination of a few cameras or networks of cameras will continue. Networks of ASIs covering several hundred square kilometers are an option to create highly resolved nowcasts for whole regions. The combination of many cameras also allows for an increase in the forecast horizon and accuracy. In addition, downward-looking shadow cameras on mountains, buildings, or other elevated positions to derive irradiance forecasts is a promising topic of research (Kuhn et al. 2017, Kuhn et al., 2019, Wilbert et al. 2020).

Current evaluation software is often simplistic, and many approximations are applied. ASI images contain a large amount of information that is currently not fully used to avoid these approximations. Related to software developments, the application of artificial intelligence will certainly increase for ASI forecasts.

10.3.3 Artificial Intelligence for Solar Forecast

The predictive capabilities of artificial intelligence hold a lot of promise for solar forecasting, and for that reason efforts are increasing to identify their applications to improve NWP models. Among those models, it is important to highlight machine learning and, specifically, deep learning. The term *machine learning* encompasses all artificial intelligence techniques that give computers the ability to learn without being explicitly programmed to do so. Although machine learning was first used in the late 1950s, the current form of machine learning is commonly assumed to have started in the 1980s because of the increased amount of available data and novel approaches to treat them. *Deep learning* is a recent (circa 2010) subset of machine learning that makes the computation of multilayer neural

[85] This point should also be extended to deterministic solar forecasts.

networks feasible and enhances the capability to find patterns in unstructured or unlabeled data.

A promising application of deep learning neural networks is to replace computationally expensive parameterizations of certain physical schemes in NWP models because they involve modeling at scales much greater than the actual phenomena. The search for less expensive models favors higher resolution simulations for generating short-term forecasts at the local scale that need to be computed within short periods of time. Deep learning has also gained interest in satellite meteorology because it can provide rapid answers from models trained with tens of thousands of images, and its applications to solar forecasts could be explored for resolving weather patterns (in urban areas or large solar power plants) that are not achievable by traditional NWP models. In particular, *convolutional neural networks* (a class of deep neural networks) can be explored to provide forecasts as an image-to-image translation problem based on a filtering process that can be used to detect meaningful patterns. Within this data-driven (or "physics-free") approach, the atmospheric physical processes are emulated from the training examples alone—not by incorporating a priori knowledge of how the atmosphere actually works—which can generate nearly instantaneous forecasts. The accuracy and the temporal and spatial resolutions of this approach are yet to be explored.

Finally, to exploit the capabilities that artificial intelligence can bring to solar forecasting, models should be trained by vast amounts of granular data captured with a network of measuring instruments. This could comprise low-cost, good-performance radiometers measuring solar radiation, sky cameras providing cloud screening, and spaceborne instruments dedicated to the observation of clouds, aerosols, and climate change indicators (Gueymard 2017). In addition, especially in urban environments, Internet of Things sensors (such as street cameras, connected cars, drones, or cell towers) can be useful for this purpose, where high spatial resolution could probably be achieved. In the same vein, smart sensors might be useful for monitoring accurate demand forecasting together with renewable generation forecasting in the search for the optimization of economic load dispatch and to improve demand-side management and efficiency.

Yet the lack of transparency that usually accompanies artificial intelligence models (i.e., retracing the path that the model took to reach its conclusion) has drawbacks: the difficulty of translating the information generated into basic principles (or physics) and interpreting the information to determine what is happening in the natural world and apply the knowledge gained at a particular project site to other regions. Consequently, an appropriate strategy could benefit from the optimized combination of both physical and artificial intelligence-based models.

10.3.4 Firm Photovoltaic Power

Grid-connected solar power generation, either dispersed or centralized, has developed and grown at the margin of a core of dispatchable and baseload conventional generation. Its economics and management have required increasingly versatile and precise historical and operational solar resource information with increasing penetration levels. Operational solar forecasts have become central to transmission system operation in regions with significant solar penetration levels—for example, energy markets and load ramp management.

The challenge ahead for grid-connected solar is to go beyond the margin and the context of underlying conventional generation management. For wind, the transformation of intermittent variable solar power generation into firm, effectively dispatchable power generation is a prerequisite to the gradual displacement of the underlying conventional generation core. The IEA PVPS Task 16 will focus on this variable-to-firm generation transformation by developing

and analyzing the data, methodologies, and models that will cost-optimally enable this transformation in pertinent grid-connected contexts defined by:

- Their geographic extent (from single plants to balancing area fleets)
- Their level of penetration, from current to ultrahigh levels
- The considered solar technologies: PV and/or CST
- The economics of firm power generation enablers, in particular storage technologies, including conventional electrochemical batteries, thermal storage, and pumped hydropower
- The economics of nontraditional firm power generation enablers, such as operational curtailment; whereas some years ago output curtailment of expensive PV (e.g., via peak output inverter limitation) was not economically sensible, it will likely become standard practice in future systems.

A logical initial step in the direction of firm solar power generation is *firm solar power forecasting*, where forecast errors are operationally balanced by these enablers. The end-game objective is the delivery of 24/7 energy capable of entirely displacing conventional generation.

10.4 Additional Parameters

Although direct normal irradiance, global horizontal irradiance, and global tilted irradiance are the most important meteorological input parameters for solar power plant yield, several additional parameters must be provided at high resolution for accurate yield analysis. Solar energy-specific measurands include the soiling rate of plant components, albedo, spectral mismatch factors, the sunshape/circumsolar radiation, and the extinction of radiation between the mirrors and the receiver of tower power plants. Often, no site-specific information on these properties is available, which results in remarkable impacts on the accuracy of the yield prediction; hence, these parameters must be studied in more detail in the future. This topic will continue to be investigated under Subtask 1 of the IEA PVPS Task 16. Similar to the increasing interest in albedo data for bifacial PV modules, other technological developments might also trigger research on further additional parameters.

10.5 Effects of Climate Change on Solar Resource Assessments

Changes in atmospheric aerosol loading from natural causes or industrial pollution, changing patterns of clouds, relative humidity, precipitation, and other climatic variables might have recently affected solar resource availability and could affect it further in the future (Huber et al. 2016).

This could be important when estimating the performance of a solar power plant throughout the system's design life (approximately 25 years). Research is needed to advance climate modeling capabilities and to merge the outputs of these models with advanced system performance models. The climate of the future can follow different scenarios, and aerosol scenarios are expected to matter most with respect to the solar resource. In contemporary climate modeling, aerosol pollution scenarios are considered independent from greenhouse gas scenarios. Rao et al. (2017) describe various aerosol scenarios in terms of "shared socioeconomic pathways" that depend on assumed "strong," "medium," and "weak" policies against aerosol pollution. These scenarios are included in the current generation of climate model runs (Collins et al. 2017). In parallel, geoengineering experiments, aiming at injecting various types of reflecting particles into the stratosphere as an attempt to curb climate

change, are already starting. Such experiments, if generalized, might completely disrupt all current estimates of the future solar resource (Smith et al. 2017).

The identification and treatment of years with impacts of exceptionally strong volcanic eruptions should be standardized because they impact the probabilities of exceedance, which are a key factor in the bankability of large solar systems. Further investigation is needed, including liaising with the volcanology scientific community. The last major eruption with a global effect on aerosols happened in 1991 at Mount Pinatubo in the Philippines, before solar energy applications were widespread, so such eruptions have been forgotten by the solar energy industry. Additional focus will be put on climate change effects when conducting long-term analyses. Subtask 2 of IEA PVPS Task 16 will seed further progress in this area, e.g., to precisely assess the risk of major volcanic eruptions.

10.6 References

Antonanzas, J., N. Osorio, R. Escobar, R. Urraca, F. J. Martinez-de-Pison, and F. Antonanzas-Torres. 2016. "Review of Photovoltaic Power Forecasting." *Solar Energy* 136: 78–111. https://doi.org/10.1016/j.solener.2016.06.069.

Bakker, K., K. Whan, W. Knap, and M. Schmeits. 2019. "Comparison of statistical post-processing methods for probabilistic NWP forecasts of solar radiation." *Solar Energy* 191: 138–50. https://doi.org/10.1016/j.solener.2019.08.044.

Collins, W. J., J.-F. Lamarque, M. Schulz, O. Boucher, V. Eyring, M. I. Hegglin, A. Maycock, G. Myhre, M. Prather, D. Shindell, and S. J. Smith. 2017. "AerChemMIP: Quantifying the Effects of Chemistry and Aerosols in CMIP6." *Geoscientific Model Development* 10: 585–607.

Davò, F., S. Alessandrini, S. Sperati, L. Delle Monache, D. Airoldi, and M. T. Vespucci. 2016. "Postprocessing Techniques and Principal Component Analysis for Regional Wind Power and Solar Irradiance Forecasting." *Solar Energy* 134: 327–38. https://doi.org/10.1016/j.solener.2016.04.049.

Doubleday, K., V. V. S. Hernandez, and B.-M. Hodge. 2020. "Benchmark Probabilistic Solar Forecasts: Characteristics and Recommendations." *Solar Energy* 206: 52–67. https://doi.org/10.1016/j.solener.2020.05.051.

Gastón, M., C. F. Peruchena, A. Bernardos, and J. L. Casado. 2018. "Statcasting: A Machine Learning Based Methodology for Post-Processing Ensemble Predictions of Direct Normal Solar Irradiance." *AIP Conference Proceedings* 2033 (1): 190006. https://doi.org/10.1063/1.5067191.

Golestaneh, F., H. B. Gooi, and P. Pinson. 2016. "Generation and Evaluation of Space–Time Trajectories of Photovoltaic Power." *Applied Energy* 176: 80–91. https://doi.org/10.1016/j.apenergy.2016.05.025.

Guermoui, M., F. Melgani, K. Gairaa, and M. L. Mekhalfi. 2020. "A Comprehensive Review of Hybrid Models for Solar Radiation Forecasting." *Journal of Cleaner Production* 258: 120357.

Gueymard, C. 2017. "A Personal Vision: The Future of Solar Energy and why it Matters." *Open Access Journal of Photoenergy* 1: 2. https://doi.org/10.15406/mojsp.2017.01.00002.

Huber, I., L. Bugliaro, M. Ponater, H. Garny, C. Emde, and B. Mayer. 2016. "Do Climate Models Project Changes in Solar Resources?" Solar Energy 129: 65–84. https://doi.org/10.1016/j.solener.2015.12.016.

International Renewable Energy Agency (IRENA). 2019. Solar Simulators: Application to Developing Cities. Abu Dhabi. ISBN: 978-92-9260-099-0. https://www.irena.org/-/media/Files/IRENA/Agency/Publication/2019/Jan/IRENA_Solar_simulators_2019.PDF.

Kuhn P., S. Wilbert, C. Prahl, D. Schüler, T. Haase, T. Hirsch, M. Wittmann, L. Ramirez, L. Zarzalejo, A. Meyer, L. Vuilleumier, P. Blanc, and R. Pitz-Paal. 2017. "Shadow Camera System for the Generation of Solar Irradiance Maps." Solar Energy 157: 157–70. https://doi.org/10.1016/j.solener.2017.05.074.

Kuhn, P., D. Garsche, S. Wilbert, B. Nouri, N. Hanrieder, C. Prahl, L. Zarzarlejo, J. Fernández, A. Kazantzidis, T. Schmidt, D. Heinemann, P. Blanc, and R. Pitz-Paal. 2019. "Shadow-Camera Based Solar Nowcasting System for Shortest-Term Forecasts." Meteorologische Zeitschrift. https://doi.org/DOI 10.1127/metz/2019/0954.

Kurtz, B., F. A. Mejia, and J. Kleissl. 2017. "A Virtual Sky Imager Testbed for Solar Energy Forecasting." *Solar Energy* 158: 753–59.

Lauret, P., M. David, and P. Pinson. 2019. "Verification of Solar Irradiance Probabilistic Forecasts." *Solar Energy* 194: 254–71. https://doi.org/10.1016/j.solener.2019.10.041.

Li, B., and J. Zhang. 2020. "A Review on the Integration of Probabilistic Solar Forecasting in Power Systems." *Solar Energy* 210: 68–86.

Long, C. N., and Y. Shi. 2008. "An Automated Quality Assessment and Control Algorithm for Surface Radiation Measurements." *The Open Atmospheric Science Journal* 2: 23–37.

Marquez, R., H. T. C. Pedro, and C. F. M. Coimbra. 2013. "Hybrid Solar Forecasting Method Uses Satellite Imaging and Ground Telemetry as Inputs to ANNs." *Solar Energy* 92: 176–88.

Maxwell, E., S. Wilcox, and M. Rymes. 1993. *User's Manual for SERI QC Software—Assessing the Quality of Solar Radiation Data* (NREL/TP-463-5608). Golden, CO: National Renewable Energy Laboratory. http://www.nrel.gov/docs/legosti/old/5608.pdf.

Pinson, P. 2013. "Wind Energy: Forecasting Challenges for Its Operational Management." *Statistical Science* 28, 564–85. https://doi.org/10.1214/13-STS445.

Rao, S., et al. 2017. "Future Air Pollution in the Shared Socio-Economic Pathways." *Global Environmental Change* 42: 346–58.

Schalkwijk, J., H. J. Jonker, A. P. Siebesma, and E. Van Meijgaard. 2015. "Weather Forecasting Using GPU-Based Large-Eddy Simulations." *Bulletin of the American Meteorological Society* 96 (5): 715–23.

Smith, C. J., J. A. Crook, R. Crook, L. S. Jackson, S. M. Osprey, and P. M. Forster. 2017. "Impacts of Stratospheric Sulfate Geoengineering on Global Solar Photovoltaic and Concentrating Solar Power Resource." Journal of Applied Meteorology and Climatology 56: 1483–97. http://dx.doi.org/10.1175/ JAMC-D-16-0298.s1.

Van der Meer, D. W., J. Widén, and J. Munkhammar. 2018. "Review on Probabilistic Forecasting of Photovoltaic Power Production and Electricity Consumption." *Renewable and Sustainable Energy Reviews* 81: 1484–512.

Von Loeper, F., P. Schaumann, M. de Langlard, R. Hess, R. Bäsmann, and V. Schmidt. 2020. "Probabilistic Prediction of Solar Power Supply to Distribution Networks, Using Forecasts of Global Horizontal Irradiation." *Solar Energy* 203: 145–56. https://doi.org/10.1016/j.solener.2020.04.001.

Walch, A., R. Castello, N. Mohajeri, and J.-L. Scartezzini. 2020. "Big Data Mining for the Estimation of Hourly Rooftop Photovoltaic Potential and its Uncertainty." *Applied Energy* 262: 114404. https://doi.org/10.1016/J.APENERGY.2019.114404.

Wilbert, S., B. Nouri, N. Kötter-Orthaus, N. Hanrieder, C. Prahl, P. Kuhn, L. Zarzalejo, and R. Lázaro. 2020. “Irradiance Maps from a Shadow Camera on a Mountain Range.” *Proceedings of the SolarPACES Conference*.

Yagli, G. M., D. Yang, and D. Srinivasan. 2020. “Ensemble Solar Forecasting Using Data-Driven Models with Probabilistic Post-Processing through GAMLSS.” *Solar Energy* 208: 612–22.

Yang, D. 2019. “A Universal Benchmarking Method for Probabilistic Solar Irradiance Forecasting.” *Solar Energy* 184: 410–16.

Yang, D., J. Kleissl, C. A. Gueymard, H. T. C. Pedro, and C. F. M. Coimbra. 2018. “History and Trends in Solar Irradiance and PV Power Forecasting: A Preliminary Assessment and Review Using Text Mining.” *Solar Energy* 168: 60–101. https://doi.org/10.1016/j.solener.2017.

ISBN 978-3-907281-19-2